

# ***CARBON NANOMATERIALS***

# **Advanced Materials Series**

*Series Editor:*

**Yury Gogotsi**, *Drexel University, Philadelphia, Pennsylvania, USA*

*series includes:*

**Carbon Nanomaterials**

Yury Gogotsi

**Nanotubes and Nanofibers**

Yury Gogotsi

# ***CARBON NANOMATERIALS***

***Edited By***

***Yury Gogotsi***

*Drexel University,  
Philadelphia, Pennsylvania, USA*



**Taylor & Francis**

Taylor & Francis Group  
Boca Raton London New York

---

CRC is an imprint of the Taylor & Francis Group,  
an informa business

This material was previously published in the *Nanomaterials Handbook* © 2006 by Taylor and Francis Group, LLC.

CRC Press  
Taylor & Francis Group  
6000 Broken Sound Parkway NW, Suite 300  
Boca Raton, FL 33487-2742

© 2006 by Taylor and Francis Group, LLC  
CRC Press is an imprint of Taylor & Francis Group, an Informa business

No claim to original U.S. Government works  
Printed in the United States of America on acid-free paper  
10 9 8 7 6 5 4 3 2 1

International Standard Book Number-10: 0-8493-9386-8 (Hardcover)  
International Standard Book Number-13: 978-0-8493-9386-0 (Hardcover)  
Library of Congress Card Number 2006012298

This book contains information obtained from authentic and highly regarded sources. Reprinted material is quoted with permission, and sources are indicated. A wide variety of references are listed. Reasonable efforts have been made to publish reliable data and information, but the author and the publisher cannot assume responsibility for the validity of all materials or for the consequences of their use.

No part of this book may be reprinted, reproduced, transmitted, or utilized in any form by any electronic, mechanical, or other means, now known or hereafter invented, including photocopying, microfilming, and recording, or in any information storage or retrieval system, without written permission from the publishers.

For permission to photocopy or use material electronically from this work, please access [www.copyright.com](http://www.copyright.com) (<http://www.copyright.com/>) or contact the Copyright Clearance Center, Inc. (CCC) 222 Rosewood Drive, Danvers, MA 01923, 978-750-8400. CCC is a not-for-profit organization that provides licenses and registration for a variety of users. For organizations that have been granted a photocopy license by the CCC, a separate system of payment has been arranged.

**Trademark Notice:** Product or corporate names may be trademarks or registered trademarks, and are used only for identification and explanation without intent to infringe.

---

#### Library of Congress Cataloging-in-Publication Data

---

Carbon nanomaterials / Yury Gogotsi, editor.

p. cm.

Includes bibliographical references and index.

ISBN 0-8493-9386-8 (978-0-8493-9386-0 : alk. paper)

1. Nanostructured materials. 2. Carbon. I. Gogotsi, IU. G., 1961-

TA418.9.N35C34 2006

620!5--dc22

2006012298

---

Visit the Taylor & Francis Web site at  
<http://www.taylorandfrancis.com>

and the CRC Press Web site at  
<http://www.crcpress.com>

*This book is dedicated to my children, Pavel and Natalie,  
who have always served as a source of my inspiration.*

---

# Preface

Nanomaterials, which are materials with structural units on a nanometer scale in at least one direction, is the fastest growing area in materials science and engineering. Material properties become different on the nanoscale: for example, the theoretical strength of materials can be reached or quantum effects may appear. Carbon is as important for nanotechnology as silicon is for electronics, and certainly carbon nanomaterials deserve a separate book. I realized the need for such a book when I started to offer a graduate course on nanostructured carbon materials at Drexel University. I have taught it three times since 2002, and had to use handouts because Hugh O. Pierson's *Handbook of Carbon, Graphite, Diamond and Fullerenes* provides only a basic coverage of traditional carbon materials and its fullerene chapter is short and dated. While separate books have been written on carbon nanotubes and fullerenes, there is no single volume covering all nanostructured carbons, such as nanodiamonds, fullerenes, nanotubes, nanofibers, cones, and whiskers.

Carbon nanotubes, whiskers, and nanofibers are not only excellent tools for studying one-dimensional phenomena, but they are also among the most important and promising nanomaterials and nanostructures. The role of nanomaterials in industries is growing. Nanofibers are already used for insulation and reinforcement of composites, and many materials and structures incorporating nanotubes are under development. Extensions to conical and rod-like or wire-like structures provide the scope for new discoveries and novel applications. We may find ourselves in the carbon age within less than a decade.

This book describes a large variety of carbon nanomaterials, including fullerenes, nanotubes, whiskers, cones, and nanodiamonds. They include the hardest material known (diamond) and some of the softest (graphite and fullerene crystals). There are semiconductors, metals, and dielectrics among carbons; moreover, the band gap of semiconducting nanotubes can be tuned by changing the tube diameter. Carbons can be transparent or opaque, and their surfaces may be passive (basal planes of graphite) or chemically active (edge planes of graphite). Thus, virtually any combination of mechanical, electrical, or chemical properties can be achieved by using carbon and controlling its structure and surface chemistry. Some of the more conventional and well known carbon nanomaterials, such as soot, carbon black, or intercalated graphite, have not been included in this book. Carbon nanotubes (Chapters 2 and 3) receive special attention in this book, because they have been receiving more attention than any other nanomaterials. Sumio Iijima's discovery of carbon nanotubes in 1991 stimulated the development of the whole nanotechnology field. A dramatic progress in synthesis and purification of nanotubes has been achieved and many applications are emerging. After carbon, many other materials have been produced in the tubular shape with nanometer diameters.

Designed specifically to provide an overview of carbon nanomaterials for today's scientists, graduate students, and engineering professionals; this book will treat the subject using the terms familiar to a materials scientist or engineer. The book consists of nine chapters selected from the recently published *Nanomaterials Handbook* and written by the leading researchers in the field. Providing coverage of the latest material developments in the United States, Asia, and Europe, it describes both commercially available and emerging materials. While this book is written as a reference book for specialists working in the field, it also provides a sufficiently broad coverage of all carbon nanomaterials and can be used as a textbook for teaching a graduate course on carbon nanomaterials.

Finally, I would like to acknowledge all the people who have helped make this book possible. My family was very patient and understanding, and my students and post-docs did a great job allowing me to concentrate on the book project. My research on carbon nanomaterials was funded over the past decade by the U.S. National Science Foundation (NSF), Department of Energy (DOE), Defense Advanced Research Projects Agency (DARPA) via the Office of Naval Research (ONR), and private corporations. The staff of Taylor & Francis helped immensely in preparing this volume for publication.

Yury Gogotsi  
Philadelphia, PA

---

# Editor

**Dr. Yury Gogotsi** is professor of materials science and engineering at Drexel University in Philadelphia, Pennsylvania. He also holds appointments in the Departments of Chemistry and Mechanical Engineering at Drexel University and serves as director of the A.J. Drexel Nanotechnology Institute and associate dean of the College of Engineering. He received his M.S. (1984) and Ph.D. (1986) degrees from Kiev Polytechnic and a D.Sc. degree from the Institute of Materials Science, Ukrainian Academy of Science, in 1995. His research group works on carbon nanotubes, nanoporous carbide-derived carbons, and nanofluidics. He has also contributed to the areas of structural ceramics, corrosion of ceramic materials, and pressure-induced phase transformations, creating a new research field called high pressure surface science and engineering. He has coauthored 2 books, edited 9 books, obtained more than 20 patents, and authored about 200 journal papers and 12 book chapters. He has advised a large number of M.S., Ph.D., and post-doctoral students at Drexel University and University of Illinois at Chicago.

Gogotsi has received several awards for his research, including I.N. Frantsevich Prize from the Ukrainian Academy of Science, S. Somiya Award from the International Union of Materials Research Societies, G.C. Kuczynski Prize from the International Institute for the Science of Sintering, and Roland B. Snow Award from the American Ceramic Society (twice). He has been elected a fellow of the American Ceramic Society, academician of the World Academy of Ceramics, and full member of the International Institute for the Science of Sintering.



---

# Contributors

**François Béguin**

Centre de Recherche sur la Matière Divisée  
CNRS-Université  
Orléans, France

**J.D. Carey**

Advanced Technology Institute  
University of Surrey  
Guildford, United Kingdom

**Svetlana Dimovski**

Department of Materials Science and  
Engineering  
Drexel University  
Philadelphia, Pennsylvania

**Fangming Du**

Department of Chemical and Biomolecular  
Engineering  
University of Pennsylvania  
Philadelphia, Pennsylvania

**John E. Fischer**

Department of Materials Science and  
Engineering  
University of Pennsylvania  
Philadelphia, Pennsylvania

**Elzbieta Frackowiak**

Institute of Chemistry and Technical  
Electrochemistry  
Poznań University of Technology  
Poznań, Poland

**Yury Gogotsi**

Department of Materials Science and  
Engineering  
Drexel University  
Philadelphia, Pennsylvania

**Aurelio Mateo-Alonso**

Dipartimento di Scienze Farmaceutiche  
Università degli Studi di Trieste  
Trieste, Italy

**Gary McGuire**

International Technology Center  
Research Triangle Park, North Carolina

**Alexi Nikitin**

Department of Materials Science and  
Engineering  
Drexel University  
Philadelphia, Pennsylvania

**Maurizio Prato**

Dipartimento di Scienze Farmaceutiche  
Università degli Studi di Trieste  
Trieste, Italy

**Eduard G. Rakov**

D.I. Mendeleev University of Chemical  
Technology  
Moscow, Russia

**Olga Shenderova**

International Technology Center  
Research Triangle Park, North Carolina

**S.R.P. Silva**

Advanced Technology Institute  
University of Surrey  
Guildford, United Kingdom

**Nikos Tagmatarchis**

Dipartimento di Scienze Farmaceutiche  
Università degli Studi di Trieste  
Trieste, Italy

**Karen I. Winey**

Department of Materials Science and  
Engineering  
University of Pennsylvania  
Philadelphia, Pennsylvania

**Gleb Yushin**

Department of Materials Science and  
Engineering  
Drexel University  
Philadelphia, Pennsylvania

---

# Table of Contents

<b>Chapter 1</b> Fullerenes and Their Derivatives .....	1
<i>Aurelio Mateo-Alonso, Nikos Tagmatarchis, and Maurizio Prato</i>	
<b>Chapter 2</b> Carbon Nanotubes: Structure and Properties.....	41
<i>John E. Fischer</i>	
<b>Chapter 3</b> Chemistry of Carbon Nanotubes .....	77
<i>Eduard G. Rakov</i>	
<b>Chapter 4</b> Graphite Whiskers, Cones, and Polyhedral Crystals .....	149
<i>Svetlana Dimovski and Yury Gogotsi</i>	
<b>Chapter 5</b> Nanocrystalline Diamond .....	175
<i>Olga Shenderova and Gary McGuire</i>	
<b>Chapter 6</b> Carbide-Derived Carbon .....	211
<i>Gleb Yushin, Alexi Nikitin, and Yury Gogotsi</i>	
<b>Chapter 7</b> Nanotubes in Multifunctional Polymer Nanocomposites.....	255
<i>Fangming Du and Karen I. Winey</i>	
<b>Chapter 8</b> Nanostructured Materials for Field Emission Devices.....	275
<i>J.D. Carey and S.R.P. Silva</i>	
<b>Chapter 9</b> Nanotextured Carbons for Electrochemical Energy Storage.....	295
<i>François Béguin and Elzbieta Frackowiak</i>	

---

# 1 Fullerenes and Their Derivatives

*Aurelio Mateo-Alonso, Nikos Tagmatarchis, and  
Maurizio Prato*

Dipartimento di Scienze Farmaceutiche, Università degli Studi  
di Trieste, Trieste, Italy

## CONTENTS

1.1	Introduction .....	1
1.2	Functionalization of Fullerenes .....	2
1.2.1	Cycloadditions .....	2
1.2.1.1	[2+2] Cycloadditions .....	2
1.2.1.2	[3+2] Cycloadditions .....	3
1.2.1.3	[4+2] Cycloadditions .....	10
1.2.2	Cyclopropanation Reactions .....	11
1.3	Self-Assembled Fullerene Architectures .....	15
1.3.1	Rotaxanes, Catenanes, Pseudorotaxanes .....	15
1.3.2	Nanorings, Peapods .....	19
1.3.3	Supramolecular Assemblies with Porphyrins .....	22
1.3.4	Complementary Hydrogen Bonded Supramolecular Systems .....	22
1.4	Applications .....	24
1.4.1	Donor–Acceptor Systems .....	24
1.4.1.1	Dyads Containing Photoactive Electron Donors .....	25
1.4.1.2	Dyads Containing Nonphotoactive Electron Donors .....	26
1.4.1.3	Polyads .....	28
1.4.2	Plastic Solar Cells .....	28
1.5	Conclusions .....	33
	Acknowledgments .....	33
	References .....	33

## 1.1 INTRODUCTION

Since the discovery<sup>1</sup> and the bulk production<sup>2,3</sup> of fullerenes an integrated research field involving organic transformations of these all-carbon hollow-cluster materials has emerged. C<sub>60</sub> has been the most thoroughly studied member of fullerenes because it (1) is produced abundantly in the carbon soot by the arc discharge of graphite electrodes, (2) has high symmetry (icosahedral I<sub>h</sub> with all 60 carbons chemically equivalent), (3) is less expensive, (4) is relatively inert under mild conditions, and (5) shows negligible toxicity. Electronically, C<sub>60</sub> is described as having a closed-shell configuration consisting of 30 bonding molecular orbitals with 60 p electrons,<sup>4</sup> which give rise to a completely full fivefold degenerate h<sub>u</sub> highest occupied molecular orbital that is energetically located approximately 1.5 to 2.0 eV lower than the corresponding antibonding lowest unoccupied molecular orbital (LUMO) one.<sup>5,6</sup> The first electron in the reduction of C<sub>60</sub> is added to a triply degenerate

$t_{1u}$  unoccupied molecular orbital and is highly delocalized.<sup>7</sup> This threefold-degeneracy, together with the low-energy possession of the LUMO, make  $C_{60}$  a fairly good electron acceptor with the ability of reversibly gaining up to six electrons upon reduction.<sup>8,9</sup> The facile reduction contrasts with its difficult oxidation. Only the first three reversible oxidation waves have been observed.<sup>10</sup> This high degree of symmetry in the arrangement of the molecular orbitals of  $C_{60}$  provides the foundation for a plethora of intriguing physicochemical, electronic, and magnetic properties. Semiconducting,<sup>11</sup> magnetic,<sup>12–16</sup> and superconducting<sup>17–19</sup> properties of unmodified  $C_{60}$  have been intensively investigated; however, these properties remain to be explored for functionalized fullerenes. On the other hand, nonlinear optical and photophysical properties of functionalized fullerene materials have already been under investigation.

The skeleton of  $C_{60}$  consists of 20 hexagonal and 12 pentagonal rings fused all together. The chemical reactivity of  $C_{60}$  is that of a strained electron deficient polyalkene, with rather localized double bonds. Cycloaddition reactions have been widely applied for the functionalization of fullerenes. Usually, addition occurs across [6,6] ring junctions where electron density is much higher than at the [6,5] ones. Other reactions that take place on the spherically shaped carbon core of fullerenes involve additions of nucleophiles, free radicals, and carbenes as well as  $\eta^2$ -complexation with various transition metal elements. In such fullerene adducts, the functionalized carbon atoms change their hybridization from a trigonal  $sp^2$  to a less strained tetrahedral  $sp^3$  configuration; thus, the primary driving force for addition reactions is the relief of strain in the fullerene cage. Furthermore, the regiochemistry of the addition is governed by the minimization of the 5,6-double bonds within the fullerene skeleton. Therefore, any 1,2-addition reactions occur to produce ring-closed 6,6-adducts, having two  $sp^3$  carbon atoms on the fullerene framework. However, sometimes ring-opened 6,5-adducts (fulleroids) are formed, keeping all fullerene carbon atoms  $sp^2$ -hybridized.

The main advantage gained upon functionalization of fullerenes is a substantial increase in their solubility. The existence of a great diversity of synthetic protocols combined with the high number of chemical reactions that have been mainly applied to  $C_{60}$  has led to the formation of a wide variety of functionalized fullerenes.

The special characteristics of the added groups, coupled with the unique structural, physicochemical, and electronic properties of fullerenes (which in most of the cases are retained after functionalization), have aided the development of new materials with tremendous potential in fascinating and widespread technological applications such as electronic and optoelectronic devices, light-emitting diodes photovoltaics, and thermotropic liquid crystals. This chapter highlights the rapid progress made in the above scientific areas by the syntheses and applications of some novel functionalized fullerene materials.

## 1.2 FUNCTIONALIZATION OF FULLERENES

### 1.2.1 CYCLOADDITIONS

Fullerenes behave as  $2\pi$  electron-deficient dienophiles and dipolarophiles and, therefore undergo cycloaddition reactions such as [2+2], [3+2], and [4+2]. These have been carried out either thermally or photochemically, and they typically take place on the 6,6-ring junctions of the fullerene skeleton.

#### 1.2.1.1 [2+2] Cycloadditions

Four-membered rings fused to 6,6-ring junctions are formed upon [2+2] cycloadditions. The first example of this procedure was the [2+2] thermal addition of benzyne to  $C_{60}$ .<sup>20,21</sup> Schuster and coworkers<sup>22–25</sup> reported photochemical [2+2] cycloadditions of cyclic enones and 1,3-diones, while Liou and Cheng<sup>26</sup> reported the addition of electron-deficient alkenes. It can be concluded from their experiments that (1) photocycloadditions cannot proceed at wavelengths where only  $C_{60}$  absorbs light (i.e., 532 nm); (2) better yields are obtained either by increasing the concentration of the enone or by

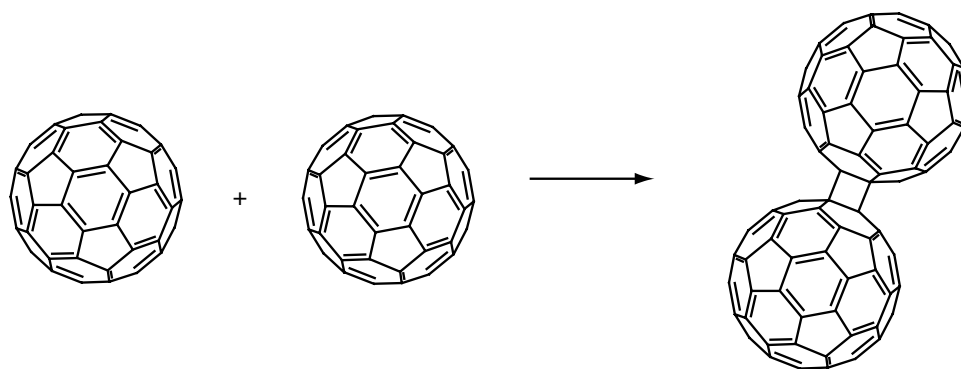
decreasing the concentration of the fullerene; (3) the [2+2] cycloaddition takes place between the ground state of the  $C_{60}$  and the enone triplet excited state via an intermediate triplet 1,4-biradical.

The addition of diethylaminopropyne to  $C_{60}$  resulted in a [2+2] adduct that can be ring-opened under acidic conditions. Then, novel fullerene lactones were obtained under oxidative cyclization conditions in the presence of activated carbon.<sup>27</sup>

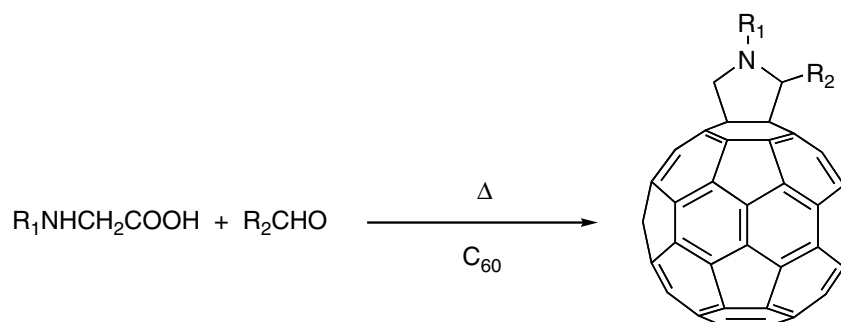
Recently, the interest in the synthesis of fullerene dimers has increased,<sup>28</sup> as they can be used as building blocks for nanotechnological applications (Scheme 1.1). The first procedure was published by Komatsu and coworkers;<sup>29,30</sup> the experiments yielded the dimer when carried out using high-speed vibration milling (HSVM) in the presence of potassium cyanide, while in solution<sup>31</sup> only  $C_{60}$ -cyanated derivatives were obtained. This technique has also been applied to the reaction between  $C_{60}$  and pentanocene<sup>32</sup> and to the dimerization of  $C_{70}$ <sup>33</sup> and  $C_{60}$ - $C_{70}$  cross-dimers.<sup>34</sup>

### 1.2.1.2 [3+2] Cycloadditions

Five-membered rings fused to 6,6-junctions can be formed upon [3+2] cycloadditions to fullerenes. The 1,3-dipolar cycloaddition of azomethine ylides has been shown as one of the most versatile tools for functionalization of fullerenes and has been widely used.<sup>35-38</sup> Azomethine ylides are reactive intermediates that can be generated *in situ* by one of the following protocols: (1) decarboxylation of immonium salts derived from thermal condensation of  $\alpha$ -amino acids (Scheme 1.2) and aldehydes (alternatively ketones), or (2) thermal ring opening of aziridines. 1,3-Dipolar addition of azomethine ylides to  $C_{60}$  yields fulleropyrrolidines that are formed across the 6,6-junction of the fullerene core. The key features of this type of reaction are summarized as: (1) utilization of functionalized aldehydes leads to the formation of 2-substituted fulleropyrrolidines, whereas utilization of *N*-substituted glycines affords *N*-substituted fulleropyrrolidines (Scheme 1.2); and (2) mono-fulleropyrrolidines are formed by controlling the stoichiometry of the reagents and the reaction conditions. Therefore, through this methodology, structurally different fullerene derivatives for different



**SCHEME 1.1** [2+2] Cycloaddition  $C_{60}$  dimer.



**SCHEME 1.2** [3+2] Cycloaddition using azomethine ylides.

applications are obtained, either by using properly functionalized azomethine ylides or by modifying a fulleropyrrolidine intermediate. The characteristics of the fullerene skeleton combined with the properties of the substituents introduced, leads to the construction of fullerene-based materials with novel properties.

When the highly hydrophobic fullerenes are derivatized with hydrophilic residues, fullerene-based amphiphilic derivatives are obtained. Such materials are suitable for the construction of Langmuir–Blodgett (LB) films. Amphiphilic fulleropyrrolidines bearing suitable hydrophilic addends (Figure 1.1) have been found to form true monolayers that can be eventually transferred onto solid substrates while the formation of LB films could not be equally realized with their corresponding hydrophobic analogs.<sup>39–55</sup>

*N*-substituted fulleropyrrolidines can be *N*-alkylated to give fulleropyrrolidinium salts. The insertion of positive charges increases substantially the solubility of such compounds in aqueous media, which have been used for the construction of supramolecular architectures. *N*-functionalization with oligoethylene glycol chains bearing terminal ammonium salts enhanced the solubility in water, while the fullerene–fullerene interactions were responsible for aggregation due to hydrophobicity. The combination of these properties led to the formation of spheres, nanorods, or nanotubules in water (Figure 1.2).<sup>56</sup> When porphyrins were inserted, the molecules assembled in nanotubules, but the removal of the porphyrin fragment generated nanometer level structures characterized by long uniform bundles of tens of aligned parallel nanotubules with

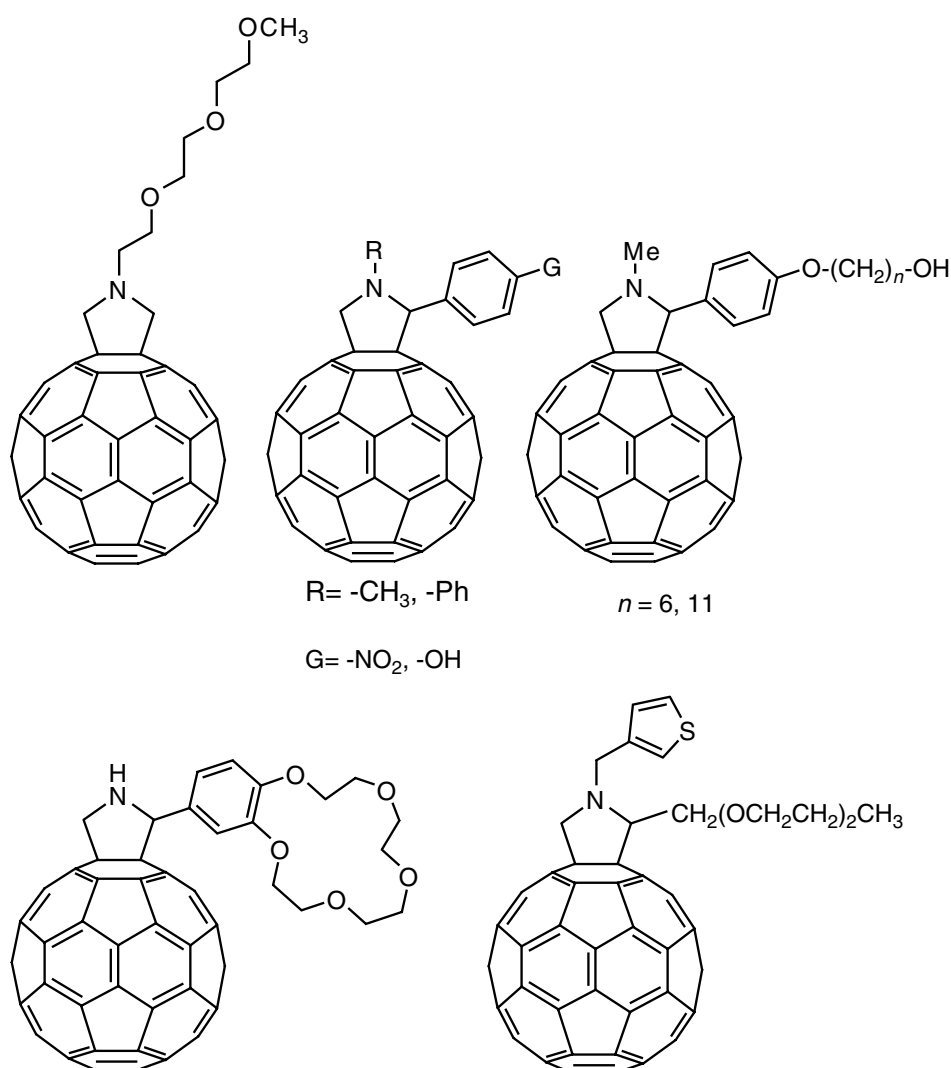


**FIGURE 1.1** Fullerenes functionalized with hydrophilic addends.

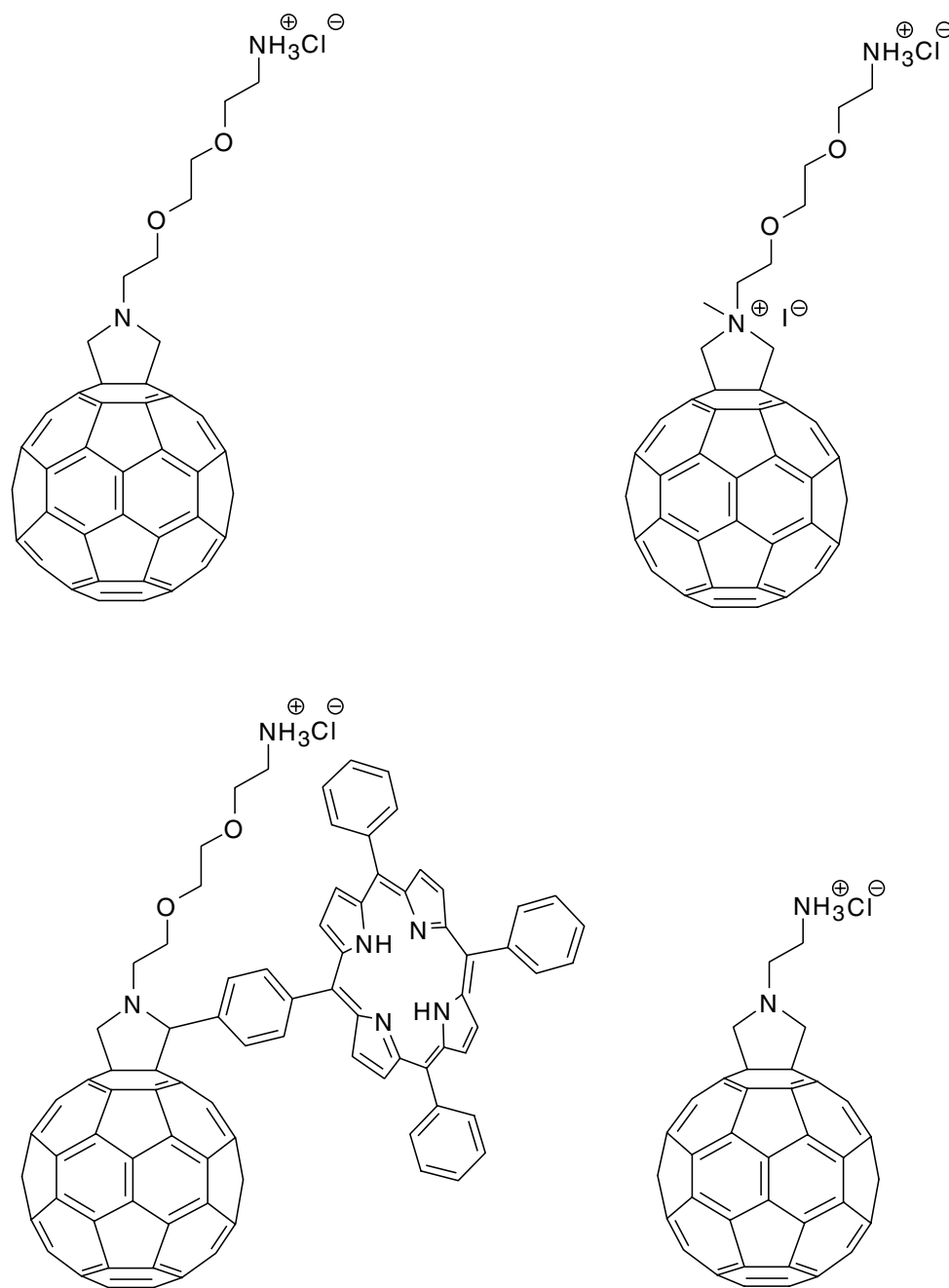


**FIGURE 1.2** Fulleropyrrolidine salts.

diameters of about 4 nm and lengths of several microns. If the porphyrin fragment is removed, the driving force for the formation of well-defined nanotubes is less favorable, resulting in one-dimensional linear structures, which are rather different from the relatively common spherical systems obtained by fullerenes derivatives. Removal of the long oligoethylene glycol chains in favor of a short aliphatic chain results in spherical aggregates, thereby recovering the supramolecular topology of  $C_{60}$  mesoscopic aggregates. Therefore, it is reasonable to assume that molecular tailoring or different solution treatment of such amphiphilic organofullerene materials induces different kinds of assembly.<sup>57</sup>

The solubility in water of this type of fulleropyrrolidine derivative allowed its insertion into the interlayer space of smectite clays leading to a new family of organic–inorganic nanocomposites.<sup>58</sup> The positively charged fulleropyrrolidines were introduced into the clay galleries by cation exchange, replacing the charge-balancing cations such as  $Na^+$  (Figure 1.3).

The solubilization of fullerenes in water allows the possibility to explore their properties in different fields such as medicinal chemistry and biotechnology. Again the functionalization with polar side-chains<sup>59</sup> and with positively charged groups<sup>60</sup> enhanced the solubility to sufficiently high concentrations ( $10^{-4}$  to  $10^{-5}$  M) to study the biological activity of fulleropyrrolidines.<sup>61</sup>

In another very recent report, a fulleropyrrolidine–mercaptophenyl hybrid material was synthesized and self-assembled in two-dimensional arrays.<sup>62</sup> The self-assemblies of this novel material have shown reversible electrochemistry and intriguing electronic properties suitable for constructing well-ordered nanostructural morphologies and thin film functional materials.

1,3-Dipolar additions have also been used in the preparation of novel compounds such as fulleroproline, the biggest unnatural amino acid<sup>63</sup> that comprises a natural  $\alpha$ -amino acid proline condensed to a 6,6 ring junction of  $C_{60}$ .<sup>64</sup> When glycine *t*-butyl ester was condensed with formaldehyde in refluxing toluene, followed by removal of the protecting group under acidic conditions, fulleroproline was generated that turned out to be insoluble in any kind of solvent (Scheme 1.3). However, derivatization of the pyrrolidine nitrogen with either an acylating agent (i.e., acetic anhydride) or a protecting group (i.e., Fmoc fluorenylmethyloxycarbonyl or Boc, *tert*-butyloxycarbonyl) affords a compound that can be easily characterized for further peptide synthesis.

Alternatively, fulleroprolines can be obtained via the thermal ring opening of aziridines (Scheme 1.4).<sup>65</sup> In this case, the fulleroproline results orthogonally protected at the *N*- and *C*-termini. In addition, di- and tripeptides have already been prepared by incorporating fulleroproline at their *N*- or *C*-terminal parts.<sup>66–68</sup>

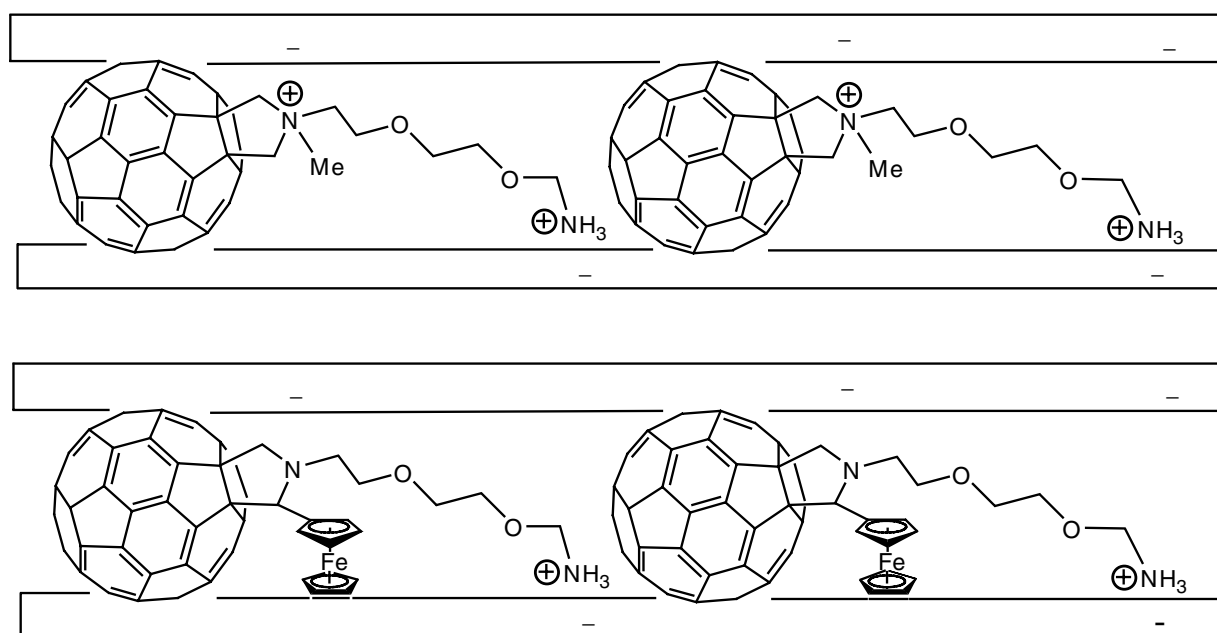
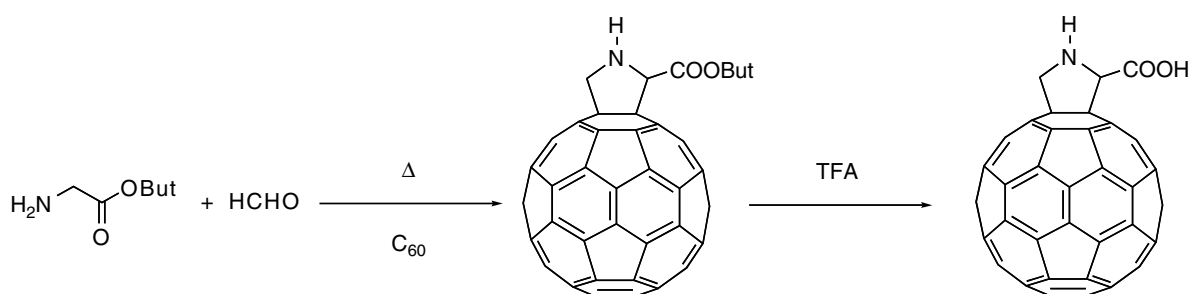
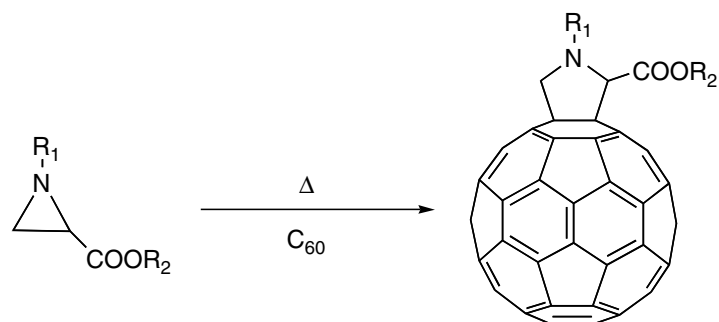


FIGURE 1.3 Fullerene inserted in clay galleries.



SCHEME 1.3 Synthesis of fulleroproline.





**SCHEME 1.4** [3+2] Cycloaddition by thermal opening of azyridines.

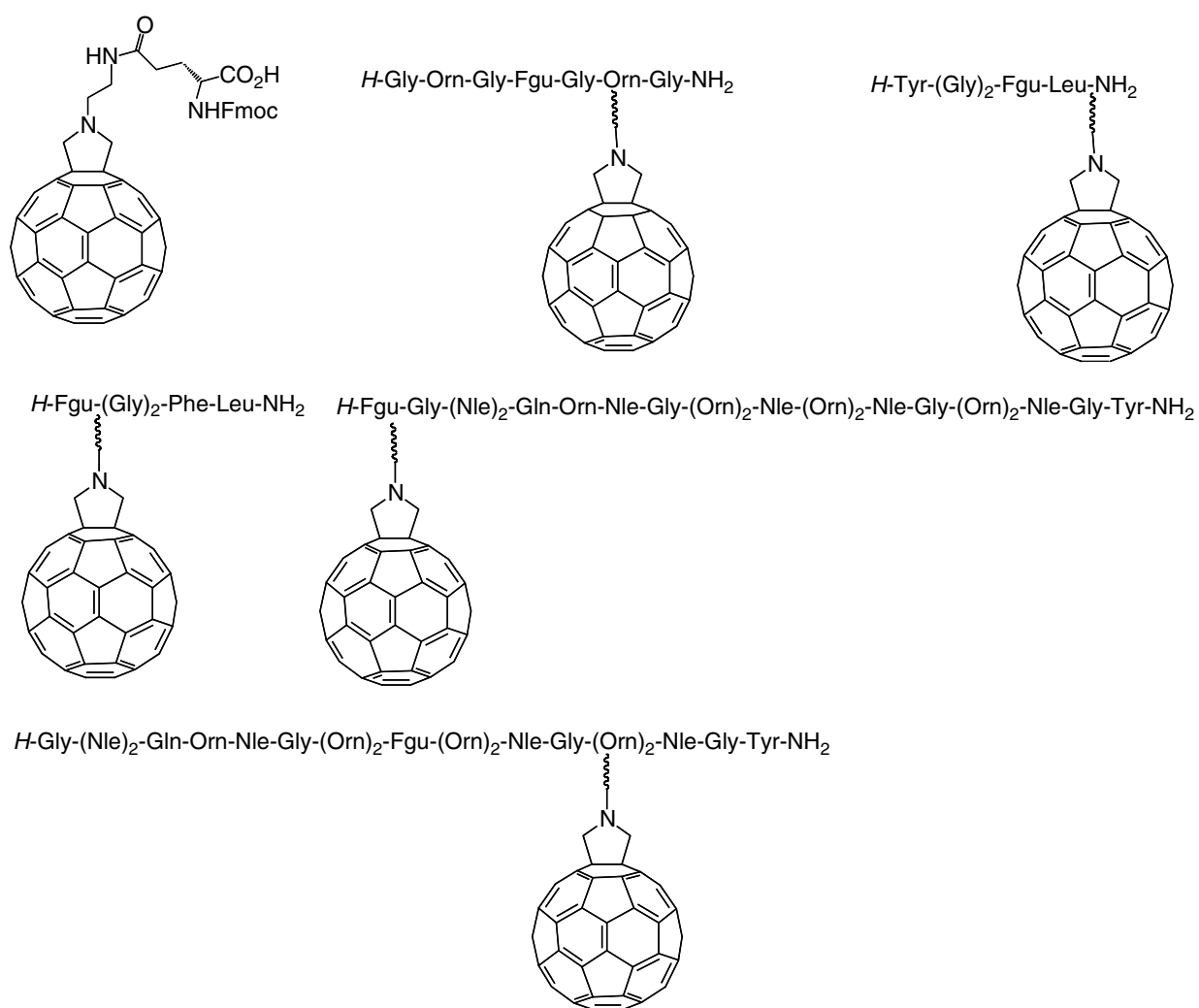


**FIGURE 1.4** Fullerene peptides.

For more complex fullerene-modified peptides, a protocol for the solid phase using the fulleropyrrolidino-glutamic acid, was developed. Such protocol was used to insert a series of different peptides, including Leu-enkephalins analogs and antimicrobial sequences (Figure 1.4).<sup>69</sup>

Dendrimers can serve as building blocks for the construction of organized materials with nano-size precision due to the well-defined three-dimensional structure they possess. An issue of great importance is to incorporate photoactive and/or redox-active units at the center of the dendrimer in order to establish this type of materials as molecular devices. Through 1,3-dipolar addition, a wide

variety of fullerodendrimers containing oligoethylene glycol as well as with oligophenylenevinylene have been synthesized.<sup>70–72</sup>

Recently, the synthesis of a functionalized fullerene having a DNA minor groove binder and an oligonucleotide chain covalently linked to a fullerene cage via a fused pyrrolidine ring was reported.<sup>73–75</sup> The design of the latter synthesis was based on an already established idea that coupling of fullerenes to a minor groove binder leads to higher affinity and specificity of the derivatives toward target DNA.<sup>76</sup> The construction of fullerene–DNA hybrid materials allows transmission electron microscopy (TEM) imaging of deoxyribonucleic acid without the use of any heavy metal. Recently, such compounds became available and showed to bind to DNA through electrostatic interactions with the phosphorylated groups providing excellent contrast for imaging individual DNA molecules.<sup>77</sup>

Fulleropyrrolidine-based steroid hybrids were synthesized and found to decrease both the ATP hydrolysis and  $\text{Ca}^{2+}$  uptake activity of sarcoplasmic reticulum  $\text{Ca}^{2+}$ -ATPase while the inhibitions were concentration-dependent.<sup>78</sup> Recently, a range of fullerene–flavanoid dyads were synthesized.<sup>79–81</sup> The idea of preparing such systems stemmed from the fact that flavanoids possess significant antioxidant activity, can act as anticarcinogens, and express beneficial effects in inflammatory and immunomodulatory systems.

Bisadducts can also be produced using [3+2] cycloaddition methodology (Figure 1.5). The isolation and full characterization of the whole series of the pyrrolidine bisadducts (*trans*-1, -2, -3, -4, equatorial, *cis*-3, -2, and -1).<sup>82</sup> Although some of these patterns had been partly characterized before,<sup>83–85</sup> the isolation and full characterization of the never observed *cis*-3, -2, and -1 fulleropyrrolidine isomers were achieved.

In a recent paper,<sup>86</sup> the bisadducts were prepared and separated by high-performance liquid chromatography (HPLC), following the previous procedure. It should be noted that *trans*-2, *trans*-3, and *cis*-3 enantiomers display  $C_2$  symmetry and are chiral due to their addition pattern. Then, each couple of these enantiomers was separated by chiral HPLC. The resulting enantiomerically pure isomers were transformed into fulleropyrrolidinium salts. The *trans*-3 enantiomers were used successfully to induce chiral helicity, in opposite directions of negatively charged polymer backbones.

In a different work<sup>87</sup> that focused on the biological and medicinal application of fullerenes, different  $C_{60}$  bisadducts containing polyethyleneglycol chains and ammonium salts were prepared to prevent aggregation and increase the solubility in water. Only *trans*-2, -3, -4 and equatorial isomers were completely purified by HPLC, showing an increase of solubility in water by 100 times compared with the corresponding monoadducts, and also exhibited high solubility on a phosphate-buffered solution.

The influence on the reduction potentials of the different substitution patterns in fulleropyrrolidines and fulleropyrrolidinium salts have been studied.<sup>88</sup> This concept has been extended efficiently to the preparation of molecules in other applications, such as cation recognition.<sup>89</sup> Bisfunctionalized crown ethers have been attached very close to the fullerene sphere using 1,3-dipolar additions. An electrochemical signal is obtained from the variation of the redox potentials of the fullerene when different cations are binded. The responses were favorable showing reduction potential shifts between 15 and 38 mV depending on the cation.

Among other examples, the thermal [3+2] cycloaddition of azides to  $C_{60}$ <sup>90–92</sup> should be highlighted as it is the first step toward [60]azafullerenes (Scheme 1.5).<sup>93–95</sup> When the reaction is carried out at temperatures  $<80^\circ\text{C}$ , the cycloaddition takes place preferentially in the 6,6-ring junctions, affording thermally labile triazolines. Owing to the lower symmetry  $D_{5h}$  of  $C_{70}$  as compared with  $I_h$  symmetrical  $C_{60}$ , the regiochemistry of [3+2] cycloadditions of azides gives isomeric mixture of [70]triazolines that can be eventually separated and serve as precursors in the synthetic route to [70]azafullerenes.<sup>96–98</sup>

Diazo compounds are added to fullerenes across a 6,6-double bond yielding fulleropyrrazolines, which decompose to mixtures of methanofullerenes and methanofulleroids either thermally or photochemically.<sup>99</sup>

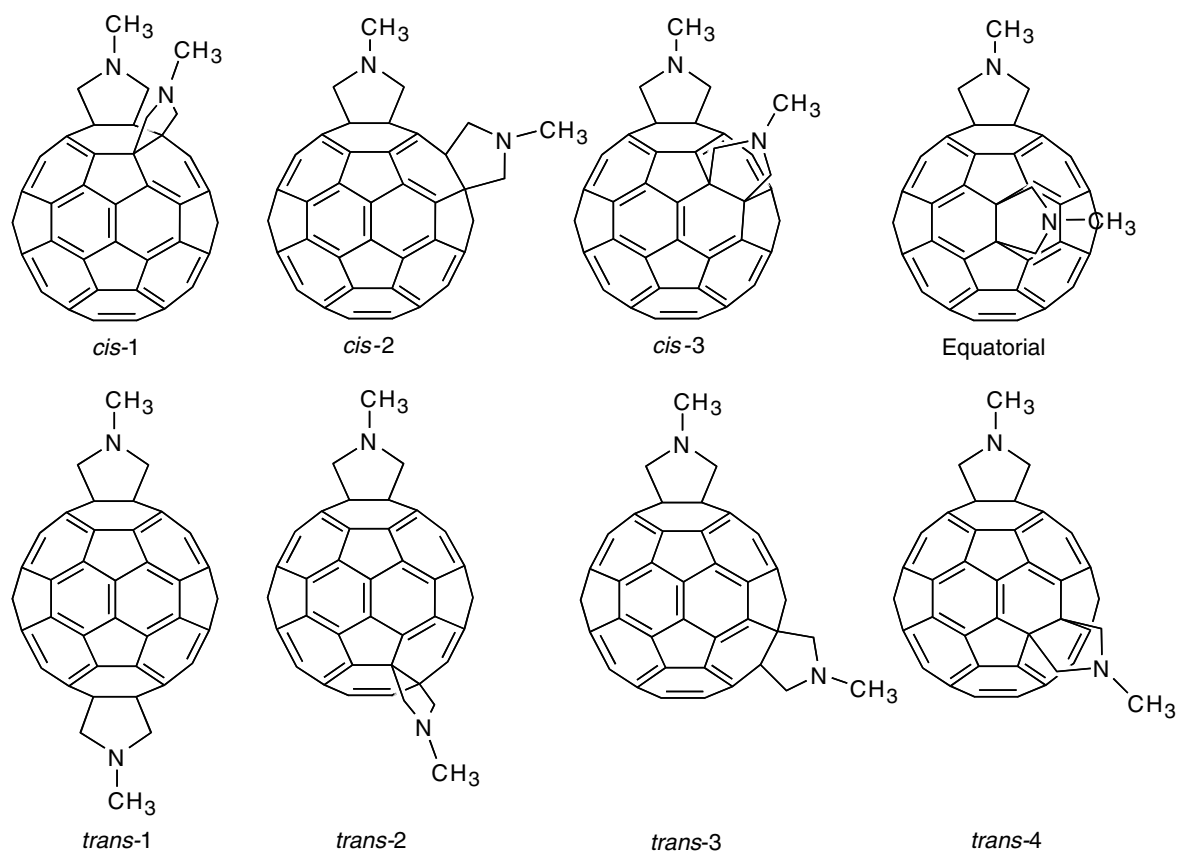
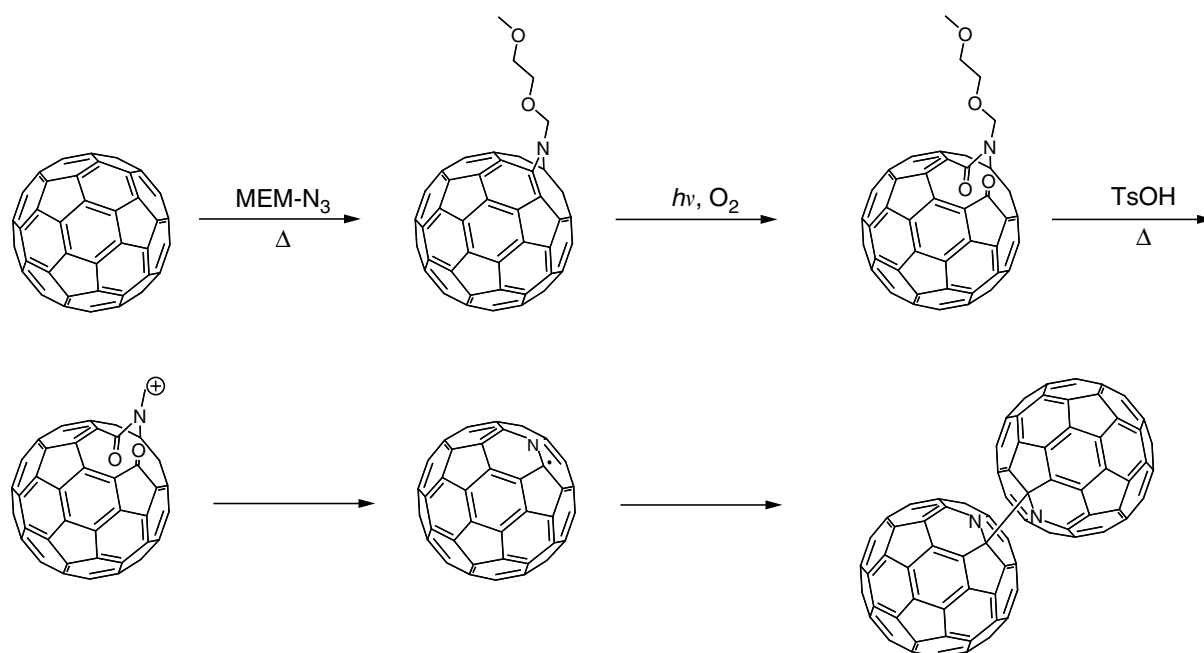


**FIGURE 1.5** All fullerene bisadducts.



**SCHEME 1.5** Synthesis of [60]aza fullerene.

Buta-2,3-dienoates and buta-2-ynoates, in the presence of phosphine as catalyst, have been found to react with  $\text{C}_{60}$  in a [3+2] fashion,<sup>100,101</sup> contrary to the early observations of yielding [2+2] cycloadducts.<sup>102</sup>

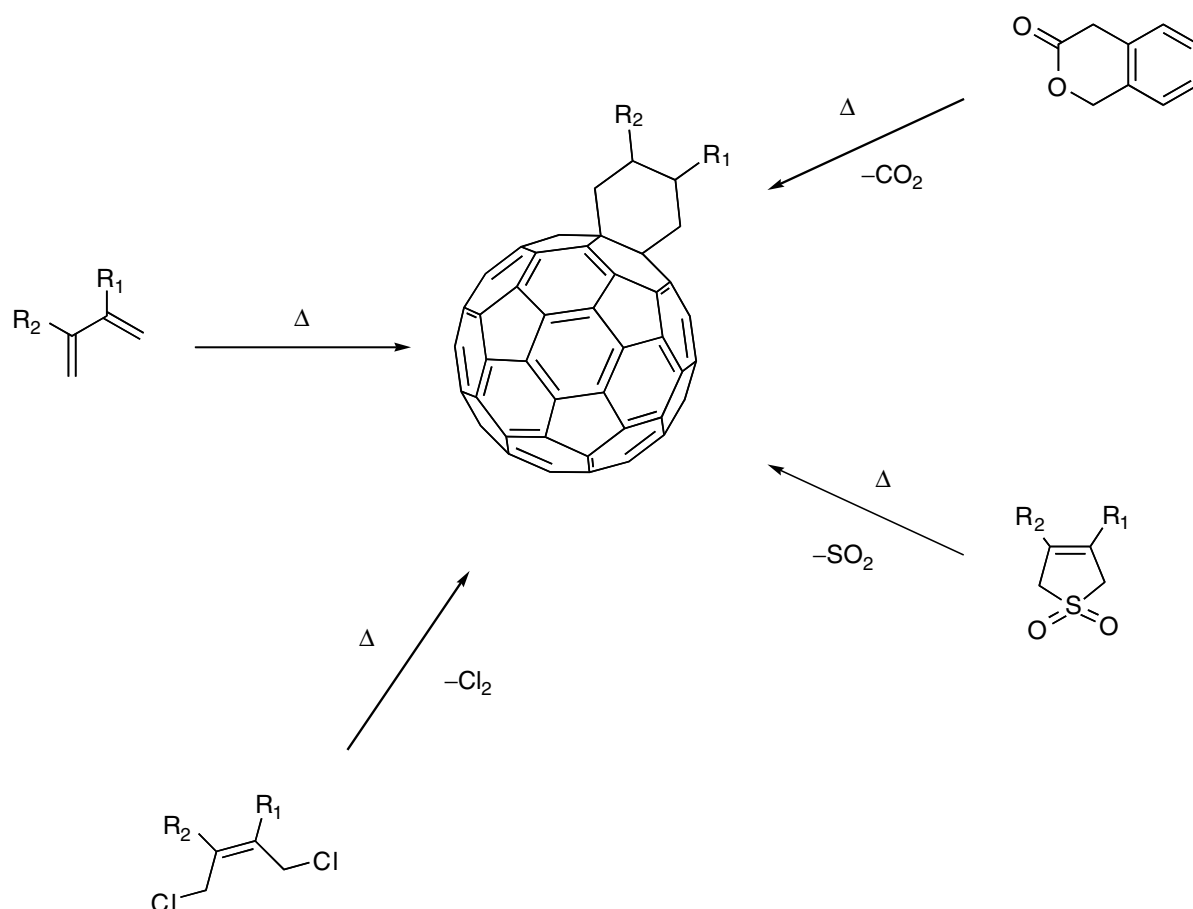
### 1.2.1.3 [4+2] Cycloadditions

In the [4+2] Diels–Alder cycloaddition, 1,3-dienes are added to 6,6-junctions of fullerenes. This type of cycloaddition offers the great advantage of controlling the degree of functionalization as well as the site of addition. However, it also offers the disadvantage of being reversible in most cases. Therefore, the cycloadditions are normally unstable. There are several examples of these cycloadditions reported in the literature, which can be divided into two main categories: (1) those in which the 1,3-dienes are cycloadded directly to the fullerene skeleton and (2) those in which the 1,3-dienes are generated *in situ* from the used reactants (Scheme 1.6).

In the first category, the addition of several analogs of Danishefsky dienes is highlighted, yielding fullerene-fused cyclohexanones.<sup>103</sup> The presence of the carbonyl group makes this system suitable for further chemical transformations on the carbonyl group leading to useful materials in nanotechnological areas.

A different example showed the reversible addition of a water-soluble fullerodendrimer with biotechnological applications.<sup>104</sup> A dendrimeric anthracene unit was successfully attached to C<sub>60</sub> using the Diels–Alder cycloaddition, providing solubility to the whole system in water. The reversibility of the reaction allows the possibility of removal of the solubilizing group that could release C<sub>60</sub> intracellularly.

Solid state reactions between C<sub>60</sub> and aromatic compounds such as anthracene, tetracene, pentacene, and naphtho[2,3-a]pyrene were carried out under HSVM conditions, to yield the corresponding [4+2]cycloadducts.<sup>32</sup> When the reaction was carried out with anthracene, the same product as in solution was obtained,<sup>105–107</sup> but with better yields. While in the case of pentacene, the reaction gave a different adduct to the one obtained in solution, in which pentacene was attached to two C<sub>60</sub>



**SCHEME 1.6** [4+2] Cycloaddition to C<sub>60</sub>.

molecules. Moreover, the reaction with tetracene and naphtho[2,3-a]pyrene afforded the expected [4+2] cycloadducts, similar to the case when the reactions were carried out in solution. Other Diels–Alder reactions between electron-deficient dienes with fullerenes involved tropones,<sup>108</sup> 1,3-butadienes substituted with electron-withdrawing groups<sup>109</sup> as well as 2-pyrone.<sup>110</sup>

The second category of [4+2] cycloadditions, which involves the *in situ* generation of the diene, has been applied to prepare novel organofullerene materials bearing fused furan and thiophene rings,<sup>111,112</sup> which are suitable for nanoelectronics and photovoltaics applications. Other examples include reactive *o*-quinodimethanes species created *in situ* by thermolysis of cyclic sulfones,<sup>113</sup> substituted cyclo-<sup>113,114</sup> or benzocyclo-butanones<sup>115</sup> and 1,4-elimination of dibromides.<sup>115</sup>

The reaction of “masked” *o*-benzoquinone<sup>116</sup> with C<sub>60</sub> was also studied.<sup>117</sup> The [4+2] cycloaddition reaction of such electron-deficient dienes with fullerenes resulted in the formation of highly functionalized bicyclo[2.2.2] octenone-fused fullerenes. The reactants were generated *in situ* by oxidation of the readily available 2-methoxy phenols.

Heterocyclic analogs of *o*-quinodimethane have become increasingly popular for Diels–Alder functionalization of C<sub>60</sub>, since methods for generating these highly reactive species have been developed. However, most attention has been paid to their generation via chelotropic elimination of SO<sub>2</sub> from heteroaromatic-fused 3-sulfolenes and 1,4-elimination from the corresponding  $\alpha,\alpha'$ -dihalides.<sup>118–122</sup>

Some novel C<sub>60</sub>-based [4+2] adducts were recently synthesized through 1,4-dihalide elimination, giving fused tetrathiafulvalene–C<sub>60</sub> dyads and C<sub>60</sub>–tetrathiafulvalene–C<sub>60</sub> dumbbell triads, in which the fullerene acceptor is doubly tethered to the donor tetrathiafulvalene through a rigid cyclohexene ring.<sup>123</sup> With this novel approach, control of the relative orientation as well as the distance between the donor and acceptor units was achieved. Thereby, through-space interactions were expected to dominate because of the special topology of the constructed molecules. More examples of such donor–acceptor hybrid systems are discussed in following sections.

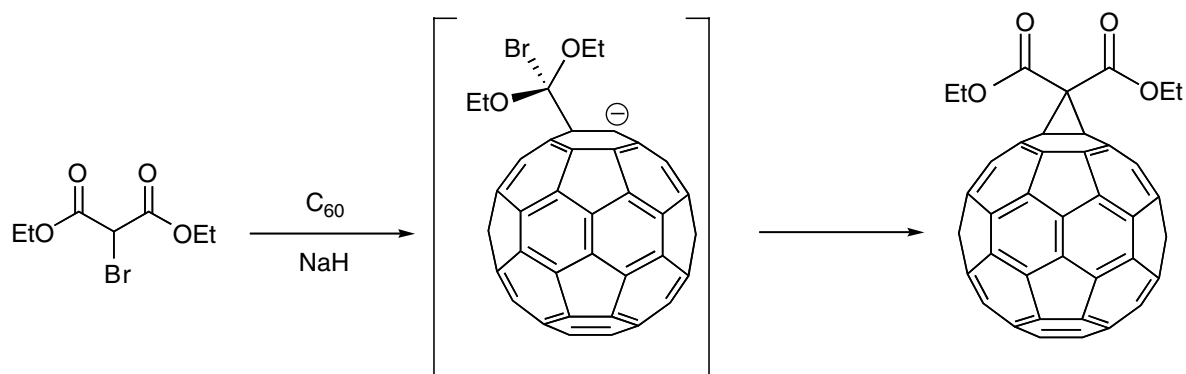
All the work cited in this section refers to monoaddition of dienes to fullerenes. By using an excess of a diene the formation of multi-adducts is increased. Following these conditions, hexakisadducts fullerenes have been prepared upon cycloaddition of 2,3-dimethyl-1,3-butadiene to C<sub>60</sub>.<sup>124,125</sup> Different bisadducts<sup>126</sup> containing crown ethers have been prepared by 1,4-dihalide elimination depending on the size of the crown ether used. Various properties of these derivatives with potential applications in the field of molecular sensors, including complexation, electrochemical, and fluorescence emission behaviors have been studied.

A few examples of [4+2] cycloadditions to higher fullerenes have been described, which lead to isomeric mixtures due to their lower molecular symmetry. Such works involved cycloadditions of *in situ* created reactive *o*-quinodimethane to C<sub>70</sub> and C<sub>76</sub><sup>127,128</sup> as well as pentamethylcyclopentadiene<sup>129</sup> to C<sub>70</sub>.

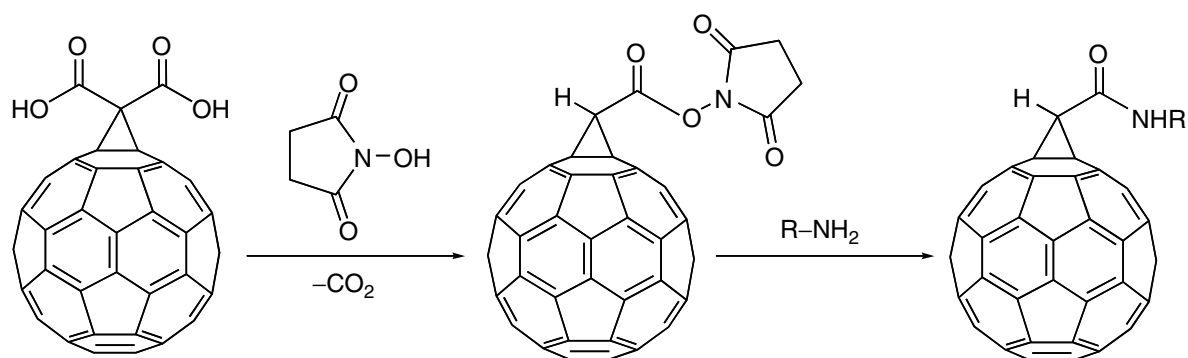
## 1.2.2 CYCLOPROPANATION REACTIONS

Cyclopropanation reactions are considered among the widely used methods for regioselective functionalization of fullerenes. In general, cyclopropanated fullerenes (methanofullerenes) can be synthesized either by (i) generation of carbon nucleophiles from  $\alpha$ -halo esters and their subsequent addition to C<sub>60</sub> (Bingel method), (ii) thermal addition of diazo compounds followed by thermolysis or photolysis, or (iii) addition of free carbene species.

In the Bingel cyclopropanation reaction<sup>130</sup> (addition–elimination), the addition of anions of  $\alpha$ -haloesters to fullerenes is followed by an intramolecular substitution of the halide by the intermediate fullerene anion to give the corresponding methanofullerene derivative (Scheme 1.7). The addition takes place exclusively on double bonds between two six-membered rings of the fullerene skeleton. The versatility of the reaction is justified in terms of the ready availability of the starting ester compounds. Furthermore, additional chemical transformations to the ester addend group of an already synthesized methanofullerene could occur. For example, activation of malonic acid



SCHEME 1.7 Bingel reaction.



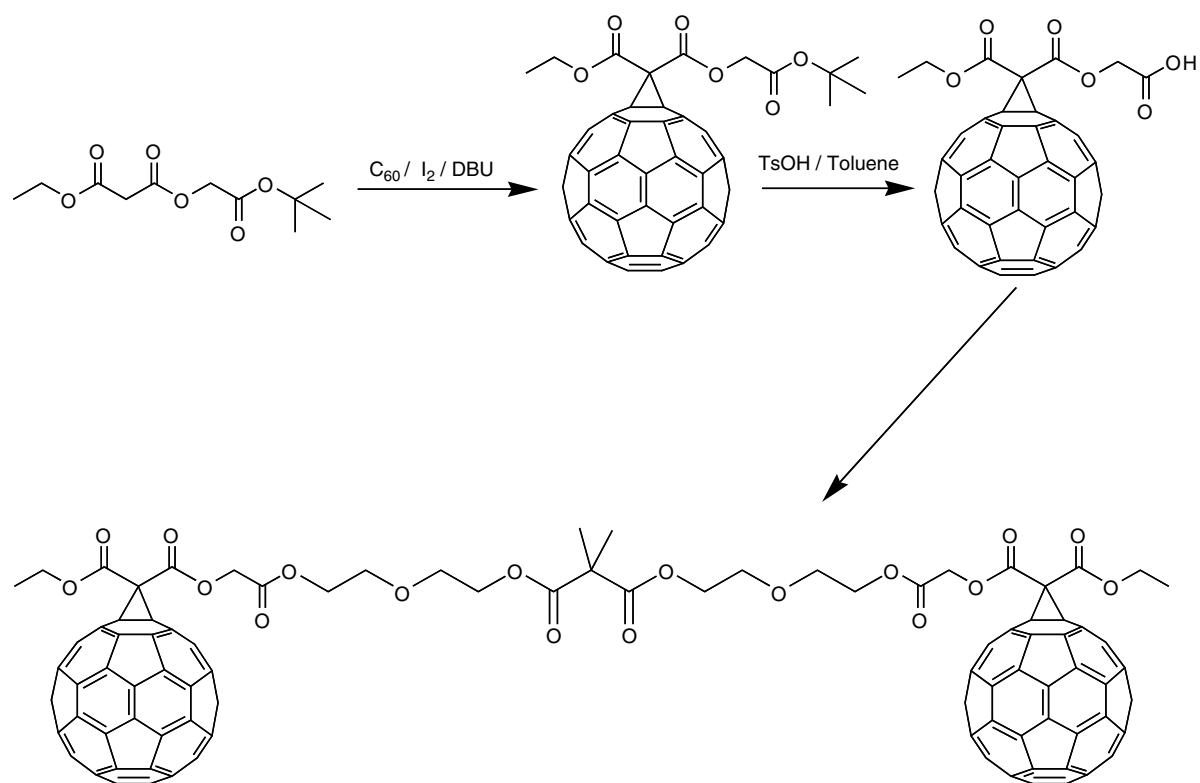
SCHEME 1.8 Chemical modification of Bingel adducts.

methanofullerene material with *N*-hydroxysuccinimide and subsequent reaction with amines furnishes the corresponding methanofullerene amides, as shown in Scheme 1.8.

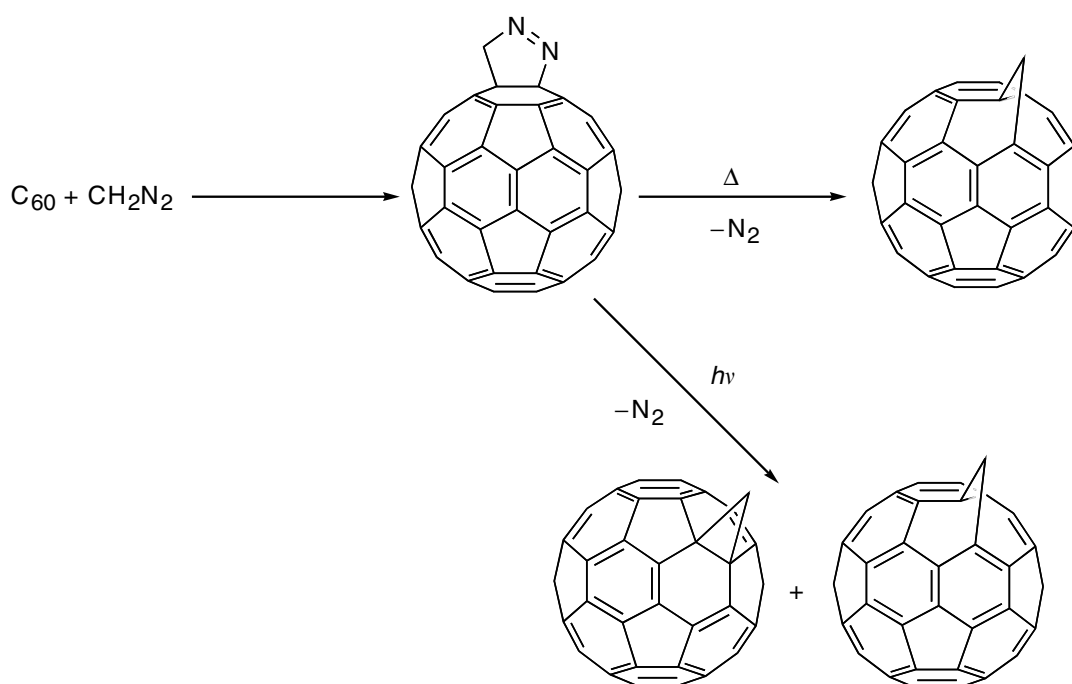
It is worth mentioning that during the activation of malonic acid on the methanofullerene material with *N*-hydroxysuccinimide, decarboxylation occurs. Therefore, to prevent decarboxylation a spacer was introduced between the bridging carbon atom of the methanofullerene and the reacting carboxylic acid unit in such systems. This route ultimately provides access to the construction of methanofullerene derivative bearing a free carboxylic acid moiety as a versatile building block as shown in Scheme 1.9. In this instance, the reaction has been used for the construction of a novel structure consisting of alternating  $C_{60}$ – $C_{70}$  methanofullerene units. The novel features of this material are summarized in its electronic absorption spectrum that shows the characteristic absorptions of both  $C_{60}$  and  $C_{70}$  subunits as well as in the cyclic voltammogram which indicates that each fullerene unit behaves as an independent redox center.<sup>131</sup>

Recently, modifications of the original Bingel cyclopropanation have been performed, thereby expanding the use and applicability of the reaction and increasing the construction of novel fullerene-based materials. For example, alternative pathways generation *in situ* of the reactive halo-malonate intermediate have been developed.<sup>132,133</sup> Additionally, a series of phosphonium<sup>134</sup> and sulfur<sup>135</sup> ylides have been reacted with  $C_{60}$ , following a similar addition–elimination pathway, yielding the corresponding methanofullerenes. However, the yields of these reactions can vary significantly depending on the nature of the ylide used.

A different way to synthesize methanofullerene materials is upon addition of diazo compounds to fullerenes via formation of unstable pyrazoline derivatives,<sup>136,137</sup> where nitrogen is thermally or photochemically released (Scheme 1.10). Two different compounds were formed: thermally the [5,6]-open fulleroid is obtained upon addition on a 5,6-junction;<sup>138</sup> while photochemically a mixture of the 5,6-open fulleroid as well as the methanofullerene upon addition to a 6,6-ring junction is



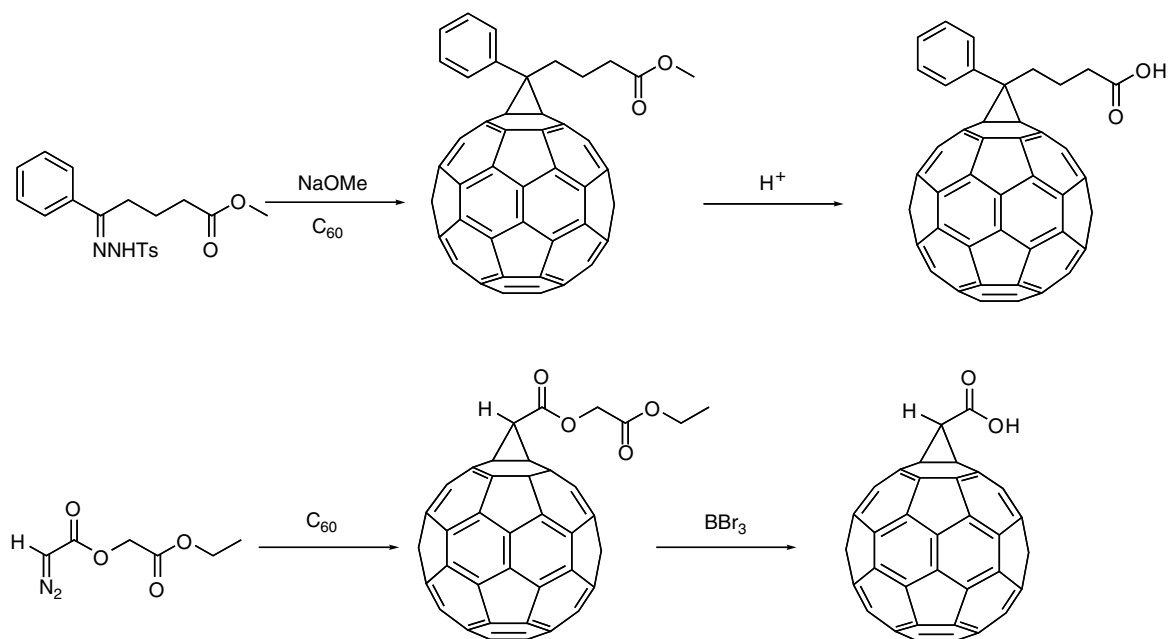
**SCHEME 1.9** Bingel building blocks.



**SCHEME 1.10** Synthesis of methanofullerenes by addition of diazocompounds.

formed.<sup>138,139</sup> The ratio of the 5,6-fulleroid and 6,6-methanofullerene formed is highly dependent on the starting diazo compound used.<sup>140–143</sup>

Given the wide variety of substituted diazomethanes that can be used<sup>144–149</sup> as well as other chemical methods for *in situ* generation of diazo compounds,<sup>146,150–152</sup> a variety of ethanofullerene materials with diverse functional groups has been synthesized and studied. A representative



**SCHEME 1.11** Addition of tosyl hydrazones and diazomalonates.

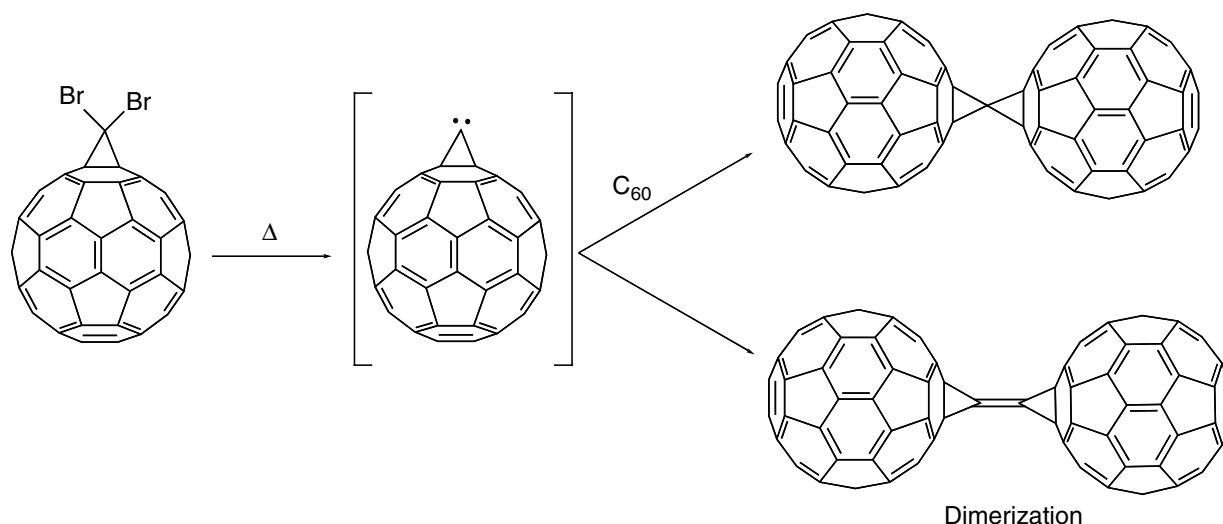
example of base-induced decomposition of tosylhydrazones and immediate entrapment by C<sub>60</sub> of the *in situ* generated diazo compounds and electron-deficient diazomalonates is presented in Scheme 1.11. In the former case, the methyl ester of the corresponding methanofullerene material can be further transformed to the carboxylic acid giving access to a variety of methanofullerene-based derivatives,<sup>153–155</sup> while in the latter case a methanofullerene-carboxylic acid material is generated.<sup>141,156</sup> In either case, esterification or amidation condensation reactions can be easily performed in order to construct useful methanofullerene-based materials for LB films, electron-donor hybrids for technological applications.<sup>157–161</sup>

In an intriguing example based on the Bingel cyclopropanation reaction, diethylmalonate in the presence of an auxiliary base was reacted with (C<sub>60</sub>)<sub>2</sub> dimer to yield a mixture of monoadducts. The monoaddition reaction can be considered as “bisfunctionalization” of one of the C<sub>60</sub> cages explaining the formation of isomers. The same reaction was also carried out on dimeric material encapsulating <sup>3</sup>He in one of the C<sub>60</sub> cages. However, functionalization was more complicated with regio-isomeric products arising from addends either on an empty C<sub>60</sub> cage or a <sup>3</sup>He-encapsulating one.<sup>162</sup>

At this point it should be mentioned that an important field, where the cyclopropanation has been widely used, is the construction of fullerene-dendrimers,<sup>71,72,163–165</sup> possessing fullerenes as either functional cores<sup>51,131,166–171</sup> or branches.<sup>50,172–175</sup> An example of an organofullerene material that has the potential to serve as a core building block for the construction of dendrimeric compounds (as well as a precursor to C<sub>2v</sub> symmetrical pentakisadducts) has been recently synthesized. Thus, utilizing Bingel cyclopropanation reaction under template activation conditions, a highly symmetrical decakisadduct of (C<sub>60</sub>)<sub>2</sub> was produced.<sup>176</sup> Furthermore, several cyclopropanated organofullerene materials have been synthesized for the preparation of fullerene-containing thermotropic liquid crystals. A wide variety of such liquid-crystalline materials was synthesized possessing mono-,<sup>177–179</sup> hexa-addition pattern<sup>180</sup> or even dendritic addends.<sup>181–183</sup>

Finally, the third way that gives access to methanofullerene materials is based on the addition of highly reactive free carbenes to fullerenes. A representative example is the reaction under pyrolytic conditions of sodium trichloroacetate that generates dichlorocarbene, which effectively adds to C<sub>60</sub> furnishing the corresponding methanofullerene derivative.<sup>184</sup> Another interesting example concerns the all-carbon fullerene dimers C<sub>121</sub> and C<sub>122</sub>, which have been synthesized via an intermediate methanofullerene carbene<sup>185,186</sup> as shown in the following [Scheme 1.12](#).





**SCHEME 1.12** Generation and reactivity of fullerene carbenes.

Cyclopropanation reaction has been successfully applied for the functionalization of endohedral metallofullerenes.<sup>187–190</sup> Gd@C<sub>60</sub> endohedral metallofullerene has been derivatized with multiple malonate ester units to increase the solubility.<sup>191</sup> The decakisadduct of Gd@C<sub>60</sub>[C(COOCH<sub>2</sub>CH<sub>3</sub>)<sub>2</sub>]<sub>10</sub> was easily converted into the water-soluble Gd@C<sub>60</sub>[C(COOH)<sub>2</sub>]<sub>10</sub> material, which was medically evaluated and suitable for future biotechnological applications. In another recent example, the isolation and crystallographic characterization of a paramagnetic endohedral metallofullerene cyclopropanated derivative based on *in situ* generated carbene attack from 2-adamantene-2,3-[3H]-diazirine onto the  $\pi$ -spherical network of La@C<sub>82</sub> was reported.<sup>192</sup>

It should be mentioned that cyclopropanations can also be achieved in the solid state with active methylene compounds in the presence of a base under HSVM conditions.<sup>193</sup>

Bisadducts can also be obtained through this procedure. Tether-directed remote multifunctionalization is probably one of the most effective means for controlling multiple additions. It was introduced in 1994 by Isaacs et al.<sup>194</sup> and reviewed in 1999 by Diederich and Kessinger.<sup>195</sup> By controlling the length and geometry of the tether, bis- and trisadduct structures can be almost exclusively obtained. Recent examples appeared in the literature showing the regio- and stereoselective synthesis of bisadducts using bismalonates connected to different carbazol moieties<sup>196</sup> or Tröger bases.<sup>197</sup> The success of the latter relied on the existence of two chiral nitrogen centers, the rigidity and the folded geometry of the Tröger base.

An independent study<sup>198</sup> showed how bis- $\alpha$ -halophenylacetates of the same length produced almost exclusively *trans*-2 or equatorial bisadducts depending on the halogen used. It could be concluded that the nature of the leaving group as well as that of the tether part also plays an important role on the regioselectivity.

### 1.3 SELF-ASSEMBLED FULLERENE ARCHITECTURES

Supramolecular architectures containing fullerenes have attracted a lot of attention.<sup>199,200</sup> Fullerenes can be incorporated into well-ordered arrays by means of different intermolecular interactions, including hydrogen bonding,  $\pi$ -stack interactions, and metal templates. In recent years, novel supramolecular systems have been developed with a wide variety of architectures with very interesting properties.

#### 1.3.1 ROTAXANES, CATENANES, PSEUDOROTAXANES

[2]Rotaxanes are interlocked molecules formed by a macrocycle and a thread (Figure 1.6). The macrocycle is trapped within the thread by two terminal bulky stoppers. These can be obtained by

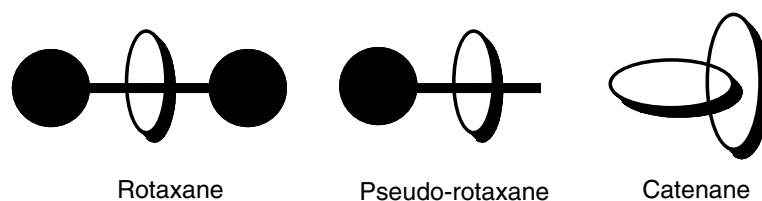


**FIGURE 1.6** Different interlocked architectures.

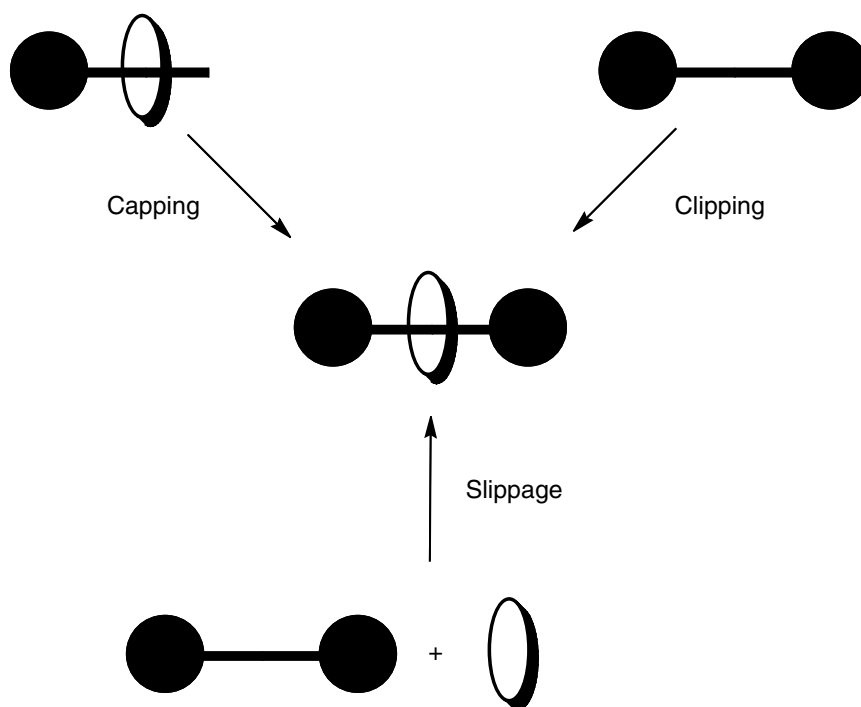


**FIGURE 1.7** Strategies for the preparation of rotaxanes.

different strategies, such as clipping, capping, or slippage (Figure 1.7). The applications of these systems have generated a lot of expectation as they can be used as different molecular devices with applications in energy conversion and storage, information storage, and nanosensing.

Fullerenes have been incorporated into these supramolecular structures as stoppers or as units in the macrocycle, in order to exploit their photo- and electrochemical properties.

The very first example of a rotaxane, including two fullerenes as stoppers, was reported by Diederich and collaborators<sup>201</sup> (Figure 1.8). It was obtained by the capping strategy where the thread contained a phenanthroline unit and a fullerene as a stopper. Then, by coordination of the two phenanthroline units with copper, the macrocycle was introduced into the thread and was locked by the addition of another fullerene stopper.

More recently, Schuster and coworkers<sup>202</sup> have successfully used this metal-templated strategy to build similar structures containing fullerenes as stoppers but including a porphyrin unit into the macrocycle. The fullerenes were functionalized using the Bingel reaction. These systems containing porphyrins are used to transmit and process solar energy into other energy sources. This topic will be analyzed in depth in forthcoming sections.

In a different article from Schuster's laboratory,<sup>203</sup> an analogous rotaxane was prepared. The fullerene unit was contained in the macrocycle and the porphyrins were used as stoppers. The macrocycle was threaded following metal-templated capping strategy. The structural distribution allowed the preparation of novel catenane systems by complexation of the two terminal Zn-porphyrins when one equivalent of a bidentate ligands, such as 1,4-Diazabicyclo[2.2.2]octane

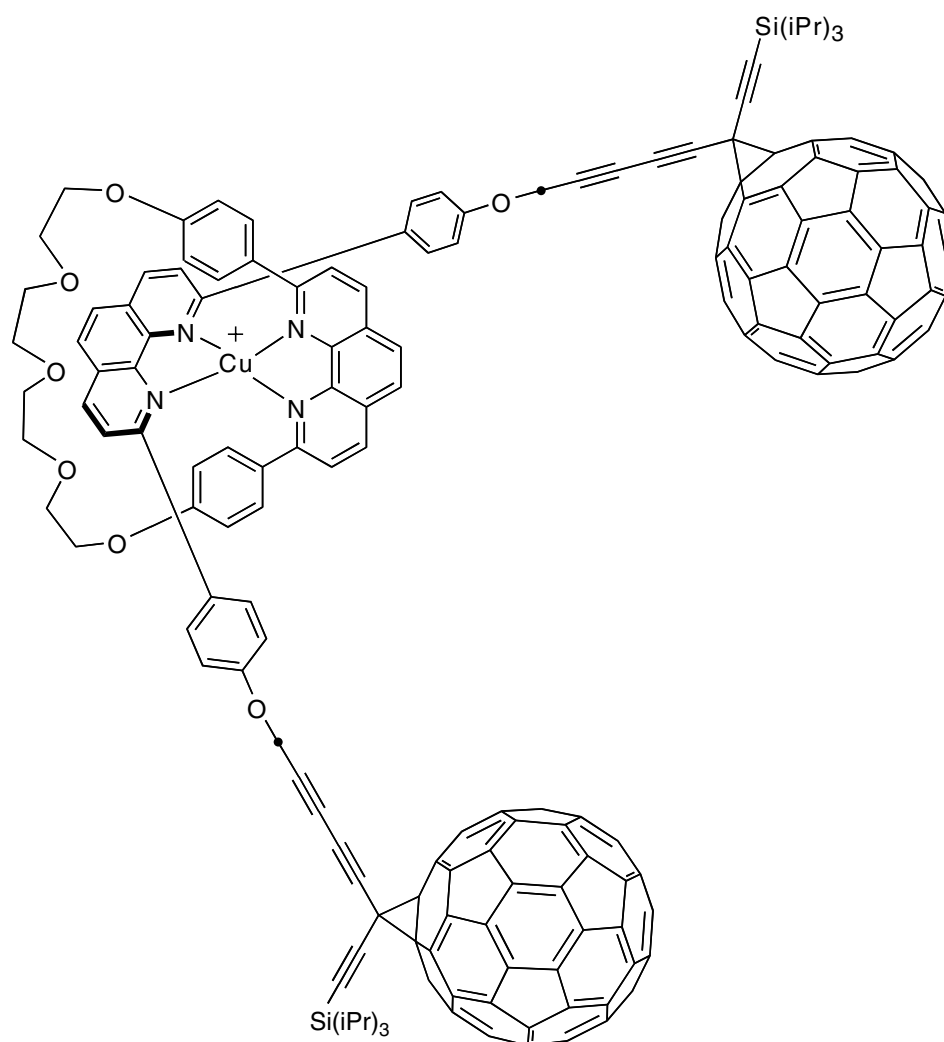


**FIGURE 1.8** Phenantroline based fullerene rotaxane.

(DABCO) and 4,4'-bipyridine, were used. A subsequent addition of one extra equivalent of the bidentate ligand converted the 1:1 catenane supramolecular complex into a 2:1 rotaxane complex.

Catenanes consist of two or more interlocked macrocycles (Figure 1.6). The first example of a catenane containing a fullerene was first reported in a collaborative work between Stoddard and Diederich<sup>204</sup> (Figure 1.9). The [2]catenane was obtained by molecular recognition between  $\pi$ -electron-rich aromatic and  $\pi$ -electron-deficient aromatic units. A bisfunctionalized fullerene prepared by tether addition, contained the  $\pi$ -electron-rich aromatic unit. Then the  $\pi$ -electron-deficient aromatic unit was used to clip the second macrocycle.

Following this methodology, rotaxanes and catenanes have been prepared.<sup>205</sup> A thread was synthesized with one fullerene as a stopper, a naphthalenetetracarboxylic diimide moiety and a 1,3-dicarboxylic acid unit at the other end. The electron-deficient diimide was capable of recognizing an electron-rich naphthocrown ether. When the reaction was carried out in the presence of 1,8-Diazabicyclo[5.4.0]undec-7-ene (DBU), an excess of  $C_{60}$  a [2]rotaxane was obtained. But if the experiment was carried out only with DBU, a [2]catenane was obtained by the formation of a Bingel bisadduct.

Rotaxanes can be assembled using other molecular interactions, such as hydrogen bonds. In a collaborative work between Prato and Leigh groups,<sup>206</sup>  $C_{60}$  was functionalized following the 1,3-dipolar fashion (Figure 1.10). A glycyglycine template was introduced into the molecule, as well as a long alkyl chain and a phenolic stopper. Macrocyclization of *p*-xylylenediamine and isophthaloyl

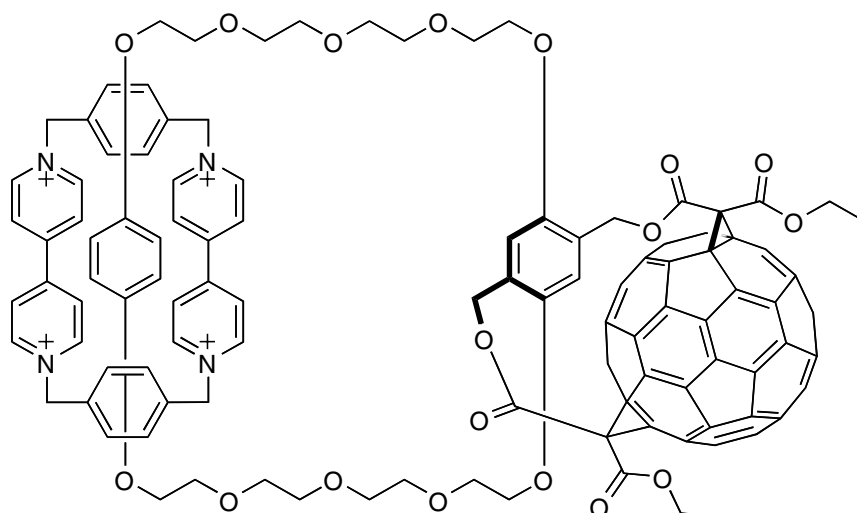


FIGURE 1.9 Fullerene catenane.

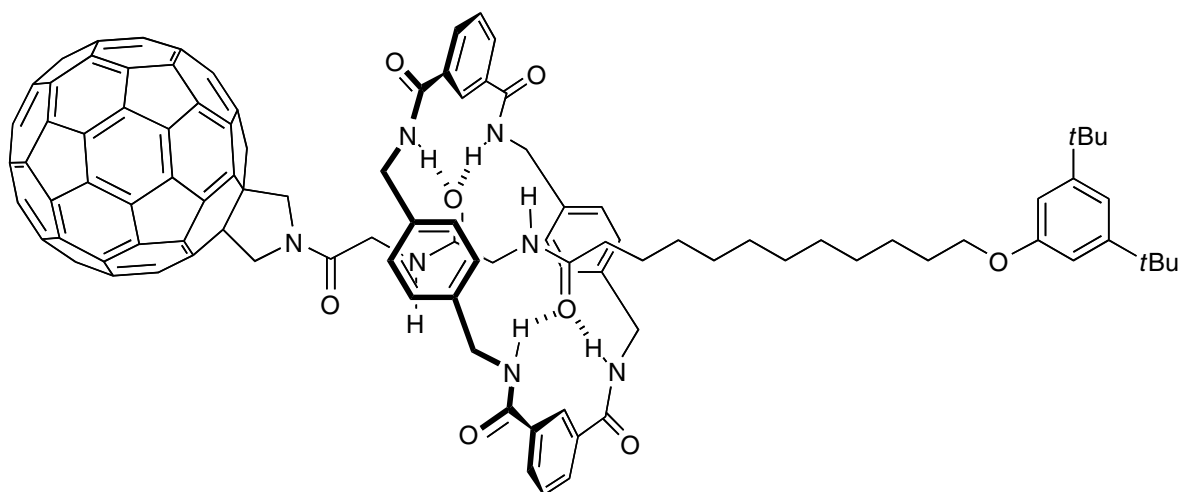


FIGURE 1.10 Hydrogen bond assembled rotaxane.

dichloride templated by hydrogen bond clipped the rotaxane around the glycylglycine residue. The importance of this work relied on the possibility of switching the macrocycle within the thread. The macrocycle bonds to the peptide residue in solvents such as chloroform or dichloromethane. In highly polar solvents such as Dimethylsulfoxide (DMSO), the hydrogen bonds were disrupted and the macrocycle was preferentially located over the alkyl chain. The location of the macrocycle can be monitored by means of NMR spectroscopy and time-resolved spectroscopy.

In another example of rotaxanes assembled by hydrogen bonding, the thread was capped in the macrocycle and stoppered by two porphyrins.<sup>207</sup> The macrocycle functionalized with the hydrogen bond template and butadiene sulfone. Then,  $C_{60}$  was added to the macrocycle using Diels–Alder cycloaddition, as 1,3-butadiene was generated *in situ* from butadiene sulfone.

Other structures known as pseudorotaxanes, analogous to rotaxanes but with none, or only one stopper, have also generated a lot of interest (Figure 1.6). These assemblies are not interlocked, so both the thread and the macrocycle are free to dissociate. The first pseudorotaxane bearing a fullerene was published in 1999.<sup>208</sup> It was prepared by complexation between two  $C_{60}$  units functionalized via Bingel. One of them was functionalized with a crown ether, while the other one was functionalized with a secondary amine. The secondary amine was transformed into an ammonium salt. Then the fullerene crown ether bound the ammonium salt and the association constant was

determined by NMR as  $K_a = 970 M^{-1}$ . An interesting feature regarding the reversibility of these systems should be highlighted. When the fullerene ammonium salt was complexed with dibenzo-24-crown-8, the fluorescence of the macrocycle was quenched by proximity of the fullerene. Then, in the presence of a base the ammonium salt was transformed in the free base and the two units disassembled switching “on” the fluorescence of the system.

Similar systems have been successfully prepared by coordination of fullerene ammonium salts with phthalocyanine<sup>209,210</sup> (Figure 1.11) and porphyrin<sup>211</sup> crown ethers. The association constants, respectively, were  $K_a = 153,000$  and  $K_a = 375,000 M^{-1}$ ; such high values can be associated with the stabilization of the supramolecular complex by  $\pi$ -stacking interactions between the heterocycles and  $C_{60}$ . The quenching of the fluorescence of both the phthalocyanine and the porphyrin was observed.

### 1.3.2 NANORINGS, PEAPODS

New supramolecular motifs of fullerenes with concave–convex structures have been developed very recently by  $\pi$ -stack interactions. It comprises interactions between fullerenes and different curved carbon structures, such as nanorings or nanotubes. Both structures have  $\pi$ -orbitals oriented radially, as well as the fullerenes.

Nanorings are closed loops formed by conjugated  $\pi$ -orbitals. They are very interesting from the point of view that they can host different molecules depending on the size of the ring. Fullerenes can be hosted by nanorings as shown by Kawase and Oda.<sup>212</sup> They prepared [6]- and [8]paraphenyleneacetylene and studied their complexation with  $C_{60}$  and with *bis*(ethoxycarbonyl)methanofullerene. The experiments with  $C_{60}$  showed the formation of a 1:1 supramolecular complex with [6]paraphenyleneacetylene (Figure 1.12) and the association constant was determined ( $K_a = 16,000 M^{-1}$ ). The same measurements were attempted with *bis*(ethoxycarbonyl)methanofullerene but the changes in absorption were too small to measure a reliable association constant. On the other hand, it was possible to obtain an X-ray structure from the fullerene monoadduct and [6]paraphenyleneacetylene, confirming the structure of the complex. The experiments with [8]paraphenyleneacetylene showed none or very small complexation with  $C_{60}$ .

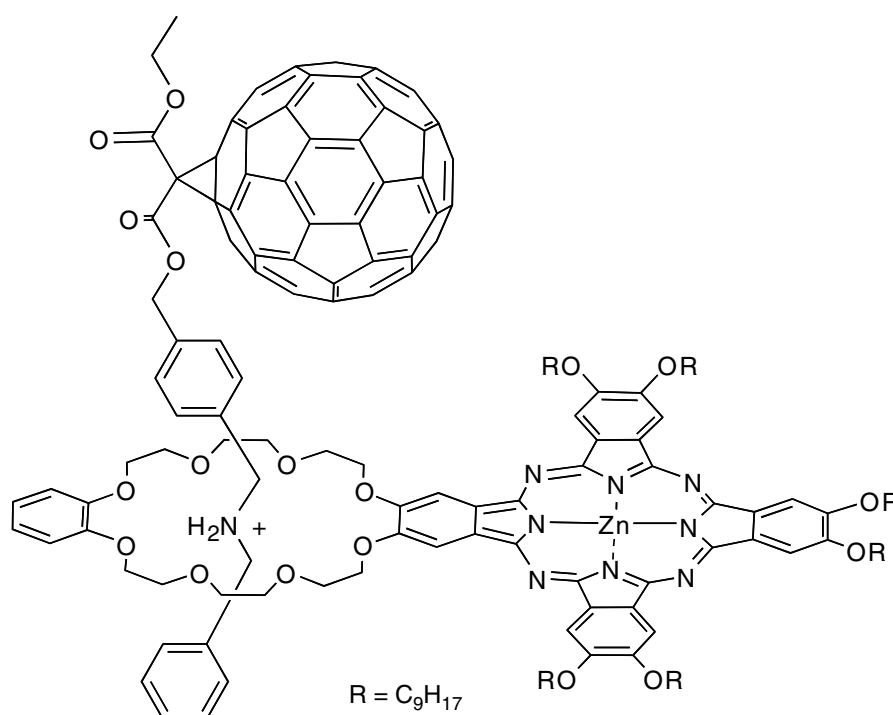


FIGURE 1.11 Phthalocyanine–fullerene pseudorotaxane.

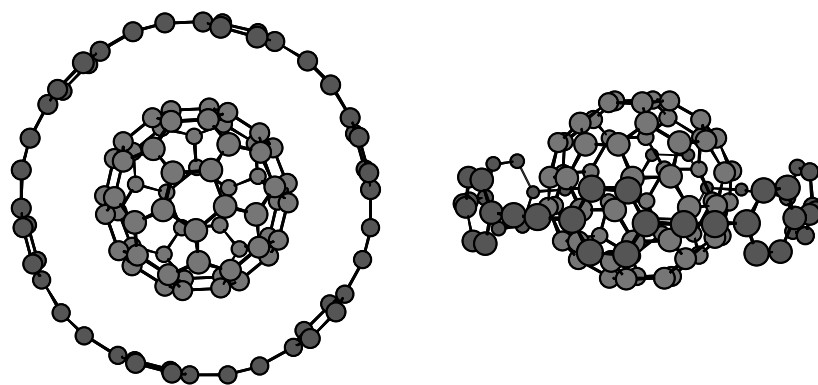


FIGURE 1.12  $C_{60}$ -nanoring complex.

In a different article from the same authors,<sup>213</sup> the complexation of  $C_{60}$  and  $C_{70}$  with [6]- and [7]paraphenyleneacetylene was studied. Also other complexation studies were carried out with the novel isomers of [7]paraphenyleneacetylene that have 1,4- or 2,6-naphthylene units diametrically opposed. The calculation of the association constants was attempted but they were too large to be determined precisely ( $>5 \times 10^4$ ), which indicated that very stable complexes were formed. Fluorescent measurements were carried out from these complexes, providing a lot of information about the estimated relative stability of the whole series of rings with  $C_{60}$  and  $C_{70}$ . The results were consistent with the values of the association constants and also showed that the new naphthylene nanorings are very efficient fluorescent sensors for fullerenes.

During the synthesis and purification of the different paraphenyleneacetylene and 1,4-naphthyleneacetylene nanorings, it was found that big rings could form inclusion complexes with smaller rings.<sup>214</sup> [6]Paraphenyleneacetylene could be inserted within the larger [9]paraphenyleneacetylene, the association constant could only be determined at  $-60^\circ\text{C}$  ( $K_a = 340 \pm 45 \text{ M}^{-1}$ ). The same behavior was observed with the analogous 1,4-naphthyleneacetylene nanorings showing much higher association constants at  $-60^\circ\text{C}$  ( $K_a = 11,000 \pm 1400 \text{ M}^{-1}$ ) because of the larger contact area. In order to prepare complexes including fullerenes,  $C_{60}$  was first included within the smaller ring as done in previous experiments and subsequently these complexes were then assembled with the larger ring. NMR experiments proved the formation of these onion-type complexes (Figure 1.13). The association constants could only be calculated for the [9]paraphenyleneacetylene $\supset$ ([6]paraphenyleneacetylene $\supset$  $C_{60}$ ) complex at  $-60^\circ\text{C}$  ( $K_a = 410 \pm 80 \text{ M}^{-1}$ ).

Other interesting structures known as carbon peapods have been developed in the last years. Carbon peapods are single-walled carbon nanotubes (SWCNTs) that are filled with fullerenes (Figure 1.14). They are considered as a new supramolecular carbon allotrope. Carbon peapods were first reported in 1998<sup>215</sup> when they were detected by high-resolution transmission electron microscopy (HRTEM) as side products during the production of carbon nanotubes. Since then, several methods for the efficient filling of empty SWCNTs have been developed.

The first production method was reported by Luzzi and Smith in 2000.<sup>216</sup> Carbon peapods were prepared from raw nanotubes produced by pulsed laser vaporization. Several defects (such as side-wall holes and open ends) were introduced on the surface of the nanotubes by refluxing the material in nitric acid, thus facilitating the insertion of fullerenes. Subsequently they were annealed at high temperatures and low pressures.  $C_{60}$  was only inserted in 1.3 to 1.4 nm diameter SWCNTs that are the only ones that permit the preferred graphitic 0.3 nm van der Waals separation between the fullerene and the nanotube.

Endohedral fullerenes such as  $\text{Ce}@C_{82}$ ,<sup>217,218</sup>  $\text{Gd}@C_{82}$ ,<sup>219</sup>  $\text{Dy}@C_{82}$ ,<sup>220</sup>  $\text{La}@C_{82}$ ,<sup>221</sup>  $\text{Sm}@C_{82}$ ,<sup>221</sup>  $\text{Ti}_2@C_{82}$ ,<sup>222</sup>  $\text{La}_2@C_{82}$ ,<sup>223</sup> and  $\text{Gd}_2@C_{82}$ ,<sup>224</sup> have been introduced in carbon nanotubes. Different motions have been observed by HRTEM of peapods containing  $\text{Ce}@C_{82}$ .<sup>217</sup> The images showed the translational motion of the fullerenes inside the nanotubes, as well as rotation of the fullerene units.

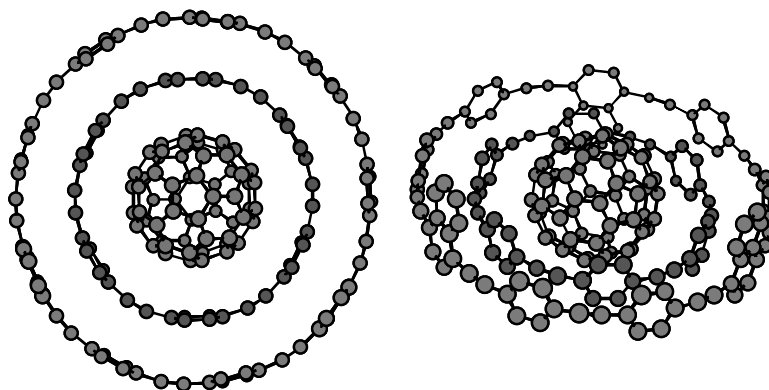


FIGURE 1.13  $C_{60}$  Onion type complex.

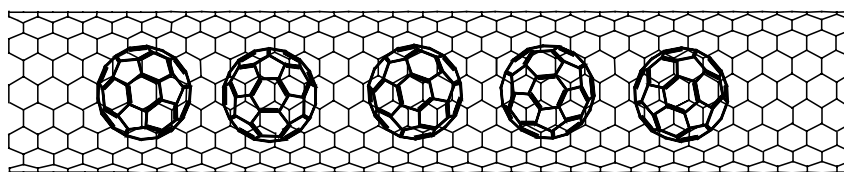


FIGURE 1.14 Carbon peapods.

Yudasaka and coworkers<sup>225</sup> introduced two very interesting and simple methods that do not require extreme conditions for the preparation of carbon peapods. These processes are known as nano-extraction and nano-condensation and are easy to apply and require no special skills. First, commercial SWCNTs were treated under extreme conditions to open holes in sidewalls and ends. In nano-extraction,  $C_{60}$  crystallites were sonicated in ethanol, then the nanotubes were added to the solution and left at room temperature for 1 day. TEM images showed  $(C_{60})_n@SWCNTs$  in a 50 to 70 filling percentage. The success of this method relies on the high affinity of the fullerenes for the nanotubes that was enhanced by the medium, due to the low affinity of the SWCNTs and  $C_{60}$  to ethanol. In nano-condensation, SWCNTs were deposited on a grid surrounded by filter paper. After the addition of a saturated solution of  $C_{60}$  in toluene, the SWCNTs were filled in at 50 to 70% as estimated by TEM, in only a few seconds. The mechanism of this process was not completely understood. These two methods demonstrated that high temperatures are not needed for filling SWCNTs, therefore other molecules that are not stable to sublimation or evaporation temperatures could also be inserted.

Briggs and coworkers<sup>218,226</sup> have discovered that SWCNTs can be filled with fullerenes in supercritical fluids using low temperatures (30 to 50°C). These low-temperature conditions allowed the SWCNTs to fill with empty, endohedral, and functionalized fullerenes. Nanotubes were produced by the arc discharge method. During purification, the ends were opened and also sidewall holes were introduced. Then a mixture of nanotubes and  $C_{60}$  was exposed to pressurized supercritical  $CO_2$  to 150 bar at 50°C and the cycle was repeated six times yielding  $(C_{60})_n@SWCNTs$  in an ~70% filling factor. The general applicability to this filling procedure has been demonstrated by the introduction of different functionalized fullerenes such as  $C_{61}(COOEt)_2$  or  $Er_3N@C_{80}$ . However, experiments<sup>226</sup> carried out with  $C_{61}(COOH)_2$  showed that the fullerene derivative was preferentially coordinated outside the SWCNTs rather than forming peapods. Supercritical  $CO_2$  showed to facilitate the penetration of the fullerene derivatives inside the nanotubes by different factors. These include (1) low solvation of both fullerenes and SWCNTs, (2) low viscosity and lack of surface tension that promote the solvent to flow through the nanotubes without being encapsulated, thus leaving free room for the insertion of fullerenes, and (3) cleans the surface and the holes as well as separates the nanotube bundles.

### 1.3.3 SUPRAMOLECULAR ASSEMBLIES WITH PORPHYRINS

Surprisingly, fullerene derivatives can form complexes with planar electron-rich macrocycles, such as porphyrins. The association between fullerenes and porphyrins was first observed by x-ray crystallography in a covalently linked fullerene–porphyrin.<sup>227,228</sup> Since then, a variety of x-ray structures from co-crystals of different fullerenes and porphyrins have been reported.<sup>229,230</sup> The nature of the supramolecular interactions between these two units is not fully understood. It has been suggested that the association can be due to van der Waal interactions<sup>229,231</sup> to electrostatic interactions,<sup>232</sup> and to charge-transfer interactions.<sup>233,234</sup> Theoretical calculations<sup>235</sup> showed that the electrostatic interactions contribute approximately 50 to 60% of the total attractive interactions. Also, a charge transfer contribution of about 0.10 to 0.14 electrons from the porphyrin to the fullerene was observed. More importantly, the high affinity of fullerenes and porphyrins was not only observed in the solid state, but also in solution as shown by upfield shifts in both <sup>1</sup>H- and <sup>13</sup>C-NMR experiments in toluene.<sup>229</sup>

These results stimulated further work, and new porphyrin hosts were designed and synthesized for binding fullerenes. A type of bis-porphyrin systems, known as “porphyrin jaws,” were prepared by Reed and coworkers.<sup>236</sup> The complexation of several “jaws” with fullerenes was studied both in solid state and in solution. The most successful binding was obtained with a palladium-based “jaw” (Figure 1.15) as observed by MALDI mass spectrometry. Also, mass spectrometry experiments with mixtures of fullerenes were carried out, showing the different affinities. Association constants around 490 to 5200  $M^{-1}$  were determined between bis-metalated porphyrin “jaws” and  $C_{60}$  using NMR. The highest association constant was obtained for the free bis-porphyrin.

Novel supramolecular peapod systems<sup>237</sup> have been developed using dendrimeric “jaws.” Once the porphyrin “jaws” complexed with  $C_{60}$  or  $C_{70}$ , the hexacarboxylic porphyrins polymerized unidirectionally through hydrogen bond dimerization of the side acid functionalization affording the supramolecular peapods with the dendrimeric envelope. The fibers observed by TEM displayed a constant diameter of 12 to 15 nm, which agreed with the diameter estimated from the molecular model.

Cyclic porphyrin dimers show high affinity for  $C_{60}$  ( $K_a = 670,000 M^{-1}$ ) (Figure 1.16).<sup>238</sup> Dendrimeric systems containing this cyclic bis-porphyrin dimers have also been prepared.<sup>239</sup> The high affinity of this system for fullerenes was observed even with the high branched dendrimers for both  $C_{60}$  ( $K_a = 15,000 M^{-1}$ ) and  $C_{70}$  ( $K_a = 230,000 M^{-1}$ ). Different lengths with bis-porphyrin cyclic hosts have been investigated<sup>240</sup> in order to separate different fullerenes from fullerene mixtures obtained directly from the carbon-soot method. The extraction experiments showed that the different size bis-porphyrin hosts extracted selectively the higher fullerenes as was verified by HPLC–MS. The association constants were calculated by spectroscopic titration showing 118 and 16 times larger affinities for  $C_{96}$  ( $K_a = 3.0 \times 10^7 M^{-1}$ ) than those obtained for  $C_{60}$  ( $K_a = 5.1 \times 10^5 M^{-1}$ ) and  $C_{70}$  ( $K_a = 1.3 \times 10^7 M^{-1}$ ).

### 1.3.4 COMPLEMENTARY HYDROGEN BONDED SUPRAMOLECULAR SYSTEMS

Complex supramolecular architectures can be prepared by complementary hydrogen-bond donor–acceptor systems. Hydrogen bonds not only provide a high directionality and selectivity, but also introduce the possibility of multiple bonding in complementary donor–acceptor patterns, thus increasing the stability and the selectivity of the supramolecular system.

Hummelen<sup>241</sup> and Martin<sup>242</sup> pioneered the introduction of self-complementary hydrogen bond patterns in functionalized fullerenes. Quadrupole hydrogen bond motifs based on 2-uridopyrimidin-4-ones, were used to prepare self-assembled fullerene dimers (Figure 1.17). The dimers were successfully assembled and a high association constant was measured ( $K_a = 1 \times 10^6 M^{-1}$ ).<sup>241</sup> Moreover, a fluorescence quench of 50% was observed in the assembled dimer.<sup>242</sup> On the other hand, an enhancement of the fluorescence was detected when disrupting hydrogen bond solvents were added. These results evidenced the strong electronic coupling occurring through the hydrogen bond.

More sophisticated systems have been prepared following the quadrupole hydrogen bond strategy. Fullerenes were assembled with oligo(*p*-phenylenevinylene)s (OPVs), and the photo- and electrochemical properties of these new materials with applications in the field of plastic solar cells



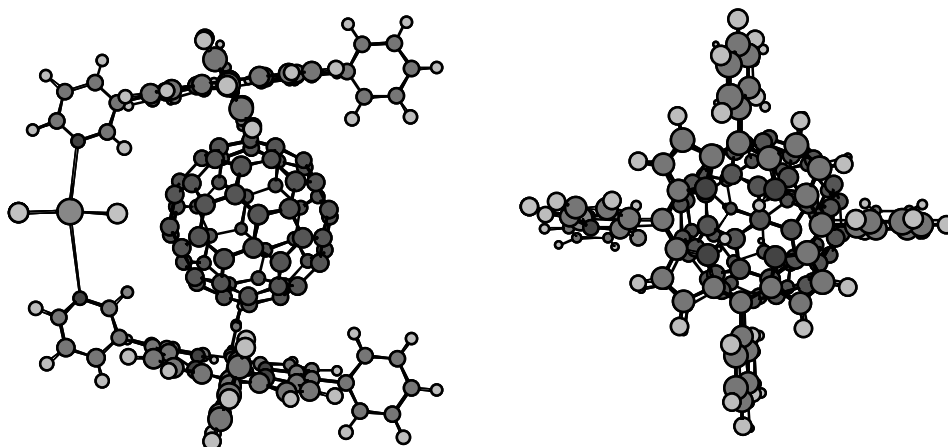


FIGURE 1.15 Porphyrin jaws. Left: Side view. Right: Top view.

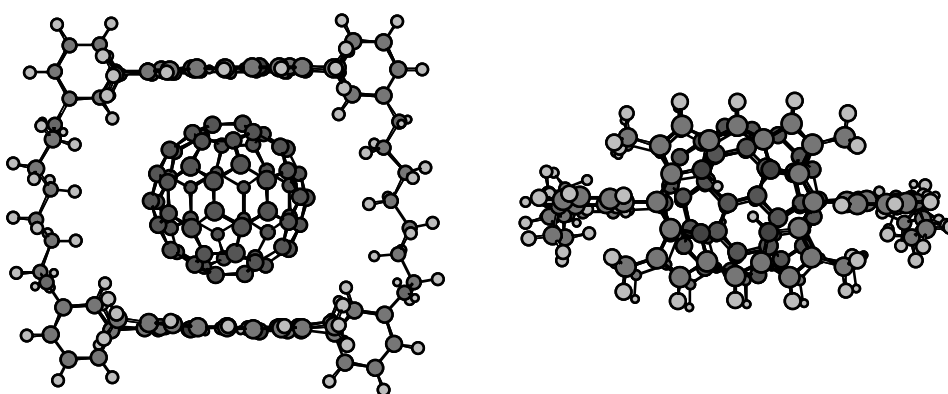


FIGURE 1.16  $C_{60}$ -porphyrin dimer complex. Left: Side view. Right: Top view.

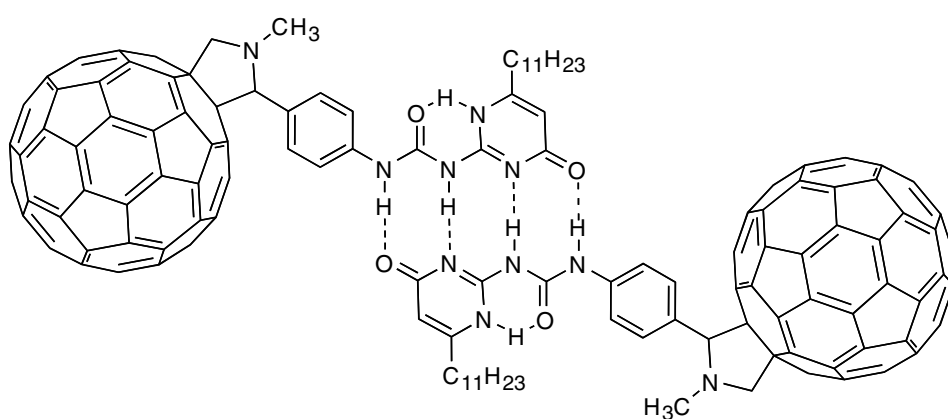


FIGURE 1.17 Self assembled fullerene dimer.

were studied (Figure 1.18).<sup>243,244</sup> Additionally,  $C_{60}$  was functionalized with two 2-uridopyrimidin-4-one moieties, which self-assembled as a linear supramolecular fullerene polymer<sup>245</sup> as well as other motifs with bis-functional OPVs.<sup>246</sup>

Hydrogen bond assemblies are not restricted to 2-uridopyrimidin-4-ones motifs. In an elegant example from Martin and collaborators,<sup>247</sup> a wide variety of fullerene-tetrathiafulvalene systems was prepared through complementary recognition between carboxylates and guanidinium salts by donor-donor/acceptor-acceptor hydrogen bond motifs (Figure 1.19).

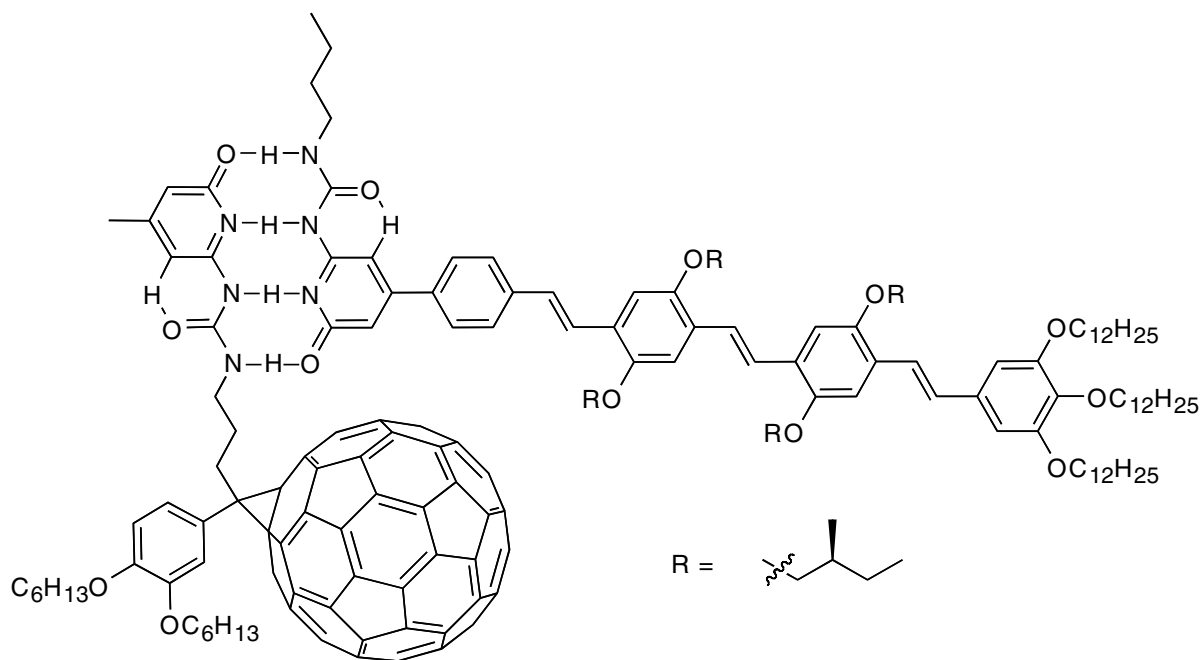


FIGURE 1.18 OPV-C<sub>60</sub> hydrogen bond assembly.

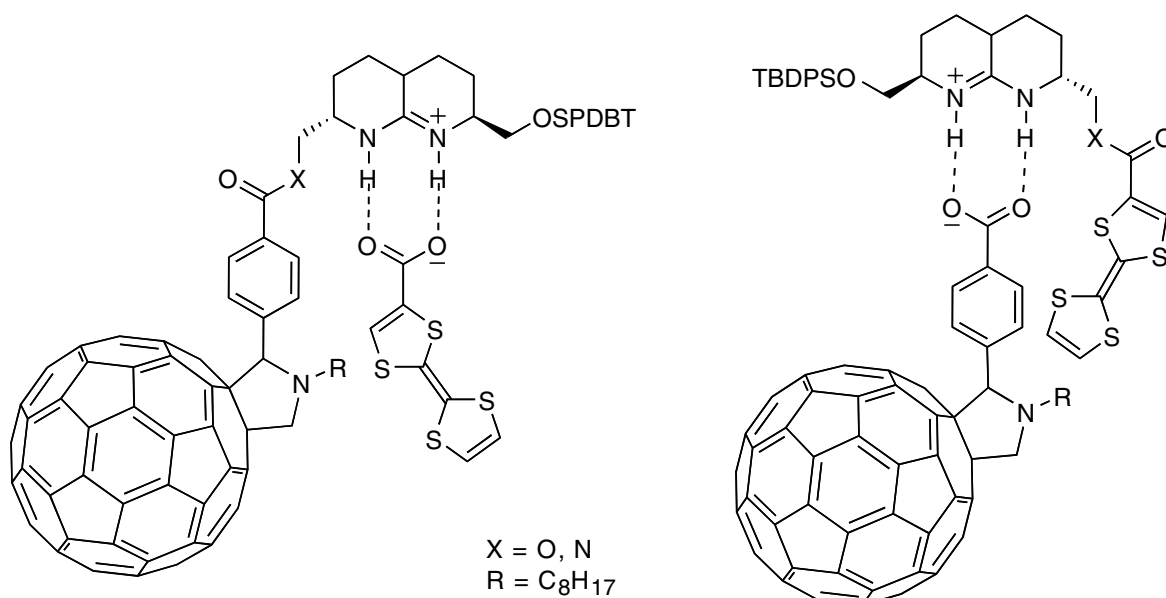


FIGURE 1.19 Recognition between carboxylates and guanidinium salts.

## 1.4 APPLICATIONS

In the last few years, scientists have employed the different methodologies for the functionalization of fullerenes, as well as the different types of supramolecular interactions to build a variety of very interesting molecular architectures with efficient applications. In the next section, some of the most promising fields of application of fullerene-containing systems will be summarized. The inherent photo- and electrochemical properties of fullerenes have played an active role in the performance of the system.

### 1.4.1 DONOR–ACCEPTOR SYSTEMS

The research on donor–acceptor systems involving fullerenes has attracted a lot of attention, as they can be used as artificial photosynthetic systems to transform light into chemical energy.

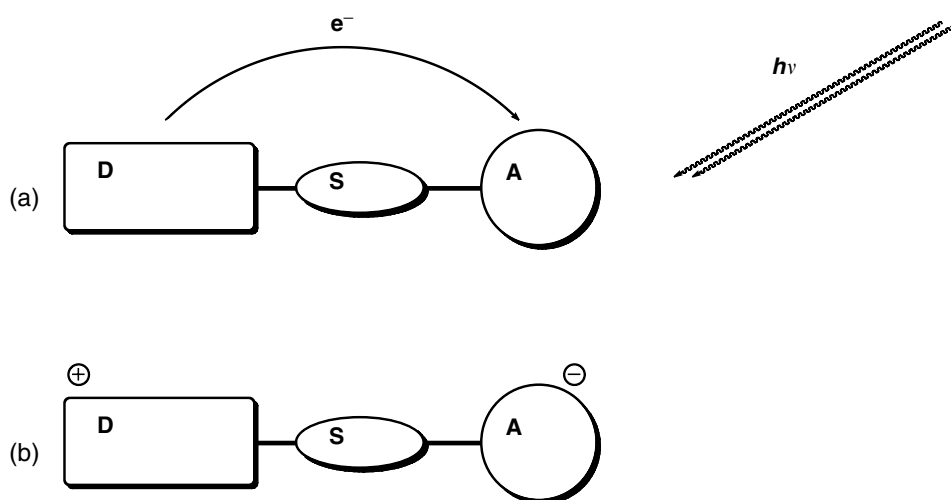


**FIGURE 1.20** (a) Photoinduced electron transfer; (b) radical pair formed.

The simplest systems, known as dyads, can be described as the result of two units, an electron donor (D) and an electron acceptor (A), linked together through covalent or noncovalent interactions. After photostimulation,<sup>248</sup> the charge transfer is induced between the two units leading to a charge-separated state where the energy is stored (Figure 1.20).

An important feature that should be taken into account is the lifetime of the charge-separated state formed. The excited state should be sufficiently long-lived to be converted into chemical energy. In order to increase the lifetimes, C<sub>60</sub> has been widely used as an electron-acceptor unit, not only because of the high electron affinity<sup>7–9</sup> but also because of the high delocalization of the electron in the three-dimensional  $\pi$ -system and its small reorganization energy.<sup>249</sup> Other factors such as the rate of charge recombination, affect directly the lifetime of the charge-separated state. Therefore, the selection of the linker (or spacer) between the two units is very important. It controls the distance, the orientation, and the electronic coupling between the two units, and thus the electron transfer and the rate of charge recombination. Depending on the nature of the linker, covalent or noncovalent, both the electron transfer and the charge recombination can occur through bond or through space.

Additionally, a wide range of electron donors has been explored and they will be reviewed in the following sections.

#### 1.4.1.1 Dyads Containing Photoactive Electron Donors

Electron transfer takes place easily between fullerenes and heterocycles that absorb light in the visible region of the spectrum, such as porphyrins, phthalocyanines, and subphthalocyanines.

Porphyrin dyads have been by far the most investigated systems.<sup>250–253</sup> Dyads linked through covalent spacers have been constructed and investigated. In some architectures, the porphyrin was linked close to the fullerene<sup>254–262</sup> or forced apart.<sup>159,263–265</sup>

1,3-Dipolar addition was used to prepare architectures bearing porphyrins in position 2 of fulleropyrrolidines.<sup>254–256</sup> These systems have shown the longest lifetimes reported in dyads to the moment (230  $\mu$ sec at 25°C)<sup>255</sup> and have been highlighted for their simplicity and effectiveness (Figure 1.21).<sup>266</sup>

Strapped and parachute-like fullerene–porphyrin architectures have been prepared via Bingel with flexible linkers that allow the porphyrin to get very close to the fullerene.<sup>258–262</sup>

Other systems have been assembled by means of supramolecular interactions in rotaxane architectures,<sup>202,203,207,211</sup> in sandwiched  $\pi$ -stack complexes<sup>229–234,236–240</sup> or by metal coordination.<sup>267–271</sup>

A zinc tetraphenyl porphyrin (Zn(TPP)) was noncovalently linked to a C<sub>60</sub> derivative via axial pyridine coordination to the metal (Figure 1.22).<sup>267–270,272</sup> Photoexcitation of the Zn-complex led to electron transfer with very long lifetimes of the charge-separated pairs as revealed by optical

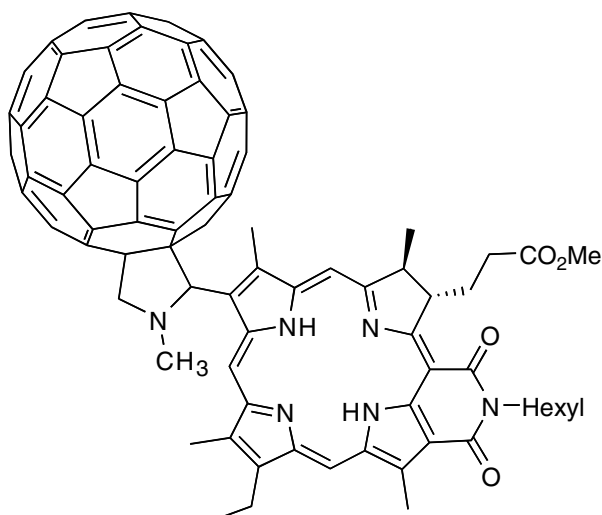


FIGURE 1.21 Simple fullerene–porphyrin dyad.

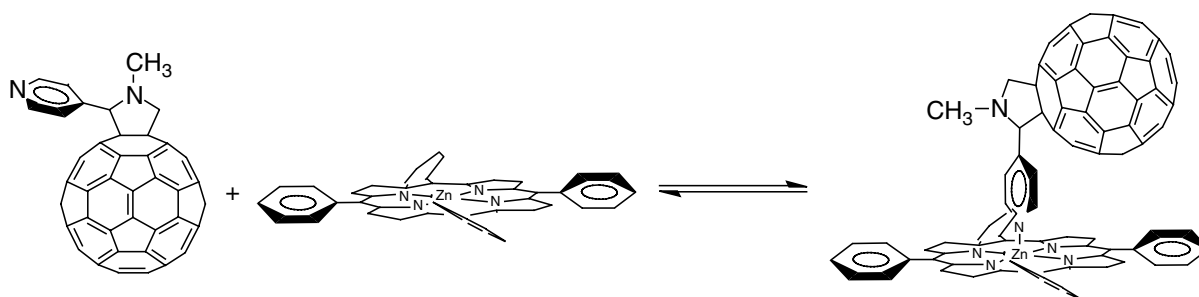


FIGURE 1.22 Preparation of dyads by metal complexation.

spectroscopy and confirmed by time-resolved electron paramagnetic resonance spectroscopy. Similar fulleropyrrolidine complexes, including porphyrins covalently linked, have been reported.<sup>269–271</sup>

Phthalocyanines and subphthalocyanines have been used for the construction of different efficient dyads. Once more, the most straightforward approach involved 1,3-dipolar addition yielding fulleropyrrolidines substituted with phthalocyanines in position 2.<sup>154,273,274</sup> Various pseudorotaxane architectures were prepared by Torres and collaborators<sup>209,210</sup> (Figure 1.11, see Section 1.3.1). The most notorious properties of these systems relied on the possibility of switching “on” and “off” the electron transfer by the addition of acid or base. Under acidic conditions the fullerene ammonium salt complexed with the phthalocyanine crown ether, allowing photoinduced electron transfer between the two units. While under basic conditions the two units are apart and no electron transfer took place.

A wide variety of substituted subphthalocyanines<sup>275,276</sup> has been assembled by complexation with 2-phenony-substituted fulleropyrrolidines. The peripheral substitution in the subphthalocyanine moiety led to the tuning of the electron-donating properties of the dyads.

#### 1.4.1.2 Dyads Containing Nonphotoactive Electron Donors

Donor–acceptor systems can also be prepared using nonphotoactive electron donors such as tetrathiafulvalene<sup>277</sup> (TTF) and ferrocene units. In this case, the fullerene unit (electron acceptor) gets excited by light irradiation to its singlet state, while the electron donor does not absorb light and remains in its ground state; this is followed by electron transfer.<sup>248</sup>

The first synthesis of C<sub>60</sub>–tetrathiafulvalene dyads was done via 1,3-dipolar cycloaddition by using the appropriate azomethine ylides substituted with a tetrathiafulvalene unit as electron donor

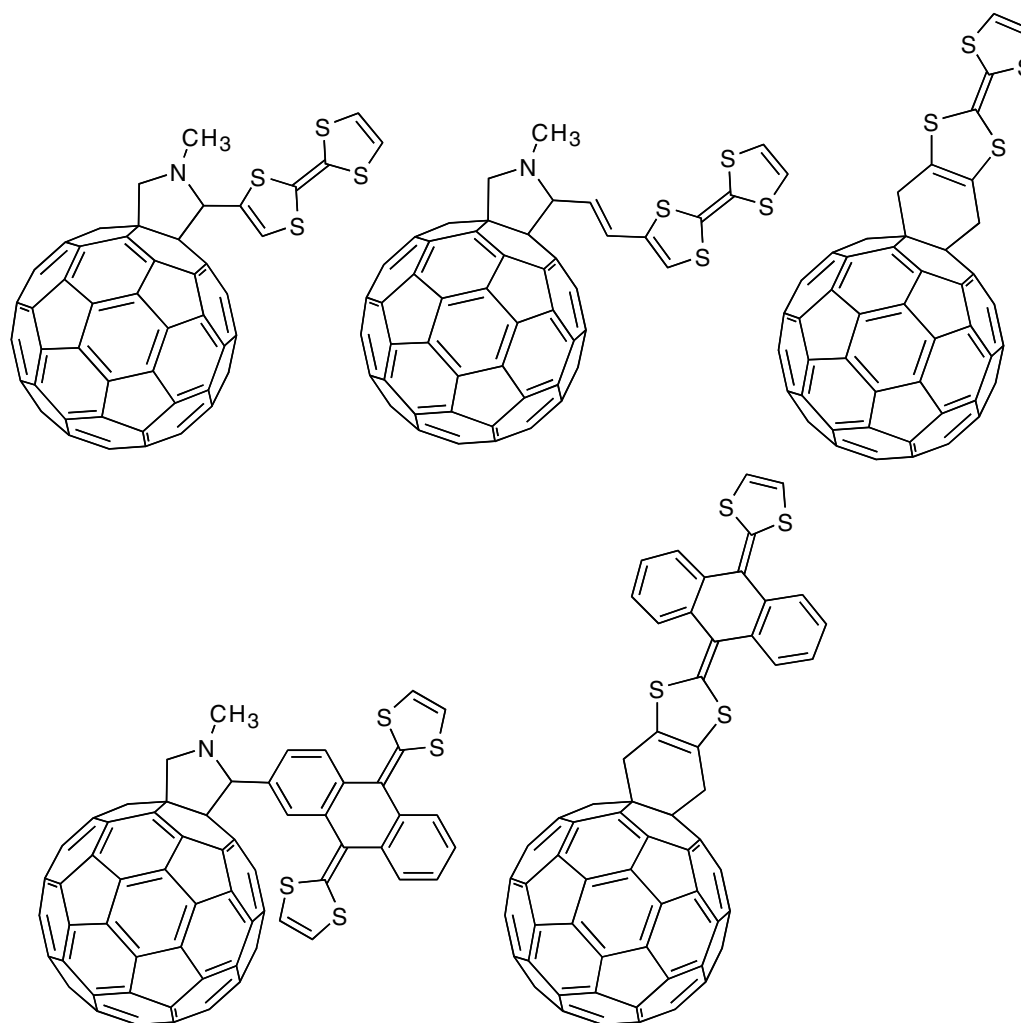


**FIGURE 1.23** Fullerene–TTF dyads.

(Figure 1.23).<sup>278,279</sup> These were followed by more sophisticated approaches that had highly conjugated tetrathiafulvalene units linked to  $C_{60}$  skeleton (Figure 1.23).<sup>280</sup> The idea for synthesizing such  $\pi$ -extended-tetrathiafulvalenes stemmed from their ability to form stable dication species that introduced electrical and magnetic properties, in sharp contrast with simple tetrathiafulvalenes that are known to form only stable radical cations.<sup>281,282</sup> However, in the early dyads, no electronic interactions between the donor–acceptor units were observed.<sup>283</sup>

When the redox units were attached via Diels–Alder cycloaddition,<sup>284–286</sup> efficient electron- and energy transfer took place between the active units of the system by a through-bond coupling mechanism (Figure 1.23).

Electron transfer events were also detected when  $C_{60}$  was functionalized by 1,3-dipolar addition, using azomethine ylides<sup>283,287</sup> with vinyl spacers bearing TTF moieties, along with azides bearing TTF<sup>288</sup> and  $\pi$ -extended-TTF units (Figure 1.23).<sup>289</sup>

Other examples of active dyads bearing TTFs functionalized by Bingel-type adducts were reported.<sup>290</sup>

Recently, a variety of supramolecular  $C_{60}$ –TTF dyads have been assembled through complementary recognition between guanidinium salts and carboxylic acids, through donor–donor–acceptor–acceptor hydrogen bond motifs.<sup>247</sup> Eight different dyads were prepared and studied displaying different functional groups and spacers (Figure 1.19, see Section 1.3.4). Intramolecular electron transfer occurred between the two units but this was not observed when solvents that disrupt hydrogen bonds were added. Alternatively, intermolecular electron transfer was detected.

Ferrocene (Fc) is another good example of electron donor that is not excited upon light irradiation. Some fullerene–ferrocene dyads have been synthesized following the methodology of 1,3-dipolar cycloaddition to  $C_{60}$ , with either variable spacing building blocks or rigid linkers, in order to tune the redox properties of the system.<sup>177,279,291–294</sup> Another novel dyad that contained two covalently bound ferrocene units was recently synthesized via cyclopropanation of the fullerene core.<sup>295</sup>

Recently, liquid-crystalline fullerene–ferrocene dyads<sup>296</sup> were prepared by 1,3-dipolar additions leading to fulleropyrrolidines bearing functionalized fullerene unit and a mesomorphic dendrimer. Photoinduced intramolecular electron transfer was observed (Figure 1.24).

### 1.4.1.3 Polyads

More complicated systems bearing more than two electroactive units have been built and studied.<sup>252,297</sup> In this case, the donor–acceptor systems are called triads, tetrads, pentads, hexads, etc., depending on the number of electroactive units that can work both as donors and acceptors. The objective is to build an optimal distance for long-lived charge-separated states by means of a series of short distance and efficient electron transfer events.

A variety of triads and tetrads displaying combinations of fullerenes, porphyrins, Zn-porphyrins, and ferrocenes were synthesized and studied by Imahori and collaborators. In a very elegant work, ZnP– $H_2P$ – $C_{60}$  (Figure 1.25) was synthesized and investigated.<sup>298,299</sup> After photostimulation, energy transfer took place from the ZnP to the  $H_2P$  followed by an electron transfer from the excited  $H_2P$  to  $C_{60}$  giving a long distance charge-separated state.

Analogous Fc–ZnP– $C_{60}$  and Fc– $H_2P$ – $C_{60}$  (Figure 1.25) triads that contain a terminal ferrocene unit<sup>299,300</sup> were prepared and examined. When irradiated, two consecutive electron transfers took place, first from the porphyrin to  $C_{60}$  and then from the ferrocene to the porphyrin leading to the charge-separated state. By combination of these two systems, a tetrad was reported,<sup>301</sup> which showed the longest charge-separated state to date, as the product of a sequence of energy and multistep electron transfer events (Figure 1.25).

Novel multicomponent polyads have been prepared and analyzed, based on linear<sup>302,303</sup> and branched<sup>304</sup> multiporphyrin polyads (Figure 1.26), including a ferrocene–multiporphyrin pentad.<sup>305</sup>

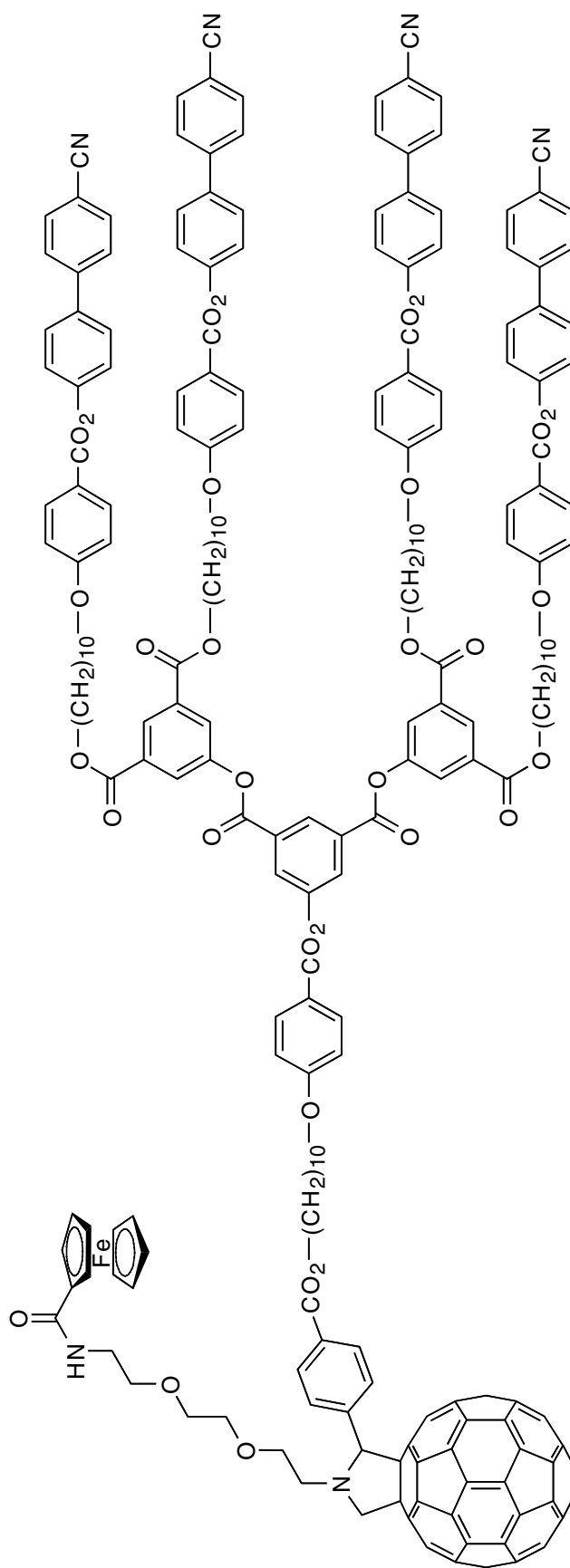
Multiple donor–acceptor systems containing TTF have also been explored. These include porphyrin– $C_{60}$  triads bearing terminal TTF<sup>306</sup> and  $\pi$ -extended-TTF<sup>307</sup> moieties (Figure 1.27).

Series of triads based on a terminal  $\pi$ -extended-TTF unit linked to  $C_{60}$  through a polyphenylenevinylene (PPV) molecular wire have been recently reported.<sup>308</sup> After light irradiation, electron transfer occurred leading to a 40 Å charge-separated state (Figure 1.28).

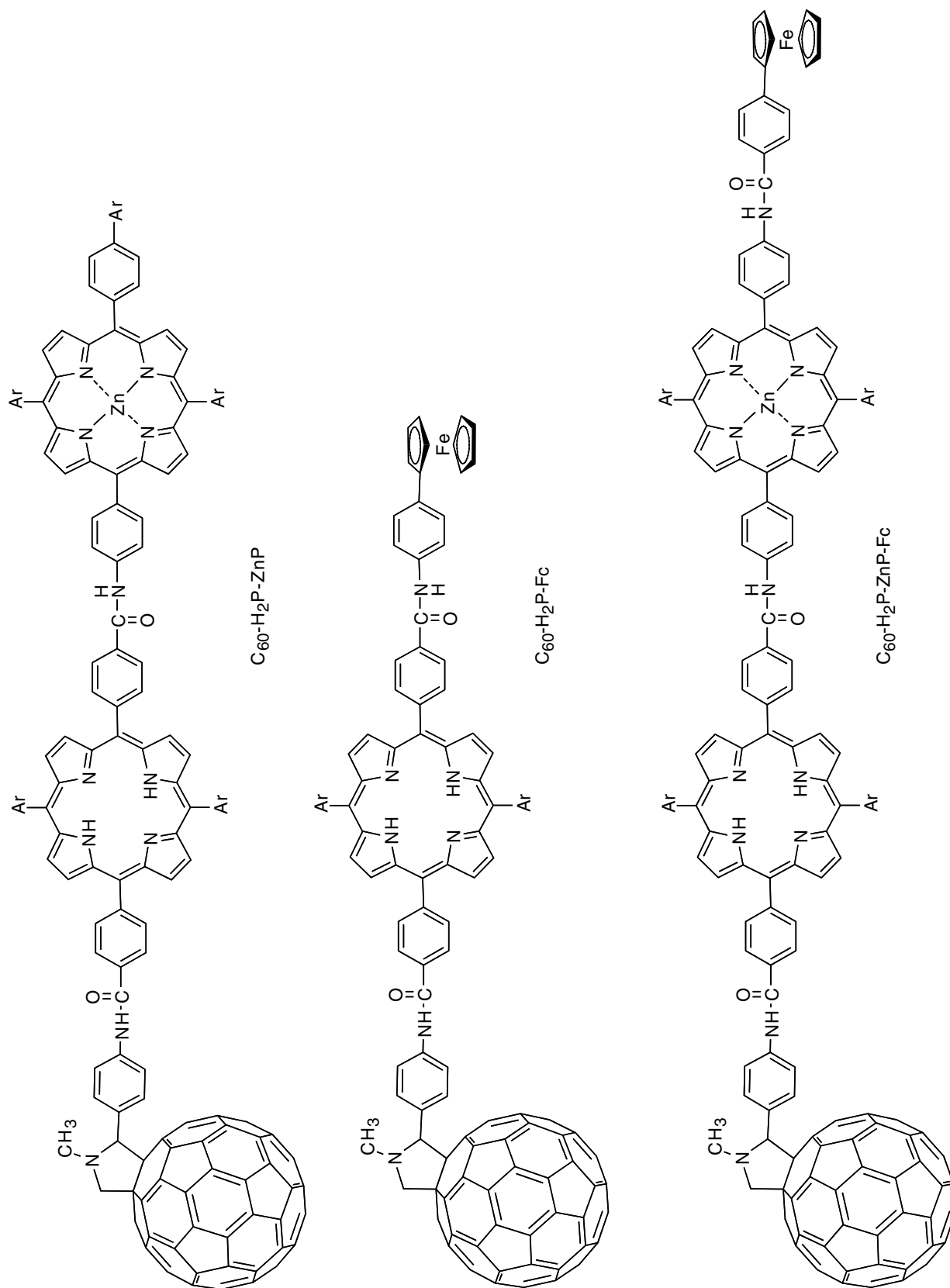
## 1.4.2 PLASTIC SOLAR CELLS

Fullerenes participate in the formation of charge-transfer complexes with weak electron donors, such as conjugated polymers. Upon photoexcitation, electron transfer takes place between the  $S_1$  excited state of the polymer and the more electronegative  $C_{60}$ .<sup>309</sup> The addition of  $C_{60}$  to conjugated polymers increased the photoconductivities<sup>310,311</sup> to a large extent, as a result of the photoinduced electron transfer. Due to these properties, fullerene-based plastic solar cells are shown as one of the most promising applications of these composite materials. This field has been extensively reviewed.<sup>312,313</sup>

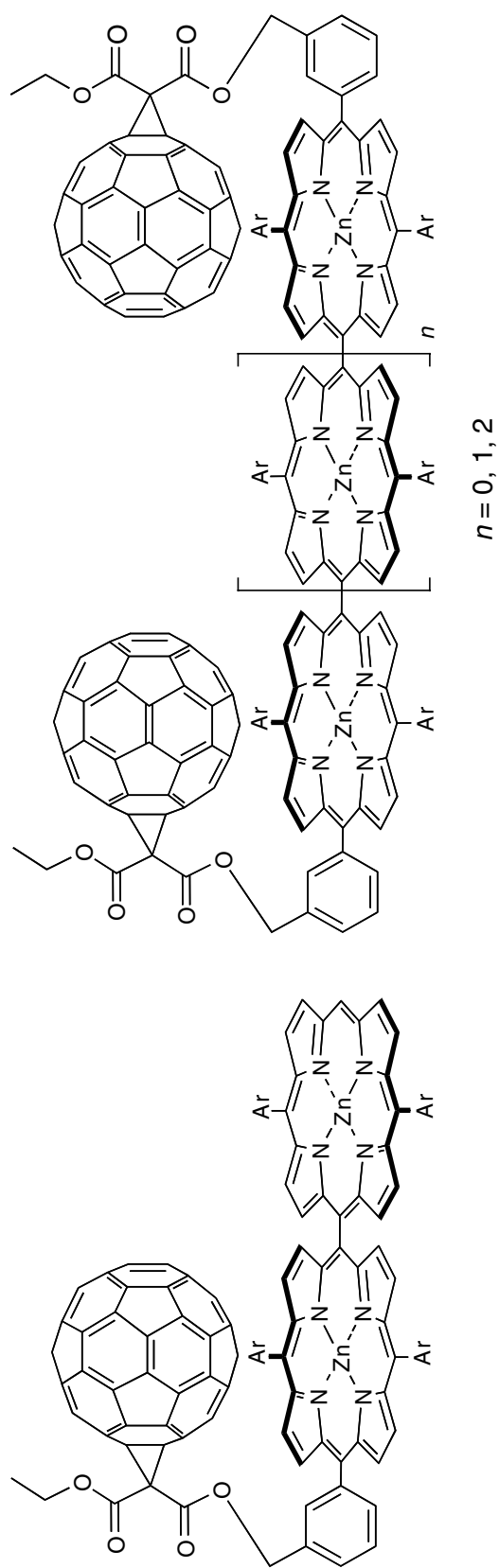
In the first example,<sup>309</sup>  $C_{60}$  was added to PPV and electron transfer occurred from the excited state of the polymer to  $C_{60}$ . It was observed that the charged-separated state was long-lived enough to allow the charges to migrate to the anode and the cathode, and thus the first fullerene-based photodiode was constructed.<sup>314</sup> Nevertheless, the interactions between the acceptor and the donor were limited by the flat geometry of the interface. When functionalized fullerenes were adopted, the photodiodes displayed better photoconversions.<sup>146,315–317</sup> The use of functionalized fullerenes decreased the aggregation and increased the interaction with the soluble conjugated polymer



**FIGURE 1.24** Liquid crystalline fullerene-ferrocene dyad.

**FIGURE 1.25** C<sub>60</sub>-porphyrin-ferrocene polyads.



**FIGURE 1.26** Oligoporphyryin polyads.

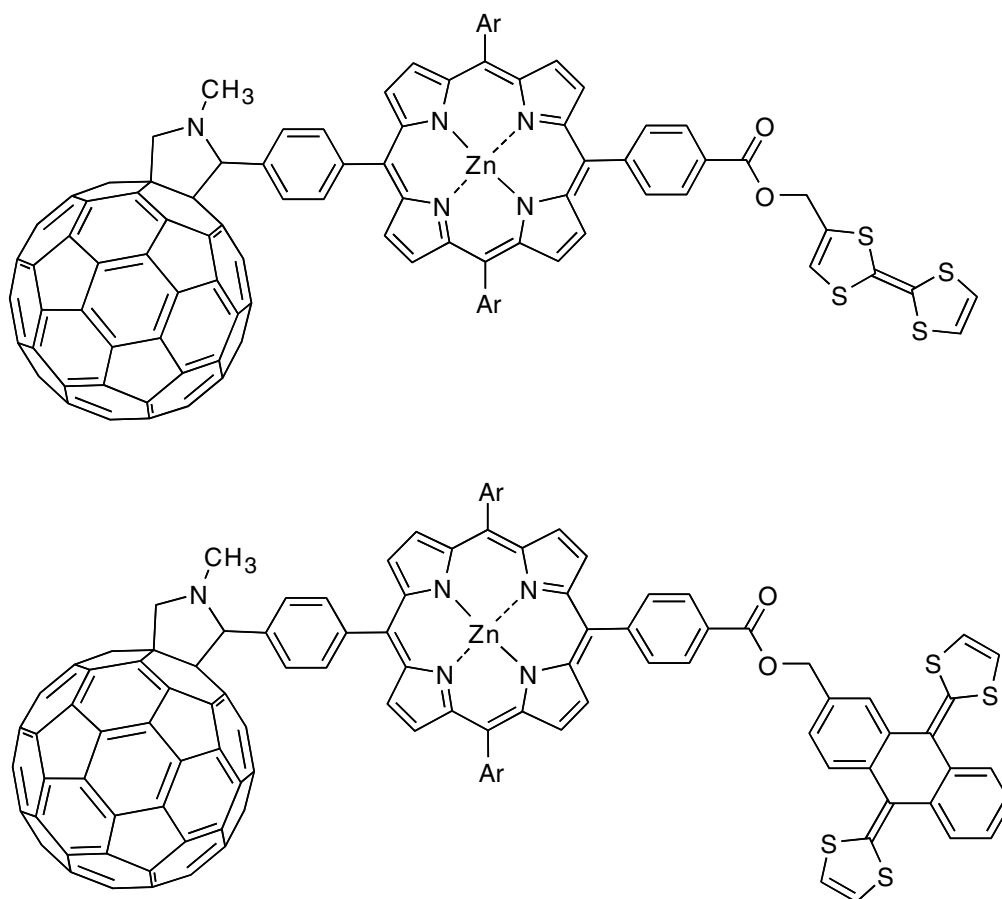


FIGURE 1.27 TTF-porphyrin- $C_{60}$  triads.

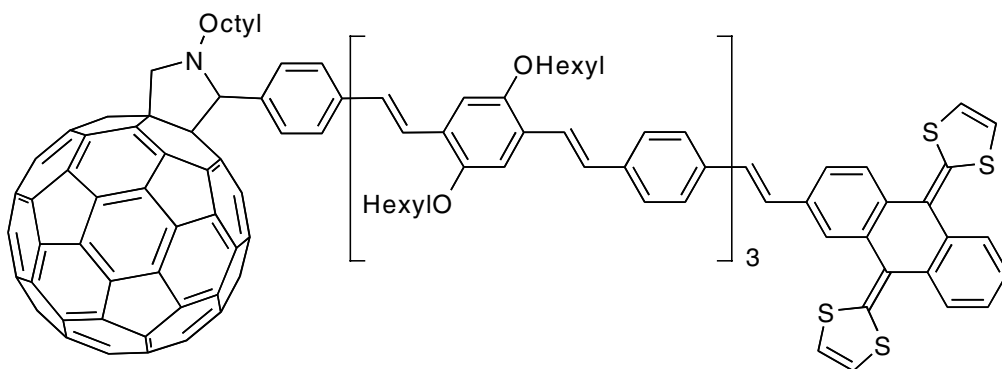


FIGURE 1.28 Molecular wire.

enhancing the generation of a photocurrent circuit.<sup>312,315</sup> Also, it has been shown that the morphology of the so called “bulk heterojunction” has a very important influence in the power conversion efficiency.<sup>317</sup> Hence, diverse strategies have been proposed to improve the processibility of functionalized fullerene materials and obtain their intimate mixing with conjugated polymers to control both electronic and morphological properties.

1-(3-methoxycarbonyl)-propyl-1-1-(6'6) $C_{61}$  (PCBM) has been widely used as acceptor in multiple bulk heterojunction solar cells. More recently, new fullerenes acceptors were studied including DPM-12<sup>318</sup> and mixtures of isomers of [70]PCBM.<sup>319</sup>

In more detail, the following systems have already been designed and tested to a great extent as useful photodiodes: (1) diblock-copolymers (i.e., conjugated donor block polymer plus fullerene-bearing

block)<sup>320</sup> and (2) conjugated oligomer–fullerene dyads with different conjugation length of the donor moiety.<sup>321–328</sup>

Novel hybrid materials have been realized in which fullerenes participate in composite films with  $\pi$ -conjugated polymer-electron donors such as oligothiophenes. Established studies have already shown that the photoinduced electron transfer is rather enhanced between  $\pi$ -conjugated polymers and fullerenes, while back electron transfer is considerably slower.<sup>309,316,329,330</sup> Electrosynthesized polythiophene with pendant fullerene substituents was recently obtained from the corresponding bithiophene–fulleropyrrolidine dyad.<sup>331</sup> The novel described material has the potential of a double-cable polymer, heavily loaded with fullerene electron-conducting moieties.

Studies dealing with the incorporation of conjugated oligomeric units in fullerene dyads systems have been increased, especially after the observation of electron transfer from conducting oligomers (or polymers) to  $C_{60}$ .<sup>309,332</sup> Some further examples on such materials involved the construction of organofullerene materials in which two oligo-phenylenevinylene,<sup>333</sup> or two oligo-thienyleneviylenes<sup>334</sup> units, have been attached on the skeleton of  $C_{60}$  via a fused pyrrolidine ring. Further works utilizing oligo-phenylenevinylenes<sup>335,336</sup> and oligo-naphthylenevinylenes<sup>337–339</sup> in fullerene hybrids systems have been performed and found to possess intriguing physicochemical properties including singlet–singlet energy transfer as well as intramolecular electron-transfer interactions.

Recently, self-assembly of complementary hydrogen bond motifs have been introduced in both fullerenes and conjugated oligo(*p*-phenylenevinylene)s in order to control the morphology of the fullerene–oligomer mixture and obtain better photoconversions.<sup>243,244,246</sup>

## 1.5 CONCLUSIONS

The organic functionalization of  $C_{60}$  has produced a wide range of derivatives, which retain the basic properties of pristine fullerene. Among the many possible reactions available, cycloadditions have been most widely used, along with cyclopropanation (nucleophilic) reactions. The products have now improved the solubility and processibility and can be used in several applications including electron-transfer reactions, liquid crystals, polymers, dendrimers, and solar cells. The continuous evolution of fullerene science and technology, accompanying the progress obtained in the functionalization chemistry, has led to the production of more and more compounds that open new horizons in the potential applications of these fascinating molecules.

## ACKNOWLEDGMENTS

Part of the work described in this chapter was supported by the European Union through grants HPRN-CT-2002-00168 and HPRN-CT-2002-00177, and by MIUR (PRIN 2004, prot. 2004035502).

## REFERENCES

1. Kroto, H.W., et al., *Nature*, 318, 162, 1985.
2. Krätschmer, W., et al., *Nature*, 347, 354, 1990.
3. Haufler, R.E., et al., *J. Phys. Chem.*, 94, 8634, 1990.
4. Haddon, R.C., Brus, L.E., and Raghavachari, K., *Chem. Phys. Lett.*, 125, 459, 1986.
5. Haddon, R.C., Brus, L.E., and Raghavachari, K., *Chem. Phys. Lett.*, 131, 165, 1986.
6. Yang, S.H., et al., *Chem. Phys. Lett.*, 139, 233, 1987.
7. Echegoyen, L., Diederich, F., and Echegoyen, L.E., *Electrochemistry of Fullerenes*, in *Fullerenes: Chemistry, Physics, and Technology*, Kadish, K.M. and Ruoff, R.S., Eds., Wiley, New York, 2000, p. 1.
8. Echegoyen, L. and Echegoyen, L.E., *Acc. Chem. Res.*, 31, 593, 1998.
9. Arias, F., et al., *J. Am. Chem. Soc.*, 117, 1422, 1995.
10. Bruno, C., Doubitski, I., Marcaccio, M., Paolucci, F., Paolucci, D., and Zaopo, A., *J. Am. Chem. Soc.*, 125, 15738–15739, 2003.

11. Haddon, R.C., et al., *Appl. Phys. Lett.*, 67, 121, 1995.
12. Allemand, P.M., et al., *Science*, 253, 301, 1991.
13. Makarova, T.L., et al., *Science*, 253, 301, 2001.
14. Lappas, A., et al., *Science*, 267, 1799, 1995.
15. Narymbetov, B., et al., *Nature*, 407, 883, 2000.
16. Mizoguchi, K., et al., *Phys. Rev. B*, 6314, 2001.
17. Hebard, A.F., et al., *Nature*, 350, 600, 1991.
18. Grant, P., *Nature*, 413, 264, 2001.
19. Dagotto, E., *Science*, 293, 2410, 2001.
20. Hoke II, S.H., et al., *J. Org. Chem.*, 57, 5069, 1992.
21. Tsuda, M., et al., *Chem. Lett.*, 2333, 1992.
22. Wilson, S.R., et al., *J. Am. Chem. Soc.*, 115, 8495, 1993.
23. Wilson, S.R., et al., *J. Org. Chem.*, 58, 6548, 1993.
24. Schuster, D.I., et al., *J. Am. Chem. Soc.*, 118, 5639, 1996.
25. Jensen, A.W., et al., *J. Am. Chem. Soc.*, 119, 7303, 1997.
26. Liou, K.-F. and Cheng, C.-H., *J. Chem. Soc. Chem. Commun.*, 2473, 1995.
27. Bernstein, R. and Foote, C.S., *Tetrahedron Lett.*, 39, 7051, 1998.
28. Segura, J.L. and Martin, N., *Chem. Soc. Rev.*, 29, 13, 2000.
29. Wang, G.W., et al., *Nature*, 387, 583, 1997.
30. Komatsu, K., et al., *J. Org. Chem.*, 63, 9358, 1998.
31. Keshavarz-K., M., et al., *J. Am. Chem. Soc.*, 117, 11371, 1995.
32. Murata, Y., et al., *J. Org. Chem.*, 64, 3483, 1999.
33. Forman, G.S., Tagmatarchis, N. and Shinohara, H., *J. Am. Chem. Soc.*, 124, 178, 2002.
34. Tagmatarchis, N., et al., *Synlett*, 235, 2002.
35. Wilson, S., et al., Organic chemistry of Fullerenes, in *Fullerenes: Chemistry, Physics, and Technology*, Kadish, K.M. and Ruoff, R.S., Eds., Wiley, New York, 2000, chap. 3.
36. Maggini, M., Scorrano, G., and Prato, M., *J. Am. Chem. Soc.*, 115, 9798, 1993.
37. Prato, M. and Maggini, M., *Acc. Chem. Res.*, 31, 519, 1998.
38. Tagmatarchis, N. and Prato, M., *Synlett*, 768, 2003.
39. Wang, P., et al., *J. Mater. Chem.*, 7, 2397, 1997.
40. Wang, P., Metzger, R.M. and Chen, B., *Thin Solid Films*, 329, 96, 1998.
41. Guo, Z., et al., *Synth. Commun.*, 28, 1957, 1998.
42. Murakami, H., et al., *Chem. Lett.*, 815, 1999.
43. Ge, Z.X., et al., *Tetrahedron Lett.*, 40, 5759, 1999.
44. Guo, Z., et al., *Synth. Met.*, 102, 1567, 1999.
45. Leo, L., et al., *Langmuir*, 16, 4599, 2000.
46. Zhang, S., Gan, L., and Huang, C., *Chem. Phys. Lett.*, 331, 143, 2000.
47. Guo, Z., et al., *Appl. Phys. B*, 70, 257, 2000.
48. Ge, X.Z., *Thin Solid Films*, 368, 147, 2000.
49. Carano, M., et al., *Electrochim. Acta*, 46, 265, 2000.
50. Nierengarten, J.F., *Chem. Eur. J.*, 6, 3667, 2000.
51. Rio, Y., et al., *Tetrahedron Lett.*, 41, 10207, 2000.
52. Guo, Z., *Appl. Phys. B*, 71, 545, 2001.
53. Angelini, G., et al., *Langmuir*, 17, 6404, 2001.
54. Hernandez, M.P., *Langmuir*, 17, 2001.
55. Nakashima, N., et al., *Chem. Eur. J.*, 7, 1766, 2001.
56. Georgakilas, V., et al., *Proc. Natl. Acad. Sci. U.S.A.*, 99, 5075, 2002.
57. Cassell, A.M., Asplund, C.L., and Tour, J.M., *Angew. Chem. Int. Ed. Engl.*, 38, 2403, 1999.
58. Gournis, D., et al., *J. Am. Chem. Soc.*, 126, 8561, 2004.
59. Tomberli, V., et al., *Carbon*, 38, 1551, 2000.
60. Bosi, S., et al., *Bioorg. Med. Chem. Lett.*, 10, 1043, 2000.
61. Kordatos, K., et al., *J. Org. Chem.*, 66, 4915, 2001.
62. Kang, S.H., et al., *Angew. Chem. Int. Ed. Engl.*, 43, 1512, 2004.
63. Holmes, A.B. and Stephenson, G.R., *Chem. Ind.*, 303, 1994.
64. Maggini, M., et al., *J. Chem. Soc. Chem. Commun.*, 305, 1994.

65. Bianco, A., et al., *J. Am. Chem. Soc.*, 119, 7550, 1997.
66. Bianco, A., et al., *J. Am. Chem. Soc.*, 118, 4072, 1996.
67. Bianco, A., et al., *J. Pept. Res.*, 50, 159, 1997.
68. Bianco, A., et al., *J. Pept. Sci.*, 4, 364, 1998.
69. Pantarotto, D., et al., *J. Am. Chem. Soc.*, 124, 12543, 2002.
70. Nierengarten, J.F., et al., *Chem.-Eur. J.*, 9, 37, 2003.
71. Nierengarten, J.F., *Top. Curr. Chem.*, 228, 87, 2003.
72. Nierengarten, J.F., *C. R. Chim.*, 6, 725, 2003.
73. Bergamin, M., et al., *Chem. Commun.*, 17, 2001.
74. Da Ros, T., et al., *Aus. J. Chem.*, 54, 223, 2001.
75. Da Ros, T., et al., *Eur. J. Org. Chem.*, 405, 2002.
76. Nakamura, E., et al., *Bull. Chem. Soc. Jpn.*, 69, 2143, 1996.
77. Cassell, A.M., Scrivens, W.A., and Tour, J.M., *Angew. Chem. Int. Ed. Engl.*, 37, 1528, 1998.
78. Li, H.S., et al., *J. Chem. Soc. Perkin. Trans. 1*, 617, 2000.
79. de la Torre, M.D.L., et al., *Tetrahedron Lett.*, 43, 2002.
80. de la Torre, M.D.L., et al., *Tetrahedron Lett.*, 43, 4617, 2002.
81. de la Torre, M.D.L., et al., *Tetrahedron*, 60, 3581, 2004.
82. Kordatos, K., et al., *J. Org. Chem.*, 2802, 2001.
83. Lu, Q., Schuster, D.I., and Wilson, S.R., *J. Org. Chem.*, 61, 4764, 1996.
84. Pasimeni, L., et al., *J. Am. Chem. Soc.*, 119, 12896, 1997.
85. Schick, G., et al., *J. Am. Chem. Soc.*, 121, 3246, 1999.
86. Nishimura, T.T., et al., *J. Am. Chem. Soc.*, 126, 11711, 2004.
87. Bosi, S., et al., *Eur. J. Org. Chem.*, 4741, 2003.
88. Carano, M., et al., *J. Am. Chem. Soc.*, 125, 7139, 2003.
89. Smith, P.M., et al., *Chem. Commun.*, 1754, 2003.
90. Prato, M., et al., *J. Am. Chem. Soc.*, 115, 1148, 1993.
91. Hummelen, J.C., Prato, M., and Wudl, F., *J. Am. Chem. Soc.*, 117, 7003, 1995.
92. Grösser, T., et al., *Angew. Chem. Int. Ed. Engl.*, 34, 1343, 1995.
93. Hummelen, J.C., et al., *Science*, 269, 1554, 1995.
94. Hummelen, J.C., Bellavia-Lund, C., and Wudl, F., Heterofullerenes, in *Fullerenes and Related Structures*, Springer-Verlag, GmbH, 1999, p. 93.
95. Lamparth, I., et al., *Angew. Chem. Int. Ed. Engl.*, 34, 2257, 1995.
96. Nuber, B. and Hirsch, A., *Fullerene Sci. Technol.*, 4, 715, 1996.
97. Bellavia-Lund, C., and Wudl, F., *J. Am. Chem. Soc.*, 119, 943, 1997.
98. Tagmatarchis, N., et al., *Synlett*, 1761, 2001.
99. Smith, A.B., et al., *J. Am. Chem. Soc.*, 115, 5829, 1993.
100. Shu, L.H., et al., *Chem. Commun.*, 79, 1997.
101. O'Donovan, B.F., et al., *Chem. Commun.*, 81, 1997.
102. Zhang, C.L.X., *J. Org. Chem.*, 60, 2906, 1997.
103. Ohno, M., et al., *Tetrahedron*, 52, 4983, 1996.
104. Takaguchi, Y., et al., *Angew. Chem. Int. Ed. Engl.*, 41, 817, 2002.
105. Komatsu, K., et al., *Tetrahedron Lett.*, 34, 8473, 1993.
106. Schlueter, J.A., et al., *J. Chem. Soc., Chem. Commun.*, 972, 1993.
107. Tsuda, M., et al., *J. Chem. Soc., Chem. Commun.*, 1296, 1993.
108. Mori, A., Takamori, Y., and Takeshita, H., *Chem. Lett.*, 395, 1997.
109. Ohno, M., Shirakawa, Y., and Eguchi, S., *Synthesis*, 1812, 1998.
110. Mori, S., et al., *Synth. Commun.*, 27, 1475, 1997.
111. Jonas, U., et al., *Chem. Eur. J.*, 1, 243, 1995.
112. Ohno, M., et al., *Tetrahedron*, 53, 9075, 1997.
113. Walter, M., et al., *Fullerene Sci. Technol.*, 4, 101, 1996.
114. Mattay, J., et al., *J. Phys. Chem. Solids*, 58, 1929, 1997.
115. Nakamura, Y., et al., *J. Chem. Soc., Perkin Trans. 2*, 2351, 1995.
116. Liao, C.C. and Peddinti, R.K., *Acc. Chem. Res.*, 35, 856, 2002.
117. Yen, C.F., Peddinti, R.K., and Liao, C.C., *Org. Lett.*, 2, 2909, 2000.
118. Tome, A.C., et al., *Tetrahedron Lett.*, 38, 2557, 1997.

119. Boule, C., et al., *Tetrahedron Lett.*, 38, 81, 1997.
120. AlHariri, M., et al., *J. Org. Chem.*, 62, 405, 1997.
121. Segura, J.L. and Martin, N., *Chem. Rev.*, 99, 3199, 1999.
122. Liu, J.H., et al., *J. Org. Chem.*, 65, 3395, 2000.
123. Kreher, D., et al., *J. Mater. Chem.*, 12, 2137, 2002.
124. Kräutler, B. and Maynollo, J., *Angew. Chem. Int. Ed. Engl.*, 34, 87, 1995.
125. Krautler, B. and Maynollo, J., *Tetrahedron*, 52, 5033, 1996.
126. Nakamura, Y., et al., *J. Am. Chem. Soc.*, 124, 4329, 2002.
127. Hermann, A., et al., *Helv. Chim. Acta*, 77, 1689, 1994.
128. Seiler, P., Herrmann, A., and Diederich, F., *Helv. Chim. Acta*, 78, 344, 1995.
129. Meidine, M.F., et al., *J. Chem. Soc. Perkin Trans. 2*, 1189, 1994.
130. Bingel, K., *Chem. Ber.*, 126, 1957, 1993.
131. Nierengarten, J.-F., et al., *Helv. Chim. Acta*, 80, 2238, 1997.
132. Nierengarten, J.-F., et al., *Angew. Chem. Int. Ed. Engl.*, 35, 2101, 1996.
133. Camps, X. and Hirsch, A., *J. Chem. Soc. Perkin Trans. 1*, 1595, 1997.
134. Bestmann, H.J., et al., *Tetrahedron Lett.*, 35, 9017, 1994.
135. Wang, Y., et al., *Tetrahedron Lett.*, 36, 6843, 1995.
136. Wudl, F., *Acc. Chem. Res.*, 25, 157, 1992.
137. Suzuki, T., et al., *Science*, 254, 1186, 1991.
138. Suzuki, T., et al., *J. Am. Chem. Soc.*, 114, 7301, 1992.
139. Smith, A.B., III, et al., *J. Am. Chem. Soc.*, 115, 5829, 1993.
140. Diederich, F., Isaacs, L., and Philp, D., *Chem. Soc. Rev.*, 23, 243, 1994.
141. Isaacs, L. and Diederich, F., *Helv. Chim. Acta*, 76, 2454, 1993.
142. Hall, M.H., Lu, H.J., and Shevlin, P.B., *J. Am. Chem. Soc.*, 123, 1349, 2001.
143. Janssen, R.A.J., Hummelen, J.C., and Wudl, F., *J. Am. Chem. Soc.*, 117, 544, 1995.
144. Osterodt, J., et al., *Chem. Ber.*, 126, 2331, 1993.
145. Wilson, S.R. and Wu, Y., *J. Chem. Soc., Chem. Commun.*, 784, 1993.
146. Hummelen, J.C., et al., *J. Org. Chem.*, 60, 532, 1995.
147. Tomioka, H. and Yamamoto, K., *J. Chem. Soc., Perkin Trans. 1*, 63, 1996.
148. Knol, J. and Hummelen, J.C., *J. Am. Chem. Soc.*, 122, 3226, 2000.
149. Meijer, M.D., et al., *Tetrahedron Lett.*, 39, 6773, 1998.
150. An, Y.-Z., et al., *J. Org. Chem.*, 59, 2927, 1994.
151. Anderson, H.L., et al., *Angew. Chem. Int. Ed. Engl.*, 33, 1366, 1994.
152. Li, Z., Bouhadir, K.H., and Shevlin, P.B., *Tetrahedron Lett.*, 37, 4651, 1996.
153. Ravaine, S., et al., *New J. Chem.*, 19, 1, 1995.
154. Sastre, A., et al., *Org. Lett.*, 1, 1807, 1999.
155. Ravaine, S., et al., *J. Phys. Chem.*, 99, 9551, 1995.
156. Isaacs, L., Wehrsig, A., and Diederich, F., *Helv. Chim. Acta*, 76, 1231, 1993.
157. Safonov, I.G., Baran, P.S., and Schuster, D.I., *Tetrahedron Lett.*, 38, 8133, 1997.
158. Baran, P.S., et al., *J. Am. Chem. Soc.*, 119, 8363, 1997.
159. McMahan, S., et al., *J. Org. Chem.*, 66, 5449, 2001.
160. Jonas, U., et al., *Chem. Eur. J.*, 1, 243, 1995.
161. Cardullo, F., et al., *Langmuir*, 14, 1955, 1998.
162. Fujiwara, K., et al., *J. Am. Chem. Soc.*, 123, 10715, 2001.
163. Even, M., et al., *Chem. Eur. J.*, 7, 2595, 2001.
164. Guillon, D., et al., *Macromol. Symp.*, 192, 63, 2003.
165. Hirsch, A. and Vostrowsky, O., *Top. Curr. Chem.*, 217, 51, 2001
166. Camps, X., Schönberger, H., and Hirsch, A., *Chem. Eur. J.*, 3, 561, 1997.
167. Catalano, V.J. and Parodi, N., *Inorg. Chem.*, 36, 537, 1997.
168. Brettreich, M. and Hirsch, A., *Tetrahedron Lett.*, 39, 2731, 1998.
169. Camps, X., et al., *Chem. Eur. J.*, 5, 2362, 1999.
170. Herzog, A., Hirsch, A., and Vostrowsky, O., *Eur. J. Org. Chem.*, 171, 2000.
171. Schwell, M., et al., *Chem. Phys. Lett.*, 339, 25, 2001.
172. Nierengarten, J.F., Felder, D., and Nicoud, J.F., *Tetrahedron Lett.*, 40, 269, 1999.
173. Nierengarten, J.F., Felder, D., and Nicoud, J.F., *Tetrahedron Lett.*, 40, 273, 1999.

174. Nierengarten, J.F., Felder, D., and Nicoud, J.F., *Tetrahedron Lett.*, 41, 41, 2000.
175. Felder, D., et al., *New J. Chem.*, 24, 687, 2000.
176. Fujiwara, K. and Komatsu, K., *Chem. Commun.*, 1986, 2001.
177. Chuard, T. and Deschenaux, R., *Helv. Chim. Acta*, 79, 736, 1996.
178. Deschenaux, R., Even, M., and Guillon, D., *Chem. Commun.*, 537, 1998.
179. Dardel, B., et al., *Macromolecules*, 32, 5193, 1999.
180. Chuard, T., et al., *Chem. Commun.*, 2103, 1999.
181. Tirelli, N., et al., *J. Chem. Soc. Perkin Trans. 2*, 193, 2000.
182. Campidelli, S. et al., R., *Helv. Chim. Acta*, 84, 589, 2001.
183. Dardel, B., et al., *J. Mater. Chem.*, 11, 2814, 2001.
184. Tsuda, M., et al., *Tetrahedron Lett.*, 34, 6911, 1993.
185. Osterodt, J. and Vögtle, F., *Chem. Commun.*, 547, 1996.
186. Dragoe, N., et al., *Chem. Commun.*, 85, 1999.
187. Chai, Y., et al., *J. Phys. Chem.*, 95, 7564, 1991.
188. Bethune, D.S., et al., *Nature*, 366, 123, 1993.
189. Nagase, S., Kobayashi, K., and Akasaka, T., *Bull. Chem. Soc. Jpn.*, 69, 2131, 1996.
190. Shinohara, H., *Rep. Prog. Phys.*, 63, 843, 2000.
191. Bolskar, R.B., et al., *J. Am. Chem. Soc.*, 123, 5741, 2001.
192. Maeda, Y., et al., *J. Am. Chem. Soc.*, 126, 6858, 2004.
193. Zhang, T.H. et al., *Org. Biomol. Chem.*, 2, 1698, 2004.
194. Isaacs, L., Haldimann, R.F., and Diederich, F., *Angew. Chem. Int. Ed. Engl.*, 33, 2339, 1994.
195. Diederich, F. and Kessinger, R., *Acc. Chem. Res.*, 32, 537, 1999.
196. Nakamura, Y., et al., *Org. Lett.*, 6, 2797, 2004.
197. Sergeyev, S. and Diederich, F., *Angew. Chem. Int. Ed. Engl.*, 43, 1738, 2004.
198. Hino, T. and Saigo, K., *Chem. Commun.*, 402, 2003.
199. Diederich, F. and Gomez-Lopez, M., *Chem. Soc. Rev.*, 28, 263, 1999.
200. Guldi, D.M. and Martin, N., *J. Mater. Chem.*, 12, 1978, 2002.
201. Armaroli, N., et al., *Chem. Eur. J.*, 4, 406, 1998.
202. Li, K., et al., *J. Am. Chem. Soc.*, 126, 3388, 2004.
203. Schuster, D.I., et al., *Org. Lett.*, 6, 1919, 2004.
204. Ashton, P.R., et al., *Angew. Chem. Int. Ed. Engl.*, 36, 1448, 1997.
205. Nakamura, Y., et al., *Angew. Chem. Int. Ed. Engl.*, 42, 3158, 2003.
206. Da Ros, T., et al., *Org. Lett.*, 5, 689, 2003.
207. Watanabe, N., et al., *Angew. Chem. Int. Ed. Engl.*, 42, 681, 2003.
208. Diederich, F., et al., *J. Chem. Soc. Perkin Trans. 2*, 1577, 1999.
209. Martinez-Diaz, M.V., et al., *J. Mater. Chem.*, 12, 2095, 2002.
210. Guldi, D.M., et al., *Chem. Commun.*, 2774, 2002.
211. Solladie, N., et al., *Chem. Commun.*, 2412, 2003.
212. Kawase, T., et al., *Angew. Chem. Int. Ed. Engl.*, 42, 1624, 2003.
213. Kawase, T., et al., *Angew. Chem. Int. Ed. Engl.*, 43, 1722, 2004.
214. Kawase, T., et al., *Angew. Chem. Int. Ed. Engl.*, 42, 5597, 2003.
215. Smith, B.W., Monthieux, M., and Luzzi, D.E., *Nature*, 396, 323, 1998.
216. Luzzi, D.E. and Smith, B.W., *Carbon*, 38, 1751, 2000.
217. Khlobystov, A.N., et al., *Angew. Chem. Int. Ed. Engl.*, 43, 1386, 2004.
218. Khlobystov, A.N., et al., *J. Mater. Chem.*, 14, 2852, 2004.
219. Hirahara, K., et al., *Phys. Rev. Lett.*, 85, 5384, 2000.
220. Chiu, P.W., et al., *Appl. Phys. Lett.*, 79, 3845, 2001.
221. Okazaki, T., et al., *J. Am. Chem. Soc.*, 123, 9673, 2001.
222. Debarre, A., et al., *Chem. Phys. Lett.*, 380, 6, 2003.
223. Smith, B.W., Luzzi, D.E., and Achiba, Y., *Chem. Phys. Lett.*, 331, 137, 2000.
224. Suenaga, K., et al., *Nano Lett.*, 3, 1395, 2003.
225. Yudasaka, M., et al., *Chem. Phys. Lett.*, 380, 42, 2003.
226. Britz, D.A., et al., *Chem. Commun.*, 176, 2004.
227. Drovetskaya, T., Reed, C.A., and Boyd, P., *Tetrahedron Lett.*, 36, 7971, 1995.
228. Sun, Y.P., et al., *J. Org. Chem.*, 62, 3642, 1997.

229. Boyd, P.D.W., et al., *J. Am. Chem. Soc.*, 121, 10487, 1999.
230. Konarev, D.V., et al., *Chem. Eur. J.*, 7, 2605, 2001.
231. Schuster, D.I., et al., *J. Mater. Chem.*, 12, 2041, 2002.
232. Sun, D., et al., *Proc. Natl. Acad. Sci. U. S. A.*, 99, 5088, 2002.
233. Guldi, D.M., et al., *J. Am. Chem. Soc.*, 123, 9166, 2001.
234. Guldi, D.M., et al., *Chem. Commun.*, 373, 2000.
235. Wang, Y.-B.L., et al., *J. Am. Chem. Soc.*, 125, 6072, 2002.
236. Sun, D.Y., et al., *J. Am. Chem. Soc.*, 124, 6604, 2002.
237. Yamaguchi, T., et al., *J. Am. Chem. Soc.*, 125, 13934, 2003.
238. Tashiro, K., et al., *J. Am. Chem. Soc.*, 121, 9477, 1999.
239. Nishioka, T., et al., *Macromolecules*, 33, 9182, 2000.
240. Shoji, Y., Tashiro, K., and Aida, T., *J. Am. Chem. Soc.*, 126, 6570, 2004.
241. Rispens, M.T., et al., *Chem. Commun.*, 161, 2001.
242. Gonzalez, J.J., et al., *Chem. Commun.*, 163, 2001.
243. Beckers, E.H.A., et al., *J. Mater. Chem.*, 12, 2054, 2002.
244. Rispens, M.T., et al., *Synth. Met.*, 135, 801, 2003.
245. Sanchez, L., Rispens, M.T., and Hummelen, J.C., *Angew. Chem. Int. Ed. Engl.*, 41, 838, 2002.
246. Beckers, E.H.A., et al., *Chem. Commun.*, 2888, 2002.
247. Segura, M., et al., *J. Am. Chem. Soc.*, 125, 15093, 2003.
248. Guldi, D.M. and Prato, M., *Acc. Chem. Res.*, 33, 695, 2000.
249. Guldi, D.M., *Chem. Commun.*, 321, 2000.
250. Imahori, H. and Sakata, Y., *Adv. Mater.*, 9, 537, 1997.
251. Imahori, H. and Sakata, Y., *Eur. J. Org. Chem.*, 2445, 1999.
252. Guldi, D.M., *Chem. Soc. Rev.*, 31, 22, 2002.
253. Guldi, D.M., *Pure Appl. Chem.*, 75, 1069, 2003.
254. Kashiwagi, Y., et al., *Org. Lett.*, 5, 2719, 2003.
255. Ohkubo, K., et al., *Angew. Chem. Int. Ed. Engl.*, 43, 853, 2004.
256. Guldi, D.M., et al., *J. Mater. Chem.*, 14, 303, 2004.
257. Bourgeois, J.P., et al., *Helv. Chim. Acta*, 81, 1835, 1998.
258. Dietel, E., et al., *Chem. Commun.*, 1981, 1998.
259. Cheng, P., Wilson, S.R., and Schuster, D.I., *Chem. Commun.*, 89, 1999.
260. Schuster, D.I., et al., *J. Am. Chem. Soc.*, 121, 11599, 1999.
261. Sutton, L.R., et al., *J. Am. Chem. Soc.*, 126, 10370, 2004.
262. Schuster, D.I., et al., *J. Am. Chem. Soc.*, 126, 7257, 2004.
263. Maggini, M., et al., *Chem. Eur. J.*, 4, 1992, 1998.
264. Bell, T.D.M., et al., *Chem. Phys. Lett.*, 268, 223, 1997.
265. Fong, R., Schuster, D.I., and Wilson, S.R., *Org. Lett.*, 1, 729, 1999.
266. Harriman, A., *Angew. Chem. Int. Ed. Engl.*, 43, 2, 2004.
267. Da Ros, T., et al., *Chem. Commun.*, 635, 1999.
268. Da Ros, T., et al., *Chem. Eur. J.*, 7, 816, 2001.
269. D'Souza, F., et al., *Chem. Commun.*, 267, 2001.
270. D'Souza, F., et al., *Inorg. Chem.*, 38, 2157, 1999.
271. D'Souza, F., et al., *J. Am. Chem. Soc.*, 123, 5277, 2001.
272. Wilson, S.R., et al., *Chem. Commun.*, 226, 2003.
273. Guldi, D.M., et al., *Chem. Commun.*, 2056, 2002.
274. Loi, M.A., et al., *J. Mater. Chem.*, 13, 700, 2003.
275. Gonzalez-Rodriguez, D., et al., *Org. Lett.*, 4, 335, 2002.
276. Gonzalez-Rodriguez, D., et al., *J. Am. Chem. Soc.*, 126, 6301, 2004.
277. Segura, J.L. and Martin, N., *Angew. Chem. Int. Ed. Engl.*, 40, 1372, 2001.
278. Martin, N., et al., *Tetrahedron Lett.*, 37, 5979, 1996.
279. Prato, M., et al., *Tetrahedron*, 52, 5221, 1996.
280. Martin, N., et al., *J. Org. Chem.*, 62, 5690, 1997.
281. Yamashita, Y., Kobayashi, Y., and Miyashi, T., *Angew. Chem. Int. Ed. Engl.*, 28, 1052, 1989.
282. Bryce, M.R., et al., *Angew. Chem. Int. Ed. Engl.*, 29, 1450, 1990.
283. Martin, N., et al., *J. Phys. Chem. A*, 104, 4648, 2000.
284. Llacay, J., et al., *Chem. Commun.*, 659, 1997.



285. Llacay, J., et al., *J. Org. Chem.*, 63, 5201, 1998.
286. Mas-Torrent, M., et al., *J. Org. Chem.*, 67, 566, 2002.
287. Martin, N., et al., *Carbon*, 38, 1577, 2000.
288. Guldi, D.M., et al., *J. Org. Chem.*, 65, 1978, 2000.
289. Gonzalez, S., et al., *Org. Lett.*, 5, 557, 2003.
290. Gonzalez, S., Martin, N., and Guldi, D.M., *J. Org. Chem.*, 68, 779, 2003.
291. Maggini, M., et al., *J. Chem. Soc. Chem. Commun.*, 589, 1994.
292. Guldi, D.M., et al., *J. Am. Chem. Soc.*, 119, 974, 1997.
293. Guldi, D.M., et al., *Nano Lett.*, 2, 775, 2002.
294. Guldi, D.M., et al., *Chem. Commun.*, 2320, 2002.
295. Kay, K.Y., Kim, L.H., and Oh, I.C., *Tetrahedron Lett.*, 41, 1397, 2000.
296. Campidelli, S., et al., *J. Mater. Chem.*, 14, 1266, 2004.
297. Imahori, H., *Org. Biomol. Chem.*, 2, 1425, 2004.
298. Luo, C., et al., *J. Am. Chem. Soc.*, 122, 6535, 2000.
299. Imahori, H., et al., *J. Am. Chem. Soc.*, 123, 2607, 2001.
300. Fujitsuka, M., et al., *Chem. Lett.*, 721, 1999.
301. Imahori, H., et al., *J. Am. Chem. Soc.*, 123, 6617, 2001.
302. Bonifazi, D. and Diederich, F., *Chem. Commun.*, 2178, 2002.
303. Bonifazi, D., et al., *Angew. Chem. Int. Ed. Engl.*, 42, 4966, 2003.
304. Kuciauskas, D., et al., *J. Am. Chem. Soc.*, 121, 8604, 1999.
305. Imahori, H., et al., *Chem. Eur. J.*, 10, 3184, 2004.
306. Liddell, P.A., et al., *Helv. Chim. Acta*, 84, 2765, 2001.
307. Kodis, G., et al., *J. Mater. Chem.*, 12, 2100, 2002.
308. Giacalone, F., et al., *J. Am. Chem. Soc.*, 126, 5340, 2004.
309. Sariciftci, N.S., et al., *Science*, 258, 1474, 1992.
310. Lee, C.H., et al., *Phys. Rev. B*, 48, 15425, 1993.
311. Morita, S., Zakhidov, A.A., and Yoshino, K., *Solid State Commun.*, 82, 249, 1992.
312. Cravino, A. and Sariciftci, N.S., *J. Mater. Chem.*, 12, 1931, 2002.
313. Hoppe, H. and Sariciftci, N.S., *J. Mater. Res.*, 19, 1924, 2004.
314. Sariciftci, N.S., et al., *Appl. Phys. Lett.*, 62, 585, 1993.
315. Janssen, R.A.J., et al., *J. Chem. Phys.*, 103, 788, 1995.
316. Yu, G., et al., *Science*, 270, 1789, 1995.
317. Shaheen, S.E., et al., *Appl. Phys. Lett.*, 78, 841, 2001.
318. Riedel, I., et al., *Thin Solid Films*, 451–52, 43, 2004.
319. Wienk, M.M., et al., *Angew. Chem. Int. Ed. Engl.*, 42, 3371, 2003.
320. Stalmach, U., et al., *J. Am. Chem. Soc.*, 122, 5464, 2000.
321. Martin, N., et al., *Chem. Rev.*, 98, 2527, 1998.
322. Liu, S.G., et al., *J. Org. Chem.*, 64, 4884, 1999.
323. Knorr, S., et al., *J. Chem. Phys.*, 110, 3502, 1999.
324. Yamashiro, T., et al., *Chem. Lett.*, 443, 1999.
325. Nierengarten, J.F., et al., *Chem. Commun.*, 617, 1999.
326. van Hal, P.A., et al., *J. Phys. Chem. A*, 104, 5974, 2000.
327. Peeters, E., et al., *J. Phys. Chem. B*, 104, 10174, 2000.
328. Martini, I.B., et al., *Chem. Phys. Lett.*, 327, 253, 2000.
329. Roman, L.S., et al., *Adv. Mater.*, 9, 1164, 1997.
330. Fromherz, T., et al., *Sol. Energy Mater. Sol. Cells*, 63, 61, 2000.
331. Cravino, A., et al., *Chem. Commun.*, 2487, 2000.
332. Pasimeni, L., et al., *Chem. Commun.*, 429, 1999.
333. Armaroli, N., et al., *Chem. Commun.*, 599, 2000.
334. Martineau, C., et al., *Adv. Mater.*, 14, 283, 2002.
335. Gu, T. and Nierengarten, J.F., *Tetrahedron Lett.*, 42, 3175, 2001.
336. Gu, T., et al., *Chem. Phys. Chem.*, 3, 124, 2002.
337. Segura, J.L. and Martin, N., *Tetrahedron Lett.*, 40, 3239, 1999.
338. Segura, J.L., et al., *Chem. Commun.*, 701, 2000.
339. Guldi, D.M., et al., *J. Org. Chem.*, 67, 1141, 2002.

---

# 2 Carbon Nanotubes: Structure and Properties

*John E. Fischer*

Department of Materials and Engineering,  
University of Pennsylvania, Philadelphia, Pennsylvania

## CONTENTS

2.1	Introduction .....	41
2.2	Structure .....	43
2.2.1	Single-Wall Tubes, Bundles, and Crystalline Ropes .....	43
2.2.2	Multiwall Tubes .....	45
2.2.3	Macroscopic Nanotube Materials .....	45
2.2.4	Fibers .....	47
2.2.5	Filled Tubes .....	47
2.2.6	Nanotube Suspensions .....	50
2.3	Physical Properties .....	51
2.3.1	Mechanical Properties .....	52
2.3.2	Thermal Properties .....	53
2.3.3	Electronic Properties .....	58
2.3.4	Magnetic and Superconducting Properties .....	70
2.4	Summary and Prospects .....	71
	Acknowledgments .....	71
	References .....	71

## 2.1 INTRODUCTION

Carbon nanotubes were discovered in 1991 as a minor byproduct of fullerene synthesis [1]. Remarkable progress has been made in the ensuing 14 years, including the discovery of two basic types of nanotubes (single-wall and multiwall); great strides have been taken in their synthesis and purification, elucidation of the fundamental physical properties, and important steps are being taken toward realistic practical applications.

Carbon nanotubes are long cylinders of 3-coordinated carbon, slightly pyramidalized by curvature [2] from the pure  $sp^2$  hybridization of graphene, toward the diamond-like  $sp^3$ . Infinitely long in principle, a perfect tube is capped at both ends by hemi-fullerenes, leaving no dangling bonds. A single-walled carbon nanotube (SWNT) is one such cylinder, while multiwall tubes (MWNT) consist of many nested cylinders whose successive radii differ by roughly the interlayer spacing of graphite (see [Figure 7.1](#) in the chapter by Du and Winey [3]). The minimum diameter of a stable freestanding SWNT is limited by curvature-induced strain to  $\sim 0.4$  nm [4]. MWNT may have outer shells  $>30$  nm

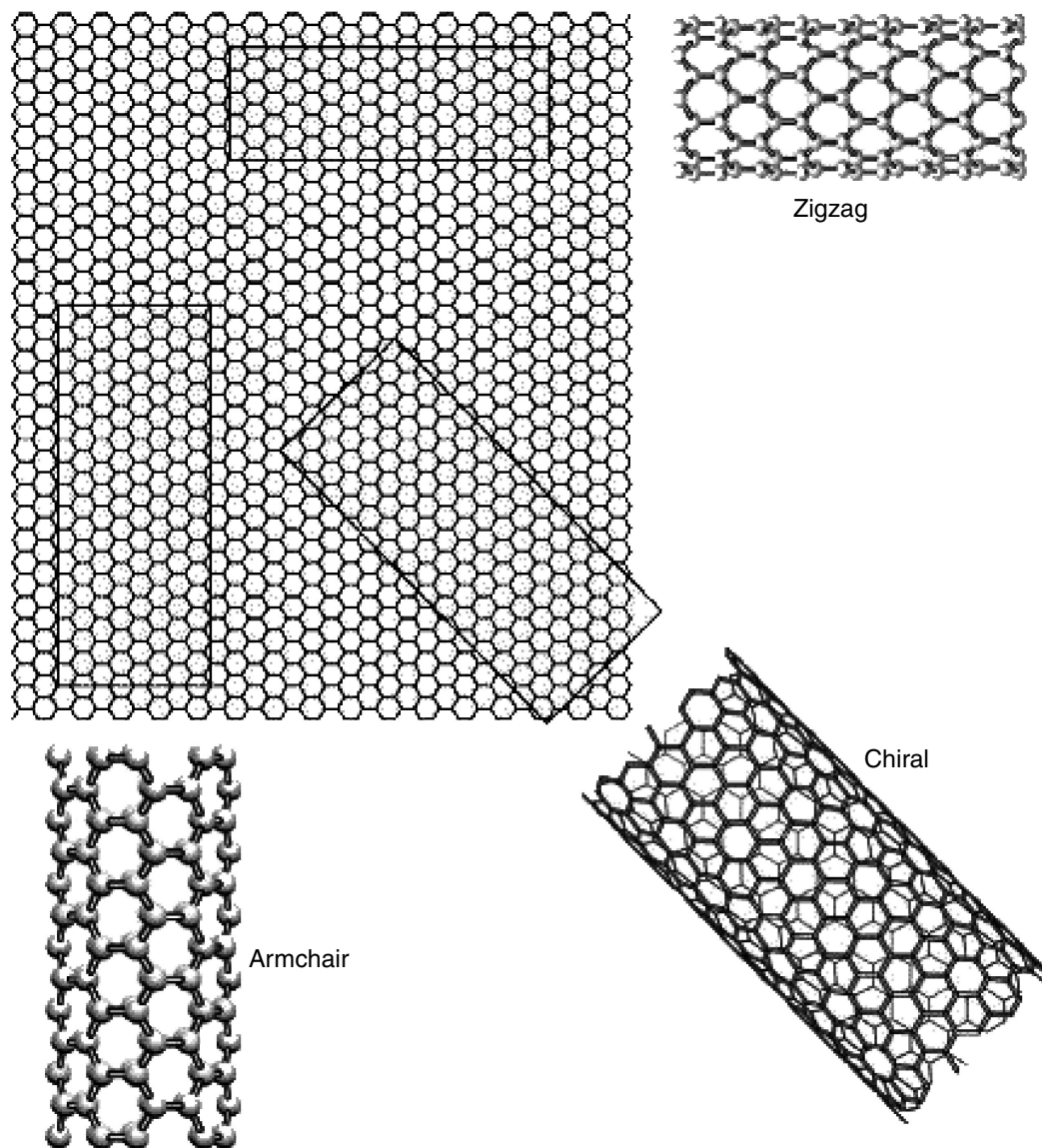


**FIGURE 2.1** Schematic representation of the relation between nanotubes and graphene. The three rectangles can be rolled up into seamless nanotubes; the short side, referred to as the roll-up vector  $\mathbf{R}$ , becomes the circumference.  $\mathbf{R} = n\mathbf{a}_1 + m\mathbf{a}_2$ , is a graphene 2D lattice vector, where  $\mathbf{a}_1$  and  $\mathbf{a}_2$  are unit vectors. Integers  $n$  and  $m$  uniquely define the tube: diameter, chirality, metal vs. semiconducting nature, and band gap, if semiconducting. In a bulk polydisperse sample consisting of a distribution of diameters, the larger the average diameter, the greater the number of  $n, m$  pairs that will satisfy the seamless roll-up condition.

in diameter, with varying numbers of shells, affording a range of empty core diameters. Lengths up to 3 mm have been reported [5]. Nanotubes are distinguished from less-perfect quasi-one-dimensional carbon materials by their well-developed parallel wall structure. Other elements too can be made into nanotubes, so one often encounters the term “SWCNT” to distinguish them from noncarbon tubes, i.e., BN, BCN, metal dichalcogenides [6]. The unique feature of carbon nanotubes is that they exist in both metallic and semiconducting varieties, a blessing or a curse depending on the context.

SWNTs can be conceptualized as seamless cylinders rolled up from graphene rectangles (cf. Figure 2.1), or as cylindrical isomers of large fullerenes.  $C_{70}$  is the smallest nanotube; compared with  $C_{60}$  it contains an extra belt of hexagons normal to the fivefold axis of the hemi- $C_{60}$  caps. Adding more belts leads to longer tubes of the metallic (5,5) armchair category as defined later. According to theory, cylindrical fullerene isomers are less stable than the more nearly spherical ones because the 12 pentagons necessary to ensure closure are localized on the two caps. This

results in strain concentrations at the ends of closed tubes, which in turn makes it easier to perform additional chemistry on the ends than on the sidewalls [7].

There exist many quasi-one-dimensional all-carbon structures, which are neither SWNT nor MWNT. Composite materials reinforced with carbon or graphite fibers are often used in sporting goods, high-performance aircraft, and other applications where high stiffness and light weight are required. Companies such as Hyperion sell commodity quantities of vapor-grown carbon fibers as conductivity additives for paints and plastics. Carbon nanohorns have received a good deal of attention lately as catalyst supports, fuel cell, and battery electrodes [8]. Such materials lack the atomic perfection of nanotubes, but are nonetheless crucially important in science and industry.

The discovery and rapid evolution of carbon nanotubes has played a major role in triggering the explosive growth of R & D in nanotechnology. Many of the early lessons learned carried over to rapid developments in inorganic semiconductor nanowire science and engineering, in particular, field effect transistor (FET)-like switching devices, and chemical and biological sensors. The nanotube field *per se* has fanned out to encompass molecular electronics, multifunctional composites, flat-panel display technology, high-strength lightweight structural materials, nanoscale metrology (mass, heat, functional scanning probe tips, etc.), and others. In this chapter, I attempt to provide a broad-brush introduction to the materials responsible for all this excitement. My selection of sources is personal. Apologies in advance to friends, colleagues, and others whose work I fail to mention.

This chapter is a survey of the physical properties of carbon nanotubes, with emphasis on macroscopic assemblies of engineering interest. The important subjects of synthesis, purification, and composite materials are covered elsewhere in this volume [3,7]. Contact is made with single-tube properties where appropriate; an obvious issue is the extent to which properties of macroscopic material approach those of ideal individual tubes. Materials scientists will immediately note with dismay the paucity of information relating to defects and their influence on properties. In this important arena theory and simulations are far ahead of experiments. Atomic-scale defects may be at the resolution limit of high-resolution transmission electron microscopy (HRTEM). Their presence can be inferred from the breakup of individual tube device characteristics into multiple quantum dots defined by defect-related internal barriers [9].

## 2.2 STRUCTURE

We start the discussion by considering a single isolated tube. Is it a molecule? If so, we might be able to dissolve it in order to perform high-resolution  $^{13}\text{C}$  NMR, the method which proved that the carbons in  $\text{C}_{60}$  were all equivalent, thus confirming the soccer-ball structure. So far, no true solvent for pristine nanotubes has been found. The surfactants, or chemical functionalization, necessary to obtain stable suspensions must perturb the intramolecular structure however slightly. Worse yet, we still lack even minute samples consisting of a single type of nanotube, so even if we had an NMR spectrum, it would be impossible to interpret. HRTEM is a borderline technique for resolving individual carbon atoms 0.14 nm apart. Electron diffraction from a single tube is possible in principle. The most convincing images are from scanned probe microscopy at low temperatures. The example shown in [Figure 2.2\(a\)](#) has a screw axis and “handedness” like DNA, and is referred to as a chiral SWNT.

### 2.2.1 SINGLE-WALL TUBES, BUNDLES, AND CRYSTALLINE ROPES

An SWNT can be envisioned as a narrow rectangular strip of nanoscale graphene “chicken wire” with carbon atoms 0.14 nm apart at each apex, rolled up into a seamless cylinder 1–10 nm in diameter and as long as several micrometers. “Graphene” refers to a monolayer of  $\text{sp}^2$ -bonded carbon atoms. Several possibilities for legal strips, those that will roll up seamlessly, are shown in [Figure 2.1](#). Because the length and width of legal strips are “quantized,” so too are the lengths and diameters of the tubes. The short side of the rectangle becomes the tube diameter and therefore is “quantized” by the requirement that the rolled-up tube must have a continuous lattice structure. Similarly,

the rectangle must be properly oriented with respect to the flat hexagonal lattice, which allows only a finite number of roll-up choices. The longer the short side, the larger the tube diameter *and* the larger the number of choices. Two of them correspond to high-symmetry SWNT; in “zigzag” tubes (top), some of the C–C bonds lie parallel to the tube axis, while in “armchair” tubes (bottom left), some bonds are perpendicular to the axis. Intermediate orientations of the rectangle produce chiral tubes when wrapped, as in Figure 2.2(a).

The different wrappings have profound consequences on the electronic properties. The allowed electron wave functions are no longer those of the unwrapped infinite two-dimensional graphene; the rolling operation imposes periodic boundary conditions for propagation around the circumference, the consequences of which depend on the symmetry. This is the reason why SWNT can either be metallic or insulating.

SWNT in close proximity can self-assemble into more or less close-packed parallel arrays, referred to as ropes or bundles according to whether the arrays are well ordered or not, respectively. These can be directly visualized in the electron microscope when a rope accidentally curves upward from the grid such that the focal plane cuts normally through the rope, as shown in Figure 2.2(b). The driving force is the van der Waals (vdW) attraction, amplified by the considerable lengths involved. Figure 2.2(b) shows a well-ordered rope consisting of  $\sim 100$  tubes with similar diameters. In principle there is no limit to the number of tubes per rope, while the perfection of the 2D organization is directly related to the diameter polydispersity and thus to the synthesis method. The 2D triangular lattice implied by Figure 2.2(b) has been studied quantitatively using x-ray, neutron, and electron diffraction. Data analysis for materials containing highly ordered ropes has advanced to the point that diameter dispersivity, finite size, and the filling of the interior lumen can all be accounted for.

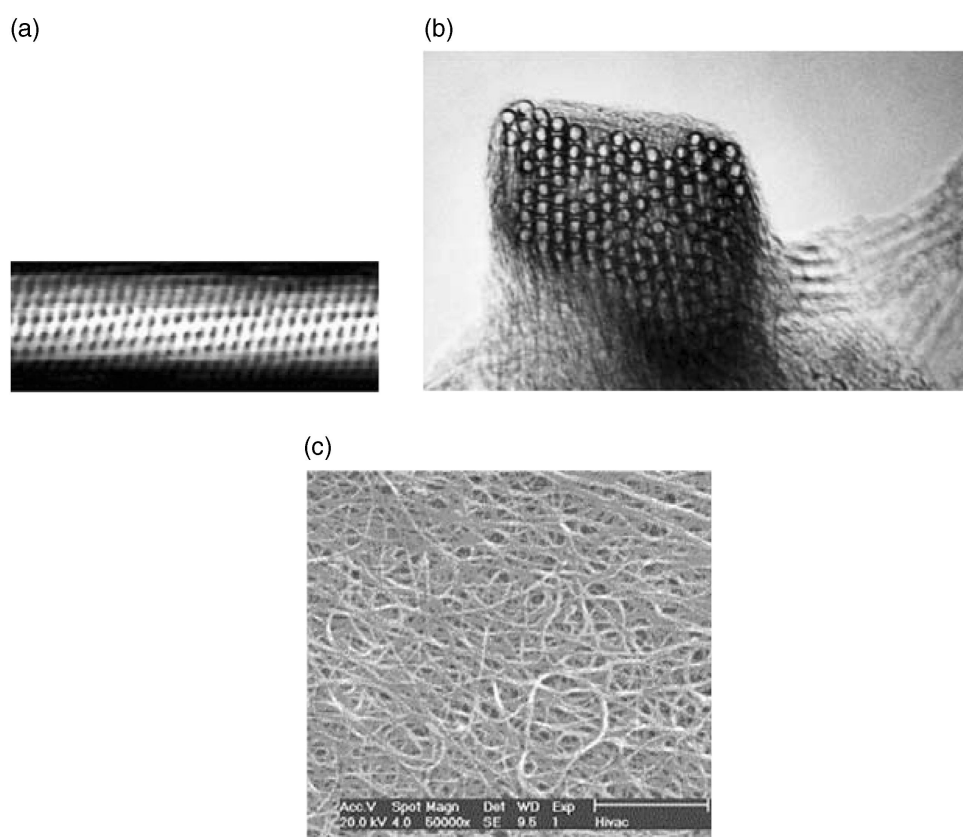


**FIGURE 2.2** Single-wall carbon nanotube images at different length scales. (a) Scanning tunneling microscope image of a chiral SWNT (image by Clauss, W.); (b) HRTEM image of a nanotube rope (from Thess, A. et al., *Science* **273**, 483 (1996), with permission); (c) tangled spaghetti of purified SWNT ropes and bundles (Smalley, R. E., website).

Long-range order in three dimensions is generally frustrated. The 2D close-packed lattice imposes threefold rotational symmetry, while the point symmetry normal to the molecular axes will be modulo 3 only in special cases. This observation has important consequences for the nature of electronic tube–tube interactions in macroscopic materials.

Crystalline ropes are observed in some raw nanotube soots; others show TEM evidence for bundles, but with little or no 2D diffraction intensity. Crystallinity can often be improved by anaerobic thermal annealing, which is generally interpreted as minor rearrangements of misaligned tubes in a bundle, as opposed to grain growth by long-range migration of individuals accreting onto a small primordial rope. Purified bulk material resembles a spaghetti of nanotube ropes depicted in the SEM image in [Figure 2.2\(c\)](#).

Van der Waals bonding among the tubes in a rope implies that the equation of state should be closely related to those of graphite and solid  $C_{60}$  (similar bonding in 2, 1, and 3 directions, respectively [10]). The compressibility in a hydrostatic diamond anvil-cell environment, as determined by x-ray diffraction, is not consistent with the trend established by the other two carbon isomorphs, suggesting that the tubes become polygonalized into hexagonal cross sections at rather modest pressures [11]. The volume compressibility has been measured up to 1.5 GPa as  $0.024 \text{ GPa}^{-1}$ . The deformation of the nanotube lattice is reversible up to 4 GPa, beyond which the nanotube lattice is destroyed. Similarly, the thermal expansion of the 2D triangular lattice [12] of the rope does not follow the pattern of interlayer graphite and FCC  $C_{60}$ . One possibility is that the circular cross section of a tube is only an idealization, with the time-averaged cross-sectional shape changing with temperature due to thermally driven radial fluctuations.

### 2.2.2 MULTIWALL TUBES

Multiwall tubes have two advantages over their single-wall cousins. The multishell structure is stiffer than the single-wall one, especially in compression. Large-scale syntheses by enhanced chemical vapor deposition (CVD) processes are many, while for single-wall tubes, only the Rice HiPco process appears to be scaleable. The special case of double-wall tubes is under intense investigation; the coaxial structure of two nested tubes is well defined by the synthesis conditions, and large enhancement in stiffness over the single wall has already been achieved [13]. Multiwall structures are intrinsically frustrated since it is impossible to satisfy epitaxy simultaneously, or compatibility of wrapping indices ( $n, m$ ) on adjacent shells, with the very strong tendency to maintain the intershell spacing close to that of the graphite interlayer spacing of  $3.35 \text{ \AA}$ . Experimentally, the intershell correlations in MWNT are characteristic of turbostratic graphite in which the ABAB stacking order is severely disrupted [14].

Are multiwall tubes really concentric “Russian doll” structures, or are they perhaps scrolled? A minority of TEM studies suggests scrolling by virtue of observing  $n$  and  $n+1$  graphene layers on opposite sides of the MWNT. One such example [14] is shown in [Figure 2.3](#). On the other hand, attempts to intercalate bulk MWNT samples result in destruction of the cylindrical morphology, which would not be the case if the MWNT were a continuous graphene sheet rolled into a seamless scroll [15].

Several unique features of multiwall tubes should be noted here. Hydrothermal synthesis results in water-filled tubes, a natural model system for studying 1D nanofluidics and exploiting these as nanoreactors [16]. Synthetic methods can be adapted to allow direct fiber production from the primordial soot or the hot reactor plume [17,18], or by twisting fibers from vertically aligned MWNT grown as a carpet-like array on a substrate [19,20]. Current pulses, through individual MWNT, controllably remove one shell at a time, permitting the custom construction of devices to order, with metallic or semiconducting outer shells [21].

### 2.2.3 MACROSCOPIC NANOTUBE MATERIALS

Individual nanotubes can be used to construct electronic devices, gas and biosensors, sensitive nanobalances, NEMS resonators, scanning probe tips, etc. [22]. As the cost of production decreases

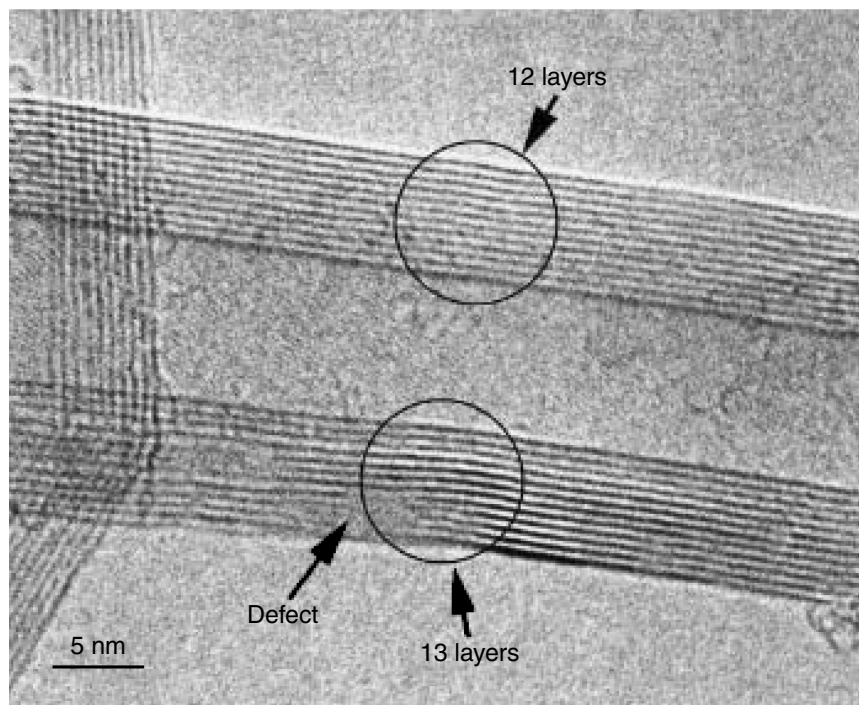


**FIGURE 2.3** HRTEM image of an MWCNT. The number of graphene layer images on the two edges of the tube differs by 1, implying a scroll structure rather than the assumed-to-be-universal Russian doll morphology. (From Lavin, J. G. et al., *Carbon* **40**, 1123–1130 (2002), with permission.)

with time, applications involving macroscopic nanotube-derived materials become feasible. Such materials should obviously be strong and lightweight. Prospects for replacing traditional materials rest on opportunities to design in multifunctional combinations of mechanical, electrical, thermal, dielectric, magnetic, and optical properties.

Macroscopic nanotube materials are available in many forms: compressed random mats of raw or purified soot, filter-deposited foils (“buckypaper”) [23], spin-coated or solvent-cast films [24], and various forms of all-nanotube [25,26], or composite [3,27] fibers. Property optimization for these complex materials depends on many factors. For example, the degree of preferred nanotube orientation within a macroscopic body determines the extent to which one takes advantage of the excellent but anisotropic intrinsic nanotube properties. Another major factor is the macroscopic density. This is important from several aspects. Empty space means missing material in the body, such that most properties will never be optimal. On the other hand, porosity on different length scales can be useful, e.g., for perm-selective membranes, fast diffusion for ionic conduction in electrochemical devices [28], and tailored nanoporosity for filtering, storage, or sequestration of specific molecular-scale analytes.

Materials of SWNT can be partially aligned by mechanical shear [15], anisotropic flow [3,26], gel extrusion [29], filter deposition from suspension in strong magnetic fields [30], or the application of electric fields during or after growth [31]. Fibers exhibit axially symmetric alignment with mosaic spreads of a few degrees in composites [3], and as low as 20° for all-SWNT post-stretched gel fibers [25]. Ordinary filter-deposited or solvent-cast films exhibit substantial adventitious alignment of tube axes in the film plane due simply to the rather gentle landing of rigid sticks on a flat surface [32].

The most complete characterization of the degree of alignment is obtained by combining the best features of Raman scattering [33] and traditional x-ray fiber diagrams [34]. With two independent experimental parameters, texture can be modeled as a “two-phase” system consisting of an aligned fraction, characterized by the angular distribution of tube axes about the preferred direction, plus a completely unaligned fraction to account for SWNT aggregates, which are insufficiently dispersed

to respond to the aligning field. The model distribution function, shown schematically in Figure 2.4, is represented by a Gaussian “bugle horn” for the axially aligned fraction sitting atop a right-circular cylinder, which accounts for the unaligned fraction. X-ray two-dimensional fiber diagrams unambiguously give the Gaussian width from the azimuthal dependence of either a Bragg intensity or form factor diffuse scattering if the material is not sufficiently crystalline. A similar method was previously applied to texture studies of oriented films and fibers of conjugated polymers [35]. This approach can be applied to thin films cut into strips and carefully stacked in a capillary as well as to fibers. Both geometries are shown schematically in Figure 2.5. Angle-dependent polarized Raman scattering, using the x-ray-derived distribution width as input unambiguously gives the unaligned fraction. This is because the resonantly enhanced Raman contribution from the SWNT contribution dominates over all the other constituents of the sample [36], even at the 1% loading level [37]. An example of this combined fitting approach is shown in Figure 2.6 for nanotube fibers extruded from strong acid solution with no post stretching [34]. Here we deduce a mosaic distribution width of  $55^\circ$  full-width at half-maximum (FWHM) and an aligned fraction of 90%. In the case of magnetically aligned buckypapers, these parameters can be correlated with measurements of electrical resistivity  $\rho$  and thermal conductivity  $\kappa$  parallel and perpendicular to the alignment direction [30]. Differences between 7 and 26 T aligning magnetic fields give some clues about the alignment mechanism and strategies for improving the process.

#### 2.2.4 FIBERS

The best alignment achieved so far is in polymer–SWNT composites [3,27]. Here the “dope” consists of either a polymer melt with SWNT dispersed at concentrations up to 10 wt%, or mixtures of polymer and SWNT in the same organic “solvent.” This is extruded through a small orifice after twin-screw mixing and then stretched by take-up spindles. The extensional flow through the orifice, combined with shear flow during stretching, combine to yield FWHMs of the order of a few degrees in the best cases [3]. SWNT–(poly)vinyl alcohol (PVA) composite fibers exhibit modest alignment as extruded, but this can be greatly improved by controlled elongation prior to removal of the PVA by heat treatment [25,38]. Nanotube fibers consisting mainly of MWNT can be obtained directly during carbon arc synthesis [18], or by agglomeration as the tubes are pulled off a substrate [19]. Nothing quantitative is known yet about the degree of alignment in these and related materials [20].

#### 2.2.5 FILLED TUBES

Carbon soot produced by arcing in helium or laser ablation contains both fullerenes (mainly  $C_{60}$ ) and nanotubes, the proportions varying with the amount of transition metal catalysts in the graphite

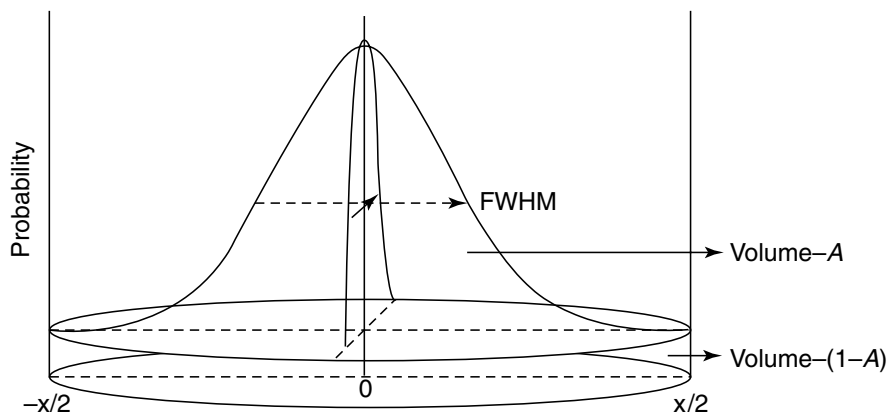


**FIGURE 2.4** Two-phase model for the axially symmetric distribution of nanotube axes in oriented fibers. The inverted horn is the aligned fraction, characterized by an FWHM. The pillbox on top of which the horn is positioned is the unaligned fraction, characterized by its volume relative to the total.



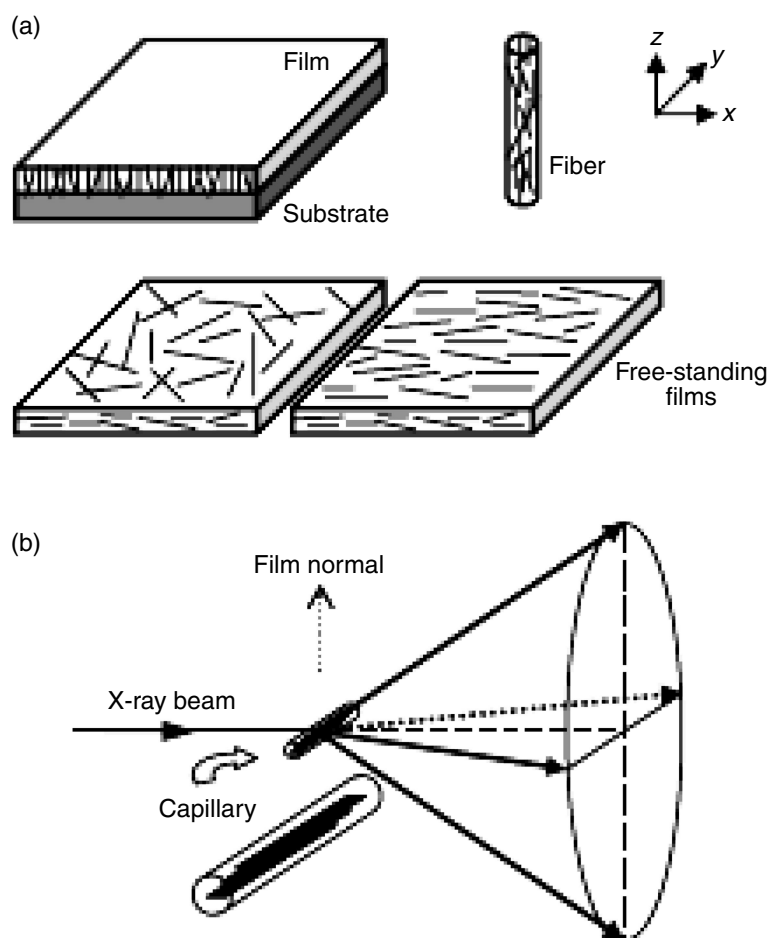


**FIGURE 2.5** Schematic of the experimental setup for measuring out-of-plane mosaic. The film plane is parallel to the incident x-ray beam. Out-of-plane preferred orientation results in azimuth ( $\chi$ )-dependent anisotropic scattering within the 2D detector plane, (a) and (b) refer to films and fibers, respectively.

electrode or target, as discussed previously. Acid purification of nanotube-rich soot reveals the presence of “peapods” — SWNT with chains of  $C_{60}$  inside [39], in substantial amounts [40], denoted by “ $C_{60}$ @SWNT.” It is now understood that acid etching opens holes in the SWNT, either by decapitation or creation of sidewall defects. Fullerenes and other species can diffuse in and be trapped by annealing after filling [41]. Rational synthesis now achieves  $>80\%$  filling routinely [42]. The process has been extended to higher fullerenes [43], endofullerenes [44] and other substances [7]. We speculated early on that host–guest interactions might favor commensurate packings, in which case the ideal container for  $C_{60}$  would be the (10,10) tube. The interior lumen is a good fit for  $C_{60}$  (vdW diameter  $\sim 1$  nm), and, with armchair symmetry, exactly four “belts” of hexagons would be commensurate with one  $C_{60}$  [45]. This turned out not to be important after all, implying very weak interactions between the pea and the pod. There are indeed strong steric constraints on the tube diameter, which will accept a perfect 1D chain [46], while there seems to be no effect of symmetry on filling probability. Global filling fractions depend strongly on diameter dispersivity; HiPco tubes have broad diameter distributions and generally give at best 50–60% filling.

Films of crystalline peapods exhibit unique “fiber diagrams” using the 2D detector (cf. Figure 2.5). Figure 2.7 shows an example of a detector image from such a film. Diffraction peaks from the 1D lattice of close-packed  $C_{60}$  peas are concentrated in the horizontal direction, perpendicular to those from the 2D pod lattice. This separation is a consequence of the out-of-plane preferred orientation; the sample is neither a “perfect powder” nor a single crystal, but rather a “mosaic crystal” with identical orientation distributions exhibited by  $[0\ 0\ L]$  and  $[H\ K\ 0]$  families of reflections [32]. The absence of mixed  $[H\ K\ L]$  indicates that the peas in different pods “float” along the tube axis

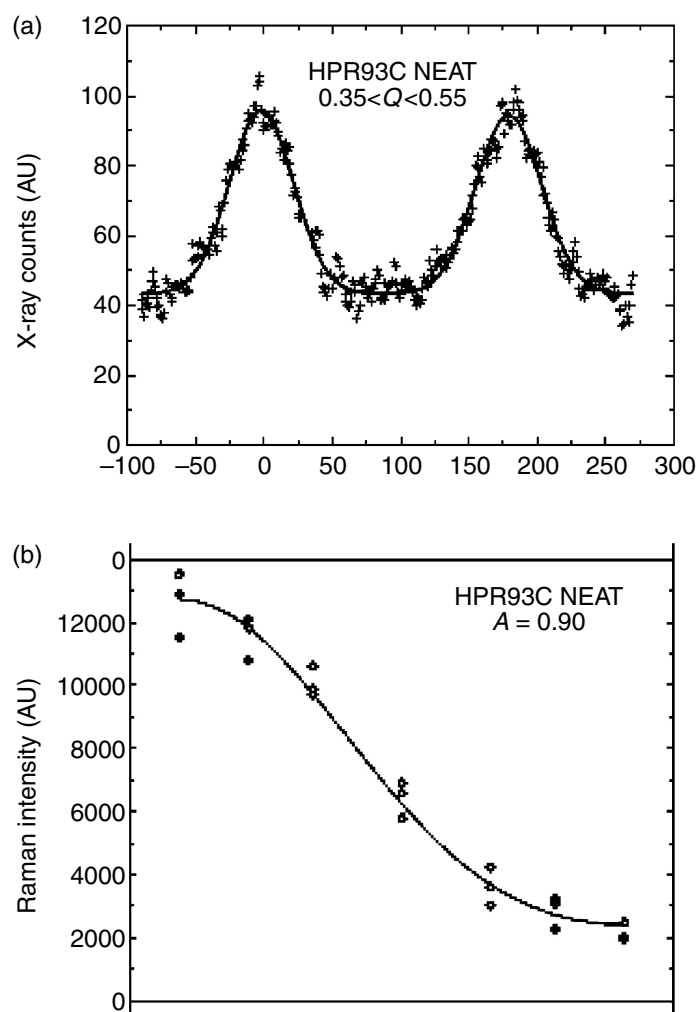


**FIGURE 2.6** Combining x-ray fiber diagrams and angle-dependent polarized Raman scattering to solve the texture problem in SWNT materials. (a) Background-subtracted X-ray counts, summed over different  $Q$  intervals, every  $1^\circ$  in  $\chi$ . Symbols represent data; smooth curves are fits to two Gaussians plus a constant. (b) Angle-dependent polarized Raman data (open circles) and fits (solid curves). A two-parameter model was used, with one (FWHM) fixed at the value determined from (a). (From Zhou, W. et al., *J. Appl. Phys.* **95**, 649 (2004), with permission.)

with respect to each other; there are no 3D correlations among peas in different pods [32,41]. Also shown are radial cuts through 2D images of an unfilled control sample [0 0  $L$ ] I, the filled sample [0 0  $L$ ] II, and [ $H$   $K$  0] III. Note that the filling of  $C_{60}$  into nanotubes significantly changes the diffraction profile. The (0 0 1) and (0 0 2) peaks from the 1D  $C_{60}$  chains are easily detected. Filling fractions can be obtained from detailed curve fits; these seem to be limited only by the diameter dispersion of the starting material, i.e., a real-world sample will always contain some tubes which are too small to be filled [42,46].

One of the most significant developments in the peapod arena is their exploitation as precursors to the formation of highly perfect double-wall nanotubes [13]. Thermal decomposition inside the original SWNT container leads to rearrangement of broken bonds on near-neighbor tubes into a smaller seamless cylinder whose diameter respects the usual vdW spacing requirement. This process takes place at a temperature considerably below those of the amorphization of FCC  $C_{60}$  [47] and enormously below the gas-phase decomposition temperature [48]. Clearly, the coordination and packing environment in the condensed phase leads to facile destruction of the icosahedral molecule by rather violent near-neighbor collisions, more effective in the 12-coordinated 3D solid than in the 2-coordinated chain structure of the “peas.”

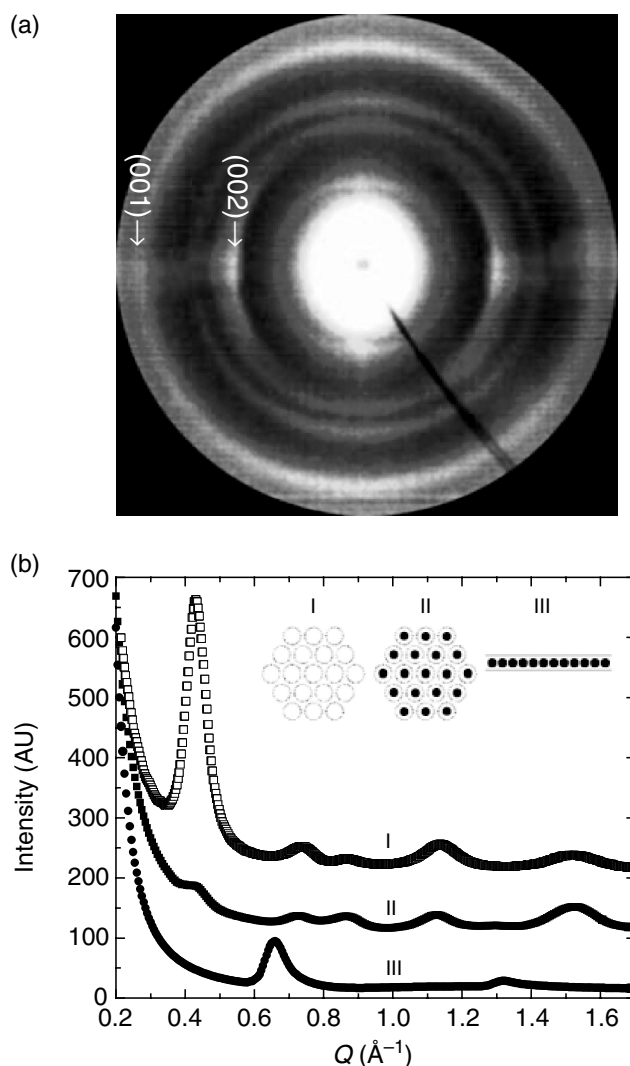


**FIGURE 2.7** (a) Detector image from a  $C_{60}$ @SWNT peapod film. Diffraction peaks from the 1D  $C_{60}$  lattice are concentrated in the direction perpendicular to those from the 2D pod lattice, a consequence of the out-of-plane preferred orientation. (b) X-ray diffraction patterns from starting SWNT film (control sample), and  $C_{60}$ @SWNT film (peapod sample). Note that the filling of  $C_{60}$  into nanotubes significantly changes the diffraction profile. The (0 0 1) and (0 0 2) peaks from the 1D  $C_{60}$  chains are easily detected. (From Zhou, W. et al., *Appl. Phys. Lett.* **84**, 2172 (2004), with permission.)

The extent to which nanotube properties are affected by the endohedral doping is controversial and will be discussed later.

### 2.2.6 NANOTUBE SUSPENSIONS

It is appropriate to conclude our discussion of structure in nanotube materials with a few words about tubes in solution or suspension. These are important for fundamental and technological reasons. Absorption spectroscopy of isolated tubes [49] reveals important aspects of their presumed simple electronic structure and its dependence on tube diameter and symmetry as well as the importance of excitonic and other higher order effects [50]. Nanotube suspensions also provide a unique system in which to study rigid rod-phase behavior [51] and network formation at higher concentrations. Furthermore, an improved understanding of suspension structure should lead to better control of solution processes such as phase separation, chemical derivatization, control and improvement of polymer/nanotube composite properties, and optimization of the “dope” from which fibers are spun.

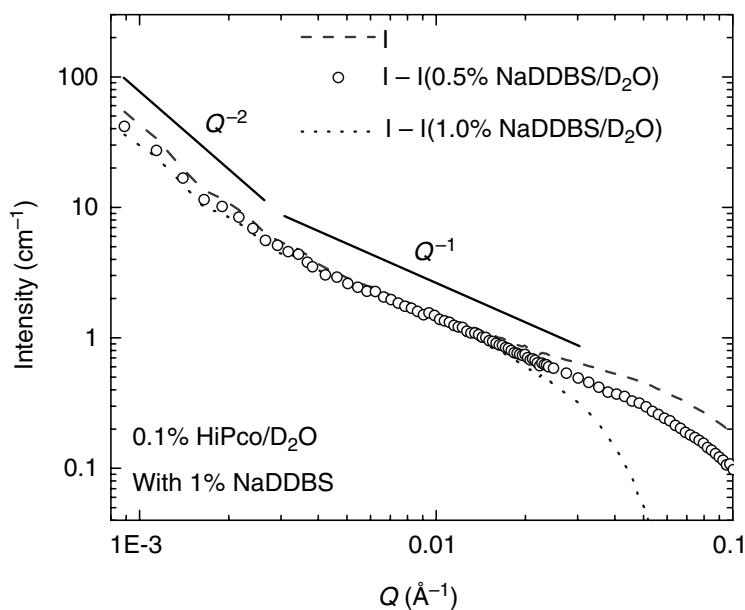


**FIGURE 2.8** Analysis of SANS data from nanotubes in surfactant/heavy water suspension. Subtraction of surfactant contribution from total intensity for HiPco tubes. Dashed and dotted lines correspond to the extreme assumptions of no excess surfactant and no surfactant on the tubes, respectively. A  $Q^{-1}$  slope is clearly visible from 0.003 to 0.02  $\text{\AA}^{-1}$ , no matter what fraction of surfactant intensity is subtracted. There is also a crossover to  $-2$  exponent at 0.004  $\text{\AA}^{-1}$ , suggesting the formation of a dilute network with a mesh size  $\sim 160$  nm. (From Zhou, W. et al., *Chem. Phys. Lett.* **384**, 185–189 (2004), with permission.)

Individual SWNTs with diameters 1–2 nm and lengths 100 nm to several micrometers can be envisioned as rigid rods, and if sufficiently dilute, should display a correspondingly simple structure factor in scattering experiments (light, x-rays, neutrons, etc.). In particular, the scattered intensity,  $I$ , from a suspension of isolated rigid rods with diameter  $D$  and length  $L$  should follow a  $Q^{-1}$  law for scattering wave vectors  $2\pi/L < (Q = 4\pi \sin \theta/\lambda) < 2\pi/D$  [52]. This is generally not observed; suggesting that even at very low concentrations, the SWNTs tend to form loose networks with node spacings of the order of the tube length. One exception is the dilute suspensions using the ionic surfactant sodium dodecylbenzene sulfonate (NaDDBS) and its relatives [52]. It is believed that the benzenoid moiety provides  $\pi$  stacking interactions with the graphene-like tube wall structure, of sufficient strength to adhere to single tubes and thus preventing them from aggregating. Figure 2.8 shows small-angle neutron scattering data for HiPco SWNT in 1% NaDDBS/ $D_2O$  suspensions. After correcting for scattering from NaDDBS micelles and incoherent proton background, one indeed observes a linear regime at intermediate values of  $Q$ . There is a crossover from  $Q^{-1}$  to  $Q^{-2}$  behavior at about 0.004  $\text{\AA}^{-1}$ , corresponding to average tube length  $\sim 160$  nm. This is precisely what is found from atomic force microscopy (AFM) image analysis of  $>1000$  tubes, confirming that we have truly isolated tubes at this very low concentration, i.e.,  $10^{-3}$  wt%. Linear regimes are not observed at any practicable concentration using Triton-X, polymer melts, or superacids. Fiber spinning requires much higher concentrations, so we must accept some degree of aggregation as the dope is being extruded out of the orifice or spinneret. How this limits the properties of the ensuing fibers has not been determined as yet.

### 2.3 PHYSICAL PROPERTIES

We focus on the properties of macroscopic nanotube materials. These ultimately derive from the intrinsic attributes of single tubes, vastly complicated by defects, impurities, preferred orientation, network connectivity, large-scale morphology, etc. Theory does a reasonable job of predicting, rationalizing, and explaining single-tube properties, while structure–property relations in macroscopic

assemblies are still in a rudimentary state. For composites in particular, properties of the simplest materials show large deviations from the rule of mixture behavior.

To achieve viability in practice, any class of new materials must have some property that surpasses the state of the art sufficiently to justify replacement. Alternatively, new materials may provide some new capability otherwise unavailable. It seems likely that the first large-scale applications for nanotubes will arise from multifunctionality, for example, stiff lightweight structural parts, which also conduct electricity and have low thermal expansion.

### 2.3.1 MECHANICAL PROPERTIES

The strength of the carbon–carbon bond gives rise to the extreme interest in the mechanical properties of nanotubes. Theoretically, they should be stiffer and stronger than any known substance. Simulations [53] and experiments [54] demonstrate a remarkable “bend, don’t break” response of individual SWNT to large transverse deformations; an example from Yakobson’s simulation is shown in Figure 2.9. The two segments on either side of the buckled region can be bent into an acute angle without breaking bonds; simulations and experiments show the full recovery of a straight perfect tube once the force is removed.

Young’s modulus of a cantilevered individual MWNT was measured as 1.0 to 1.8 TPa from the amplitude of thermally driven vibrations observed in the TEM [55]. At the low end, this is only ~20% better than the best high-modulus graphite fibers. Exceptional resistance to shock loads has also been demonstrated [56]. Both the modulus and strength are highly dependent on the nanotube growth method and subsequent processing, due no doubt to variable and uncontrolled defects. Values of Young’s modulus as low as 3 to 4 GPa have been observed in MWNT produced by pyrolysis of organic precursors [57]. TEM-based pulling and bending tests gave more reasonable moduli and strength of MWNT of 0.8 and 150 GPa, respectively [58].

Multiwall nanotubes and SWNT bundles may be stiffer in bending but are expected to be weaker in tension due to “pullout” of individual tubes. In one experiment, 15 SWNT ropes under tension broke at a strain of 5.3% or less. The stress–strain curves suggest that the load is carried primarily by SWNT on the periphery of the ropes, from which the authors deduce breaking strengths from 13 to 52 GPa [59]. This is far less than that reported for a single MWNT [58]. On the other hand, the mean value of tensile modulus was 1 TPa, consistent with near-ideal behavior. Clearly, the effects of nonideal structure and morphology have widely different influences on modulus and strength. There is always some ambiguity in choosing the appropriate cross-sectional area to use in evaluating stress–strain data. On a density-normalized basis the nanotubes look much better [22]; modulus and strength are, respectively, 19 and 56 times better than steel.

Figure 2.10 shows the formation of a remarkable nanotube yarn by pulling and (optionally) twisting material from a “forest” of vertically aligned MWNT grown by a CVD process [19]. The untwisted yarns are very weak; if they accidentally touch a surface while being pulled off the substrate, they immediately break. On the other hand, twisted single-strand yarns exhibited strengths in the range 150 to 300 MPa; this improved to 250 to 460 MPa in the two-ply yarns. Further gain



**FIGURE 2.9** MD simulation of a large-amplitude transverse deformation of a carbon nanotube, apparently beyond the elastic limit. In fact, the tube snaps back once the computer-generated force is removed, and there is no plastic deformation or permanent damage. (From Yakobson, B. I., *Appl. Phys. Lett.* **72**, 918–920 (1998), with permission.)

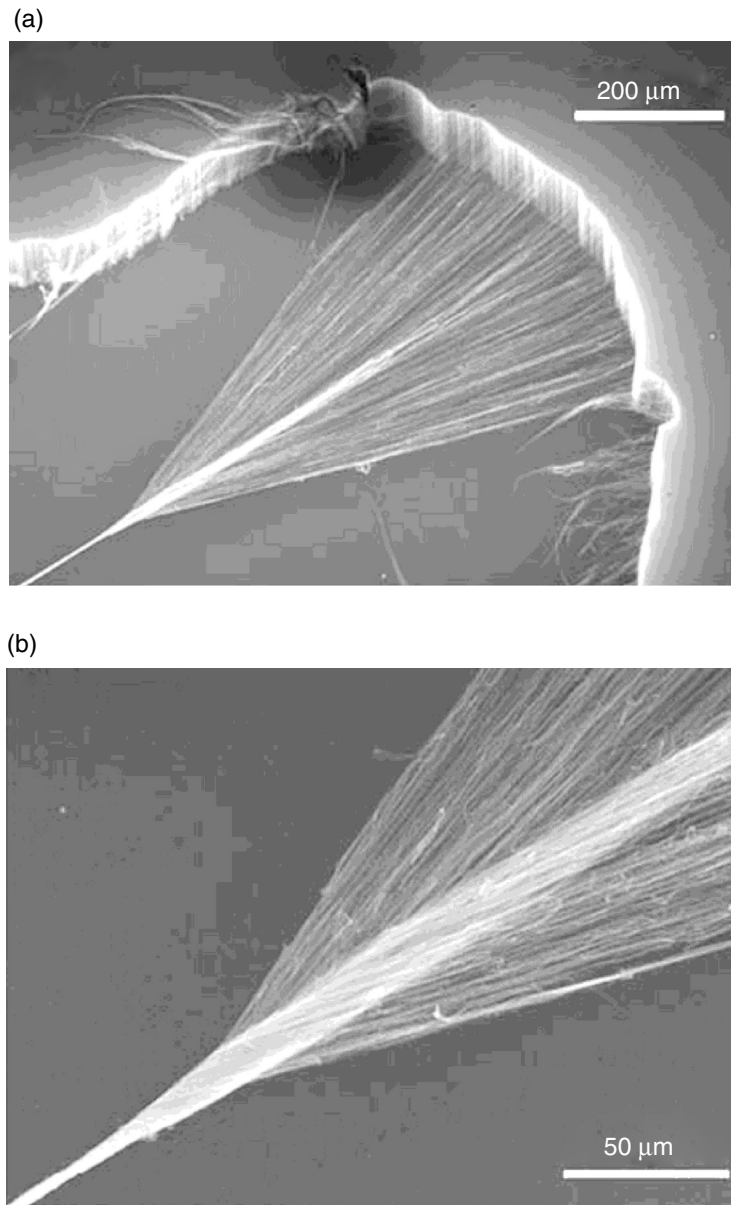


**FIGURE 2.10** *Ex situ* SEM snapshots of a carbon nanotube yarn in the process of being drawn and twisted. The MWNTs,  $\sim 10$  nm in diameter and  $100\ \mu\text{m}$  long, form small bundles of a few nanotubes each in the forest. Drawing fiber normal (a) and parallel (b) to the edge of the forest of nanotubes. (From Zhang, M. et al., *Science*, **306**, 1358 (2004), with permission.)

to 850 MPa was achieved by infiltration with PVA [19], which also improved the strain-to-failure to 13%. Toughness, the so-called “artificial muscle” [60], is a major issue in the optimization of nanotube actuators, where the figure of merit is the work done per cycle.

Another form of nanotube material useful for sensors and actuators are thin films or buckypapers. A typical result for solution-cast film with random SWNT orientations in the plane [32] is described in [61]. The tensile modulus, strength, and elongation-to-break values are 8 GPa (at 0.2% strain), 30 MPa, and 0.5%, respectively, much lower than what can be routinely achieved in fibers. This suggests that failure in the films occurs via interfibrillar slippage rather than fracture within a fibril.

### 2.3.2 THERMAL PROPERTIES

The thermal conductivity  $\kappa$  of carbon materials is dominated by atomic vibrations or phonons. Even in graphite, a good electrical conductor, the electronic density of states is so low that thermal transport via

“free” electrons is negligible at all temperatures. Thus, roughly speaking,  $\kappa(T)$  is given by the product of (1) the temperature-dependent lattice specific heat  $C_p$ , a measure of the density of occupied phonon modes at a given temperature; (2) the group velocity of the phonon modes (speed of sound  $V_s$  for acoustic branches, not strongly  $T$ -dependent); and (3) a mean free path accounting for elastic and inelastic, intrinsic and extrinsic phonon-scattering processes. It was conjectured early on that nanotubes would be excellent heat conductors [62]; the axial stiffness conduces to large  $V_s$ , the 1D structure greatly restricts the phase space for phonon–phonon (Umklapp) collisions, and the presumed atomic perfection largely eliminates elastic scattering from defects. Calculations of the lattice contribution to  $\kappa$ , pioneered by the Tomanek group [63], yield values in the range of 2800 to 6000 W/mK.

Experiments on individual tubes are extremely difficult, and so far have been limited to MWNT [64]. Figure 2.11 shows the temperature-dependent thermal conductance of a 14-nm-diameter, 2.5- $\mu\text{m}$ -long MWNT;  $\kappa(T)$  based on an effective cross-sectional area is shown in the inset. The salient features are a peak value  $\sim 3000$  W/mK at 320 K, in good agreement with the perfect-tube calculations, and a roll-off in  $\kappa$  above 320 K signaling the onset of Umklapp scattering. For bulk MWNT foils,  $\kappa$  is only 20 W/mK [65], suggesting that thermally opaque junctions between tubes severely limit the large-scale diffusion of phonons. The temperature dependence below 150 K reflects the effective dimensionality of the phonon dispersion, a subtlety that is more pronounced in SWNT and will be discussed later. The onset of Umklapp scattering at 320 K is highly significant. Knowing  $C_p$  and  $V_s$  from other experiments and theoretical estimates, the mean free path is  $\sim 500$  nm, comparable to the length of the sample. This means that phonon transport at low  $T$  is essentially ballistic; on average a phonon scatters only a few times as it traverses the sample. There is no corresponding rollover in the data from bulk nanotube samples.

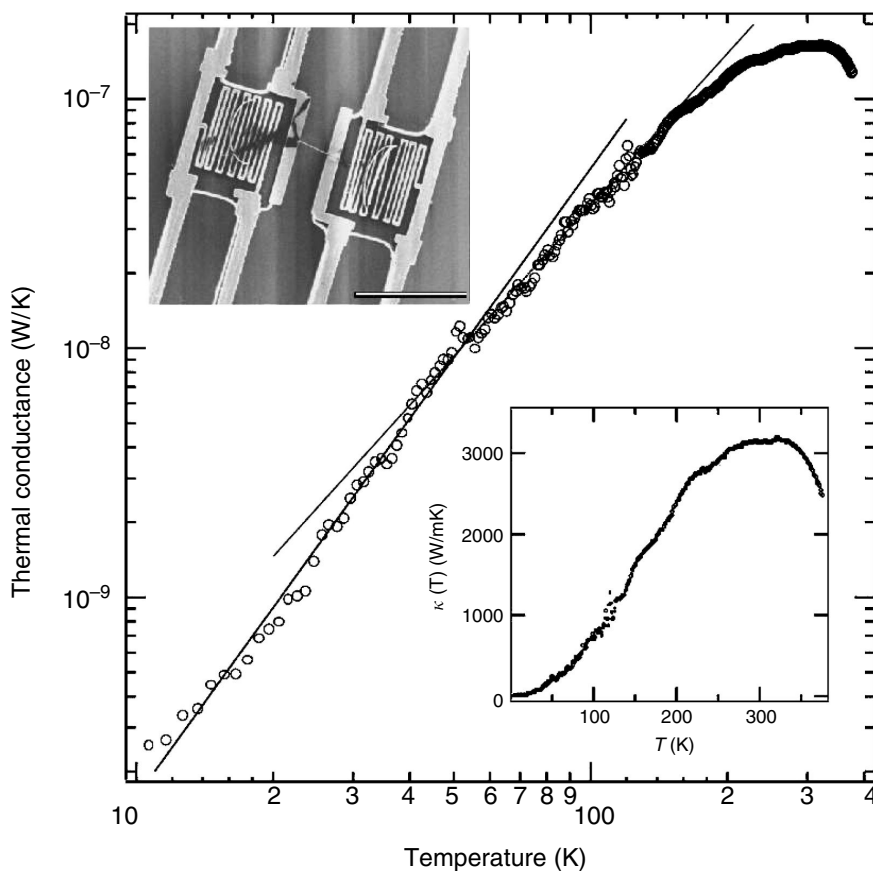


**FIGURE 2.11** Thermal conductance of an individual MWNT of 14 nm diameter. The power law slope decreases from  $\sim 2.5$  to  $\sim 2.0$  above  $\sim 5$  K. Saturation occurs at 340 K, the thermal conductance decreasing at higher  $T$ . Lower inset shows the thermal conductivity, for which some assumptions about effective area are required. (From Kim et al., *Phys. Rev. Lett.* **87**, 215502 (2001), with permission.)

One of the most important concepts in nanotube physics is quantization of the electronic states by the restricted 1D geometry. Analogous 1D phonon quantization is difficult to observe because of the far smaller energy/temperature scale. In general, the smaller the object, the higher the temperature at which quantum confinement effects can be detected, so SWNT with radii  $\sim 2$  nm raise the temperature to practicable values. Temperature-dependent heat capacity of purified SWNT shows direct evidence for 1D quantized phonon subbands [66] (see Figure 2.12). The sample is  $\sim 40$  mg of purified HiPco SWNT, for which the 2D triangular lattice is not well developed. This material was chosen in the hope that the 1D physics would not be obscured by tube–tube coupling. However, a good fit to the data (solid dots) requires an anisotropic, weakly 3D Debye model, shown in the inset, which accounts for weak coupling between SWNT in a rope (black curve). Below 8 K, only the acoustic branch contributes (blue curve), while above 8 K the first optic subband becomes significant (red curve). The key point is that this subband “turns on” at a temperature high enough to be detected, yet low enough not to be buried by graphene-like 2D contributions. The relevant fitting parameters are 4.3 meV for the  $Q = 0$  subband energy (in reasonable agreement with predictions for this diameter) and 1.1 meV for the transverse Debye energy, signaling very weak intertube coupling. It would be of interest to repeat this experiment on samples with weaker or stronger tube–tube coupling, the former, for example, by intercalation with large dopant ions [67]. Above 25 K,  $C_p$  of bulk SWNT is indistinguishable from that of graphite. Extension of the measurement on the same sample down to the milliKelvin regime [68], confirmed the importance of 3D effects at the lowest temperatures; a definitive analysis was impeded by a strong nuclear hyperfine contribution from residual Ni catalyst.

Both SWNT and MWNT materials and composites are being actively studied for thermal management applications, either as “heat pipes” or as alternatives to metallic or alumina particle additives to low thermal resistance adhesives. The individual MWNT results are promising; similar data for SWNT are not yet available. In the case of polymer composites, the important limiting factors are quality of the dispersion and interphase thermal barriers [3]. What limits  $\kappa$  in all-nanotube

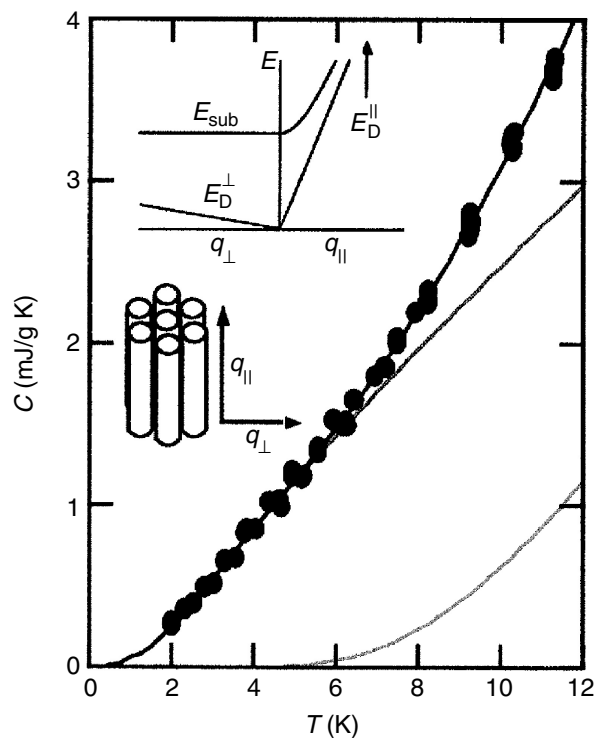


**FIGURE 2.12** Specific heat vs.  $T$  of SWCNTs (dots) fitted to an anisotropic two-band Debye model that accounts for weak coupling between SWNT in a rope (solid curve). The rope structure and ensuing phonon dispersion are shown as insets. (From Hone, J. et al., *Science* **289**, 1730 (2000), with permission.)

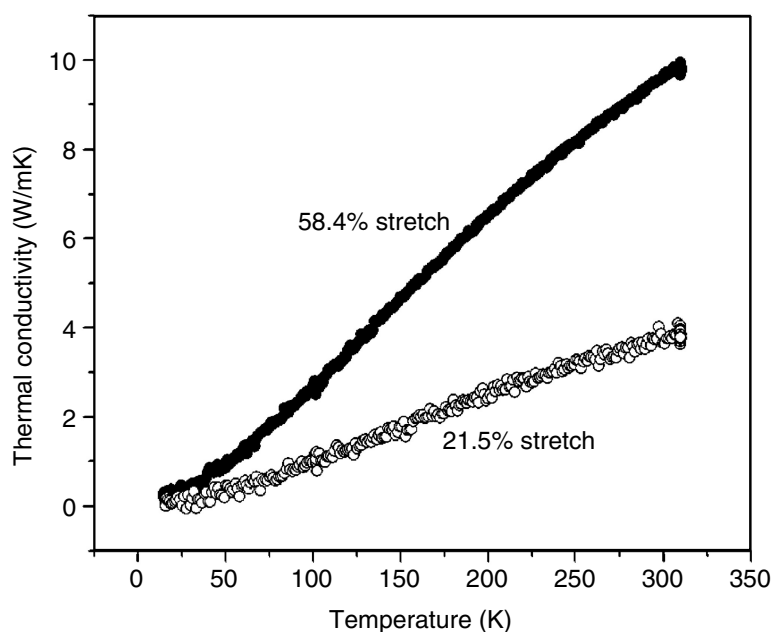


fibers, sheets, etc.? Tube wall defects can be minimized by avoiding long sonication and extended exposure to acids in the fabrication process. In one example, partial alignment of nanotube axes in buckypaper yielded anisotropic thermal conductivities, with  $\kappa_{//}/\kappa_{\perp} \sim 5$  to 10 [69].

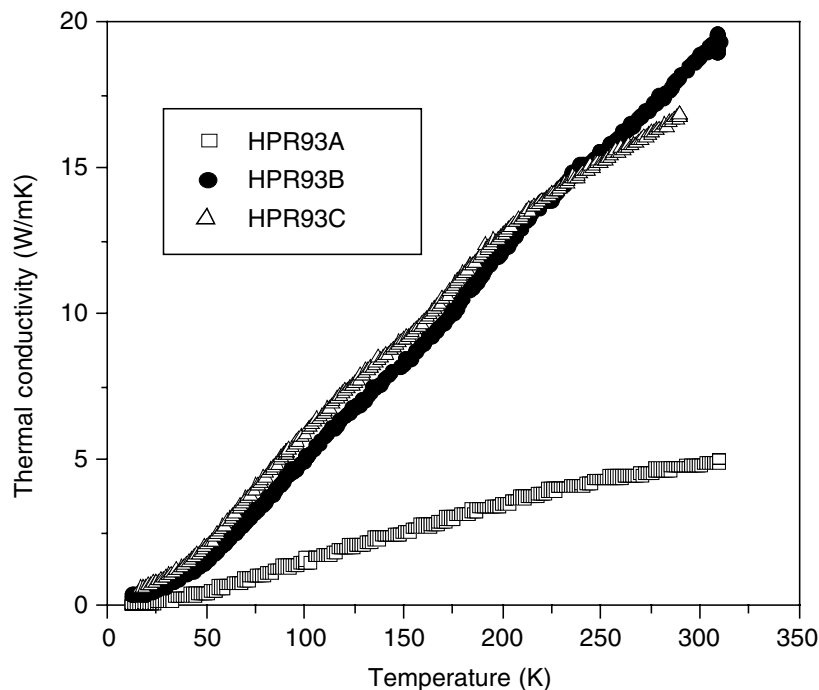
Experimental determinations of  $\kappa$  are subject to many pitfalls, one of which is the problem of defining the cross-sectional area through which the heat is flowing. This is similar to the dimensional ambiguity we encountered with Young's modulus. There are many well-tested methods for measuring thermal conductance  $G$ , but translating that into thermal conductivity  $\kappa$  is not straightforward. This is illustrated by two different results from the magnetic field-aligned buckypaper mentioned above. In the first method, sample dimensions were deduced from a measurement of electrical resistance of the  $\kappa$  sample and scaling to the resistivity of a different sample, with well-defined geometry, taken from the same batch. This assumed that the resistivity is uniform over centimeter length scales in the original piece of buckypaper, and gave  $\kappa$  parallel to the average tube axis  $\sim 250$  W/mK. A second measurement in which the actual dimensions were carefully measured gave a more modest 60 W/mK.

Figure 2.13 shows the effect of stretch alignment on the thermal conductivity of SWNT fibers gel extruded from water/PVA suspensions [25]. Here the fibers are statically stretched in a PVA/water bath by suspending a weight on the end of a length of pristine fiber. Vacuum annealing after elongation eliminates the PVA, so the fiber properties are entirely due to aligned nanotubes. Reducing the mosaic by increasing the elongation, from  $23^\circ$  to  $15^\circ$  FWHM, gives an almost three-fold increase in  $\kappa$  (300 K). In contrast to the individual MWNT data (Figure 2.11), there is no evidence for  $\kappa(T)$  saturation or rolloff at high temperature. This almost certainly means that  $\kappa$  is limited by interparticle barriers and not by the Umklapp mean free path.

Figure 2.14 shows  $\kappa(T)$  for similar fibers extruded from superacid suspension but not stretched [34]. Here the correlations are with nanotube concentration and syringe orifice diameter. Concentration dictates the phase of the rigid rod suspension [26] and controls the viscosity, while the orifice diameter affects the degree of flow-induced alignment. From the three examples shown, and from other observations, the authors find that (1) annealing to remove acid residues and the attendant p-type metallic doping (see below) has no effect on  $\kappa$  at any temperature; (2) reducing the



**FIGURE 2.13** Thermal conductivity vs. temperature for annealed nanotube fibers, which have been stretch-aligned to 21% (lower curve) and 58% (upper curve). Additional alignment of the latter yields a factor of  $\sim 2$  further enhancement of  $\kappa$ . The temperature dependence is dominated by that of the lattice specific heat, as is generally observed. (From Badaire, S. et al., *J. Appl. Phys.* **96**, 7509 (2004), with permission.)



**FIGURE 2.14** Thermal conductivity  $\kappa$  vs. temperature of three HiPco fibers. HPR93 exhibits the broadest mosaic distribution of nanotube axes, as determined from the x-ray fiber diagrams.

concentration from 8 to 6%, or reducing the syringe diameter from 500 to 250  $\mu\text{m}$  improves  $\kappa$  (300 K) fourfold; and (3) further syringe diameter reduction to 125  $\mu\text{m}$  yields no further improvement. The syringe diameter effects are clearly due to improved alignment; the smallest orifice gives the smallest mosaic, 45° FWHM compared to 65° with the 500  $\mu\text{m}$  one. The best  $\kappa$  value is still orders of magnitude below graphite and ideal MWNT, most probably due to thermal barriers. It may be significant that the highest macroscopic  $\kappa$  was obtained for materials made from pulsed laser vaporization (PLV) SWNT without extended exposure to strong acids. PLV tubes made thus are known to be highly perfect, while acid immersion can lead to defects and ultimately to very short tubes. Either way, the phonon mean free path in such materials may be quite low.

Thermal conductivity of peapods is enhanced relative to that of empty tubes, and the enhancement exhibits interesting temperature dependence [70,71]. Difference data,  $\kappa(\text{filled}) - \kappa(\text{empty})$ , from 10 to 285 K are shown in Figure 2.15. Three distinct regions are evident. Region I is dominated by the contribution from the very soft  $C_{60}$ - $C_{60}$  acoustic modes. A 1D Debye temperature of 90 K is estimated for these modes using a Lennard-Jones potential. At  $T_D$  all the LA modes are excited, the excess heat capacity saturates and  $\Delta\kappa$  levels off to a constant value (region II). The filling fraction of this sample is well below 50%, and the theory predicts the existence of  $C_{60}$  capsules separated by lengths of empty tubes to account for the unfilled sites [46]. We imagine the onset of a new thermal transport mechanism (region III), beginning at temperatures sufficiently high to break the weak vdW bond between a terminal  $C_{60}$  and its capsule. This will happen more efficiently at the hot end, and, once liberated, the free  $C_{60}$  will thermally diffuse to, and join, the end of a cold capsule, as shown schematically in the inset. The internal degrees of freedom represent an additional thermal transport process accompanying the mass transport inside the tube. The rate of this process increases with increasing  $T$  and will saturate at a very high  $T$ , which transforms the assembly of capsules to a 1D gas. This scenario is speculative at this point since it has been observed only in one sample. A rigorous test of the mechanism would be to find out if the effect disappears in a completely filled sample. Other endohedral species may give larger enhancements, and these materials may then become candidates for thermal management applications such as additives to conducting adhesives.

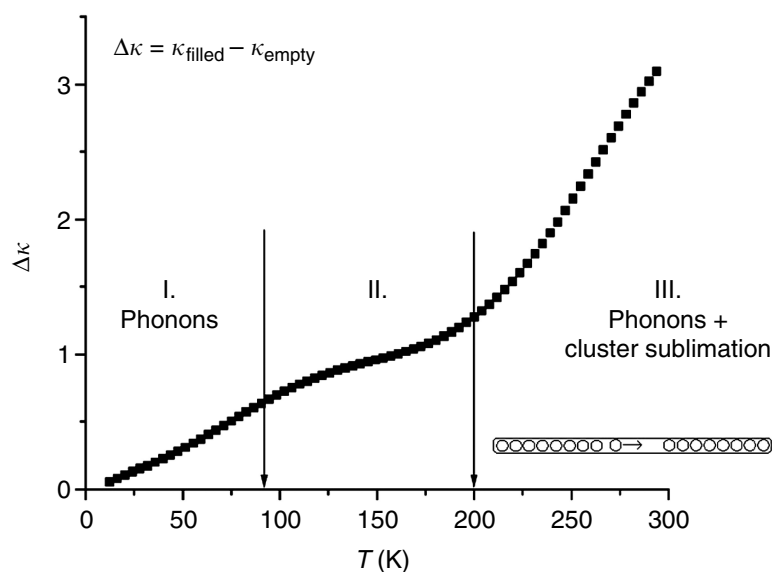


**FIGURE 2.15** Excess thermal conductivity in a partially filled  $C_{60}$ @SWNT buckypaper. Enhancement in regime I attributed to the 1D LA phonons on the  $C_{60}$  chains. Saturation in regime II after  $T > T_{\text{Debye}} \sim 90$  K of the 1D molecular modes. Further enhancement in regime III assigned to hot  $C_{60}$  molecules subliming off the end of a capsule, diffusing to the end of a colder capsule while carrying internal vibrations as a combined heat and mass transfer.

### 2.3.3 ELECTRONIC PROPERTIES

At the last count Google.scholar gave 4400 hits on this rubric, so this section will be highly selective.

Theory led experiment in this important aspect of nanotube properties, and the most important results emerge from a simple idea. One monolayer of graphene has two energy bands  $E_n(k)$  which cross at the Fermi energy  $E_F$ , so the system is on the cusp of a metal–insulator (MI) transition. The electronic ground state can therefore be described either as a zero-gap semiconductor or as a metal with infinitesimal density of states at the Fermi energy  $N(E_F)$ . In 3D graphite, the interlayer interaction causes a transition to a semimetal which conducts well, because the  $\sim 10^{18}$  charge carriers/cm<sup>3</sup> have very high mobility. On the other hand, rolling a single sheet into a tube is a symmetry-breaking transition, which leads to semiconducting or metallic ground states, depending on the choice of wrapping (Figure 2.1). The band structure of a single tube consists of unusual 1D subbands resulting from the requirement that the radial wave function be commensurate with the circumference of the tube. The larger the tube, the smaller the subband spacing; in the 2D graphene limit, there are only the two bands mentioned above. The longitudinal dispersion is linear for a range of energies close to zero.

As noted earlier, bulk properties are generally dominated by extrinsic effects, although some of the 1D subtleties remain, especially in oriented material. The properties of the principal techniques are resistivity and its temperature dependence, density of states spectroscopy using electron energy loss and photoemission, optical absorption, and reflectivity. In a few cases, thermoelectric power and conduction electron spin resonance have also been applied to nanotube physics.

The electrical properties of bulk nanotube materials have evolved considerably since the first experiments 10 years ago. Early samples consisted of pressed “mats” of nanotube soots from carbon arc or laser ablation processes, which contained only 10 to 30 wt% tubes. Major impurities were amorphous carbon, metal catalyst particles, and fullerenes, mainly  $C_{60}$ . Mat densities were as low as 1% of the crystallographic value computed from a triangular lattice of 1.4 nm diameter SWNT. On the other hand, long high-quality tubes could be found in these soots. This is because they had not been subjected to acid treatment or sonication in attempts to remove impurities, both of which are now known to create sidewall defects and ultimately to cut tubes into shorter lengths.

The prevailing attitude at the time was that only single-tube measurements would give useful information. Nevertheless, some valuable information, still valid today, was obtained from four-probe measurements on these mats. First, correcting for the missing material,  $\rho$  (300 K) values within 1–2 decades of in-plane graphite were obtained, suggesting that bulk SWNT materials could be developed into strong, lightweight synthetic metals [72]. Second, the very modest temperature dependence in the range  $80 \text{ K} < T < 350 \text{ K}$  changed from nonmetallic to weakly metallic at  $\sim 200 \text{ K}$ , suggesting a phonon-scattering mechanism at high temperatures. Third, experiments extended to very low  $T$  showed a strong divergence in  $\rho(T)$  as  $T \rightarrow 0$ , indicating strong localization of carriers [73]. Finally, chemical doping with bromine or potassium [67,74] showed that like graphite, bulk SWNT material acted as an amphoteric host for redox doping. All of these phenomena have since been revisited using purified samples with SWNT content approaching 100%.

Figure 2.16 shows the anisotropy of  $\rho(T)$  measured parallel and perpendicular to the alignment direction for the case of buckypaper deposition in a magnetic field [30]. The temperature dependence is weakly nonmetallic and quite similar for both orientations. Furthermore, the anisotropy is independent of temperature. These observations indicate that we are not observing the intrinsic anisotropy of aligned SWNT; transport in the perpendicular direction is dominated by misaligned bundles or fibrils, which short out the larger intertube/interbundle resistance. The nonmetallic  $T$ -dependence is consistent with previous results on unoriented buckypaper after similar acid purification and high-temperature vacuum annealing. These processes are presumed to reduce the mean free path for electron–phonon scattering via defect creation or tube cutting, and thus eliminate the high-temperature regime of positive  $d\rho/dT$ . At 295 K, the measured  $\rho_{\parallel}$  for 7 T field alignment is  $0.91 \text{ m}\Omega \text{ cm}$ . Accounting for gross porosity raises this to  $0.41 \text{ m}\Omega \text{ cm}$ .

The weak anisotropy can be accounted for by a simple model of 1D paths in the plane of the sample, each sample containing on average  $n$  elements (ropes, tubes) of fixed length and resistance. The resistance of each path is linearly proportional to  $n$  and, since for a fixed number of elements, the number of paths is inversely proportional to  $n$ , the resistance of the ensemble of paths in parallel is

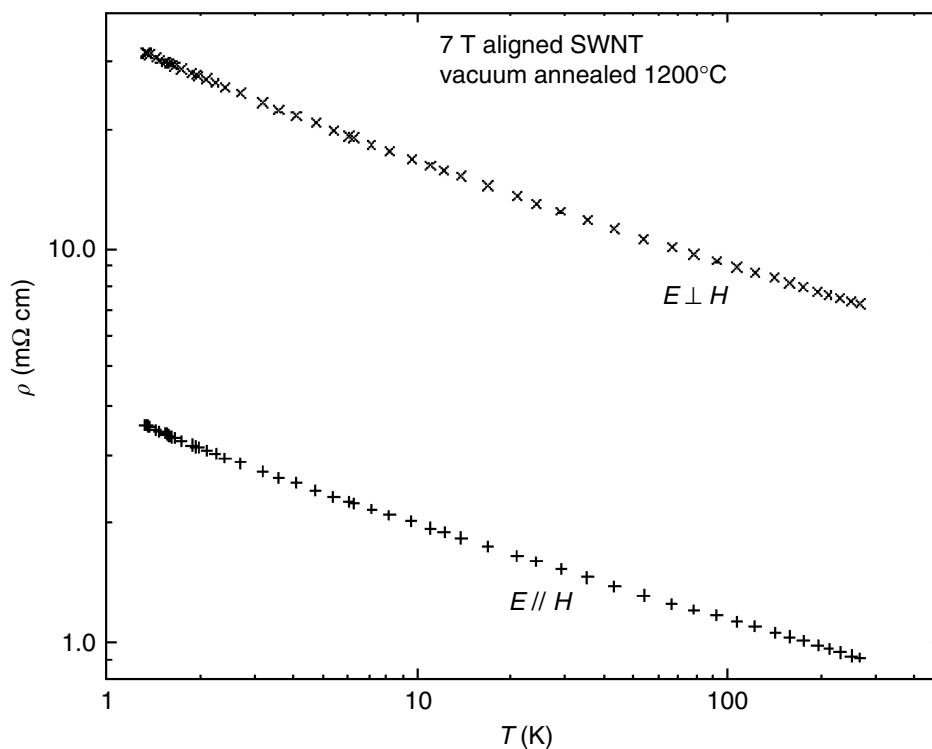


**FIGURE 2.16** Resistivity vs. temperature for annealed 7 T-aligned bucky paper, measured with current perpendicular and parallel to the average alignment axis on two different samples with in-line four-probe contacts. (From Fischer, J. E. et al., *J. Appl. Phys.* **93**, 2157 (2003), with permission.)

proportional to  $n^2$ . The average number of elements  $n$  required for current to flow through the sample is equal to  $L/\lambda$ , where  $L$  is the length of the sample and  $\lambda$  is the mean projection of the element length in the current direction:  $\lambda$  depends on the distribution width and aligned fraction. Using x-ray and Raman data as input, very good agreement is obtained between predicted and measured  $\rho_{\parallel}/\rho_{\perp}$  for 7 and 26 T data.

How does the experimental  $\rho_{\parallel}$  (300 K) compare with that of an assembly of ballistic conductors? Assume that each metallic tube in a perfectly aligned sample is comprised of finite-length ballistic conductors in series, the length being the mean free path  $\lambda$  for electron–phonon backscattering. Each tube has two transport channels corresponding to the two bands degenerate at  $E_F$ . Taking  $\lambda = 300$  nm [75],  $\rho_{\parallel} = (\text{area}/\text{tube})/(2G_0 \times 300 \text{ nm}) = 1.5 \times 10^{-5} \Omega \text{ cm}$ , where  $G_0$  is the conductance quantum  $(12.6 \text{ K } \Omega)^{-1}$ . Assuming further that tube growth is stochastic with respect to wrapping indices, only one third of the tubes will be metallic at 300 K and so  $\rho_{\parallel} \sim 50 \mu\Omega \text{ cm}$ , roughly twice the value for graphite. This is a surprising result because there are many factors which will increase this number in real samples: finite distribution width of tube axes, unaligned tubes, empty volume (porosity), junction resistance between tube segments and between ropes, incoherent intertube scattering within a rope, and elastic scattering from tube ends, defects, and impurities. These may be partially offset by p doping of the semiconducting tubes by acid residues from purification and by atmospheric oxygen.

Pure nanotube fibers offer the prospect of even lower resistivities since they are readily aligned during extrusion and can be further aligned by stretching. We discuss next the results of transport measurements on the two sets of fibers described above: syringe extruded from oleum suspensions and PVA/water mixtures.

Figures 2.17(a) and (b) show the effects of extrusion conditions and post-extrusion annealing on the temperature-dependent resistivity of fibers extruded from anhydrous sulfuric acid, or oleum [34]. Varying degrees of alignment were obtained from HPR93 fibers extruded using three different combinations of SNWT concentration and orifice diameter. The texture results of these have been discussed above. Annealing was carried out in vacuum or flowing argon at 1100°C for 24 h. In the neat state, all three fibers exhibit low resistance with metallic temperature dependence above 200 K, as shown in Figure 2.17(a). The best alignment is obtained for HPR93B, which correlates nicely with the lowest  $\rho$  (300 K) = 0.24 m $\Omega$  cm, about a factor 10 less than graphite. For all three neat fibers, both the small values and the weak temperature dependence are due to the strong redox doping effect of bisulfate from the acid suspension. The nondivergent low- $T$  behavior in the neat state can be ascribed to interparticle tunneling induced by thermal fluctuations [76].

The effect of annealing on  $\rho(T)$  is shown in Figure 2.17(b), which displays the results of a series of successively higher annealing temperatures at constant time intervals. All three annealed samples show large increases in resistivity at all  $T$ , in addition to notably steeper nonmetallic temperature dependence. In general, annealing removes dopant molecules and the fibers become more resistive with higher annealing temperatures. This effect is more pronounced at low  $T$ . Note that for HPR93B,  $d\rho/dT$  still becomes more negative with decreasing  $T$  at our lower limit of 1.3 K, unlike the nondivergent behavior of the neat fibers. These results suggest that removing dopant molecules leads to localization of charge carriers within the ropes.

A similar study of fibers spun from PVA–water–surfactant [29] focused on the effect of post-extrusion stretching while the green “gel” fiber still contained  $\sim 50\%$  PVA. The effect on  $\rho$  (300 K) is shown in Figure 2.18 [25]. An initial decrease by a factor  $\sim 4$  up to 21% stretch is followed by saturation beyond  $\sim 35\%$  stretch. Surprisingly, the x-ray-derived-distribution width is narrowing continuously over the whole range of stretching (up to 80%), suggesting that above an intermediate degree of alignment,  $\rho$  (297 K) is limited by some other factor which does not improve with further stretching. Note also that for these composite gel fibers,  $\rho$  (300 K) is 20 to 30 times larger than for the neat oleum-based fibers. Here, the insulating PVA impedes long-range transport while the presence of trace p-type dopants enhances the neat conductivity of the oleum fibers.

Selected fibers were annealed in  $\text{H}_2$  at 1000°C after stretching, to remove the insulating PVA and thereby obtain more highly conducting material. This process leads to a strong reduction in

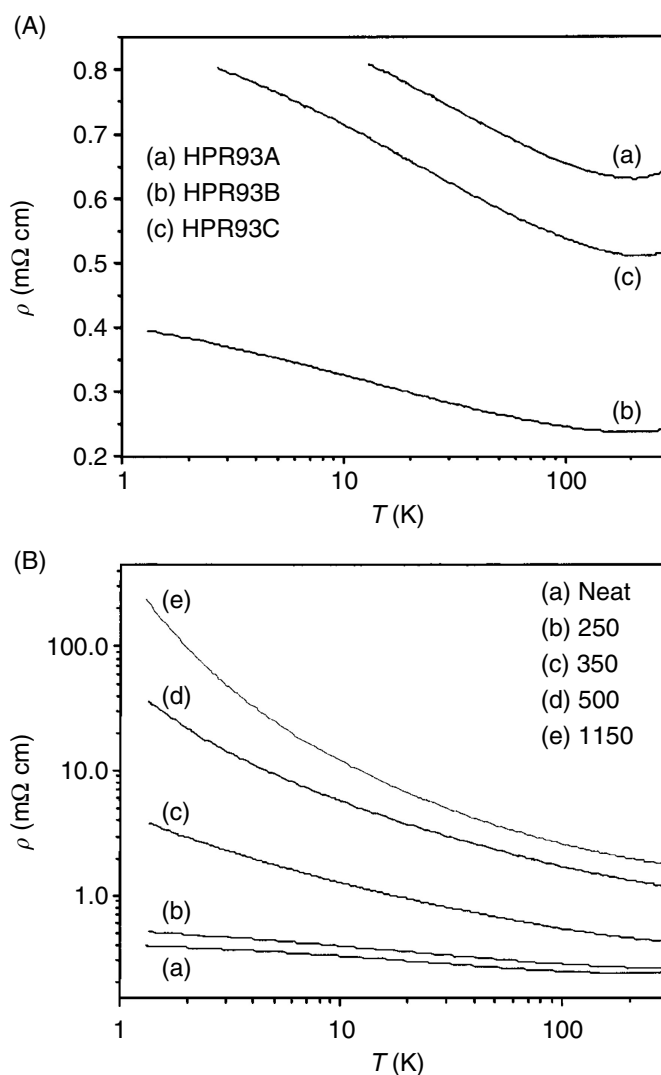


**FIGURE 2.17** (a) Four-point resistivity vs. temperature for three neat SWNT fibers extruded from oleum suspension.  $\rho$  decreases at all  $T$  as alignment improves. Nonmetallic behavior at low  $T$  levels off as  $T \rightarrow 0$  (non-divergent behavior) while metallic behavior is observed above 200 K. (b) Effect of vacuum annealing on  $\rho(T)$  for HPR93B; note log–log scale.  $\rho$  increases as the bisulfate p-dopants are removed, especially at very low  $T$  (factor  $\sim 500$  at 1.3 K). Metallic behavior is lost, and the slope  $d\rho/dT$  continues to increase as  $T \rightarrow 0$  (divergent behavior). (From Zhou, W. et al., *J. Appl. Phys.* **95**, 649 (2004), with permission.)

$\rho$  (300 K) and a flattening of the  $\rho(T)$  curve to a much weaker  $T$  dependence than in the green gel fiber. The data for green PVA/SWNT composite fiber and for the PVA-free annealed one are shown in Figure 2.19. Both have been stretch-aligned as indicated in the figure legend; note the log–log scale. At 300 K,  $\rho$  for the composite fiber exceeds that of the annealed one by 40 to 50 times. Here, the elimination of PVA removes high-resistance interbundle contacts so the macroscopic carrier transport is more efficient. At low temperature the difference is more dramatic, suggesting that the presence of PVA enhances the effects of carrier localization by disorder. The composite fiber resistance becomes too high to measure at the lowest temperature. Extrapolating to 2 K, we deduce a resistance ratio of at least 11 decades, strongly suggesting totally different conduction mechanisms in the two morphologies. It is obvious from the data that disorder dominates charge transport in both states. Furthermore, the disorder is most likely to encompass all three dimensions since the fibers consist of coupled and intertwined objects. In particular, we expect that the disorder is neither limited to 1D carrier localization on individual tubes or bundles, nor to defect scattering/trapping on single tubes. The huge effect of PVA, which permeates the interbundle volumes in the composite

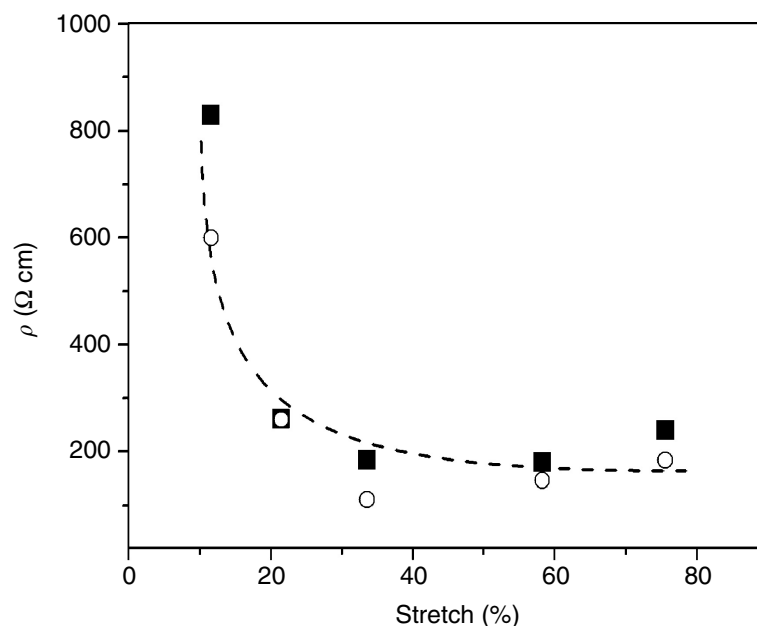


**FIGURE 2.18** Four-probe electrical resistivity at room temperature vs. stretch ratio for PVA composite nanotube fibers. The experiments have been conducted on two series of samples (black squares, open circles). Accurate cross-sectional areas were obtained from SEM image analysis. The resistivity decreases with stretch ratio by a factor between three and four for the two sets of data. The absolute value is intermediate between all-SWNT fibers and polymer composites. The dashed line is a guide to the eye. (From Badaire, S. et al., *J. Appl. Phys.* **96**, 7509 (2004), with permission.)

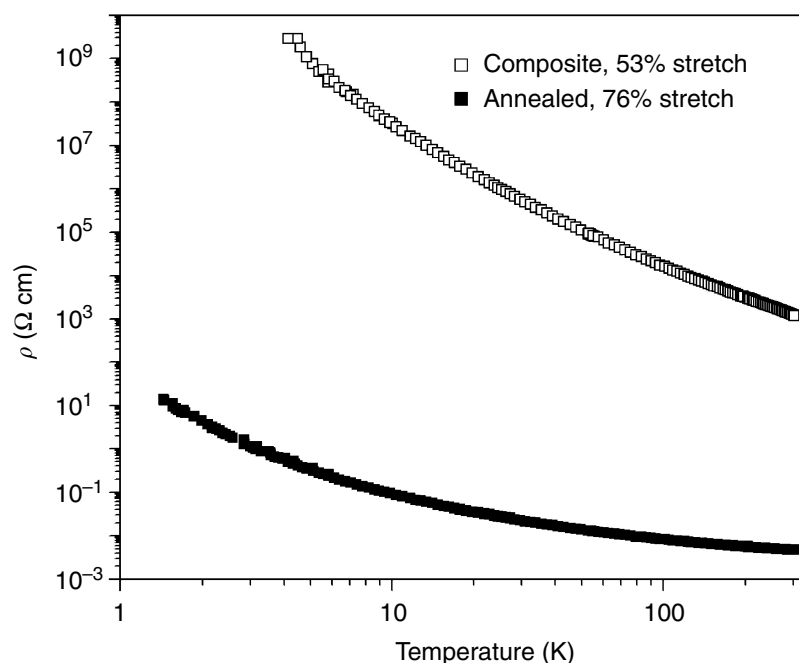


**FIGURE 2.19** Resistivity vs. temperature for composite (53% stretch) and annealed (76% stretch) nanotube fibers (note log–log scale). Note that  $\rho(T)$  for the composite fiber is more strongly divergent as  $T \rightarrow 0$  as compared to the annealed one. (From Badaire, S. et al., *J. Appl. Phys.* **96**, 7509 (2004), with permission.)

fibers, cannot possibly be 1D. It is interesting to note that for both fiber series, one ends up with about the same  $\rho$  (300 K) after annealing, whereas this value is approached from opposite directions in the two different processes.

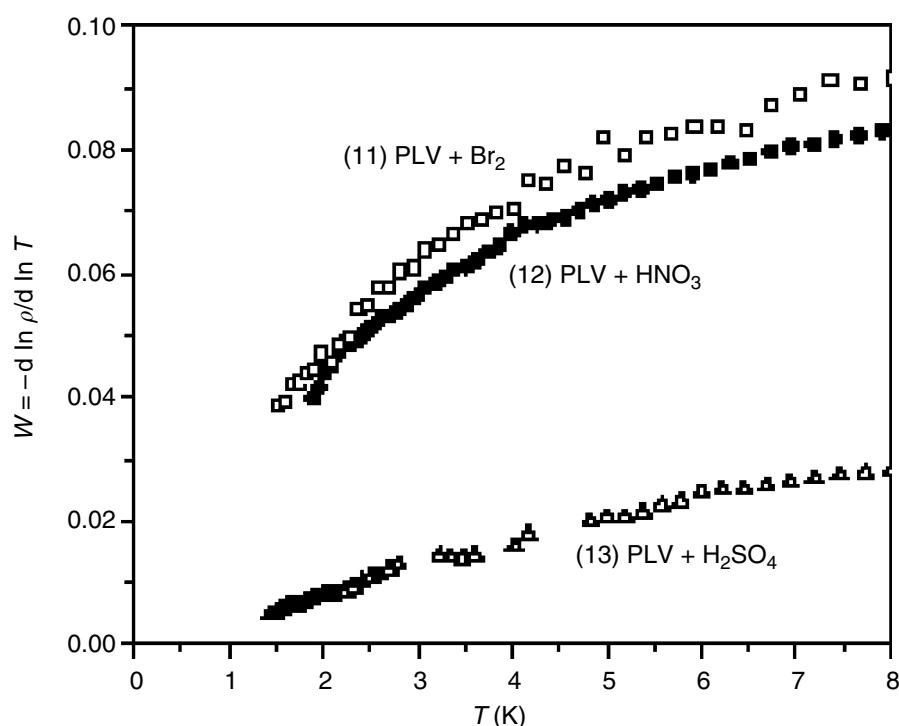
The qualitatively different  $\rho(T)$  behaviors in the two sets of fibers can be attributed to an MI transition as a function of doping level [77]. On the metallic side for heavily doped tubes,  $\rho$  tends

to a finite value as  $T$  approaches zero, and the effective band gap,  $-\text{dln}\rho/\text{d}T$ , vanishes as  $T$  approaches zero; examples of this behavior are shown in Figure 2.20. On the insulating side for PVA-rich gel fibers or annealed oleum fibers,  $\rho$  diverges as  $T$  approaches zero, and the exponential  $T$  dependence can be ascribed to strong localization and either 3D Mott or Coulomb gap variable-range hopping [77]. The MI transition is revealed by systematic measurements of resistivity and transverse magnetoresistance (MR) in the ranges 1.9 to 300 K and 0 to 9 T, as a function of p-type redox doping. The observed changes in transport properties are explained by the effect of doping on semiconducting SWNTs and tube–tube coupling.

How does the presence of endohedral  $C_{60}$  affect the electronic properties of peapods? Despite predictions based on work function differences between peas and pod, there is no evidence for charge transfer redox doping by the endofullerenes. Figure 2.21 shows  $\rho(T)$  data for a peapod sample and an unfilled control [70,71]. Near 300 K the resistivities are the same within experimental error, and the peapod temperature dependence is steeper suggesting stronger disorder effects compared with the empty tubes.

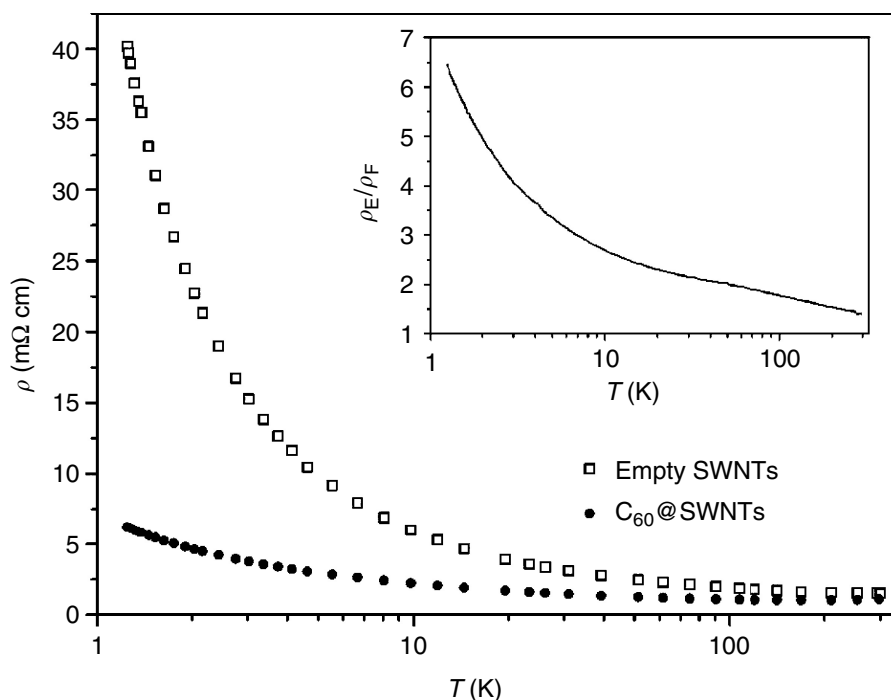
More fundamental than electron transport properties is the spectrum of allowed electron energies or density of states  $N(E)$ . This can be measured on individual tubes using scanning tunneling spectroscopy, which yields much important information. For bulk materials, one measures the related quantities such as electron energy loss function, using electron energy loss spectroscopy (EELS), absorption spectroscopy using thin films, or reflection spectroscopy if flat and reasonably smooth surfaces are available. We close this section by giving a few examples.

Figure 2.22 shows the loss function of a 100-nm-thick film of ~60% SWNT deposited on a TEM grid [78]. Both energy and momentum of the transmitted electrons can be determined, so the observed transitions can be separated into dispersing and nondispersing, which correspond to “collective” (plasmon) and “localized” interband processes, respectively. The inset shows the loss function over a wide energy range, in which the plasmons representing collective excitations of the  $\pi$  and  $\pi + \sigma$  electrons can be clearly seen at 5.2 and 21.5 eV, respectively, in agreement with the theory. Features in the loss function at 0.85, 1.45, 2.0, and 2.55 eV are independent of  $q$  and are therefore assigned to interband transitions. Their nature is revealed by a Kramers–Kronig transform



**FIGURE 2.20** Reduced activation energy  $W$  vs.  $T$  for the most conductive p-doped SWNT samples. Extrapolating from the lowest data point 1.3 K to  $T = 0$  shows that  $W$ , and any possible energy gap, vanishes, signaling a true metallic state. (From Vavro, J. et al., *Phys. Rev. B* **71**, 155410 (2005), with permission.)





**FIGURE 2.21** Four-point resistivity vs.  $T$  for C<sub>60</sub>@SWNT (filled circles) and empty nanotubes (open squares). The ratio empty/filled is shown in the inset. At ambient temperature the resistivities are indistinguishable. (From Vavro, J. et al., *Appl. Phys. Lett.* **80**, 1450 (2002), with permission.)

to obtain real and imaginary parts of the dielectric function,  $\epsilon_2$  being directly proportional to the optical absorption coefficient. The results are shown in [Figure 2.23](#), which reveals three interband transitions at 0.65, 1.2, and 1.8 eV. These are the energy separations of the 1D van Hove singularities, slightly broadened by diameter dispersivity in bulk samples. We now understand the sequence of transitions as  $E_{11}^S$ ,  $E_{22}^S$ , and  $E_{11}^M$  where  $n$  is the band index and S and M denote semiconducting and metallic tubes, respectively.

EELS also gives important information about the effects of redox doping on electronic properties [79]. [Figure 2.24](#) shows how the loss function evolves with potassium concentration. The upshift in the  $\pi$  plasmon near 6.5 eV is due to the gradual addition of an extra electron per  $n$  carbons to the previously empty  $\pi^*$  conduction band. The extra delocalized electron is charge-compensated by  $K^0$  oxidizing to  $K^+$  during intercalation. [Figure 2.24\(b\)](#) shows this relation explicitly, with  $K/C$  determined from core-level spectroscopy. The disappearance of fine structure below 2 eV signals the upshift in  $E_F$ , which quenches the van Hove interband transitions since the final states in the neutral material ([Figure 2.23](#)) are now occupied by doping.

Optical absorption and reflectance are complementary to EELS. The energy resolution is higher, polarization and selection rule information is accessible, and the spectra extend to lower energies which would otherwise be obscured in EELS by the tail of the  $\sim 100$  kV incident electron beam. The lower energy cutoff permits accurate measurements of the so-called Drude plasmon, a collective excitation of the delocalized electrons, and how it evolves with doping.

[Figure 2.25](#) shows the reflectance of an unoriented undoped film [80]. The solid curve is a model fit, including a free carrier Drude term and several interband Lorentz oscillators. These results confirm that undoped material consists of a mixture of conducting and semiconducting nanotubes, typical for bulk samples. The interband transition energies are consistent with electronic structure calculations for 1.4-nm-diameter tubes, and with EELS described above. The theory predicts that because these transitions involve 1D van Hove singularities, they should be completely polarized along the nanotube axis, i.e., they should vanish when the incident and transmitted beams are cross polarized. This was proved in a clever experiment on magnetically aligned SWNT suspensions with

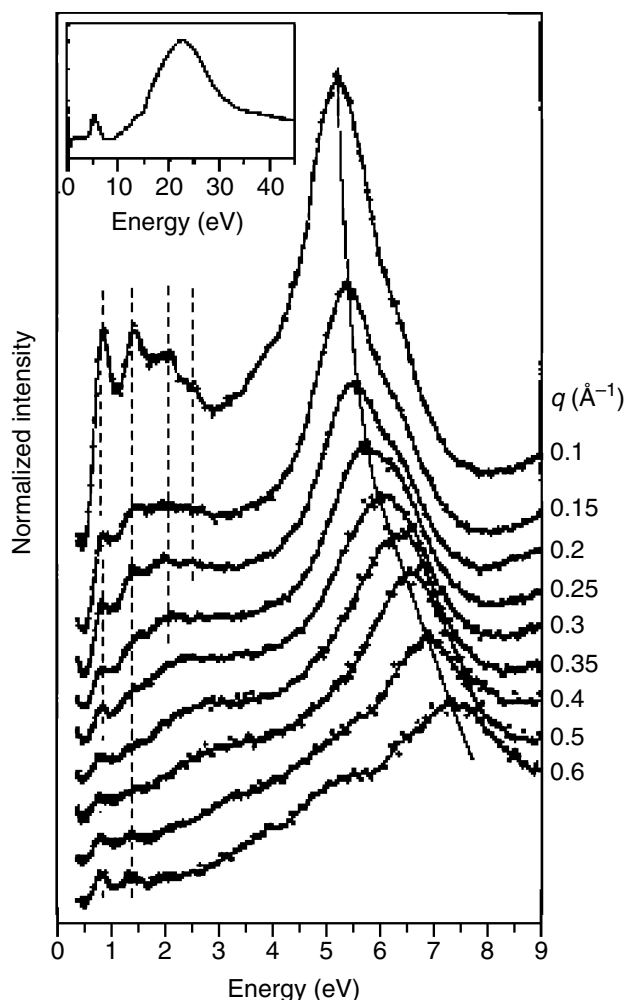


**FIGURE 2.22** The loss function of purified SWNT from EELS in transmission for the different  $q$  values is shown. The contributions from the elastic peak have been subtracted. The inset contains the loss function over an extended energy range, showing the  $\pi$  plasmon and the  $\pi + \sigma$  plasmon at around 5 and 22 eV, respectively. (From Pichler, T. et al., *Phys. Rev. Lett.* **80**, 4729 (1998), with permission.)

the alignment locked in place by gelation [81]. Polarized Raman scattering was used to quantify the degree of alignment. Combined with absorbance data from the partly aligned sample, the intrinsic polarized absorbance is recovered. The fitted Drude plasma frequency  $\omega_p$  is 0.29 eV, characteristic of a small concentration of conduction electrons or holes.

Chemical doping is revealed in absorption and reflectance spectroscopy by several mechanisms. The higher concentration of free carriers shifts the Drude edge to higher energy. The Drude scattering time may be affected by doping-induced disorder or dimensional crossover. Low-energy interband transitions may be quenched by the  $E_F$  shift through valence or conduction band singularities. Examples of these phenomena are evident in the reflectance spectra shown in Figure 2.26 for potassium-doped purified SWNT bucky paper [82]. These experiments were performed in sealed quartz tubes to avoid air exposure; consequently, the results differ significantly from those quoted in an earlier publication in which such precautions were not taken [83]. Data recorded in the range 0.07 to 4 eV show clearly that with increasing K concentration, the 1D van Hove transitions disappear and the Drude edge shifts progressively to higher energies into the visible spectrum [84]. Colors from purple to golden-brown, reminiscent of alkali graphite compounds, are observed as the K concentration increases to saturation. The Drude edge blue-shifts strongly, signaling a large increase in conduction electron concentration after doping. Now the fitted value of  $\sigma_p$  is 1.85 eV. In the free-electron model for metals, the DC conductivity is proportional to  $\omega_p^2$ . This implies a  $\sim 40\times$

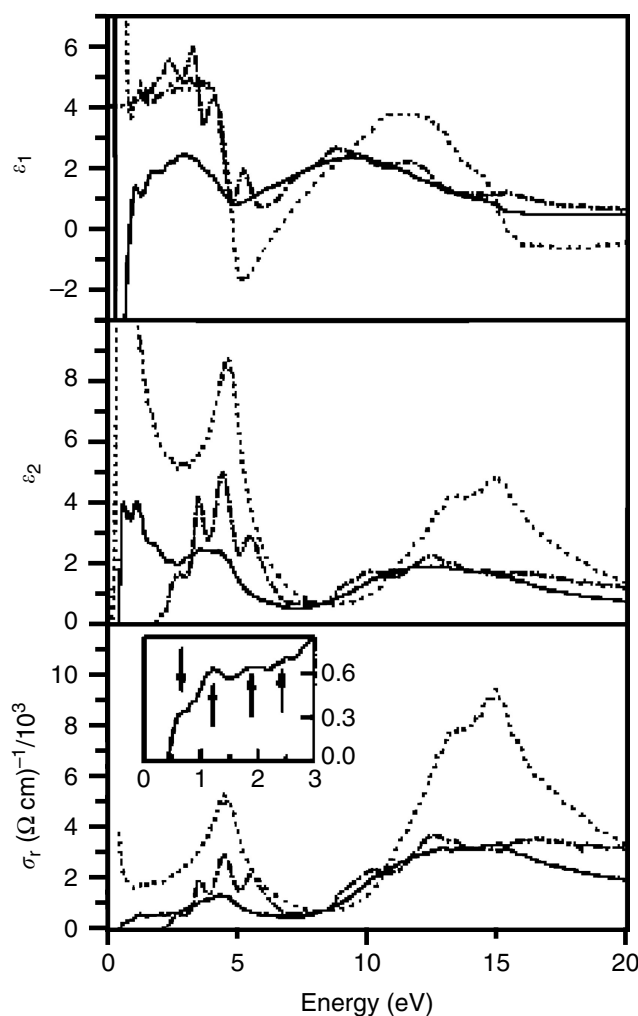


**FIGURE 2.23** Real and imaginary parts of the dielectric function (upper panels) and the real part of the optical conductivity for SWNT (solid curves),  $C_{60}$  (dot-dash curves), and graphite (dotted curves). (From Pichler, T. et al., *Phys. Rev. Lett.* **80**, 4729 (1998), with permission.)

enhancement in  $\sigma$  by saturation doping, in excellent agreement with direct measurements. Reference [83] reports a much smaller enhancement, underscoring the importance of avoiding air exposure. Similar experiments with electron acceptor doping show a maximum upshift to only 1.2 eV. The weaker effect on  $\omega_p$  with acceptors is again familiar from graphite intercalation compounds, in which the fraction of a free hole per intercalated molecule is considerably less than the fraction of a free electron per alkali ion.

A key parameter in characterizing doped bulk SWNT samples is the position of the Fermi energy, above or below the neutrality point for donors and acceptors, respectively. This is straightforward in electrochemical experiments, in which temperatures are limited to near ambient and the sample is not optically accessible at all wavelengths. An alternative is provided by the phonon drag, or electron-phonon scattering contribution to the thermopower. The basic idea is quite simple [85], and is shown schematically in Figure 2.27(a). The Fermi surface of a 1D metal consists of two points separated in  $k$  by a wave vector of amplitude  $|Q|$ . Momentum-conserving (inelastic) electron-phonon scattering thus requires participation of acoustic phonons with wave vector  $Q$ , which are absorbed or emitted as electrons scatter from the left- to right-moving branch of  $E(k)$ . Thus, the temperature dependence will reflect the temperature dependence of the heat capacity, and phonon drag is quenched below a characteristic temperature  $T_0$  given approximately by  $0.2\pi\hbar\omega_Q/k_B$  (cf. Figure 2.27(a)).  $|Q|$  is set by the chemical potential  $\mu$ , which in turn is controlled by the doping level;  $h$  and  $k_B$  are the Planck and Boltzmann constants, respectively. Operationally (Figure 2.27(b)), one records thermopower vs. temperature, locates  $T_0$  from the peak in the derivative, and backs out  $E_F$  from the

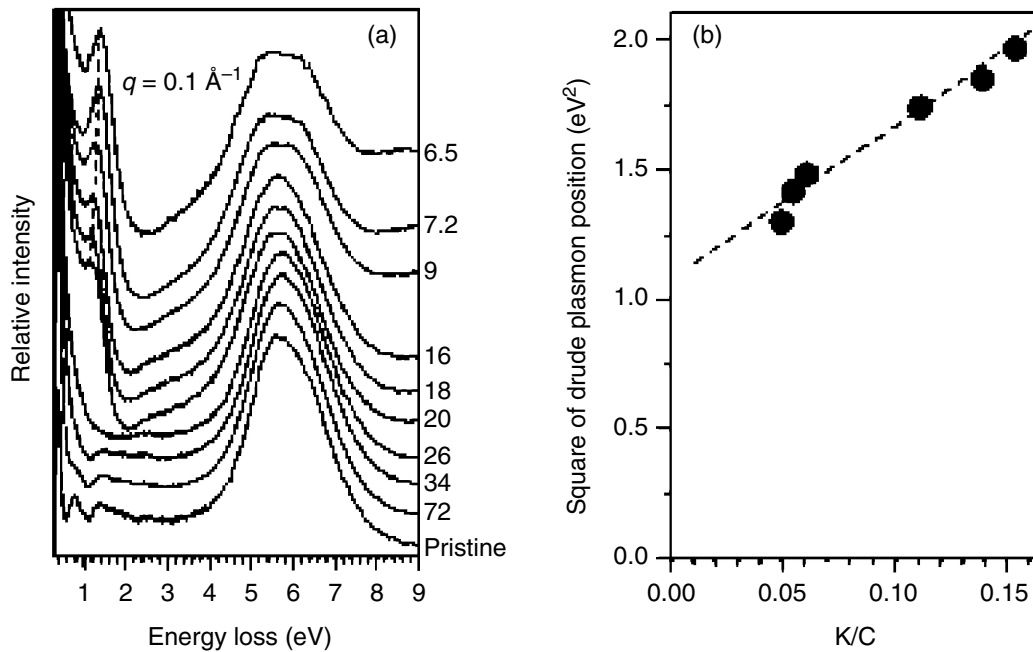


**FIGURE 2.24** (a) The loss function of pristine and potassium-intercalated SWNT; the potassium concentration increases from bottom to top. The dashed line indicates the shift of the position of the charge carrier plasmons with increasing concentration. (b) The quantitative relation between the square of the energy position of the charge carrier plasmon and the relative potassium concentration. (From Liu, X. et al., *Phys. Rev. B* **67**, 125403 (2003), with permission.)

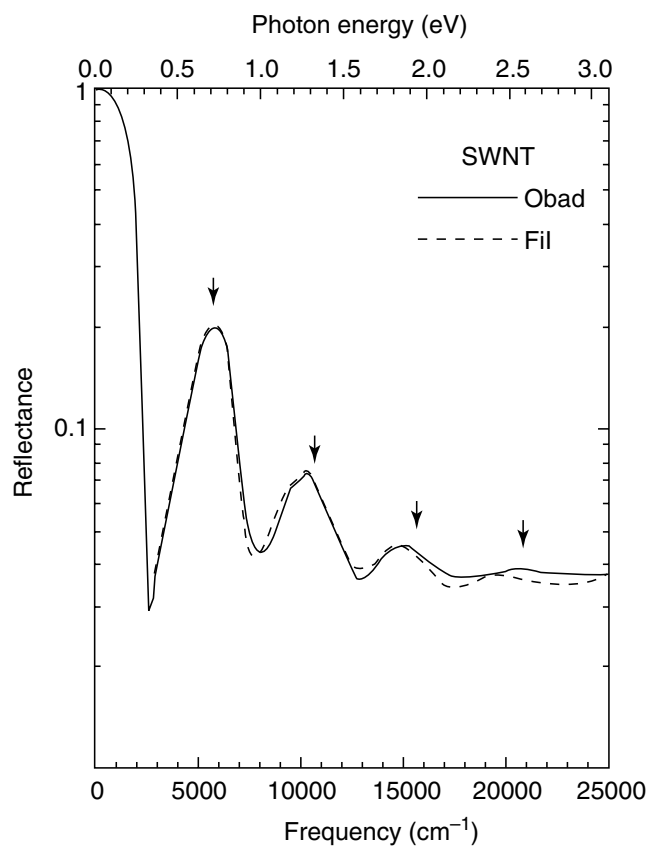


**FIGURE 2.25** Reflectance of an unaligned SWNT mat measured from 25 to 25,000 cm<sup>-1</sup> (lower scale), corresponding to the energy interval 0.003–3 eV (upper scale).  $R$  approaches 1 at  $E = 0$ , characteristic of a metal. Four interband transitions involving 1D van Hove singularities are identified by the downward arrows. (From Hwang, J. et al., *Phys. Rev. B* **62**, R13310 (2000), with permission.)

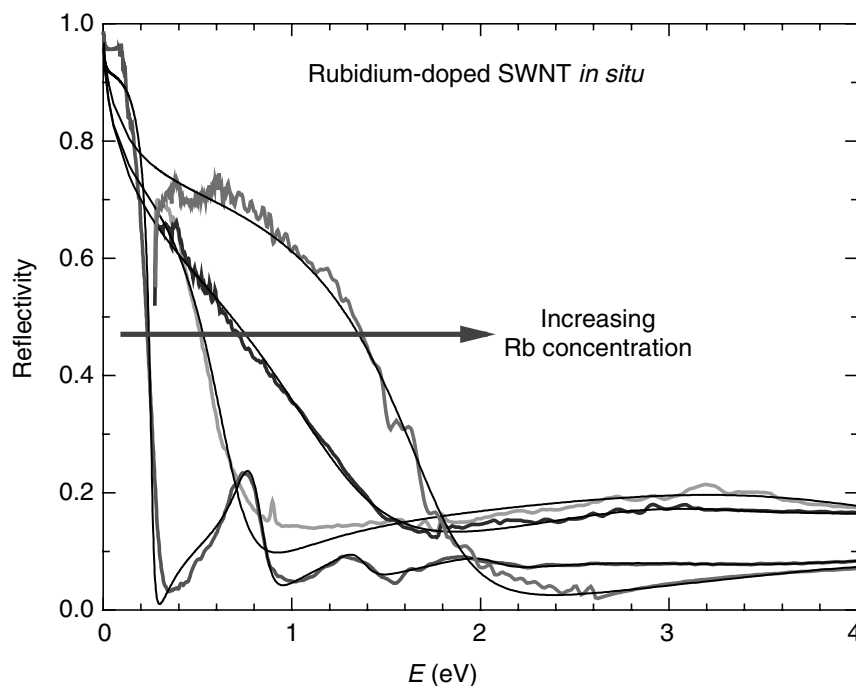


**FIGURE 2.26** Reflectance vs. photon energy for four SWNT buckypaper samples with increasing carrier concentration from alkali doping. Leftmost curve is for undoped SWNT. Doping causes a strong blueshift of the free carrier Drude edge, and quenches the interband transitions as  $E_F$  increases through the first two-conduction band van Hove singularities. (From Zhou, W. et al., *Phys. Rev. B* **71**, 205423 (2005), with permission.)

relevant dispersion relations. In the example shown, we see the sharp contrast between undoped and sulfuric acid-doped data from which a Fermi level depression of 0.5 eV is obtained.

The phonon drag method for locating  $E_F$  suffers one major drawback — it relies on a model for the energy band dispersion  $E(k)$ . The original one-electron tight-binding models have been extremely useful [86], while the importance of higher order effects is becoming evident [87]. For studies of the metallic state of doped nanotube materials, it would be helpful to have a characterization technique which directly measures the free carrier concentration (Hall effect), or at least the density of states at the Fermi energy  $N(E_F)$ . The Pauli paramagnetism of conduction electrons provides one option. This is difficult to observe directly in magnetization measurements due to strong diamagnetic corrections, which are not well quantified. This limitation is overcome by conduction electron spin resonance (CESR), which in essence is the Zeeman effect of delocalized electrons. Evidence for Pauli spins in raw SWNT soot was reported 10 years ago [88]. This was controversial because (1) it was believed that the random orientation combined with anisotropic metallic properties would broaden the CESR beyond recognition, and (2) assuming stochastic growth such that only approximately one third of the tubes is metallic, and given the theoretical result that  $N(E_F)$  per mole is only approximately one fourth that of 3D graphite, these few intrinsic metallic spins might be undetectable. The original interpretation was supported by subsequent measurements of the temperature dependence of integrated CESR linewidth [89]. While the more typical paramagnetic resonance associated with localized spins obeys a Curie law temperature dependence, susceptibility  $\chi \sim 1/T$ , the nanotube  $\chi$  was independent of  $T$  in the range 70 to 300 K. The same sample exhibited the aforementioned shallow minimum in resistivity vs.  $T$  at about 200 K, so the  $T$  independence of  $\chi_{\text{Pauli}}$  ruled out an MI transition in the undoped material.

CESR was extended to alkali-doped buckypaper using *in situ* electrochemical doping to follow the resonance vs. K concentration [90]. Figure 2.28(a) shows the evolution of the full profile, which consists of a narrow Pauli contribution, magnified in Figure 2.28(b), superposed on a broad anti-ferromagnetic resonance (AFMR) associated with residual transition metal catalyst. The Pauli

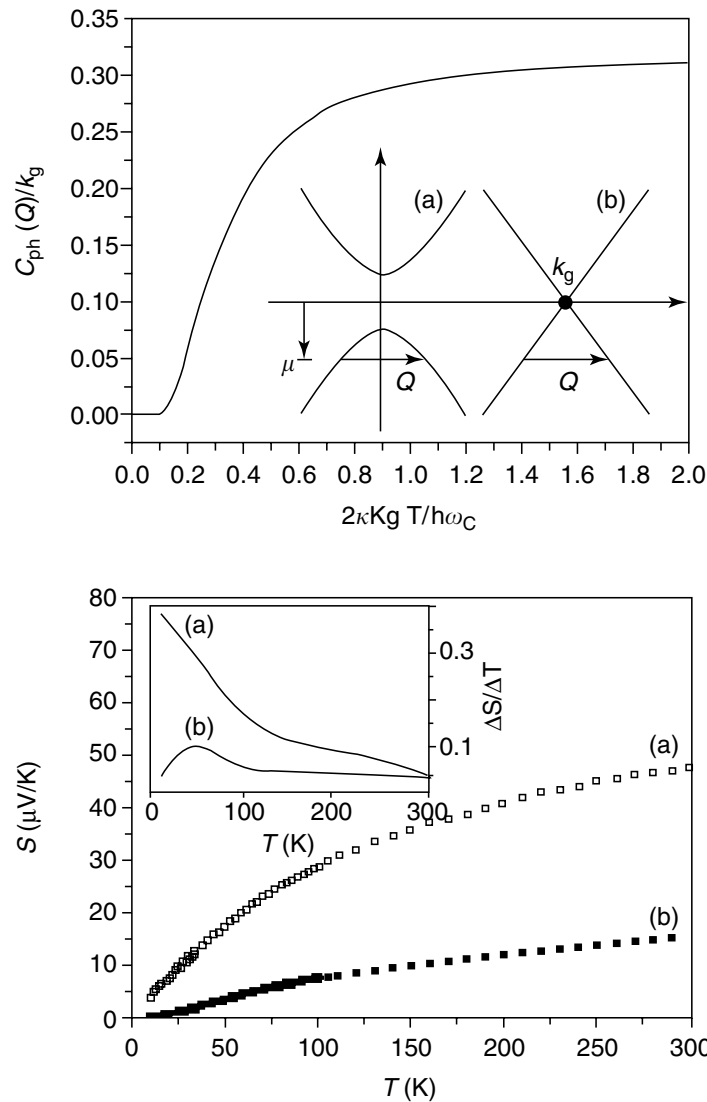


**FIGURE 2.27** Phonon drag in SWNT. Top: calculated phonon heat capacity vs.  $T$  for p-type doped nanotubes with chemical potential  $\mu$  applicable to semiconducting or metallic tubes is shown in the inset. The cutoff in occupied phonon energies leads to a weak threshold in thermopower  $S$ . Bottom:  $S(T)$  and its derivative for SWNT fibers extruded from sulfuric acid (b) and after annealing to remove the acid and return  $\mu$  toward zero. The peak in the derivative (b) is a measure of the doping-induced downshift in  $E_F$ . (From Vavro, J. et al., *Phys. Rev. Lett.* **90**, 065503 (2003), with permission.)

CESR grows in intensity with increasing K concentration, while the position and width are constant. The AFMR intensity diminishes as the sample becomes more conducting and the microwave skin depth decreases. Figure 2.28(b) shows that  $\chi_{\text{Pauli}}$ , proportional to the double integral of the CESR line, increases monotonically with K/C. Now that an absolute scale is established, the absence of CESR in this undoped material is surprising since there is ample sensitivity.

It also calls into question the origin of the  $T$ -independent signal observed previously in unpurified soot [89]. Figure 2.29 shows that  $\chi_{\text{Pauli}}$  is independent of  $T$  for two saturation-doped samples, from 30 to 290 K. This proves beyond doubt that alkali-doped SWNTs are true metals. The absolute value  $5 \times 10^{-8}$  emu/g translates to  $N(E_F) = 0.015$  states/eV per carbon per spin, approximately five times smaller than a theoretical estimate [91]. The anomalously small value in doped material, and the absence of a true ESR signal in clean undoped material, remain to be resolved.

The independence of the CESR linewidth on temperature is unusual. The inverse of the width is proportional to the spin relaxation rate, which is usually dominated by spin-orbit interaction with

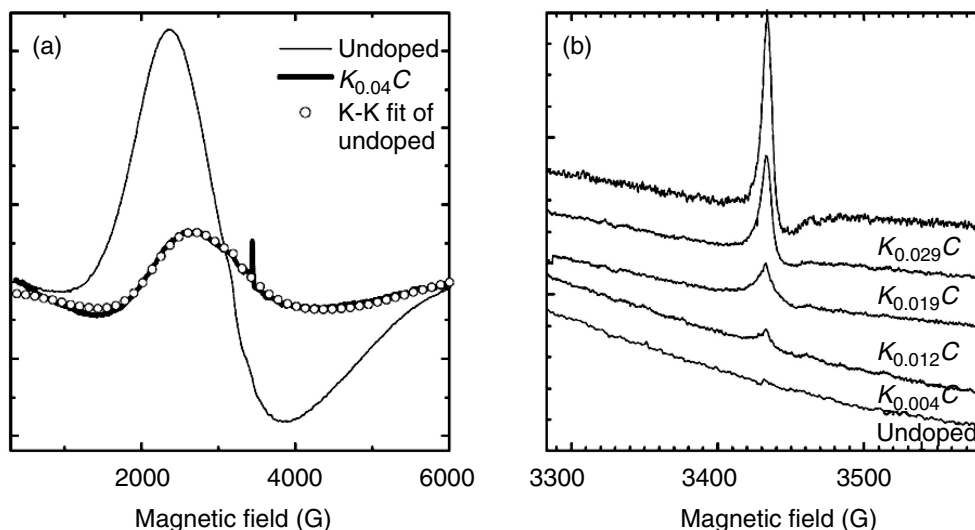


**FIGURE 2.28** Conduction electron spin resonance in K-doped SWNT. (a) Ferromagnetic resonance of Ni catalyst particles in undoped and fully doped SWNT (light and heavy curves, respectively). The narrow CESR peak is not seen in the undoped sample, and the Ni resonance changes line shape as the sample becomes more conducting and the skin depth decreases. (b) The CESR line grows continuously with increasing K concentration, while the spin relaxation rate (line width) and  $g$  factor (position) remain constant. (From Claye, A. S. et al., *Phys. Rev. B* **62**, R4845 (2000), with permission.)

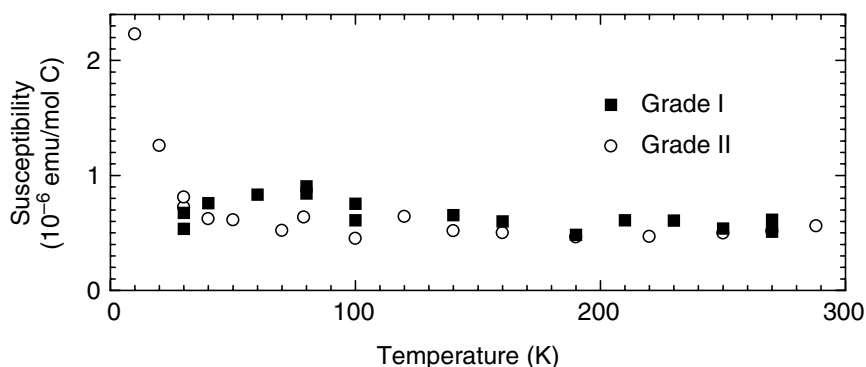


**FIGURE 2.29** The Pauli spin susceptibility vs.  $T$  for saturation-doped SWNT is independent of  $T$  above 30 K, characteristic of a metallic state. (From Claye, A. S. et al., *Phys. Rev. B* **62**, R4845 (2000), with permission.)

the dopants. The only explanation is inhomogeneous doping; small saturation-doped regions are created at the outset, and their number density increases with global K/C without affecting their size. This model is supported by accompanying x-ray diffraction data [90].

### 2.3.4 MAGNETIC AND SUPERCONDUCTING PROPERTIES

We close with a brief mention of these collective phenomena in bulk nanotube materials. An excellent entrée to the magnetism controversy is the recent paper by Cesvedes et al. and references therein [92]. The authors prove convincingly that there is no bulk magnetism in a clean multiwall nanotube sample. On the other hand, when placed on a flat ferromagnetic substrate, fringing fields can be observed by magnetic force microscopy. Thus, the prospect for “contact-induced magnetism” and the application of carbon nanotubes to nanoscale spintronic devices remain open. Magnetic contrast is observed for carbon nanotubes placed on cobalt or magnetite substrates, but is absent on silicon, copper, or gold. Spin transfer of about 0.1  $\mu$ B per contact carbon atom is obtained.

The dialog about nanotube superconductivity began with a very simple argument [93]: if one could tune the chemical potential to the peak of a van Hove singularity, either chemically or electrostatically,

one should have a high  $N(E_F)$  value, a prerequisite for BCS superconductivity. The obvious problem in applying this to bulk material is the diameter dispersivity. Even in single tubes, higher order interactions will broaden the square-root energy divergences. This has not prevented some from conjecturing  $T_c$  above 400 K for nanotube superconductors. Super-current flow through an SWNT with low-resistance contacts was reported in 1999 [94]; analogous to contact-induced magnetism, no claims were made for bulk nanotube superconductivity. Evidence for a bulk anisotropic Meissner effect below 20 K in aligned 0.4-nm-diameter SWNT was claimed and justified by the argument that small-diameter tubes will be the stiffest, and thus, the average phonon energy in the BCS equation will be favorable [95]. This dramatic result has not been reproduced by other researchers since it appeared 4 years ago. As with bulk magnetism, it would appear that the jury is still out concerning bulk superconductivity in carbon nanotubes and other nanostructures.

## 2.4 SUMMARY AND PROSPECTS

It is difficult to counter the argument that carbon is the most amazing element in the Periodic Table. In the space of a mere 30 years, we have experienced the discovery of (or renaissance in) three material families: graphite intercalation compounds (GICs), fullerene solids, and nanotubes. GICs provided a wealth of detailed chemical and physical information, while immediate applications were frustrated by cost, lack of air stability, and most importantly, the lack of new or greatly improved applications and properties. Though the foundations of physics and chemistry remain unshaken, the Li ion battery industry has certainly benefited greatly from this store of knowledge. Fullerene solids fared better, and may yet surprise us in the practical world; while no large volume application has yet emerged, the elucidation of electronic properties in this highly correlated system has made invaluable contributions to fundamental science. Nanotubes may offer the best prospects yet; money is already being made on some small-scale applications. The combination of enhanced properties encourages the drive to multifunctional materials, and also affords an excellent laboratory for studying 1D phenomena. Extensions to other tubular and nanowire-like materials provide ample scope for new discoveries.

## ACKNOWLEDGMENTS

The nanotube phase of my research life has been enriched by delightful interactions with numerous students, postdocs, colleagues and collaborators. This chapter draws heavily from the work of recently awarded theses of Roland Lee, Zdenek Benes, Agnes Claye, Norbert Nemes, Juraj Vavro, and Marc Llaguno, and soon to be awarded theses of Wei Zhou and Csaba Guthy. Funding from the National Science Foundation, the Office of Naval Research, and especially the Department of Energy are gratefully acknowledged. I am grateful as well to Linda Fischer for a most thorough proofreading.

## REFERENCES

1. S. Iijima, Helical microtubules of graphitic carbon, *Nature* **354**, 56–58 (1991).
2. R. C. Haddon and S.-Y. Chow, Hybridization as a metric for the reaction coordinate of the chemical reaction: concert in chemical reactions, *Pure Appl. Chem.* **71**, 289–294 (1999).
3. F. Du and K. I. Winey, this volume.
4. N. Wang, G. D. Li and Z. K. Tang, Mono-sized and single-walled 4 Å carbon nanotubes, *Chem. Phys. Lett.* **339**, 47 (2001).
5. G. Eres, A. A. Puzos, D. B. Geohegan and H. Cui, In situ control of the catalyst efficiency in chemical vapor deposition of vertically aligned carbon nanotubes on predeposited metal catalyst films, *Appl. Phys. Lett.* **84**, 1759–1761 (2004).
6. R. Tenne, this volume.



7. E. G. Rakov, this volume.
8. T. Yoshitake, Y. Shimakawa, S. Kuroshima, H. Kimura, T. Ichihashi, Y. Kubo, D. Kasuya, K. Takahashi, F. Kokai, M. Yudasaka and S. Iijima, Preparation of fine platinum catalyst supported on single-wall carbon nanohorns for fuel cell application, *Physica B* **323**, 124–126 (2002).
9. M. Freitag, A. T. Johnson, S. V. Kalinin and D. A. Bonnell, Role of single defects in electronic transport through carbon nanotube field-effect transistors, *Phys. Rev. Lett.* **89**, 216801 (2002).
10. J. E. Fischer, P. A. Heiney, A. R. McGhie, W. J. Romanow, A. M. Denenstien, J. P. McCauley Jr. and A. B. Smith III, Compressibility of solid C<sub>60</sub>, *Science* **252**, 1288 (1991).
11. J. Tang, L.-C. Qin, T. Sasaki, M. Yudasaka, A. Matsushita and S. Iijima, Compressibility and poly-gonization of single-walled carbon nanotubes under hydrostatic pressure, *Phys. Rev. Lett.* **85**, 1887 (2000).
12. Y. Maniwa, R. Fujiwara, H. Kira, H. Tou, H. Kataura, S. Suzuki, Y. Achiba, E. Nishibori, M. Takata, M. Sakata, A. Fujiwara and H. Suematsu, Thermal expansion of single-walled carbon nanotube (SWNT) bundles: X-ray diffraction studies, *Phys. Rev. B* **64**, 241402 (2001).
13. S. Bandow, G. Chen, G. U. Sumanasekera, R. Gupta, M. Yudasaka, S. Iijima and P. C. Eklund, Diameter-selective resonant Raman scattering in double-wall carbon nanotubes, *Phys. Rev. B* **66**, 075416 (2002).
14. J. G. Lavin, S. Subramoney, R. S. Ruoff, S. Berber and D. Tomanek, Scrolls and nested tubes in multiwall carbon nanotubes, *Carbon* **40**, 1123–1130 (2002).
15. L. Jin, C. Bower and O. Zhou, Alignment of carbon nanotubes in a polymer matrix by mechanical stretching, *Appl. Phys. Lett.* **73**, 1197 (1998).
16. Y. Gogotsi, J. A. Libera, A. Güvenç-Yazicioglu, and C. M. Megaridis, In-situ multiphase fluid experiments in hydrothermal carbon nanotubes, *Appl. Phys. Lett.* **79**, 1021–1023 (2001).
17. H. W. Zhu, C. L. Xu, D. H. Wu, B. Q. Wei, R. Vajtal and P. M. Ajayan, Direct synthesis of long single-walled carbon nanotube strands, *Science* **296**, 884 (2002).
18. Y.-L. Li, I. A. Kinloch and A. H. Windle, Direct spinning of carbon nanotube fibers from chemical vapor deposition synthesis, *Science* **304**, 276 (2004).
19. M. Zhang, K. R. Atkinson and R. H. Baughman, Multifunctional carbon nanotube yarns by downsizing an ancient technology, *Science* **306**, 1358 (2004).
20. K. Hata, D. N. Futaba, K. Mizuno, T. Namai, M. Yumura and S. Iijima, Water-assisted highly efficient synthesis of impurity-free single-walled carbon nanotubes, *Science* **306**, 1362 (2004).
21. P. G. Collins, M. S. Arnold and P. Avouris, Engineering carbon nanotubes and nanotube circuits using electrical breakdown, *Science* **292**, 706–709 (2001).
22. R. H. Baughman, A. A. Zakhidov and W. A. De Heer, Carbon nanotubes — the route toward applications, *Science* **297**, 787–792 (2002).
23. A. G. Rinzler, J. Liu, P. Nikolaev, C. B. Huffman, F. J. Rodriguez-Macias, P. J. Boul, A. H. Lu, D. Heymann, D. T. Colbert, R. S. Lee, J. E. Fischer, A. M. Rao, P. C. Eklund and R. E. Smalley, Large-scale purification of single-wall carbon nanotubes: process, product, and characterization, *Appl. Phys. A* **67**, 29 (1998).
24. T. V. Sreekumar, T. Liu, S. Kumar, L. M. Ericson, R. H. Hauge and R. E. Smalley, Single-wall carbon nanotube films, *Chem. Mater.* **15**, 175 (2003).
25. S. Badaire, C. Zakri, P. Poulin, V. Pichot, P. Launois, J. Vavro, M. Chen and J. E. Fischer, Correlation of properties with preferred orientation in extruded and stretch-aligned single wall carbon nanotubes, *J. Appl. Phys.* **96**, 7509 (2004).
26. L. M. Ericson, H. Fan, H. Peng, V. A. Davis, J. Sulpizio, Y. Wang, R. Booker, W. Zhou, J. Vavro, C. Guthy, S. Ramesh, C. Kittrell, G. Lavin, H. Schmidt, W. W. Adams, M. Pasquali, W.-F. Hwang, R. H. Hauge, J. E. Fischer and R. E. Smalley, Macroscopic, neat, single-walled carbon nanotube fibers, *Science* **305**, 1447 (2004).
27. R. Haggmueller, W. Zhou, J. E. Fischer and K. I. Winey, Production and characterization of polymer nanocomposites with highly aligned single-walled carbon nanotubes, *J. Nanosci. Nanotech.* **3**, 105 (2003).
28. A. S. Claye, J. E. Fischer, C. B. Huffman, A. G. Rinzler and R. E. Smalley, Solid-state electrochemistry of the Li single-wall carbon nanotube system, *J. Electrochem. Soc.* **147**, 2845 (2000).
29. B. Vigolo, A. Penicaud, C. Coulon, C. Sauder, R. Pallier, C. Journet, P. Bernier and P. Poulin, Macroscopic fibers and ribbons of oriented carbon nanotubes, *Science* **290**, 1331 (2000).

30. J. E. Fischer, W. Zhou, J. Vavro, M. C. Llaguno, C. Guthy, R. Haggenueller, M. J. Casavant, D. E. Walters and R. E. Smalley, Magnetically aligned single wall carbon nanotube films: preferred orientation and anisotropic transport properties, *J. Appl. Phys.* **93**, 2157 (2003).
31. S. Huang, X. Cai and J. Liu, Growth of millimeter-long and horizontally aligned single-walled carbon nanotubes on flat substrates, *J. Am. Chem. Soc.* **125**, 5636–5637 (2003).
32. W. Zhou, K. I. Winey, J. E. Fischer, S. Kumar and H. Kataura, Out-of-plane mosaic of single-wall carbon nanotube films, *Appl. Phys. Lett.* **84**, 2172 (2004).
33. H. H. Gommans, J. W. Alldredge, H. Tashiro, J. Park, J. Magnuson and A. G. Rinzler, Fibers of aligned single-walled carbon nanotubes: polarized Raman spectroscopy, *J. Appl. Phys.* **88**, 2509 (2000).
34. W. Zhou, J. Vavro, C. Guthy, K. I. Winey, J. E. Fischer, L. M. Ericson, S. Ramesh, R. Saini, V. A. Davis, C. Kittrell, M. Pasquali, R. H. Hauge and R. E. Smalley, Single wall carbon nanotube fibers extruded from super-acid suspensions: preferred orientation, electrical, and thermal transport, *J. Appl. Phys.* **95**, 649 (2004).
35. J. E. Fischer, Q. Zhu, X. Tang, E. M. Scherr, A. G. MacDiarmid and V. B. Cajipe, Polyaniline fibers, films, and powders — X-ray studies of crystallinity and stress-induced preferred orientation, *Macromolecules* **27**, 5094 (1994).
36. M. A. Pimenta, A. Marucci, A. Empedocles, M. G. Bawendi, E. B. Hanlon, A. M. Rao, P. C. Eklund, R. E. Smalley, G. Dresselhaus and M. S. Dresselhaus, Raman modes of metallic carbon nanotubes, *Phys. Rev. B* **58**, R16 016 (1998).
37. R. Haggenueller, H. H. Gommans, A. G. Rinzler, J. E. Fischer and K. I. Winey, Aligned single-wall carbon nanotubes in composites by melt processing methods, *Chem. Phys. Lett.* **330**, 219 (2000).
38. P. Launois, A. Marucci, B. Vigolo, A. Derre and P. Poulin, Structural characterization of nanotube fibers by x-ray scattering, *J. Nanosci. Nanotechnol.* **1**, 125–128 (2001).
39. B. W. Smith, M. Monthieux and D. E. Luzzi, Encapsulated C-60 in carbon nanotubes, *Nature* **396**, 323 (1998).
40. B. Burtiaux, A. Claye, B. W. Smith, M. Monthieux, D. E. Luzzi and J. E. Fischer, Abundance of encapsulated C-60 in single-wall carbon nanotubes, *Chem. Phys. Lett.* **310**, 21 (1999).
41. B. W. Smith, R. M. Russo, S. B. Chikkannanavar and D. E. Luzzi, High-yield synthesis and one-dimensional structure of C<sub>60</sub> encapsulated in single-wall carbon nanotubes, *J. Appl. Phys.* **91**, 9333 (2002).
42. X. Liu, T. Pichler, M. Knupfer, M. S. Golden, J. Fink, H. Kataura, Y. Achiba, K. Hirahara and S. Iijima, Filling factors, structural, and electronic properties of C<sub>60</sub> molecules in single-wall carbon nanotubes, *Phys. Rev. B* **65**, 045419 (2002).
43. P. M. Rafailov, C. Thomsen and H. Kataura, Resonance and high-pressure Raman studies on carbon peapods, *Phys. Rev. B* **68**, 193411 (2003).
44. T. Okazaki, K. Suenaga, K. Hirahara, S. Bandow, S. Iijima and H. Shinohara, Electronic and geometric structures of metallofullerene peapods, *Physica B: Cond. Matt.* **323**, 97–99 (2002).
45. B. W. Smith and J. E. Fischer, unpublished.
46. M. Hodak and L. A. Girifalco, Ordered phases of fullerene molecules formed inside carbon nanotubes, *Phys. Rev. B* **67**, 075419 (2003).
47. M. R. Stetzer, P. A. Heiney, J. E. Fischer and A. R. McGhie, Thermal stability of solid C<sub>60</sub>, *Phys. Rev. B* **55**, 127 (1997).
48. E. Kolodny, B. Tsipinyuk and A. Budrevich, The thermal stability and fragmentation of C<sub>60</sub> molecule up to 2000 K on the milliseconds time scale, *J. Chem. Phys.* **100**, 8542 (1994).
49. S. M. Bachilo, M. S. Strano, C. Kittrell, R. H. Hauge and B. R. Weisman, Structure-assigned optical spectra of single-walled carbon nanotubes, *Science* **298**, 2361–2366 (2002).
50. C. L. Kane and E. J. Mele, Ratio problem in single-carbon nanotube fluorescence spectroscopy, *Phys. Rev. Lett.* **90**, 207401 (2003).
51. V. A. Davis, L. M. Ericson, A. N. G. Parra-Vasquez, H. Fan, Y. Wang, V. Prieto, J. A. Longoria, S. Ramesh, R. K. Saini, C. Kittrell, W. E. Billups, W. W. Adams, R. H. Hauge, R. E. Smalley and M. Pasquali, Phase behavior and rheology of SWNTs in superacids, *Macromolecules* **37**, 154–160 (2004).
52. W. Zhou, M. F. Islam, H. Wang, D. L. Ho, A. G. Yodh, K. I. Winey and J. E. Fischer, Small angle neutron scattering from single-wall carbon nanotube suspensions: evidence for isolated rigid rods and rod networks, *Chem. Phys. Lett.* **384**, 185–189 (2004).
53. B. I. Yakobson, Mechanical relaxation and “intramolecular plasticity” in carbon nanotubes, *Appl. Phys. Lett.* **72**, 918–920 (1998).

54. M. R. Falvo, G. J. Clary, R. M. Taylor II, V. Chi, F. P. Brooks, J. R. Washburn and R. Superfine, Bending and buckling of carbon nanotubes under large strain, *Nature* **389**, 582–584 (1997).
55. M. Treacy, T. W. Ebbesen and J. M. Gibson, Exceptionally high Young's modulus observed for individual carbon nanotubes, *Nature* **381**, 678–680 (1996).
56. Y. Q. Zhu, T. Sekine, T. Kobayashi, E. Takazawa, M. Terrones and H. Terrones, Collapsing carbon nanotubes and diamond formation under shock waves, *Chem. Phys. Lett.* **287**, 689–693 (1998).
57. F. Li, H. M. Cheng, S. Bai, G. Su and M. S. Dresselhaus, Tensile strength of single-walled carbon nanotubes directly measured from their macroscopic ropes, *Appl. Phys. Lett.* **20**, 3161–3163 (2000).
58. Z. L. Wang, R. P. Gao, P. Poncharal, W. A. De Heer, Z. R. Dai and Z. W. Pan, Mechanical and electrostatic properties of carbon nanotubes and nanowires, *Mater. Sci. Eng. C* **16**, 3–10 (2001).
59. M.-F. Yu, B. S. Files, S. Arepalli and R. S. Ruoff, Tensile loading of ropes of single-wall carbon nanotubes and their mechanical properties, *Phys. Rev. Lett.* **84**, 5552 (2000).
60. O. Inganäs and I. Lundström, Carbon nanotube muscles, *Science* **284**, 1281–1282 (1999).
61. T. V. Sreekumar, Tao Liu, S. Kumar, L. M. Ericson, R. H. Hauge and R. E. Smalley, Single-wall carbon nanotube films, *Chem. Mater.* **15**, 175–178 (2003).
62. J. Hone, M. Whitney, C. Piskoti, and A. Zettl, Thermal conductivity of single-walled carbon nanotubes, *Phys. Rev. B* **59**, R2514 (1999).
63. S. Berber, Y. K. Kwon and D. Tomanek, Unusually high thermal conductivity of carbon nanotubes, *Phys. Rev. Lett.* **84**, 4613 (2000).
64. P. Kim, L. Shi, A. Majumdar and P. L. McEuen, Thermal transport measurements of individual multiwalled nanotubes, *Phys. Rev. Lett.* **87**, 215502 (2001).
65. W. Yi, L. Lu, D. L. Zhang, Z. W. Pan and S. S. Xie, Linear specific heat of carbon nanotubes, *Phys. Rev. B* **59**, R9015 (1999).
66. J. Hone, B. Batlogg, Z. Benes, A. T. Johnson and J. E. Fischer, Quantized phonon spectrum of single-wall carbon nanotubes, *Science* **289**, 1730 (2000).
67. J. E. Fischer, Chemical doping of single-wall carbon nanotubes, *Acc. Chem. Res.* **35**, 1079 (2002).
68. J. C. Lasjaunias, K. Biljacović, Z. Benes, J. E. Fischer and P. Monceau, Low-temperature specific heat of single-wall carbon nanotubes, *Phys. Rev. B* **65**, 113409 (2002).
69. J. Hone, M. C. Llaguno, N. M. Nemes, J. E. Fischer, D. E. Walters, M. J. Casavant, J. Schmidt and R. E. Smalley, Electrical and thermal transport properties of magnetically aligned single-wall carbon nanotube films, *Appl. Phys. Lett.* **77**, 666 (2000).
70. J. Vavro, M. C. Llaguno, B. C. Satishkumar, D. E. Luzzi and J. E. Fischer, Electrical and thermal properties of C-60-filled single-wall carbon nanotubes, *Appl. Phys. Lett.* **80**, 1450 (2002).
71. J. Vavro, M. C. Llaguno, B. C. Satishkumar, R. Haggemueller, K. I. Winey, D. E. Luzzi, J. E. Fischer, G. U. Sumanasekera and P. C. Eklund, Electrical and thermal properties of C-60-filled single-wall carbon nanotubes, in *Molecular Nanostructures*, H. Kuzmany, J. Fink, M. Mehring and S. Roth, Eds., *AIP Conf. Proc.* **633**, 127 (2002).
72. J. E. Fischer, H. Dai, A. Thess, R. Lee, N. M. Hanjani, D. DeHaas and R. E. Smalley, Metallic resistivity in crystalline ropes of single-wall carbon nanotubes, *Phys. Rev. B* **55**, R4921 (1997).
73. M. S. Fuhrer, M. L. Cohen, A. Zettl and V. Crespi, Localization in single-walled carbon nanotubes, *Solid State Commun.* **109**, 105 (1998).
74. R. S. Lee, H. J. Kim, J. E. Fischer, A. Thess and R. E. Smalley, Conductivity enhancement in single-walled carbon nanotube bundles doped with K and Br, *Nature* **388**, 255 (1997).
75. M Radosavljevic, Improving carbon nanotube nanodevices: ambipolar field effect transistors and high current interconnects, PhD thesis, University of Pennsylvania (2001).
76. P. Sheng, Fluctuation-induced tunneling conduction in disordered materials, *Phys. Rev. B* **21**, 2180 (1980).
77. J. Vavro, J. M. Kikkawa and J. E. Fischer, Metal–insulator transition in doped single-wall carbon nanotubes, *Phys. Rev. B* **71**, 155410 (2005).
78. T. Pichler, M. Knupfer, M. S. Golden, J. Fink, A. Rinzler and R. E. Smalley, Localized and delocalized electronic states in single-wall carbon nanotubes, *Phys. Rev. Lett.* **80**, 4729 (1998).
79. X. Liu, T. Pichler, M. Knupfer and J. Fink, Electronic and optical properties of alkali-metal-intercalated single-wall carbon nanotubes, *Phys. Rev. B* **67**, 125403 (2003).
80. J. Hwang, H. H. Gommans, A. Ugawa, H. Tashiro, R. Haggemueller, K. I. Winey, J. E. Fischer, D. B. Tanner and A. G. Rinzler, Polarized spectroscopy of aligned single-wall carbon nanotubes, *Phys. Rev. B* **62**, R13310 (2000).

81. M. F. Islam, D. E. Milkie, C. L. Kane, A. G. Yodh, and J. M. Kikkawa, Direct measurement of the polarized optical absorption cross section of single-wall carbon nanotubes, *Phys. Rev. Lett.* **93**, 037404 (2004).
82. N. M. Nemes, J. E. Fischer, K. Kamarás, D. B. Tanner and A. G. Rinzler, Synthesis, isolation and characterisation of new alkaline earth endohedral fullerenes, in *Molecular nanostructures*, H. Kuzmany, J. Fink, M. Mehring and S. Roth, Eds., *AIP Conf. Proc.* **633**, 259 (2002).
83. B. Ruzicka, L. Degiorgi, R. Gaal, L. Thien-Nga, R. Bacsá, J.-P. Salvetat and L. Forró, Optical and dc conductivity study of potassium-doped single-walled carbon nanotube films, *Phys. Rev. B* **61**, R2468 (2000).
84. W. Zhou, J. Vavro, N. M. Nemes, J. E. Fischer, F. Borondics, K. Kamarás and D. B. Tanner, *Phys. Rev. B* **71**, 205423 (2005).
85. J. Vavro, M. C. Llaguno, J. E. Fischer, S. Ramesh, R. K. Saini, L. M. Ericson, V. A. Davis and R. E. Smalley, Thermoelectric power of p-doped single-wall carbon nanotubes and the role of phonon drag, *Phys. Rev. Lett.* **90**, 065503 (2003).
86. C. L. Kane and E. J. Mele, Size, shape, and low-energy electronic structure of carbon nanotubes, *Phys. Rev. Lett.* **78**, 1932 (1997).
87. C. L. Kane and E. J. Mele, Ratio problem in single-carbon nanotube fluorescence spectroscopy, *Phys. Rev. Lett.* **90**, 207401 (2003).
88. A. Thess, R. Lee, P. Nikolaev, H. Dai, P. Petit, J. Robert, C. Xu, H. Lee, S. G. Kim, D. T. Colbert, G. Scuseria, D. Tomanek, J. E. Fischer and R. E. Smalley, Crystalline ropes of metallic carbon nanotubes, *Science* **273**, 483 (1996).
89. P. Petit, E. Jouguet, J. E. Fischer, A. Thess and R. E. Smalley, Electron spin resonance and microwave resistivity of single-wall carbon nanotubes, *Phys. Rev. B* **56**, 9275 (1997).
90. A. S. Claye, N. M. Nemes, A. Janossy and J. E. Fischer, Structure and electronic properties of potassium-doped single-wall carbon nanotubes, *Phys. Rev. B* **62**, R4845 (2000).
91. A. A. Maarouf, C. L. Kane, and E. J. Mele, Electronic structure of carbon nanotube ropes, *Phys. Rev. B* **61**, 156 (2000).
92. O. Cespedes, M. S. Ferreira, S. Sanvito, M. Kociak and J. M. D. Coey, Contact-induced magnetism in carbon nanotubes, *J. Phys.: Condens. Matter* **16**, L155–L161 (2004).
93. R. Saito, G. Dresselhaus and M. S. Dresselhaus, *Physical properties of carbon nanotubes*, Imperial College Press, London, 1999.
94. A. Yu. Kasumov, R. Deblock, M. Kociak, B. Reulet, H. Bouchiat, I. I. Khodos, Yu. B. Gorbatov, V. T. Volkov, C. Journet and M. Burghard, Supercurrents through single-walled carbon nanotubes, *Science* **284**, 1508–1511 (1999).
95. Z. K. Tang, L. Zhang, N. Wang, X. X. Zhang, G. H. Wen, G. D. Li, J. N. Wang, C. T. Chan and P. Sheng, Superconductivity in 4 Å single-walled carbon nanotubes, *Science* **292**, 2462–2465 (2001).

---

# 3 Chemistry of Carbon Nanotubes

*Eduard G. Rakov*

D.I. Mendeleev University of Chemical Technology,  
Moscow, Russia

## CONTENTS

Abstract .....	78
3.1 Introduction.....	78
3.2 Carbon Nanotube Morphology and Structure .....	79
3.3 Synthesis of Carbon Nanotubes .....	80
3.4 Opening of Carbon Nanotubes .....	81
3.5 Functionalization of Carbon Nanotubes.....	82
3.5.1 Attachment of Oxidic Groups .....	83
3.5.2 Reactions of Carboxylic Groups Attached to Nanotubes.....	83
3.5.3 Fluorination.....	87
3.5.4 Amidation .....	88
3.5.5 Other Types of Covalent Bonding .....	90
3.5.6 Noncovalent Bonding .....	93
3.5.7 Dispersions in Oleum .....	96
3.5.8 Self-Assembly, Film, and Fiber Formation .....	96
3.6 Filling the Inner Cavity of Carbon Nanotubes.....	99
3.6.1 <i>In Situ</i> Filling.....	100
3.6.2 Post-Processing Filling.....	101
3.6.2.1 Filling from Liquid Media .....	101
3.6.2.2 Filling from Gas Phase.....	103
3.6.3 Reactions inside Nanotube .....	104
3.6.4 The Structure of Crystals inside Nanotubes.....	105
3.7 Adsorption and Storage of Gases .....	106
3.7.1 Hydrogen Problem.....	107
3.7.2 Carbon Nanotube Gas Sensors .....	109
3.8 Attachment of Biomolecules .....	110
3.8.1 Biosensors.....	110
3.8.2 Other Fields of Application .....	112
3.9 Nanotubes as Templates .....	112
3.9.1 Substitution of the Carbon Atoms of Nanotubes .....	112
3.9.2 Decoration of Carbon Nanotubes .....	113
3.10 Intercalation of “Guest” Moieties.....	115
3.11 Summary and Conclusions .....	117
Acknowledgments .....	117
References .....	117

## ABSTRACT

The main trends and recent achievements in carbon nanotube chemistry are reviewed. Apart from “traditional” subjects such as opening, filling, and decoration of nanotubes, some new subjects have also been discussed. A special emphasis has been placed on the functionalization and solubilization of carbon nanotubes, their self-assembly, film and fiber formation, and sensor and biosensor preparation. Some basics on carbon nanotubes are introduced.

## 3.1 INTRODUCTION

Owing to their electronic, mechanical, optical, and chemical characteristics, carbon nanotubes (NTs) attract a good deal of attention from physicists, chemists, biologists, and scientists from several other fields.<sup>1–5</sup> Possible applications in the fields of molecular electronics, nanomechanic devices, information display, sensing, energy storage, and composite materials are of interest for industry.<sup>6</sup>

The perspectives of NT application are greatly dependent on NT chemistry. Chemical behavior of NTs is very diverse and the processes of NT synthesis, purification, modification, and solubilization<sup>7,8</sup> all contribute to this diversity.

There are different ways to modify NTs:

- Partial oxidation and decapping (opening) of NTs
- Attachment of functional groups to the open ends of NTs
- Attachment of functional groups to the sidewalls of NTs
- Chemical reactions of functionalities attached to NTs
- Filling of inner cavities of the NTs with different substances (gaseous, liquid, or solid) and carrying out a chemical reaction inside the NTs
- Replacement of the carbon atoms of NTs by atoms of other chemical elements or groups
- Intercalation (insertion) of “guest” atoms or molecules into the intertubular space of single-wall NTs (SWNTs) bundles or in between the walls of multi-wall NTs (MWNTs)
- Decoration of outer walls of NTs and using NTs as templates
- Adsorption of gases

NTs having very large molecular weights cannot form true solutions. Therefore, solubilization of NT means the formation of their colloid solutions (dispersions). The solubilization can be subdivided into the formation of aqueous, organic, or polymeric dispersions.

The geometry and size of NTs allows them to take part in self-assembly and aligning processes. The directional deposition on certain surfaces, structuring by Langmuir–Blodgett films and by liquid crystals, and formation of colloidal systems are mentioned here.

In its chemical behavior, NTs partially resemble graphite and fullerenes; however, there are also noticeable differences from both graphite and fullerenes.<sup>8,9</sup> Graphite represents a typical layered polymeric crystal and each fullerene can be considered as a molecule which can form molecular crystals (fullerites). However, a great many NTs cannot be classified as either usual molecules or crystals. SWNTs are similar to polymeric molecules of simple substances and MWNTs resemble structured nanoparticles. The individual NT can be also assumed as 1-D crystal and well-ordered NT bundles as 2-D crystals.

Graphite has planar structure corresponding to  $sp^2$  for  $\sigma$  bonds and  $p$  for  $\pi$  bond. Fullerenes and NTs have hybrid bonding orbitals between  $sp^2$  and  $sp^3$ . NTs having low percentage of  $sp^3$  bonds are in this regard nearer to graphite. All these bonds in straight NTs are concentrated in half-spherical or conical caps, and in curved NT they are concentrated in the bends. The difference in chemical activity between NT caps and sidewalls as well as between straight and curved NTs is determined by the  $sp^2:sp^3$  bonds ratio.

Specific chemical properties of graphite, fullerenes, and NTs as well as of fullerenes or NTs of different diameters are also different owing to dissimilar surface curvatures.<sup>10</sup>

The chemistry of new carbon allotropes has been described with a pyramidalization angle  $\theta_p$  formalism.<sup>11</sup> For graphite,  $\theta_p = 0^\circ$ . All carbon atoms in  $C_{60}$  have  $\theta_p = 11.6^\circ$ . Pyramidalization angle of SWNTs ( $n, n$ ) of various  $n$  ( $n = 2$  to 10) is calculated to vary between  $14\text{--}17^\circ$  and  $2^\circ$ .<sup>12</sup> Pyramidalization changes the hybridization of atomic orbitals at the C atom so that the  $\pi$  orbital contains different portions of s and p orbitals, leading to different chemical reactivity. Because of this hybridization, fullerenes and NTs are known to be more reactive than graphite. The deformation energy of  $sp^2$  bond is inversely proportional to the diameter of NT, and therefore tubes with smaller diameter have greater reactivity. The enthalpy of the reaction decreases with increase in the diameter. The enthalpy of homolytic reactions of H atoms and methyl radicals with atoms of curved carbon plane is linearly dependent on the pyramidalization angle and can differ by 1 eV.<sup>13</sup>

The cups of NT, which are often similar to fullerene molecule halves, contain more reactive C atoms, than the sidewalls. Experimental evidence of the higher chemical reactivity of conformationally strained carbon sites in MWNTs has been reported.<sup>14</sup>

NTs exhibit more differences owing to various structure and morphology (kinked, branched, conical NTs, etc.).<sup>15</sup> The NTs differ from fullerenes by the larger size of internal cavity, and from graphite by the greater share of accessible surface sites.

Fullerites, graphite, and NTs contain van der Waals gaps, which on being filled can form intercalates, or “guest–host” compounds. The dimensionality of such compounds is different: 0-D for fullerites, 2-D for graphite, and 1-D for NTs. NTs can form “guest–host” compounds of different types: for instance, the “guests” can exist in the inner cavity of SWNT or MWNT, in the intertube space of the bundled NTs, or in between the walls of MWNTs having scroll structure.

The development of the chemistry of NTs will determine the fields of their practical application. Primarily, NT chemistry is involved with the rational routes of NT purification and sorting. Chemical modification of NTs can open the way to modify the properties of these materials.

Unlike physical investigation of the solid-state properties of NTs, the study of their chemical reactivity is still in its infancy. At the same time, there have been very impressive achievements in the study of the chemistry of NTs in recent years. There are a large number of original publications and some reviews on the subject.<sup>8,10,16–21</sup> The present review pertains mainly to works in the last five years.

### 3.2 CARBON NANOTUBE MORPHOLOGY AND STRUCTURE

Dozens of different morphological varieties of filamentous carbon nanoparticles were revealed in a remarkably short period of time after the discovery of “classical” NTs. As was mentioned by Hilding et al.,<sup>10</sup> NTs can differ by “aspect ratio, NT diameters, surface structures, defect densities, and physical entanglements.”

The NT of the “classical” type represents a cylindrical particle formed from graphene — a flat carbon net with the atoms located in the corners of joined hexagons. They may be single-walled with a diameter between  $\sim 0.3$  and  $\sim 5.0$  nm (typical SWNTs have diameters of 1.0 to 1.4 nm, and length up to 50 to 100  $\mu\text{m}$ ) or multi-walled. SWNTs as a rule contain less topological defects and possess better mechanical and electrophysical properties. The specific surface area of SWNTs is independent of their diameter and is equal to  $1315 \text{ m}^2/\text{g}$  (for outer surface).

MWNTs consist of several (from two to tens) coaxial tubes, with outer diameter of  $\sim 1.4$  to 100 nm. Their specific surface area depends on the number of walls, and to a lesser extent on the diameter of the inner tube. The theoretical surface area of double-wall NTs is between 700 and 800  $\text{m}^2/\text{g}$ , and of ten-wall NTs is about 200  $\text{m}^2/\text{g}$ . Nanofibers (NFs) have a diameter from tens to hundreds of nanometers.

Some MWNTs and NFs have internal cross connections formed by curved graphenes. A moderate relative number (density) of cross connections correspond to a “bamboo-like” structure of

MWNT, while a high relative number of connections may be attributed to conical structures such as “herringbone-like” or “cup-stacked” types. The angle of conicity in the conical structures varies from 15 to 85°. Grafene layers in NFs may also be located perpendicular to the fiber axis. Nanofibers having regularly changing diameter (“nanobeads”) have been synthesized.<sup>22</sup> And finally, there are amorphous NTs or NFs.

SWNTs, MWNTs, and NFs can spontaneously form “secondary” structures. A classification of carbon nanotubular particles into primary, secondary, and tertiary forms was first introduced by De Jong and Geus.<sup>23</sup> The most popular secondary form of the SWNT is a bundle (“rope”), which consists of tubes in a 2-D triangular lattice, with a lattice constant of 1.7 nm. The bundles usually have greater lengths as compared to individual NTs. For example, 1-m-long bundles of NTs have been produced. They can combine to form a structure of higher order. Tangled SWNTs or MWNTs can form “bucky paper” (“nanopaper” and “nanomats”).

Single-walled nanohorns (nanocones) quite often combine to produce flower- or bud-like structures.

“Secondary” structures formed by MWNTs are more diverse. The formation of bundles of MWNT is less typical. More often, kinked (L-shaped) and branched (Y-, T-, H-like, “octopus,” tree-like) forms were synthesized. Tangled MWNTs form aggregates up to 3 mm in diameter (“worms” and “boiled spaghetti”). The aggregates along with conical “cedar forest,” “bucky pearl” and some others are the members of “tertiary” structure.

A pyrolytic synthesis sometimes yields coiled NTs, helices, double helices, helices inside NTs, and even more complex structures, such as brushes, entangled worm-like features, and foil-like structures at the nanometer scale. Transitional forms, such as nanopeas (fullerenes inside SWNTs), are also among the structures formed.

The chemistry of different structures must be notably diverse. This diversity has not been studied yet, and the overwhelming majority of published results pertain to SWNTs, SWNT bundles, and MWNTs.

### 3.3 SYNTHESIS OF CARBON NANOTUBES

There are two main methods or groups of processes of NT synthesis: sublimation of graphite with subsequent desublimation, and decomposition of carbon-containing compounds.<sup>5,7,24</sup> The first group of processes is associated with high temperatures (up to 4000°C), which can be obtained in electric arcs (see, for example, Refs. 25–29), by the process of laser ablation,<sup>29–34</sup> by focused solar radiation,<sup>34,35</sup> or by resistive heating of graphite.

The arc process is remarkable for the larger number of versions, among which some versions allow the realization of a semicontinuous process in automated facilities. Arching process in liquid nitrogen,<sup>36,37</sup> in water,<sup>36</sup> and in aqueous solutions<sup>38,39</sup> have also been developed.

Arching processes in gaseous<sup>40</sup> or liquid<sup>41,42</sup> hydrocarbons are classified as combined methods, where the pyrolysis of hydrocarbons takes place along with the sublimation–desublimation of graphite.

The arc-discharge technique is a popular method. The main disadvantages of the method lies in the difficulty of organizing a continuous process, the concurrent formation of amorphous carbon, metal clusters coated with carbon and in some cases fullerenes along with NTs. The total yield of SWNT, as a rule, does not exceed 20 to 40%.

The second group of methods has its own variations: pyrolysis of gases (chemical vapor deposition, CVD process), solids (e.g., pyrolysis of polymers), aqueous solutions (hydrothermal synthesis),<sup>43,44</sup> or organic solutions (supercritical toluene).<sup>45</sup>

The CVD method can produce NTs in large quantities and can be realized at temperatures of 500 to 1300°C. In accordance with the chemical composition of the carbon source, the method can be subdivided on the disproportionation of CO,<sup>29,33,46</sup> the pyrolysis of hydrocarbons (CH<sub>4</sub>, C<sub>2</sub>H<sub>2</sub>, C<sub>6</sub>H<sub>6</sub>, etc., including polymers),<sup>23,47–49</sup> pyrolysis of CH<sub>x</sub>O<sub>y</sub> compounds (for example, alcohols<sup>50</sup>), and pyrolysis of heteroatomic CH<sub>x</sub>A<sub>y</sub>B<sub>z</sub> compounds (A, B = N, O, S, Cl, ..., e.g., amines).



It is also possible to synthesize NTs via a template method, applying, for example, porous anodic alumina membrane. CVD using hydrocarbons as NT precursors over patterned catalyst arrays leads to the formation of different complex structures and opens up exciting opportunities in nanotechnology.<sup>48</sup>

The thermal disproportionation of CO is realized in two main variants: HiPco<sup>2,5,46</sup> and CoMoCAT.<sup>5,51</sup> These methods are considered by American researchers as the most promising for the commercial production of SWNTs.

High-value NTs, viz. SWNTs, are produced at temperatures of 900 to 1200°C, mainly using CO or CH<sub>4</sub> as a precursor. The availability of precursors, such as C<sub>2</sub>H<sub>2</sub>, methanol, and ethanol, for SWNT synthesis is also shown. SWNTs in all instances are produced only by catalytic reactions.

Methods other than the ones mentioned above, for example, thermal decomposition of metal carbides<sup>7,52,53</sup> or carbonitrides,<sup>54</sup> chlorination of carbides,<sup>7</sup> electrolysis of molten salts,<sup>7</sup> interaction of cesium metal with microporous carbon,<sup>7</sup> defoliation of graphite by forming and subsequent transformation of “guest-host” intercalated compound, transformation of fullerenes C<sub>60</sub> and C<sub>70</sub>,<sup>55</sup> “rapid thermal processing” of amorphous carbon film containing iron,<sup>56</sup> sonochemical production,<sup>57</sup> AC plasma processing,<sup>58</sup> etc., are not widely used.

### 3.4 OPENING OF CARBON NANOTUBES

Independent of their synthesis method, pristine SWNTs have large aspect ratio (10<sup>3</sup> to 10<sup>4</sup>) and closed ends. Open-ended NTs offer unique possibilities as conduits for flow of low-surface-tension fluids through their cylindrical pores. Applications of NTs in molecule separation devices, in biocatalysis, in molecule detection, and as encapsulation media have been proposed. The end cups on NTs must be destroyed to make the inner cavity available for filling. The simplest method to open NTs is their oxidative treatment. The oxidation tends to initiate on the end cups, thus providing a mechanism for opening the NT. The treatment is accompanied by functionalization of NTs with oxygen-containing groups (see below).

Liquid or gaseous chemical agents are used as oxidants. Refluxing, sonication, or microwave (MW) digestion in concentrated acids, such as HNO<sub>3</sub>, H<sub>2</sub>SO<sub>4</sub> and their mixtures, are the most popular methods of oxidation. Refluxing of MWNTs in concentrated HNO<sub>3</sub> leads not only to oxidative opening, but also in the reduction of the NT length and diameter as well as the breaking of entangled MWNTs.<sup>59</sup> Treatment of SWNTs results in tube cutting and narrowing of diameter distribution.<sup>60,61</sup> The bundles of SWNTs become disordered and partly exfoliated, when they are immersed in 70% HNO<sub>3</sub> for a long period of time.<sup>62</sup> Nitric acid can be intercalated into SWNT bundles, in that way disintegrates the tube walls into graphitic flakes, and then reforms them into various multi-shell phases such as MWNTs, cone-shaped phases, and onion-like phases.<sup>63</sup> A prolonged treatment of SWNTs leads to amorphization and complete destruction of the tubes.

Bundles in raw SWNT material are significantly thinner (<10 NTs) than those found in sonicated and HNO<sub>3</sub>-oxidized samples (>30 NTs).<sup>64,65</sup> It has been suggested that this thickening is promoted by the H-bonding between –COOH sidegroups formed during oxidation.

The concentrated H<sub>2</sub>SO<sub>4</sub>/HNO<sub>3</sub> mixture (3:1) is a better agent for cutting SWNTs<sup>60,66</sup> and for enrichment of large-diameter SWNTs.<sup>67,68</sup>

Oxidation of SWNTs with H<sub>2</sub>O<sub>2</sub> is a common tube-opening procedure.<sup>69–71</sup> SWNTs react exothermically with the H<sub>2</sub>SO<sub>4</sub>/H<sub>2</sub>O<sub>2</sub> mixture.<sup>60</sup> Oxidation in solution (HNO<sub>3</sub>/H<sub>2</sub>O<sub>2</sub>/H<sub>2</sub>SO<sub>4</sub>) has been found to be effective for opening SWNTs. Aqueous solutions of OsO<sub>4</sub>, OsO<sub>4</sub>/NaIO<sub>3</sub>,<sup>72</sup> RuO<sub>4</sub>, KMnO<sub>4</sub>, H<sub>2</sub>SO<sub>4</sub>/KMnO<sub>4</sub>, H<sub>2</sub>SO<sub>4</sub>/(NH<sub>4</sub>)<sub>2</sub>S<sub>2</sub>O<sub>8</sub><sup>73</sup> have also been successively used to open NTs. Superacids such as HF–BF<sub>3</sub> have been shown to act as an etchant of NTs at room temperature.

The opening of MWNTs can be realized at room temperature electrochemically in H<sub>2</sub>SO<sub>4</sub><sup>74</sup> or in dilute aqueous KCl solutions.<sup>75</sup> Supercritical water acts on MWNT as an opening and thinning agent.<sup>76</sup>

Gaseous thermal oxidation is more effective than acid treatment. Thinner SWNTs burn more quickly than thicker SWNTs during oxidation by oxygen gas.<sup>77,78</sup> Fixed ambient air,<sup>79,80</sup> fixed air activated by microwave irradiation,<sup>81</sup> air flow,<sup>82–84</sup> 5% O<sub>2</sub>/Ar mixture,<sup>85,86</sup> reduced O<sub>2</sub> atmosphere,<sup>61</sup> O<sub>2</sub>/H<sub>2</sub>S mixture,<sup>87,88</sup> O<sub>2</sub>, and H<sub>2</sub>O plasma<sup>89</sup> are used for oxidation. It has been shown that the oxidative stability of SWNT is higher than that of amorphous carbon but lower than the oxidative stability of graphitic carbon.

The pore structure and specific surface area of SWNT aggregates are changed by air oxidation.<sup>82</sup> However, unlike oxidation with H<sub>2</sub>SO<sub>4</sub>/HNO<sub>3</sub> (3:1) solution, the air oxidation process preferentially oxidizes SWNTs without introducing sidewall defects.<sup>90</sup> The air oxidation rate of SWNTs is clearly correlated to the amount of metal impurity. Ultrafine gold particles catalyze the oxidation.<sup>91</sup>

A mechanism for oxidative etching by O<sub>2</sub> includes adsorption of O<sub>2</sub> molecules on the tube cup or wall, successive transformation of adsorbed molecules, and tube cup being etched away.<sup>92</sup> Defective sites on the ends and the walls of MWNTs facilitate the thermal oxidative destruction of the tubes.<sup>93</sup> The kinetics of oxidation in an air flow has been studied at 400 to 450°C.<sup>94</sup> The apparent activation energy of oxidation has been found to be equal to 150 kJ/mol and corresponds to the data for oxidation of carbon soot.<sup>95</sup> A kinetic model of the process has been proposed.<sup>84</sup>

Ozone at reduced or room temperature<sup>96–101</sup> and CO<sub>2</sub>/Ar (2:1) mixture at 600°C<sup>102</sup> are suitable for the oxidation of NTs.

As a rule, the oxidation procedure is used for the purification of crude SWNTs and MWNTs containing amorphous carbon, catalyst, and graphitic nanoparticles. Acid reflux followed by thermal oxidation or reciprocal manner of treatment are common.<sup>5,9,10,79,83,85,86,103–105</sup> Acid treatment of SWNTs in combination with tangential filtration<sup>106</sup> or centrifugation<sup>104</sup> have been tested. Microwave acid digestion allows a reduction in the operational time.<sup>107</sup> In some cases, HCl<sup>71,108</sup> or HF<sup>109,110</sup> is used for the dissolution of metal impurities. Multi-step purification procedures including acid treatment<sup>80,111</sup> or air oxidation<sup>112,113</sup> have been developed. Hydrogen peroxide has been shown to be an effective agent in the process of carbon nanostructure purification from amorphous carbon impurities.<sup>114</sup> The methods that are usually used to remove impurities from the as-prepared SWNT material lead to hole-doped purified SWNTs.<sup>115</sup>

### 3.5 FUNCTIONALIZATION OF CARBON NANOTUBES

Functionalization allows the segregation of entangled or bundled NTs for their subsequent alignment. It is widely used for solubilization of NTs and for purification and classification of NTs in solutions. The surface modification of NTs plays an important role in their use in composites, providing strong fiber–matrix bonding and thus improving the mechanical properties of the material. The integration of NTs into integrated circuits and working devices, such as sensors and actuators, requires robust, well-defined connections, for which few processes are better than covalent functionalization.

All the existing methods of chemical derivatization of NTs are divided into two groups, depending on whether attached moieties are introduced onto the NT tips or sidewalls. The use of the latter offers wider opportunities to change the original NT properties, since it allows high coverage with attached groups. The attachment can be realized either by covalent bond formation, or by simple adsorption via noncovalent interactions (hydrophobic,  $\pi$  stacking, etc.).

The covalent bonding can be realized via chemical or electrochemical reactions. The chemical functionalization involves oxidation, fluorination, amidation, and other reactions. Two main paths are usually followed for the functionalization of NTs: attachment of organic moieties either to carboxylic groups that are formed by oxidation of NTs with strong acid, or by direct bonding to the surface double bonds.<sup>116</sup>

Using NTs as either anode or cathode in an electrochemical cell enables oxidation or reduction of small molecules on the surface of the NT, leading to the formation of radical species which can be covalently bonded.

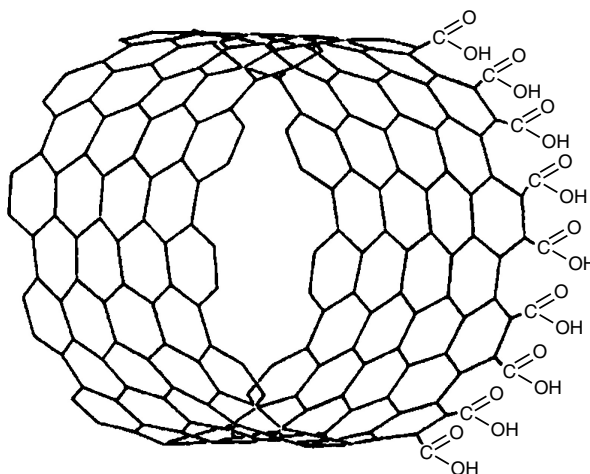


**FIGURE 3.1** Structure of (10,10) SWNT-COOH.

### 3.5.1 ATTACHMENT OF OXIDIC GROUPS

By analogy with other carbonaceous materials, concentrated  $\text{HNO}_3$  and mixtures of  $\text{H}_2\text{SO}_4$  with  $\text{HNO}_3$ ,  $\text{H}_2\text{O}_2$ , or  $\text{KMnO}_4$  have been widely used for attaching acidic functionalities to NTs. First, acidic groups are attached to the open ends of SWNTs (Figure 3.1).

Refluxing NTs in a  $\text{H}_2\text{SO}_4/\text{HNO}_3$  mixture results in a clear, colorless solution, which on evaporation of the solvent and removal of excess acid, gives a white solid containing functionalized NTs.<sup>72</sup> Neutralization of the acidic solution by alkali results in precipitation of a brown solid containing nanotubes.

The main acidic functionalities comprise  $-\text{COOH}$ ,  $-\text{C}=\text{O}$ , and  $-\text{OH}$  groups<sup>117</sup> approximately in the proportion of 4:2:1.<sup>118</sup> The concentration of surface acid groups in the NTs treated by different oxidants varies in the range of  $2 \times 10^{20}$  to  $10 \times 10^{20}$  sites/g.<sup>72</sup> On a molar basis, the concentration of acid groups is equal to 5.5 to 6.7%,<sup>119</sup> ~6%,<sup>120</sup> ~5%<sup>121</sup> for shortened SWNTs or ~4% for full-length SWNTs.<sup>122</sup> Simple acid–base titration method shows that three different samples of purified SWNTs had about 1 to 3% of acidic sites and about 1 to 2% of  $-\text{COOH}$  functionalities.<sup>123</sup> The functional group concentration is time-dependent.

Treatment of SWNTs with concentrated  $\text{H}_2\text{SO}_4$  containing  $(\text{NH}_4)_2\text{S}_2\text{O}_7$  and  $\text{P}_2\text{O}_5$ , followed by treatment with  $\text{H}_2\text{SO}_4$  and  $\text{KMnO}_4$ , results in the formation of material containing C/O/H in the atomic ratio of 2.7:1.0:1.2.<sup>73</sup>

A “one-pot” oxidative method via ozonolysis of the NT sidewall has been developed.<sup>99</sup> The ozonized NTs can react with several types of reagents, thus providing control over functional groups (Table 3.1).

Along with functionalization with carboxylic, alcoholic, aldehydic, and ketonic groups, acidic treatment leads to sizeable attaching of protons. The MWNTs, after acidic purification, contain 76.6%  $\text{CH}_x$ , 13.0% C–O, 4.2% C=O, and 6.2% N–C=O and O–C=O groups<sup>124</sup>  $-\text{CSO}_3\text{H}$  groups are also attached using sulfuric acid.

Acid-functionalized, purified, and shortened SWNTs can be dispersed in water by sonication.<sup>125</sup> No tube precipitation was observed with solutions containing 0.03 to 0.15 g/L after a month. The solubility and stability of the solution are pH-dependent.

### 3.5.2 REACTIONS OF CARBOXYLIC GROUPS ATTACHED TO NANOTUBES

The carboxylic groups at the SWNT tips can chemically react in organic solutions to form closed rings (Figure 3.2).<sup>126</sup> The average diameter of the rings is 540 nm with a narrow size distribution.

The most important aspect for further covalent or ionic functionalization is the possibility of exploiting carboxylic groups at the tube ends or walls. Amines are among the reagents that have drawn

**TABLE 3.1**  
**Relative Amounts of Different Surface Oxygenated Groups (%) on HiPco SWNTs Subjected to Ozonolysis at  $-78^{\circ}\text{C}$  in Methanol Followed by Selective Chemical Treatment**

Sample	C-OH	C=O	COOH, O-C=O
Ozonated	13.3	50.8	35.9
Treated with $\text{H}_2\text{O}_2$	37.0	9.4	53.6
Treated with DMS	28.7	41.1	30.2
Treated with $\text{NaBH}_4$	29.1	36.3	34.6

Source: From Banerjee, S. and Wong, S.S., *J. Chem. Phys.*, **B 106**, 12144–12151, 2002. With permission.

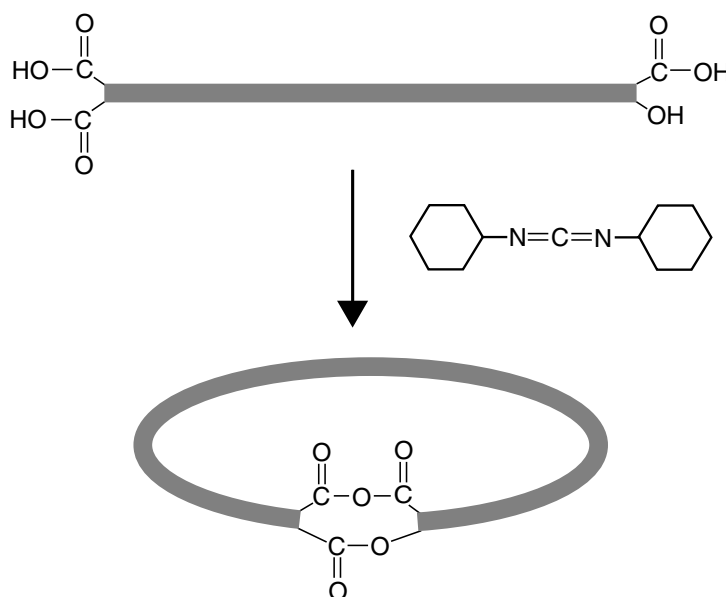


**FIGURE 3.2** A possible scheme for the ring-closure reaction with 1,3-dicyclohexylcarbodiimide. (Reprinted with permission from Sano, M. et al., *Science*, **293**, 1299–1301, 2001.)

the greatest attention. There are three types of carboxylic group reactions with amines: (1) amidation, (2) acid–base interaction, and (3) condensation. Besides, amines can be physisorbed on NT walls.

Haddon and coworkers<sup>118,120,127,128</sup> pioneered the approach of functionalizing the carboxylic groups of shortened oxidized SWNTs through amidation with amines bearing long alkyl chains. To modify SWNTs with the amide functionality, the reactions shown in [Figure 3.3](#) were used.

Shortened SWNTs were stirred in  $\text{SOCl}_2$  containing dimethylformamide (DMF) at  $70^{\circ}\text{C}$  for 24 h, and after centrifugation, decantation, washing, and drying, the residual solid was mixed with octadecylamine (ODA) and heated at 90 to  $100^{\circ}\text{C}$  for 96 h. During this process, the volume of the SWNTs expanded several times.

The second and the third routes to attach amines are the direct reactions of carboxylic groups with amine (see [Section 3.5.4](#)).

The concentration of functional groups bound in SWNTs functionalized with  $\text{SOCl}_2$  seems to be sensitive to gamma irradiation.<sup>129</sup> SWNTs and MWNTs containing acyl chloride groups are solubilized via poly(propionylethylenimine-*co*-ethylenimine) attachment.<sup>130–132</sup> Reaction with polyethyleneimine caused the formation of a product, which is soluble in chloroform.<sup>133</sup> MWNTs functionalized with  $-\text{COCl}$  groups can covalently attach polythiophene.<sup>134</sup>

The refluxing of functionalized NTs with an excess of  $\text{NaBH}_4$  in absolute ethanol leads to the reduction of the carboxylic acid groups into hydroxyl groups.

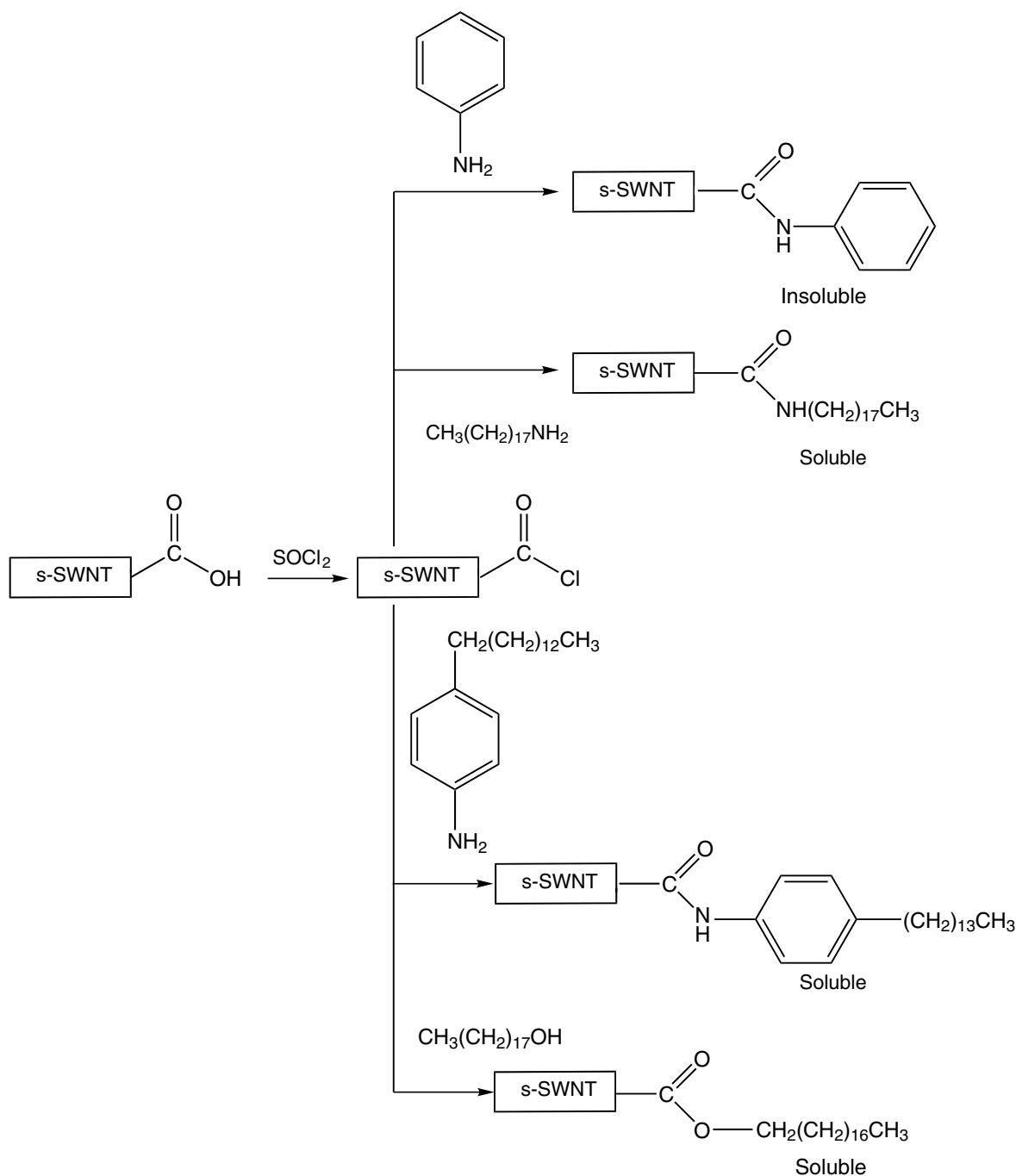
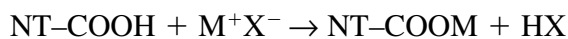


**FIGURE 3.3** Covalent chemistry at the open ends of SWNTs. (Reprinted with permission from Niyogi, S. et al., *Acc. Chem. Res.*, **35**, 1105–1113, 2002. Copyright 2002. American Chemical Society.)

Esterification of the NT ends or sidewalls after their carboxylation<sup>130,135–141</sup> differs from many other methods of functionalization in the simplicity of defunctionalization.<sup>136</sup> The attached groups can be easily removed by a hydrolysis reaction, catalyzed by acids or bases. The NTs evolve from the solution after hydrolysis.

Oxidized carbon atoms can act as specific sites for adsorption of metal ions.<sup>142,143</sup> The simplest reaction may be expressed by the equation



Individual  $\text{Pb}^{2+}$ ,  $\text{Cu}^{2+}$ , and  $\text{Cd}^{2+}$  ion-adsorption capacities are equal to 97, 28, and 11 mg/g, respectively.<sup>143</sup>  $\text{Hg(II)}$  ions form groups of two types:  $(-\text{COO})_2\text{Hg}$  and  $(-\text{O})_2\text{Hg}$ , in the ratio (%) of

30:70.<sup>142</sup> Ultrasonication of a dispersion of MWNTs in water–isopropanol solution containing  $\text{RuCl}_3 \cdot 3\text{H}_2\text{O}$  leads to Ru attachment.<sup>144</sup> The surface carboxylic groups are used to attach the relatively bulky metal complexes such as Vaska's complex ( $\text{trans-IrCl}(\text{CO})(\text{PPh}_3)_2$ ),<sup>145</sup> Wilkinson's complex ( $\text{RhCl}(\text{PPh}_3)_3$ ),<sup>146</sup> and also  $\text{TiO}_2$  or  $\text{CdSe}$  nanoparticles.<sup>147,148</sup> It has been shown that Ir coordinates to the NTs by two distinctive pathways. With raw tubes, the metal attaches as if the tubes were electron-deficient alkenes. With oxidized tubes, oxygen atoms form a hexacoordinate around the Ir atom. The Rh atom similarly coordinates to these NTs through the increased number of oxygenated species. The functionalization reaction, in general, appears to increase significantly oxidized NT solubility in DMF in the case of Vaska's and in dimethyl sulfoxide (DMSO) in the case of Wilkinson's.

Among the range of reagents tested, the most effective for MWNTs silylation were *N*-(*tert*-butyldimethylsilyl)-*N*-methyltrifluoroacetamide and 1-(*tert*-butyldimethylsilyl)imidazole.<sup>149</sup>

The oxidized groups present on SWNTs allow the formation of polymer/NT films by the alternate adsorption of the polyelectrolyte and SWNTs onto substrates.<sup>150</sup> Such groups on MWNT walls can react with 3-mercaptopropyl trimethoxysilane.<sup>151</sup> Alkoxysilane-terminated amide acid oligomers are used to disperse NTs.<sup>152</sup> Alkoxysilane functional ends on the oligomer, once hydrolyzed, react with functionalities on the ends of the purified SWNTs, thus leading to polymer formation.

The formation of NT arrays by self-assembling COOH-terminated NTs onto certain metal oxide substrates (e.g., Ag, Cu, Al) has been demonstrated.<sup>153</sup> In such reactions, the ability of carboxylic groups to deprotonate in contact with metal oxides is utilized.<sup>20</sup> An assembling acid-functionalized SWNTs on patterned gold surface has been developed.<sup>154,155</sup> The reaction mechanism is presumed to include an ester intermediate formation.

The carboxylated tips of NWNT are used to force titrations by atomic force microscope (AFM).<sup>156</sup> The ability of carboxylic groups at the tips of NT to be readily derivatized by a variety of reactions allows the preparation of a wide range of molecular probes for AFM.<sup>157,158</sup>

Air heating of derivatized NTs at controlled temperatures and for controlled periods leads to the decomposition of carboxylic groups and to the formation of hydroxyl groups.<sup>159</sup> The carboxylic groups could be removed by thermal vacuum decarboxylation without damaging the electron system of the NTs, but defects remain on the tube walls.<sup>65</sup> It is generally accepted that carboxylic groups decomposed on heating to  $\text{CO}_2$  gas and carbonyl groups, desorbed in the form of CO (Figure 3.4).<sup>160,161</sup> The  $\text{CH}_x$  groups decompose giving  $\text{CH}_4$  and  $\text{H}_2$ .<sup>161</sup>

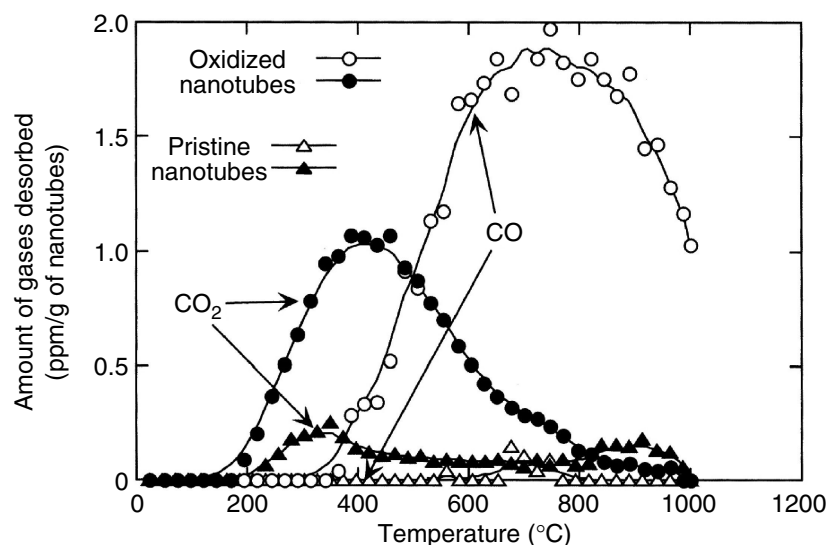


**FIGURE 3.4**  $\text{CO}_2$  and CO temperature programmed desorption patterns of oxidized and pristine NTs. (Reprinted from Kyotani, S. et al., *Carbon*, **39**, 771–785, 2001. With permission from Elsevier.)

### 3.5.3 FLUORINATION

Fluorination plays an important role in the chemistry of NTs because of the simplicity in achieving a high degree of functionalization, the very high stability of fluorinated NTs, and the possibility to change the attached fluorine atoms to other functional groups. The fluorination reaction can easily be scaled-up.

The first work devoted to fluorination of fibrous carbon material was published by Nakajima et al.<sup>162</sup> before NTs were discovered. This work showed that the reaction starts at room temperature. The composition of the products prepared at fluorine pressure of 1 atm corresponds to  $C_{8-12}F$ .

After a decade, MWNTs were fluorinated at different temperatures and the formation of  $(CF)_n$  at 500°C was documented.<sup>163</sup> A year later, French specialists, using a mixture of  $F_2$ -HF- $IF_5$  for fluorination of MWNTs, observed a modification of NT structure after reaction at high temperatures, and studied the electrochemical behavior of the fluorinated NT (“fluorotubes”) as electrode material in a lithium cell.<sup>164,165</sup> The fluorination of MWNTs by vapor over a solution of  $BrF_3$  in liquid  $Br_2$  at room temperature revealed a decrease of cage nanoparticles in the fluorinated material relative to the pristine sample, which was connected with unrolling the NTs during fluorination.<sup>166</sup> Insufficient purity of the samples used in these works makes the full interpretation of the results difficult.

The amount of doped fluorine increases with increasing doping temperature. Doping at lower temperatures resembles the intercalation of graphite with fluorine and leads to the buckling of the outer MWNT walls.<sup>167</sup>

The fluorination of the internal surfaces of NTs, prepared by a template carbonization technique and which are less crystalline than those synthesized by arc discharge or laser methods, by elemental fluorine at 200°C shows that the resulting compound corresponds to  $CF_{1.42}$ .<sup>168</sup>

Fluorination of purified SWNTs in the form of “bucky paper,” by flow of fluorine gas diluted by helium at a reaction time of 5 h demonstrated that the composition of fluorinated NTs varied from  $CF_{0.1}$  at 150°C to  $CF_{1.0}$  at 600°C.<sup>169</sup> It appeared that fluorination at 400°C and higher temperatures leads to destruction (e.g., “unzipping”) of SWNTs, to the formation of structures resembling MWNTs, and to the evolution of gaseous products such as  $CF_4$ ,  $C_2F_4$ ,  $C_2F_6$ . Once fluorinated at temperatures up to 325°C, which corresponds to the formation of  $C_2F$ , SWNTs were defluorinated with anhydrous hydrazine and were rejuvenated. Partial or complete elimination of fluorine can be done by  $LiBH_4/LiAlH_4$  treatment.<sup>170</sup>

In their subsequent works, Peng et al.<sup>171</sup> realized the fluorination of purified SWNTs with  $F_2/HF$  mixture at 250°C (HF acts as a catalyst).

Heat annealing of fluorinated SWNTs having C/F ratios between 2.0 and 2.3, in a flow of noble gas, indicates that NTs could be recovered at 100°C.<sup>172</sup> Tubes fluorinated at 250°C to a  $CF_{0.43}$  stoichiometry lose fluorine on annealing under flowing helium gradually with increasing temperature.<sup>173</sup> Upon heating, the largest fluorine loss occurred between 200 and 300°C.

The fluorination of purified HiPco tubes to a stoichiometry  $CF_x$  ( $x \leq 0.2$ ) followed by pyrolysis of partially fluorinated material up to 1000°C was found to have “cut” the NTs.<sup>174</sup> In an argon atmosphere, the fluorine was driven off the NT structure in the form of gaseous  $CF_4$  and  $COF_2$ . Short bundles comprising strongly interacting individual NTs were found in the cut nanotube sample.

As a result of band-gap enlargement, the resistivity of fluorinated SWNT mat increases with increasing fluorination temperature, i.e., fluorine content.<sup>175</sup> The electronic properties are also altered by fluorination. As they are fluorinated, NTs reduce their tendency to self-agglomerate.

The most important property of fluorotubes is their ability to form soluble derivatives (Figure 3.5).<sup>176-179</sup>

Sidewall-alkylated NTs are obtained by interaction of fluorinated NTs with alkyl magnesium bromides in a Grignard synthesis or by reaction with alkyllithium precursors. The alkylated NTs are soluble in various organic solvents, including chloroform, methylene chloride, and tetrahydrofuran. For example, the solubility of hexyl-solubilized SWNTs in chloroform is up to ~0.6 g/L,

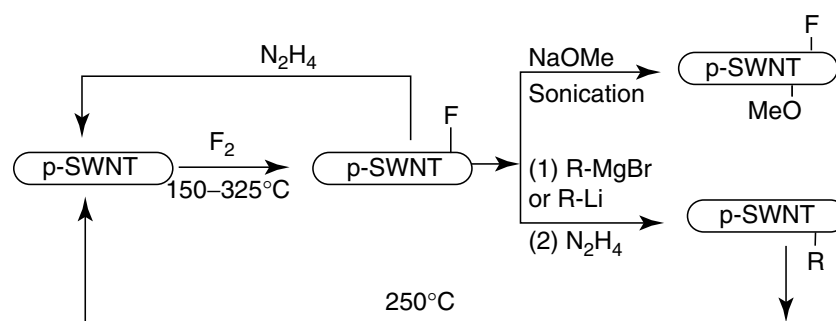


**FIGURE 3.5** Sidewall fluorination of SWNTs and fluorine substitution reactions. (Reprinted with permission from Niyogi, S. et al., *Acc. Chem. Res.*, **35**, 1105–1113, 2002. Copyright 2002. American Chemical Society.)

in tetrahydrofuran to  $\sim 0.4$  g/L, in methylene chloride to  $\sim 0.3$  g/L, as compared with maximum concentration of 0.1 g/L of pristine NTs in DMF.

Sonication of SWNTs in some solvents for  $\sim 5$  min also results in the selective solubilization of highly fluorinated (isopropanol) or sparsely fluorinated (DMF) samples. Fluorotubes can be solvated in alcohols yielding metastable solutions. Of the solvent used, 2-propanol and 2-butanol seemed to be the best, reaching SWNT concentration of 1 g/L. A probable mechanism of such solvation would be hydrogen bonding between the hydroxyl hydrogen atom in alcohol and NT-bound fluorine. Water, diethylamine, perfluorinated solvents, or acetic acid do not solvate NTs.

Fluorotubes dissolved in alcohols can react with alkoxides or terminal diamines such as  $\text{H}_2\text{N}(\text{CH}_2)_n\text{NH}_2$  ( $n = 2, 3, 4, 6$ ). They are capable of reacting with hydrogen peroxide, organic peroxides (e.g., lauroyl, benzoyl, *tert*-butyl), and with a number of solid inorganic compounds, such as alkali halides,  $\text{Li}_2\text{S}$ ,  $\text{ZnS}$ ,  $\text{Li}_2\text{O}_2$ , and AlP.

The atomic and electronic structures of fluorinated SWNTs have been examined in a few experimental and theoretical works.<sup>175,180–188</sup> As a result of fluorination, a significant charge transfer occurs from the NT wall to the fluorine atoms, resulting in partially ionic bonds. This transforms the non-polar SWNT to the polar one.

X-ray photoelectron spectroscopy can identify the type of bonding within  $\text{CF}_x$  compounds. The spectra of fluorinated samples give peaks appearing at 287 eV (semi-ionic C–F), at 288 to 299 eV (nearly covalent C–F), and at 292.0 to 294.05 eV (covalent  $\text{CF}_2$  and  $\text{CF}_3$ ).<sup>175</sup>

Fluorinated SWNTs are used to form composites with poly(ethylene oxide).<sup>189</sup>

### 3.5.4 AMIDATION

Amines, particularly ODA, have attracted special attention in the studies of functionalization of CNs. The SWNT–COOH product treated with oxalyl chloride at  $0^\circ\text{C}$  and then heated with ODA at  $100^\circ\text{C}$ , after purification contains 4 mol% of amine.<sup>190</sup> Shortened MWNTs attach considerably larger amounts of ODA, up to 41.7 wt%, after 96-h functionalization.<sup>191</sup>

Acid-chloride-functionalized SWNTs are used to attach glucosamine,<sup>192</sup> didecylamine,<sup>193,194</sup> 4-dodecyl-aniline, and 4- $\text{CH}_3(\text{CH}_2)_{13}\text{C}_6\text{H}_4\text{NH}_2$ .<sup>118</sup> NTs functionalized with aniline prove to be soluble only in aniline, whereas NTs derivatized with tetradecylaniline are soluble in  $\text{CS}_2$  and aromatic solvents. The anilination reaction solubilizes SWNTs and allows their purification chromatographically using excess of adsorbed aniline. A product with the ratio of NT carbons to aniline sites of 360:1 has been prepared by refluxing oxidatively end-cut SWNTs.<sup>195</sup> The functionalized group of MWNTs modified with aniline was determined to be  $\text{C}_6\text{H}_6\text{N}^-$ .<sup>196</sup> The terminal chlorinated carboxylic groups were used to append pyrenyl subunits<sup>197</sup> and *n*-pentyl ethers.<sup>141</sup>

SWNTs absorb MW radiation, and thus tubes can be rapidly heated by radiation. A procedure based on MW heating, which allows the attachment of monoamine-terminated poly(ethylene glycol) molecules to shortened SWNTs–COCl, has been developed.<sup>198</sup>

The acid-chloride-functionalized SWNTs were attached in pyridine suspension to chemically functionalized Si surfaces.<sup>199</sup>



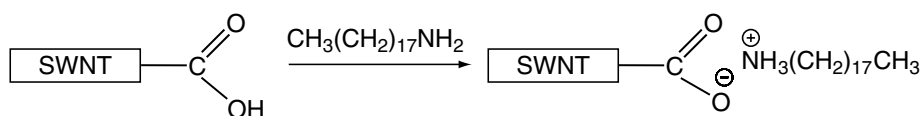


**FIGURE 3.6** Zwitter-ionic functionalization of SWNTs. (Reprinted with permission from Niyogi, S. et al., *Acc. Chem. Res.*, **35**, 1105–1113, 2002. Copyright 2002. American Chemical Society.)

It is supposed that SWNT in DMF can form covalent bonds with tenth generation poly(amidoamine) starburst dendrimer.<sup>200</sup> A “grafting-from” method has been developed for production of hyperbranched poly(amidoamine)-modified NTs.<sup>201</sup>

Solution of SWNTs in DMF derivatized with ODA is used for chromatographic purification procedure.<sup>202</sup> The NT end-to-side or end-to-end junctions are created by the reaction between modified NTs and diamines.<sup>203,204</sup>

The CdSe quantum dots were coupled to individual acid-chloride-modified SWNTs via amide-bond formation.<sup>205</sup>

Oxygen-containing groups that are present on NT tips can condense with alkoxy silane groups-terminated amide acid polymers and facilitate the formation of NT/polymer films for electrostatic charge mitigation.<sup>152,206</sup>

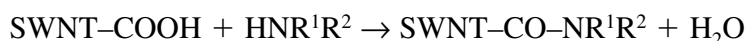
The simplest possible route to the solubilization of SWNTs is direct reaction of the molten amine with the shortened SWNT–COOH. Thus a simple acid–base reaction is realized and zwitterions are formed (Figure 3.6).<sup>118</sup> The products of the reaction are found to be soluble in tetrahydrofuran (THF) and CH<sub>2</sub>Cl<sub>2</sub>. Zwitterion-functionalized shortened SWNTs are used for length separation via gel permeation chromatography<sup>207</sup> and for selective precipitation of metallic SWNTs upon solvent evaporation.<sup>208</sup> The method is used to solubilize full-length SWNTs.<sup>122</sup> The derivatization of the oxidized MWNTs with triethylenetetramine leads to subsequent covalent bonding with the epoxy resin used as a matrix for MWNTs.<sup>209</sup> +NH<sub>3</sub>(CH<sub>2</sub>)<sub>17</sub>CH<sub>3</sub> ions, as has been stated, can readily exchange with other ions, e.g., metal ions.<sup>11</sup> Cysteamine allows the realization of thiolization reaction of carboxyl-terminated SWNTs and deposition of the NTs onto a gold surface.<sup>210</sup> A version of region-specific NT deposition onto prepatterned surface via amidation of acid-functionalized NTs is described.<sup>211,212</sup>

Sun et al.<sup>213</sup> studied the reaction and dispersal of noncarboxylated SWNTs by refluxing in aniline. Dark-red complexes are formed in the process. The solubility of SWNTs in aniline is up to 8 g/L. This aniline–NT solution can be readily diluted with other organic solvents such as acetone, THF, and DMF. As evidenced by their relatively high solubility in aniline, NTs may form donor–acceptor interactions with aniline.<sup>213</sup> Complexing with aromatic amines makes both single- and multi-wall tubes dispersible in organic solvents.

The condensation reaction of acid-functionalized SWNTs with 2-aminoethanesulfonic acid allows to supply the end of SWNT with sulfonic groups and enhance its solubility in water.<sup>214</sup> This technique has been used for attachment of aminopolymers.<sup>132</sup> The amidation of NT-bound carboxylic acids can be accomplished in diimide-activated reactions. Functionalization with poly(propionylethylenimine-*co*-ethylenimine) in the presence of 1-ethyl-3-(3-dimethylaminopropyl)carbodiimide has been found to be significantly improved in both efficiency and yield by sonication under ambient conditions.<sup>215</sup>

The attachment of poly(styrene-*co*-aminomethylstyrene) is possible under amidation reaction.<sup>139</sup> The ball-milling process in ammonia atmosphere allows the introduction of amine and amide groups onto MWNTs.<sup>216</sup>

Basiuk et al.<sup>217</sup> attempted to simplify convenient solution method, and to apply gas-phase derivatization of oxidized NTs containing carboxylic groups on their tips according to the equation



Nonylamine, dipentylamine, ethylenediamine, and propylenediamine<sup>217</sup> have been used as test compounds. This procedure consists of treating SWNTs with amine vapors under reduced pressure and at a temperature of 160 to 170°C. Amine molecules not only formed derivatives with SWNT tips but physisorbed inside SWNTs. The content of physisorbed nonylamine is about one order of magnitude higher than the amide content.

Theoretical consideration of the amidation reaction with methylamine shows that the formation of amide derivatives on carboxylated armchair SWNT tips is more energetically preferable than that on the zigzag NTs.<sup>218</sup>

The physisorption on metallic SWNTs causes no significant change in the electrical conductance, whereas adsorption of amines (such as butylamine and propylamine) on partial length of semiconducting NTs causes modulated chemical gating.<sup>219</sup>

Other works on amidation have been published; among them is the amidation of HiPco SWNTs,<sup>220</sup> and the functionalization of SWNTs with phthalocyanine molecules through amide bonds.<sup>221</sup>

### 3.5.5 OTHER TYPES OF COVALENT BONDING

Direct covalent functionalization of NT can be realized via addition of carbenes,<sup>127,222–226</sup> nitrenes,<sup>223,227–229</sup> 1,3-dipoles,<sup>230–232</sup> aryl cations,<sup>19,233,234</sup> and radicals (Figure 3.7).<sup>19,233,235–241</sup>

For direct functionalization, one can use processes such as ultrasonication in organic media,<sup>10</sup> plasma treatment, UV irradiation, or irradiation with energetic particles.

Carbenes have the general formula  $CRR'$ , where  $R, R' = H$ , halogen, organic residuum, etc., and represent unstable compounds of bivalent carbon. Dichlorocarbene is an electrophilic reagent that adds to deactivated double bonds, but not to benzene. It is capable of attacking  $C=C$  bonds, replacing them by  $CCl_2$  bridges. The addition of dichlorocarbene took place at the sidewall of both insoluble SWNT<sup>222</sup> and shortened SWNTs (s-SWNTs).<sup>127</sup> It was reacted with NTs in a refluxing chloroform/water suspension. Around 5% of chlorine was incorporated into or onto the SWNTs.<sup>222</sup>

Hu et al.<sup>225</sup> used dichlorobenzene solution of  $PhCCl_2HgBr$  and showed that the addition of dichlorocarbene converts metallic SWNTs to semiconducting SWNTs. Thermal treatment of (s-SWNT) $CCl_2$  above 300°C results in the breakage of  $C-Cl$  bonds, but the electronic structure of the SWNTs was not recovered. Monthieux<sup>224</sup> published a method for dichlorocarbene formation and attachment to the SWNT by the decomposition of chloroform under UV irradiation. The  $C=Cl_2$  bridges are assumed to be removed under UV treatment.

The two-level Our own n-layered Integrated molecular Orbital + molecular mechanics Method (ONIOM) technique has been employed to study the [2 + 1] cycloadditions of dichlorocarbene, silylene, germilene, and oxycarbonitrene onto the sidewall of SWNT.<sup>226</sup> Results showed that the reactions are site-selective and yield three-membered ring species. The thermal stability of the SWNT derivatives follows the order oxycarbonitrene  $\gg$  dichlorocarbene  $>$  silylene  $>$  germilene. The derivatives can be good starting points for further functionalization.

Nitrenes are analogs of carbenes; they represent unstable compounds of monovalent nitrogen and have general formula  $RN$ , where  $R =$  alkyl, aryl, getaryl,  $NR'_2$ ,  $CN$ , etc. Among the methods of nitrene generation, thermal and photochemical decomposition of azides and other compounds should be mentioned. The addition of (R-)-oxycarbonyl nitrenes allows the bonding of a variety of different groups such as alkyl chains, aromatic groups, dendrimers, crown ethers, and oligoethylene glycol units.<sup>227</sup>

For functionalization based on the 1,3-dipolar cycloaddition of azomethine ylides,<sup>230–232</sup> the heterogeneous reaction mixture of SWNTs suspended in DMF together with excess aldehyde and modified glycine was heated at 130°C for 5 days. The modified NTs are remarkably soluble in most organic solvents ( $CHCl_3$ ,  $CH_2Cl_2$ , acetone, methanol and ethanol) and even in water. The solubility of SWNTs in  $CHCl_3$  is close to 50 g/L without sonication. The reactions were successful with the use of either short-oxidized or long-nonoxidized SWNTs, without notable differences in their solubility. The functionalized NTs are less soluble in toluene and THF, and practically insoluble in less polar solvents including diethyl ether and hexane.

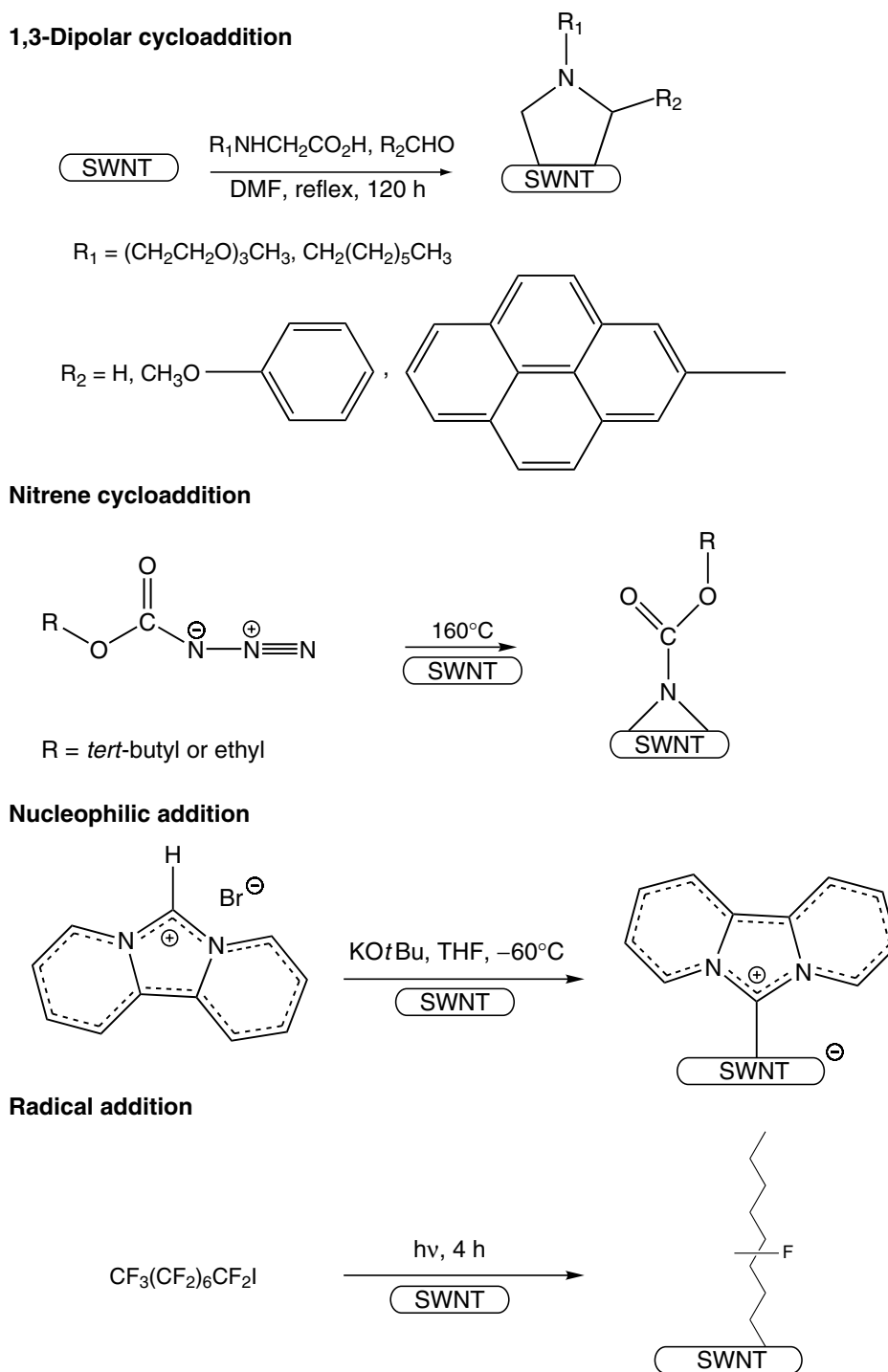


**FIGURE 3.7** Sidewall covalent chemistry on SWNTs. (Reprinted with permission from Niyogi, S. et al., *Acc. Chem. Res.*, **35**, 1105–1113, 2002. Copyright 2002. American Chemical Society.)

It was reported that sonication and homogenization of a mixture of SWNTs and a monochlorobenzene solution of poly(methylmetacrylate) increased the ratio of shorter and thinner SWNTs<sup>242–244</sup> and led to the chemical modification of SWNTs.<sup>245</sup> Organic molecules decompose at the hot spots, and reactive species react with damaged SWNT sidewalls. FT-IR spectra show the formation of C–H and C=O groups. The sonication of purified SWNTs in monochlorobenzene solution leads to the formation of two kinds of modified SWNTs.<sup>243,244</sup> Sonochemical decomposition of *o*-dichlorobenzene<sup>246</sup> and 1,2-dichlorobenzene<sup>247</sup> also leads to the attachment of decomposition products to SWNTs and to the stabilization of SWNT dispersions.

Other organic solvents formed NT dispersions under sonication (see the next section) most likely by an analogous mechanism.

For the purpose of SWNT sidewalls functionalization using organic radicals, Ying et al.<sup>239</sup> decomposed benzoyl peroxide in the presence of alkyl iodides and obtained phenyl radicals. These radicals reacted with alkyl iodides, which generated iodobenzene and alkyl radicals. The procedure allowed them to attach long-chain alkanes, alkyl halides, amides, nitriles, and ethers to the sidewalls of the NTs. Methyl radicals can also bond to the sidewalls, but the resulting NTs are generally insoluble in organic solvents.

Water-soluble diazonium salts can react with NTs.<sup>233,235,237</sup> A reactive radical can be produced by electrochemical reduction of different aryl diazonium salts using a bucky-paper electrode.<sup>235</sup> The estimated degree of functionalization is up to 5% of carbon atoms. Along with reductive coupling, it is possible to provide oxidative coupling (Figure 3.8).<sup>238,248</sup> The derivatization with aryl diazonium salts is not limited to the electrochemically induced reaction.<sup>237</sup>

NTs derivatized with a 4-*tert*-butylbenzene moiety exhibit the highest solubility in organic solvents. Solvent-free functionalization has short reaction times.<sup>233</sup>

Addition of diazonium salts to NTs suspended in aqueous solution opens a way to select chemically and separate NTs based on their electronic structure. Metallic NTs under certain controlled conditions give up electrons more readily than semiconducting NTs, a factor that the diazonium reagent can respond to.<sup>240</sup> The chemistry is reversible. Heating of the functionalized NTs in inert media at 300 to 400°C stimulates pyrolysis of arene groups and leads to restoration of the pristine electronic structure of NTs. This work also proves that the assumption that NT chemistry is controlled solely by their diameter (with smaller-diameter NTs being less stable) is in fact not always true.

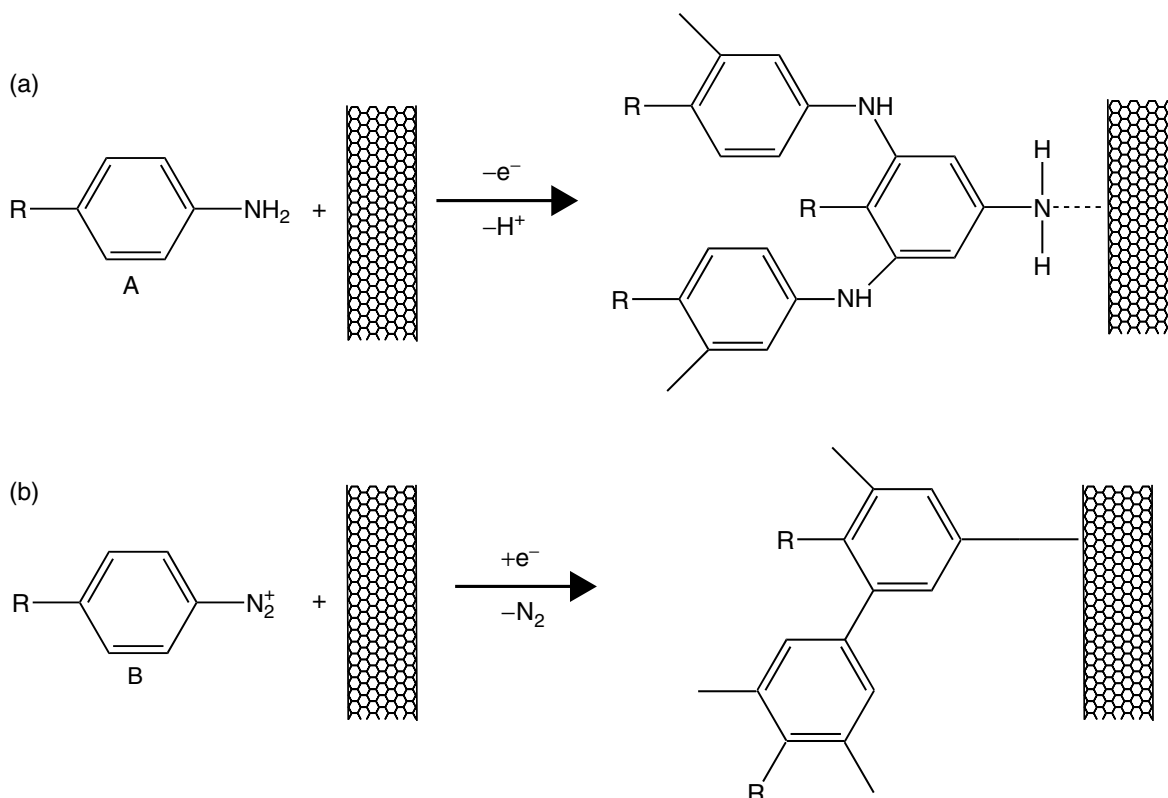


**FIGURE 3.8** Oxidative (a) and reductive (b) electrochemical modification of SWNTs. The broken line in (a) indicates the formation of electro-polymerized layers of A on the SWNT, without the creation of chemical bonds. (Reprinted with permission from K. Balasubramanian, et al., *Adv. Mater.*, **15**, 1517–1518 (2003)).

Since organic thiol derivatives are generally well known to interact strongly with noble metal surfaces, therefore, the selective thiolation may be used to make a good electrical junction between a NT and a metal electrode, or to position the NT relative to a metal surface. The first thiolated NTs, NT-(CH<sub>2</sub>)<sub>11</sub>-SH, with long alkyl chains, were synthesized by Smalley and coworkers.<sup>66</sup> Because of the long and flexible alkyl chain, the latter compounds do not anchor on a metal surface in a specific orientation and give rise to a large contact resistivity. To overcome these problems, another type of compound, NT-CONH-(CH<sub>2</sub>)<sub>2</sub>SH, with a shorter alkyl chain, was synthesized.<sup>210</sup> The compound, however, contains an amide bond that tends to react easily in an acid or basic environment.

The new form of thiolated NT, which contains thiol groups almost directly linked to the body of NT, was synthesized by Lim et al.<sup>249</sup> The formation of NT-CH<sub>2</sub>-SH is achieved via successive carboxylation, reduction, chlorination, and thiolation of the open ends of NTs.

Time-dependent plasma etching and irradiation with energetic particles can provide controlled introduction of defects and functionalities into NTs. Irradiation creates links between NTs, and leads to coalescence and welding of NTs (see, e.g., Refs. 250 and 251). Argon ion irradiation enhances the field emission of NTs.<sup>252</sup>

It has been shown that H<sub>2</sub>O plasma can be used to open end-caps selectively of perpendicularly aligned NTs without any structural change.<sup>253</sup> The treatment of NTs with oxygen plasma at a low pressure for some minutes results in an oxygen concentration up to 14% and formation of outer layers consisting of hydroxide, carbonyl, and carboxyl groups.<sup>254</sup>

Interaction of SWNTs with high-energy protons at low irradiation doses causes the formation of wall defects.<sup>255</sup> The NTs curve at higher doses (>0.1 mC) and degrade into amorphous material at even higher doses (approaching 1 mC). The hydrogenation of NTs can be achieved in a cold MW plasma at low pressure.<sup>256</sup> A 30 sec exposure to a plasma of H<sub>2</sub> generated by glow-discharge results in near-saturation coverage of SWNT with atomic hydrogen.<sup>257</sup>

Calculations using molecular dynamics show that CH<sub>3</sub> radicals with energies of higher than 19 eV can attach to NT sidewalls.<sup>258,259</sup> The heat of the attachment reaction changes from ~0.8 eV for graphite to ~1.6 eV for fullerene C<sub>60</sub>, and has intermediate, close to figures for graphite, values for NTs.<sup>13</sup>

The experiments show evidence of chemical functionalization of MWNTs by attachment of CF<sub>3</sub><sup>+</sup> ions at incident energies of 10 and 45 eV.<sup>259</sup> The exposure of SWNTs to CF<sub>4</sub> gaseous plasma leads to the formation of semi-ionic and covalent C-F bonds.<sup>260,261</sup> The ion bombardment does not result in loss of NT structure.<sup>261</sup>

Ion beams of certain energies can be used to create nanotube-based composites with improved adhesion between the filler and polymer matrixes as well as to create covalent cross-links between NTs and the C<sub>60</sub> molecules.<sup>262</sup>

The modification of NTs is possible with acetaldehyde plasma activation.<sup>212</sup> Plasma-modified NTs improve the properties of nanotube-epoxy composites.<sup>263</sup> The hydrogen plasma treatment enhances field emission of NTs.<sup>264</sup> By using hydrothermal synthesis it is possible to produce hydrophilic SWNTs or MWNTs that are wetted by water and water solutions, because their outer and inner surfaces are terminated with OH groups.

An electrochemical derivatization method can also be used to attach carboxylate groups to NT walls (see Ref. 265 and references therein).

### 3.5.6 NONCOVALENT BONDING

Carbon NTs have been solubilized in water with the aid of surfactants, which can deposit on the NT surface and help to form stable colloidal dispersion. The repulsive force introduced by the surfactant overcomes the van der Waals attractive force between the carbon surfaces. However, there is a problem when the surfactant is removed from the NT surface.

Sodium dodecyl sulfate (NaDDS,  $\text{CH}_3(\text{CH}_2)_{11}\text{OSO}_3\text{Na}$ ),<sup>266–276</sup> lithium dodecyl sulfate (LiDDS,  $\text{CH}_3(\text{CH}_2)_{11}\text{OSO}_3\text{Li}$ ),<sup>277–279</sup> and sodium dodecylbenzene sulfonate (NaDDBS,  $\text{C}_{12}\text{H}_{25}\text{C}_6\text{H}_4\text{SO}_3\text{Na}$ )<sup>280–284</sup> are among the simplest and most popular surfactants used for NT solubilization.

At low NaDDS concentration, large and dense clusters of the initial NTs were still found after sonication. At higher surfactant concentrations, black and apparently homogeneous solutions, stable over several weeks, were obtained.<sup>269</sup> The phase diagram of the NaDDS–SWNT–water system is not a simple one.<sup>271</sup> The domain of homogeneously dispersed NTs is limited and has an optimum (good NT solubility and system stability) at ~0.35 wt% in NTs and 1.0 wt% in NaDDS.

Suspensions of MWNTs or SWNTs in water stabilized by 0.25% NaDDS solution have been used for purification and size separation of tubes.<sup>266–268</sup> An individual SWNT encased in close-packed columnar NaDDS micelle has a specific gravity of ~1.0, whereas that of an NaDDS-coated bundle has a specific gravity of ~1.2 or more.<sup>270</sup> Therefore, NaDDS suspensions (2 g/L) prepared by sonication of raw, solid SWNTs in 0.5% NaDDS solution are capable of separating bundled SWNTs from isolated individuals.<sup>272</sup> The MWNT dispersion stabilized by NaDDS allows the production of MWNTs/hydroxyapatite composites.<sup>276</sup>

Non-specific physical adsorption of NaDDBS allows the solubilization of lightweight fraction SWNTs in water.<sup>280,282</sup> The NT stabilization depends on the structure of surfactant molecules that lie on the tube, parallel to the cylindrical axis (Figure 3.9). It was possible to achieve relatively high SWNT concentration (up to 10 g/L as a mixture of isolated and small bundles of SWNTs) without nematic ordering in suspension. The optimum NT/surfactant ratio was found to be 1:10 (by weight). The properties of a dispersion depend on the sonication technique used (high-power or mild mode of operation, tip or bath sonicator). The mechanism of NT solubilization determines the hydrophobic forces between the surfactant tail and the NT surface. Each NT is covered by a monolayer of NaDDBS molecules, in which the heads form a compact outer surface of a cylindrical micelle.<sup>283</sup> The aqueous ( $\text{D}_2\text{O}$ ) suspension in the presence of NaDDBS surfactant exhibits the presence of SWNT aggregates, but not rigid rods.<sup>284</sup>

The dispersing power of Triton X-100 (TX-100,  $\text{C}_8\text{H}_{17}\text{C}_6\text{H}_4(\text{OCH}_2\text{CH}_2)_n\text{OH}$ ;  $n \sim 9.5$ ),<sup>60,66,131,280,285–288</sup> sodium octylbenzene sulfonate ( $\text{C}_8\text{H}_{17}\text{C}_6\text{H}_4\text{SO}_3\text{Na}$ ),<sup>280</sup> sodium butylbenzene sulfonate ( $\text{C}_4\text{H}_9\text{C}_6\text{H}_4\text{SO}_3\text{Na}$ ),<sup>280</sup> sodium benzoate ( $\text{C}_6\text{H}_5\text{CO}_2\text{Na}$ ),<sup>280</sup> dodecyltrimethylammonium bromide (DTAB,  $\text{CH}_3(\text{CH}_2)_{11}\text{N}(\text{CH}_3)_3\text{Br}$ ),<sup>280,289,290</sup> cetyltrimethylammonium bromide ( $\text{C}_{16}\text{TMAB}$ ,  $\text{CH}_3(\text{CH}_2)_{14}\text{CH}_2\text{N}(\text{CH}_3)_3\text{Br}$ ),<sup>291</sup> cetyltrimethylammonium chloride ( $\text{CH}_3(\text{CH}_2)_{14}\text{CH}_2\text{N}(\text{CH}_3)_3\text{Cl}$ ),<sup>289</sup> cetyl alcohol derivative ( $\text{CH}_3(\text{CH}_2)_{14}\text{CH}_2(\text{OC}_2\text{H}_5)_{10}\text{OH}$ ),<sup>291</sup> pentaoxoethylenedodecyl ether ( $\text{C}_{12}\text{E}_5$ ),<sup>289</sup> and hexadecyltrimethylammonium bromide ( $\text{CH}_3(\text{CH}_2)_{16}\text{N}(\text{CH}_3)_3\text{Br}$ )<sup>292</sup> have been studied. Both NaDDBS and TX-100 dispersed the NTs better than NaDDS, because of their benzene rings; NaDDBS dispersed better than TX-100 because of its headgroups and slightly longer alkyl chain.<sup>280</sup> DTAB and  $\text{C}_{12}\text{E}_5$  solutions, at concentrations ranging from 0.05% to a few percent, do not stabilize the NTs.<sup>289</sup>

Ultrasonication of a mixture of distilled water and MWNTs in the presence of 5 vol% TX-100, followed by centrifugation to remove unsuspended material allows the production of a suspension of

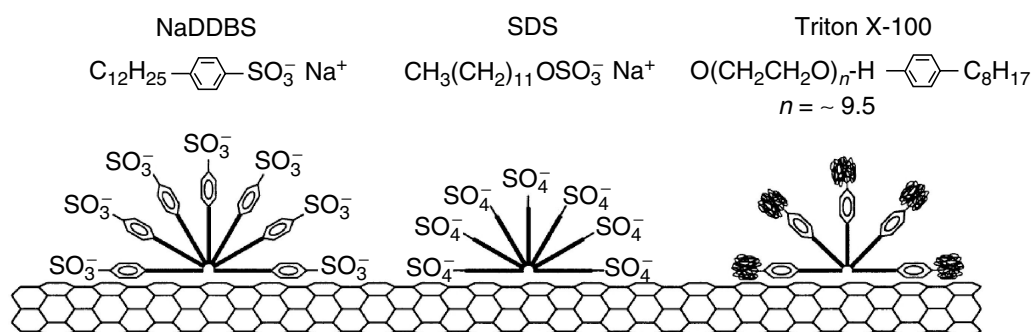


**FIGURE 3.9** A representation of surfactant molecules adsorbed onto NT surface. (Reprinted with permission from Islam, M.F. et al., *Nano Lett.*, **3**, 269–273, 2003. Copyright 2003. American Chemical Society.)

concentration of 0.1 g/L.<sup>287</sup> An aqueous (or alcoholic) solution of TX-100 has been used to prepare SWNT dispersion, followed by alignment under AC electric field.<sup>286</sup> Such dispersions are suitable to prepare thin film coatings on flexible plastic substrates.<sup>288,291</sup>

Spectral study reveals that the most essential spectral shift of lines compared with the spectrum of SWNT in KBr pellet is observed for NT aqueous solutions with the surfactants containing charged groups.<sup>293</sup>

Acidification of a solution of surfactant-dispersed SWNTs in water in the pH region of 6.0 to 2.5 results in the reversible and selective reaction of protons at the sidewall of SWNTs.<sup>290</sup> The equilibrium constants are dependent on the NT band gap, and metallic NTs appear more sensitive to acidity of the solution. A crucial role is played by adsorbed O<sub>2</sub>, which controls both the rate and equilibrium extent of the reaction. The results of this investigation hold promise for chemical separation and sorting of NTs having different electronic structures.

C<sub>16</sub>TMAB or other surfactants are used to prepare a SiO<sub>2</sub>/NT composite.<sup>291,294</sup>

SWNTs can be solubilized in water at g/L concentrations by non-covalent wrapping them with water-soluble linear polymers, most successfully with polyvinyl pyrrolidone<sup>295,296</sup> and sodium polystyrene sulfonate.<sup>295,297,298</sup> Polymetacrylic acid,<sup>298</sup> polypyrrole,<sup>299</sup> poly(phenylacetylene),<sup>300</sup> and poly(diallyldimethylammonium chloride)<sup>301,302</sup> have also been tested. The solubilization of SWNTs by polymer wrapping might provide a series of useful techniques, such as purification, fractionation, and manipulation of the SWNTs.

For many applications, bio-compatible water-soluble derivatives of NTs are desirable. For this reason, the solubilization of NTs in cyclodextrins,<sup>303–305</sup> polysaccharides, and natural mixtures of polysaccharides such as gelatine,<sup>306,307</sup> Gum Arabic,<sup>275,289</sup> and starch<sup>308</sup> has been studied.

Nanotubes are not soluble in aqueous solutions of starch but they are soluble in a starch–iodine complex. The starch, wrapped helically around small molecules, will transport NTs into aqueous solutions.<sup>308</sup> The process is reversible at high temperatures which permits the separation of NTs in their starch-wrapped form. The addition of glucosidases to these starched NTs results in the precipitation of the NTs from the solution. Readily available starch complexes can be used to purify NTs. An effective process to produce colloidal solution of SWNT–amylose complexes is elaborated.<sup>309</sup> The solubility of sonicated NTs improves by dilution of water with DMSO (10 to 25 vol%). Some natural polysaccharides wrap SWNTs, forming helical suprastructures.<sup>310</sup>

An amphiphilic  $\alpha$ -helical peptide specifically designed not only to coat and solubilize NTs, but also to control the assembly of the peptide-coated NTs into macromolecular structures, is described.<sup>311</sup> The NTs can be recovered from their polymeric wrapping by changing their solvent system.

As for the solubility of pure SWNTs in organic solvents, these solvents are divided into three groups.<sup>285</sup> The “best” solvents are *N*-methylpyrrolidone (NMP), DMF, hexamethylphosphoramide, cyclopentanone, tetramethylene sulfoxide, and  $\epsilon$ -caprolactone, which readily disperse SWNTs, forming light-gray, slightly scattering liquid phases. All of these solvents are nonhydrogen-bonding Lewis bases. Group 2 includes DMSO, acrylonitrile, 4-chloroanisole, and ethylisothiocyanate. The third group includes 1,2-dichlorobenzene, 1,2-dimethylbenzene, bromobenzene, iodobenzene, and toluene.

Using solvchromic and thermochemical parameters of different solvents Torrens also categorized them into three groups.<sup>312</sup> The first group include the “best” solvents mentioned earlier. In the group of “good” solvents, he includes toluene, 1,2-dimethylbenzene, CS<sub>2</sub>, 1-methylnaphthalene, iodobenzene, chloroform, bromobenzene, and *o*-dichlorobenzene. Group 3 are the “bad” solvents, *n*-hexane, ethyl isothiocyanate, acrylonitrile, DMSO, water, and 4-chloroanisole.

As reported earlier, the best solvents for generating SWNT dispersions in organic solvents are amides, particularly DMF and NMP.<sup>176</sup> The solubilities of SWNTs in 1,2-dichlorobenzene, chloroform, 1-methylnaphthalene, and 1-bromo-2-methylnaphthalene are equal to 95, 31, 25, and 23 mg/L,<sup>247</sup> respectively. Solubilities of purified and functionalized SWNTs in ethanol, acetone, and DMF is 0.5, 1.06, and 2.0 mg/L,<sup>313</sup> respectively. According to Ref. 247, the solubilities are <1, <1, and 7.2 mg/L.

MWNTs cannot be dispersed in toluene into the level of single tubes even when diluted to a concentration of  $\sim 10^{-3}$  g/L.<sup>314</sup> It has been found that the aggregation decreases with increasing temperature.

A procedure for the quantitative evaluation of the purity of bulk quantities of SWNT soot on the basis of near infrared (NIR) spectroscopy of a sample dispersed in DMF is described.<sup>315</sup>

Organic solutions of NTs in poly(*p*-phenylenevinylene-*co*-2,5-dioctoxy-*m*-phenylenevinylene),<sup>316</sup> poly(*m*-phenylenevinylene-*co*-2,5-dioctoxy-*p*-phenylenevinylene),<sup>317</sup> and poly(2,6-pyridinylenevinylene-*co*-2,5-dioctoxy-*p*-phenylenevinylene),<sup>317</sup> a family of poly(*m*-phenylenevinylene-*co*-*p*-phenylenevinylene)s,<sup>318</sup> can be formed due to the physical adsorption of polymers. Certain polymers such as polyphenylenevinylene derivatives, and vinyl-based polymers such as polyvinylalcohol and polyvinylpyrrolidone tend to disperse NTs, while rejecting other carbon-based impurities (see Ref. 319).

The solubilization of small-diameter NTs is possible using rigid side-chain poly(aryleneethylene).<sup>320</sup> The method includes the dissolution of SWNTs in methylene chloride and polymer under vigorous stirring or sonication, and yields a solubility as high as 2.2 g/L. Researchers believe that the most probable mechanism is a  $\pi$  stacking, which stabilizes the polymer–NT interaction.

Noncovalent solubilization of NTs can be realized by encapsulation of SWNTs by metallo-macrocyclic rings.<sup>216,321</sup> A DMF solution of poly(vinylidene fluoride) can be used for size fractionation of MWNTs.<sup>322</sup>

### 3.5.7 DISPERSIONS IN OLEUM

Successive dispersion of SWNTs in oleum at concentrations up to 4 wt% was first achieved at Rice University.<sup>323</sup> It was shown that at very low concentrations of SWNTs (<0.25 wt%), a single phase with uniformly dispersed tubes was formed. The SWNTs in the dilute system behave as Brownian (noninteracting) rods. The SWNT concentration in the dispersion can be increased up to 10 wt%; the dispersion process is promoted by the protonation of the SWNT sidewall, and the tubes are stabilized against aggregation due to the formation of electrostatic double layer of protons and negatively charged counterions.<sup>324</sup> Increasing the concentration of SWNTs in the acid leads to the formation of a highly unusual nematic phase of spaghetti-like, self-assembled supra-molecular strands of SWNTs. As concentration increases (to 4 vol% in 102% H<sub>2</sub>SO<sub>4</sub>), the strands self-assemble into a single-phase nematic liquid crystal. If a small amount of water is added, the liquid crystal separates into ~20  $\mu$ m long, needle-like strands of highly aligned SWNTs, termed “alewives.” This phase can be processed, under anhydrous conditions, into highly aligned fibers of pure SWNTs with a typical alignment ratio of 20:1 to 30:1. A syringe pump was used to extrude the mixture through a 0.15-mm internal diameter needle, followed by spinning the neat SWNT fibers up to 1 m long. The detailed structure and properties of the fiber have been studied.<sup>325</sup> High-temperature annealing of the fibers does not affect the SWNT alignment.

A solution of purified SWNTs in oleum (H<sub>2</sub>SO<sub>4</sub>/30% SO<sub>3</sub>) was used to cast optically isotropic film exhibiting fibrillar morphology.<sup>326</sup> The electrical conductivity of this film ( $1 \times 10^5$  S/m) is about an order of magnitude higher than that for the SWNT bucky paper.

Chlorosulfonic acid, triflic acid, and anhydrous HF–BF<sub>3</sub> solution can also be used for the solubilization of NTs.

### 3.5.8 SELF-ASSEMBLY, FILM, AND FIBER FORMATION

A promising feature of NTs in nanotechnology is that they are potentially amenable to a “bottom-up,” self-assembly-based manufacturing approach. It is essential to fabricate well-aligned structures of NTs for various electric and optical applications. The necessity for aligned and micropatterned NTs has been elaborated in many articles.

There are two general strategies to align NTs: (1) *in situ* synthesis and (2) postsynthesis ordering. The first approach includes CVD processes on a prepatterned (with catalyst) surface or a template-based synthesis.<sup>20,48,327</sup> This approach is not considered here.

The second approach includes a variety of chemical or electrochemical processes<sup>9</sup> such as different functionality reactions and noncovalent (e.g., electrostatic) interactions between the NTs and surface-bound moieties.



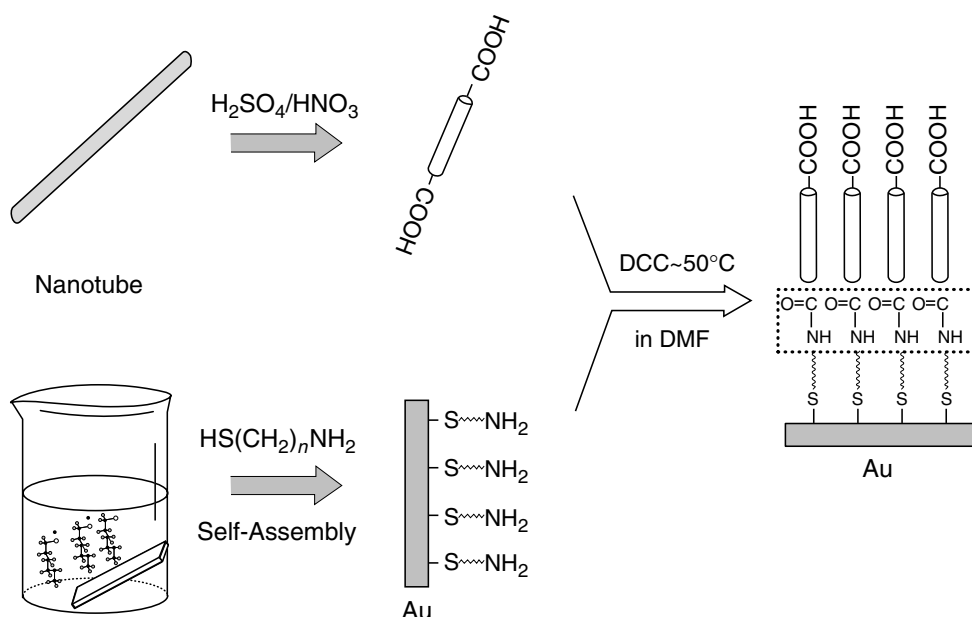


**FIGURE 3.10** Schematic illustration of the formation of highly aligned SWNTs on gold surface. (Reprinted from Nan, X. et al., *J. Colloid Interf. Sci.*, **245**, 311–318, 2002. Copyright 2002. With permission from Elsevier.)

To organize NTs on gold or silver substrates, the carboxylic groups at the end of NTs were thiol-functionalized to form Au–S or Ag–S chemical bonds (Figure 3.10).<sup>153–155,210–212</sup> Flexible SWNTs with many thiol groups at their ends are more likely to bend on metal surface to form the “bow-type” structure, while a more rigid form of SWNT or MWNT with less thiol groups will stand upright on the surface, forming a rod-like structure.<sup>249</sup> The monolayer of randomly tangled SWNTs is attached to a gold surface containing HS–(CH<sub>2</sub>)<sub>10</sub>–COOH.<sup>328</sup>

It is possible to use a patterned self-assembled monolayer which can either enhance or deter NT adherence.<sup>329–330</sup> Silicon wafers can be coated with either nonpolar methyl groups or with polar carboxyl and amino groups.<sup>199,331</sup> When the substrate is placed in a suspension of SWNTs, the tubes are attracted toward the polar regions and self-assemble to organize pre-designed structures. To form self-assembled monolayers with amino-terminated surface, silicon wafers were silanized using 3-aminopropyltriethoxysilane.<sup>332</sup> The octadecyltrichlorosilane is used to attach methyl-terminated groups.

Polyelectrolyte layers on a silicon substrate have been used to align MWNTs.<sup>333</sup> The carboxylate anion groups of MWNTs bind on the oppositely charged polycationic poly(diallyldimethylammonium chloride) (PDSC). The possibility of forming multi-layer assemblies such as Si/PDSC/PSS/PDSC/MNT (where PSS stands for poly(sodium 4-styrenesulfonate)) using coulombic interaction has been demonstrated.

An original method to produce a hollow spherical cage of nested SWNTs using self-assembly technique consists of attaching of NTs to amidated silica gel spheres and subsequent drying and dissolution of the template.<sup>334</sup>

The aligning of NTs can be realized under the influence of the capillary force and the tensile force that appear in the process of solvent evaporation.<sup>335–339</sup> The vacuum evaporation of concentrated (20 to 50 g/L) aqueous dispersion of purified MWNTs at 100°C yields long ribbons of aligned NTs, self-assembled on the wall of the container.<sup>337</sup> The ribbons form in one of the two orthogonal orientations to the bottom of the container (glass beaker): perpendicular when vacuum is applied, and parallel when no vacuum is applied. The ribbons are 50 to 100 μm wide, 4 to 12 μm thick, and 100 mm long. Presumably, the key factor is the rate of evaporation.

Using a dispersion of shortened purified SWNTs in de-ionized water, Shimoda et al.<sup>338,339</sup> formed a thin film on the surface of a soaked glass substrate with natural vaporization of water. The

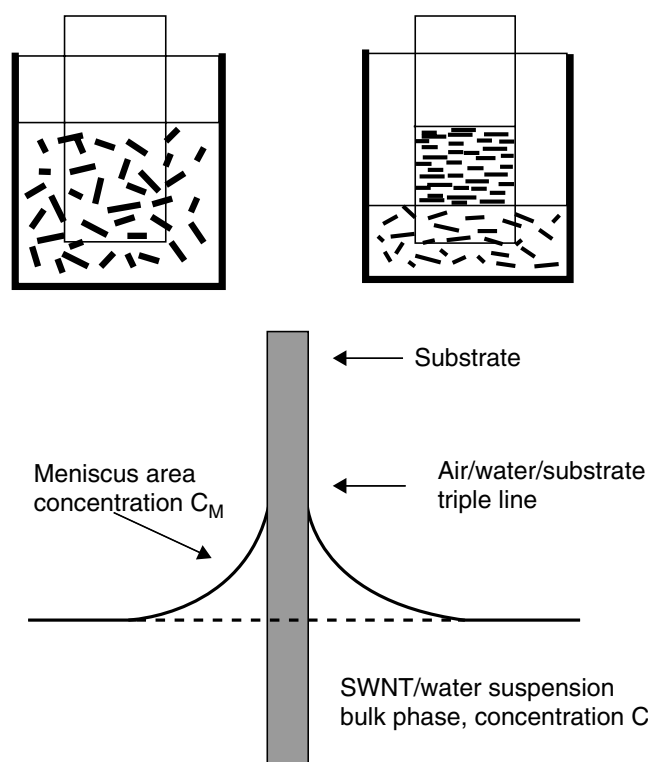


**FIGURE 3.11** Self-assembly process of shortened SWNTs onto a hydrophilic glass slide.

SWNT bundles were uniaxially aligned parallel to the bottom of the container (Figure 3.11). In this process, SWNT bundles are first dispersed at a concentration of 0.5 to 1.0 g/L. Then a clean hydrophilic glass sheet is immersed vertically into the suspension. As the water evaporates, the NTs deposit near the triple borderline air/water/NTs and the deposit progresses downward. By means of patterned hydrophilic regions, patterned deposits were produced in the form of squares and strips, 100  $\mu\text{m}$  in width.

Capillary forces arising during the evaporation of liquids from dense NT arrays were used to re-assemble the NTs into 2-D contiguous cellular foams.<sup>340</sup>

Natural self-assembly and cooperative mechanisms of liquid crystals can be employed to manipulate the alignment of NTs.<sup>341</sup> Thermotropic liquid crystals used as a solvent provide a tool for aligning SWNTs and MWNTs.<sup>342</sup> The broad range of possibilities of liquid crystals has been demonstrated.

An alignment of NTs can be realized under the electric field with both DC and AC voltage between the electrodes.<sup>343</sup> This method allows the orientation and spatial positioning of the SWNTs<sup>344</sup> to be controlled. The room-temperature method, called “minimal-lithography” technique, has been used to prepare crossbars of SWNT ropes and deterministic wiring networks from SWNTs. Electrophoretic deposition of NT films<sup>345</sup> and dielectrophoretic formation of fibrils<sup>346</sup> has been demonstrated.

Multi-layer polymer/SWNT films can be formed by electrostatic assembly.<sup>150</sup> The Langmuir–Blodgett method is used to deposit thin uniform films of SWNTs onto substrates.<sup>277,347,348</sup> Thin films have been made with NTs embedded in a surfactant matrix suspended on top of an aqueous subphase and then pulling the substrate through the surface. The Langmuir–Blodgett method has been used to prepare a monolayer of crown ether-modified full-length MWNTs and SWNTs.<sup>349</sup> A method of laying down thin uniform films of NTs on substrates of arbitrary composition resembling the Langmuir–Blodgett deposition technique has been developed.<sup>350</sup> The composite Langmuir–Schaefer conducting organic/MWNT films with useful optical and electrochemical properties have been studied.<sup>351</sup>

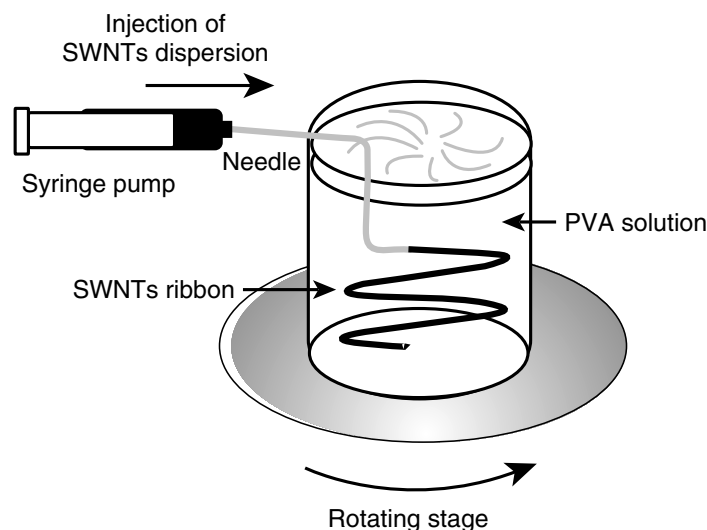


**FIGURE 3.12** Simplified drawing of the experimental setup used to make NT ribbons. (From Poulin, P. et al., *Carbon*, **40**, 1741–1749, 2002. With permission.)

Fukushima et al.<sup>352</sup> have found a way to distribute NTs evenly through a gel, to form an electrically versatile material. The “bucky gel” materials were produced by grinding suspensions of SWNTs in imidazolium cation-based ionic liquids in an agate mortar. The gel can be printed using inkjet printer or polymerized. Lowering the temperature of the gels results in long-range ordering of the ionic liquid molecules and formation of crystal-like materials.

Yodh and his colleagues embedded isolated SWNTs coated with NaDDBS into a cross-linked polymer matrix, an *N*-isopropyl acrylamide gel.<sup>281</sup> The volume of the gel is highly temperature-dependent, and a change in temperature results in volume-compression transition. The condensed gel thus creates concentrations of isolated, aligned NTs that cannot be achieved when they are suspended in water.

Re-condensing of surfactant-stabilized NT solutions is used for the formation of aligned NT fibers.<sup>269,353</sup> In this method, NTs are sonicated in an aqueous solution of NaDDS. The dispersion is injected into a co-flowing stream of poly(vinyl alcohol) (PVA) via capillary tube. This principle was modified to produce long aligned fibers of NTs.<sup>278</sup> The process consists of introducing SWNT dispersion into a co-flowing stream of PVA in a cylindrical pipe, thereby causing the agglomeration of the SWNTs into a ribbon. The fibers are then unwound and passed through a series of washing stages to remove the excess PVA.

The extrusion of aqueous dispersions of NTs into rotating viscous solution of PVA leads to aggregation of NTs into narrow strips (Figure 3.12).<sup>269</sup> These strips, a few micrometers thick and a few millimeters wide, contract when dried in air forming dense fibers.

Electro-spinning allows the fabrication of an oriented poly(ethylene oxide) NFs in which MWNTs are embedded mostly aligned along the fiber axis (Figure 3.13).<sup>275</sup> The feasibility of this electrostatically induced self-assembly process for incorporation of NTs into NFs, production of membranes, and nanofiber yarn have been demonstrated.<sup>354,355</sup>

Macroscopic fibers have been produced from NT dispersions in oleum by spinning technique.<sup>324,325</sup>

### 3.6 FILLING THE INNER CAVITY OF CARBON NANOTUBES

Numerous attempts to fill the nanoscale cavities of NTs have been made following the discovery of these materials. The filling was attempted to achieve one of the two goals. First, being a kind of template synthesis, filling allows the preparation of nanostructured materials with controlled size, shape, and purity. Secondly, doping can modify the electronic properties of NTs. The thus prepared

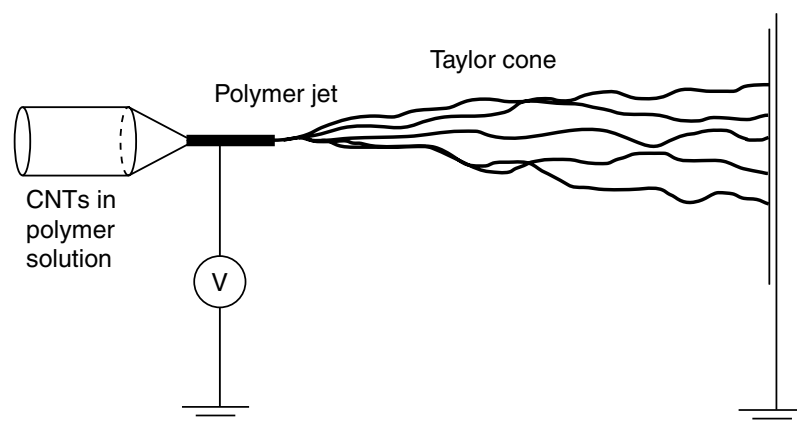


**FIGURE 3.13** Schematic of the electrospinning process used to form SWNT-filled composites.

compounds are also interesting as nanosized objects to investigate size–crystal structure relations and size effects.

The filling of SWNTs attracts more attention than filling of MWNTs due to the smaller diameter of SWNT inner cavities, better stability, and more perfect structure of SWNTs. The afterward removal of SWNT used as nanomolds is a more easy procedure than removing the MWNT shield.

The filler can exist either in solid, liquid, or gaseous state. As far as solid materials are concerned, the inner cavity of NTs can be filled with single crystalline nanorods, polycrystalline nanorods, amorphous nanorods, or discrete nanoparticles.

Many solid substances can fill the inner cavities of NTs. The list of fillers includes metals (Cs, Cu, Ag, Au, Sn, Fe, Co, Ni, Pd, Rh, etc.), alloys (Fe–Ni, Fe–Pt, Pt–Ru,  $\text{Nd}_2\text{Fe}_{14}\text{B}$ ), nonmetals (Ge, S, Se, Te,  $\text{I}_2$ , etc.), oxides ( $\text{SnO}$ ,  $\text{Sb}_2\text{O}_3$ ,  $\text{NiO}$ ,  $\text{UO}_{2-x}$ ), hydroxides ( $\text{Ni}(\text{OH})_2$ ), halides ( $\text{KI}$ ,  $\text{LaCl}_3$ ,  $\text{ZrCl}_4$ ), salts ( $\text{AgNO}_3$ ), carbides ( $\text{B}_4\text{C}$ ,  $\text{LaC}_x$ ,  $\text{NbC}_x$ ,  $\text{FeC}_x$ ), sulfides ( $\text{AuS}_x$ ,  $\text{CdS}$ ,  $\text{CoS}_x$ ), nitrides ( $\text{BN}$ ,  $\text{GaN}$ ), organic substances ( $\text{CHCl}_3$ ), acids ( $\text{HNO}_3$ ), polymers (polystyrene), complex inorganic compounds and eutectic mixtures ( $\text{FeBiO}_3$ ,  $\text{CoFe}_2\text{O}_4$ ,  $\text{AgCl–AgBr}$ ,  $\text{KCl–UCl}_4$ ), and fullerene and endofullerene molecules ( $\text{C}_{60}$ ,  $\text{Gd@C}_{82}$ ), complex hybrid materials ( $\text{FeCl}_3\text{–C}_{60}$ ,  $\text{K–C}_{60}$ ,  $\text{Pt–WO}_3$ ).<sup>7,8,224,356–358</sup> Quantum chemical simulations predicted the stability of alkali metal compounds ( $\text{Na@SWNT}$ ) and metallocarbohedrene derivatives ( $\text{Ti}_8\text{C}_{12}\text{@SWNT}$ ).

Water, inorganic acids, aqueous solutions,  $\text{CHCl}_3$  solutions, and molten salts are among liquid substances suitable to fill NTs.

The solid and liquid substances can fill the cavity entirely or partially. Materials produced by filling of NT inner cavities can be used as magnetic media, catalysts, sorbents, quantum wires, field emitters, electromagnetic shielding, etc.

The results of theoretical calculations show that the radius as well as the helicity of the most stably doped SWNT are different for different kinds of impurity atoms.<sup>359</sup>

There are two basic strategies of filling: *in situ* synthesis of filled NTs or post-production methods that require an opening of the tubes.

### 3.6.1 IN SITU FILLING

All synthesis strategies may be accompanied by filling of NTs produced. In an arching process, the filler precursor can be introduced either by graphite anode doping (the most commonly used technique) or by dissolution in a liquid medium (if the process takes place in liquid environment). In the first stage of NT study, most information was obtained by using arc-discharge method in an inert gas flow. For filling of arc-produced NTs, a variety of metals, oxides, or salts have been used to dope the anode. With a few exclusions (Co, Cu, Pd), the encapsulated materials were always carbides.

Close-capped NTs can be filled *in situ* with metallic Co, S, and  $\text{CoS}_x$  from aqueous solution of  $\text{CoSO}_4$  by arching.<sup>38</sup> A simplified arc-discharge in aqueous solution of  $\text{PdCl}_2$  yields Pd-nanoparticles-filled NTs.<sup>360</sup>

All types of pyrolytic synthesis of NTs (using supported, dissolved, or floating catalysts, different physical activation methods) are inevitably accompanied by capture of some part of the catalyst and encapsulation of catalyst particles. Consequent purification with boiling  $\text{HNO}_3$  or other oxidants cannot eliminate the metals completely.<sup>361</sup> The filling can be controlled to some extent by varying the process parameters, but sometimes, relative amounts of incorporated material reach substantial values.

For example, the HiPco technique results in SWNTs partially filled with Fe (total Fe content in crude product is about 20 to 30%). The oxidation treatment of  $\text{LaNi}_2$  alloy followed by CVD process using a  $\text{CH}_4/\text{Ar}$  mixture at  $550^\circ\text{C}$  leads to the formation of MWNTs filled with single-crystal Ni nanowires.<sup>362</sup> The synthesis of NTs filled with Ni by CVD over the Raney-Ni catalyst gives straight and two types of bamboo-shaped NTs.<sup>363</sup> The synthesis of Fe-, Ni-, and Co-filled NTs by using the pyrolysis of metallocenes (cyclopentadienyls) has been performed at 900 to  $1150^\circ\text{C}$ .<sup>364,365</sup> Invar ( $\text{Fe}_{65}\text{Ni}_{35}$ ) has been introduced into NTs by pyrolyzing an atomized solution of  $\text{NiCp}_2/\text{FeCp}_2$  in  $\text{C}_6\text{H}_6$  at  $800^\circ\text{C}$  (Cp stands for cyclopentadiene).<sup>366</sup> The pyrolysis of methane over  $\text{Fe}_2\text{O}_3/\text{Al}_2\text{O}_3$  binary aerogel at  $880^\circ\text{C}$  yields multi-wall nanohorns filled with Fe nanoparticles.<sup>367</sup> The decomposition of gaseous  $\text{Fe}(\text{CO})_5$  in a mixture with CO or  $\text{C}_6\text{H}_6$  yields NTs partially filled with Fe.<sup>368</sup> MWNT-encapsulated Co particles have been produced by the catalytic method using water-soluble  $\text{NaCl}/\text{NaF}$  mixture as a support for the metal.<sup>369</sup>

Plasma-enhanced CVD on Si wafers allows the production of NTs-containing magnetic Fe,  $\text{Nd}_2\text{Fe}_{14}\text{B}$ , or Fe–Pt nanoparticles.<sup>358</sup> The formation of simple and branched Cu-filled NTs has been observed in the plasma-activated CVD process.<sup>370</sup> The Cu electrodes serve as a metal source in this process. Microwave-plasma-enhanced CVD process yields almost 100% GaN-filled NTs.<sup>371</sup>

“Double template” synthesis demands exploration of a material with aligned micropores. For example, NTs filled with Co have been synthesized using the CVD method and molecular sieve AlPO-5 and AlPO-31 as a primary template to formulate NTs.<sup>372</sup>

A high-temperature process interaction of pulverized  $\text{Fe}(\text{NO}_3)_3$  solution with carbon black and boron precursor results in the formation of Fe nanowire encapsulated in the inner cavity of carbon NT having an inner layer of BN.<sup>373</sup> The mechanism of the phase separation between C and BN is not clear.

An original, but complicated, method to produce relatively long cobalt nanowires filling the NT consists of a reaction of  $\text{Co}(\text{CO})_3\text{NO}$  with magnesium in closed vessel cell.<sup>374,375</sup>

During a hydrothermal synthesis of MWNTs, some gases, particularly  $\text{CO}_2$ ,  $\text{H}_2\text{O}$ , and  $\text{CH}_4$  can be trapped in the inner cavity of the tube.<sup>376</sup> Theoretical analysis of phase equilibria in such systems reveals an enhanced layering effect in the liquid phase.<sup>377</sup>

### 3.6.2 POST-PROCESSING FILLING

Nanotubes of two types are used in the filling process: NT synthesized by a usual method and NTs prepared by a template method in pores of  $\text{Al}_2\text{O}_3$ , AlPO-5, AlPO-31, or other suitable membranes. The usual methods lead to the formation of NTs of different diameters, whereas membrane synthesis (“double template” or “second-order” template synthesis) allows for the preparation of NTs of similar diameter and therefore in the production of encapsulated materials of uniform size. The second method is more complex and less productive.

#### 3.6.2.1 Filling from Liquid Media

Filling by capillarity is possible only if the NTs are opened. The classification of liquid fillers or precursors includes:

- water and aqueous solutions
- liquid organic compounds

- hydrothermal solutions
- supercritical solutions
- molten metals, salts, and molten eutectic mixtures

The wetting properties of different carbons have been found to depend on the surface tension of the fluid, with a threshold value of 100 to 200 mN/m. Therefore, water having surface tension of 72 mN/m should wet NTs.<sup>378,379</sup> The boundary value is dependent on the inner diameter of NT.

The study of the filling of NT with water is of considerable importance in many biological systems and for the development of molecular devices. The behavior of water in the inner channel of NT has been discussed in a set of works.<sup>380–387</sup> Hummer et al.<sup>380</sup> showed, by molecular dynamics simulations that water molecules enter NTs of diameter greater than 0.81 nm even though carbon is hydrophobic. The possibility of transport of an electrolytic solution (KCl) through a carbon NT by a molecular dynamics simulation has also been explored.<sup>388</sup>

Certain metal oxides (V, Bi, Mo, Mn, Fe) can be doped by refluxing closed NTs with HNO<sub>3</sub> in the presence of metal nitrate and by subsequent calcination of metal nitrates inside NTs.<sup>389,390</sup> Filling with Ag (presumably silver oxide) has been achieved using concentrated aqueous solution of AgNO<sub>3</sub>.<sup>391</sup> Aligned, open MWNTs can also be filled with Ag nanorods of up to 9 μm in length, using aqueous nitrate solution.<sup>89</sup> The reduction to metal Ag was achieved with CH<sub>3</sub>COOH at 300°C. Interaction of the opened MWNTs with inner channel diameter of 60 nm with aqueous nitrate solution, and subsequent heat treatment under inert atmosphere at 100°C, leads to the formation of spinel CoFe<sub>2</sub>O<sub>4</sub> in the form of nanowire several micrometers long.<sup>392–394</sup> Immersion of a sample of pre-treated SWNT in a saturated aqueous solution of RuCl<sub>3</sub> leads to filling with this salt.<sup>395</sup>

Platinum–ruthenium nanoparticle (1.6 nm) filled NTs have been prepared by immersing the carbon/alumina template composite in an aqueous solution of H<sub>2</sub>PtCl<sub>2</sub> and RuCl<sub>3</sub> for 5 h, and subsequently drying at room temperature, reducing in H<sub>2</sub> at 550°C, and dissolution of the membrane.<sup>396,397</sup> This method was used to load Pt, Pt–Ru, and Pt–WO<sub>3</sub> nanoparticles inside NTs.<sup>398,399</sup> A second-order template method was used for electrochemical Ni deposition inside NTs.<sup>400</sup> Highly crystalline nanorods of α-Fe<sub>2</sub>O<sub>3</sub> were synthesized in the cavity of carbon NTs by hydrothermal treatment with NaOH aqueous solution.<sup>401</sup>

A solution of chromium(III) oxide in hydrochloric acid is used to fill NTs with the oxide at room temperature.<sup>391,402</sup> Wet chemical techniques to produce CuO nanoparticles, 20 to 90 nm in diameter and 250 to 700 nm in length, using MWNTs as templates has been developed.<sup>403</sup>

Gold nanoparticles can be introduced into the inner cavity of MWNT after its heat treatment in NH<sub>3</sub>.<sup>404</sup>

The rapid filling of metals (Pd, Ni, and Cu) into MWNTs can be achieved using super-critical CO<sub>2</sub> as the reaction medium.<sup>405</sup> Britz et al.<sup>406</sup> used a metal-β-diketone complex M(hfa)<sub>2</sub> (hfa stands for hexafluoroacetylacetonate), which was reduced by H<sub>2</sub> dissolved in super-critical CO<sub>2</sub>. Super-critical CO<sub>2</sub> solutions were used to fill SWNTs with C<sub>60</sub> and C<sub>61</sub>(COOEt)<sub>2</sub> molecules.

The solvent method of peapod preparation based on the refluxing of *n*-hexane suspension makes it possible to get a high yield of C<sub>60</sub>@SWNT, C<sub>70</sub>@SWNT, and to synthesize N@C<sub>60</sub>:C<sub>60</sub>@SWNT.<sup>407</sup> Two other methods of nanopeapod formation consist of establishing a contact of SWNT and fullerene ethanol or toluol solutions/suspensions (Figure 3.14).<sup>408</sup>

A synthetic method of integrating organic molecules, such as *tetrakis*(dimethyl-amino)ethylene and tetracyanoquinodimethane into SWNTs<sup>409</sup> has strong potential for molecular electronics. Molecular dynamic simulations have indicated that even DNA could be encapsulated inside NTs in a water solute environment via an extremely rapid dynamic interaction process, provided that the tube size exceeds a certain critical value.<sup>410</sup>

Capillary filling with molten oxides,<sup>411,412</sup> molten metal salts, such as chlorides,<sup>395,413–415</sup> and some molten metals<sup>416,417</sup> is also widely used. Metal nanowires encapsulated in NTs have been obtained by treating SWNTs with metal salts at melting temperatures in vacuum-sealed quartz tubes, followed by reduction with hydrogen.

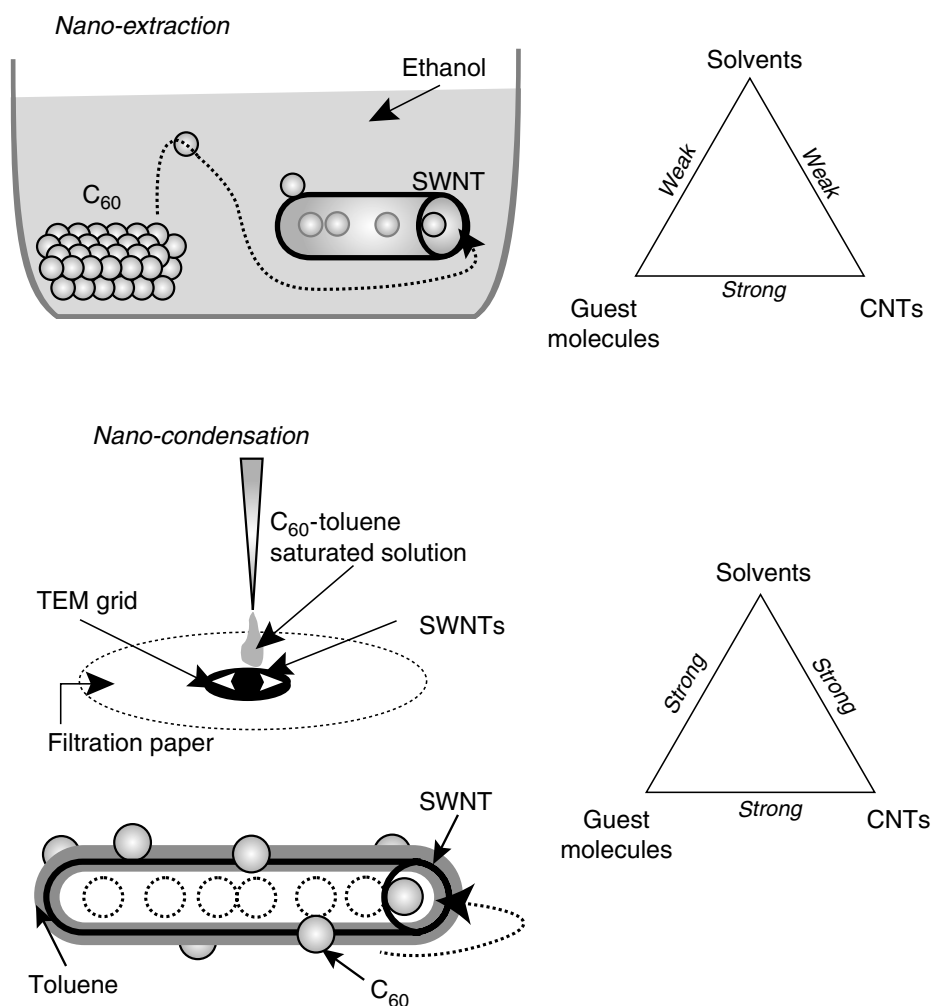


**FIGURE 3.14** Schemes of nanoextraction and nanocondensation methods. The difference in relative affinities among the three components are shown in the triangles. (From Yudasaka, M. et al., *Chem. Phys. Lett.*, **380**, 42–46, 2003. With permission.)

The doping of SWNT bundles by immersion in molten iodine gives quite different results compared to using iodine vapors. This is due to the dissociative character of the melt.<sup>418</sup> Iodine atoms form charged polyiodide chains inside MWNTs of different inner diameter.<sup>419</sup>

A carbon nanotube 75 nm in diameter and 10  $\mu\text{m}$  long, filled with liquid Ga, acts as a thermometer as claimed by Gao and Bando.<sup>420</sup> The height of the continuous, unidirectional column of Ga inside the nanotube varies linearly with temperatures ranging from 50 to 500°C.

### 3.6.2.2 Filling from Gas Phase

In SWNTs with open ends, nitrogen and oxygen are adsorbed first in the inside of the tubes, and next in the interstitial channels of bundles (see Section 3.7).<sup>421</sup> In each site, gases can be adsorbed with the stoichiometry of  $\text{C}_{20}\text{N}_2$  or  $\text{C}_{20}\text{O}_2$ , as a monolayer.

Theoretical analysis of the behavior of some of the simplest molecules (methane, ethane, ethylene) in the NT cavity predicts normal-mode molecular diffusion for methane, and intermediate between molecular diffusion and single-file diffusion for ethane and ethylene at room temperature.<sup>422,423</sup>

The filling of NT with vapors of halogenes (Se),<sup>390</sup> hydrides ( $\text{SiH}_4$ ),<sup>424</sup> metal halogenides ( $\text{ZrCl}_4$ ),<sup>425</sup> fullerenes ( $\text{C}_{60}$ ,  $\text{Sc}_2@C_{84}$ ,  $\text{La}@C_{82}$ ),<sup>426–429</sup> and metallocenes ( $\text{Fe}(\text{Cp})_2$ , and  $\text{Ni}(\text{Cp})_2$ )<sup>429–432</sup> has been studied. Volatile metal carbonyls, metal diketonates, and metal phthalocyanines can also be used.

Reaction with Se in vapor phase using the two-bulb method allows to reach a filling of 50 to 80% of NTs.<sup>390</sup> The thermal decomposition of SiH<sub>4</sub> inside NTs by double-template technique leads to the formation of NTs/Si core-sheath composite.<sup>424</sup> Filling of SWNTs by ZrCl<sub>4</sub> is possible by heating of the mixture of components with mass ratio of 1:1, in a sealed ampoule at 623 K.<sup>425</sup> It is possible that under the experimental conditions (under pressure), ZrCl<sub>4</sub> formed melt and the NT filling is induced by capillary effect. Filling of opened NTs with fullerene molecules is possible by heating the mixture of components at 400 to 650°C in a sealed quartz or glass tube.<sup>426,428</sup> Mechanochemical activation under nitrogen atmosphere of solid-phase mixture of SWNTs and C<sub>60</sub> fullerene leading to fullerene-modified NTs<sup>433</sup> presumably involved evaporation of fullerene.

An unusual process of Cs encapsulation inside SWNT via plasma-ion irradiation has also been demonstrated.<sup>434</sup>

### 3.6.3 REACTIONS INSIDE NANOTUBE

Many interesting chemical reactions can be performed inside NT cavities. Among these are:

- thermal decomposition of salts (e.g., metal nitrates)
- thermal decomposition and pyrolysis of volatile compounds (e.g., silane, metallocenes)
- chemical reduction of salts (e.g., metal halides or nitrates)
- air oxidation (e.g., metal halides)
- hydrolysis and pyrohydrolysis (metal halogenides, trimethylaluminum)
- polymerization (styrene, C<sub>60</sub>)
- formation of complex salts (CoFe<sub>2</sub>O<sub>4</sub>)
- alloy formation (Nd<sub>2</sub>Fe<sub>14</sub>B)
- sorption of vapors
- photolytic reduction

Some processes are complex and involve reactions of different types, e.g., thermal decomposition, reduction, and alloying. It is also possible to modify the inserted solid materials by *in situ* electron irradiation at intermediate accelerating voltages (100 to 400 kV). Electron<sup>435</sup> or carbon-ion<sup>436</sup> beam irradiation can form a connection between NTs. The structural change observed in NTs with encapsulated Ni particles is quite different as compared to empty samples, and leads to the formation of short-range fibrous or amorphous structures instead of a layered structure.<sup>437</sup> The crystalline–amorphous phase transformation has been observed under irradiation of encapsulated Fe.<sup>438</sup>

The first example of a chemical reaction inside SWNT is the H<sub>2</sub> reduction of RuCl<sub>3</sub> yielding Ru metal.<sup>395</sup> Some other examples of reactions (thermal decomposition of AgNO<sub>3</sub> to produce Ag nanowire, reduction of the salts, and CVD processes) have been mentioned earlier. One-dimensional crystals may be reduced to form metallic wires or templated 0-D nanocrystals of regulated sizes.

The reaction of trimethylaluminum and water vapor at 300°C using atomic-layer deposition technique yields Al<sub>2</sub>O<sub>3</sub> nanorods inside MWNTs.<sup>439</sup>

Bando and coworkers<sup>440</sup> revealed that MWNT filled with Ga at 800°C can effectively absorb copper vapor, forming Ga–Cu alloy. The absorption rate for sealed tubes was equal to or even greater than the rate for open-ended tubes. This is presumably due to the fact that the Ga vapor pressure within a closed NT is much higher than that in an open one, and the Cu penetrates inside via defects.

Polymerization of C<sub>60</sub> and generation of double-wall NTs takes place under heat treatment (the temperature must be above ~800°C) or irradiation.<sup>116,441–443</sup> Photopolymerization of C<sub>60</sub> or C<sub>70</sub> inside NT under blue-laser irradiation has also been detected.<sup>444</sup> A Raman investigation revealed that inner SWNTs produced by polymerization are remarkably defect-free.<sup>443</sup> It is interesting that in the polymerization of C<sub>60</sub>, short inner NTs with diameters of ~0.7 nm are preferentially formed first. Such short NTs merge together and lengthen with diameter increasing in the course of polymerization.<sup>445,446</sup>



The polymerization of  $C_{60}$  fullerenes takes place also after heavy doping of the peapod system with an alkali metal.<sup>116</sup> A polymeric phase of  $K_6C_{60}$  has not been observed so far outside the NTs. The coalescence of  $Sm@C_{82}$  has been observed under electron irradiation.<sup>447</sup>

In contrast to fullerenes, in the case of  $LnCl_3$  and  $ZrCl_4$ , the formation of clusters has been observed.<sup>414,425</sup>

MWNTs can be hydrothermally synthesized from different precursors in the presence of metal powder catalyst. One of the important features of some MWNTs produced in hydrothermal conditions is their large inner diameter, well suited for inner-tubular chemical reactions.<sup>43</sup> Since a part of these MWNTs have closed tips and contain encapsulated water and gases (supercritical mixtures of  $CO$ ,  $CO_2$ ,  $H_2O$ ,  $H_2$ , and  $CH_4$ ),<sup>43,44,448</sup> it was important to investigate interaction between the fluid and inner carbon walls.<sup>376</sup> It has been shown that strong interaction between the tube wall and aqueous mixture results in penetration of liquid between the graphitic layers, swelling of the inner wall layers, bending of graphite layers toward the tube center, and inter-calation of several inner layers with O–H species, and interlayer spacing increasing to 0.61 nm. The chemical interaction leads to dissolution of the tube wall and increase in the internal diameter of the tube in the vicinity of the liquid inclusions.

Recently, NTs with an outer diameter of ~90 nm and tube walls inclined with respect to the tube axis were found to form at 770°C and 50 to 90 MPa.<sup>449</sup> The conical-scroll structure of these tubes, with a high density of graphene edges at both inner and outer surfaces, enables functionalization of both surfaces. The outer wall of these NTs is shown to be covered by a hair-like layer of functional groups containing oxygen and carbon, thus making the hydrothermal NTs hydrophilic.

It is expected that nanopeapods could be used as chemical nanoreactors.<sup>445,447</sup>

Selectively opened NTs with 2.0 nm opening would allow many organic molecules to enter and leave. As pointed out by Green,<sup>450</sup> rather than having a “ship-in-the-bottle” situation, one would have what could be described as a “fleet-in-the-harbor,” and the idea of NT catalysis is very attractive. Encapsulation of polystyrene within MWNTs can be realized using solutions of monomer styrene and benzoyl peroxide (initiator) in super-critical  $CO_2$ .<sup>451</sup>

Some inner-tubular chemical and physical processes of NTs have been reviewed by Yang et al.<sup>452</sup>

### 3.6.4 THE STRUCTURE OF CRYSTALS INSIDE NANOTUBES

The restricted diameter range of NT confines the crystals formed inside the NT cavity. As nanocrystal size decreases, surface energy becomes an increasing factor in structural stability. For a given size, surface energy also influences the structural phase diagram in the temperature–pressure plane. Simple thermodynamic models, which predict a lowering of the melting point if the surface energy of the solid is higher than that of the liquid, describe the data semi-quantitatively.

The size of an NT inner cavity is usually small enough to show the dimension effect on embedded particles. The effect consists, for example, of size dependency of melting temperature of encapsulated nanocrystals.<sup>453</sup> But, besides enhanced surface energy, there are other factors affecting the crystal structure of material inside NT; e.g., van der Waals interaction and interaction with the NT wall.

The structure of the encapsulated materials significantly deviates from the structure of bulk materials, with lower surface coordination and substantial lattice distortion. The most noticeable studies in these fields were carried out at Oxford University and Cambridge University (see [Refs. 414, 454, 455](#) and references therein).

The “Feynman crystal’s” growth inside SWNTs is atomically regulated. One-dimensional KI having nine atoms in cross section (inside an NT of 1.6 nm diameter) and four atoms (inside NT of 1.4 nm diameter) were among the first such crystals studied.<sup>453,456</sup> In both cases, the crystal structure peculiar to the bulk crystal is distorted due to interaction with NT walls and change in the coordination number (CN). Especially, noticeable contraction was observed in  $4 \times 4$  crystals, in which crystal parameters were about 4/9 of the standard ones for the bulk crystal. Novel, low-dimensional crystal structures, such as “twisted” crystals, were found.<sup>457,458</sup>

**TABLE 3.2**  
**Packing Behavior Observed in SWNTs as a Function of Bulk Structure Type**

Halide Filling	Common Bulk Structure Type	CN in Bulk	Structure Inside SWNTs	CNs Observed or Predicted within SWNTs <sup>a</sup>
KI	3-D rock salt	6	Rock salt	<b>4, 5, 6</b>
AgX <sup>b</sup>	3-D rock salt	6	Rock salt	4, 5, 6
	Wurzite	4	Wurzite	<b>3, 4</b>
SrI <sub>2</sub>	3-D network	7	1-D PHC <sup>c</sup>	<b>4, 6</b>
BaI <sub>2</sub>	3-D network	7 + 2	1-D PHC	<b>5, 6</b>
PbI <sub>2</sub>	2-D layered	6	1-D PHC	<b>5, 6</b>
LnCl <sub>3</sub> <sup>d</sup>	2-D layered	6	1-D PHC	<b>5, 6</b>

<sup>a</sup> CNs in bold have been observed experimentally. Bulk coordination is predicted for polyhedra in the center of wide capillary SWNTs.

<sup>b</sup> X includes Cl or Br and I.

<sup>c</sup> 1-D PHC, 1-D polyhedral chain.

<sup>d</sup> Ln = La to Tb (UCI<sub>3</sub>-type) only, Ln = Tb to Lu (PuBr<sub>3</sub>-type) only.

Source: From Sloan, J. et al., *Chem. Commun.*, 1319–1332, 2002. With permission.

It was stated later that the form of the structures varies depending on whether the bulk material is a single packed structure (e.g., rocksalt or wurzite) or represents 1-D chain structure of simple coordination polyhedra (Table 3.2).

The chains of lanthanoide halides<sup>415</sup> and zirconium tetrachloride<sup>425</sup> consist of edge-shared MCl<sub>6</sub> polyhedra. “Twisted” CdCl<sub>2</sub> structure closely resembles helical iodine chains.<sup>418</sup> Double-helix iodine chains with the period of ~5 nm correspond to a composition of IC<sub>20</sub>.

In the case of Sb<sub>2</sub>O<sub>3</sub> filling, the material is identified as a single crystal in the valentinite form (i.e., the high-pressure modification as opposed to its senarmontite form). In comparison to the bulk structure of valentinite, the encapsulated crystal shows a longitudinal contraction of ~13% and significant lattice distortions.

The fullerenes inside NTs of appropriate diameter (close to that of (10,10) NT for C<sub>60</sub>) form 1-D molecular chains. Two different domains, where the dominant alignment of C<sub>70</sub> molecular long axis is standing or lying with respect to the NT axis, have been observed.<sup>459</sup> The ratio of the standing to the lying C<sub>70</sub> domains is roughly 7:3.

Molecular dynamic simulations show that water molecules inside NTs at 300 K and 1 atm tend to organize themselves into solid-like wrapped-around ice sheets.<sup>384</sup> A variety of new ice phases that are not seen in bulk ice, and a solid–liquid critical point where the distinction between solid and liquid phases disappears, are observed.<sup>383</sup> The water has been observed to exhibit first-order freezing transition to hexagonal and heptagonal ice nanotubes, as also a continuous phase transformation into solid-like square or pentagonal ice nanotubes.

### 3.7 ADSORPTION AND STORAGE OF GASES

Owing to the specific structure and morphology of NTs, there are a variety of possible sites available for adsorption. In ideal, defect-free, and bundled SWNTs, the sites having different energy of gas adsorption include (1) the internal cavity of opened SWNTs, (2) the interstitial channels between NTs in bundles, and (3) the grooves at the periphery of the bundles (Figure 3.15). Adsorptive capacity of single-wall nanohorns (nanocones) differs from the capacity of SWNTs. The surface structure of MWNTs may be more complex due to different topological defects, such as

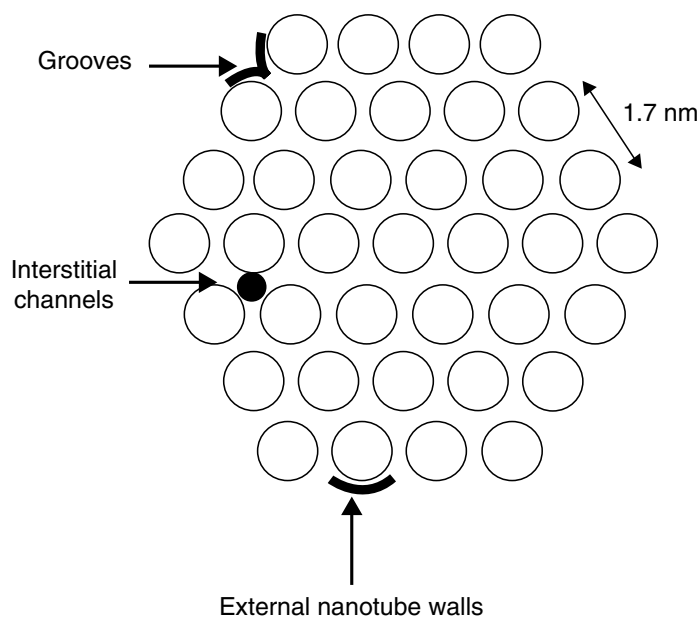


**FIGURE 3.15** The three possible adsorption sites on a bundle of SWNTs with closed ends. (From Babaa, M.R. et al., *Carbon*, **42**, 1549–1554, 2004. With permission.)

pentagons and heptagons, holes and dislocations in sidewalls, etc. The structure of MWNT can be scroll-like, branched, or coiled. The tubes can form second- and third-order structures (see [Section 3.2](#)) and aligned arrays. Therefore the adsorption behavior of MWNTs is more complicated than that of SWNTs. Admixtures such as amorphous carbon, graphitic nanoparticles, or catalyst residues, attached to tube walls functionalities, exert influence upon the adsorption characteristics.

### 3.7.1 HYDROGEN PROBLEM

Hydrogen is an ideal fuel for the future. If hydrogen fuel cells were used to power automobiles and other vehicles, air pollution would be reduced. But the problem is not only to develop effective fuel cells or cost-effective methods of hydrogen production. It is necessary to supply every vehicle with a safe, cheap, compact on-board hydrogen accumulator. The nearest goal is to achieve an adsorption capacity of 6.5 wt% or 62 kg H<sub>2</sub> m<sup>-3</sup> at room temperature.

There are two methods to store hydrogen in NTs: one is to store it under high gas pressure, and the other is to employ an electrochemical charge–discharge cycling method.<sup>5</sup>

The first article on the possibility of hydrogen storage in NTs was published in 1997.<sup>460</sup> Dillon et al.<sup>460</sup> estimated that SWNTs can adsorb from 5 to 10 wt% of hydrogen under ambient conditions. In 1998, Rodriguez and coworkers<sup>461</sup> claimed that certain graphite NFs can store more than 50 wt% at room temperature. In 1999, Chen et al.<sup>462</sup> reported hydrogen uptake at 300 K and a pressure of 0.1 MPa up to 20 wt% by alkali metal-doped MWNTs. Aligned MWNTs with diameters of 50 to 100 nm show a reversible hydrogen storage capacity of 5 to 7 wt% at room temperature under 1 MPa pressure.<sup>463</sup> Pre-treatments of MWNTs increase the storage capacity up to 13 wt%.

Subsequent studies could not confirm these results. Other experimental data are given in [Table 3.3](#).

Most of the work given in [Table 3.3](#) have been done with minor quantities of highly impure and badly characterized samples of NT materials, and only some of the latest publications seemed to be accurate. Therefore the measurements using samples up to 85 g show low adsorptive capacities of MWNTs.<sup>486</sup> The thermal desorption spectra show that hydrogen desorbs below 300 K and at 656 K.<sup>495</sup> The D<sub>2</sub> sorption at 77 K has been found to be 0.45 wt% in raw SWNTs and 0.67 wt% in potassium-doped SWNTs.<sup>496</sup>

Results indicate that hydrogen uptake by metal-containing NT bundles is substantially enhanced compared with uptake by pure tubes. MWNTs seems to be more promising materials than SWNTs.

**TABLE 3.3**  
**Hydrogen Adsorption Levels in NTs**

NT Type	Adsorption Conditions	Adsorption Capacity (wt%)	Year	Reference
SWNTs	300 K, 0.1 MPa, E <sup>a</sup>	0.35	1999	464
SWNTs	300 K, 0.1 MPa, E <sup>a</sup>	2.9	2000	465
SWNTs	300 K, 0.1 MPa	0.04–1.5	2001	466
SWNTs	300 K, 0.1 MPa, E <sup>a</sup>	1.84	2002	467
SWNTs	300 K, 0.1 MPa, E <sup>a</sup>	6	2002	468
SWNTs	300 K, 0.1 MPa	1.8	2004	469
SWNTs	300 K, 0.1 MPa	0.01	2004	470
SWNTs	295 K, 0.1 MPa	0.93	2002	471
SWNTs	300 K, 9 MPa	0.3	2003	472
SWNTs	300 K, 9 MPa	0.3–0.4	2004	473
SWNTs	300 K, 10 MPa	3.5	2001	474
SWNTs	300 K, 10 MPa	<0.2	2002	475
SWNTs	300 K, 12 MPa	4.2	1999	476
SWNTs	253 K, 6 MPa	1	2004	477
SWNTs	77 K, 0.04 MPa	3	2004	478
SWNTs	77 K, 0.1 MPa	1	2004	470
SWNTs	77 K, 0.1 MPa	2.37	2002	471
SWNTs	77 K, 0.2 MPa	6	2002	479
SWNTs	77 K, 1 MPa	0.7	2002	475
SWNTs	77 K, 2 MPa	0.6	2003	480
SWNTs	77 K, 2.5 MPa	2.4	2003	474
SWNTs	77 K, 10 MPa	8.2	1999	481
MWNTs	300 K, 0.1 MPa	0.25	2000	482
MWNTs	300 K, 0.1 MPa, E <sup>a</sup>	0.7	2000	483
MWNTs	300 K, 0.1 MPa, E <sup>a</sup>	0.1–1.6	2001	484
MWNTs	300 K, 0.1 MPa, E <sup>a</sup>	1.6	2003	74
MWNTs	300 K, 0.1 MPa, E <sup>a</sup> , Li	0.6–2.3	2001	484
MWNTs	300 K, 0.1 MPa, Li, K	1.8–2.5	2000	485
MWNTs	300 K, 0.1 MPa	0.30	2004	486
MWNTs	300 K, 3 MPa	<0.2	2002	475
MWNTs	300 K, 10 MPa	0.7–2.4	2001	487
MWNTs	300 K, 10 MPa	0.5–2	2001	488
MWNTs	300 K, 10 MPa	1.16–2.67	2000	489
MWNTs	290 K, 10 MPa	3.4	2001	490
MWNTs	300 K, 12 MPa, KNO <sub>3</sub>	3.2	2002	491
MWNTs	300 K, 13.5 MPa	2.5–4.6	2003	492
MWNTs	77 K, 0.1 MPa	2.27	2004	486
MWNTs	77 K, 3 MPa	~0.3	2002	475
NFs	300 K, 0.1 MPa, KNO <sub>3</sub>	5.1	2003	493
NFs	300 K, 12 MPa	6.5	2002	494

<sup>a</sup>E = electrochemical storage.

The results of theoretical calculations on hydrogen sorption in NTs<sup>5,497–515</sup> are also controversial. It is clear that purified SWNTs store hydrogen in the molecular form. The hydrogen uptake is due to physisorption, therefore the relative amount of adsorbed hydrogen is proportional to the specific surface area of the sorbent material (1.5 wt% per 1000 m<sup>2</sup>/g at 77 K). It has been shown that different

forms of carbon are essentially the same for hydrogen molecules.<sup>516</sup> Close-ended SWNTs and open SWNTs have relatively low accessible surface areas due to bundling of the tubes.

MWNTs can be used as additives to metal adsorbents.<sup>517</sup> Mg–5 wt% MWNTs composite absorbed 4.86 wt% (80% maximum hydrogen storage capacity) within 1 min at 553 K, under 2.0 MPa.

The problem has been discussed in the reviews.<sup>518–527</sup> One can trace the change from rather optimistic estimations of the prospects to use NTs as effective storage media in early publications, to more cautious conclusions and even to a pessimistic point of view in the latest ones. Today, it is still unclear whether NTs will have real practical applications in the hydrogen storage area. Addition of some metals and salts to the NTs, chemical activation, and aligning of NTs leads to an increase in adsorption capacity. However, some other problems which need to be solved include achievement of fast kinetics of discharge, high stability during cycling, low self-discharge level, etc.

### 3.7.2 CARBON NANOTUBE GAS SENSORS

The adsorption of different gases and vapors in NT materials as reported in publications up to year 2000 has been briefly reviewed earlier.<sup>8</sup> Apart from hydrogen, adsorption of noble gases,<sup>528–532</sup> nitrogen,<sup>531–534</sup> oxygen,<sup>531,532,534–536</sup> carbon monoxide,<sup>534</sup> carbon dioxide,<sup>531,533,537–539</sup> nitrogen dioxide,<sup>531,540</sup> ammonia,<sup>531,540</sup> water vapor,<sup>531,534</sup> methane,<sup>528,531,533,541–544</sup> acetylene,<sup>545</sup> acetone,<sup>546</sup> carbon tetrachloride,<sup>547</sup> carbon tetrafluoride,<sup>530</sup> sulfur hexafluoride,<sup>530</sup> methanol,<sup>548</sup> ethanol,<sup>548,549</sup> linear-chain alkanes, and fatty acids<sup>550</sup> has been characterized in the last 5 years. The gas transport properties of NTs have been measured.<sup>551,552</sup>

NTs have been found to be an effective separation media for removing some admixtures from flue gases; they can store gases having relatively high molecular mass (e.g., methane). However, the most promising field of their application is the development of new sensing devices. Sensing gaseous molecules is important in environmental monitoring, control of chemical processes and agriculture, and biological and medical applications. NT-based sensors have huge prospects in outer planetary exploration and for incorporation into yarns and fabrics.

Chemical doping of NTs, particularly of SWNTs, changes their electronic properties and can induce strong changes in conductance<sup>48,553,554</sup> and in thermoelectric power.<sup>555–557</sup> Chemical sensors are measurement devices that convert a chemical or physical property of a specific analyte into a measurable signal whose magnitude is usually proportional to the concentration of the analyte. For sensing applications, NTs have advantages, such as small size with larger surface, high sensitivity, fast response, and good reversibility.

The first sensor based on SWNTs was reported by Dai and coworkers,<sup>558</sup> who demonstrated that small concentrations of NO<sub>2</sub> produced large changes in sensor conduction. To clarify the reason for the discrepancy of recovery time between theoretical results and experimental data, the formation of adsorbed NO<sub>3</sub> has been postulated.<sup>559</sup> Recent works<sup>560,561</sup> show the possibility of using MWNT thin films for measuring sub-ppm NO<sub>2</sub> concentrations (10 to 100 ppb) in dry air, with the maximum response at 165°C. The gas-sensing properties of NT thin films depend on the nature of the defect and concentration.<sup>562</sup>

Gas-sensing characteristics of MWNTs as applied to humidity, NH<sub>3</sub>, CO, and CO<sub>2</sub> partial pressure have been studied.<sup>563</sup> A practical gas sensor for ammonia and water vapor, based on measuring the variation of the electrical conductivity of MWNT ropes, has been proposed.<sup>564</sup> In particular, the absorption of different gases in the MWNT/SiO<sub>2</sub> layer changes the permittivity and conductivity of the material, consequently altering the resonant frequency of the sensor, which is tracked remotely, using a loop antenna.<sup>564</sup> Detecting properties of MWNTs for NH<sub>3</sub> allow the exploitation of the sensor at room temperature.<sup>565</sup>

The construction of gas sensors based on MWNT thin films to measure NO<sub>2</sub>, CO, NH<sub>3</sub>, H<sub>2</sub>O, and C<sub>2</sub>H<sub>5</sub>OH concentrations has been described.<sup>561</sup>

The thermoelectric response due to the interaction of adsorbed molecules with NT walls can be used to detect gases such as He, N<sub>2</sub>, and H<sub>2</sub>.<sup>566</sup>

The viability of using boron- or nitrogen-doped NT films as sensors has been suggested<sup>567</sup> and verified.<sup>568</sup> It was shown that sensors fabricated using individual films of  $CN_x$  NTs have a fast response for  $NH_3$  and reach saturation within 2 to 3 sec. The experiments also indicate a great potential in the manufacture of solvent vapor sensors, and especially for ethanol, acetone, and chloroform detection. The simple casting of SWNTs on an inter-digitated electrode allows the fabrication of a gas sensor for detection of  $NO_2$  and nitrotoluene.<sup>569</sup>

Rational chemical modification of NTs leads to the fabrication of a sensor having good molecular selectivity. A selective molecular hydrogen sensor has been formed using SWNTs decorated with Pd nanoparticles.<sup>570</sup> Sensing properties of NTs can be amplified using conjugated polymer composites (see Ref. 571 and references therein).

### 3.8 ATTACHMENT OF BIOMOLECULES

NTs are considered to be biocompatible<sup>572–576</sup> and attract great interest as a material for biological applications. The main fields of such applications include: (1) fabrication of bioprobes and biosensors, (2) synthesis of molecular structures for the transport of vaccines and drugs, especially water-insoluble substances into the body or to a certain body organ, (3) formation of anti-fouling surfaces (enzyme-containing composites), (4) use of NTs as a template to grow cells, and (5) creation of implantable bioelectronic devices.

#### 3.8.1 BIOSENSORS

The development of biosensors has taken greater importance in the past years of heightened security. Biosensors are defined as analytical devices incorporating biological material (e.g., DNA, enzymes, antibodies, microorganisms, etc.) associated with or integrated within a physico-chemical transducer. In contrast to gas sensors, biosensors act in the aqueous phase, particularly in physiological solutions. NTs have definite advantages in sensing applications: small size, large specific surface, high sensitivity, fast response, and good reversibility.<sup>577</sup>

Amperometric sensors are based on the reaction between a biomolecule immobilized on the sensor electrode with the analyte. The reaction produces an electric current, which is proportional to the analyte concentration and can be measured.

The NT film can be easily fabricated on a glassy carbon or edge-plane carbon surfaces to form an electrode.<sup>576</sup> Nonfunctionalized NT electrodes have been used in electrochemical oxidation of dopamine and norepinephrine<sup>578,579</sup> and to determine thyroxine.<sup>580</sup> The NT sidewalls can be functionalized for biocompatibility and to display selective binding sites for specific biological analytes.<sup>573</sup> Different bio-molecules, such as proteins, enzymes, and DNAs, can be attached to the NTs. The attachment can be covalent or noncovalent. The noncovalent linking of DNA is a usual way to modify NTs.<sup>573,581–584</sup> The method elaborated by Chen et al.<sup>583</sup> involves a bi-functional molecule, 1-pyrenebutanoic acid, and succinimidyl ester, irreversibly adsorbed onto the inherently hydrophobic surfaces of SWNTs in an organic solvent. Succinimidyl ester groups are highly reactive to nucleophilic substitution by primary and secondary amines that exist in abundance on the surface of most proteins.

The covalent binding of DNA with NTs has been described.<sup>585–587</sup> A major area of interest for biosensor developers is the study of human DNA. The NT array electrode functionalized with DNA/PNA can detect the hybridization of targeted DNA/RNA from the sample. A nanoelectrode array based on vertically aligned MWNTs embedded in  $SiO_2$  has been reported by Li et al.<sup>588</sup> and Koehne et al.<sup>589</sup> Oligonucleotide probes were selectively attached to the ends of the MWNTs. The hybridization of subattomole DNA targets was detected by combining the electrode array with ruthenium bipyridine-mediated guanine oxidation.

Such electro-chemical assay provides enhanced daunomycin signals.<sup>590</sup> A MWNTs-COOH-modified glassy carbon electrode was fabricated and oligonucleotides with 5'-amino groups were covalently bonded to the carboxyl group of NTs.

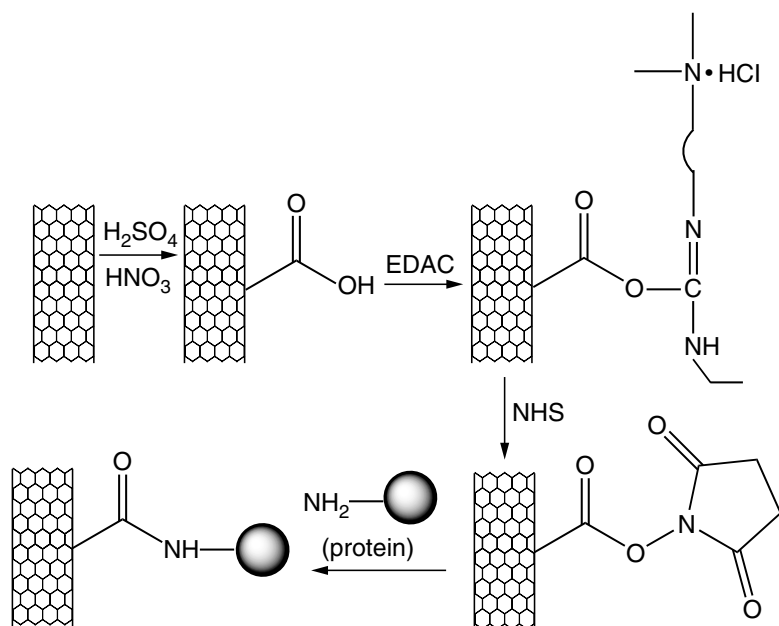


**FIGURE 3.16** The attachment of proteins to NTs via a two-step process of diimide-activated amidation. (From Jiang, K. et al., *J. Mater. Chem.*, **14**, 37–39, 2004. With permission.)

Trace levels of oligonucleotides and polynucleotides can be readily detected following short accumulation periods with detection limits of 25, 60, 126, and 219  $\mu\text{g/L}$  for oligo(dG)(21), oligo(dG)(11), ss, and da calf thymus DNA, respectively.<sup>591</sup>

A novel glucose biosensor based on NT-modified electrode is also of great practical interest. Glucose oxidase (GOx) is a flavine enzyme used commercially on a massive scale to monitor blood glucose levels in diabetics. The GOx adsorbs spontaneously on NT sheets and can be reversibly oxidized without complete loss of enzymatic activity.<sup>592</sup> A vertical array of MWNTs with GOx molecules is adsorbed non-specifically on the exposed ends.<sup>593</sup> The electrode exhibits an amperometric response in the presence of varying glucose concentrations. Different methods of GOx immobilization onto NTs have been described.<sup>594–596</sup>

SWNTs fabricated into field effect transistors have several advantages over conventional sensor systems, providing high sensitivity and allowing real-time detection.<sup>597</sup> This approach has been used to fabricate biosensors for streptavidin recognition.<sup>598</sup> NT coated with a polymer functional layer was functionalized with protein biotin, thus providing specific molecular detection.

The immobilization of different proteins and enzymes onto NTs for the development of new biosensors has been described.<sup>599–606</sup> Two different methods were employed for NTs functionalization with bioactive peptides:<sup>607</sup> (1) fragment condensation of fully protected peptides and (2) selective chemical ligation. The latter is shown in Figure 3.16.

Biosensors can be applied for detecting of diseases, particularly in cancer diagnostics.<sup>608,609</sup>

Detection of organophosphorus pesticides and nerve gases by biosensors is possible.<sup>610</sup> Detection of pathogens and toxins, and direct determination of total cholesterol in blood, has been studied. Bacterial binding has been used to create biosensors.<sup>611</sup> The capture of specific bacteria by particular antibodies can be detected by different sensor platforms, e.g., by acoustic wave sensors, using piezoelectric resonator. NTs can also be potentially used as ion channel biosensors.<sup>388</sup>

The study of the kinetics and thermodynamics of biological redox processes by biosensors is an important part of biochemistry.<sup>576,612</sup> As per theory, NIR-radiation-excited NT ropes could control the activity of proteins *in vivo*.<sup>613</sup>

### 3.8.2 OTHER FIELDS OF APPLICATION

Enzyme-containing polymer/SWNT composites have been explored as unique biocatalytic materials.<sup>614</sup> NTs functionalized with bioactive peptides act as a medium to transfer peptides across the cell membranes.<sup>615</sup>

MWNTs functionalized with hemin are able to detect oxygen in solution.<sup>616,617</sup> Bucky paper can be used for transplanting cells into the retina. In experiments, the substrate worked as a scaffold for the growth of the retinal cells taken from white rabbits, for implanting in other rabbits. The NTs served as substrates for neuronal growth.<sup>618,619</sup>

Some biomolecules solubilize NTs. Lipid rings<sup>620</sup> and DNA<sup>621</sup> have been studied as solubilizers to dissolve NTs in aqueous solutions. The solubility of  $\beta$ -galactoside-modified SWNTs in water was shown to be increased by adsorption of lectin molecules.<sup>622</sup> NTs in the presence of galactose-specific lectins form micrometer-sized nanostructures.

Solubilization using single-stranded DNA allows the purification and separation of NTs.<sup>623,624</sup> By screening a library of oligonucleotides, scientists found that a certain sequence of single-stranded DNA self-assembles into a helical structure around individual NTs. Since NT/DNA hybrids have different electrostatic properties that depend on the NT diameter and electronic structure, they can be separated and sorted using anion-exchange chromatography. DNA-stabilized dispersions of NTs prepared by Barisci et al.<sup>625</sup> are concentrated (up to 1%, by mass) and are better suited for fiber spinning than conventional surfactants.

Selective localization of SWNTs on aligned DNA molecules on surfaces is an important tool in bottom-up bio-templated nanofabrication.<sup>626</sup> Self-assembly based on molecular recognition could be the best approach for constructing complex architectures (e.g., field-effect transistor<sup>627</sup>) for miniature biological electronics and optical devices. The attachment of DNA to oxidatively opened ends of MWNT arrays<sup>587</sup> and the DNA-guided assembly of NTs<sup>628</sup> have been studied.

## 3.9 NANOTUBES AS TEMPLATES

### 3.9.1 SUBSTITUTION OF THE CARBON ATOMS OF NANOTUBES

The incorporation of some chemical elements in carbon NTs leads to a new nanomaterial without a significant modification of the NT structure, but with possible improvement of their properties. Substitution of carbon atoms with nitrogen or boron atoms is most interesting from a practical standpoint. It allows the formation of hetero-junctions within a single NT, and opens a way to use such a tube in electronic devices. Besides, substitution with silicon has also been studied.

Tight-binding calculations show that the presence of nitrogen atoms is responsible for introducing donor states near Fermi level.<sup>629,630</sup> Nitrogen-doped carbon NTs have been found to be metals<sup>630,631</sup> (earlier it was stated that the modified tubes were metals or semiconductors depending on the relative position of nitrogen and carbon atoms<sup>632</sup>).

Arc-discharge process<sup>633,634</sup> and pyrolysis<sup>629,635–646</sup> are the main methods of nitrogen-substituted carbon NT synthesis. The third method is carbon-resistive heating under high isostatic nitrogen pressure.<sup>647</sup>

The incorporation of nitrogen into carbon NTs grown by arc-discharge method takes place in a helium–nitrogen atmosphere<sup>633</sup> or by introducing nitrogen-rich organic or inorganic precursors into the anode rods.<sup>634</sup> Metal phthalocyanines,<sup>636,641</sup> methane and nitrogen mixtures,<sup>637–639,646</sup> ferrocene and melamine mixtures,<sup>629,640</sup> acetylene/ammonia/iron carbonyl mixtures,<sup>642</sup> acetylene/ammonia/hydrogen mixtures,<sup>643</sup> and acetonitrile or acetonitrile/hydrogen mixtures<sup>644,645</sup> have been used in CVD processes.

The amount of incorporated nitrogen varies from some tenths of a percent to 9%<sup>641</sup> and even 13%.<sup>647</sup> The nitrogen incorporation enhances the growth of NTs by the CVD process and induces visible changes in the NT structure and morphology. Overall, the presence of nitrogen suppresses the formation of bundles, changes the tube conformation, and leads to the NT texturing.

All boron-doped carbon NTs exhibit highly metallic electronic character. Boron has been shown to play a key role at the open end of a growing carbon NT, thus increasing its overall length.



Boron-substituted NTs are formed by arc-discharge<sup>634,648,649</sup> or CVD<sup>650,651</sup> methods. Moreover, solid-state<sup>652–655</sup> and gas–solid<sup>656,657</sup> reactions are also employed to prepare the material.

It is possible to reach boron-substitutional level up to 20%<sup>653,654</sup> and synthesize carbon-free BN nanotubes.<sup>656,658</sup> The methods described allow the preparation of B–C–N NTs<sup>635</sup> and NFs.<sup>634,658–661</sup>

The determined properties of silicon-doped carbon NTs and a suggestion how such tubes can be synthesized have been published.<sup>662,663</sup> The interaction of carbon NTs with SiO<sub>2</sub> or Si yields SiC nanorods (see the next section). Some substitution reactions have been developed to produce hetero-structures of SWNTs and metal-carbide nanorods.<sup>664</sup>

### 3.9.2 DECORATION OF CARBON NANOTUBES

Surface-modified carbon NTs, inorganic NTs, and nanorods are of great significance in various practical applications, such as catalysis, electrocatalysis, photocatalysis, ion-exchange and gas sorption, electron emitter and nanodevice fabrication, and production of composites. “Decoration” is often referred to as a process of covering NTs with a substance that does not form strong chemical bonds with carbon atoms. At the same time, several decoration processes yield a covering substance linked by weak chemical or electrostatic forces to the NTs.

NTs can be decorated with metals (Cu, Ag, Au, Al, Ti, Ni, Pt, Pd), alloys (Co–B, Ni–P, Mo–Ge), nonmetals (Se), metal oxides (ZnO, CdO, Al<sub>2</sub>O<sub>3</sub>, CeO<sub>2</sub>, SnO<sub>2</sub>, SiO<sub>2</sub>, TiO<sub>2</sub>, V<sub>2</sub>O<sub>5</sub>, Sb<sub>2</sub>O<sub>5</sub>, MoO<sub>2</sub>, MoO<sub>3</sub>, WO<sub>3</sub>, RuO<sub>2</sub>, IrO<sub>2</sub>), metal chalcogenides (ZnS, CdS, CdSe, CdTe), metal carbides (SiC), metal nitrides (SiN<sub>x</sub>, AlN), and polymers (polyaniline, polypyrrole). The list of such substances can go on. It is possible to prepare the covering of NTs in the form of quantum dots and nanoparticles, to isolate nanotubules or nanorods and nanowires. The surface structure of NTs, and the strategy and extent of deposition greatly influence the morphology of a coating.

The approaches to decoration of NTs include physical evaporation, electroless deposition, electroplating, CVD, sol–gel process, chemical attachment of metal ions or complexes with subsequent reduction or thermal decomposition, solid-state reactions, solid–gas reactions, self-assembling, polymerization, and other chemical processes.

The decoration of NTs with nickel is achieved by electroless plating method,<sup>665–668</sup> by electrochemical deposition process,<sup>669,670</sup> by chemical reduction of NiCl<sub>2</sub> with hydrogen,<sup>671</sup> or by electron-beam evaporation of the metal.<sup>672,673</sup> Copper has been deposited onto NTs by electroless plating<sup>667</sup> or by reduction of CuCl<sub>2</sub> with hydrogen.<sup>674</sup> Cobalt has been plated onto NTs via electroless plating<sup>675</sup> or by reduction of Na<sub>2</sub>Co(OH)<sub>4</sub> using KBH<sub>4</sub> solution.<sup>676</sup> Electroless plating usually demands preliminary chemical activation of a substrate.

Several procedures have been used to decorate acid-treated NTs with nanoscale clusters of Ag, Au, Pt, and Pd. For instance, Satishkumar et al.<sup>677</sup> carried out the refluxing with HAuCl<sub>4</sub> and HNO<sub>3</sub> or *tetrakis* hydroxymethyl phosphonium chloride, with H<sub>2</sub>PtCl<sub>6</sub> and HNO<sub>3</sub> or ethylene glycol, and with AgNO<sub>3</sub> and HNO<sub>3</sub>; Li et al.<sup>678</sup> refluxed NTs for 6 h with H<sub>2</sub>PtCl<sub>6</sub> dissolved in ethylene glycol. The activity of Pt cathode catalyst for direct methanol fuel cells has been shown to be dependent on the ratio of water/ethylene glycol.<sup>679</sup> Pt/NTs composite prepared by reduction of H<sub>2</sub>PtCl<sub>6</sub> with Na<sub>2</sub>S<sub>2</sub>O<sub>6</sub> in water/alcohol solution exhibited good catalytic properties.<sup>69</sup> It is possible to use sorption of Pd<sup>2+</sup> ions from solution with subsequent hydrogen reduction.<sup>680,681</sup> Contact of an acetone solution of H<sub>2</sub>PtCl<sub>6</sub> with NTs allows production of NTs decorated with platinum clusters without any surface functionalization.<sup>682</sup> Decomposition and reduction of H<sub>2</sub>PtCl<sub>6</sub>, HPdCl<sub>3</sub>, HAuCl<sub>4</sub>, or AgNO<sub>3</sub> dispersed on NTs at temperatures from 300 to 700°C gives metal nanoparticles with average size of 7 to 17 nm.<sup>683</sup> Nanoparticle/NT hybrid structures have been prepared by forming Au and Pd nanoparticles on the sidewalls of SWNTs using reducing reagents or catalyst-free electroless deposition, as a result of direct redox reaction between metal ions and NTs.<sup>684</sup> Because Au<sup>3+</sup> and Pt<sup>2+</sup> have much higher reduction potential than NTs, they are reduced spontaneously. Hydrogen reduction of a Pd(II)-β-diketone precursor in super-critical carbon dioxide produces Pd nanoparticles on MWNTs.<sup>405,685</sup>

As for gold and silver nanoparticles, the usual thiol-linking procedure can be used to anchor them to NTs.<sup>686–688</sup> Silver clusters on SWNT surface have been grown by the decomposition of (cycloocta-1,5-diene)(hexafluoroacetylacetonate)silver(I).<sup>686</sup> A highly selective electroless deposition of gold nanoparticles on SWNTs has been reported.<sup>684</sup> Sonication allows the deposition of gold onto MWNTs directly from gold colloid solution.<sup>689</sup> A method to fabricate gold nanowires using NTs as positive templates has been demonstrated.<sup>690</sup> The first step was to self-assemble gold nanocrystals along NTs. After thermal treatment, the nanocrystal assemblies were transformed into continuous polycrystalline gold nanowires. Monolayer-protected Au clusters strongly adsorb onto both end-opened and solubilized when refluxed in aniline SWNTs.<sup>195</sup>

Formation of different metal nanowires using NTs as positively charged templates has been described.<sup>691</sup>

To form a  $\text{SiO}_2$  or  $\text{SiO}_x$  coating on NTs as well as to prepare silica nanotubes, silica nanorods and silica/NT composites, sol-gel technique has been employed by many researchers.<sup>692–696</sup> Tetraethoxysilane (tetraethyl-*o*-silicate) was the usual precursor in this process. Silica-coated SWNTs have also been produced by adding silica/ $\text{H}_2\text{SiF}_6$  solution to a surfactant-stabilized dispersion of SWNTs<sup>697</sup> or by hydrolysis of 3-aminopropyltriethoxysilane.<sup>698</sup>

NTs have been coated with titania by using titanium *bis*-ammonium lactato dihydroxide,<sup>699</sup> tetraethyl-*o*-titanate,<sup>696,700</sup> titanium tetraisopropoxide,<sup>147,700</sup> titanium oxysulfate,<sup>700</sup> and titanium tetrachloride<sup>701</sup> as precursors. Sol-gel method has been used to sheathe NT tips for field emission electron emitters (Figure 3.17).<sup>702</sup> The coating morphology depends on the precursor composition and method of deposition.<sup>700</sup> Covalent linking of  $\text{TiO}_2$  nanocrystals to SWNTs by short-chain organic molecule linker is demonstrated.<sup>147</sup>

Coating of NTs with alumina<sup>692,696,703</sup> or  $\text{Al}(\text{OH})_3$ <sup>704</sup> is possible by either thermal or chemical decomposition of aluminum sources, such as aluminum isopropoxide, aluminum trichloride, or aluminum nitrate. Oxidation of a powdered aluminum metal/MWNT mixture with  $\text{O}_2$  or air leads to the formation of  $\text{Al}_2\text{O}_3$  nanotubes or nanowires.<sup>705</sup> Treating the same mixture in  $\text{NH}_3$  atmosphere at 300 to 500°C yields AlN nanowires or particles.<sup>705</sup>

SWNTs and MWNTs can be coated with a thin or thick film of  $\text{SnO}_2$ .<sup>706–708</sup> Heat treatment of MWNTs with zinc at various temperatures gives ultra-thin films of ZnO on the tubes, ZnO quantum dots, or nanowires.<sup>709</sup> Deposition of  $\text{CeO}_2$  nanoparticles on the surface of MWNTs by hydrolysis of  $\text{CeCl}_3$  in aqueous solution has been described.<sup>710</sup> Covering of NTs with oxides of different metals (V, Sb, Mo, Ir, Ru) has been characterized.<sup>711,712</sup>

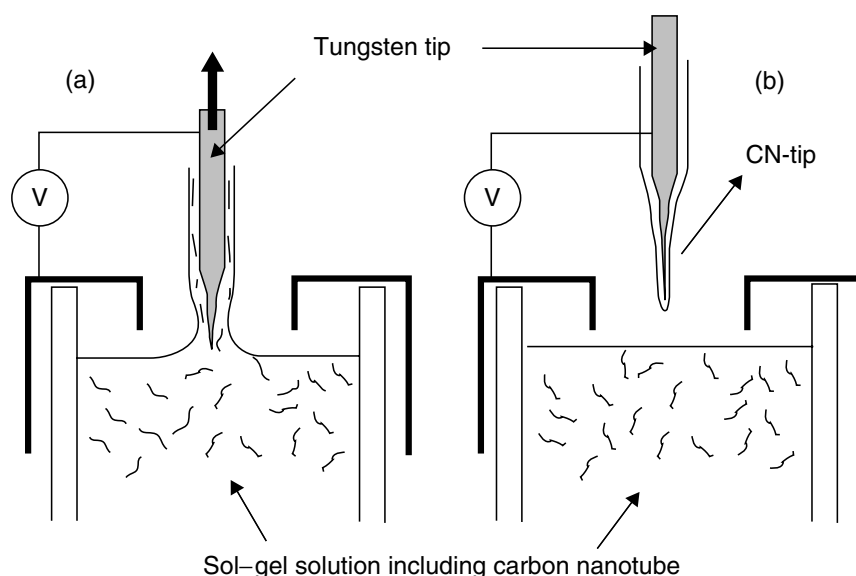


**FIGURE 3.17** Schematic illustration of the sol-gel coating process under DC voltage. (From Brioude, A. et al., *Appl. Surf. Sci.*, **221**, 4–9, 2004. With permission.)

Semiconductor metal chalcogenide nanoparticles such as CdS,<sup>713</sup> CdSe,<sup>147,205,714,205</sup> CdTe,<sup>148</sup> and ZnS<sup>715,714</sup> have been bound to the surfaces of NTs. The example of an attachment process is presented in Figure 3.18.

Reaction of carbon NTs and carbon NFs with silicon<sup>716,717</sup> as well as with silica<sup>718</sup> allows the production of SiC coatings, NFs, or nanorods. The plasma enhanced CVD (PECVD) method using mixtures of SiH<sub>4</sub> with C<sub>2</sub>H<sub>2</sub> or with NH<sub>3</sub> introduced into the reaction chamber at 250°C has been used to coat MWNTs with amorphous films of SiC or SiN<sub>x</sub>.<sup>719</sup> A process of simultaneous growth of carbon NTs and SiC nanorods has been realized by means of CVD.<sup>720</sup>

The aligned NTs can be used to make conducting polymer/NT coaxial nanowires by electrochemical deposition of a concentric layer of conducting polypyrrole.<sup>721</sup> Ultra-thin films of pyrrole were deposited on the surfaces of MWNTs using a plasma polymerization technique.<sup>722</sup> Polymer nanoshells on NTs can be formed via layer-by-layer deposition on NT template.<sup>723</sup>

Interesting and unusual nanowires of rare-earth phthalocyanine have been produced via the templated assembly method.<sup>724</sup> When the solvent is evaporated gradually, RErPc<sub>2</sub> nanoparticles and nanowires are found to self-assemble on the exterior walls of NTs.

### 3.10 INTERCALATION OF “GUEST” MOIETIES

Similar to graphite, NTs can form guest–host compounds with electron acceptors (e.g., bromine, iodine, interhalogens, FeCl<sub>3</sub>, HNO<sub>3</sub>) and electron donors (alkali metals).<sup>8,16,18</sup> The guest species can be inserted between the graphene shells of MWNTs or in the open inter-tubular spaces inside the bundles of SWNTs. Reversible inter-cation proceeds by both direct vapor/liquid contacting and electrochemical insertion of ions. The doping is accompanied by charge transfer and enhancement of NT conductivity.

The inter-cation of bromine into MWNTs at 50°C shows an unusual ordered accumulation along the direction perpendicular to the NT surface.<sup>725</sup> Iodine reversibly forms charged polyiodide chains into SWNT bundles,<sup>726</sup> which is similar to the chains in iodine-doped SWNTs<sup>418</sup> and MWNTs.<sup>419</sup>

The behavior of MWNTs depends on their structure. In addition to FeCl<sub>3</sub>, other metal chlorides (ZnCl<sub>2</sub>, CdCl<sub>2</sub>, AlCl<sub>3</sub>, and YCl<sub>3</sub>) formed inter-cation compounds with MWNTs having scroll structure.<sup>18</sup>

The HNO<sub>3</sub> molecules intercalate into the bundles of SWNT,<sup>727</sup> and HNO<sub>3</sub>, H<sub>2</sub>SO<sub>4</sub>, and HCl intercalate into the SWNT film (“bucky paper”).<sup>728</sup> In all cases, an acceptor-type doping of the SWNTs has been observed.

Fluorine, as was mentioned earlier (see Section 3.5.3), forms strong semi-ionic or covalent bonds with carbon atoms of NTs and cannot be deintercalated in diatomic molecular form.

Much more information has been obtained on NT doping with alkali metals. Some theoretical models of inter-cation products have been offered.<sup>16,18</sup> Potassium and other heavy-weight alkali metals at saturation state form MC<sub>8</sub> compounds corresponding to the first-stage graphite inter-cation compounds (GIC).<sup>16,18</sup> The doping of SWNTs is diameter-selective.<sup>729,730</sup> The dopant atoms initially deposited on the tips of aligned MWNTs diffuse toward their roots at extremely small rates.<sup>731</sup>

The rapid development of lithium-ion batteries, which use graphite or carbonaceous materials as one of the electrodes, gives rise to a great interest in NT material inter-cation with lithium.<sup>5,522</sup> A significant reversible capacity has been found.<sup>732</sup> SWNTs can be reversibly inter-cated with lithium up to Li<sub>1.7</sub>C<sub>6</sub> composition.<sup>733</sup> The reversible lithium storage capacity after etching of SWNTs increases to Li<sub>2</sub>C<sub>6</sub>.<sup>734,735</sup> Moreover, this saturation composition increases to Li<sub>2.7</sub>C<sub>6</sub> by applying a suitable ball-milling treatment to the purified SWNTs.<sup>736</sup> It means that SWNTs can contain roughly twice the energy density of graphite. To explain the results of Refs. 732 and 736, a non-GIC mechanism of storage has been proposed.<sup>737</sup> In this mechanism, except for the lithium intercalated between graphene layers to form GIC, the higher charge capacity should be related to lithium doped into disordered graphitic structures, defects, microcavities, and edge of graphitic layers.

The reversible capacity increases as compared to that of raw NTs after treatment with lithium compounds such as LiNO<sub>2</sub>.<sup>738</sup> The lithium diffusion coefficient decreases with an increase of the

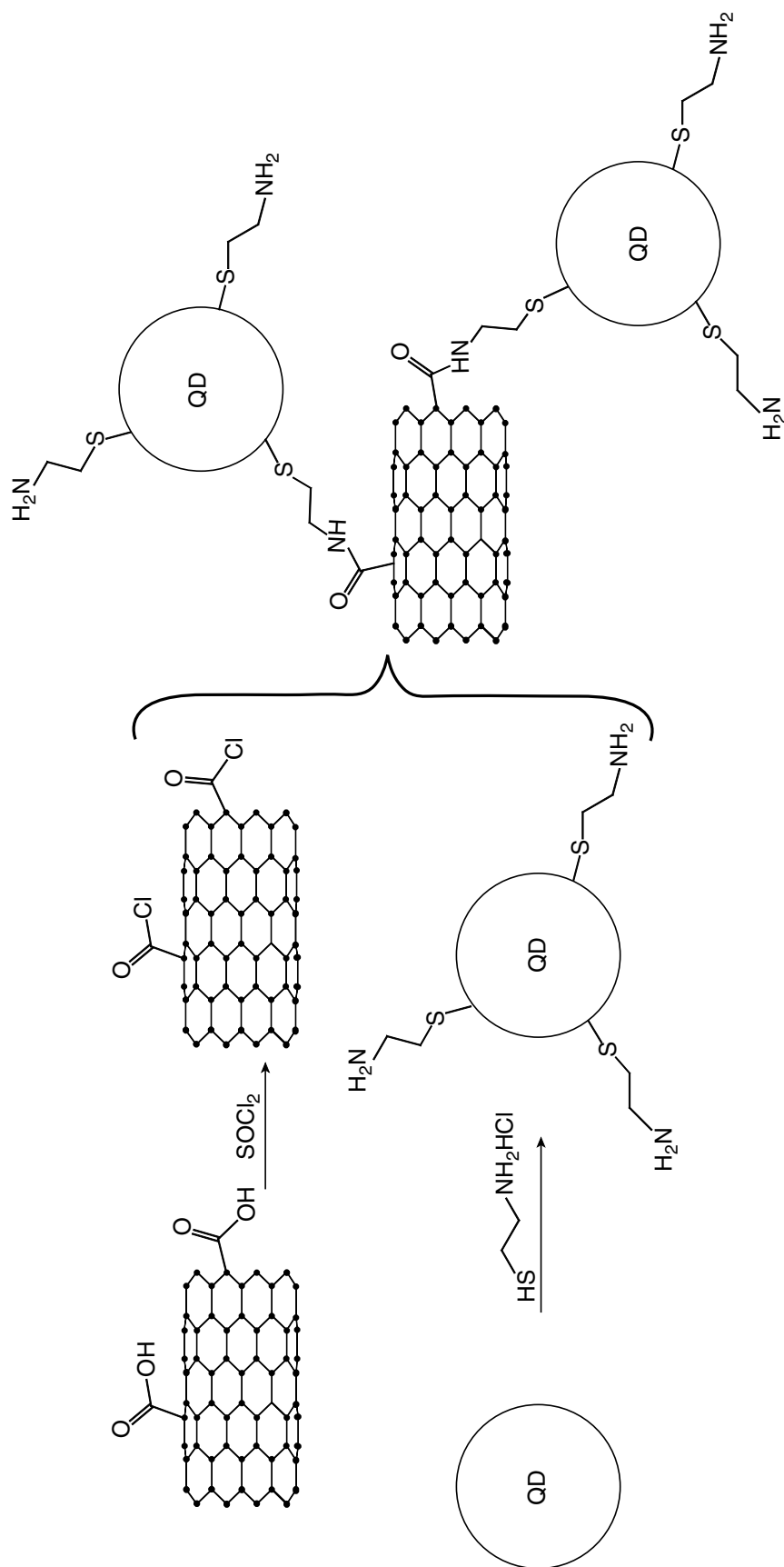


**FIGURE 3.18** Quantum dots (QD) attachment at cut ends or at defects along NT sidewall. (From Haremza, J.M. et al., *Nano Lett.*, **2**, 1253–1258, 2002. With permission.)

open-circuit voltage. This phenomenon is presumably connected with a change of composition and properties of thin inorganic film covering the NTs.

### 3.11 SUMMARY AND CONCLUSIONS

Carbon NTs represent a set of materials including numerous variants with different structure, morphology, and properties. Some of these materials are now coming to the industrial arena as new attractive resources with many remarkable properties and dozens of promising applications. Several scaleable continuous chemical methods of NT production have been elaborated and scaled.

The practical significance of carbon NT chemistry and its achievements is sharply increased. Today, this branch of NT “general chemistry” subdivides into carbon NT inorganic, organic, bioorganic, colloidal, and polymeric chemistry. NT chemistry now occurs in solution, in such a way that it opens many new possibilities to purify, sort, and modify the material and to integrate it in electronic devices.

Carbon NTs are among the most important materials of modern nanoscience and nanotechnology, including molecular electronics, and the chemistry of NTs play a remarkable role in the development of this interdisciplinary area.

### ACKNOWLEDGMENTS

The author is grateful to Mr. I. Anoshkin and Mr. Nguyen Tran Hung for their helpful assistance.

### REFERENCES

1. J.-M. Bonard, H. Kind, T. Stöckli, and L.-O. Nilsson, Field emission from carbon nanotubes: the first five years, *Solid-State Electron.* **45**, 893–914 (2001).
2. R.H. Baughman, A.A. Zakhidov, and W.A. de Heer, Carbon nanotubes — the route toward applications, *Science* **297**, 787–792 (2002).
3. Ph. Avouris, Carbon nanotube electronics, *Chem. Phys.* **281**, 429–445 (2002).
4. T.W. Odom, J.-L. Huang, and C.M. Lieber, Single-walled carbon nanotubes: from fundamental studies to new device concepts, *Ann. N.Y. Acad. Sci.* **960**, 203–215 (2002).
5. M. Daenen, R.D. de Fouw, B. Hamers, P.G.A. Janssen, K. Schouteden, and M.A.J. Veld, *The Wondrous World of Carbon Nanotubes. A Review of Current Carbon Nanotube Technologies*. Eindhoven University of Technology, 2003, p. 93.
6. *Nanotubes: Technology and Directions*. Business Communication Co., Inc., 2003, p. 280 [<http://www.marketresearch.com/map/prod/967076.html>].
7. E.G. Rakov, Methods for preparation of carbon nanotubes, *Russ. Chem. Rev.* **69**, 35–52 (2000).
8. E.G. Rakov, The chemistry and application of carbon nanotubes, *Russ. Chem. Rev.* **70**, 827–863 (2001).
9. O. Zhou, H. Shimoda, B. Gao, S. Oh, L. Fleming, and G. Yue, Materials science of carbon nanotubes: fabrication, integration, and properties of macroscopic structures of carbon nanotubes, *Acc. Chem. Res.* **35**, 1045–1053 (2002).
10. J. Hilding, E.A. Grulke, Z.G. Zhang, and F. Lockwood, Dispersion of carbon nanotubes in liquids, *J. Disp. Sci. Technol.* **24**, 1–41 (2003).
11. S. Niyogi, M.A. Hamon, H. Hu, B. Zhao, P. Bhowmik, R. Sen, M.E. Itkis, and R.C. Haddon, Chemistry of single-walled carbon nanotubes, *Acc. Chem. Res.* **35**, 1105–1113 (2002).
12. Z. Chen, W. Thiel, and A. Hirsch, Reactivity of the convex and concave surfaces of single-walled carbon nanotubes (SWNTs) toward addition reactions: dependence on the carbon-atom pyramidalization, *Chem. Phys. Chem.* **4**, 93–97 (2003).
13. T. Yu. Astakhova, G.A. Vinogradov, O.D. Gurin, and M. Menon, Effect of local strain on the reactivity of carbon nanotubes, *Russ. Chem. Bull.* **51**, 704–708 (2002).
14. K.D. Ausman, H.W. Rohrs, M. Yu, and R.S. Ruoff, Nanostressing and mechanochemistry, *Nanotechnology* **10**, 258–262 (1999).

15. D. Srivastava, D.W. Brenner, J.D. Schall, K.D. Ausman, M.F. Yu, and R.S. Ruoff, Predictions of enhanced chemical reactivity at regions of local conformational strain on carbon nanotubes: kinky chemistry, *J. Phys. Chem. B* **103**, 4330–4337 (1999).
16. J.E. Fischer, Chemical doping of single-wall carbon nanotubes, *Acc. Chem. Res.* **35**, 1079–1086 (2002).
17. Y.-P. Sun, K. Fu, Y. Lin, and W. Huang, Functionalized carbon nanotubes: properties and applications, *Acc. Chem. Res.* **35**, 1096–1104 (2002).
18. L. Duclaux, Review of the doping of carbon nanotubes (multiwalled and single-walled), *Carbon* **40**, 1751–1764 (2002).
19. A. Hirsch, Functionalization of single-walled carbon nanotubes, *Angew. Chem. Int. Edit.* **41**, 1853–1859 (2002).
20. L. Dai, A. Patil, X. Gong, Z. Guo, L. Liu, Y. Liu, and D. Zhu, Aligned nanotubes, *Chem. Phys. Chem.* **4**, 1150–1169 (2003).
21. T. Lin, V. Bajpai, T. Ji, and L. Dai, Chemistry of carbon nanotube, *Aust. J. Chem.* **56**, 635–651 (2003).
22. J.-M. Ting and J.B.C. Lan, Beaded carbon tubes, *Appl. Phys. Lett.* **75**, 3309–3311 (1999).
23. K.De Jong and J.W. Geus, Carbon nanofibers: catalytic synthesis and applications, *Catal. Rev. Sci. Eng.* **42**, 481–510 (2000).
24. C.T. Kingston and B. Simard, Fabrication of carbon nanotubes, *Anal. Lett.* **36**, 3119–3145 (2003).
25. C. Journet, W.K. Maser, P. Bernier, A. Loiseau, M. Lamy de la Chapelle, S. Lefrant, P. Deniard, R. Lee, and J.E. Fischer, Large-scale production of single-walled carbon nanotubes by the electric-arc technique, *Nature* **388**, 756–758 (1997).
26. Z. Shi, Y. Lian, X. Zhou, Z. Gu, Y. Zhang, S. Iijima, L. Zhou, K.T. Yue, and S. Zhang, Mass-production of single wall carbon nanotubes by arc discharge method, *Carbon* **37**, 1449–1453 (1999).
27. M. Takizawa, S. Bandow, M. Yudasaka, Y. Ando, H. Shimoyama, and S. Iijima, Change of tube diameter distribution of single-wall carbon nanotubes induced by changing the bimetallic ratio of Ni and Y catalysts, *Chem. Phys. Lett.* **326**, 351–357 (2000).
28. M. Cadek, R. Murphy, B. McCarthy, A. Drury, B. Lahr, R.C. Barklie, M. in het Panhuis, J.N. Coleman, and W.J. Blau, Optimization of the arc-discharge production of multi-wall carbon nanotubes, *Carbon* **40**, 923–928 (2002).
29. A.V. Krestinin, N.A. Kiselev, A.V. Raevskii, A.G. Ryabenko, D.N. Zakharov, and G.I. Zvereva, Perspectives of single-wall carbon nanotube production in the arc discharge process, *Euras. Chem. Tech. J.* **5**, 7–18 (2003).
30. T. Guo, P. Nikolaev, A. Thess, D.T. Colbert, and R.E. Smalley, Catalytic growth of single-walled nanotubes by laser vaporization, *Chem. Phys. Lett.* **243**, 49–54 (1995).
31. M. Yudasaka, T. Komatsu, T. Ichihashi, and S. Iijima, Single-wall carbon nanotube formation by laser ablation using double-targets of carbon and metal, *Chem. Phys. Lett.* **278**, 102–106 (1997).
32. O. Jost, A.A. Gorbunov, J. Möller, W. Pompe, A. Graff, R. Friedlein, X. Liu, M.S. Golden, and J. Fink, Impact of catalyst coarsening on the formation of single-wall carbon nanotubes, *Chem. Phys. Lett.* **339**, 297–304 (2001).
33. D.T. Colbert and R.E. Smalley, Past, present and future of fullerene nanotubes: buckytubes. *Perspectives of Fullerene Nanotechnology*. Ed. E. Osawa. Kluwer Academic Publishers, 2002, pp. 3–10.
34. W.K. Maser, A.M. Benito, and M.T. Martínez, Production of carbon nanotubes: the light approach, *Carbon* **40**, 1685–1695 (2002).
35. D. Laplaze, P. Bernier, W.K. Maser, G. Flamant, T. Guillard, and A. Loiseau, Carbon nanotubes: the solar approach, *Carbon* **36**, 685–688 (1998).
36. M.V. Antisari, R. Marazzi, and R. Krsmanovic, Synthesis of multiwall carbon nanotubes by electric arc discharge in liquid environments, *Carbon* **41**, 2393–2401 (2003).
37. N. Sano, J. Nakano, and T. Kanki, Synthesis of single-walled carbon nanotubes with nanohorns by arc in liquid nitrogen, *Carbon* **42**, 686–688 (2004).
38. Y.L. Hsin, K.C. Hwang, F.-R. Chen, and J.-J. Kai, Production and in-situ metal filling of carbon nanotubes in water, *Adv. Mater.* **13**, 830–833 (2001).
39. H.W. Zhu, X.S. Li, B. Jiang, C.L. Xu, Y.F. Zhu, D.H. Wu, and X.H. Chen, Formation of carbon nanotubes in water by the electric-arc technique, *Chem. Phys. Lett.* **366**, 664–669 (2002).
40. K. Shimotani, K. Anazawa, H. Watanabe, and M. Shimizu, New synthesis of multi-walled carbon nanotubes using an arc discharge technique under organic molecular atmospheres, *Appl. Phys.* **73 A**, 451–454 (2001).

41. V.A. Ryzhkov, On producing carbon nanotubes by a self-regulated electric contact arc discharge in hydrocarbon liquids. *NANOTUBE'02 Workshop*, Abstr. P-103 [<http://dielc.kaist.ac.kr/nt02/abstracts/P103.shtml>].
42. V.A. Ryzhkov, Use of self-regulated arc discharge in hydrocarbon liquids for bulk production of carbon nanotubes, *Int. Conf. Sci. Applic. Nanotubes 2003*, July 7–11, 2003, Seoul, Korea [<http://nt03.skku.ac.kr/abstract/view.html?idx=NTqRCh4KAnABY>].
43. Y. Gogotsi, J.A. Libera, and M. Yoshimura, Hydrothermal synthesis of multiwall carbon nanotubes, *J. Mater. Res.* **15**, 2591–2594 (2000).
44. J.A. Libera and Y. Gogotsi, Hydrothermal synthesis of graphite tubes using Ni catalyst, *Carbon* **39**, 1307–1318 (2001).
45. D.C. Lee, F.V. Mikulec, and B.A. Korgel, Carbon nanotube synthesis in supercritical toluene, *J. Am. Chem. Soc.* **126**, 4951–4957 (2004).
46. P. Nikolaev, M.J. Bronikowski, R.K. Bradley, F. Rohmumnd, D.T. Colbert, K.A. Smith, and R.E. Smalley, Gas-phase catalytic growth of single-walled carbon nanotubes from carbon monoxide, *Chem. Phys. Lett.* **313**, 91–97 (1999).
47. R. Andrews, D. Jacques, D. Qian, and T. Rantell, Multiwall carbon nanotubes: synthesis and application, *Acc. Chem. Res.* **35**, 1008–1017 (2002).
48. H. Dai, Carbon nanotubes: synthesis, integration, and properties, *Acc. Chem. Res.* **35**, 1035–1044 (2002).
49. K.B.K. Teo, C. Singh, M. Chhowalla, and W.I. Milne, Catalytic synthesis of carbon nanofibers. *Encyclopedia of Nanoscience and Nanotechnology*. Ed. H.S. Nalwa. Vol. 10, American Sci. Pub. 2003, pp. 1–22.
50. S. Maruyama, R. Kojima, Y. Miyauchi, S. Chiashi, and M. Kohno, Low-temperature synthesis of high-purity single-walled carbon nanotubes from alcohol, *Chem. Phys. Lett.* **360**, 229–234 (2002).
51. CoMoCat Process (University of Oklahoma, School Chem. Eng. Mater. Sci.) [<http://www.ou.edu/engineering/nanotube/comocat.html>].
52. M. Kusunoki, T. Suzuki, C. Honjo, T. Hirayama, and N. Shibata, Selective synthesis of zigzag-type aligned carbon nanotubes on SiC (000-1) wafers, *Chem. Phys. Lett.* **366**, 458–462 (2002).
53. T. Nagano, Y. Ishikawa, and N. Shibata, Preparation of silicon-on-insulator substrate on large free-standing carbon nanotube film formation by surface decomposition of SiC film, *Jpn. J. Appl. Phys.* **42**, 1717–1721 (2003).
54. Y.L. Li, Y.D. Yu, and Y. Liang, A novel method for synthesis of carbon nanotubes: low temperature solid pyrolysis, *J. Mater. Res.* **12**, 1678–1680 (1997).
55. S. Maruyama, Y. Miyauchi, T. Edamura, Y. Igarashi, S. Chiashi, and Y. Murakami, Synthesis of single-walled carbon nanotubes with narrow diameter-distribution from fullerene, *Chem. Phys. Lett.* **375**, 553–559 (2003).
56. T.S. Wong, C.T. Wang, K.H. Chen, L.C. Chen, and K.J. Ma, Carbon nanotube growth by rapid thermal processing, *Diamond Rel. Mater.* **10**, 1810–1813 (2001).
57. R. Katoh, Y. Tasaka, E. Sekreta, M. Yumura, F. Ikazaki, Y. Kakudate, and S. Fujiwara, Sonochemical production of a carbon nanotube. *Ultrason. Sonochem.* **6**, 185–187 (1999).
58. F. Fabry, T.M. Gruenberger, J. Gonzalez-Aguilar, H. Okuno, E. Grivei, N. Probst, L. Fulcheri, G. Flamant, and J.-C. Charlier, Continuous mass production of carbon nanotubes by 3-phase AC plasma processing, *Nanotech 2004, Vol. 3, Techn. Proc. of the 2004 NSTI Nanotechnology Conf. and Trade Show*, 228–231 (2004). March 7–11, Boston Sheraton Hotel & Copley Convention Center, Boston, MA.
59. Z. Jia, Z. Wang, J. Liang, B. Wei, and D. Wu, Production of short multi-walled carbon nanotubes, *Carbon* **37**, 903–906 (1999).
60. E. Farkas, M.E. Anderson, Z. Chen, and A.G. Rinzler, Length sorting *cut* single wall carbon nanotubes by high performance liquid chromatography, *Chem. Phys. Lett.* **363**, 111–116 (2002).
61. E. Borowiak-Palen, T. Pichler, X. Liu, M. Knupfer, A. Graff, O. Jost, W. Pompe, R.J. Kalenczuk, and J. Fink, Reduced diameter distribution of single-wall carbon nanotubes by selective oxidation, *Chem. Phys. Lett.* **363**, 567–572 (2002).
62. C. Bower, A. Kleinhammes, Y. Wu, and O. Zhou, Intercalation and partial exfoliation of single-walled carbon nanotubes by nitric acid, *Chem. Phys. Lett.* **288**, 481–486 (1998).
63. K.H. An, K.K. Jeon, J.-M. Moon, S.J. Eum, C.W. Yang, G.-S. Park, C.Y. Park, and Y.H. Lee, Transformation of singlewalled carbon nanotubes to multiwalled carbon nanotubes and onion-like structures by nitric acid treatment, *Synt. Met.* **140**, 1–8 (2004).
64. K.B. Shelimov, R.O. Esenaliev, A.G. Rinzler, C.B. Huffman, and R.E. Smalley, Purification of single-wall carbon nanotubes by ultrasonically assisted filtration, *Chem. Phys. Lett.* **282**, 429–434 (1998).

65. A. Kukovecz, Ch. Kramberger, M. Holzinger, H. Kuzmany, J. Schalko, M. Mannsberger, and A. Hirsch, On the stacking behavior of functionalized single-wall carbon nanotubes, *J. Phys. Chem. B* **106**, 6374–6380 (2002).
66. J. Liu, A.G. Rinzler, H. Dai, J.H. Hafner, R.K. Bradley, P.J. Boul, A. Lu, T. Iverson, K. Shelimov, C.B. Huffman, F. Rodriguez-Macias, Y.-S. Shon, T.R. Lee, D.T. Colbert, and R.E. Smalley, Fullerene pipes, *Science* **280**, 1253–1255 (1998).
67. Y. Yang, J. Zhang, X. Nan, and Z. Liu, Toward the chemistry of carboxylic single-walled carbon nanotubes by chemical force microscopy, *J. Phys. Chem. B* **106**, 4139–4144 (2002).
68. Y. Yang, H. Zou, B. Wu, Q. Li, J. Zhang, Z. Liu, X. Guo, and Z. Du, Enrichment of large-diameter single-walled carbon nanotubes by oxidative acid treatment, *J. Phys. Chem. B* **106**, 7160–7162 (2002).
69. J. Chen, C. Xu, Z. Mao, G. Chen, B. Wei, J. Liang, and D. Wu, Fabrication of Pt deposited on carbon nanotubes and performance of its polymer electrolyte membrane fuel cells, *Sci. China* **45**, 82–86 (2002).
70. F. Simon, Á. Kukovecz, and H. Kuzmany, Controlled oxidation of single-wall carbon nanotubes: a Raman study, *AIP Conf. Proc.* **685**, No. 1, 185–188 (2003).
71. Y. Feng, G. Zhou, G. Wang, M. Qu, and Z. Yu, Removal of some impurities from carbon nanotubes, *Chem. Phys. Lett.* **375**, 645–648 (2003).
72. B.C. Satishkumar, A. Govindaraj, J. Mofokeng, G.N. Subbanna, and C.N.R. Rao. Novel experiments with carbon nanotubes: opening, filling, closing and functionalizing, *J. Phys. B* **29**, 4925–4934 (1996).
73. N.I. Kovtyukhova, T.E. Mallouk, L. Pan, and E.C. Dickey, Individual single-walled nanotubes and hydrogels made by oxidative exfoliation of carbon nanotube ropes, *J. Am. Chem. Soc.* **125**, 9761–9769 (2003).
74. J.M. Skowroński, P. Scharff, N. Pfänder, and S. Cui, Room temperature electrochemical opening of carbon nanotubes followed by hydrogen storage, *Adv. Mater.* **15**, 55–57 (2003).
75. T. Ito, L. Sun, and R.M. Crooks, Electrochemical etching of individual multiwall carbon nanotubes, *Electrochem. Solid-State Lett.* **6**, C4–C7 (2003).
76. J.-Y. Chang, A. Ghule, J.-J. Chang, S.-H. Tzing, and Y.-C. Ling, Opening and thinning of multiwall carbon nanotubes in supercritical water, *Chem. Phys. Lett.* **363**, 583–590 (2002).
77. S. Nagasawa, M. Yudasaka, K. Hirahara, T. Ichihashi, and S. Iijima, Effect of oxidation on single-wall carbon nanotubes, *Chem. Phys. Lett.* **328**, 374–380 (2000).
78. E. Borowiak-Palen, X. Liu, T. Pichler, M. Knupfer, J. Fink, and O. Jost, Diameter control of single-walled carbon nanotubes by selective oxidation, *NANOTUBE'02 Workshop*, Sa-RS2-Sy46, Log Number: P-53 [<http://dielc.kaist.ac.kr/nt02/abstracts/P53.shtml>].
79. J.-M. Moon, K.H. An, Y.H. Lee, Y.S. Park, D.J. Bae, and G.-S. Park, High-yield purification process of singlewalled carbon nanotubes, *J. Phys. Chem. B* **105**, 5677–5681 (2001).
80. P.X. Hou, S. Bai, Q.H. Yang, C. Liu, and H.M. Cheng, Multi-step purification of carbon nanotubes, *Carbon* **40**, 81–85 (2002).
81. E. Vázquez, V. Georgakilas, and M. Prato, Microwave-assisted purification of HiPCO carbon nanotubes, *Chem. Commun.* 2308–2309 (2002).
82. C.-M. Yang, K. Kaneko, M. Yudasaka, and S. Iijima, Effect of purification on pore structure of HiPco single-walled carbon nanotube aggregates, *Nano Lett.* **2**, 385–388 (2002).
83. C. Xu, E. Flahaut, S.R. Bailey, G. Brown, J. Sloan, K.S. Coleman, V.C. Williams, and M.L.H. Green, Purification of single-walled carbon nanotubes grown by a chemical vapour deposition (CVD) method, *Chem. Res. Chinese Univ.* **18**, 130–132 (2002).
84. S. Gajewski, H.-E. Maneck, U. Knoll, D. Neubert, I. Dörfel, R. Mach, B. Strauß, and J.F. Friedrich, Purification of single walled carbon nanotubes by thermal gas phase oxidation, *Diamond Rel. Mater.* **12**, 816–820 (2003).
85. I.W. Chiang, B.E. Brinson, R.E. Smalley, J.L. Margrave, and R.H. Hauge, Purification and characterization of single-wall carbon nanotubes, *J. Phys. Chem. B* **105**, 1157–1161 (2001).
86. I.W. Chiang, B.E. Brinson, A.Y. Huang, P.A. Willis, M.J. Bronikowski, J.L. Margrave, R.E. Smalley, and R.H. Hauge, Purification and characterization of single-wall carbon nanotubes (SWNTs) obtained from gas-phase decomposition of CO (HiPco process), *J. Phys. Chem. B* **105**, 8297–8301 (2001).
87. T. Jeong, W.-Y. Kim, and Y.-B. Hahn, A new purification method of single-wall carbon nanotubes using H<sub>2</sub>S and O<sub>2</sub> mixture gas, *Chem. Phys. Lett.* **344**, 18–22 (2001).
88. T. Jeong, T.H. Kim, W.-Y. Kim, K.-H. Lee, and Y.-B. Hahn, High yield purification of carbon nanotubes with H<sub>2</sub>S–O<sub>2</sub> mixture, *Korean J. Chem. Eng.* **19**, 519–523 (2002).
89. S. Huang and L. Dai, Plasma etching for purification and controlled opening of aligned carbon nanotubes, *J. Phys. Chem. B* **106**, 3543–3545 (2002).



90. J.G. Wiltshire, A.N. Khlobystov, L.J. Li, S.G. Lyapin, G.A.D. Briggs, and R.J. Nicholas, Comparative studies on acid and thermal based selective purification of HiPCO produced single-walled carbon nanotubes, *Chem. Phys. Lett.* **386**, 239–243 (2004).
91. E. Mizoguti, F. Nihey, M. Yudasaka, S. Iijima, T. Ichihashi, and K. Nakamura, Purification of single-wall carbon nanotubes by using ultrafine gold particles, *Chem. Phys. Lett.* **321**, 297–301 (2000).
92. C.-Y. Moon, Y.-S. Kim, E.-C. Lee, Y.-G. Jin, and K.J. Chang, Mechanism for oxidative etching in carbon nanotubes, *Phys. Rev. B* **65**, 155401.1–4 (2002).
93. D. Bom, R. Andrews, D. Jacques, J. Anthony, B. Chen, M.S. Meier, and J.P. Selegue, Thermogravimetric analysis of the oxidation of multiwalled carbon nanotubes: evidence for the role of defect sites in carbon nanotube chemistry, *Nano Lett.* **2**, 615–619 (2002).
94. E.G. Rakov, I.G. Ivanov, S.N. Blinov, N.V. Kazakov, V.V. Skudin, N.G. Digurov, and A.K. Bogdanovich, Kinetics of carbon multi-wall nanotube synthesis by catalytic pyrolysis of methane, *Fullerenes Nanotubes Carbon Nanostruct.* **12**, 29–32 (2004).
95. Summary of oxidation studies pertinent to soot and carbon solids [<http://me.lsu.edu/~mechar/current/sootoxid.html>].
96. D.B. Mawhinney, V. Naumenko, A. Kuznetsova, J.T. Yates, Jr., J. Liu, and R.E. Smalley, Infrared spectral evidence for the etching of carbon nanotubes: ozone oxidation at 298 K, *J. Am. Chem. Soc.* **122**, 2383–2384 (2000).
97. X. Lu, L. Zhang, X. Xu, N. Wang, and Q. Zhang, Can the sidewalls of single-wall carbon nanotubes be ozonized? *J. Phys. Chem. B* **106**, 2136–2139 (2002).
98. K. Hernadi, A. Siska, L. Thiên-Nga, L. Forró, and I. Kiricsi, Reactivity of different kinds of carbon during oxidative purification of catalytically prepared carbon nanotubes, *Solid State Ionics* **141–142**, 203–209 (2001).
99. S. Banerjee and S.S. Wong, Rational sidewall functionalization and purification of single-walled carbon nanotubes by solution-phase ozonolysis, *J. Chem. Phys.* **106**, 12144–12151 (2002).
100. S. Banerjee, M.G.C. Kahn, and S.S. Wong, Rational chemical strategies for carbon nanotube functionalization, *Chem. Eur. J.* **9**, 1898–1908 (2003).
101. O. Byl, P. Kondratyuk, S.T. Forth, S.A. FitzGerald, L. Chen, J.K. Johnson, and J.T. Yates, Jr., Adsorption of CF<sub>4</sub> on the internal and external surfaces of opened single-walled carbon nanotubes: a vibrational spectroscopy study, *J. Am. Chem. Soc.* **125**, 5889–5896 (2003).
102. M.R. Smith, S.W. Hedges, R. LaCount, D. Kern, N. Shah, G.P. Huffman, and B. Bockrath, Selective oxidation of single-walled carbon nanotubes using carbon dioxide, *Carbon* **41**, 1221–1230 (2003).
103. O.P. Gorelik, P. Nikolaev, and S. Arepalli, Purification procedures for single-wall carbon nanotubes, *Report NASA/CR-2000-208926*, 2001, p. 64 [<http://mmtpdpublic.jsc.nasa.gov/hscnano/CR-2000-208926.pdf>].
104. H. Huang, H. Kajiura, A. Yamada, and M. Ata, Purification and alignment of arc-synthesis single-walled carbon nanotube bundles, *Chem. Phys. Lett.* **356**, 567–572 (2002).
105. K.L. Strong, D.P. Anderson, K. Lafdi, and J.N. Kuhn, Purification process for single-wall carbon nanotubes, *Carbon* **41**, 1477–1488 (2003).
106. L. Vaccarini, C. Goze, R. Aznar, V. Micholet, C. Journet, and P. Bernier, Purification procedure of carbon nanotubes, *Synt. Met.* **103**, 2492–2493 (1999).
107. M.T. Martinez, M.A. Callejas, A.M. Benito, W.K. Maser, M. Cochet, J.M. Andrés, J. Schreiber, O. Chauvet, and J.L.G. Fierro, Microwave single walled carbon nanotubes purification, *Chem. Commun.* 1000–1001 (2002).
108. F. Li, H.M. Cheng, Y.T. Xing, P.H. Tan, and G. Su, Purification of single-walled carbon nanotubes synthesized by the catalytic decomposition of hydrocarbons, *Carbon* **38**, 2041–2045 (2000).
109. J.-F. Colomer, P. Piedigrosso, I. Willems, C. Journet, P. Bernier, G. Van Tendeloo, A. Fonseca, and J.B. Nagy, Purification of catalytically produced multi-wall carbon nanotubes, *J. Chem. Soc. Faraday Trans.* **94**, 3753–3758 (1998).
110. J.-F. Colomer, P. Piedigrosso, A. Fonseca, and J.B. Nagy, Different purification methods of carbon nanotubes produced by catalytic synthesis, *Synth. Met.* **103**, 2482–2483 (1999).
111. S.R.C. Vivekchand and A. Govindaraj, A new method of preparing single-walled carbon nanotubes, *Proc. Indian Acad. Sci.* **115**, 509–518 (2003).
112. Y. Sato, T. Ogawa, K. Motomiya, K. Shinoda, B. Jeyadevan, K. Tohji, A. Kasuya, and Y. Nishina, Purification of MWNTs combining wet grinding, hydrothermal treatment, and oxidation, *J. Phys. Chem. B* **105**, 3387–3392 (2001).

113. H. Kajiura, S. Tsutsui, H. Huang, and Y. Murakami, High-quality single-walled carbon nanotubes from arc-produced soot, *Chem. Phys. Lett.* **364**, 586–592 (2002).
114. W.-K. Choi, S.-G. Park, H. Takahashi, and T.-H. Cho, Purification of carbon nanofibers with hydrogen peroxide, *Synth. Met.* **139**, 39–42 (2003).
115. M.E. Itkis, S. Niyogi, M.E. Meng, M.A. Hamon, H. Hu, and R.C. Haddon, Spectroscopic study of the Fermi level electronic structure of single-walled carbon nanotubes, *Nano Lett.* **2**, 155–159 (2002).
116. H. Kuzmany, A. Kukovecz, F. Simon, M. Holzweber, Ch. Kramberger, and T. Pichler, Functionalization of carbon nanotubes, *Synth. Met.* **141**, 113–122 (2004).
117. K. Esumi, M. Ishigami, A. Nakajima, K. Sawada, and H. Honda, Chemical treatment of carbon nanotubes, *Carbon* **34**, 279–281 (1996).
118. M.A. Hamon, J. Chen, H. Hu, Y. Chen, M.E. Itkis, A.M. Rao, P.C. Eklund, and R.C. Haddon, Dissolution of single-walled carbon nanotubes, *Adv. Mater.* **11**, 834–840 (1999).
119. A. Kuznetsova, I. Popova, J.T. Yates Jr., M.J. Bronikowski, C.B. Huffman, J. Liu, R.E. Smalley, H.H. Hwu, and J.G. Chen, Oxygen-containing functional groups on single-wall carbon nanotubes: NEXAFS and vibrational spectroscopic studies, *J. Am. Chem. Soc.* **123**, 10699–10704 (2001).
120. M.A. Hamon, H. Hu, P. Bhowmik, S. Niyogi, B. Zhao, M.E. Itkis, and R.C. Haddon, End-group and defect analysis of soluble single-walled carbon nanotubes, *Chem. Phys. Lett.* **347**, 8–12 (2001).
121. D.B. Mawhiney, V. Naumenko, A. Kuznetsova, J.T. Yates Jr., J. Liu, and R.E. Smalley, Surface defect site density on single walled carbon nanotubes by titration, *Chem. Phys. Lett.* **324**, 213–216 (2000).
122. J. Chen, A.M. Rao, S. Lyuksyutov, M.E. Itkis, M.A. Hamon, H. Hu, R.W. Cohn, P.C. Eklund, D.T. Colbert, R.E. Smalley, and R.C. Haddon, Dissolution of full-length single-walled carbon nanotubes, *J. Phys. Chem. B* **105**, 2525–2528 (2001).
123. H. Hu, P. Bhowmik, B. Zhao, M.A. Hamon, M.E. Itkis, and R.C. Haddon, Determination of the acidic sites of purified single-walled carbon nanotubes by acid-base titration, *Chem. Phys. Lett.* **345**, 25–28 (2001).
124. L. Liu, Y. Qin, Z.-X. Guo, and D. Zhu, Reduction of solubilized multi-walled carbon nanotubes, *Carbon* **41**, 331–335 (2003).
125. W. Zhao, C. Song, and P.E. Pehrsson, Water-soluble and optically pH-sensitive single-walled carbon nanotubes from surface modification, *J. Am. Chem. Soc.* **124**, 12418–12419 (2002).
126. M. Sano, A. Kamino, J. Okamura, and S. Shinkai, Ring closure of carbon nanotubes, *Science* **293**, 1299–1301 (2001).
127. J. Chen, M.A. Hamon, H. Hu, Y. Chen, A.M. Rao, P.C. Eklund, and R.C. Haddon, Solution properties of single-walled carbon nanotubes, *Science* **282**, 95–98 (1998).
128. B. Zhao, H. Hu, S. Niyogi, M.E. Itkis, M.A. Hamon, P. Bhowmik, M.S. Meier, and R.C. Haddon, Chromatographic purification and properties of soluble single-walled carbon nanotubes, *J. Am. Chem. Soc.* **123**, 11673–11677 (2001).
129. V. Skakalova, U. Dettlaff-Weglikowska, and S. Roth, Gamma-irradiated and functionalized single wall nanotubes, *Diamond Rel. Mater.* **13**, 296–298 (2004).
130. J.E. Riggs, Z. Guo, D.L. Carroll, and Y.-P. Sun, Strong luminescence of solubilized carbon nanotubes. *J. Am. Chem. Soc.* **122**, 5879–5880 (2000).
131. J.E. Riggs, D.B. Walker, D.L. Carroll, and Y.-P. Sun, Optical limiting properties of suspended and solubilized carbon nanotubes, *J. Phys. Chem. B* **104**, 7071–7076 (2000).
132. Y. Lin, A.M. Rao, B. Sadanadan, E.A. Kenik, and Y.-P. Sun, Functionalizing multiple-walled carbon nanotubes with aminopolymers, *J. Phys. Chem. B* **106**, 1294–1298 (2002).
133. I. Yamaguchi and T. Yamamoto, Soluble self-doped single-walled carbon nanotube, *Mater. Lett.* **58**, 598–603 (2004).
134. B. Philip, J. Xie, A. Chandrasekhar, J. Abraham, and V.K. Varadan, A novel nanocomposite from multiwalled carbon nanotubes functionalized with a conducting polymer, *Smart Mater. Struct.* **13**, 295–298 (2004).
135. Y.-P. Sun, W. Huang, Y. Lin, K. Fu, A. Kitaygorodsky, L.A. Riddle, Y.J. Yu, and D.L. Carroll, Soluble dendron-functionalized carbon nanotubes: preparation, characterization and properties, *Chem. Mater.* **13**, 2864–2869 (2001).
136. K. Fu, W. Huang, Y. Lin, L.A. Riddle, D.L. Carroll, and Y.-P. Sun, Defunctionalization of functionalized carbon nanotubes, *Nano Lett.* **1**, 439–441 (2001).
137. Y.-P. Sun, B. Zhou, K. Henbest, K. Fu, W. Huang, Y. Lin, S. Taylor, and D.L. Carroll, Luminescence anisotropy of functionalized carbon nanotubes in solution, *Chem. Phys. Lett.* **351**, 349–353 (2002).

138. M.A. Hamon, H. Hui, P. Bhowmik, M.E. Itkis, and R.C. Haddon, Ester-functionalized soluble single-walled carbon nanotubes, *Appl. Phys. A* **74**, 333–338 (2002).
139. D.E. Hill, Y. Lin, L.F. Allard, and Y.-P. Sun, Solubilization of carbon nanotubes via polymer attachment, *Int. J. Nanosci.* **1**, 213–221 (2002).
140. S. Qin, D. Qin, W.T. Ford, D.E. Resasco, and J.E. Herrera, Polymer brushes on single-walled carbon nanotubes by atom transfer radical polymerization of *n*-butyl methacrylate, *J. Am. Chem. Soc.* **126**, 170–176 (2004).
141. M. Alvaro, P. Atienzar, P. de la Cruz, J.L. Delgado, H. Garcia, and F. Langa, Synthesis and photochemistry of soluble, pentyl ester-modified single wall carbon nanotube, *Chem. Phys. Lett.* **386**, 342–345 (2004).
142. A.M. Bond, W. Miao, and C.L. Raston, Mercury(II) immobilized on carbon nanotubes: synthesis, characterization, and redox properties, *Langmuir* **16**, 6004–6012 (2000).
143. Y.-H. Li, J. Ding, Z. Luan, Z. Di, Y. Zhu, C. Xu, D. Wu, and B. Wei, Competitive adsorption of  $Pb^{2+}$ ,  $Cu^{2+}$  and  $Cd^{2+}$  ions from aqueous solutions by multiwalled carbon nanotubes, *Carbon* **41**, 2787–2792 (2003).
144. G. Arabale, D. Wagh, M. Kulkarni, I.S. Mulla, S.P. Vernekar, K. Vijayamohan, and A.M. Rao, Enhanced supercapacitance of multiwalled carbon nanotubes functionalized with ruthenium oxide, *Chem. Phys. Lett.* **376**, 207–213 (2003).
145. S. Banerjee and S.S. Wong, Functionalization of carbon nanotube with a metal-containing molecular complex, *Nano Lett.* **2**, 49–53 (2002).
146. S. Banerjee and S.S. Wong, Structural characterization, optical properties, and improved solubility of carbon nanotubes functionalized with Wilkinson's catalyst, *J. Am. Chem. Soc.* **124**, 8940–8948 (2002).
147. S. Banerjee and S.S. Wong, Synthesis and characterization of carbon nanotube-nanocrystal heterostructures, *Nano Lett.* **2**, 195–200 (2002).
148. S. Banerjee and S.S. Wong, In situ quantum dot growth on multiwalled carbon nanotubes, *J. Am. Chem. Soc.* **125**, 10342–10350 (2003).
149. M. Aizawa and M.S.P. Shaffer, Silylation of multi-walled carbon nanotubes, *Chem. Phys. Lett.* **368**, 121–124 (2003).
150. J.H. Rouse and P.T. Lillehei, Electrostatic assembly of polymer/single walled carbon nanotube multilayer films, *Nano Lett.* **3**, 59–62 (2003).
151. C. Velasco-Santos, A.L. Martínez-Hernández, M. Lozada-Cassou, A. Alvarez-Castillo, and V.M. Castaño, Chemical functionalization of carbon nanotubes through an organosilane, *Nanotechnology* **13**, 495–498 (2002).
152. J.G. Smith Jr., K.A. Watson, C.M. Thompson, and J.W. Connell, Carbon nanotube/space durable polymer nanocomposite films for electrostatic charge dissipation, p. 12, 2002 [<http://techreport.larc.nasa.gov/ltrs/PDF/2002/mtg/NASA-2002-34sampe-jgs.pdf>].
153. B. Wu, J. Zhang, Z. Wei, S. Cai, and Z. Liu, Chemical alignment of oxidatively shortened single-walled carbon nanotubes on silver surface, *J. Phys. Chem. B* **105**, 5075–5078 (2002).
154. X.-L. Nan, J. Zhang, Z.-F. Liu, Z.-J. Shi, and Z.-N. Gu, Patterned assembly of shortened single-walled carbon nanotubes on gold surface, *Acta Phys. Chim. Sin.* **17** (5), 393–396 (2001).
155. X. Nan, Z. Gu, and Z. Liu, Immobilizing shortened single-walled carbon nanotubes (SWNTs) on gold using a surface condensation method, *J. Colloid Interf. Sci.* **245**, 311–318 (2002).
156. S.S. Wong, A.T. Woolley, E. Joselevich, and C.M. Lieber, Functionalization of carbon nanotube AFM probes using tip-activated gases, *Chem. Phys. Lett.* **306**, 219–225 (1999).
157. S.S. Wong, E. Joselevich, A.T. Woolley, C.L. Cheung, and C.M. Lieber, Covalently functionalized nanotubes as nanometre-sized probes in chemistry and biology, *Nature* **394**, 52–55 (1998).
158. S.S. Wong, A.T. Woolley, E. Joselevich, C.L. Cheung, and C.M. Lieber, Covalently-functionalized single-walled carbon nanotube probe tips for chemical force microscopy, *J. Am. Chem. Soc.* **120**, 8557–8558 (1998).
159. M. Sano, A. Kamino, and S. Shinkai, Activation of hydroxyl groups on carbon nanotubes by thermal treatment in air, *NANOTUBE'02 Workshops Sa-P71-Sy17*. Log Number: P160 [<http://dielc.kaist.ac.kr/nt02/abstracts/P160.shtml>].
160. T. Kyotani, S. Nakazaki, W.-H. Xu, and A. Tomita, Chemical modification of the inner walls of carbon nanotubes by  $HNO_3$  oxidation, *Carbon* **39**, 771–785 (2001).
161. A. Kuznetsova, D.B. Mawhinney, V. Naumenko, J.T. Yates Jr., J. Liu, and R.E. Smalley. Enhancement of adsorption inside of single-walled nanotubes: opening the entry ports, *Chem. Phys. Lett.* **321**, 292–296 (2000).

162. T. Nakajima, N. Watanabe, I. Kameda, and M. Endo, Preparation and electrical conductivity of fluorine-graphite fiber intercalation compound, *Carbon* **24**, 343–351 (1986).
163. T. Nakajima, S. Kasamatsu, and Y. Matsuo, Synthesis and characterization of fluorinated carbon nanotubes, *Eur. J. Solid State Inorg. Chem.* **33**, 831–840 (1996).
164. A. Hamwi, H. Alvergnat, S. Bonnamy, and F. Béguin, Fluorination of carbon nanotubes, *Carbon* **35**, 723–728 (1997).
165. A. Hamwi, P. Gendrand, H. Gaucher, S. Bonnamy, and F. Béguin, Electrochemical properties of carbon nanotube fluorides in a lithium cell system, *Mol. Cryst. Liq. Cryst.* **310**, 185–190 (1998).
166. A.V. Okotrub, N.F. Yudanov, A.L. Chuvilin, I.P. Asanov, Yu.V. Shubin, L.G. Bulusheva, A.V. Gusel'nikov, and I.S. Fyodorov, Fluorinated cage multiwall carbon nanoparticles, *Chem. Phys. Lett.* **322**, 231–236 (2000).
167. H. Touhara and F. Okino, Property control of carbon material by fluorination, *Carbon* **38**, 241–267 (2000).
168. Y. Hattori, Y. Watanabe, S. Kawasaki, F. Okino, B.K. Pradhan, T. Kyotani, A. Tomita, and H. Touhara, Carbon-alloying of the rear surfaces of nanotubes by direct fluorination, *Carbon* **37**, 1033–1038 (1999).
169. E.T. Mickelson, C.B. Huffman, A.G. Rinzler, R.E. Smalley, R.H. Hauge, and J.L. Margrave, Fluorination of single-wall carbon nanotubes, *Chem. Phys. Lett.* **296**, 188–194 (1998).
170. I.W. Chiang, E.T. Mickelson, P.J. Boul, R.H. Hauge, R.E. Smalley, and J.L. Margrave, Fluorination, defluorination, and derivatization of single-wall carbon nanotubes, *Abstr. Pap. — Am. Chem. Soc.* **2000**, 220th, IEC-153. Washington, DC, Aug. 20–24, 2000.
171. H. Peng, Z. Gu, J. Yang, J.L. Zimmerman, P.A. Willis, M.J. Bronikowski, R.E. Smalley, R.H. Hauge, and J.L. Margrave, Fluorotubes as cathodes in lithium electrochemical cells, *Nano Lett.* **1**, 625–629 (2001).
172. W. Zhao, C. Song, B. Zheng, J. Liu, and T. Viswanathan, Thermal recovery behavior of fluorinated single-walled carbon nanotubes, *J. Phys. Chem.* **B 106**, 293–296 (2002).
173. P.E. Pehrsson, W. Zhao, J.W. Baldwin, C. Song, J. Liu, S. Kooi, and B. Zheng, Thermal fluorination and healing of single-wall carbon nanotubes, *J. Phys. Chem.* **B 107**, 5690–5695 (2003).
174. Z. Gu, H. Peng, R.H. Hauge, R.E. Smalley, and J.L. Margrave, Cutting single-wall carbon nanotubes through fluorination, *Nano Lett.* **2**, 1009–1013 (2002).
175. Y.S. Lee, T.H. Cho, B.K. Lee, J.S. Rho, K.H. An, and Y.H. Lee, Surface properties of fluorinated single-walled carbon nanotubes, *J. Fluor. Chem.* **120**, 99–104 (2003).
176. P.J. Boul, J. Liu, E.T. Mickelson, C.B. Huffman, L.M. Ericson, I.W. Chiang, K.A. Smith, D.T. Colbert, R.H. Hauge, J.L. Margrave, and R.E. Smalley, Reversible sidewall functionalization of buckytubes, *Chem. Phys. Lett.* **310**, 367–372 (1999).
177. K.F. Kelly, I.W. Chiang, E.T. Mickelson, R.H. Hauge, J.L. Margrave, X. Wang, G.E. Scuseria, C. Radloff, and N.J. Halas, Insight into the mechanism of sidewall functionalization of single-walled nanotubes: an STM study, *Chem. Phys. Lett.* **313**, 445–450 (1999).
178. E.T. Mickelson, I.W. Chiang, J.L. Zimmerman, P.J. Boul, J. Lozano, J. Liu, R.E. Smalley, R.H. Hauge, and J.L. Margrave, Solvation of fluorinated single-wall carbon nanotubes in alcohol solvents, *J. Phys. Chem.* **B 103**, 4318–4322 (1999).
179. V.N. Khabashesku, W.E. Billups, and J.L. Margrave, Fluorination of single-wall carbon nanotubes and subsequent derivatization reactions, *Acc. Chem. Res.* **35**, 1087–1095 (2002).
180. D.V. Kirin, N.N. Breslavskaya, and P.N. D'yachkov, Heterojunctions based on chemically modified carbon nanotubes, *Doklady Phys. Chem.* **374**, 161–166 (2000).
181. H.F. Bettinger, K.N. Kudin, and G.E. Scuseria, Thermochemistry of fluorinated single wall carbon nanotubes, *J. Am. Chem. Soc.* **123**, 12849–12856 (2001).
182. K.N. Kudin, H.F. Bettinger, and G.E. Scuseria, Fluorinated single-wall carbon nanotubes, *Phys. Rev.* **B 63**, 045413.1–8 (2001).
183. T. Hayashi, M. Terrones, C. Scheu, Y.A. Kim, M. Rühle, T. Nakajima, and M. Endo, NanoTeflons: structure and EELS characterization of fluorinated nanotubes and nanofibers, *Nano Lett.* **2**, 491–496 (2002).
184. P.R. Marcoux, J. Schreiber, P. Batail, S. Lefrant, J. Renouard, G. Jacob, D. Albertini, and J.-Y. Mevellec, A spectroscopic study of the fluorination and defluorination reactions on single-walled carbon nanotubes, *Phys. Chem. Phys.* **4**, 2278–2285 (2002).
185. H.F. Bettinger, Experimental and computational investigation of the properties of fluorinated single-walled carbon nanotubes, *Chem. Phys. Chem.* **4**, 1283–1289 (2003).
186. K.H. An, K.A. Park, J.G. Heo, J.Y. Lee, K.K. Jeon, S.C. Lim, C.W. Yang, Y.S. Lee, and Y.H. Lee, Structural transformation of fluorinated carbon nanotubes induced by in situ electron-beam irradiation, *J. Am. Chem. Soc.* **125**, 3057–3061 (2003).

187. K.A. Park, Y.S. Choi, and Y.H. Lee, Atomic and electronic structures of fluorinated single-walled carbon nanotubes, *Phys. Rev. B* **68**, 045429.1–8 (2003).
188. R.L. Jaffe, Quantum chemistry study of fullerene and carbon nanotube fluorination, *J. Phys. Chem. B* **107**, 10378–10388 (2003).
189. H. Geng, R. Rosen, B. Zheng, H. Shimoda, L. Fleming, J. Liu, and O. Zhou, Fabrication and properties of composites of poly(ethylene oxide) and functionalized carbon nanotubes, *Adv. Mater.* **14**, 1387–1390 (2002).
190. R.L. Jaffe, Quantum chemistry study of chemical functionalization reactions of fullerenes and carbon nanotubes, *Proc. Electrochem. Soc.* **12**, 153–162 (1999). Fullerenes Vol. 7: Recent Advances in the Chemistry and Physics of Fullerenes and Related Mater. (12th Int. Symp.), K.M. Kadish, P.V. Kamat, and D.M. Guldi, PV 99–12, Seattle, Washington, Spring 1999.
191. M. Xu, Q. Huang, Q. Chen, P. Guo, and Z. Sun, Synthesis and characterization of octadecylamine grafted multi-walled carbon nanotubes, *Chem. Phys. Lett.* **375**, 598–604 (2003).
192. F. Pompeo and D.E. Resasco, Water solubilization of single-walled carbon nanotubes by functionalization with glucosamine, *Nano Lett.* **2**, 369–373 (2002).
193. L. Liu, S. Zhang, T. Hu, Z.-X. Guo, C. Ye, L. Dai, and D. Zhu, Solubilized multi-walled carbon nanotubes with broadband optical limiting effect, *Chem. Phys. Lett.* **359**, 191–195 (2002).
194. W. Wu, J. Li, L. Liu, L. Yanga, Z.-X. Guo, L. Dai, and D. Zhu, The photoconductivity of PVK-carbon nanotube blends, *Chem. Phys. Lett.* **364**, 196–199 (2002).
195. J. Zhang, G. Wang, Y.-S. Shon, O. Zhou, R. Superfine, and R.W. Murray, Interactions of small molecules and Au nanoparticles with solubilized single-wall carbon nanotubes, *J. Phys. Chem. B* **107**, 3726–3732 (2003).
196. W.-Y. Chen, C.-Y. Chen, K.-Y. Hsu, C.-C. Wang, and Y.-C. Ling, Reaction monitoring of polyaniline film formation on carbon nanotubes with TOF-SIMS, *Appl. Surf. Sci.* **231–232**, 845–849 (2004).
197. M. Álvaro, P. Atienzar, J.L. Bourdelande, and H. García, An organically modified single wall carbon nanotube containing a pyrene chromophore: fluorescence and diffuse reflectance laser flash photolysis study, *Chem. Phys. Lett.* **384**, 119–123 (2004).
198. F. Della Negra, M. Meneghetti, and E. Menna, Microwave-assisted synthesis of a soluble single wall carbon nanotube derivative, *Fullerenes Nanotubes Carbon Nanostruct.* **11**, 25–34 (2003).
199. H.-J. Lee, H. Park, S. Koo, and H. Lee, Vertical alignments of single-walled carbon nanotubes on chemically functionalized silicon substrates [<http://otlf.hanyang.ac.kr/publications/pdf/2003/Vertical%20alignments%20of%20SWNTs%20on%20chemical%20functionalized%20silicon%20substrates.pdf>].
200. M. Sano, A. Kamino, and S. Shinkai, Construction of carbon nanotube “stars” with dendrimers, *Angew. Chem. Int. Edit.* **40**, 4661–4663 (2001).
201. L. Cao, W. Yang, J. Yang, C. Wang, and S. Fu, Hyperbranched poly(amidoamine)-modified multi-walled carbon nanotubes via grafting-from method, *Chem. Lett.* **33**, 490–491 (2004).
202. S. Niyogi, H. Hu, M.A. Hamon, P. Bhowmik, B. Zhao, S.M. Rozenzhak, J. Chen, M.E. Itkis, M.S. Meier, and R.C. Haddon, Chromatographic purification of soluble SWNTs, *J. Am. Chem. Soc.* **123**, 733–734 (2001).
203. P.W. Chiu, G.S. Duesberg, U. Dettlaff-Weglikowska, and S. Roth, Interconnection of carbon nanotubes by chemical functionalization, *Appl. Phys. Lett.* **80**, 3811–3813 (2002).
204. K. Niesz, Z. Kónya, A.A. Koós, L.P. Biró, Á. Kukovecz, and I. Kiricsi, Synthesis procedures for production of carbon nanotube junctions, *AIP Conf. Proc.* **685**, No. 1, 253–256 (2003).
205. J.M. Haremza, M.A. Hahn, T.D. Krauss, S. Chen, and J. Calcines, Attachment of single CdSe nanocrystals to individual single-walled carbon nanotubes, *Nano Lett.* **2**, 1253–1258 (2002).
206. J.G. Smith Jr., J.W. Connell, D.M. Delozier, P.T. Lillehei, K.A. Watson, Y. Lin, B. Zhou, and Y.-P. Sun, Space durable polymer/carbon nanotube films for electrostatic charge mitigation, *Polymer* **45**, 825–836 (2004).
207. D. Chattopadhyay, S. Lastella, S. Kim, and F. Papadimitrakopoulos, Length separation of zwitterion-functionalized single wall carbon nanotubes by GPC, *J. Am. Chem. Soc.* **124**, 728–729 (2002).
208. D. Chattopadhyay, I. Galeska, and F. Papadimitrakopoulos, A route to bulk separation of semiconducting from metallic single-wall carbon nanotubes, *J. Am. Chem. Soc.* **125**, 3370–3375 (2003).
209. F. Gojny, J. Nastalczyk, Z. Roslaniec, and K. Schulte, Surface modified multi-walled carbon nanotubes in CNT/epoxy composites, *Chem. Phys. Lett.* **370**, 820–824 (2003).

210. Z. Liu, Z. Shen, T. Zhu, S. Hou, L. Ying, Z. Shi, and Z. Gu, Organizing single-walled carbon nanotubes on gold using a wet chemical self-assembling technique, *Langmuir* **16**, 3569–3573 (2000).
211. Q. Chen and L. Dai, Plasma patterning of carbon nanotubes, *Appl. Phys. Lett.* **76**, 2719–2721 (2000).
212. Q. Chen, L. Dai, M. Gao, S. Huang, and A. Mau, Plasma activation of carbon nanotubes for chemical modification, *J. Phys. Chem. B* **105**, 618–622 (2001).
213. Y. Sun, S.R. Wilson, and D.I. Schuster, High dissolution and strong light emission of carbon nanotubes in aromatic amine solvents, *J. Am. Chem. Soc.* **123**, 5348–5349 (2001).
214. B. Li, Z. Shi, Y. Lian, and Z. Gu, Aqueous soluble single-wall carbon nanotube, *Chem. Lett.* 2001, 598–599.
215. W. Huang, Y. Lin, S. Taylor, J. Gaillard, A.M. Rao, and Y.-P. Sun, Sonication-assisted functionalization and solubilization of carbon nanotubes, *Nano Lett.* **2**, 231–234 (2002).
216. Z. Kónya, I. Vesselenyi, K. Niesz, A. Kukovecz, A. Demortier, A. Fonseca, J. Delhalle, Z. Mekhalif, J.B. Nagy, A.A. Koós, Z. Osváth, A. Kocsonya, L.P. Biró, and I. Kiricsi, Large scale production of short functionalized carbon nanotubes, *Chem. Phys. Lett.* **360**, 429–435 (2002).
217. E.V. Basiuk, V.A. Basiuk, J.-G. Bañuelos, J.-M. Saniger-Blesa, V.A. Pokrovskiy, T.Yu. Gromovoy, A.V. Mischanchuk, and B.G. Mischanchuk. Interaction of oxidized single-walled carbon nanotubes with vaporous aliphatic amines, *J. Phys. Chem. B* **106**, 1588–1597 (2002).
218. V.A. Basiuk, ONIOM studies of chemical reactions on carbon nanotube tips: effects of the lower theoretical level and mutual orientation of the reactants, *J. Phys. Chem. B* **107**, 8890–8897 (2003).
219. J. Kong and H. Dai, Full and modulated chemical gating of individual carbon nanotubes by organic amine compounds, *J. Phys. Chem. B* **105**, 2890–2893 (2001).
220. F. Hennrich, M.M. Kappes, M.S. Strano, R.H. Hauge, and R.E. Smalley, Infrared analysis of amine treated single-walled carbon nanotubes produced by decomposition of CO, *AIP Conf. Proc.* **685**, No. 1, 197–201 (2003).
221. G. de la Torre, W. Blau, and T. Torres, A survey on the functionalization of single-walled nanotubes. The chemical attachment of phthalocyanine moieties, *Nanotechnology* **14**, 765–771 (2003).
222. Y. Chen, R.C. Haddon, S. Fang, A.M. Rao, P.C. Eklund, W.H. Lee, E.C. Dickey, E.A. Grulke, J.C. Pendergrass, A. Chavan, B.E. Haley, and R.E. Smalley, Chemical attachment of organic functional groups to single-walled carbon nanotube material, *J. Mater. Res.* **13**, 2423–2431 (1998).
223. M. Holzinger, O. Vostrowsky, A. Hirsch, F. Hennrich, M. Kappes, R. Weiss, and F. Jellen, Sidewall functionalization of carbon nanotubes, *Angew. Chem. Int. Edit.* **40**, 4002–4005 (2001).
224. M. Monthieux, Filling single-wall carbon nanotubes, *Carbon* **40**, 1809–1823 (2002).
225. H. Hu, B. Zhao, M.A. Hamon, K. Kamaras, M.E. Itkis, and R.C. Haddon, Sidewall functionalization of single-walled carbon nanotubes by addition of dichlorocarbene, *J. Am. Chem. Soc.* **125**, 14893–14900 (2003).
226. X. Lu, F. Tian, and Q. Zhang, The [2+1] cycloadditions of dichlorocarbene, silylene, germylene, and oxycarbonylnitrene onto the sidewall of armchair (5,5) single-wall carbon nanotube, *J. Phys. Chem. B* **107**, 8388–8391 (2003).
227. M. Holzinger, J. Abraham, P. Whelan, R. Graupner, L. Ley, F. Hennrich, M. Kappes, and A. Hirsch, Functionalization of single-walled carbon nanotubes with (R)-oxycarbonyl nitrenes, *J. Am. Chem. Soc.* **125**, 8566–8580 (2003).
228. J. Abraham, P. Whelan, A. Hirsch, F. Hennrich, M. Kappes, D. Samaille, P. Bernier, A. Vencelová, R. Graupner, and L. Ley, Covalent functionalization of arc discharge, laser ablation and HiPCO single-walled carbon nanotubes, *AIP Conf. Proc.* **685**, No. 1, 291–296 (2003).
229. S. Qin, D. Qin, W.T. Ford, D.E. Resasco, and J.E. Herrera, Functionalization of single-walled carbon nanotubes with polystyrene via grafting to and grafting from methods, *Macromolecules* **37**, 752–757 (2004).
230. V. Georgakilas, K. Kordatos, M. Prato, D.M. Guldi, M. Holzinger, and A. Hirsch, Organic functionalization of carbon nanotubes, *J. Am. Chem. Soc.* **124**, 760–761 (2002).
231. V. Georgakilas, D. Voulgaris, E. Vázquez, M. Prato, D.M. Guldi, Kukovecz, and H. Kuzmany, Purification of HiPCO carbon nanotubes via organic functionalization. *J. Am. Chem. Soc.* **124**, 14318–14319 (2002).
232. N. Tagmatarchis and M. Prato, Functionalization of carbon nanotubes via 1,3-dipolar cycloadditions, *J. Mater. Chem.* **14**, 437–439 (2004).
233. C.A. Dyke and J.M. Tour, Solvent-free functionalization of carbon nanotubes, *J. Am. Chem. Soc.* **125**, 1156–1157 (2003).
234. C.A. Dyke and J.M. Tour, Overcoming the insolubility of carbon nanotubes through high degrees of sidewall functionalization, *Chem. Eur. J.* **10**, 812–817 (2004).

235. J.L. Bahr, J. Yang, D.V. Kosynkin, M.J. Bronikowski, R.E. Smalley, and J.M. Tour, Functionalization of carbon nanotubes by electrochemical reduction of aryl diazonium salts: a bucky paper electrode, *J. Am. Chem. Soc.* **123**, 6536–6542 (2001).
236. J.L. Bahr and J.L. Tour, Highly functionalized carbon nanotubes using in situ generated diazonium compounds, *Chem. Mater.* **13**, 3823–3824 (2001).
237. J.L. Bahr and J.M. Tour, Covalent chemistry of single-wall carbon nanotubes, *J. Mater. Chem.* **12**, 1952–1958 (2002).
238. S.E. Kooi, U. Schlecht, M. Burghard, and K. Kern, Electrochemical modification of single carbon nanotubes, *Angew. Chem. Int. Ed.* **41**, 1353–1355 (2002).
239. Y. Ying, R.K. Saini, F. Liang, A.K. Sadana, and W.E. Billups, Functionalization of carbon nanotubes by free radicals, *Org. Lett.* **5**, 1471–1473 (2003).
240. M.S. Strano, C.A. Dyke, M.L. Usrey, P.W. Barone, M.J. Allen, H. Shan, C. Kittrell, R.H. Hauge, J.M. Tour, and R.E. Smalley, Electronic structure control of single-walled carbon nanotube functionalization, *Science* **301**, 1519–1522 (2003).
241. P. Umek, J.W. Seo, K. Hernadi, A. Mrzel, P. Pechy, D.D. Mihailovic, and L. Forro, Addition of carbon radicals generated from organic peroxides to single wall carbon nanotubes, *Chem. Mater.* **15**, 4751–4755 (2003).
242. M. Yudasaka, M. Zhang, C. Jabs, and S. Iijima, Effect of an organic polymer in purification and cutting of single-wall carbon nanotubes, *Appl. Phys. A* **71**, 449–451 (2000).
243. M. Zhang, M. Yudasaka, A. Koshio, and S. Iijima, Effect of polymer and solvent on purification and cutting of single-wall carbon nanotubes, *Chem. Phys. Lett.* **349**, 25–30 (2001).
244. M. Zhang, M. Yudasaka, A. Koshio, and S. Iijima, Thermogravimetric analysis of single-wall carbon nanotubes ultrasonicated in monochlorobenzene, *Chem. Phys. Lett.* **364**, 420–426 (2002).
245. A. Koshio, M. Yudasaka, M. Zhang, and S. Iijima, A simple way to chemically react single-wall carbon nanotubes with organic materials using ultrasonication, *Nano Lett.* **1**, 361–363 (2001).
246. S. Niyogi, M.A. Hamon, D.E. Perea, C.B. Kang, B. Zhao, S.K. Pal, A.E. Wyant, M.E. Itkis, and R.C. Haddon, Ultrasonic dispersions of single-walled carbon nanotubes, *J. Phys. Chem. B* **107**, 8799–8804 (2003).
247. J.L. Bahr, E.T. Mickelson, M.J. Bronikowski, R.E. Smalley, and J.M. Tour, Dissolution of small diameter SWNTs in organic solvents? *Chem. Commun.* 193–194 (2001).
248. K. Balasubramanian, M. Friedrich, C. Jiang, Y. Fan, A. Mews, M. Burghard, and K. Kern, Electrical transport and confocal Raman studies of electrochemically modified individual carbon nanotubes, *Adv. Mater.* **15**, 1515–1518 (2003).
249. J.K. Lim, W.S. Yun, M.-h. Yoon, S.K. Lee, C.H. Kim, K. Kim, and S.K. Kim, Selective thiolation of single-walled carbon nanotubes, *Synt. Met.* **139**, 521–527 (2003).
250. A.V. Krasheninnikov and K. Nordlund, Irradiation effects in carbon nanotubes, *Nucl. Instr. Meth. Phys. Res. B* **216**, 355–366 (2004).
251. A.V. Krasheninnikov and K. Nordlund, Signatures of irradiation-induced defects in scanning-tunneling microscopy images of carbon nanotubes, *Phys. Solid State* **44**, 470–472 (2002).
252. D.-H. Kim, H.-S. Jang, C.-D. Kim, D.-S. Cho, H.-D. Kang, and H.-R. Lee, Enhancement of the field emission of carbon nanotubes straightened by application of argon ion irradiation, *Chem. Phys. Lett.* **378**, 232–237 (2003).
253. L. Dai, H.J. Griesser, and A.W.H. Mau, Surface modification by plasma etching and plasma patterning, *J. Phys. Chem. B* **101**, 9548–9554 (1997).
254. H. Bubern, S. Haiber, W. Brandl, G. Marginean, M. Heintze, and V. Brüser, Characterization of the uppermost layer of plasma-treated carbon nanotubes, *Diamond Rel. Mater.* **12**, 811–815 (2003).
255. V.A. Basiuk, K. Kobayashi, T. Kaneko, Y. Negishi, E.V. Basiuk, and J.-M. Saniger-Blesa, Irradiation of single-walled carbon nanotubes with high-energy protons, *Nano Lett.* **2**, 789–791 (2002).
256. B.N. Khare, M. Meyyappan, A.M. Cassell, C.V. Nguyen, and J. Han, Functionalization of carbon nanotubes using atomic hydrogen from a glow discharge, *Nano Lett.* **2**, 73–77 (2002).
257. B.N. Khare, M. Meyyappan, J. Kralj, P. Wilhite, M. Sisay, H. Imanaka, J. Koehne, and C.W. Bauschlicher Jr., A glow-discharge approach for functionalization of carbon nanotubes, *Appl. Phys. Lett.* **81**, 5237–5239 (2002).
258. B. Ni and S.B. Sinnott, Chemical functionalization of carbon nanotubes through energetic radical collisions, *Phys. Rev. B* **61**, R16343–R16346 (2000).

259. B. Ni, R. Andrews, D. Jacques, D. Qian, M.B.J. Wijesundara, Y. Choi, L. Hanley, and S.B. Sinnott, A combined computational and experimental study of ion-beam modification of carbon nanotube bundles, *J. Phys. Chem. B* **105**, 12719–12725 (2001).
260. N.O.V. Plank, L. Jiang, and R. Cheung, Fluorination of carbon nanotubes in CF<sub>4</sub> plasma, *Appl. Phys. Lett.* **83**, 2426–2428 (2003).
261. N.O.V. Plank and R. Cheung, Functionalization of carbon nanotubes for molecular electronics, *Microelectronic Eng.* **73–74**, 578–582 (2004).
262. Y. Hu and S. Sinnott, Nanometer-scale engineering of composites, *11th Foresight Conf. Molec. Nanotech.* [<http://www.foresight.org/Conferences/MNT11/Abstracts/Hu/>].
263. Y. Breton, S. Delpeux, R. Benoit, J.P. Salvetat, C. Sinturel, F. Beguin, S. Bonnamy, G. Desarmot, and L. Boufendi, Functionalization of multiwall carbon nanotubes: properties of nanotubes-epoxy composites, *Mol. Cryst. Liq. Cryst.* **387**, 135–140 (2002).
264. C.Y. Zhi, X.D. Bai, and E.G. Wang, Enhanced field emission from carbon nanotubes by hydrogen plasma treatment, *Appl. Phys. Lett.* **81**, 1690–1692 (2002).
265. S.A. Miller, V.Y. Young, and C.R. Martin, Electroosmotic flow in template-prepared carbon nanotube membranes, *J. Am. Chem. Soc.* **123**, 12335–12342 (2001).
266. G.S. Duesberg, J. Muster, V. Krstic, M. Burghard, and S. Roth, Chromatographic size separation of single-wall carbon nanotubes, *Appl. Phys. A* **67**, 117–119 (1998).
267. G.S. Duesberg, M. Burghard, J. Muster, G. Philipp, and S. Roth, Separation of carbon nanotubes by size exclusion chromatography, *Chem. Commun.* 435–436 (1998).
268. G.S. Duesberg, W. Blau, H.J. Byrne, J. Muster, M. Burghard, and S. Roth, Chromatography of carbon nanotubes, *Synth. Met.* **103**, 2484–2485 (1999).
269. B. Vigolo, A. Pénicaud, C. Coulon, C. Sauder, R. Pailler, C. Journet, P. Bernier, and P. Poulin, Macroscopic fibers and ribbons of oriented carbon nanotubes, *Science* **290**, 1331–1334 (2000).
270. M.J. O'Connell, S.M. Bachilo, C.B. Huffman, V.C. Moore, M.S. Strano, E.H. Haroz, K.L. Rialon, P.J. Boul, W.H. Noon, C. Kittrell, J. Ma, R.H. Hauge, R.B. Weisman, and R.E. Smalley, Band gap fluorescence from individual single-walled carbon nanotubes, *Science* **297**, 593–596 (2002).
271. P. Poulin, B. Vigolo, and P. Lannois, Films and fibers of oriented single wall nanotubes, *Carbon* **40**, 1741–1749 (2002).
272. S.K. Doorn, M.S. Strano, M.J. O'Connell, E.H. Haroz, K.L. Rialon, R.H. Hauge, and R.E. Smalley, Capillary electrophoresis separation of bundled and individual carbon nanotubes, *J. Phys. Chem. B* **107**, 6063–6069 (2003).
273. A.V. Neimark, S. Ruetsch, K.G. Kornev, P.I. Ravikovitch, P. Poulin, S. Badaire, and M. Maugey, Hierarchical pore structure and wetting properties of single-wall carbon nanotube fibers. *Nano Lett.* **3**, 419–423 (2003).
274. J. Wang, R.P. Deo, P. Poulin, and M. Maugey, Carbon nanotube fiber microelectrodes, *J. Am. Chem. Soc.* **125**, 14706–14707 (2003).
275. Y. Dror, W. Salalha, R.L. Khalfin, Y. Cohen, A.L. Yarin, and E. Zussman, Carbon nanotubes embedded in oriented polymer nanofibers by electrospinning, *Langmuir* **19**, 7012–7020 (2003).
276. L. Zhao and L. Gao, Novel in situ synthesis of MWNTs-hydroxyapatite composites, *Carbon* **42**, 423–426 (2004).
277. V. Krstic, G.S. Duesberg, J. Muster, M. Burghard, and S. Roth, Langmuir-Blodgett films of matrix-diluted single-walled carbon nanotubes, *Chem. Mater.* **10**, 2338–2340 (1998).
278. A.B. Dalton, S. Collins, E. Muñoz, J.M. Razal, Von H. Ebron, J.P. Ferraris, J.N. Coleman, B.G. Kim, and R. Baughman, Super tough carbon nanotube fibers, *Nature* **423**, 703 (2003).
279. A.B. Dalton, S. Collins, J. Razal, E. Munoz, Von H. Ebron, B.G. Kim, J.N. Coleman, J.P. Ferraris, and R. Baughman, Continuous carbon nanotube composite fibers: properties, potential applications, and problems, *J. Mater. Chem.* **14**, 1–3 (2004).
280. M.F. Islam, E. Rojas, D.M. Bergey, A.T. Johnson, and A.G. Yodh, High weight-fraction surfactant solubilization of single-wall carbon nanotubes in water, *Nano Lett.* **3**, 269–273 (2003).
281. M.F. Islam, A.M. Alsayed, Z. Dogic, J. Zhang, T.C. Lubensky, and A.G. Yodh, Nematic nanotube gels, *Phys. Rev. Lett.* **92**, 1–4 (2004).
282. J.I. Paredes and M. Burghard, Dispersions of individual single-walled carbon nanotubes of high length, *Langmuir*, **20**, 5149–5152 (2004).
283. O. Matarredona, H. Rhoads, Z. Li, J.H. Harwell, L. Balzano, and D.E. Resasco, Dispersion of single-walled carbon nanotubes in aqueous solutions of the anionic surfactant NaDDBS, *J. Phys. Chem. B* **107**, 13357–13367 (2003).



284. W. Zhou, M.F. Islam, H. Wang, D.L. Ho, A.G. Yodh, K.I. Winey, and J.E. Fischer, Small angle neutron scattering from single-wall carbon nanotube suspensions: evidence for isolated rigid rods and rod networks, *Chem. Phys. Lett.* **384**, 185–189 (2004).
285. K.D. Ausman, R. Piner, O. Lourie, R.S. Ruoff, and M. Korobov, Organic solvent dispersions of SWNTs: toward solutions of pristine nanotubes, *J. Phys. Chem.* **B 104**, 8911–8915 (2000).
286. X. Liu, J.L. Spencer, A.B. Kaiser, and W.M. Arnold, Electric-field oriented carbon nanotubes in different dielectric solvents, *Curr. Appl. Phys.* **4**, 125–128 (2004).
287. Z. Hongbing, C. Wenzhe, W. Minquan, Zhengchan, and Z. Chunlin, Optical limiting effects of multi-walled carbon nanotubes suspension and silica xerogel composite, *Chem. Phys. Lett.* **382**, 313–317 (2003).
288. N. Saran, K. Parikh, D.-S. Suh, E. Muñoz, H. Kolla, and S.K. Manohar, Fabrication and characterization of thin films of single-walled carbon nanotube bundles on flexible plastic substrates, *J. Am. Chem. Soc.* **126**, 4462–4463 (2004).
289. R. Bandyopadhyaya, E. Nativ-Roth, O. Regev, and R. Yerushalmi-Rosen, Stabilization of individual carbon nanotubes in aqueous solutions, *Nano Lett.* **2**, 25–28 (2002).
290. M.S. Strano, C.B. Huffman, V.C. Moore, M.J. O’Connell, E.H. Haroz, J. Hubbard, M. Miller, K. Rialon, C. Kittrell, S. Ramesh, R.H. Hauge, and R.E. Smalley, Reversible, band-gap-selective protonation of single-walled carbon nanotubes in solution, *J. Phys. Chem.* **B 107**, 6979–6985 (2003).
291. J. Ning, J. Zhang, Y. Pan, and J. Guo, Surfactants assisted processing of carbon nanotube-reinforced SiO<sub>2</sub> matrix composites, *Ceramics Int.* **30**, 63–67 (2004).
292. Z. Jin, L. Huang, S.H. Goh, G. Xu, and W. Ji, Characterization and nonlinear optical properties of a poly(acrylic acid)–surfactant–multi-walled carbon nanotube complex, *Chem. Phys. Lett.* **332**, 461–466 (2000).
293. V.A. Karachevtsev, A.Yu. Glamazda, U. Dettlauff-Weglikowska, V.S. Leontiev, A.M. Plokhotnichenko, and S. Roth, Spectroscopy study of SWNT in aqueous solution with different surfactants, *AIP Conf. Proc.* **685**, No. 1, 202–206 (2003).
294. G.L. Hwang and K.C. Hwang, Carbon nanotube reinforced ceramics, *J. Mater. Chem.* **11**, 1722–1725 (2001).
295. K.D. Ausman, M.J. O’Connell, P. Boul, L.M. Ericson, M.J. Casavant, D.A. Walters, C. Huffman, R. Saini, Y. Wang, E. Haroz, E.W. Billups, and R.E. Smalley, Roping and wrapping carbon nanotubes [<http://smalley.rice.edu/rick's%20publications/ausman.pdf>].
296. M.J. O’Connell, P. Boul, L.M. Ericson, C. Huffman, Y. Wang, E. Haroz, C. Kuper, J. Tour, K.D. Ausman, and R.E. Smalley, Reversible water-solubilization of single-walled carbon nanotubes by polymer wrapping, *Chem. Phys. Lett.* **342**, 265–271 (2001).
297. D.W. Schaefer, J.M. Brown, D.P. Anderson, J. Zhao, K. Chokalingam, D. Tomlin, and J. Ilavsky, Structure and dispersion of carbon nanotubes, *J. Appl. Cryst.* **36**, 553–557 (2003).
298. D.W. Schaefer, J. Zhao, J.M. Brown, D.P. Anderson, and D.W. Tomlin, Morphology of dispersed carbon single-walled nanotubes, *Chem. Phys. Lett.* **375**, 369–375 (2003).
299. G.Z. Chen, M.S.P. Shaffer, D. Coleby, G. Dixon, W. Zhou, D.J. Fray, and A.H. Windle, Carbon nanotube and polypyrrole composites: coating and doping, *Adv. Mater.* **12**, 522–526 (2000).
300. B.Z. Tang and H. Xu, Preparation, alignment, and optical properties of soluble poly(phenylacetylene)-wrapped carbon nanotubes, *Macromolecules* **32**, 2569–2576 (1999).
301. D. Li, H. Wang, J. Zhu, X. Wang, L. Lu, and X. Yang, Dispersion of carbon nanotubes in aqueous solutions containing poly(diallyldimethylammonium chloride), *J. Mater. Sci. Lett.* **22**, 253–255 (2003).
302. B. Kim, H. Park, and W.M. Sigmund, Electrostatic interactions between shortened multiwall carbon nanotubes and polyelectrolytes, *Langmuir* **19**, 2525–2527 (2003).
303. J. Chen, M.J. Dyer, and M.-F. Yu, Cyclodextrin-mediated soft cutting of single-walled carbon nanotubes, *J. Am. Chem. Soc.* **123**, 6201–6202 (2001).
304. H. Dodziuk, A. Ejchart, W. Anczewski, H. Ueda, E. Krinichnaya, G. Dolgonos, and W. Kutner, Determination of the number of different types of SWNTs by complexation with  $\eta$ -cyclodextrin, *Chem. Commun.* 986 (2003).
305. Z.H. Wang, G.A. Luo, and S.F. Xiao, Functionalization of cyclodextrins-incorporated carbon nanotube electrodes for neutral nitrophenol recognition, *Sensors, 2003. Proceedings of IEEE*. Vol. 2, 941–945 (2003).
306. T. Takahashi, K. Tsunoda, H. Yajima, and T. Ishii, Isolation of single-wall carbon nanotube bundles through gelatin wrapping and unwrapping processes, *Chem. Lett.* **31**, 690–691 (2002).
307. H. Li, D.Q. Wang, H.L. Chen, B.L. Liu, and L.Z. Gao, A novel gelatin-carbon nanotubes hybrid hydrogel, *Macromol. Biosci.* **3**, 720–724 (2003).

308. A. Star, D.W. Steuerman, J.R. Heath, and J.F. Stoddart, Starched carbon nanotubes, *Angew. Chem. Int. Edit.* **41**, 2508–2512 (2003).
309. O.-K. Kim, J. Je, J.W. Baldwin, S. Kooi, P.E. Pehrsson, and L.J. Buckley, Solubilization of single-wall carbon nanotubes by supramolecular encapsulation of helical amylose, *J. Am. Chem. Soc.* **125**, 4426–4427 (2003).
310. M. Numata, M. Asai, K. Kaneko, T. Hasegawa, N. Fujita, Y. Kitada, K. Sakurai, and S. Shinkai, Curdlan and schizophylan ( $\beta$ -1,3-glucans) can entrap single-wall carbon nanotubes in their helical superstructure, *Chem. Lett.* **33**, 232–233 (2004).
311. G.R. Dieckmann, A.B. Dalton, P.A. Johnson, J. Razal, J. Chen, G.M. Giordano, E. Muñoz, I.H. Musselman, R.H. Baughman, and R.K. Draper, Controlled assembly of carbon nanotubes by designed amphiphilic peptide helices, *J. Am. Chem. Soc.* **125**, 1770–1777 (2003).
312. F. Torrens, Calculation on solvent dispersions of carbon nanotubes, *The Electrochem. Soc. 205th Meet.*, Abs. 457 (2004).
313. Z. Shi, Y. Lian, X. Zhou, Z. Gu, Y. Zhang, S. Iijima, Q. Gong, H. Li, and S.-L. Zhang, Single-wall carbon nanotube colloids in polar solvents, *Chem. Commun.* 461–462 (2000).
314. X. Gao, T. Hu, L. Liu, and Z. Guo, Self-assembly of modified carbon nanotubes in toluene, *Chem. Phys. Lett.* **370**, 661–664 (2003).
315. M.E. Itkis, D.E. Perea, S. Niyogi, S.M. Rickard, M. Hamon, H. Hu, B. Zhao, and R.C. Haddon, Purity evaluation of as-prepared single-walled carbon nanotube soot by use of solution-phase near-IR spectroscopy, *Nano Lett.* **3**, 309–314 (2003).
316. A.B. Dalton, W.J. Blau, G. Chambers, J.N. Coleman, K. Henderson, S. Lefrant, B. McCarthy, C. Stephan, and H.J. Byrne, A functional conjugated polymer to process, purify and selectively interact with single wall carbon nanotubes, *Synth. Met.* **121**, 1217–1218 (2001).
317. D.W. Steuerman, A. Star, R. Narizzano, H. Choi, R.S. Ries, C. Nicolini, J.F. Stoddart, and J.R. Heath, Interactions between conjugated polymers and single-walled carbon nanotubes, *J. Phys. Chem. B* **106**, 3124–3130 (2002).
318. A. Star, Y. Liu, K. Grant, L. Ridvan, J.F. Stoddart, D.W. Steuerman, M.R. Diehl, A. Boukai, and J.R. Heath, Noncovalent side-wall functionalization of single-walled carbon nanotubes, *Macromolecules* **36**, 553–560 (2003).
319. J.N. Coleman, D.F. O'Brien, M. in het Panhuis, A.B. Dalton, B. McCarthy, R.C. Barklie, and W.J. Blau, Solubility and purity of nanotubes in arc discharge carbon powder, *Synth. Met.* **121**, 1229–1230 (2001).
320. J. Chen, H. Liu, W.A. Weimer, M.D. Halls, D.H. Waldeck, and G.C. Walker, Noncovalent engineering of carbon nanotube surface by rigid functional conjugated polymers, *J. Am. Chem. Soc.* **124**, 9034–9035 (2002).
321. J.-M. Nam, M.A. Ratner, X. Liu, and C.A. Mirkin, Single-walled carbon nanotubes and C<sub>60</sub> encapsulated by a molecular macrocycles, *J. Phys. Chem. B* **107**, 4705–4710 (2003).
322. Z. Jin, L. Huang, S.H. Goh, G. Xu, and W. Ji, Size-dependent optical limiting behavior of multi-walled carbon nanotubes, *Chem. Phys. Lett.* **352**, 328–333 (2002).
323. V.A. Davis, L.M. Ericson, R. Saini, R. Sivarajan, R.H. Hauge, R.E. Smalley, and M. Pasquali, Rheology, phase behavior, and fiber spinning of carbon nanotube dispersion, *Paper prepared for presentation at the 2001 AIChE annual meeting, 9 November, 2001, T7019 session.*
324. V.A. Davis, L.M. Ericson, A.N.G. Parra-Vasquez, H. Fan, Y. Wang, V. Prieto, J.A. Longoria, S. Ramesh, R.K. Saini, C. Kittrell, W.E. Billups, W.W. Adams, R.H. Hauge, R.E. Smalley, and M. Pasquali, Phase behavior and rheology of SWNTs in superacids, *Macromolecules* **37**, 154–160 (2004).
325. W. Zhou, J. Vavro, C. Guthy, K.I. Winey, J.E. Fisher, L.M. Ericson, S. Ramesh, R. Saini, V.A. Davis, C. Kittrell, M. Pasquali, R.H. Hauge, and R.E. Smalley, Single wall carbon nanotube fibers extruded from super-acid suspensions: preferred orientation, electrical, and thermal transport, *J. Appl. Phys.* **95**, 649–655 (2004).
326. T.V. Sreekumar, T. Liu, S. Kumar, L.M. Ericson, R.H. Hauge, and R.E. Smalley, Single-wall carbon nanotube films, *Chem. Mater.* **15**, 175–178 (2003).
327. H. Dai, J. Kong, C. Zhou, N. Franklin, T. Tombler, A. Cassell, S. Fan, and M. Chapline, Controlled chemical routes to nanotube architectures, physics, and devices, *J. Phys. Chem. B* **103**, 11246–11255 (1999).
328. X. Yu, T. Mu, H. Huang, Z. Liu, and N. Wu, The study of the attachment of a single-walled carbon nanotube to a self-assembled monolayer using X-ray photoelectron spectroscopy, *Surf. Sci.* **461**, 199–207 (2000).

329. J. Liu, M.J. Casavant, M. Cox, D.A. Walters, P. Boul, W. Lu, A.J. Rimerberg, K.A. Smith, D.T. Colbert, and R.E. Smalley, Controlled deposition of individual single-walled carbon nanotubes on chemically functionalized templates, *Chem. Phys. Lett.* **303**, 125–129 (1999).
330. K.H. Choi, J.P. Bourgoïn, S. Auvray, D. Esteve, G.S. Duesberg, S. Roth, and M. Burghard, Controlled deposition of carbon nanotubes on a patterned substrate, *Surf. Sci.* **462**, 195–202 (1999).
331. S.G. Rao, L. Huang, W. Setyawan, and S. Hong, Large-scale assembly of carbon nanotubes, *Nature* **425**, 36 (2003).
332. B. Wincheski, J. Smits, M. Namkung, J. Ingram, N. Watkins, J.D. Jordan, and R. Louie, Nanomanipulation and lithography for carbon nanotube based nondestructive evaluation sensor development [<http://techreports.larc.nasa.gov/ltrs/PDF/2002/mtg/NASA-2002-sem-bw.pdf>].
333. B. Kim and W.M. Sigmund, Self-alignment of shortened multiwall carbon nanotubes on polyelectrolyte layers, *Langmuir* **19**, 4848–4851 (2003).
334. M. Sano, A. Kamino, J. Okamura, and S. Shinkai, Non-covalent self-assembly of carbon nanotubes for construction of ‘cages’, *Nano Lett.* **2**, 531–533 (2002).
335. J. Chen and W.A. Weimer, Room-temperature assembly of directional carbon nanotube strings, *J. Am. Chem. Soc.* **124**, 758–759 (2002).
336. Y. Yang, H. Zou, B. Wu, J. Zhang, Z. Liu, X. Guo, and Z. Du, Directional carbon nanotube assembly via solvent evaporation induced mechanical stretching, *Advanced Nanomaterials Nanodevices (IUMRS-ICEM 2002, Xian, China, 10–14 June 2002)*. 12–22 (2002).
337. Y.-H. Li, C. Xu, B. Wei, X. Zhang, M. Zheng, D. Wu, and P.M. Ajayan, Self-organized ribbons of aligned carbon nanotubes, *Chem. Mater.* **14**, 483–485 (2002).
338. H. Shimoda, S.J. Oh, H.Z. Geng, R.J. Walker, X.B. Zhang, L.E. McNeil, and O. Zhou, Self-assembly of carbon nanotubes, *Adv. Mater.* **14**, 899–901 (2002).
339. H. Shimoda, L. Fleming, K. Horton, and O. Zhou, Formation of macroscopically ordered carbon nanotube membranes by self-assembly, *Physica B* **323**, 135–136 (2002).
340. N. Chakrapani, B. Wei, A. Carrillo, P.M. Ajayan, and R.S. Kane, Capillary-driven assembly of two-dimensional cellular carbon nanotube foams, *Proc. Nat. Acad. Sci.* **101**, 4009–4012 (2004).
341. I. Dierking, G. Scalia, P. Morales, and D. LeClere, Aligning and re-orienting carbon nanotubes by nematic liquid crystals [<http://www.mat.casaccia.enea.it/link6.pdf>].
342. M.D. Lynch and D.L. Patrick, Organizing carbon nanotubes with liquid crystals, *Nano Lett.* **2**, 1197–1201 (2002).
343. M. Senthil Kumar, T.H. Kim, S.H. Lee, S.M. Song, J.W. Yang, K.S. Nahm, and E.-K. Suh, Influence of electric field type on the assembly of single walled carbon nanotubes, *Chem. Phys. Lett.* **383**, 235–239 (2004).
344. M.R. Diehl, S.N. Yaliraki, R.A. Beckman, M. Barahona, and J.R. Heath, Self-assembled, deterministic carbon nanotube wiring networks, *Angew. Chem. Int. Ed.* **41**, 353–356 (2002).
345. B. Gao, G.Z. Yue, Q. Qiu, Y. Cheng, H. Shimoda, L. Fleming, and O. Zhou, Fabrication and electron field emission properties of carbon nanotube films by electrophoretic deposition, *Adv. Mater.* **13**, 1770–1774 (2001).
346. J. Tang, B. Gao, H. Geng, O.D. Velev, L.-C. Qin, and O. Zhou, Assembly of 1D nanostructures into sub-micrometer diameter fibrils with controlled and variable length by electrophoresis, *Adv. Mater.* **15**, 1352–1355 (2003).
347. M. Burghard, G. Duesberg, G. Philipp, J. Muster, and S. Roth, Controlled adsorption of carbon nanotubes on chemically modified electrode arrays, *Adv. Mater.* **10**, 584–588 (1998).
348. Y. Guo, J. Wu, and Y. Zhang, Manipulation of single-wall carbon nanotubes into aligned molecular layers, *Chem. Phys. Lett.* **362**, 314–318 (2002).
349. L. Feng, H. Li, F. Li, Z. Shi, and Z. Gu, Functionalization of carbon nanotubes with amphiphilic molecules and their Langmuir-Blodgett films, *Carbon* **41**, 2385–2391 (2003).
350. N.P. Armitage, J.-C.P. Gabriel, and G. Grüner, Quasi-Langmuir-Blodgett thin film deposition of carbon nanotubes, *J. Appl. Phys.* **95**, 3328–3330 (2004).
351. V. Bavastrello, S. Carrara, M.K. Ram, and C. Nicolini, Optical and electrochemical properties of poly(*o*-toluidine) multiwalled carbon nanotubes composite Langmuir-Schaefer films, *Langmuir* **20**, 969–973 (2004).
352. T. Fukushima, A. Kosaka, Y. Ishimura, T. Yamamoto, T. Takigawa, N. Ishii, and T. Aida, Molecular ordering of organic molten salts triggered by single-walled carbon nanotubes, *Science* **300**, 2972–2974 (2003).

353. B. Vigolo, P. Poulin, M. Lukas, P. Launois, and P. Bernier, Improved structure and properties of single wall carbon nanotube spun fibers, *Appl. Phys. Lett.* **81**, 1210–1212 (2002).
354. F. Ko, Y. Gogotsi, A. Ali, N. Naguib, H. Ye, G. Yang, C. Li, and P. Willis, Electrospinning of continuous carbon nanotube filled nanofiber yarns, *Adv. Mater.* **15**, 1164–1165 (2003).
355. R. Sen, B. Zhao, D. Perea, M.E. Itkis, H. Hu, J. Love, E. Bekyarova, and R.C. Haddon, Preparation of single-walled carbon nanotube reinforced polystyrene and polyurethane nanofibers and membranes, *Nano Lett.* **4**, 459–464 (2004).
356. T.E. Müller, D.G. Reid, W.K. Hsu, J.P. Hare, H.W. Kroto, and D.R.M. Walton, Synthesis of nanotubes via catalytic pyrolysis of acetylene: a SEM study, *Carbon* **35**, 951–966 (1997).
357. Y.K. Chen, A. Chu, J. Cook, M.L.H. Green, P.J.F. Harris, R. Heesom, M. Humphries, J. Sloan, S.C. Tsang, and J.F.C. Turner, Synthesis of carbon nanotubes containing metal oxides and metals of the d-block and f-block transition metals and related studies, *J. Mater. Sci.* **7**, 545–549 (1997).
358. C.T. Kuo, C.H. Lin, and A.Y. Lo, Feasibility studies of magnetic particle-embedded carbon nanotubes for perpendicular recording media, *Diamond Rel. Mater.* **12**, 799–805 (2003).
359. H. Liu, J.-M. Dong, M.-C. Qian, and X.-G. Wan, Dependence of in-tube doping on the radius and helicity of single-wall carbon nanotubes, *Chinese Phys.* **12**, 542–547 (2003).
360. D. Bera, S.C. Kuiry, M. McCutchen, A. Kruize, H. Heinrich, M. Meyyappan, and S. Seal, In-situ synthesis of palladium nanoparticles-filled carbon nanotubes using arc-discharge in solution, *Chem. Phys. Lett.* **386**, 364–368 (2004).
361. E. Dujardin, C. Meny, P. Panissod, J.-P. Kintzinger, N. Yao, and T.W. Ebbesen, Interstitial metallic residues in purified single shell carbon nanotubes, *Solid State Commun.* **114**, 543–546 (2000).
362. X.P. Gao, Y. Zhang, X. Chen, G.L. Pan, J. Yan, F. Wu, H.T. Yuan, and D.Y. Song, Carbon nanotubes filled with metallic nanowires, *Carbon* **42**, 47–52 (2004).
363. C.H. Liang, G.W. Meng, L.D. Zhang, N.F. Shen, and X.Y. Zhang, Carbon nanotubes filled partially or completely with nickel, *J. Cryst. Growth* **218**, 136–139 (2000).
364. B.C. Satishkumar, A. Govindaraj, P.V. Vanitha, A.K. Raychaudhuri, and C.N.R. Rao, Barkhausen jumps and related magnetic properties of iron nanowires encapsulated in aligned carbon nanotube bundles, *Chem. Phys. Lett.* **362**, 301–306 (2002).
365. A. Leonhardt, M. Ritschel, R. Kozhuharova, A. Graff, T. Mühl, R. Huhle, I. Mönch, D. Elefant, and C.M. Schneider, Synthesis and properties of filled carbon nanotubes, *Diamond Rel. Mater.* **12**, 790–793 (2003).
366. N. Grobert, M. Mayne, M. Terrones, J. Sloan, R.E. Dunin-Borkowski, R. Kamalakaran, T. Seeger, H. Terrones, M. Rühle, D.R.M. Walton, H.W. Kroto, and J.L. Hutchison, Alloy nanowires: invar inside carbon nanotubes, *Chem. Commun.* 471–472 (2001).
367. X. Li, Z. Lei, R. Ren, J. Liu, X. Zuo, Z. Dong, H. Wang, and J. Wang, Characterization of carbon nanohorn encapsulated Fe particles, *Carbon* **41**, 3068–3072 (2003).
368. R. Sen, A. Govindaraj, and C.N.R. Rao, Metal-filled and hollow carbon nanotubes obtained by the decomposition of metal-containing free precursor molecules, *Chem. Mater.* **9**, 2078–2081 (1997).
369. B.H. Liu, J. Ding, Z.Y. Zhong, Z.L. Dong, T. White, and J.Y. Lin, Large-scale preparation of carbon-encapsulated cobalt nanoparticles by the catalytic method, *Chem. Phys. Lett.* **358**, 96–102 (2002).
370. G.Y. Zhang and E.G. Wang, Cu-filled carbon nanotubes by simultaneous plasma-assisted copper incorporation, *Appl. Phys. Lett.* **82**, 1926–1928 (2003).
371. C.Y. Zhi, D.Y. Zhong, and E.G. Wang, GaN-filled carbon nanotubes: synthesis and photoluminescence, *Chem. Phys. Lett.* **381**, 715–719 (2003).
372. A.K. Sinha, D.W. Hwang, and L.-P. Hwang, A novel approach to bulk synthesis of carbon nanotubes filled with metal by a catalytic chemical vapor deposition method, *Chem. Phys. Lett.* **332**, 455–460 (2000).
373. R. Ma, Y. Bando, and T. Sato, Coaxial nanocables: Fe nanowires encapsulated in BN nanotubes with intermediate C layers, *Chem. Phys. Lett.* **350**, 1–5 (2001).
374. S. Liu and J. Zhu, Carbon nanotubes filled with long continuous cobalt nanowires, *Appl. Phys. A* **70**, 673–675 (2000).
375. S. Liu, S. Zhu, Y. Mastai, I. Felner, and A. Gedanken, Preparation and characteristics of carbon nanotubes filled with cobalt, *Chem. Mater.* **12**, 2205–2211 (2000).
376. Y. Gogotsi, N. Naguib, and J.A. Libera, In situ chemical experiments in carbon nanotubes, *Chem. Phys. Lett.* **356**, 354–360 (2002).
377. J.L. Rivera, C. McCabe, and P.T. Cummings, Layering behavior and axial phase equilibria of pure water and water + carbon dioxide inside single wall carbon nanotubes, *Nano Lett.* **2**, 1427–1431 (2002).

378. E. Dujardin, T.W. Ebbesen, H. Hiura, and K. Tanigaki, Capillarity and wetting of carbon nanotubes, *Science* **265**, 1850–1852 (1994).
379. E. Dujardin, T.W. Ebbesen, A. Krishnan, and M.M. Treacy, Wetting of single shell carbon nanotubes, *Adv. Mater.* **10**, 1472–1475 (1998).
380. G. Hummer, J.C. Rasaiah, and J.P. Noworyta, Water conduction through the hydrophobic channel of a carbon nanotube, *Nature* **414**, 188–190 (2001).
381. M.S.P. Sansom and P.C. Biggin, Biophysics: water at the nanoscale, *Nature* **414**, 156 (2001).
382. J. Martí and M.C. Gordillo, Temperature effects on the static and dynamic properties of liquid water inside nanotubes. *Phys. Rev. E* **64**, 21504.1–6 (2001).
383. K. Koga, G.T. Gao, H. Tanaka, and X.C. Zeng, Formation of ordered ice nanotubes inside carbon nanotubes, *Nature* **412**, 802–805 (2001).
384. W.H. Noon, K.D. Ausman, R.E. Smalley, and J. Ma, Helical ice-sheets inside carbon nanotubes in the physiological condition, *Chem. Phys. Lett.* **355**, 445–448 (2002).
385. A. Waghe, J.C. Rasaiah, and G. Hummer, Filling and emptying kinetics of carbon nanotubes in water, *J. Chem. Phys.* **117**, 10789–10795 (2002).
386. A. Kalra, S. Garde, and G. Hummer, Osmotic water transport through carbon nanotube membranes, *Proc. Nat. Acad. Sci. USA* **100**, 10175–10180 (2003).
387. M.P. Rossi, H. Ye, Y. Gogotsi, S. Babu, P. Ndungu, and J.-C. Bradley, Environmental scanning electron microscopy study of water in carbon nanopipes, *Nano Lett.* **4**, 989–993 (2004).
388. S. Joseph, R.J. Mashl, E. Jacobsson, and N.R. Aluru, Ion channel based biosensors: ionic transport in carbon nanotubes, *Nanotech 2003*, **1**, 158–161 (2003) [<http://www.nsti.org/procs/Nanotech2003v1/8/T23.05>].
389. S.C. Tsang, Y.K. Chen, P.J.F. Harris, and M.L. Green, A simple chemical method of opening and filling carbon nanotubes, *Nature* **372**, 159–162 (1994).
390. J. Chancelon, F. Archaimbault, S. Delpeux, A. Pineau, M.L. Saboungi, and S. Bonnamy, Filling of multiwalled carbon nanotubes with oxides and metals, *AIP Conf. Proc.* **633**, No. 1, 131–134 (2002).
391. P. Corio, A.P. Santos, P.S. Santos, M.L.A. Temperini, V.W. Brar, M.A. Pimenta, and M.S. Dresselhaus, Characterization of single wall carbon nanotubes filled with silver and with chromium compounds, *Chem. Phys. Lett.* **383**, 475–480 (2004).
392. C. Pham-Huu, N. Keller, C. Estournès, G. Ehret, and M.J. Ledoux, Synthesis of  $\text{CoFe}_2\text{O}_4$  nanowire in carbon nanotubes. A new use of confinement effect, *Chem. Commun.* 1882–1883 (2002).
393. C. Pham-Huu, N. Keller, C. Estournès, G. Ehret, J.M. Grenèche, and M.J. Ledoux, Microstructural investigation and magnetic properties of  $\text{CoFe}_2\text{O}_4$  nanowires synthesized inside carbon nanotubes, *Phys. Chem. Chem. Phys.* **5**, 3716–3723 (2003).
394. N. Keller, C. Pham-Huu, C. Estournès, J.-M. Grenèche, G. Ehret, and M.J. Ledoux, Carbon nanotubes as a template for mild synthesis of magnetic  $\text{CoFe}_2\text{O}_4$  nanowires, *Carbon* **42**, 1395–1399 (2004).
395. J. Sloan, J. Hammer, M. Zwiefka-Sibley, and M.L.H. Green, The opening and filling of single walled carbon nanotubes (SWTs), *Chem. Commun.* 347–348 (1998).
396. B. Rajesh, K.R. Thampi, J.-M. Bonard, and B. Viswanathan, Preparation of a Pt–Ru bimetallic system supported on carbon nanotubes, *J. Mater. Chem.* **10**, 1757–1759 (2000).
397. B. Rajesh, K.R. Thampi, J.-M. Bonard, and B. Viswanathan, Preparation of Pt–Ru bimetallic catalyst supported on carbon nanotubes, *Bull. Mater. Sci.* **23**, 341–344 (2000).
398. B. Rajesh, V. Karthik, S. Karthikeyan, K.R. Thampi, J.-M. Bonard, and B. Viswanathan, Pt– $\text{WO}_3$  supported on carbon nanotubes as possible anodes for direct methanol fuel cells, *Fuel* **81**, 2177–2190 (2002).
399. B. Rajesh, K.R. Thampi, J.-M. Bonard, N. Xanthopoulos, H.J. Mathieu, and B. Viswanathan, Carbon nanotubes generated from template carbonization of polyphenyl acetylene as the support for electrooxidation of methanol, *J. Phys. Chem. B* **107**, 2701–2708 (2003).
400. J. Bao, Q. Zhou, J. Hong, and Z. Xu, Synthesis and magnetic behavior of an array of nickel-filled carbon nanotubes, *Appl. Phys. Lett.* **81**, 4592–4594 (2002).
401. K. Matsui, T. Kyotani, and A. Tomita, Hydrothermal synthesis of nano-sized iron oxide crystals in the cavity of carbon nanotubes, *Mol. Cryst. Liq. Cryst.* **387**, 1–5 (2002).
402. J. Mittal, M. Monthieux, H. Allouche, and O. Stephan, Room temperature filling of single-wall carbon nanotubes with chromium oxide in open air, *Chem. Phys. Lett.* **339**, 311–318 (2001).
403. H.-Q. Wu, X.-W. Wei, M.-W. Shao, J.-S. Gu, and M.-Z. Qu, Synthesis of copper oxide nanoparticles using carbon nanotubes as templates, *Chem. Phys. Lett.* **364**, 152–156 (2002).

404. L. Jiang and L. Gao, Modified carbon nanotubes: an effective way to selective attachment of gold nanoparticles, *Carbon* **41**, 2923–2929 (2003).
405. X.-R. Ye, Y. Lin, C. Wang, and C.M. Wai, Supercritical fluid fabrication of metal nanowires and nanorods templated by multiwalled carbon nanotubes, *Adv. Mater.* **15**, 316–319 (2003).
406. D.A. Britz, A.N. Khlobystov, J. Wang, A.S. O’Neil, M. Poliakoff, A. Ardavan, and G.A.D. Briggs, Selective host-guest interaction of single-walled carbon nanotubes with functionalized fullerenes, *Chem. Commun.* 176–177 (2004).
407. F. Simon, H. Kuzmany, H. Rauf, T. Pichler, J. Bernardi, H. Peterlik, L. Korecz, F. Fülöp, and A. Jánossy, Low temperature fullerene encapsulation in single wall carbon nanotubes: synthesis of N@C<sub>60</sub>@SWCNT, *Chem. Phys. Lett.* **383**, 362–367 (2004).
408. M. Yudasaka, K. Ajima, K. Suenaga, T. Ichihashi, A. Hashimoto, and S. Iijima, Nano-extraction and nano-condensation for C<sub>60</sub> incorporation into single-wall carbon nanotubes in liquid phases, *Chem. Phys. Lett.* **380**, 42–46 (2003).
409. T. Takenobu, T. Takano, M. Shiraiishi, Y. Murakami, M. Ata, H. Kataura, Y. Achiba, and Y. Iwasa, Stable and controlled amphoteric doping by encapsulation of organic molecules inside carbon nanotubes, *Nat. Mater.* **2**, 683–688 (2003).
410. H. Gao, Y. Kong, D. Cui, and C.S. Ozkan, Spontaneous insertion of DNA oligonucleotides into carbon nanotubes, *Nano Lett.* **3**, 471–473 (2003).
411. S. Friedrichs, R.R. Meyer, J. Sloan, A.I. Kirkland, J.L. Hutchison, and M.L.H. Green, Complete characterization of a Sb<sub>2</sub>O<sub>3</sub>/(21,–8)SWNT inclusion composite, *Chem. Commun.* 929–930 (2001).
412. S. Friedrichs, J. Sloan, M.L.H. Green, J.L. Hutchison, R.R. Meyer, and A.I. Kirkland, Simultaneous determination of inclusion crystallography and nanotube conformation for a Sb<sub>2</sub>O<sub>3</sub>/single-walled nanotube composite, *Phys. Rev.* **B 64**, 045406.1–8 (2001).
413. J. Sloan, D.M. Wright, H.-G. Woo, S. Bailey, G. Brown, A.P.E. York, K.S. Coleman, J.L. Hutchison, and M.L.H. Green, Capillarity and silver nanowire formation observed in single walled carbon nanotubes, *Chem. Commun.* 699–700 (1999).
414. J. Sloan, A.I. Kirkland, J.L. Hutchison, and M.L.H. Green, Integral atomic layer architectures of 1D crystals inserted into single walled carbon nanotubes, *Chem. Commun.* 1319–1332 (2002).
415. C. Xu, J. Sloan, G. Brown, S. Bailey, V.C. Williams, S. Friedrichs, K.S. Coleman, E. Flahaut, J.L. Hutchison, R.E. Dunin-Borkowski, and M.L.H. Green, 1D lanthanide halide crystals inserted into single-walled carbon nanotubes, *Chem. Commun.* 2427–2428 (2000).
416. C.-H. Kiang, J.-S. Choi, T.T. Tran, and A.D. Bacher, Molecular nanowires of 1 nm diameter from capillary filling of single-walled nanotubes, *J. Phys. Chem.* **B 103**, 7449–7451 (1999).
417. C.-H. Kiang, Electron irradiation induced dimensional change in bismuth filled carbon nanotubes, *Carbon* **38**, 1699–1701 (2000).
418. X. Fan, E.C. Dickey, P.C. Eklund, K.A. Williams, L. Grigorian, R. Buczko, S.T. Pantelides, and S.J. Pennycook, Atomic arrangement of iodine atoms inside single-walled carbon nanotubes, *Phys. Rev. Lett.* **84**, 4621–4624 (2000).
419. W. Zhou, S. Xie, L. Sun, D. Tang, Y. Li, Z. Liu, L. Ci, X. Zou, G. Wang, P. Tan, X. Dong, B. Xu, and B. Zhao, Raman scattering and thermogravimetric analysis of iodine-doped multiwall carbon nanotubes, *Appl. Phys. Lett.* **80**, 2553–2555 (2002).
420. Y. Gao and Y. Bando, Carbon nanothermometer containing gallium, *Nature* **415**, 599 (2002).
421. A. Fujiwara, K. Ishii, H. Suematsu, H. Kataura, Y. Maniwa, S. Suzuki, and Y. Achiba, Gas adsorption in the inside and outside of single-walled carbon nanotubes, *Chem. Phys. Lett.* **336**, 205–211 (2001).
422. Z. Mao, A. Garg, and S.B. Sinnott, Molecular dynamics simulations of the filling and decorating of carbon nanotubules, *Nanotechnology* **10**, 273–277 (1999).
423. Z. Mao and S.B. Sinnott, A computational study of molecular diffusion and dynamic flow through carbon nanotubes, *J. Phys. Chem.* **B 104**, 4618–4624 (2000).
424. M. Li, M. Lu, C. Wang, and H. Li, Preparation of well-aligned carbon nanotubes/silicon nanowires core-sheath composite structure arrays in porous anodic aluminium oxide templates, *Sci. China* **45 B**, No. 4, 435–444 (2002).
425. G. Brown, S.R. Bailey, J. Sloan, C. Xu, S. Friedrichs, E. Flahaut, K.S. Coleman, J.L. Hutchison, R.E. Dunin-Borkowski, and M.L.H. Green, Electron beam induced *in situ* characterization of 1D ZrCl<sub>4</sub> chains within single-walled carbon nanotubes, *Chem. Commun.* 845–846 (2001).
426. H. Kataura, Y. Maniwa, T. Kodama, K. Kikuchi, K. Hirahara, K. Suenaga, S. Iijima, S. Suzuki, Y. Achiba, and W. Krätschmer, High-yield fullerene encapsulation in single-wall carbon nanotubes, *Synth. Met.* **121**, 1195–1196 (2001).

427. K. Hirahara, K. Suenaga, S. Bandow, H. Kato, T. Okazaki, H. Shinohara, and S. Iijima, One-dimensional metallofullerene crystal generated inside single-walled carbon nanotubes, *Phys. Rev. Lett.* **85**, 5384–5387 (2000).
428. K. Hirahara, S. Bandow, K. Suenaga, H. Kato, T. Okazaki, H. Shinohara, and S. Iijima, Electron diffraction study of one-dimensional crystals of fullerenes, *Phys. Rev.* **B 64**, 115420.1–5 (2001).
429. A.R. Harutyunyan, B.K. Pradhan, G.U. Sumanasekera, E.Yu. Korobko, A.A. Kuznetsov, Carbon nanotubes for medical applications, *Eur. Cells Mater.* **3**, Suppl. 2, 84–87 (2002).
430. B.K. Pradhan, T. Toba, T. Kyotani, and A. Tomita, Inclusion of crystalline iron oxide nanoparticle in uniform carbon nanotubes prepared by a template carbonization method, *Chem. Mater.* **10**, 2510–2515 (1998).
431. B.K. Pradhan, T. Kyotani, and A. Tomita, Nickel nanowires of 4 nm diameter in the cavity of carbon nanotubes, *Chem. Commun.* 1317–1318 (1999).
432. K. Matsui, B.K. Pradhan, T. Kyotani, and A. Tomita, Formation of nickel oxide nanoribbons in the cavity of carbon nanotubes, *J. Phys. Chem.* **B 105**, 5682–5688 (2001).
433. X. Li, L. Liu, Y. Qin, W. Wu, Z.-X. Guo, L. Dai, and D. Zhu, C<sub>60</sub> modified single-walled carbon nanotubes, *Chem. Phys. Lett.* **377**, 32–36 (2003).
434. G.-H. Jeong, A.A. Farajian, T. Hirata, R. Hatakeyama, K. Tohji, T.M. Briere, H. Mizuseki, and Y. Kawazoe, Encapsulation of cesium inside single-walled carbon nanotubes by plasma-ion irradiation method, *Thin Solid Films* **435**, 307–311 (2003).
435. F. Banhart, The formation of a connection between carbon nanotubes in an electron beam, *Nano Lett.* **1**, 329–332 (2001).
436. Z. Wang, L. Yu, W. Zhang, Y. Ding, Y. Li, Z. Zhu, J. Han, H. Xu, G. He, Y. Chen, and G. Hu, Amorphous molecular junctions by ion irradiation on carbon nanotubes, *Phys. Lett. A* **324**, 321–325 (2004).
437. D. Ding and J. Wang, Electron irradiation of multi-walled carbon nanotubes with encapsulated Ni particles, *Carbon* **40**, 787–803 (2002).
438. R. Che, L.-M. Peng, Q. Chen, X.F. Duan, B.S. Zou, and Z.N. Gu, Controlled synthesis and phase transformation of ferrous nanowires inside carbon nanotubes, *Chem. Phys. Lett.* **375**, 59–64 (2003).
439. J.S. Lee, B. Min, K. Cho, S. Kim, J. Park, Y.T. Lee, N.S. Kim, M.S. Lee, S.O. Park, and J.T. Moon, Al<sub>2</sub>O<sub>3</sub> nanotubes and nanorods fabricated by coating and filling of carbon nanotubes with atomic-layer deposition, *J. Cryst. Growth* **254**, 443–448 (2003).
440. Z. Liu, Y. Gao, and Y. Bando, Highly effective metal vapor absorbents based on carbon nanotubes, *Appl. Phys. Lett.* **81**, 4844–4846 (2002).
441. B.W. Smith, M. Monthieux, and D.E. Luzzi, Encapsulated C<sub>60</sub> in carbon nanotubes, *Nature* **396**, 323–324 (1998).
442. J. Sloan, R.E. Dunin-Borkowski, J.L. Hutchison, K.S. Coleman, V.C. Williams, J.B. Claridge, A.P.E. York, C. Xu, S.R. Bailey, G. Brown, S. Friedrichs, and M.L.H. Green, The size distribution, imaging and obstructing properties of C<sub>60</sub> and higher fullerenes formed within arc-grown single walled carbon nanotubes, *Chem. Phys. Lett.* **316**, 191–198 (2000).
443. R. Pfeiffer, Ch. Kramberger, Ch. Schaman, A. Sen, M. Holzweber, H. Kuzmany, T. Pichler, H. Kataura, and Y. Achiba, Defect free inner tubes in DWCNTs, *AIP Conf. Proc.* **685**, No. 1, 297–301 (2003).
444. H. Kataura, Y. Maniwa, M. Abe, A. Fujiwara, T. Kodama, K. Kikuchi, M. Imahori, Y. Misaki, S. Suzuki, and Y. Achiba, Optical properties of fullerene and non-fullerene peapods, *Appl. Phys. A* **74**, 349–354 (2002).
445. S. Bandow, M. Takizawa, K. Hirahata, M. Yudasaka, and S. Iijima, Raman scattering study of double-wall carbon nanotubes derived from the chains of fullerenes in single-wall carbon nanotubes, *Chem. Phys. Lett.* **337**, 48–54 (2001).
446. S. Bandow, T. Hiraoka, T. Yumura, K. Hirahara, H. Shinohara, and S. Iijima, Raman scattering study on fullerene derived intermediates formed within single-wall carbon nanotube: from peapod to double-wall carbon nanotube, *Chem. Phys. Lett.* **384**, 320–325 (2004).
447. T. Okazaki, K. Suenaga, K. Hirahara, S. Bandow, S. Iijima, and H. Shinohara, Real time reaction dynamics in carbon nanotubes, *J. Am. Chem. Soc.* **123**, 9673–9674 (2001).
448. C.M. Megaridis, A. Güvenç Yaziciroglu, J.A. Libera, and Y. Gogotsi, Attoliter fluid experiments in individual closed-end carbon nanotubes: liquid film interface dynamics, *Phys. Fluids* **14**, L5–8 (2002).
449. H. Ye, N. Naguib, Y. Gogotsi, A.G. Yaziciroglu, and C.M. Megaridis, Wall structure and surface chemistry of hydrothermal carbon nanofibres, *Nanotechnology* **15**, 232–236 (2004).

450. M. Green, *Carbon nanotubes. Chemistry in a carbon cage*. The Institute of Applied Catalysis, 2000. [<http://www.iac.org.uk/pages/vis3.html>].
451. Z. Liu, X. Dai, J. Xu, B. Han, J. Zhang, Y. Wang, Y. Huang, and G. Yang, Encapsulation of polystyrene within carbon nanotubes with the aid of supercritical CO<sub>2</sub>, *Carbon* **42**, 423–460 (2004).
452. Q. Yang, L. Li, H. Cheng, M. Wang, and J. Bai, Inner-tubular physicochemical processes of carbon nanotubes, *Chin. Sci. Bull.* **48**, 2395–2403 (2003).
453. Q. Jiang, N. Aya, and F.G. Shi, Nanotube size-dependent melting of single crystals in carbon nanotubes, *Appl. Phys. A* **64**, 627–629 (1997).
454. J. Sloan, S. Friedrichs, R.R. Meyer, A.I. Kirkland, J.L. Hutchison, and M.L.H. Green, Structural changes induced in nanocrystals of binary compounds confined within single wall carbon nanotubes: a brief review, *Inorg. Chim. Acta* **330**, 1–12 (2002).
455. J. Sloan, A.I. Kirkland, J.L. Hutchison, and M.L.H. Green, Structural characterization of atomically regulated nanocrystals formed within single-walled carbon nanotubes using electron microscopy, *Acc. Chem. Res.* **35**, 1054–1062 (2002).
456. J. Sloan, M.C. Novotny, S.R. Bailey, G. Brown, C. Xu, V.C. Williams, S. Friedrichs, E. Flahaut, R.R. Callender, A.P.E. York, K.S. Coleman, M.L.H. Green, R.E. Dunin-Borkowski, and J.L. Hutchison, Two layer 4:4 co-ordinated KI crystals grown within single walled carbon nanotubes, *Chem. Phys. Lett.* **329**, 61–65 (2000).
457. M. Wilson, Structure and phase stability of novel ‘twisted’ crystal structures in carbon nanotubes, *Chem. Phys. Lett.* **366**, 504–509 (2002).
458. M. Wilson, The formation of low-dimensional ionic crystallites in carbon nanotubes, *J. Chem. Phys.* **116**, 3027–3041 (2002).
459. Y. Maniwa, H. Kataura, M. Abe, A. Fujiwara, R. Fujiwara, H. Kira, H. Tou, S. Suzuki, Y. Achiba, E. Nishibori, M. Takata, M. Sakata, and H. Suematsu, C<sub>70</sub> molecular stumbling inside single-walled carbon nanotubes, *J. Phys. Soc. Jpn.* **72**, 45–48 (2002).
460. A.C. Dillon, K.M. Jones, T.A. Bekkedahl, C.H. Kiang, D.S. Bethune, and M.J. Heben, Storage of hydrogen in single-walled carbon nanotubes, *Nature* **386**, 377–379 (1997).
461. A. Chambers, C. Park, R.T.K. Baker, and N.M. Rodriguez, Hydrogen storage in graphite nanofibers, *J. Phys. Chem. B* **102**, 4253–4256 (1998).
462. P. Chen, X. Wu, J. Lin, and K.L. Tan, High H<sub>2</sub> uptake by alkali-doped carbon nanotubes under ambient pressure and moderate temperatures, *Science* **285**, 91–93 (1999).
463. Y. Chen, D.T. Shaw, X.D. Bai, E.G. Wang, C. Lund, W.M. Lu, and D.D.L. Chung, Hydrogen storage in aligned carbon nanotubes, *Appl. Phys. Lett.* **78**, 2128–2130 (2001).
464. C. Nützenadel, A. Züttel, D. Chartouni, and L. Schlapbach, Electrochemical storage of hydrogen in nanotube materials, *Electrochem. Solid-State Lett.* **2**, 30–32 (1999).
465. N. Rajalakshmi, K.S. Dhathathreyan, A. Govindaraj, and B.C. Satishkumar, Electrochemical investigation of single-walled carbon nanotubes for hydrogen storage, *Electrochim. Acta* **45**, 4511–4515 (2000).
466. M. Hirscher, M. Becher, M. Haluska, U. Dettlaff-Weglikowska, A. Quintel, G.S. Duesberg, Y.-M. Choi, P. Downes, M. Hulman, S. Roth, I. Stepanek, and P. Bernier, Hydrogen storage in sonicated carbon materials, *Appl. Phys. A* **72**, 129–132 (2001).
467. G.-P. Dai, C. Liu, M. Liu, M.-Z. Wang, and H.-M. Cheng, Electrochemical hydrogen storage behavior of ropes of aligned single-walled carbon nanotubes, *Nano Lett.* **2**, 503–506 (2002).
468. F.J. Owens and Z. Iqbal, Electrochemical functionalization of carbon nanotubes with hydrogen [[www.asc2002.com/summaries/1/LP-11.pdf](http://www.asc2002.com/summaries/1/LP-11.pdf)].
469. H. Takagi, H. Hatori, Y. Soneda, N. Yoshizawa, and Y. Yamada, Adsorptive hydrogen storage in carbon and porous materials, *Mater. Sci. Eng. B* **108**, 143–147 (2004).
470. A. Ansón, M.A. Callejas, A.M. Benito, W.K. Maser, M.T. Izquierdo, B. Rubio, J. Jagiello, M. Thommes, J.B. Parra, and M.T. Martínez, Hydrogen adsorption studies on single wall carbon nanotubes, *Carbon* **42**, 1243–1248 (2004).
471. N. Nishimiya, K. Ishigaki, H. Takikawa, M. Ikeda, Y. Hibi, T. Sakakibara, A. Matsumoto, and K. Tsutsumi, Hydrogen sorption by single-walled carbon nanotubes prepared by a torch arc method, *J. Alloys Comp.* **339**, 275–282 (2002).
472. M. Shiraishi, T. Takenobu, and M. Ata, Gas-solid interactions in the hydrogen/single-walled carbon nanotube system, *Chem. Phys. Lett.* **367**, 633–636 (2003).
473. M. Shiraishi, T. Takenobu, H. Kataura, and M. Ata, Hydrogen adsorption and desorption in carbon nanotube systems and its mechanisms, *Appl. Phys. A* **78**, 947–953 (2004).



474. B.P. Tarasov, J.P. Maehlen, M.V. Lototsky, V.E. Muradyan, and V.A. Yartys, Hydrogen sorption properties of arc generated single-wall carbon nanotubes, *J. Alloys Comp.* **356–357**, 510–514 (2003).
475. P. David, T. Piquero, K. Metenier, Y. Pierre, J. Demoment, and A. Lecas-Hardit, Hydrogen adsorption in carbon materials [<http://www.waterstof.org/2003072EHECP2-200.pdf>].
476. C. Liu, Y.Y. Fan, M. Liu, H.T. Cong, H.M. Cheng, and M.S. Dresselhaus, Hydrogen storage in single-walled carbon nanotubes at room temperature, *Science* **286**, 1127–1129 (1999).
477. D. Luxembourg, G. Flamant, A. Guillot, and D. Laplaze, Hydrogen storage in solar produced single-walled carbon nanotubes, *Mater. Sci. Eng.* **B 108**, 114–119 (2004).
478. M.A. Callejas, A. Ansón, A.M. Benito, W. Maser, J.L.G. Fierro, M.L. Sanjuán, and M.T. Martínez, Enhanced hydrogen adsorption on single-wall carbon nanotubes by sample reduction, *Mater. Sci. Eng.* **B 108**, 120–123 (2004).
479. B.K. Pradhan, A.R. Harutyunyan, D. Stojkovic, J.C. Grossman, P. Zhang, M.W. Cole, V. Crespi, H. Goto, J. Fujiwara, and P.C. Eklund, Large cryogenic storage of hydrogen in carbon nanotubes at low pressures, *J. Mater. Res.* **17**, 2209–2216 (2002).
480. P. Sudan, A. Züttel, Ph. Mauron, Ch. Emmenegger, P. Wenger, and L. Schlapbach, Physisorption of hydrogen in single-walled carbon nanotubes, *Carbon* **41**, 2377–2383 (2003).
481. Y. Ye, C.C. Ahn, C. Witham, B. Fultz, J. Liu, A.G. Rinzler, D. Colbert, K.A. Smith, and R.E. Smalley, Hydrogen absorption and cohesive energy of single-walled carbon nanotubes, *Appl. Phys. Lett.* **74**, 2307–2309 (1999).
482. X.B. Wu, P. Chen, J. Lin, and K.L. Tan, Hydrogen uptake by carbon nanotubes, *Int. J. Hydrogen Energy* **25**, 261–265 (2000).
483. X. Qin, X.P. Gao, H. Liu, H.T. Yuan, D.Y. Yan, W.L. Gong, and D.Y. Song, Electrochemical hydrogen storage of multiwalled carbon nanotubes, *Electrochem. Solid-State Lett.* **3**, 532–535 (2000).
484. A.K.M. Fazle Kibria, Y.H. Mo, K.S. Park, K.S. Nahm, and M.H. Yun, Electrochemical hydrogen storage behaviors of CVD, AD and LA grown carbon nanotubes in KOH medium, *Int. J. Hydrogen Energy*, **26**, 823–829 (2001).
485. R.T. Yang, Hydrogen storage by alkali-doped carbon nanotubes — revisited, *Carbon* **38**, 623–641 (2000).
486. G.Q. Ning, F. Wei, G.H. Luo, Q.X. Wang, Y.L. Wu, and H. Yu, Hydrogen storage in multi-wall carbon nanotubes using samples up to 85 g, *Appl. Phys.* **A 78**, 955–959 (2004).
487. A. Cao, H. Zhu, X. Zhang, X. Li, D. Ruan, C. Xu, B. Wei, J. Liang, and D. Wu, Hydrogen storage of dense-aligned carbon nanotubes, *Chem. Phys. Lett.* **342**, 510–514 (2001).
488. X. Li, H. Zhu, L. Ci, C. Xu, Z. Mao, B. Wei, J. Liang, and D. Wu, Hydrogen uptake by graphitized multi-walled carbon nanotubes under moderate pressure and at room temperature, *Carbon* **39**, 2077–2079 (2001).
489. H.W. Zhu, A. Chen, Z.Q. Mao, C.L. Xu, X. Xiao, B.Q. Wei, J. Liang, and D.H. Wu, The effect of surface treatments on hydrogen storage of carbon nanotubes, *J. Mater. Sci. Lett.* **19**, 1237–1239 (2000).
490. H. Zhu, A. Cao, X. Li, C. Xu, Z. Mao, D. Ruan, J. Liang, and D. Wu, Hydrogen adsorption in bundles of well-aligned carbon nanotubes at room temperature, *Appl. Surf. Sci.* **178**, 50–55 (2001).
491. W.Z. Huang, X.B. Zhang, J.P. Tu, F.Z. Kong, J.X. Ma, F. Liu, H.M. Lu, and C.P. Chen, The effect of pretreatments on hydrogen adsorption of multi-walled carbon nanotubes, *Mater. Chem. Phys.* **78**, 144–148 (2002).
492. P.-X. Hou, S.-T. Xu, Z. Ying, Q.-H. Yang, C. Liu, and H.-M. Cheng, Hydrogen adsorption/desorption behavior of multi-walled carbon nanotubes with different diameters, *Carbon* **41**, 2471–2476 (2003).
493. K. Hanada, H. Shiono, and K. Matsuzaki, Hydrogen uptake of carbon nanofiber under moderate temperature and low pressure, *Diamond Rel. Mater.* **12**, 874–877 (2003).
494. D.J. Browning, M.L. Gerrard, J.B. Lakeman, I.M. Mellor, R.J. Mortimer, and M.C. Turpin, Studies into the storage of hydrogen in carbon nanofibers: proposal of a possible reaction mechanism, *Nano Lett.* **2**, 201–205 (2002).
495. K. Ichimura, K. Imaeda, and H. Inokuchi, Characteristic bonding of rare gases in solid carbon nanotubes, *Synth. Met.* **121**, 1191–1192 (2001).
496. S. Challet, P. Azaïs, R.J.-M. Pellenq, L. Duclaux, D<sub>2</sub> adsorption in potassium-doped single-wall carbon nanotubes: a neutron diffraction and isotherms study, *Chem. Phys. Lett.* **377**, 544–550 (2003).
497. M. Rzepka, P. Lamp, and M.A. de la Casa-Lillo, Physisorption of hydrogen on microporous carbon and carbon nanotubes, *J. Phys. Chem.* **B 102**, 10894–10898 (1998).

498. M.K. Kostov, M.W. Cole, J.C. Lewis, P. Diep, and J.K. Johnson, Many-body interactions among adsorbed atoms and molecules within carbon nanotubes and in free space, *Chem. Phys. Lett.* **332**, 26–34 (2000).
499. C.W. Bauschlicher Jr., Hydrogen and fluorine binding to the sidewalls of a (10,0) carbon nanotube, *Chem. Phys. Lett.* **322**, 237–241 (2000).
500. K.A. Williams and P.C. Eklund, Monte Carlo simulations on H<sub>2</sub> physisorption in finite-diameter carbon nanotube ropes, *Chem. Phys. Lett.* **320**, 352–358 (2000).
501. S.M. Lee, K.S. Park, Y.C. Choi, Y.S. Park, J.M. Bok, D.J. Bae, K.S. Nahm, Y.G. Choi, S.C. Yu, N.-G. Kim, T.Frauenheim, and Y.H. Lee, Hydrogen adsorption and storage in carbon nanotubes, *Synth. Met.* **113**, 209–216 (2000).
502. S.M. Lee and Y.H. Lee, Hydrogen storage in single-walled carbon nanotubes, *Appl. Phys. Lett.* **76**, 2877–2879 (2000).
503. S.-P. Chan, G. Chen, X.G. Gong, and Z.-F. Liu, Chemisorption of hydrogen molecules on carbon nanotubes under high pressure, *Phys. Rev. Lett.* **87**, 205502 (2001).
504. C. Gu, G.-H. Gao, Y.-X. Yu, and Z.-Q. Mao, Simulation study of hydrogen storage in single walled carbon nanotubes, *Int. J. Hydrogen Energy* **26**, 691–696 (2001).
505. S.M. Lee, K.H. An, Y.H. Lee, G. Seifert, and T. Frauenheim, A hydrogen storage mechanism in single-walled carbon nanotubes, *J. Am. Chem. Soc.* **123**, 5059–5063 (2001).
506. S.M. Lee, K.H. An, W.S. Kim, Y.H. Lee, Y.S. Park, G. Seifert, and T. Frauenheim, Hydrogen storage in carbon nanotubes, *Synth. Met.* **121**, 1189–1190 (2001).
507. Y. Ren and D.L. Price, Neutron scattering study of H<sub>2</sub> adsorption in single-walled carbon nanotubes, *Appl. Phys. Lett.* **79**, 3684–3686 (2001).
508. H. Cheng, G.P. Pez, and A.C. Cooper, Mechanism of hydrogen sorption on single-walled carbon nanotubes, *J. Am. Chem. Soc.* **123**, 5845–5846 (2001).
509. C.W. Bauschlicher Jr., High coverages of hydrogen on (10,0) carbon nanotube, *Nano Lett.* **1**, 223–226 (2001).
510. M.K. Kostov, H. Cheng, A.C. Cooper, and G.P. Pez, Influence of carbon curvature in carbon-based materials: a force field approach, *Phys. Rev. Lett.* **89**, 146105 (2002).
511. M.K. Kostov, H. Cheng, R.M. Herman, M.W. Cole, and J.C. Lewis, Hindered rotation of H<sub>2</sub> adsorbed interstitially in nanotube bundles, *J. Chem. Phys.* **116**, 1720–1724 (2002).
512. Y. Ma, Y. Xia, M. Zhao, and M. Ying, Hydrogen storage capacity in single-walled carbon nanotubes, *Phys. Rev. B* **65**, 155430.1–6 (2002).
513. R.A. Trasca, M.K. Kostov, and M.W. Cole, Isotopic and spin selectivity of H<sub>2</sub> adsorbed in bundles of carbon nanotubes, *Phys. Rev. B* **67**, 035410.1–8 (2003).
514. J. Li, T. Furuta, H. Goto, T. Ohashi, Y. Fujiwara, and S. Yip, Theoretical evaluation of hydrogen storage capacity in pure carbon nanostructures, *J. Chem. Phys.* **119**, 2376–2385 (2003).
515. M. Haluska, M. Hirscher, M. Becher, U. Dettlaff-Weglikowska, X. Chen, and S. Roth, Interaction of hydrogen isotopes with carbon nanostructures, *Mater. Sci. Eng. B* **108**, 130–133 (2004).
516. H.G. Schimmel, G. Nijkamp, G.J. Kearley, A. Rivera, K.P. de Jong, and F.M. Mulder, Hydrogen adsorption in carbon nanostructures compared, *Mater. Sci. Eng. B* **108**, 124–129 (2004).
517. D. Chen, L. Chen, S. Liu, C.X. Ma, D.M. Chen, and L.B. Wang, Microstructure and hydrogen storage property of Mg/MWNTs composites, *J. Alloys Comp.* **372**, 231–237 (2004).
518. B.P. Tarasov, N.G. Goldshleger, and A.P. Moravsky, Hydrogen-containing carbon nanostructures: synthesis and properties, *Russ. Chem. Rev.* **70**, 131–146 (2001).
519. H.-M. Cheng, Q.-H. Yang, and C. Liu, Hydrogen storage in carbon nanotubes, *Carbon* **39**, 1447–1454 (2001).
520. F.L. Darkrim, P. Malbrunot, and G.P. Tartaglia, Review of hydrogen storage by adsorption in carbon nanotubes, *Int. J. Hydrogen Energy* **27**, 193–202 (2002).
521. V.V. Simonyan and J.K. Johnson, Hydrogen storage in carbon nanotubes and graphitic nanofibers, *J. Alloys Comp.* **330–332**, 659–665 (2002).
522. E. Frackowiak and F. Béguin, Electrochemical storage of energy in carbon nanotubes and nanostructured carbons, *Carbon* **40**, 1775–1787 (2002).
523. A. Züttel, P. Sudan, Ph. Mauron, T. Kiyobayashi, Ch. Emmenegger, and L. Schlapbach, Hydrogen storage in carbon nanostructures, *Int. J. Hydrogen Energy* **27**, 203–212 (2002).
524. M. Becher, M. Haluska, M. Hirscher, A. Quintel, V. Skakalova, U. Dettlaff-Weglikowska, X. Chen, M. Hulman, Y. Choi, S. Roth, V. Meregalli, M. Parrinello, R. Ströbel, L. Jörissen, M.M. Kappes, J. Fink, A. Züttel, I. Stepanek, and P. Bernier, Hydrogen storage in carbon nanotubes, *C. R. Physique* **4**, 1055–1062 (2003).

525. B. Viswanathan, M. Sankaran, and M.A. Scibioh, Carbon nanomaterials – are they appropriate candidates for hydrogen storage? *Bull. Catal. Soc. India* **2**, 12–32 (2003).
526. A. Züttel, P. Wenger, P. Sudan, P. Mauron, and S.-I. Orimo, Hydrogen density in nanostructured carbon, metals and complex materials, *Mater. Sci. Eng.* **B 108**, 9–18 (2004).
527. M. Conte, P.P. Prosini, and S. Passerini, Overview of energy/hydrogen storage: state-of-the-art of the technologies and prospects for nonomaterials, *Mater. Sci. Eng.* **B 108**, 2–8 (2004).
528. S. Talapatra, A.Z. Zambano, S.E. Weber, and A.D. Migone, Gases do not adsorb on the interstitial channels of closed-ended single-walled carbon nanotube bundles, *Phys. Rev. Lett.* **85**, 138–141 (2000).
529. M.M. Calbi, S.M. Gatica, M.J. Bojan, and M.W. Cole, Phases of neon, xenon, and methane adsorbed on nanotube bundles, *J. Chem. Phys.* **115**, 9975–9981 (2001).
530. M. Muris, N. Dupont-Pavlovsky, M. Bienfait, and P. Zeppenfeld, Where are the molecules adsorbed on single-walled nanotubes? *Surf. Sci.* **492**, 67–74 (2001).
531. J. Zhao, A. Buldum, J. Han, and J.P. Lu, Gas molecule adsorption in carbon nanotubes and nanotube bundles, *Nanotechnology* **13**, 195–200 (2002).
532. B.-Y. Wei, M.-C. Hsu, Y.-S. Yang, S.-H. Chien, and H.-M. Lin, Gases adsorption on single-walled carbon nanotubes measured by piezoelectric quartz crystal microbalance, *Mater. Chem. Phys.* **81**, 126–133 (2003).
533. A. Kleinhammes, S.-H. Mao, X.-J. Yang, X.-P. Tang, H. Shimoda, J.P. Lu, O. Zhou, and Y. Wu. Gas adsorption in single-walled carbon nanotubes studied by NMR, *Phys. Rev.* **B 68**, 075418.1–6 (2003).
534. A. Goldoni, R. Larciprete, L. Petaccia, and S. Lizzit, Single-wall carbon nanotube interaction with gases: sample contaminants and environmental monitoring, *J. Am. Chem. Soc.* **125**, 11329–11333 (2003).
535. S.-H. Jhi, S.G. Loui, and M.L. Cohen, Electronic properties of oxidized carbon nanotubes, *Phys. Rev. Lett.* **85**, 1710–1713 (2000).
536. S. Dag, O. Gülseren, and S. Ciraci, A comparative study of O<sub>2</sub> adsorbed carbon nanotubes, *Chem. Phys. Lett.* **380**, 1–5 (2003).
537. M. Cinke, J. Li, C.W. Bauschlicher Jr., A. Ricca, and M. Meyyappan, CO<sub>2</sub> adsorption in single-walled carbon nanotubes, *Chem. Phys. Lett.* **276**, 761–766 (2003).
538. C. Matranga, L. Chen, M. Smith, E. Bittner, J.K. Johnson, and B. Bockrath, Trapped CO<sub>2</sub> in carbon nanotube bundles, *J. Phys. Chem.* **B 107**, 12930–12941 (2003).
539. W.-L. Yim, O. Byl, J.T. Yates Jr., and J.K. Johnson, Vibrational behavior of adsorbed CO<sub>2</sub> on single-walled carbon nanotubes, *J. Chem. Phys.* **120**, 5377–5386 (2004).
540. H. Chang, J.D. Lee, S.M. Lee, Y.H. Lee, Adsorption of NH<sub>3</sub> and NO<sub>2</sub> molecules on carbon nanotubes, *Appl. Phys. Lett.* **79**, 3863–3865 (2001).
541. S.E. Weber, S. Talapatra, C. Journet, A. Zambano, and A.D. Migone, Determination of the binding energy of methane on single-walled carbon nanotube bundles, *Phys. Rev.* **B 61**, 13150–13154 (2000).
542. H. Tanaka, M. El-Merraoui, W.A. Steele, and K. Kaneko, Methane adsorption on single-walled carbon nanotube: a density functional theory model, *Chem. Phys. Lett.* **352**, 334–341 (2002).
543. S. Talapatra and A.D. Migone, Adsorption of methane on bundles of closed-ended single-wall carbon nanotubes, *Phys. Rev.* **B 65**, 454161–454166 (2002).
544. L. Valentini, I. Armentano, L. Lozzi, S. Santucci, and J.M. Kenny, Interaction of methane with carbon nanotube thin films: role of defects and oxygen adsorption, *Mater. Sci. Eng.* **C 24**, 527–533 (2004).
545. Gy. Onyestyák, J. Vallyon, K. Hernádi, I. Kiricsi, and L.V.C. Rees, Equilibrium and dynamics of acetylene sorption in multiwalled carbon nanotubes, *Carbon* **41**, 1241–1248 (2003).
546. N. Chakrapani, Y.M. Zhang, S.K. Nayak, J.A. Moore, D.L. Carroll, Y.Y. Choi, and P.M. Ajayan, Chemisorption of acetone on carbon nanotubes, *J. Phys. Chem.* **B 107**, 9308–9311 (2003).
547. M.R. Babaa, N. Dupont-Pavlovsky, E. McRae, and K. Masenelli-Varlot, Physical adsorption of carbon tetrachloride on as-produced and on mechanically opened single walled carbon nanotubes, *Carbon* **42**, 1549–1554 (2004).
548. C.-M. Yang, H. Kanoh, K. Kaneko, M. Yudasaka, and S. Iijima, Adsorption behaviors of HiPco single-walled carbon nanotube aggregates for alcohol vapors, *J. Phys. Chem.* **B 106**, 8994–8999 (2002).
549. J.A. Nisha, M. Yudasaka, S. Bandow, F. Kokai, K. Takahashi, and S. Iijima, Adsorption and catalytic properties of single-wall carbon nanohorns, *Chem. Phys. Lett.* **328**, 381–386 (2000).
550. H. Ago, R. Azumi, S. Ohshima, Y. Zhang, H. Kataura, and M. Yumura, STM study of molecular adsorption on single-wall carbon nanotube surface, *Chem. Phys. Lett.* **383**, 469–474 (2004).
551. M. Bienfait, B. Asmussen, M. Johnson, and P. Zeppenfeld, Methane mobility in carbon nanotubes, *Surf. Sci.* **460**, 243–248 (2000).

552. S.M. Cooper, B.A. Cruden, and M. Meyyappan, Gas transport characteristics through a carbon nanotubule, *Nano Lett.* **4**, 377–381 (2004).
553. P.G. Collins, K. Bradley, M. Ishigami, and A. Zettl, Extreme oxygen sensitivity of electronic properties of carbon nanotubes, *Science* **287**, 1801–1804 (2000).
554. R. Pati, Y. Zhang, S.K. Nayak, and P.M. Ajayan, Effect of H<sub>2</sub>O adsorption on electron transport in a carbon nanotube, *Appl. Phys. Lett.* **81**, 2638–2640 (2002).
555. G.U. Sumanasekera, C.K.W. Adu, S. Fang, and P.C. Eklund, Effect of gas adsorption and collisions on electrical transport in single-walled carbon nanotubes, *Phys. Rev. Lett.* **85**, 1096–1099 (2000).
556. K. Bradley, S.-H. Jhi, P.G. Collins, J. Hone, M.L. Cohen, S.G. Louie, and A. Zettl, Is the intrinsic thermoelectric power of carbon nanotubes positive? *Phys. Rev. Lett.* **85**, 4361–4364 (2000).
557. G.U. Sumanasekera, B.K. Pradhan, H.E. Romero, K.W. Adu, and P.C. Eklund, Giant thermopower effects from molecular physisorption on carbon nanotubes, *Phys. Rev. Lett.* **89**, 166801 (2002).
558. J. Kong, N.R. Franklin, C. Zhou, M.C. Chapline, S. Peng, K. Cho, and H. Dai, Nanotube molecular wires as chemical sensors, *Science* **287**, 622–625 (2000).
559. S. Peng, K. Cho, P. Qi, and H. Dai, Ab initio study of CNT NO<sub>2</sub> gas sensor, *Chem. Phys. Lett.* **387**, 271–276 (2004).
560. C. Cantalini, L. Valentini, I. Armentano, J.M. Kenny, L. Lozzi, and S. Santucci, Carbon nanotubes as new materials for gas sensing applications, *J. Eur. Ceram. Soc.* **24**, 1405–1408 (2004).
561. L. Valentini, C. Cantalini, I. Armentano, J.M. Kenny, L. Lozzio, and S. Santucci, Highly sensitive and selective sensors based on carbon nanotubes thin films for molecular detection, *Diamond Rel. Mater.* **13**, 1301–1305 (2004).
562. L. Valentini, F. Mercuri, I. Armentano, C. Cantalini, S. Picozzi, L. Lozzi, S. Santucci, A. Sgamellotti, and J.M. Kenny, Role of the defects on the gas sensing properties of carbon nanotubes thin films: experiment and theory, *Chem. Phys. Lett.* **387**, 356–361 (2004).
563. O.K. Varghese, P.D. Kichambre, D. Gong, K.G. Ong, E.C. Dickey, and C.A. Grimes, Gas sensing characteristics of multi-wall carbon nanotubes, *Sensors Actuators B* **81**, 32–41 (2001).
564. K.G. Ong, K. Zeng, and C.A. Grimes, A wireless, passive carbon nanotube-based gas sensor, *IEEE Sensor J.* **2**, 82–88 (2002).
565. S.G. Wang, Q. Zhang, D.J. Yang, P.J. Sellin, and G.F. Zhong, Multi-walled carbon nanotube-based gas sensors for NH<sub>3</sub> detection, *Diamond Rel. Mater.* **13**, 1327–1332 (2004).
566. C.K.W. Adu, G.U. Sumanasekera, B.K. Pradhan, H.E. Romero, and P.C. Eklund, Carbon nanotubes: a thermoelectric nano-nose, *Chem. Phys. Lett.* **337**, 31–35 (2001).
567. S. Peng and K. Cho, Ab initio study of doped carbon nanotube sensors, *Nano Lett.* **3**, 513–517 (2003).
568. F. Villalpando-Páez, A.H. Romero, E. Muñoz-Sandoval, L.M. Martínez, H. Terrones, and M. Terrones, Fabrication of vapor and gas sensors using films of aligned CN<sub>x</sub> nanotubes, *Chem. Phys. Lett.* **386**, 137–143 (2004).
569. J. Li, Y. Lu, Q. Ye, M. Cinke, J. Han, and M. Meyyappan, Carbon nanotube sensors for gas and organic vapor detection, *Nano Lett.* **3**, 929–933 (2003).
570. J. Kong, M.G. Chapline, and H. Dai, Functionalized carbon nanotubes for molecular hydrogen sensors, *Adv. Mater.* **13**, 1384–1386 (2001).
571. L. Dai, P. Soundarrajan, and T. Kim, Sensors and sensor arrays based on conjugated polymers and carbon nanotubes, *Pure Appl. Chem.* **74**, 1753–1772 (2002).
572. A. Huczko, H. Lange, E. Caiko, H. Grubek-Jaworska, and P. Droszcz, Physiological testing of carbon nanotubes: are they asbestos-like? *Fullerene Sci. Technol. (Fullerenes Nanotubes Carbon Nanostruct.)* **9**, 251–254 (2001).
573. M. Shim, N.W.S. Kam, R.J. Chen, Y. Li, and H. Dai, Functionalization of carbon nanotubes for biocompatibility and biomolecular recognition, *Nano Lett.* **2**, 285–288 (2002).
574. K. Besteman, J.-O. Lee, F.G.M. Wiertz, H.A. Heering, and C. Dekker, Enzyme-coated carbon nanotubes as single-molecule biosensors, *Nano Lett.* **3**, 727–730 (2003).
575. A. Bianco and M. Prato, Can carbon nanotubes be considered useful tools for biological applications? *Adv. Mater.* **15**, 1765–1768 (2003).
576. J.J. Davis, K.S. Coleman, B.R. Azamian, C.B. Bagshaw, and M.L.H. Green, Chemical and biochemical sensing with modified single walled carbon nanotubes, *Chem. Eur. J.* **9**, 3733–3739 (2003).
577. Q. Zhao, Z. Gan, and Q. Zhuang, Electrochemical sensors based on carbon nanotubes, *Electroanalysis* **14**, 1609–1613 (2002).

578. P.J. Britto, K.S.V. Santhanam, and P.M. Ajayan, Carbon nanotube electrode for oxidation of dopamine, *Bioelectrochem. Bioenergetics* **41**, 121–125 (1996).
579. J. Wang, M. Li, Z. Shi, N. Li, and Z. Gu, Electrocatalytic oxidation of norepinephrine at a glassy carbon electrode modified with single wall carbon nanotubes, *Electroanalysis* **14**, 225–230 (2002).
580. K. Wu, X. Ji, J. Fei, and S. Hu, The fabrication of a carbon nanotube film on a glassy carbon electrode and its application to determining thyroxine, *Nanotechnology* **15**, 287–291 (2004).
581. S.C. Tsang, Z. Guo, Y.K. Chen, M.L.H. Green, H.A.O. Hill, T.W. Hambley, and P.J. Sadler, Immobilization of platinated and iodinated oligonucleotides on carbon nanotubes, *Angew. Chem. Int. Edit.* **36**, 2200–2220 (1997).
582. Z. Guo, P.J. Sadler, and S.C. Tsang, Immobilization and visualization of DNA and proteins on carbon nanotubes, *Adv. Mater.* **10**, 701–703 (1998).
583. R.J. Chen, Y. Zhang, D. Wang, and H. Dai, Noncovalent sidewall functionalization of single-walled carbon nanotubes for protein immobilization, *J. Am. Chem. Soc.* **123**, 3838–3839 (2001).
584. R.J. Chen, S. Bangsaruntip, K.A. Drouvalakis, N.W.S. Kam, M. Shim, Y. Li, W. Kim, P.J. Utz, and H. Dai, Noncovalent functionalization of carbon nanotubes for highly specific electronic biosensors, *Proc. Nat. Acad. Sci. USA* **100**, 4984–4989 (2003).
585. S.E. Baker, W. Cai, T.L. Lasseter, K.P. Weidkamp, and R.J. Hamers, Covalently bonded adducts of deoxyribonucleic acid (DNA) oligonucleotides with single-wall carbon nanotubes: synthesis and hybridization, *Nano Lett.* **2**, 1413–1417 (2002).
586. K.A. Williams, P.T.M. Veenhuizen, B.G. de la Torre, R. Eritja, and C. Dekker, Nanotechnology: carbon nanotube with DNA recognition, *Nature*, **420**, 761 (2002).
587. C.V. Nguyen, L. Delzeit, A.M. Cassell, J. Li, J. Han, and M. Meyyappan, Preparation of nucleic acid functionalized carbon nanotube arrays, *Nano Lett.* **2**, 1079–1081 (2002).
588. J. Li, H.T. Ng, A.M. Cassell, W. Fan, H. Chen, Q. Ye, J. Koehne, J. Han, and M. Meyyappan, Carbon nanotube nanoelectrode array for ultrasensitive DNA detection, *Nano Lett.* **3**, 597–602 (2003).
589. J. Koehne, H. Chen, J. Li, A.M. Cassell, Q. Ye, H.T. Ng, J. Han, and M. Meyyappan, Ultrasensitive label-free DNA analysis using an electronic chip based on carbon nanotube nanoelectrode arrays, *Nanotechnology* **14**, 1239–1245 (2003).
590. H. Cai, X. Cao, Y. Jiang, P. He, and Y. Fang, Carbon nanotube-enhanced electrochemical DNA biosensor for DNA hybridization detection, *Anal. Bioanal. Chem.* **375**, 287–293 (2003).
591. M.L. Pedano and G.A. Rivas, Immobilization of DNA on glassy carbon electrodes for the development of affinity biosensors, *Biosens. Bioelectron.* **18**, 269–277 (2003).
592. A. Guiseppi-Elie, C. Lei, and R.H. Baughman, Direct electron transfer of glucose oxidase on carbon nanotubes, *Nanotechnology* **13**, 559–564 (2002).
593. S. Sotiropoulou and N.A. Chaniotakis, Carbon nanotube array-based biosensor, *Anal. Bioanal. Chem.* **375**, 103–105 (2003).
594. L. Wang and Z. Yuan, Direct electrochemistry of glucose oxidase at a gold electrode modified with single-wall carbon nanotubes, *Sensors* **3**, 544–554 (2003).
595. J.H.T. Luong, S. Hrapovic, D. Wang, F. Bensebaa, and B. Simard, Solubilization of multiwall carbon nanotubes by 3-aminopropyltriethoxysilane towards the fabrication of electrochemical biosensors with promoted electron transfer, *Electroanalysis* **16**, 132–139 (2004).
596. K.P. Loh, S.L. Zhao, and W.D. Zhang, Diamond and carbon nanotube glucose sensors based on electropolymerization, *Diamond Rel. Mater.* **13**, 1075–1079 (2004).
597. R.J. Chen, H.C. Choi, S. Bangsaruntip, E. Yenilmez, X. Tang, Q. Wang, Y.-L. Chang, and H. Dai, An investigation of the mechanisms of electronic sensing of protein adsorption on carbon nanotube devices, *J. Am. Chem. Soc.* **126**, 1563–1568 (2004).
598. A. Star, J.-C.P. Gabriel, K. Bradley, and G. Grüner, Electronic detection of specific protein binding using nanotube FET devices, *Nano Lett.* **3**, 459–463 (2003).
599. S.C. Tsang, J.J. Davis, M.L.H. Green, H.A.O. Hill, Y.C. Leung, and P.J. Sadler, Immobilization of small proteins in carbon nanotubes: high-resolution transmission electron microscopy study and catalytic activity, *Chem. Commun.* 1803–1804 (1995).
600. J.J. Davis, M.L.H. Green, H.A.O. Hill, Y.C. Leung, P.J. Sadler, J. Sloan, A.V. Xavier, and S.C. Tsang, The immobilization of proteins in carbon nanotubes, *Inorg. Chim. Acta* **272**, 261–266 (1998).
601. F. Balavoine, P. Schultz, C. Richard, V. Mallouh, T.W. Ebbesen, and C. Mioskowski, Helical crystallization of proteins on carbon nanotubes: a first step towards development of new biosensors, *Angew. Chem. Int. Ed.* **38**, 1912–1915 (1999).

602. B.R. Azamian, J.J. Davis, K.S. Coleman, C.B. Bagshow, and M.L.H. Green, Bioelectrochemical single-walled carbon nanotubes, *J. Am. Chem. Soc.* **124**, 12664–12665 (2002).
603. W. Huang, S. Taylor, K. Fu, Y. Lin, D. Zhang, T.W. Hanks, A.M. Rao, and Y.-P. Sun, Attaching proteins to carbon nanotubes via diimide-activated amidation, *Nano Lett.* **2**, 311–314 (2002).
604. X. Yu, D. Chattopadhyay, I. Galeska, F. Papadimitrakopoulos, and J.F. Rusling, Peroxidase activity of enzymes bound to the ends of single-wall nanotube forest electrodes, *Electrochem. Commun.* **5**, 408–411 (2003).
605. M. in het Panhuis, C. Salvador-Morales, E. Franklin, G. Chambers, A. Fonseca, J.B. Nagy, W.J. Blau, and A.I. Minetta, Characterization of an interaction between functionalized carbon nanotubes and an enzyme, *J. Nanosci. Nanotech.* **3**, 209–213 (2003).
606. K. Jiang, L.S. Schadler, R.W. Siegel, X. Zhang, H. Zhang, and M. Terrones, Protein immobilization on carbon nanotubes via a two-step process of diimide-activated amidation, *J. Mater. Chem.* **14**, 37–39 (2004).
607. D. Pantarotto, C.D. Partidos, R. Graff, J. Hoebcke, J.-P. Briand, M. Prato, and A. Bianco, Synthesis, structural characterization, and immunological properties of carbon nanotubes functionalized with peptides, *J. Am. Chem. Soc.* **125**, 6160–6164 (2003).
608. R.D. Klausner, Challenges and vision for nanoscience and nanotechnology in medicine: cancer as a model, *BECON Nanoscience and Nanotechnology Symp. Report*, June 2000, 8–9.
609. M. Meyyappan, D.J. Loftus, J. Han, A.M. Cassell, J. Kaysen, C.V. Nguyen, S. Liang, R.M.D. Stevens, R. Jaffe, A. Hermone, and S. Verma, Applications of nanotube nanotechnology to biosensors and cancer research, *Principal Investigators Meeting Unconventional Innovations Program*, June 28–29, 2000, Hyatt Dulles Hotel, Herndon, Virginia, US [[http://otir.nci.nih.gov/cgi-bin/uip\\_search.cgi?ABSTRACTID=UIP-00-015](http://otir.nci.nih.gov/cgi-bin/uip_search.cgi?ABSTRACTID=UIP-00-015)].
610. Y. Lin, F. Lu, and J. Wang, Disposable carbon nanotube modified screen-printed biosensor for amperometric detection of organophosphorus pesticides and nerve agents, *Electroanalysis* **16**, 145–149 (2004).
611. T.S. Huang, Y. Tzeng, Y.K. Liu, Y.C. Chen, K.R. Walker, R. Guntupalli, and C. Liu, Immobilization of antibodies and bacterial binding on nanodiamond and carbon nanotubes for biosensor applications, *Diamond Rel. Mater.* **13**, 1098–1102 (2004).
612. Y.Z. Guo and A.R. Guadalupe, Direct electrochemistry of horseradish peroxidase adsorbed on glassy carbon electrode from organic solutions, *Chem. Commun.* 1437–1438 (1997).
613. P. Král, Control of catalytic activity of proteins in vivo by nanotube ropes excited with infrared light, *Chem. Phys. Lett.* **382**, 399–403 (2003).
614. K. Rege, N.R. Raravikar, D.-Y. Kim, L.S. Schadler, P.M. Ajayan, and J.S. Dordick, Enzyme–polymer–single walled carbon nanotube composites as biocatalytic films, *Nano Lett.* **3**, 829–832 (2003).
615. D. Pantarotto, J.-P. Briand, M. Prato, and A. Bianco, Translocation of bioactive peptides across cell membranes by carbon nanotubes, *Chem. Commun.* 16–17 (2004).
616. L. Zhang, G.-C. Zhao, X.-W. Wei, and Z.-S. Yang, Electroreduction of oxygen by myoglobin on multi-walled carbon nanotube-modified glassy carbon electrode, *Chem. Lett.* **33**, 86–87 (2004).
617. J.-S. Ye, Y. Wen, W.D. Zhang, H.-F. Cui, L.M. Gan, G.Q. Xu, and F.-S. Sheu, Application of multi-walled carbon nanotubes functionalized with hemin for oxygen detection in neutral solution, *J. Electroanal. Chem.* **562**, 241–246 (2004).
618. M.P. Mattson, R.C. Haddon, and A.M. Rao, Molecular functionalization of carbon nanotubes and use as substrates for neuronal growth, *J. Mol. Neurosci.* **14**, 175–182 (2000).
619. H. Hu, Y. Ni, V. Montana, R.C. Haddon, and V. Parpura, Chemically functionalized carbon nanotubes as substrates for neuronal growth, *Nano Lett.* **4**, 507–511 (2004).
620. C. Richard, F. Balavoine, P. Schultz, T.W. Ebbesen, and C. Mioskowski, Supramolecular self-assembly of lipid derivatives on carbon nanotubes, *Science* **300**, 775–778 (2003).
621. N. Nakashima, S. Okuzono, H. Marukami, T. Nakai, and K. Yoshikawa, DNA dissolves single-walled carbon nanotubes in water, *Chem. Lett.* **32**, 456–457 (2003).
622. K. Matsuura, K. Hayashi, and N. Kimizuka, Lectin-mediated supramolecular junctions of galactose-derivatized single-walled carbon nanotubes, *Chem. Lett.* **32**, 212–213 (2003).
623. M. Zheng, A. Jagota, M.S. Strano, A.P. Santos, P. Barone, S.G. Chou, B.A. Diner, M.S. Dresselhaus, R.S. Mclean, G.B. Onoa, G.G. Samsonidze, E.D. Semke, M. Ursey, and D.J. Walls, Structure-based carbon nanotube sorting by sequence-dependent DNA assembly, *Science* **302**, 1545–1548 (2003).

624. M. Zheng, A. Jagota, E.D. Semke, B.A. Diner, R.S. McLean, S.R. Lustig, R.E. Richardson, and N.G. Tassi, DNA-assisted dispersion and separation of carbon nanotubes, *Nat. Mater.* **2**, 338–342 (2003).
625. J.N. Barisci, M. Tahhan, G.G. Wallace, S. Badaire, T. Vaugien, M. Maugey, and P. Poulin, Properties of carbon nanotube fibers spun from DNA-stabilized dispersions, *Adv. Funct. Mater.* **14**, 133–138 (2004).
626. H. Xin and A.T. Woolley, DNA-templated nanotube localization, *J. Am. Chem. Soc.* **125**, 8710–8711 (2003).
627. K. Keren, R.S. Berman, E. Buchstab, U. Sivan, and E. Braun, DNA-templated carbon nanotube field-effect transistor, *Science* **302**, 1380–1382 (2003).
628. C. Dwyer, M. Guthold, M. Falvo, S. Washburn, R. Superfine, and D. Erie, DNA-functionalized single-walled carbon nanotubes, *Nanotechnology* **13**, 601–604 (2002).
629. R. Czerw, M. Terrones, J.-C. Charlier, X. Blase, B. Foley, R. Kamalakaran, N. Grobert, H. Terrones, D. Tekleab, P.M. Ajayan, W. Blau, M. Rühle, and D.L. Carroll, Identification of electron donor states in N-doped carbon nanotubes, *Nano Lett.* **1**, 457–460 (2001).
630. M. Terrones, N. Grobert, M. Terrones, H. Terrones, P.M. Ajayan, F. Banhart, X. Blase, D.L. Carroll, R. Czerw, J.C. Charlier, B. Foley, R. Kamalakaran, P.H. Kohler-Redlich, M. Rühle, and T. Seeger, Doping and connecting carbon nanotubes, *Mol. Cryst. Liq. Cryst.* **387**, 51–62 (2002).
631. A.H. Nevidomskyy, G. Csányi, and M.C. Payne, Chemically active substitutional nitrogen impurity in carbon nanotubes, *Phys. Rev. Lett.* **91**, 105502-1–4 (2003).
632. Y. Huang, J. Gao, and R. Liu, Structure and electronic properties of nitrogen-containing carbon nanotubes, *Synth. Met.* **113**, 251–255 (2000).
633. R. Droppa Jr., P. Hammer, A.C.M. Carvalho, M.C. dos Santos, and F. Alvarez, Incorporation of nitrogen in carbon nanotubes, *J. Non-Cryst. Solids* **299–302**, 874–879 (2002).
634. M. Glerup, J. Steinmetz, D. Samaille, O. Stéphan, S. Enouz, A. Loiseau, S. Roth, and P. Bernier, Synthesis of N-doped SWNT using the arc-discharge procedure, *Chem. Phys. Lett.* **387**, 193–197 (2004).
635. R. Sen, B.C. Satishkumar, A. Govindaraj, K.R. Harikumar, G. Raina, J.-P. Zhang, A.K. Cheetham, and C.N.R. Rao, B–C–N, C–N and B–N nanotubes produced by the pyrolysis of precursor molecules over Co catalysts, *Chem. Phys. Lett.* **287**, 671–676 (1998).
636. K. Suenaga, M. Yudasaka, C. Colliex, and S. Iijima, Radially modulated nitrogen distribution in  $CN_x$  nanotubular structures prepared by CVD using Ni phthalocyanine, *Chem. Phys. Lett.* **316**, 365–372 (2000).
637. R. Kurt and A. Karimi, Influence of nitrogen on the growth mechanism of decorated C:N nanotubes, *Chem. Phys. Chem.* **2**, 388–392 (2001).
638. R. Kurt, J.-M. Bonard, and A. Karimi, Structure and field emission properties of decorated C/N nanotubes tuned by diameter variations, *Thin Solid Films* **398–399**, 193–198 (2001).
639. R. Kurt, C. Klinke, J.-M. Bonard, K. Kern, and A. Karimi, Tailoring the diameter of decorated C–N nanotubes by temperature variations using HF-CVD, *Carbon* **39**, 2163–2172 (2001).
640. M. Terrones, P.M. Ajayan, F. Banhart, X. Blase, D.L. Carroll, J.C. Charlier, R. Czerw, B. Foley, N. Grot, R. Kamalakaran, P. Kohler-Redlich, M. Rühle, T. Seeger, and H. Terrones, N-doping and coalescence of carbon nanotubes: synthesis and electronic properties, *Appl. Phys. A* **74**, 355–361 (2002).
641. X. Wang, Y. Liu, D. Zhu, L. Zhang, H. Ma, N. Yao, and B. Zhang, Controllable growth, structure, and low field emission of well-aligned  $CN_x$  nanotubes, *J. Phys. Chem. B* **106**, 2186–2190 (2002).
642. C.J. Lee, S.C. Lyu, H.-W. Kim, J.H. Lee, and K.I. Cho, Synthesis of bamboo-shaped carbon-nitrogen nanotubes using  $C_2H_2-NH_3-Fe(CO)_5$  system, *Chem. Phys. Lett.* **359**, 115–120 (2002).
643. T.-Y. Kim, K.-R. Lee, K.Y. Eun, and K.-H. Oh, Carbon nanotube growth enhanced by nitrogen incorporation, *Appl. Phys. Lett.* **372**, 603–607 (2003).
644. H. Yan, Q. Li, J. Zhang, and Z. Liu, The effect of hydrogen on the formation of nitrogen-doped carbon nanotubes via catalytic pyrolysis of acetonitrile, *Adv. Nanomat. Nanodevices (8th International Conference on Electronic Materials, IUMRS-ICEM 2002, Xi'an, China, 10–14 June 2002)*, preprint [[http://nanotechweb.org/dl/nanomaterials/Xian\\_article\\_01\\_was153468.pdf](http://nanotechweb.org/dl/nanomaterials/Xian_article_01_was153468.pdf)].
645. H. Yan, Q. Li, J. Zhang, and Z. Liu, The effect of hydrogen on the formation of nitrogen-doped carbon nanotubes via catalytic pyrolysis of acetonitrile, *Chem. Phys. Lett.* **380**, 347–351 (2003).
646. C.H. Lin, H.L. Chang, C.M. Hsu, A.Y. Lo, and C.T. Kuo, The role of nitrogen in carbon nanotube formation, *Diamond Rel. Mater.* **12**, 1851–1857 (2003).
647. V.D. Blank, E.V. Polyakov, D.V. Batov, B.A. Kulnitskiy, U. Bangert, A. Gutiérrez-Sosa, A.J. Harvey, and A. Seepujak, Formation of N-containing C-nanotubes and nanofibres by carbon resistive heating under high nitrogen pressure, *Diamond Rel. Mater.* **12**, 864–869 (2003).

648. J. Maultzsch, S. Reich, C. Thomsen, S. Webster, R. Czerw, D.L. Carroll, S.M.C. Vieira, P.R. Birkett, and C.A. Rego, Raman characterization of boron-doped multiwalled carbon nanotubes, *Appl. Phys. Lett.* **81**, 2647–2649 (2002).
649. J. Xu, M. Xiao, R. Czerw, and D.L. Carroll, Optical limiting and enhanced optical nonlinearity in boron-doped carbon nanotubes, *Chem. Phys. Lett.* **389**, 247–250 (2004).
650. B.C. Satishkumar and C.N.R. Rao, Boron-carbon nanotubes from the pyrolysis of  $C_2H_2$ - $B_2H_6$  mixtures, *Chem. Phys. Lett.* **300**, 473–477 (1999).
651. C.F. Chen, C.L. Tsai, and C.L. Lin, The characterization of boron-doped carbon nanotube arrays, *Diamond Rel. Mater.* **12**, 1500–1504 (2003).
652. J.Y. Lao, W.Z. Li, J.G. Wen, and Z.F. Ren, Boron carbide nanolumps on carbon nanotubes, *Appl. Phys. Lett.* **80**, 500–502 (2002).
653. E. Borowiak-Palen, T. Pichler, G.G. Fuentes, A. Graff, R.J. Kalenczuk, M. Knupfer, and J. Fink, Efficient production of B-substituted single-wall carbon nanotubes, *Chem. Phys. Lett.* **378**, 516–520 (2003).
654. E. Borowiak-Palen, T. Pichler, A. Graff, R.J. Kalenczuk, M. Knupfer, and J. Fink, Synthesis and electronic properties of B-doped single wall carbon nanotubes, *Carbon* **42**, 1123–1126 (2004).
655. Y.-J. Lee, H.-H. Kim, and H. Hatori, Effects of substitutional B on oxidation of carbon nanotubes in air and oxygen plasma, *Carbon* **42**, 1053–1056 (2004).
656. W. Han, Y. Bando, K. Kurashima, and T. Sato, Synthesis of boron nitride nanotubes from carbon nanotubes by a substitution reaction, *Appl. Phys. Lett.* **73**, 3085–3087 (1998).
657. W. Han, Y. Bando, K. Kurashima, and T. Sato, Boron-doped carbon nanotubes prepared through a substitution reaction, *Chem. Phys. Lett.* **299**, 368–373 (1999).
658. D. Golberg, Y. Bando, K. Kurashima, and T. Sato, Synthesis, HRTEM and electron diffraction studies of B/N-doped C and BN nanotubes, *Diamond Rel. Mater.* **10**, 63–67 (2001).
659. X.D. Bai, J.D. Guo, J. Yu, E.G. Wang, J. Yuan, and W. Zhou, Synthesis and field-emission behavior of highly oriented boron carbonitride nanofibers, *Appl. Phys. Lett.* **76**, 2624–2626 (2000).
660. D. Golberg, Y. Bando, L. Bourgeois, K. Kurashima, and T. Sato, Large-scale synthesis and HRTEM analysis of single-walled B- and N-doped carbon nanotube bundles, *Carbon* **38**, 2017–2027 (2000).
661. D. Golberg, P. Dorozhkin, Y. Bando, M. Hasegawa, and Z.-C. Dong, Semiconducting B–C–N nanotubes with few layers, *Chem. Phys. Lett.* **359**, 220–228 (2002).
662. R.J. Baierle, S.B. Fagan, R. Mota, A.J.R. da Silva, and A. Fazzio, Electronic and structural properties of silicon-doped carbon nanotubes, *Phys. Rev. B* **64**, 085413.1–4 (2001).
663. S.B. Fagan, R. Mota, A.J.R. da Silva, and A. Fazzio, Substitutional Si doping in deformed carbon nanotubes, *Nano Lett.* **4**, 975–977 (2004).
664. Y. Zhang, T. Ichihashi, E. Landree, F. Nihey, and S. Iijima, Heterostructures of single-walled carbon nanotubes and carbide nanorods, *Science* **285**, 1719–1722 (1999).
665. Q. Li, S. Fan, W. Han, C. Sun, and W. Liang, Coating of carbon nanotube with nickel by electroless plating method, *Jpn. J. Appl. Phys.* **36 B**, L501–L503 (1997).
666. Z. Shi, X. Wang, and Z. Ding, The study of electroless deposition of nickel on graphite fibers, *Appl. Surf. Sci.* **140**, 106–110 (1999).
667. L.M. Ang, T.S.A. Hor, G.Q. Xu, C.H. Tung, S.P. Zhao, and J.L.S. Wang, Decoration of activated carbon nanotubes with copper and nickel, *Carbon* **38**, 363–372 (2000).
668. F.Z. Kong, X.B. Zhang, W.Q. Xiong, F. Liu, W.Z. Huang, Y.P. Sun, J.P. Tu, and X.W. Chen, Continuous Ni-layer on multiwall carbon nanotubes by an electroless plating method, *Surf. Coat. Technol.* **155**, 33–36 (2002).
669. Q. Xu, L. Zhang, J. Zhu, Controlled growth of composite nanowires based on coating Ni on carbon nanotubes by electrochemical deposition method, *J. Phys. Chem. B* **107**, 8294–8296 (2003).
670. S. Arai, M. Endo, and N. Kaneko, Ni-deposited multi-walled carbon nanotubes by electrodeposition, *Carbon* **42**, 641–644 (2004).
671. T.V. Reshchenko, L.B. Avdeeva, Z.R. Ismagilov, and A.L. Chuvilin, Catalytic filamentous carbon as supports for nickel catalysts, *Carbon* **42**, 143–148 (2004).
672. Y. Zhang, W. Franklin, R.J. Chen, and H. Dai, Metal coating on suspended carbon nanotubes and its implication to metal-tube interaction, *Chem. Phys. Lett.* **331**, 35–41 (2000).
673. Y. Zhang and H.J. Dai, Formation of metal nanowires on suspended single-walled carbon nanotubes, *Appl. Phys. Lett.* **77**, 3015–3017 (2000).
674. P. Chen, X. Wu, J. Lin, and K.L. Tan, Synthesis of Cu nanoparticles and microsized fibers by using carbon nanotubes as a template, *J. Phys. Chem. B* **103**, 4559–4561 (1999).



675. X. Chen, J. Xia, J. Peng, W. Li, and S. Xie, Carbon-nanotube metal-matrix composites prepared by electroless plating, *Composites Sci. Technol.* **60**, 301–306 (2000).
676. Z.-J. Liu, Z. Xu, Z.-Y. Yuan, W. Chen, W. Zhou, and L.-M. Peng, A simple method for coating carbon nanotubes with Co–B amorphous alloy, *Mater. Lett.* **57**, 1339–1344 (2003).
677. B.C. Satishkumar, E.M. Vogl, A. Govindaraj, and C.N.R. Rao, The decoration of carbon nanotubes by metal nanoparticles, *J. Phys.* **D 29**, 3173–3176 (1996).
678. W. Li, C. Liang, J. Qiu, W. Zhou, H. Han, Z. Wei, G. Sun, and Q. Xin, Carbon nanotubes as support for cathode catalyst of a direct methanol fuel cell, *Carbon* **40**, 791–794 (2002).
679. W. Li, C. Liang, W. Zhou, J. Qiu, H. Li, G. Sun, and Q. Xin, Homogeneous and controllable Pt particles deposited on multi-wall carbon nanotubes as cathode catalyst for direct methanol fuel cells, *Carbon* **42**, 436–439 (2004).
680. R. Yu, L. Chen, Q. Liu, J. Lin, K.-L. Tan, S.C. Ng, H.S.O. Chan, G.-Q. Xu, and T.S.A. Hor, Platinum deposition on carbon nanotubes via chemical modification, *Chem. Mater.* **10**, 718–722 (1998).
681. V. Lordi, N. Yao, and J. Wei, Method for supporting platinum on single-walled carbon nanotubes for a selective hydrogenation catalyst, *Chem. Mater.* **13**, 733–737 (2001).
682. S.H. Joo, S.J. Choi, I. Oh, J. Kwak, Z. Liu, O. Terasaki, and R. Ryoo, Ordered nanoporous arrays of carbon supporting high dispersions of platinum nanoparticles, *Nature* **412**, 169–172 (2001).
683. B. Xue, P. Chen, Q. Hong, J. Lin, and K. Tan, Growth of Pd, Pt, Ag and Au nanoparticles on carbon nanotubes, *J. Mater. Chem.* **11**, 2378–2381 (2001).
684. H.C. Choi, M. Shim, S. Bangsaruntip, and H. Dai, Spontaneous reduction of metal ions on the side-walls of carbon nanotubes, *J. Am. Chem. Soc.* **124**, 9058–9059 (2002).
685. X.R. Ye, Y. Lin, and C.M. Wai, Decorating catalytic palladium nanoparticles on carbon nanotubes in supercritical carbon dioxide, *Chem. Commun.* 642–643 (2003).
686. B.R. Azamian, K.S. Coleman, J.J. Davis, N. Hanson, and M.L.H. Green, Directly observed covalent coupling of quantum dots to single-wall carbon nanotubes, *Chem. Commun.* 366–367 (2002).
687. A.V. Ellis, K. Vijayamohan, R. Goswami, N. Chakrapani, L.S. Ramanathan, P.M. Ajayan, and G. Ramanath, Hydrophobic anchoring of monolayer-protected gold nanoclusters to carbon nanotubes, *Nano Lett.* **3**, 279–282 (2003).
688. L. Liu, T. Wang, J. Li, Z.-X. Guo, L. Dai, D. Zhang, and D. Zhu, Self-assembly of gold nanoparticles to carbon nanotubes using a thiol-terminated pyrene as interlinker, *Chem. Phys. Lett.* **367**, 747–752 (2003).
689. A. Fási, I. Pálkó, J.W. Seo, Z. Kónya, K. Hernadi, and I. Kiricsi, Sonication assisted gold deposition on multiwall carbon nanotubes, *Chem. Phys. Lett.* **372**, 848–852 (2003).
690. S. Fullam, D. Cottell, H. Rensmo, and D. Fitzmaurice, Carbon nanotube templated self-assembly and thermal processing on gold nanowires, *Adv. Mater.* **12**, 1430–1432 (2000).
691. W.S. Yun, J. Kim, K.H. Park, J.S. Ha, Y.-J. Ko, K. Park, S.K. Kim, Y.-J. Doh, H.-J. Lee, J.P. Salvetat, and L. Forró, Fabrication of metal nanowire using carbon nanotubes as a mask, *J. Vac. Sci. Technol. A* **18**, 1329 (2000).
692. B.C. Satishkumar, A. Govindaraj, E.M. Vogl, L. Basumallick, and C.N.R. Rao, Oxide nanotubes prepared using carbon nanotubes as templates, *J. Mater. Res.* **12**, 604–606 (1997).
693. T. Seeger, Ph. Redlich, N. Grobert, M. Terrones, D.R.M. Walton, H.W. Kroto, and M. Rühle, SiO<sub>x</sub>-coating of carbon nanotubes at room temperature, *Chem. Phys. Lett.* **339**, 41–46 (2001).
694. M. Rühle, T. Seeger, Ph. Redlich, N. Grobert, M. Terrones, D.R.M. Walton, and H.W. Kroto, Novel SiO<sub>x</sub>-coated carbon nanotubes, *J. Ceram. Process. Res.* **3**, 1–5 (2002).
695. T. Seeger, Th. Kühler, Th. Frauenheim, N. Grobert, M. Rühle, M. Terrones, and G. Seifert, Nanotube composites: novel SiO<sub>2</sub> coated nanotubes, *Chem. Commun.* 34–35 (2002).
696. K. Hernadi, E. Ljubović, J.W. Seo, and L. Forró, Synthesis of MWNT-based composite materials with inorganic coating, *Acta Mater.* **51**, 1447–1452 (2003).
697. E.A. Whitsitt and A.R. Barron, Silica coated single walled carbon nanotubes, *Nano Lett.* **3**, 775–778 (2003).
698. Q. Fu, C. Lu, and J. Han, Selective coating of single wall carbon nanotubes with thin SiO<sub>2</sub> layer, *Nano Lett.* **2**, 329–332 (2002).
699. S.W. Lee and W.M. Sigmund, Formation of anatase TiO<sub>2</sub> nanoparticles on carbon nanotubes, *Chem. Commun.* 780–781 (2003).
700. A. Jitianu, T. Cacciaguerra, R. Benoit, S. Delpeux, F. Béguin, and S. Bonnamy, Synthesis and characterization of carbon nanotubes — TiO<sub>2</sub> nanocomposites, *Carbon* **42**, 1147–1151 (2004).
701. J. Sun, M. Iwasa, L. Gao, and Q. Zhang, Single-walled carbon nanotubes coated with titania nanoparticles, *Carbon* **42**, 895–899 (2004).

702. A. Brioude, P. Vincent, C. Journet, J.C. Plenet, and S.T. Purcell, Synthesis of sheathed carbon nanotube tips by the sol-gel technique, *Appl. Surf. Sci.* **221**, 4–9 (2004).
703. Y.-H. Li, S. Wang, A. Cao, D. Zhao, X. Zhang, C. Xu, Z. Luan, D. Ruan, J. Liang, D. Wu, and B. Wei, Adsorption of fluoride from water by amorphous alumina supported on carbon nanotubes, *Chem. Phys. Lett.* **350**, 412–416 (2001).
704. K. Hernadi, E. Couteau, J.W. Seo, and L. Forró, Al(OH)<sub>3</sub>/multiwalled carbon nanotubes composite: homogeneous coverage of Al(OH)<sub>3</sub> on carbon nanotube surfaces, *Langmuir* **19**, 7026–7029 (2003).
705. Y. Zhang, J. Liu, R. He, Q. Zhang, X. Zhang, and J. Zhu, Synthesis of alumina nanotubes using carbon nanotubes as template, *Chem. Phys. Lett.* **360**, 579–584 (2002).
706. M.H. Chen, Z.C. Huang, G.T. Wu, G.M. Zhu, J.K. You, and Z.G. Lin, Synthesis and characterization of SnO-carbon nanotube composite as anode material for lithium-ion batteries, *Mater. Res. Bull.* **38**, 831–836 (2003).
707. W.-Q. Han and A. Zettl, Coating single-walled carbon nanotubes with tin oxide, *Nano Lett.* **3**, 681–683 (2003).
708. L. Zhao and L. Gao, Coating of multi-walled carbon nanotubes with thick layers of tin(IV) oxide, *Carbon* **42**, 1858–1861 (2004).
709. H. Kim and W. Sigmund, Zinc oxide nanowires on carbon nanotubes, *Appl. Phys. Lett.* **81**, 2085–2087 (2002).
710. J. Ding, Y. Li, C. Xu, and D. Wu, Depositing CeO<sub>2</sub> nano-particles on surface of carbon nanotubes, *J. Chin. Rare Earth Soc.* **21**, 441–444 (2003) (in Chinese).
711. B.C. Satishkumar, A. Govindaraj, M. Nath, and C.N.R. Rao, Synthesis of metal oxide nanorods using carbon nanotubes as templates, *J. Mater. Chem.* **10**, 2115–2119 (2000).
712. C.N.R. Rao and A. Govindaraj, Nanotubes and nanowires, *Proc. Indian Acad. Sci.* **113**, 375–392 (2001).
713. J. Shi, Y. Qin, W. Wu, X. Li, Z.-X. Guo, and D. Zhu, In situ synthesis of CdS nanoparticles on multi-walled carbon nanotubes, *Carbon* **42**, 455–458 (2004).
714. S. Ravindran, S. Chaudhary, B. Colburn, M. Ozkan, and C.S. Ozkan, Covalent coupling of quantum dots to multi-walled carbon nanotubes for electronic device applications, *Nano Lett.* **3**, 447–453 (2003).
715. H. Kim and W. Sigmund, Zinc sulfide nanocrystals on carbon nanotubes, *J. Cryst. Growth* **255**, 114–118 (2003).
716. J.W. Liu, D.Y. Zhong, F.Q. Xie, M. Sun, E.G. Wang, and W.X. Liu, Synthesis of SiC nanofibers by annealing carbon nanotubes covered with SiC, *Chem. Phys. Lett.* **348**, 357–360 (2001).
717. E. Muñoz, A.B. Dalton, S. Collins, A.A. Zakhidov, R.H. Baughman, W.L. Zhou, J. He, C.J. O'Connor, B. McCarthy, and W.J. Blau, Synthesis of SiC nanorods from sheets of single-walled carbon nanotubes, *Chem. Phys. Lett.* **359**, 397–402 (2002).
718. Y.-J. Lee, Formation of silicon carbide on carbon fibers by carbothermal reduction of silica, *Diamond Rel. Mater.* **13**, 383–388 (2004).
719. K.C. Chin, A. Gohel, H.I. Elim, W. Ji, G.L. Chong, K.Y. Lim, C.H. Sow, and A.T.S. Wee, Optical limiting properties of amorphous Si<sub>x</sub>N<sub>y</sub> and SiC coated carbon nanotubes, *Chem. Phys. Lett.* **383**, 72–75 (2004).
720. B.Q. Wei, J.W. Ward, R. Vajtai, P.M. Ajayan, R. Ma, and G. Ramanath, Simultaneous growth of silicon carbide nanorods and carbon nanotubes by chemical vapor deposition, *Chem. Phys. Lett.* **354**, 264–268 (2002).
721. M. Gao, S. Huang, L. Dai, G. Wallace, R. Gao, and Z. Wang, Aligned coaxial nanowires of carbon nanotubes sheathed with conducting polymers, *Angew. Chem. Int. Ed.* **39**, 3664–3667 (2000).
722. D. Shi, J. Lian, P. He, L.M. Wang, W.J. van Ooij, M. Schulz, Y. Liu, and D.B. Mast, Plasma deposition of ultrathin polymer films on carbon nanotubes, *Appl. Phys. Lett.* **81**, 5216–5218 (2002).
723. A.B. Artyukhin, O. Bakajin, P. Stroeve, and A. Noy, Layer-by-layer electrostatic self-assembly of polyelectrolyte nanoshells on individual carbon nanotube templates, *Langmuir* **20**, 1442–1448 (2004).
724. L. Cao, H.-Z. Chen, H.-B. Zhou, L. Zhu, J.-Z. Sun, X.-B. Zhang, J.-M. Xu, and M. Wang, Carbon-nanotube-templated assembly of rare-earth phthalocyanine nanowires, *Adv. Mater.* **15**, 909–913 (2003).
725. Z.-X. Jin, G.Q. Xu, and S.H. Goh, A preferentially ordered accumulation of bromine on multi-wall carbon nanotubes, *Carbon* **38**, 1135–1139 (2000).
726. L. Grigorian, K.A. Williams, S. Fang, G.U. Sumanasekera, A.L. Loper, E.C. Dickey, S.J. Pennycook, and P.C. Eklund, Reversible intercalation of charged iodine chains into carbon nanotube ropes, *Phys. Rev. Lett.* **80**, 5560–5563 (1998).

727. M.T. Martínez, M.A. Callejas, A.M. Benito, M. Cochet, T. Seeger, A. Ansón, J. Schreiber, C. Gordon, C. Marhic, O. Chauvet, J.L.G. Fierro, and W.K. Maser, Sensitivity of single wall carbon nanotubes to oxidative processing: structural modification, intercalation and functionalisation, *Carbon* **41**, 2247–2256 (2003).
728. R. Graupner, J. Abraham, A. Vencelová, T. Seyller, F. Hennrich, M.M. Kappes, A. Hirsch, and L. Ley, Doping of single-walled carbon nanotube bundles by Brønsted acids, *Phys. Chem. Chem. Phys.* **5**, 5472–5476 (2003).
729. A. Kukovecz, T. Pichler, R. Pfeiffer, C. Kramberger, and H. Kuzmany, Diameter selective doping of single wall carbon nanotubes, *Phys. Chem. Chem. Phys.* **5**, 582–587 (2003).
730. Y. Liu, H. Yukawa, and M. Morinaga, First-principles study on lithium absorption in carbon nanotubes, *Computat. Mater. Sci.* **30**, 50–56 (2004).
731. S. Suzuki, Y. Watanabe, T. Ogino, S. Heun, L. Gregoratti, A. Barinov, B. Kaulich, M. Kiskinova, W. Zhu, C. Bower, and O. Zhou, Extremely small diffusion constant of Cs in multiwalled carbon nanotubes, *J. Appl. Phys.* **92**, 7527–7531 (2002).
732. A.S. Claye, J.E. Fischer, C.B. Huffman, A.G. Rinzler, and R.E. Smalley, Solid-state electrochemistry of the Li-single wall carbon nanotube system, *J. Electrochem. Soc.* **147**, 2845–2852 (2000).
733. B. Gao, A. Kleinhammes, X.P. Tang, C. Bower, L. Fleming, Y. Wu, and O. Zhou, Electrochemical intercalation of single-walled carbon nanotubes with lithium, *Chem. Phys. Lett.* **307**, 153–157 (1999).
734. H. Shimoda, B. Gao, X.P. Tang, A. Kleinhammes, L. Fleming, Y. Wu, and O. Zhou, Lithium intercalation into etched single-wall carbon nanotubes, *Physica B* **323**, 133–134 (2002).
735. H. Shimoda, B. Gao, X.P. Tang, A. Kleinhammes, L. Fleming, Y. Wu, and O. Zhou, Lithium intercalation into opened single-wall carbon nanotubes: storage capacity and electronic properties, *Phys. Rev. Lett.* **88**, 015502.1–4 (2002).
736. B. Gao, C. Bower, J.D. Lorentzen, L. Fleming, A. Kleinhammes, X.P. Tang, L.E. McNeil, Y. Wu, and O. Zhou, Enhanced saturation lithium composition in ball-milled single-walled carbon nanotubes, *Chem. Phys. Lett.* **327**, 69–75 (2000).
737. C.H. Mi, G.S. Cao, and X.B. Zhao, A non-GIC mechanism of lithium storage in chemical etched MWNTs, *J. Electroanal. Chem.* **526**, 217–221 (2004).
738. Z. Yang, S. Sang, K. Huang, and H.-Q. Wu, Lithium insertion into the raw multi-walled carbon nanotubes pre-doped with lithium — an electrochemical impedance study, *Diamond Rel. Mater.* **13**, 99–105 (2004).

---

# 4 Graphite Whiskers, Cones, and Polyhedral Crystals

*Svetlana Dimovski and Yury Gogotsi*  
Department of Materials Science and Engineering,  
Drexel University, Philadelphia, Pennsylvania

## CONTENTS

Abstract .....	149
4.1 Preface .....	150
4.2 Graphite Whiskers and Cones .....	150
4.2.1 Synthetic Whiskers and Cones .....	151
4.2.1.1 Whiskers .....	151
4.2.1.2 Cones .....	153
4.2.2 Occurrence of Graphite Whiskers and Cones in Nature .....	156
4.2.3 Structure: Geometrical Considerations .....	157
4.2.4 Properties and Applications .....	161
4.2.4.1 Electronic Properties of Synthetic Whiskers and Cones .....	161
4.2.4.2 Raman Spectra .....	162
4.3 Graphite Polyhedral Crystals—Polygonal Multiwall Tubes .....	163
4.3.1 Synthesis .....	163
4.3.2 Structure of Polygonal Tubes .....	165
4.3.3 Properties and Applications .....	168
4.3.3.1 Electronic Band Structure .....	168
4.3.3.2 Raman Spectra .....	169
4.3.3.3 Chemical, Thermal, and Mechanical Stability .....	170
4.4 Conclusions .....	171
Acknowledgment .....	172
References .....	172

## ABSTRACT

Carbon nanotubes and fullerenes have been extensively studied and are described in separate chapters in this book. However, the world of carbon nanostructures is not limited to these two groups of materials. Carbon nanocones, whiskers, and larger polygonized nanotubes, called graphite polyhedral crystals, are a whole new class of carbon nanomaterials; which, along with vapor-grown carbon fibers, can be placed between graphite and fullerene families of carbon. They are elongated and, typically, axially symmetric structures. This chapter provides a comparative study of several such graphitic nanomaterials. The discussion covers the gamut of such materials — from the first

graphite cones and whiskers discovered long before the beginning of “nano” age, to the latest additions to this family of nano- and micromaterials. Some of these particles are as large as several micrometers, and they provide a bridge between carbon nanomaterials such as nanotubes, and conventional materials such as carbon fibers or planar graphite. Their structure, properties, Raman spectra, and potential applications are discussed in detail in this chapter.

## 4.1 PREFACE

Both planar graphite<sup>1</sup> and carbon nanotubes<sup>2</sup> have been extensively studied, and their structure and properties are well documented in the literature. This section is a review of the current understanding of some less common nonplanar graphitic materials, such as graphite whiskers, cones, and polygonized carbon nanotubes (graphite polyhedral crystals). Although nonplanar graphitic microstructures in the shape of cones were reported as early as 1957,<sup>3,4</sup> it is only recently<sup>5–8</sup> that attention has been paid to these exotic classes of graphitic materials. There is no doubt that this growing interest has been triggered by the discovery of fullerenes<sup>9</sup> and nanotubes,<sup>2,10</sup> which has stimulated very intensive research on carbonaceous nanomaterials over the past 20 years. While fullerenes and nanotubes have been discussed in several books during the past decade, carbon cones, whiskers, and other similar structures have received much less attention. Our intention here is to give an overview of the current understanding of their structure, synthesis methods, properties, and potential applications.

Some of the engineering disciplines that could benefit from the emergence of these forms of carbon are:

- *Materials engineering*: graphitic cones and polyhedral crystals will enable the development of new functional nanomaterials and fillers for nanocomposites.
- *Chemistry and biomedicine*: in the development of new chemical sensors, cellular probes, and micro-/nanoelectrodes.
- *Analytical tools and instrumentation development*: cones and polyhedral crystals can act as probes for atomic force and scanning tunneling microscopes.
- *Energy, transportation, and electronic devices*: as materials for energy storage, field emitters, and components for nanoelectromechanical systems.

The common features of carbon whiskers, cones, scrolls, and graphite polyhedral crystals, besides their chemistry and the graphitic nature of their bonds, are their morphology and the high length-to-diameter aspect ratio, which places them between graphite and carbon nanotube materials. In the following sections, we will examine various types of these materials, and we will show the effect of structural conformation as well as describe their properties and potential applications.

## 4.2 GRAPHITE WHISKERS AND CONES

Graphite whiskers, cones, and polyhedral crystals are all needle-like structures — meaning that their length is considerably larger than their width or diameter. The major difference between the graphitic cones and polyhedral crystals, besides their shape, is in their texture, i.e., in the orientation of the atomic planes within the structure. While graphite polyhedral crystals (GPCs) comprise (0 0 0 1) planes parallel to their main axis, carbon cones and whiskers may have various textures. Therefore, we will consider GPCs separately from cones and whiskers. The orientation and the stacking arrangement of the planes is closely related to the nucleation mechanism and the growth conditions of the cones. The following section explains currently available methods for synthesis of carbon whiskers and cones. Also, two different types of cones have also been observed in natural deposits of carbon. These are described briefly in a separate section. A detailed explanation of their structure and properties in relation to their potential applications follows.

## 4.2.1 SYNTHETIC WHISKERS AND CONES

### 4.2.1.1 Whiskers

Graphite whiskers are the first known nonplanar graphitic structures that were obtained through a controlled preparation. Bacon<sup>11</sup> succeeded in growing high-strength graphite whiskers on carbon electrodes using a DC arc under an argon pressure of 92 atm. The temperatures developed in the arc were sufficiently close to the sublimation point of graphite (above 3600°C), which enabled carbon to vaporize from the tip of the positively charged electrode, and form cylindrical deposits embedded with whiskers of up to 3 cm in length and a few microns in diameter.<sup>12</sup> Carbon deposition under extreme conditions, such as a “flash CVD” process, also resulted in the growth of very peculiar micron-sized tree-like carbon structures.<sup>13</sup>

Whiskers and filaments of graphite have also been observed to form during pyrolytic deposition of various hydrocarbon materials. Hillert and Lange<sup>14</sup> studied the thermal decomposition of n-heptane and reported the formation of filamentous graphite on iron surfaces at elevated temperatures. Pyrolysis of methane,<sup>15</sup> and carbon monoxide<sup>16</sup> on iron surfaces or heated carbon filaments<sup>17</sup> also resulted in the formation of similar structures as well as the thermal decomposition of acetylene on Nichrome wires below 700°C.<sup>18</sup>

Whisker growth during pyrolytic deposition process is generally considered as being catalyzed by metals.<sup>19,20</sup> Haanstra et al.<sup>21</sup> however, observed noncatalytic columnar growth of carbon on  $\beta$ -SiC crystals by pyrolysis of carbon monoxide at 1 atm pressure above 1800°C (Figure 4.1). The experiments showed that the growth of carbon whiskers in that case was defined by rotation twinning and stacking faults on {1 1 1} habit plane of the  $\beta$ -SiC substrate. The cylindrical carbon columns formed by this mechanism were observed to consist of parallel conical graphitic layers stacked along the column axis. Most specimens of a run had the diameter between 3 and 6  $\mu\text{m}$ , and they were several tens of microns long. The apex angle of the conical mantle was measured to be about 141°. The conical nuclei of these columns were produced on defects in twinned  $\beta$ -SiC, such as the dislocation with a screw component perpendicular to the surface.

Very similar “needle”- or “spine”-like graphitic materials were also reported by Knox et al.<sup>22</sup> In an attempt to synthesize porous graphitic carbon material that would be capable of withstanding considerable shear forces, such as those seen in high-performance liquid chromatography, they produced porous glassy carbon spheres, which in most cases contained graphitic needles. Knox et al. impregnated the high-porosity silica gel spheres with a melt of phenol and hexamethylenetetramine (hexamine) in a 6:1 weight ratio. Impregnated material was first heated gradually to 150°C to form

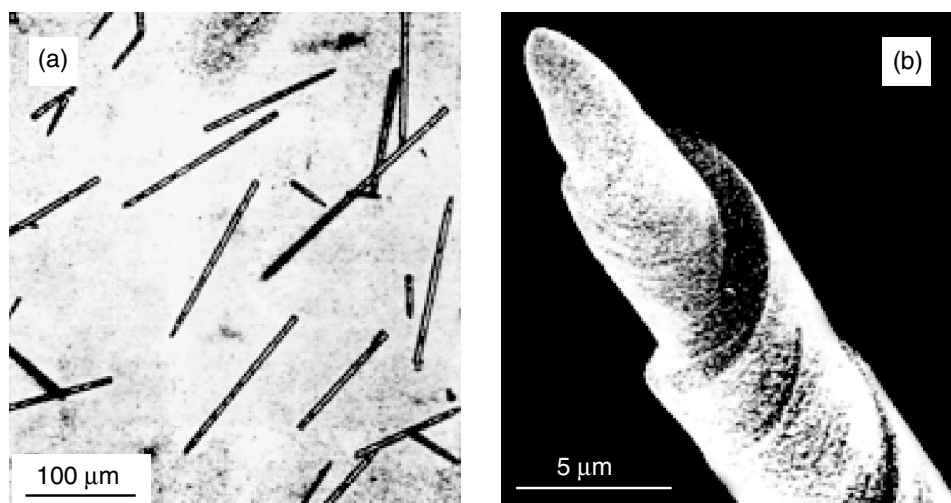


**FIGURE 4.1** Electron micrographs of (a) pencil-like carbon columns; (b) columnar carbon specimen with screw-like markings on side.<sup>21</sup>

phenol-formaldehyde resin within the pores of the silica gel, and then carbonized slowly at 900°C in a stream of oxygen-free nitrogen. The silica was then dissolved with hot aqueous potassium hydroxide (at least 99% complete), and the remaining porous glassy carbon was consequently heated up to 2500°C in oxygen-free argon.

Besides the expected glassy carbon structure, the resulting product often contained considerable amounts of needle-like material that was determined to have a three-dimensional graphitic structure. The graphitic whiskers resulting from the experiments were usually a few microns long and about 1  $\mu\text{m}$  thick. Electron diffraction and transmission electron microscopy (TEM) revealed the twinned structure of the whiskers. The angle between the layers was measured to be about 135°.

Since this material was a side product of their experiment, Knox et al. neither provided any further details of its structure nor explained the nucleation mechanism. It is, however, highly probable that their graphitic needles were nucleated and grown in pretty much the same way as were Haanstra's whiskers shown in Figure 6.1. Incomplete dissolution of the silica matrix could have caused formation of twinned  $\beta$ -SiC phase during the glassy carbon pyrolysis between 1000 and 2500°C, which further induced growth of columnar graphite from disproportionated CO within the porous glassy carbon spheres. The 135° whiskers have also been synthesized recently at 2100°C from gaseous CO and ball-milled natural graphite<sup>23,24</sup> contaminated with zirconia particles during milling. When heated above 1900°C, the zirconia particles react with the carbon to form ZrC.<sup>25</sup> The growth of the graphitic whiskers was probably initiated by screw dislocations on the surfaces of ZrC particles.

Similarly, Gillot et al.<sup>26</sup> studied the heat treatment of products of martensite electrolytic dissolution, and observed the formation of “cigar”-shaped crystals of graphite at 2800°C. The model of the texture they obtained is shown in Figure 4.2a. The length of the crystals ranged from a few microns to 250  $\mu\text{m}$  with a length-to-diameter ratio of about 10. It was suggested that the growth mechanism of the “cigars” involved mass transfer through the gas phase. The graphite layers in the whisker had the shape of an obtuse cone, the axis of which was coincident with the axis of the whisker, and had basically the same structure noted but not fully described by Knox et al. Such whiskers were assumed to be formed by a single graphene sheet coiled around the axis in a helix, each turn of the helix having the shape of a cone (Figure 4.2b). The angular shift  $\theta$  of the  $(h\ k\ 0)$  crystallographic directions from one whorl to the next one in the helix was measured to be  $\theta \approx 60^\circ$ . All graphitic layers were found to have the same stacking arrangement as of a perfect graphite crystal. Later, Double and Hellawell<sup>27</sup> proposed the cone-helix growth mechanism of such

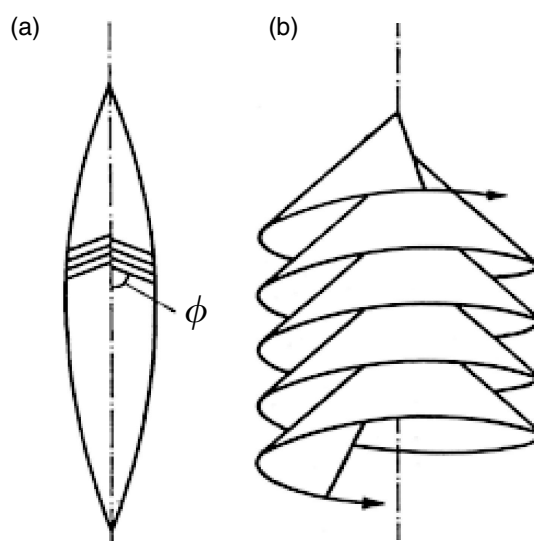


**FIGURE 4.2** Model illustrating the formation of cigar-like graphite: (a) longitudinal cross section of the cigars showing their texture; (b) cone-helix structure of graphitic filaments.<sup>26</sup>

structures, which relies on the formation of a negative wedge disclination within a graphene sheet. This model will be explained in detail in the following section.

#### 4.2.1.2 Cones

Ge and Sattler,<sup>6</sup> Sattler,<sup>7</sup> and Krishnan et al.<sup>8</sup> were among the first to observe and study fullerene nanocones, i.e., seamless conical structures formed when one or more pentagonal rings are incorporated into a graphene network. Incorporation of pentagonal and heptagonal defects into graphene sheets and nanotubes had at that time been already discussed by Iijima et al.,<sup>28</sup> Ajayan,<sup>29,30</sup> Ebbesen,<sup>31</sup> Ebbesen and Takada,<sup>32</sup> and others,<sup>33–35</sup> to explain conical morphologies of carbon nanotube tips observed by high-resolution transmission electron microscopy (HRTEM). The importance of the pentagonal defects in the formation of three-dimensional conical graphitic structures, however, was not fully recognized till the thorough investigation of their electron diffraction patterns by Amelinckx et al.,<sup>5,36,37</sup> who studied helically wound conical graphite whiskers (Figure 4.3a) by electron microscopy and electron diffraction. Whiskers gave rise to unusual diffraction effects consisting of periodically interrupted circular ring patterns (Figure 4.3b). Very similar diffraction patterns had been previously obtained from whiskers described in Ref. 21. Amelinckx et al. proposed a growth mechanism whereby the initial graphite layer adopts a slitted dome-shaped configuration (Figures 4.4a and b) by removing a sector  $\beta$  and introducing a five-fold carbon ring in the sixfold carbon network (Figure 4.4c). Successive graphene sheets were then rotated with respect to the previous one over a constant angle, thus realizing a helical cone around a “disclination,” with a five-fold carbon ring core. The model explains the morphological features and the particular diffraction effects observed on these reproducibly prepared columnar graphite crystals and it also builds on the other cone models.<sup>21,27</sup>

The first true multishell fullerene graphitic cones consisting of seamless axially stacked conical surfaces (Figure 4.5) were observed in the products of chlorination of silicon carbide at temperatures above 1000°C in 1972<sup>38</sup> and then reported by Millward and Jefferson<sup>39</sup> in 1978. Since these structures were rather singular observations in the products of the reaction, they were not recognized as a new material until much later.<sup>38</sup> Similar structures in large quantities were for the first time successfully produced by Ge and Sattler.<sup>6</sup> Up to 24 nm in length and 8 nm in base diameter, these nanometer-sized structures were generated by vapor condensation of carbon atoms on a highly oriented pyrolytic graphite substrate. All of the cones had the same apex angle  $\sim 19^\circ$ , which is the smallest among five possible opening angles for perfect graphitic cones (Figure 4.6a). The growth of these nanostructures is thought to be initiated exclusively by fullerene-type nucleation seeds with a

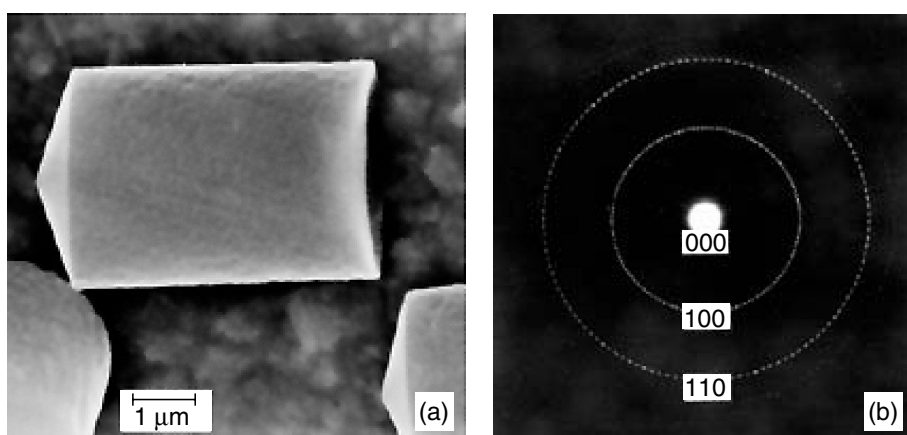


**FIGURE 4.3** Conical graphite whiskers. (a) SEM micrograph of a cleavage fragment of conically wound graphite whisker. Note the  $140^\circ$  apex angle of the conical cleavage plane. (b) Electron diffraction pattern with the incident electron beam along the normal to the cleavage ‘plane’ of the conically wound whiskers. Note the 126-fold rotation symmetry of the pattern.<sup>36</sup>



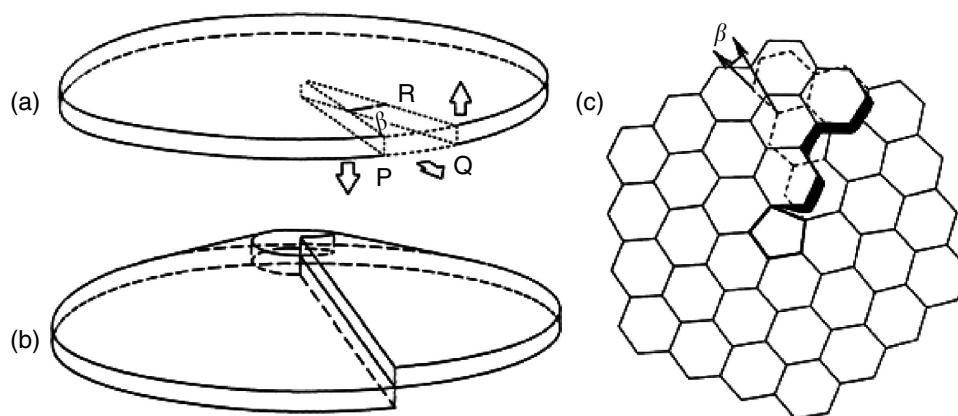


**FIGURE 4.4** Model illustrating the formation of a conical helix. (a) Sector  $\beta$  is removed from a disc. (b) The angular gap is closed and a cone is formed. (c) Twisted nucleus of the conical helix containing one pentagonal ring in the graphene network. Conical helix is formed through rotation of successive graphene sheets over a constant angle.<sup>36</sup>

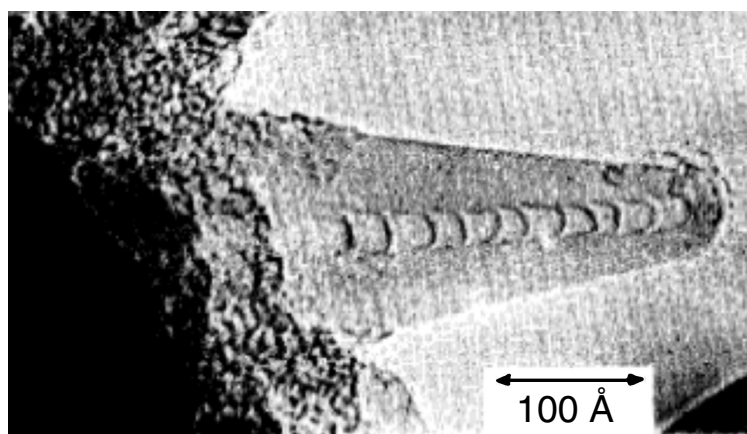


**FIGURE 4.5** Carbon cone showing separation of layers in fullerene end cups.<sup>38</sup>

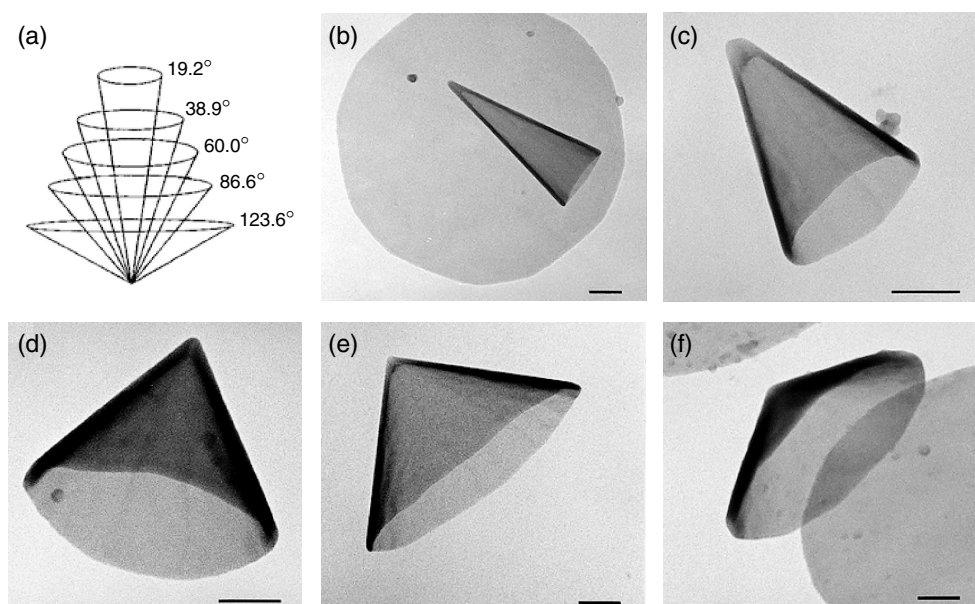


**FIGURE 4.6** Fullerene cones. (a) The five possible seamless graphitic cones, with cone angles of 19.2, 38.9, 60, 86.6, and 123.6°.<sup>6,7</sup> Electron micrographs of the corresponding five types of cones (scale bars in b–f, 200 nm). Apex angles: (b) 19.2°, (c) 38.9°, (d) 60.0°, (e) 84.6°, and (f) 112.9°.<sup>8</sup>

different number of pentagons. Fullerene cones of other apex angles corresponding to 1 to 4 pentagons were produced and reported 3 years later by Krishnan et al.<sup>8</sup> (Figures 4.6c–f). They also reproduced the  $\sim 19^\circ$  cone (Figure 4.6b).

Graphite conical crystals of very small apex angles (from  $\sim 3$  to  $\sim 20^\circ$ ) and perfectly smooth surfaces (Figure 4.7) have been reported to form in the pores of glassy carbon at high temperatures,<sup>40,41</sup> in addition to other various axial graphitic nano- and microcrystals.<sup>42</sup> Graphitic structures from the glassy carbon pores were produced from carbon-containing gas formed during decomposition of phenol formaldehyde. The size of these graphite conical crystals ranged from about 100 to 300 nm in the cone base diameter, and their lengths ranged from about 500 nm to several micrometers. Similarly, a few other conical structures of graphite were produced by thermal decomposition of hydrocarbons<sup>43</sup> with or without the aid of a catalyst, or by employing various thermochemical routes.<sup>44</sup> The structure of the majority of catalyst-free cones observed is consistent with the cone-helix growth model; however, some of the small apex angle cones ( $\sim 2.7^\circ$ ), as seen in Figure 4.7c,<sup>40,41</sup> do not conform to this rule. These are most likely carbon scroll structures.<sup>45,46</sup> Orientation of layers in catalytically produced cones is closely related to and resembles the shape of the catalyst particle.<sup>47–49</sup> Catalytically produced cones can adopt open,<sup>49–51</sup> helical,<sup>49,51</sup> or close-shell structures.<sup>49</sup>

Several other types of cones have been reported that are actually composed of cylindrical graphite sheets.<sup>52,53</sup> So-called tubular graphite cones (TGCs) (Figure 4.8) have been synthesized on an iron needle using a microwave-plasma-assisted chemical vapor deposition (MWCVD) method<sup>52</sup> in a  $\text{CH}_4/\text{N}_2$  gaseous environment. Corn-shape carbon nanofibers with metal-free tips have also been synthesized by a MWCVD method using  $\text{CH}_4$  and  $\text{H}_2$  gases.<sup>53</sup> Graphitic coils wound around a tapered carbon nanotube core have also been produced by the same technique using different substrate material.<sup>54</sup> What

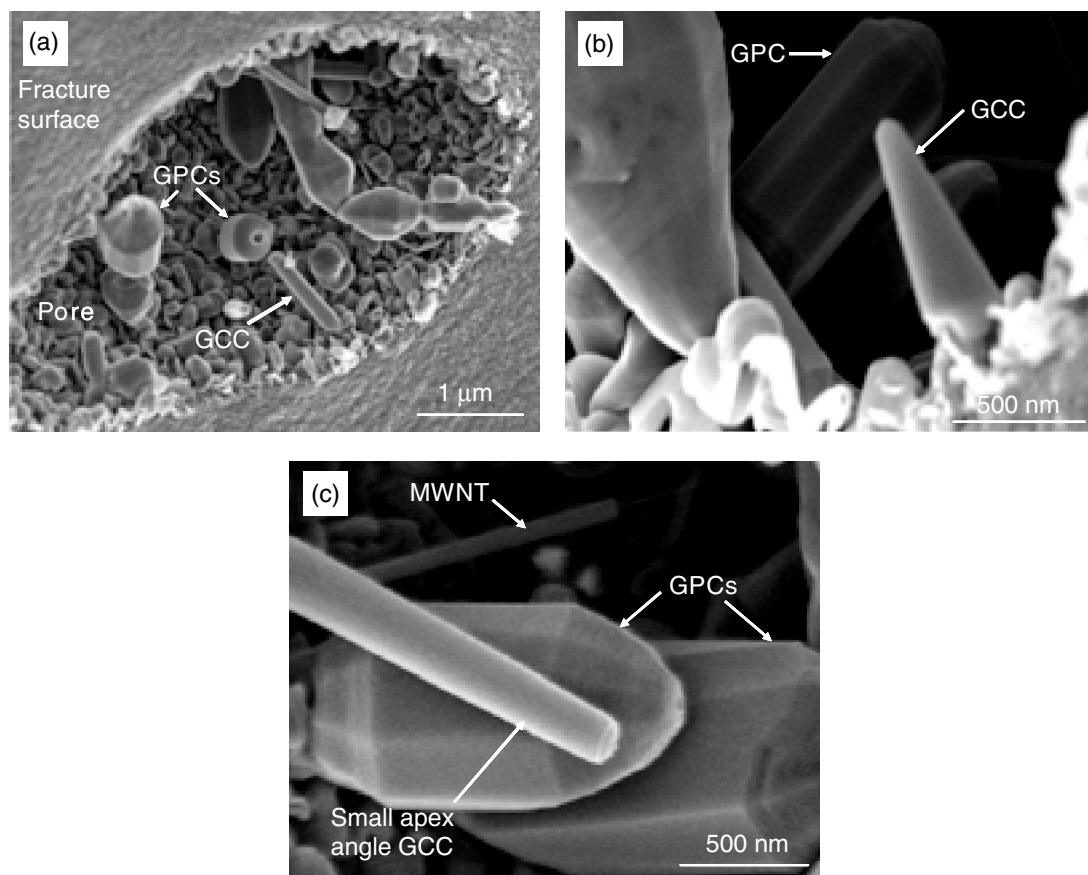


**FIGURE 4.7** SEM micrographs of carbon nano- and microcrystals found in pores of glassy carbon. (a) Fracture surface, showing crystals in a pore. (b) Graphite polyhedral crystals (GPCs) and graphite conical crystals (GCCs). (c) A small apex angle GCC growing along with GPCs, and a stylus-like multiwall carbon nanotube (MWNT).<sup>41</sup>

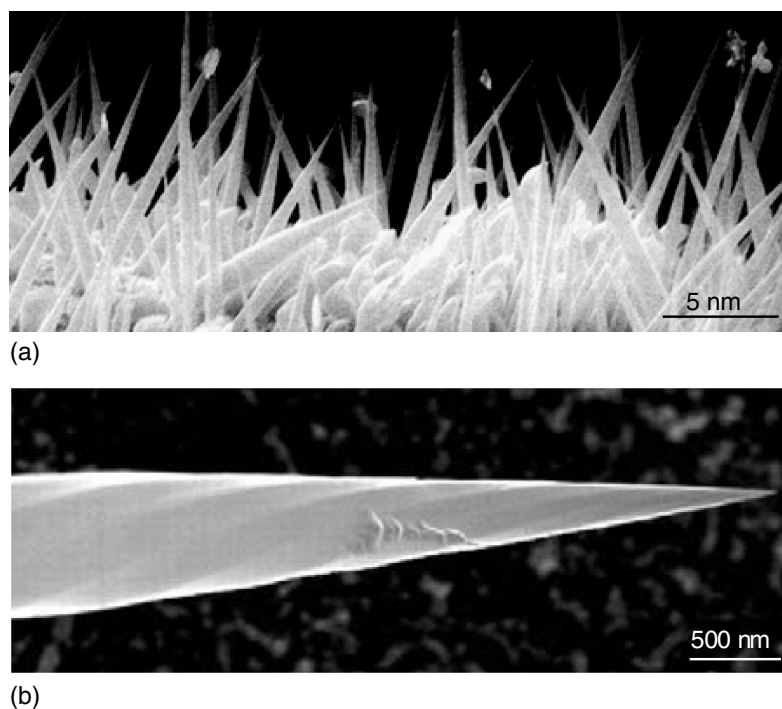


**FIGURE 4.8** Tubular graphite cones. (a) Aligned TGCs grown on an iron needle surface. (b) A high-resolution view of one TGC shows the faceted and helical appearance.<sup>52</sup>

makes these and similar structures cone-shaped is not purely an inclination of their graphitic layers with respect to the cone axis, but rather the continuous shortening of graphitic wall layers from the interior to the exterior of the structure,<sup>55</sup> or a combination of both mechanisms, as in the case of carbon nanopipettes.<sup>54</sup> Although their morphology resembles a cone, intrinsically their microstructure is that of the multiwall carbon nanotubes. This implies different mechanical and electronic properties. Tailoring carbon nanotubes to cone shapes can now be done routinely.<sup>56–59</sup>

#### 4.2.2 OCCURRENCE OF GRAPHITE WHISKERS AND CONES IN NATURE

Graphite whiskers and cones have also been observed growing on natural Ticonderoga graphite crystals,<sup>60</sup> Gooderham carbon aggregates,<sup>61</sup> and friable, radially aligned fibers of Kola graphite.<sup>62</sup> In their brief communication, Patel and Deshapande<sup>60</sup> reported the growth of 65 to 125- $\mu\text{m}$ -thick graphite whiskers in  $\langle 0001 \rangle$  direction, the  $(0001)$  planes of graphite being perpendicular to the whisker axis. The growth of the whiskers was presumed to be a result of a screw dislocation mechanism during the growth of graphite, but no details indicating the relationship of the structure and the geological origin of the sample were given. Several other exotic forms of graphite have been observed recently from two different geological environments: arrays of graphite cones in calcite from highly sheared metamorphic rocks in eastern Ontario (Gooderham graphite, Figure 4.9a),<sup>61</sup> cones, and scrolls of tubular graphite in syenitic igneous rock from the Kola Peninsula of Russia (Figures 4.9b–d).<sup>62</sup>

In a few geological occurrences, graphite forms compact spherical aggregates with radial internal textures,<sup>62–66</sup> similar to those observed in graphite spheres in cast iron.<sup>27</sup> One prominent natural occurrence is in metasedimentary rocks exposed at a roadcut, south of Gooderham, Ontario, Canada.<sup>67,68</sup> In this region, graphite crystallizes in calcite in various forms of tabular flakes, spherical, spheroidal, and triskelial polycrystalline aggregates,<sup>62,69</sup> some of which were found to contain large arrays of graphitic cones dominating the surfaces of the samples.<sup>61</sup> Cone heights ranged from less than a micron to 40  $\mu\text{m}$ , and unlike most laboratory-produced cones, they showed a wide distribution of apex angles. The apex angles were found to vary from 38 to  $\sim 140^\circ$ , with  $60^\circ$  being the most common. The cone structure can be well described by the Double and Hellawell<sup>27</sup> disclination

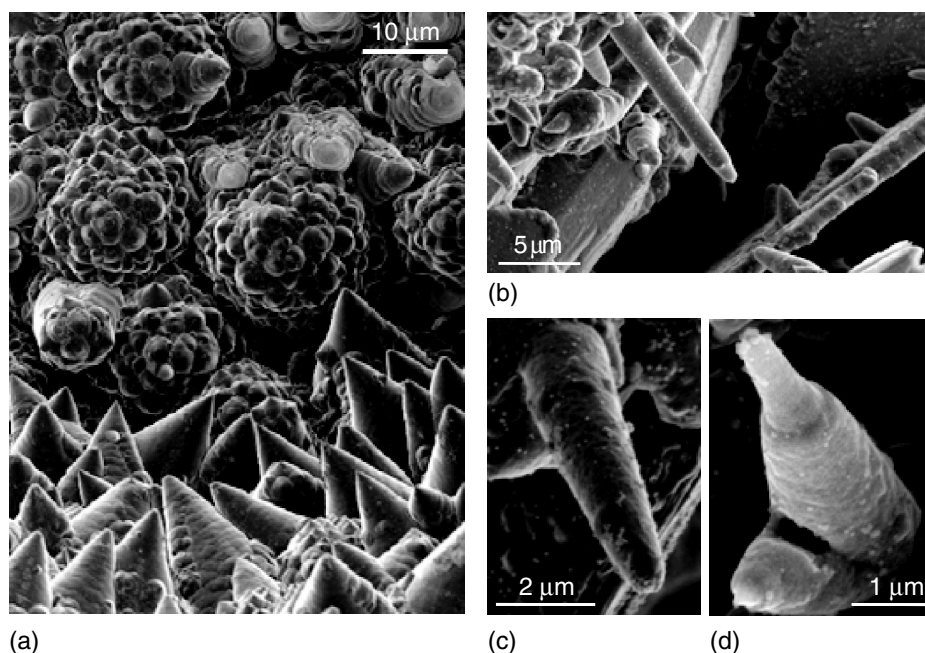


**FIGURE 4.9** FESEM images of graphite cones from (a) Gooderham, Ontario, Canada. [61] (b–d) Graphite cones, scrolls, and tubes from Hackman Valley, Kola Peninsula, Russia. A scroll-type structure is suggested in (b). Some of the Kola cones appear to be hollow, as indicated by a fractured structure (d).<sup>62</sup>

model. Other than full and solid cones, some Gooderham samples also revealed partly conical hollow structures composed of curved graphite shells (“protocones”).<sup>62</sup> These indicate a possible earlier growth stage for the cones reported in Ref. 61. Unlike large solid cones, many of these graphitic structures have partly faceted surfaces (Figure 4.10). The tips of the polygonal cones typically have six facets, and these facets only extend part way down the surfaces of the cones, which maintain a circular base.<sup>62</sup> The faceted cones are reminiscent of the polyhedral graphite crystals from glassy carbon pores.<sup>42</sup> The morphology and the surface topography of the cones and petrologic relations of the samples suggest that the cones formed from metamorphic fluids.

Numerous scroll-type graphite whiskers, up to 15 μm in length and up to 1 μm in diameter (Figures 4.9b–d), were discovered to cover inner and outer surfaces of channels comprised of tabular graphite crystals. They have been found in samples of alkaline syenitic pegmatite of Kola Peninsula, Russia.<sup>70</sup> The surfaces of cavities in the host rock were coated with a fine-grained graphite layer comprised solely of such whiskers. Some of the Kola natural graphite whiskers are cigar-like (Figure 4.9b), while others exhibit true conical (Figure 4.9c) morphologies with dome-shaped tips. The conical whiskers appear to be significantly larger and more abundant than the tube-like whiskers. Many Kola cones show distinct spiral growth steps at the surfaces of their tips, suggesting that they have a scroll-type structure, as seen previously in other synthetic whiskers.<sup>11,17,21,26</sup> SEM images of some broken cones reveal that they are hollow (Figure 4.9d).

### 4.2.3 STRUCTURE: GEOMETRICAL CONSIDERATIONS

We have seen in the previous section that, on the basis of their structure, a distinction can be made between the two major classes of graphitic cones. One type has a “scroll-helix” structure, while the second type comprises seamless conical graphene layers stacked over each other along their axis (therefore called “fullerene cones”). This classification may be considered as an equivalent to differentiating between “scroll” and “Russian-doll” type of multiwall carbon nanotubes.<sup>71</sup>

Pure “scroll-helix” cones are made up of a single graphene sheet that coils around an axis, each layer having a cone shape. The nucleation of this kind of structure is generally controlled by a line defect (dislocation), although we will see later that in addition, it always involves a screw dislocation

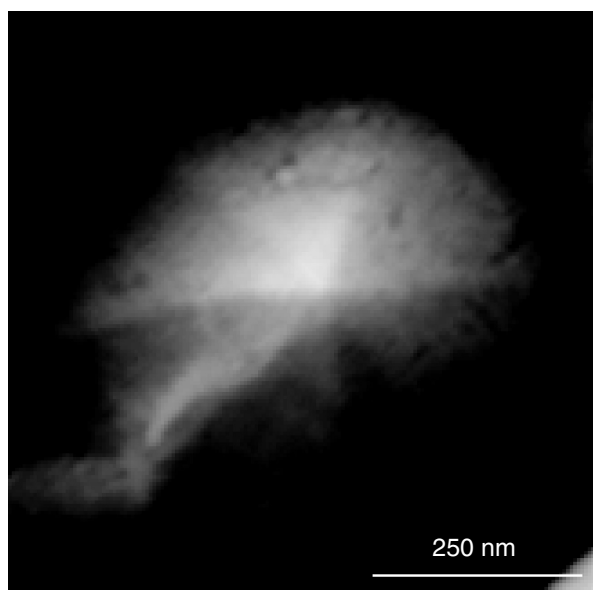


**FIGURE 4.10** FESEM micrograph of a graphite “protocone” having a faceted tip.<sup>62</sup>

and some kind of point defect at the terminated side of the dislocation line, as indicated in Figure 4.4. On the other hand, an ideal “fullerene” cone contains only point defects in the form of pentagonal, heptagonal, or lower/higher order carbon rings and their various combinations. It is also possible that some of the actual graphitic cones are neither purely helical nor purely fullerene structures, but rather a combination of the two.

Euler’s theorem<sup>72</sup> has been found particularly useful in explaining geometrical aspects and generation of fullerenes and fullerene cones. Suppose that a polyhedral object is formed by enclosing a space with polygons. The number of polygons is therefore equal to the number of faces ( $F$ ) of such object. If  $V$  is the number of vertexes,  $E$  the number of edges, and  $g$  a genus of the structure, then the four parameters correlate as follows:

$$V - E + F = 2(1 - g) \quad (4.1)$$

For bulk three-dimensional solids,  $g$  is equivalent to the number of cuts required to transform a solid structure into a structure topologically equivalent to a sphere (for instance,  $g = 0$  for a polygonal sphere such as  $C_{60}$  or  $C_{70}$ , and  $g = 1$  for a torus). Suppose, further, that the object is formed of polygons having different ( $i$ ) number of sides. The total number of faces ( $F$ ) is then

$$F = \sum N_i \quad (4.2)$$

where  $N_i$  is the number of polygons with  $i$  sides. Each edge, by definition, is shared between two adjacent faces, and each vertex between three adjacent faces, which is represented as

$$E = (1/2) \sum iN_i \quad (4.3)$$

and

$$V = (2/3)E \quad (4.4)$$

By substituting Equations (4.2) to (4.4) into (4.1), Euler’s postulate for  $i \geq 3$  is represented as

$$3N_3 + 2N_4 + N_5 - N_7 - 2N_8 - 3N_9 - \dots = 12(1 - g) \quad (4.5)$$

$$\sum (6 - i)N_i = 12(1 - g) \quad (4.6)$$

It can be observed from Equation (4.5) that the number of hexagons does not play a role, and a balance between the number of pentagons and higher order polygons ( $i \geq 7$ ) is required in order to form an enclosed structure. If each vertex is considered an atomic site containing an  $sp^2$ -hybridized C atom, and each edge is assigned to one C–C bond, then according to Equations (4.5) and (4.6), only 12 pentagons are needed to form a fullerene or a nanotube. If one heptagon is present, then 13 pentagons will close the structure.

The total disclination in a completely closed structure, such as a sphere, is  $720^\circ$  (i.e.,  $4\pi$ ). Each out of 12 pentagons contributes a positive disclination of  $720^\circ/12 = 60^\circ$ , and a heptagon, similarly, creates a negative  $60^\circ$  disclination. Incorporation of a heptagon in a graphene sheet will, therefore, produce a saddle-like deformation,<sup>73</sup> while adding pentagons will result in conical structures. Exactly five different cones (Figure 4.6) are generated by having respectively 1 to 5 pentagonal rings in their structure, as experimentally observed<sup>6,7</sup> and mentioned in a previous section. Careful examination of such cones suggests that pentagons are isolated from each other by hexagonal rings, as in fullerene molecules and fullerene nanotube caps. The apex angles for these cones can be calculated from the following relation:<sup>74</sup>

$$\sin(\theta/2) = 1 - (N_5/6) \quad (4.7)$$

where  $N_5$  is the number of pentagons in the cone structure.

Topo-combinatoric conformations of  $i$ -polygonal carbon rings (where  $i = 1, 2, 3, 4, 5, 7, 9, \dots$ ) within a hexagonal carbon network had been studied in detail even before the discovery of fullerenes, carbon nanotubes, and graphitic cones.<sup>75,76</sup> Growing interest in this topic resulted in the number of publications<sup>73,77–80</sup> that revealed the fine structure of the cone tip, such as the reconfiguration of carbon atoms and distribution of defects in the near vicinity of the tip. It had also been shown that the pentagons separated by hexagons (Figure 4.11)<sup>74</sup> make the most stable conformation of the cone tip structure, as observed experimentally. Establishing valid theoretical models of structure later helped in calculating the electronic properties of cones and curved carbon surfaces.<sup>81–84</sup>

Apart from seamless cones, there are conical structures that are formed by introducing a wedge disclination (Figure 4.12a) and a screw dislocation (Figure 4.12b) in a graphite sheet, as observed experimentally by various groups.<sup>4,5,21,22,26,36</sup> The cone-helix model<sup>27</sup> is based on growth around a positive disclination with a screw dislocation component (Figure 4.12c). As a graphene sheet wraps around the disclination, adjacent overlapping layers are rotated with respect to one another by an angle equal to the disclination angle. Among a practically unlimited number of disclination angles, some of them should be energetically more favorable (Figure 4.12c and inset table in Figure 4.13). Their value can be calculated from the following equation:

$$\alpha = n \times 60^\circ, \quad \text{or} \quad \alpha = n \times 60^\circ \pm \omega \quad (4.8)$$

where  $n = 0, 1, 2, \dots, 6$ , and  $\omega = 13.2, 21.8, 27.8^\circ, \dots$  are expected low-energy (0 0 1) twist grain-boundary angles based on lattice coincides, which are a measure of “goodness of fit,” but

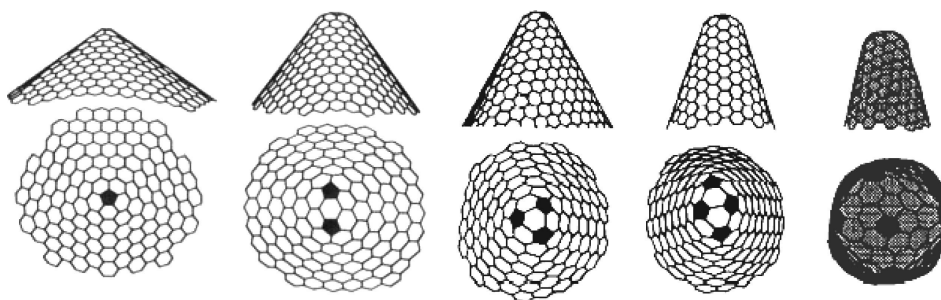


**FIGURE 4.11** Distribution of pentagonal defects within the cone tip. The apex angle changes with the number of pentagons.<sup>74</sup>

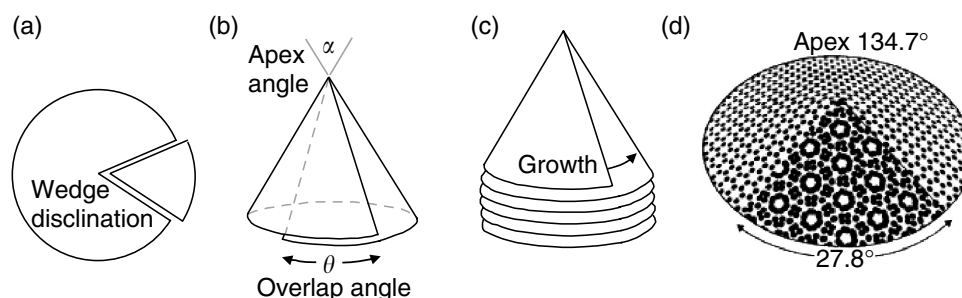


**FIGURE 4.12** Formation of helical cones. (a) Positive wedge disclination is created after a sector is removed from a graphene sheet and (b) the cone is formed by an overlap through a screw dislocation. (c) Model illustrating growth of columnar carbon, and (d) one of several energetically preferred stacking arrangements.<sup>27</sup>

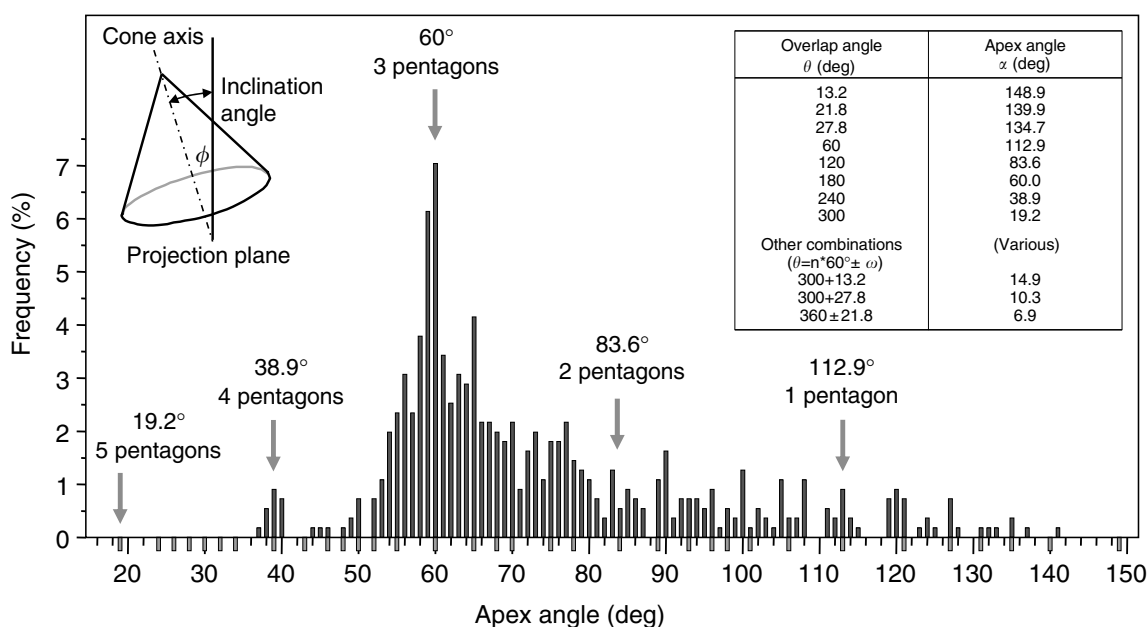


**FIGURE 4.13** Frequency of occurrence of various apex angles for natural graphite cones. The maximum is observed at  $60^\circ$ . Apex angles that correspond to “goodness” of fit are listed in the table. When measuring apex angles of cones, the inclination of cones to the projection plane of the microscope has been taken into account (inset, left).<sup>61</sup>

do not account for atomistic interactions and the curvature of the sheets. Disclinations with overlap angles equal to integer multiples of  $60^\circ$  should be energetically the most favorable, because they preserve the graphite crystal structure without stacking faults, provided the screw component of the disclination has a Burgers vector corresponding to an even multiple of the graphite’s  $c$ -axis interplanar spacing. Values of corresponding apex angles are calculated from the following relation:

$$\theta = 2 \sin^{-1}(1 - \alpha/360^\circ) \quad (4.9)$$

and they range from 6 to  $149^\circ$ . Graphitic cones having such apex angles should predominate over others.<sup>61</sup> The apex-angle distribution in a sample of natural cones is shown in Figure 4.13. Among all possible apex angles, the  $60^\circ$  angle is found to be the most frequent. Cones with smaller apex angles may be disfavored because of the higher elastic energy due to bending required to form the corresponding disclinations.

The dislocation line usually terminates with a point defect that includes bond recombination within the hexagonal network to form a pentagon or some other kind of polygon, as shown in Figure 4.4c.

## 4.2.4 PROPERTIES AND APPLICATIONS

### 4.2.4.1 Electronic Properties of Synthetic Whiskers and Cones

Carbon nanotubes are known to be either metallic or semiconducting, depending on their diameter and chirality.<sup>85–89</sup> The role of pentagon, heptagon, or pentagon–heptagon pair topological defects in structural and electronic properties of nanotubes has also been studied theoretically,<sup>81,84,90</sup> and experimentally by means of scanning tunneling microscopy (STM) and scanning tunneling spectroscopy (STS).<sup>84</sup> Special attention has been paid to curved surfaces of capped carbon nanotube tips, since these can be considered as regions of high density of defects. As the density of defect states increases at the tube ends, it can be expected that the electronic band structure of the end differs significantly from that elsewhere on the tube.<sup>81–84</sup> This has been successfully demonstrated by means of spatially resolved STM/STS carried out on a conically shaped tube end (Figures 4.14a and b),<sup>84</sup> which in fact is a fullerene-type carbon nanocone structure.

An STM image of one such conical tip is shown in Figure 4.14a. The apex of the cone has a diameter of 2.0 nm. The tunneling spectra were acquired at four different positions along the tube (marked with white letters in Figure 4.14a). Local densities of states (LDOS), derived from the scanning tunneling spectra, are represented in Figure 4.14b. In addition, the tight-binding calculations performed on two different tip morphologies are given in Figures 4.14c and d.

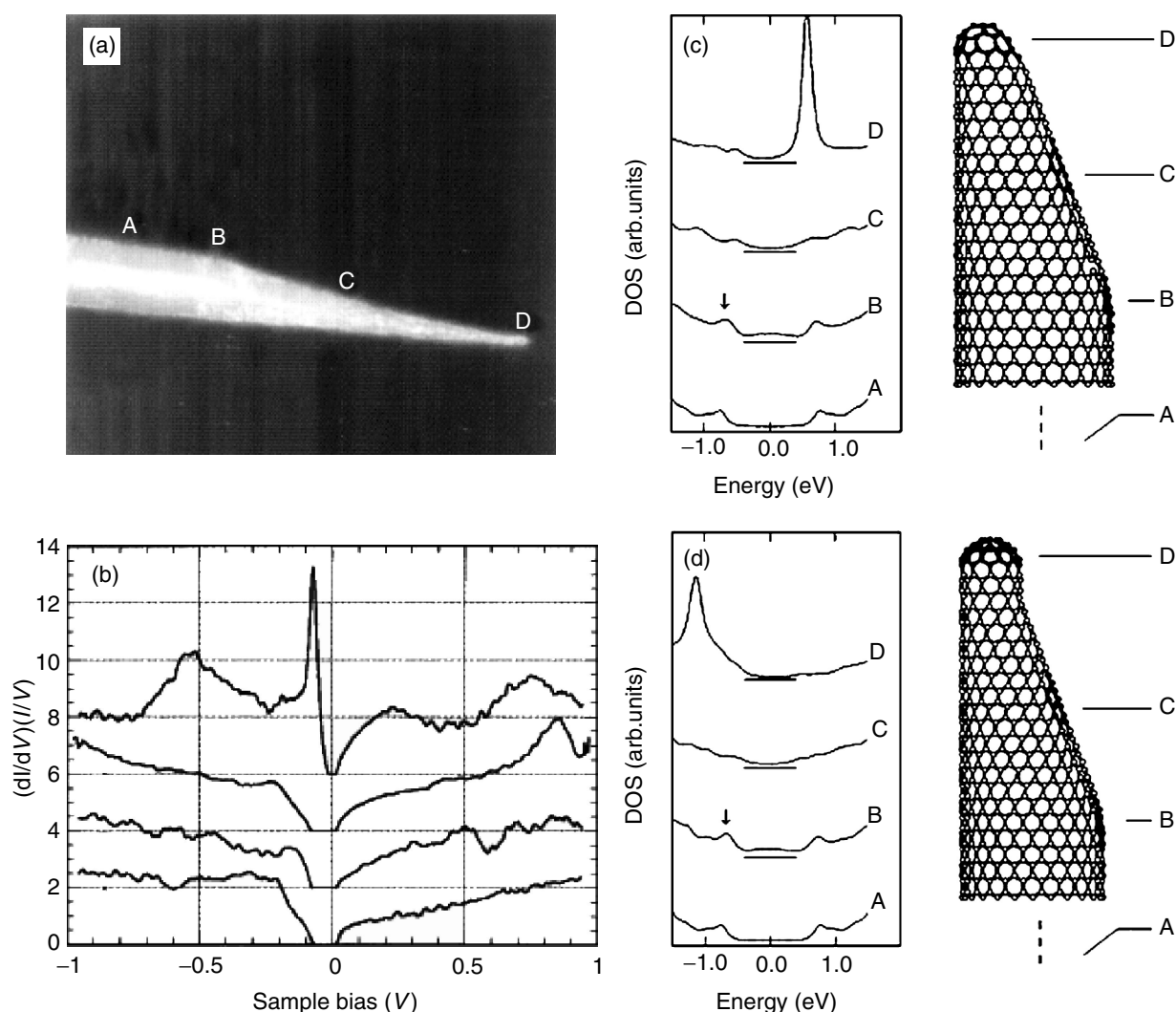


**FIGURE 4.14** Electronic structure and localized states at carbon nanotube tips: (a) STM image of a fullerene carbon cone; (b) local densities of states for a cone tip derived from scanning tunneling spectra at four (A–D) points along the tip; and (c–d) tight-binding calculations for two different configurations of cone tips.<sup>84</sup>



As we move along the tube from position A to position D, the density of topological defects increases, since the topological defects are concentrated in a smaller volume. As a result, the effect of confinement on electronic structure becomes more and more pronounced. This does not seem to be very striking in the case of the conduction band, where only a slight and broad enhancement has been noted in the LDOS at the cone apex. The valence band, however, is found to alter considerably, exhibiting sharp resonant states at the cone tip (Figure 4.14b, curve D). The strength and position of these resonant states with respect to the Fermi level is, in addition, very sensitive to the distribution and position of defects within the cone. This is illustrated with two models of cones having different morphologies obtained by altering the position of pentagons within the tip structure (Figures 4.14c and d). In the two examples, the (A), (B), and (C) LDOS calculated by the tight-binding method are very similar. Strong and sharp peaks in (D) LDOS have different shape and position in the case of models I and II. The values calculated for model II show better fit to the experimental values given in Figure 4.14b. The distribution of the defects and their effect on electronic properties of the cones have been studied in detail elsewhere.<sup>91</sup> LDOS of helix-type carbon cones are obtained by establishing the tight-binding model of a screw dislocation in graphite.<sup>81</sup>

Localized resonant states are very important in predicting the electronic behavior of carbon cones. They can also strongly influence the field emission properties of cones (For more details on field emission properties of carbon nanotubes see Chapter 8).

#### 4.2.4.2 Raman Spectra

Owing to its sensitivity to changes in the atomic structure of carbons, Raman spectroscopy has proven a useful tool in understanding the vibrational properties and the microstructure of graphitic crystals and various disordered carbon materials.<sup>92–97</sup> The relationship between the spectra and the structure has been extensively discussed in the literature, and the studies cover a wide range of carbon materials, such as pyrolytic graphite (PG)<sup>94,95</sup> and highly oriented pyrolytic graphite (HOPG),<sup>95,98,99</sup> microcrystalline graphite, amorphous carbon and glassy carbon, fullerenes, carbon onions, nanotubes, etc. Little work is carried out on the Raman scattering from graphite whiskers,<sup>100–102</sup> which usually consist of carbon layers oriented parallel to the growth axes. For such structures, it is expected that their Raman spectra will be similar to those of disordered graphite crystals and carbon fibers.

Figure 4.15 shows the Raman spectra of an individual graphite whisker and turbostratically stacked particles, using 632.8 nm excitation wavelength. Whiskers were synthesized in a graphitization furnace using a high-temperature heat-treatment method.<sup>23</sup> Carbon layers in these whiskers are almost perpendicular to their growth axes. Most of the first- and second-order Raman modes in whiskers, such as the D, G, and D' modes at  $\sim 1333$ , 1582, and 1618  $\text{cm}^{-1}$ , respectively, can be assigned to the corresponding modes in HOPG and PG.

In contrast to other carbon materials, the Raman spectra of whiskers exhibit several distinct characteristics. For example, the intensity of the 2D overtone is found to be 13 times stronger than that of the first-order G mode in whiskers. The strong enhancement of the D and 2D modes is also found in the Raman spectra of whiskers with 488.0 and 514.5 nm laser excitations.<sup>100</sup> Second, there are two additional low-frequency sharp peaks located around 228 and 355  $\text{cm}^{-1}$ , and two additional strong modes (around 1833 and 1951  $\text{cm}^{-1}$ ) observed in the second-order frequency region. The line widths of the D, G, D', 2D, and 2D' modes in whiskers are 17, 18, 10, 20, and 14  $\text{cm}^{-1}$ , respectively. Because the frequencies of the  $L_1$  and  $L_2$  modes are in the frequency region of acoustic modes, these two modes are supposed to be the resonantly excited acoustic modes in the transverse-acoustic and longitudinal-acoustic phonon branches. The two high-frequency modes at 1833 and 1951  $\text{cm}^{-1}$  are designated as  $L_1 + D'$  and  $L_2 + D'$  modes, respectively. The observed excitation-energy dependence (140  $\text{cm}^{-1} \text{eV}^{-1}$ ) of the 1833  $\text{cm}^{-1}$  mode is in excellent agreement with the theoretical value of 139  $\text{cm}^{-1} \text{eV}^{-1}$  of the  $L_1 + D'$  mode.<sup>100</sup>

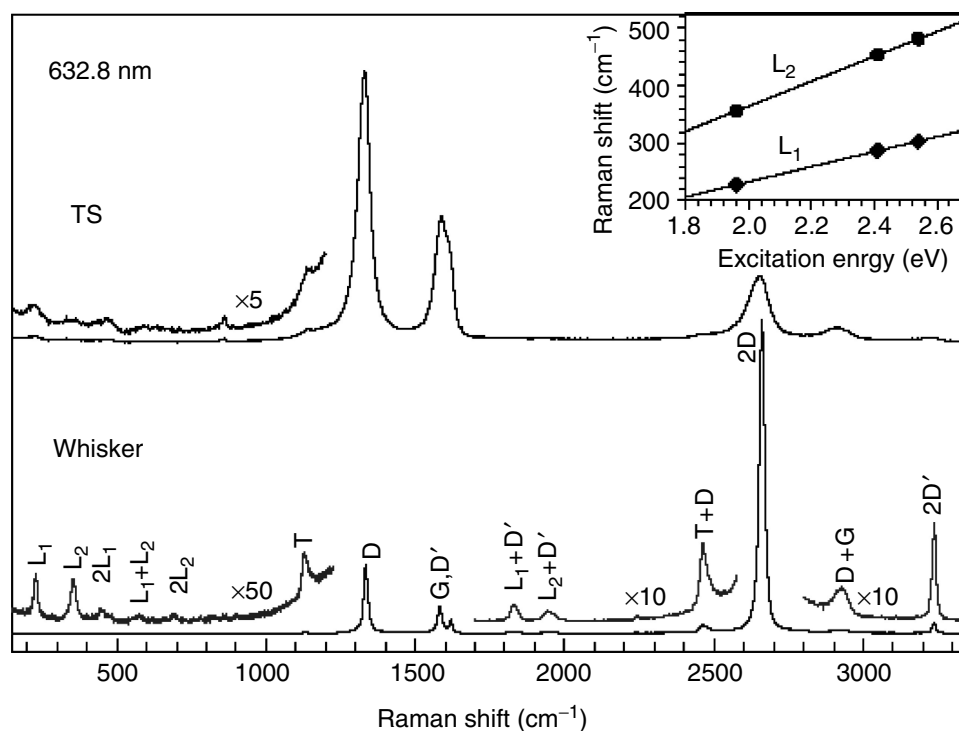


**FIGURE 4.15** Raman spectra of turbostratically stacked (TS) particles and an individual graphite whisker excited with 632.8 nm laser excitation. The inset gives the energy dependence of the frequencies of the  $L_1$  and  $L_2$  modes.<sup>102</sup>

The intensity enhancement of the dispersive modes indicates that double-resonance Raman scattering may be responsible for this phenomenon.<sup>103</sup> Such enhancement of the 2D mode is also observed in GPCs (Figure 4.17) that have a similar loop-edge structure in brim regions.<sup>42</sup>

Raman spectra from tubular, helix-type, and naturally occurring carbon cones are available elsewhere in the literature.<sup>61,102</sup>

### 4.3 GRAPHITE POLYHEDRAL CRYSTALS—POLYGONAL MULTIWALL TUBES

#### 4.3.1 SYNTHESIS

The structure of single- and multiwall carbon nanotubes, and single-wall carbon nanotube ropes have been widely studied over the last 10 years.<sup>2,31,71,104–108</sup>

While the ability of carbon to form multiwall tubular nanostructures is well known and these tubes have been studied extensively, very little information is available about carbon nanotube structures having polygonal cross sections. Although an occurrence of polygonal vapor-grown carbon fibers with a core carbon nanotube protrusion was noted by Speck et al.<sup>109</sup> as early as 1989, no details were given about core fiber structure and its polygonization.

Zhang et al.<sup>110</sup> have studied the structure of an arc-discharge-produced carbon soot by the HRTEM, and they were the first to indicate the possibility of polygonal multiwall carbon nanotubes, assuming that the tubes consisted of closed coaxial concentric layers. The first evidence for occurrence of polygonized carbon nanotubes came from Liu and Cowley,<sup>104,105,108</sup> who used nanodiffraction in conjunction with HRTEM and selected area electron diffraction to investigate the structures of carbon nanotubes having diameters of a few nanometers. Nanodiffraction is a form of convergent beam electron diffraction, which allows one to obtain a diffraction pattern from regions of the specimen about 1 nm or less in diameter. The tubes used in this study were produced by a variant of Kratschmer–Huffman arc-discharge method<sup>111</sup> in helium gas at a pressure of 550 Torr. The DC voltage applied to electrodes was 26–28 V and the corresponding current was 70 A. The carbon

nanotubes obtained at the given experimental conditions consisted of 3 to 30 carbon sheets and had a length of up to 1  $\mu\text{m}$ . The inner diameters of these tubes ranged from 2.2 to 6 nm, and the outer diameters ranged from 5 to 26 nm. In addition to nanotubes of circular cylindrical cross section, with zero, one or several helix angles, there were many tubes having polygonal cross sections, made up of flat regions joined by regions of high and uniform curvature.<sup>105</sup> An HRTEM image of one such structure is given in Figure 4.16a. Polygonization of the cross section is observed indirectly through formation of uneven patterns of lattice fringes on the two sides of the tube, with spacings varying from 0.34 nm from the circular cylinder tubes, to 0.45 nm from the regions of high curvature (Figure 4.16b).

In their study of the intershell spacing of multiwall carbon nanotubes prepared by the same Kratschmer–Huffman arc-discharge method, Kiang et al.,<sup>112</sup> similarly, found that the intershell spacing in carbon nanotubes ranged from 0.34 to 0.39 nm among different nanotubes, decreasing with the increase in the tube diameter (Figure 4.16c). Some other reports have also shown variation of the values from 0.344 nm (obtained by the electron and powder x-ray diffraction measurements)<sup>113</sup> to 0.375 nm (based on the HRTEM images).<sup>114</sup>

Faceted multiwall carbon nanotubes with larger diameters, called graphite polyhedral crystals (GPCs), have been reported to grow at high temperatures in the pores of a glassy carbon material (Figures 4.17a and b).<sup>42</sup> The glassy carbon containing polyhedral tubes was made from a thermoset phenolic resin by carbonization at 2000°C in  $\text{N}_2$  atmosphere at  $\sim 10$  Torr. The density of glassy carbon was 1.48  $\text{g}/\text{cm}^3$  with an open porosity of  $\sim 1\%$ ; its microstructure and properties are typical of other glassy carbons. After the structure of the matrix was set and some closed pores were formed, polyhedral nanotubes grew from C–H–O ( $\text{N}_2$ ) gas trapped within these pores during the resin carbonization phase.

Graphite polyhedral crystals have a very complex morphology. Their size ranges from 100 to 1000 nm in diameter and up to few micrometers in length. The number of facets can vary from 5 to 14 and more, and they may possess a helical habit or be axially true. Many of the crystals terminate with a thin protruding needle that appears to be a multiwall nanotube (Figure 4.17b), typically with

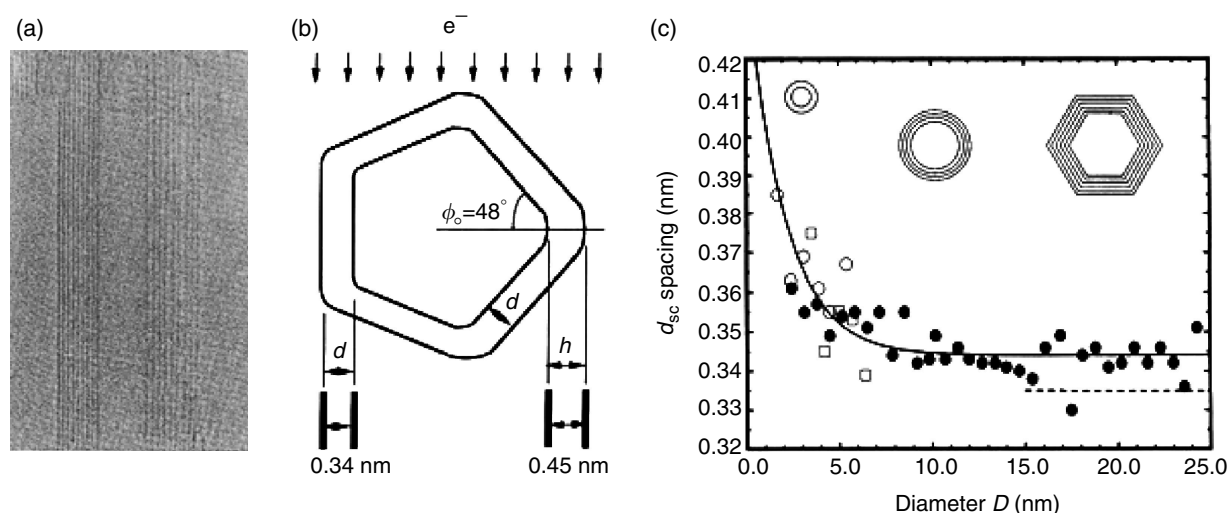


**FIGURE 4.16** (a) HRTEM image of a nine-sheet nonsymmetric tube. A  $d$  spacing of 0.34 nm is found on the left side and a  $d$  spacing of 0.45 nm is seen on the right side.<sup>108</sup> (b) Model illustrating the formation of the nonsymmetric fringes from a tube (a) with polygonal cross section.<sup>108</sup> (c) The graphitic interplanar spacing decreases as the tube diameter increases, and approaches 0.344 nm at roughly  $D = 10$  nm. The data were measured from three different nanotubes indicated by different symbols. Hollow circles: from a seven-shell tube with innermost diameter  $D_{\min} = 1.7$  nm. For large  $D$ , graphitization may occur resulting in a polygonal cross section. The broken line indicates the expected decrease in interplanar spacing owing to local graphitic stacking.<sup>112</sup>

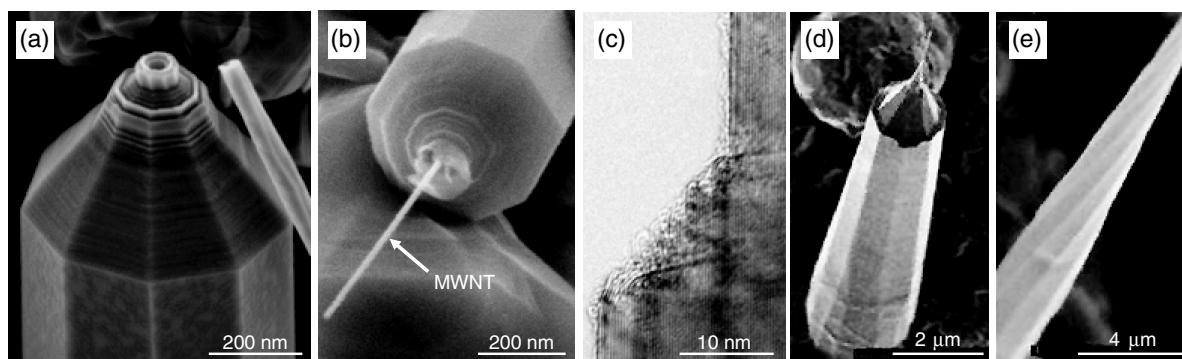


**FIGURE 4.17** Graphite polyhedral crystals (GPCs). (a) SEM micrograph of a faceted GPC.<sup>102</sup> (b) A carbon nanotube stylus is connected to a microsize body. (c) TEM image of a GPC's lattice fringes indicates that GPCs are highly graphitic and that the basal planes are terminated by a closed-loop structure.<sup>102</sup> (d–e) GPCs produced by using the flame combustion method.<sup>115</sup>

a core diameter of about 5 to 20 nm and a conical, dome-capped, or semitoroidal tip. There is no evidence about catalytic nucleation of the graphite polyhedral crystals. Formation of highly ordered structures is promoted with the high temperature of treatment, the supersaturation of the environment with carbon atoms, slow reaction kinetics, and the presence of active species such as hydrogen and oxygen atoms that balance the crystal growth rate with the surface etching rate. This explains the surprisingly large number of ordered carbon layers (up to 1500) growing on the core nanotube, resulting in complex axis-symmetric structures. GPCs of somewhat less perfect structures (Figures 4.17c and d) have been successfully produced recently by using the flame combustion method.<sup>115</sup>

Annealing of carbon nanotubes with a circular cross section at high temperatures causes polygonization of their walls. An HRTEM image of a CVD carbon nanotube sample before and after annealing is shown in Figure 4.18. The tubes were annealed for 3 h in a  $10^{-6}$  Torr vacuum at 2000°C. High-temperature annealing of carbon nanotubes in a vacuum or an inert environment allows for the transformation of circular tubes into polygonal ones. However, polygonization will not be uniform along the tube, nor will the cross section take the shape of a regular polygon.

To the best of our knowledge, natural counterparts of polygonal carbon multiwall nanotubes have not been observed so far, but it would not come as a surprise if they are discovered in the near future. Very short needle-like polygonal multiwall carbon nanotubes have also been synthesized from a supercritical C–H–O fluid by hydrothermal treatment of various carbon precursor materials<sup>116,117</sup> with and without the aid of a metal catalyst. Hollow carbon nanotubes, with multiwall structures, comprised of well-ordered concentric graphitic layers, have been produced by treating amorphous carbon in pure water at 800°C and 100 MPa.<sup>117</sup> HRTEM analysis of the reaction products indicates the presence of carbon nanotubes with polygonal cross sections (varying contrast and lattice spacing along the tube diameter) within these samples. The experimental conditions for hydrothermal synthesis of nanotubes resemble to a great extent the conditions of geological metamorphic fluids, and it is possible that some polygonal tubes are present in the Earth's crust along with the natural graphitic cones and tubules but have not been found yet.

### 4.3.2 STRUCTURE OF POLYGONAL TUBES

One of the earliest works dealing with the polygonization of the cross section of carbon nanotube is a report by Zhang et al.<sup>110</sup> Based on experimental observations, it was suggested that the fine structure of carbon nanotubes is determined by two competing accommodation mechanisms (Figure 4.19a). As a result of one of the mechanisms, the successive tube can adopt different helical shapes to accommodate the change in circumference, therefore keeping an orientationally disordered (turbostratic) stacking. As a result of the second mechanism, the rows of hexagons in successive tubes

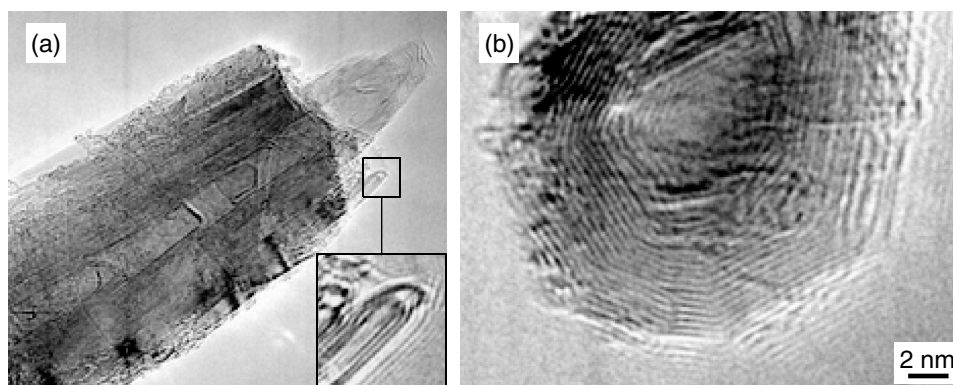


**FIGURE 4.18** Transformation of multiwall carbon nanotubes into polygonal GPC-like structures by annealing in vacuum at 2000°C. (a) TEM image of a tube with a core nanotube in the form of stylus extension. Arched semitoroidal structures, similar to that of GPCs, have been also formed (inset) through elimination of dangling bonds at high temperature. (b) Polygonized cross section and graphitic walls of an annealed hollow tube. TEM micrographs courtesy of H. Ye.

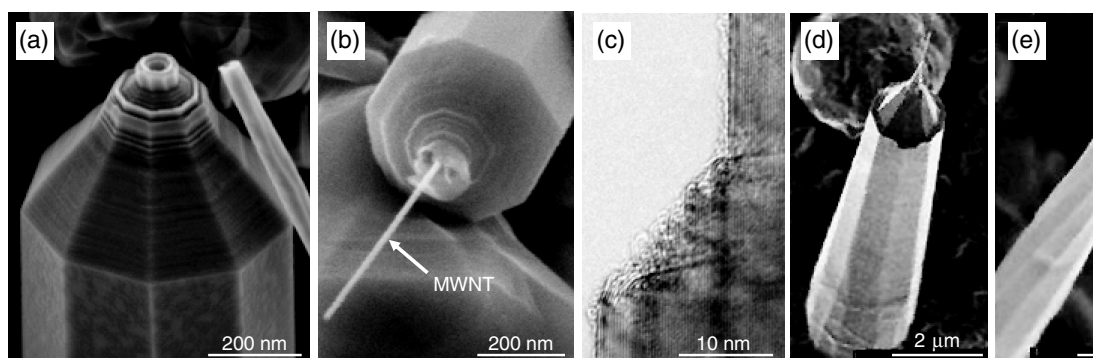


**FIGURE 4.19** (a) Schematic model of a nanotube cross section. “Interfacial dislocations” (bold lines) are introduced to accommodate the strains on the tube surfaces. The graphite stacking is maintained in the tube walls (as indicated by lines). The full circles represent the atoms in the paper plane and the open circles are projected positions of the atoms of the paper plane. (b) Defect regions in the HRTEM image of a carbon “onion.” The defect regions are characterized by their abnormal image contrast.<sup>110</sup>

remain parallel and adopt a graphitic stacking, thus inducing some regions of stacking faults due to the deformation of hexagons. The regions of stacking fault are assumed to be evenly distributed along the tube circumference,<sup>110</sup> and are separated from the graphitic structure by interfacial dislocations (bold lines in Figure 4.19a). Polygonization of carbon nanotubes therefore may appear as a result of the necessity to allow graphitic stacking of the layers, as often seen in carbon onions (Figure 4.19b).<sup>110,118,119</sup> It is easy to envision a trade-off between the energy associated with turbostratic stacking vs. the strain energy associated with shape changes and stacking faults. The mechanism prevailing depends strongly on the tube size. The relative strain required to maintain graphitic order is smaller with increasing tube size; therefore thicker tubes are expected to have graphitic ordering and polygonal cross sections with discrete regions of stacking faults, while thinner tubes are more likely to retain turbostratic concentric structures with cylindrical cross section and varying helicity between the individual shells.

In the near-planar regions of the polygonized tubes, an ordering of the stacking sequence of the carbon layers gives rise to hexagonal and possibly rhombohedral graphite structure.<sup>108</sup> The near-planar regions are connected into seamless shells through the regions of high curvature (Figure 4.16b).

A small value for the radius of curvature is preferred in regions of bending of the carbon sheets between the extended near-planar regions because of the nature of local perturbations of the carbon bonding arrangement.<sup>104,105,108</sup>

A tube structure model has been proposed to explain the variation of intershell spacing as a function of tube diameter (Figure 4.20a). Individual intershell spacings as a function of tube diameters were measured in real space from HRTEM images of various nanotubes.<sup>112</sup> The empirical equation for the best fit to these data is given as

$$\hat{d}_{002} = 0.344 + 0.1e^{-D/2} \quad (4.10)$$

The function is plotted in Figure 4.20b. The large full circles show experimental values.

The increase in the intershell spacing with decreased nanotube diameter is attributed to the high shell curvature of small diameter tubes and it has also been suggested that polygonization of the tube cross section will occur for inner tube diameters larger than ~12 nm (see Figure 4.16c). This observation is in agreement with the model suggested by Zhang et al.<sup>110</sup>

Furthermore, it has also been proposed that multiwall nanotubes most likely consist of circular core shells and polygonal outer layers.<sup>120</sup> In their pioneering work on nanodiffraction from carbon nanotubes, Liu<sup>104</sup> and Cowley<sup>105</sup> noted a possibility that there might be some nanotubes with neither entirely polygonal nor fully cylindrical cross sections. Such tubes could be considered as a mixture of the two possible morphologies, with structure varying along the tube length and the shell diameter. A schematic illustrating this model, taking into account variations of intershell spacing, is given in Figure 4.20.

In order to obtain direct evidence of tube microstructure, there have been several cross-sectional TEM studies<sup>121–124</sup>. These studies were conducted on both carbon nanotubes produced by arc-discharge method and the tubes produced by a chemical vapor deposition. A large number of defects in CVD tubes is very common, and it is an intrinsic property of the CVD process and, therefore, will not be discussed further here. HRTEM images of the cross sections of tubes reveal their nested structure, but they do not confirm models proposed by Liu,<sup>105</sup> Zhang,<sup>110</sup> and others.<sup>112,120</sup> Instead, rather random dislocation lines extending radially have been recorded.<sup>121</sup>

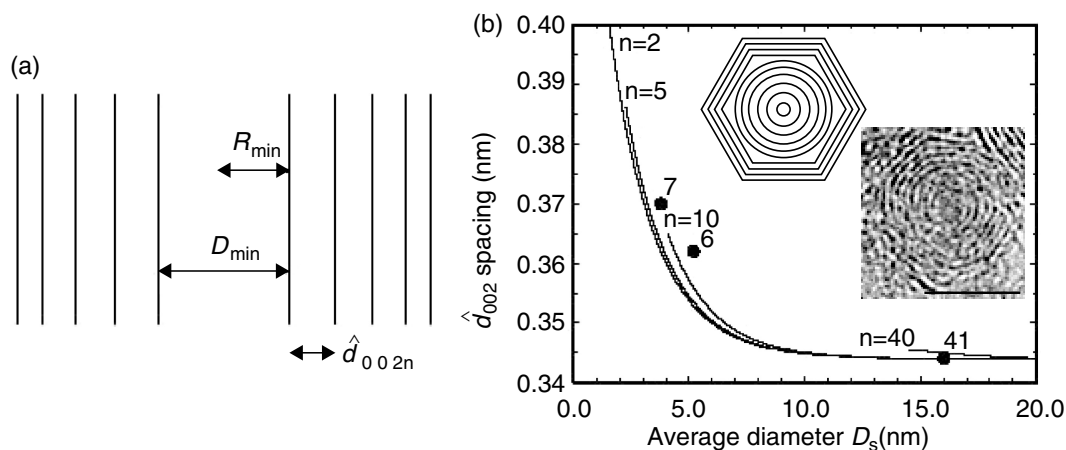


**FIGURE 4.20** Effect of tube diameter on interplanar spacing. (a) Model for a nanotube crystal with a varying intershell spacing. (b) The  $d$  spacing is given an exponential function of tube diameter (Equation [4.10]). The intershell spacing  $d$  is plotted as a function of the average tube diameter ( $D_s$ ), where  $n$  is the number of shells in a nanotube. The curves are calculated for  $n = 2, 5, 10,$  and  $40$ , using the above model and Equation (4.10). The three data points shown by the large full circles were obtained based on experimental observations.<sup>112</sup> Insets: Model illustrating change of interplanar spacing  $d$  and polygonization of tube cross section with increase of tube diameter, as observed in some TEM micrographs. (TEM image: courtesy of S. Welz; scale bar, 5 nm).

Aside from their polygonal cross section, GPCs<sup>42,115</sup> possess another important feature that may affect their electrical, chemical, and mechanical properties to a great extent. This is the several nanometer thick loop-like layer (Figure 4.17c and inset in Figure 4.18a) formed by zipping of the adjacent graphitic shells at their terminations.<sup>125,126</sup> This phenomenon is also observed in edge planes of some high-temperature planar graphites,<sup>125,127</sup> and on the surfaces of cup-like multiwalled carbon nanotubes annealed in argon atmosphere above 900°C.<sup>128</sup> In the case of planar graphite, zipping of graphitic layers (also known as “lip–lip” interactions) forms nanotube-like sleeves, while in the case of multiwall nanotubes, the resulting structure resembles concentric polygonal hemitoroidal structures.<sup>126</sup> “Lip–lip” interactions are especially pronounced when samples are annealed at temperatures above 1600°C.<sup>42,51,125,128–130</sup> The reactive edge sites transform into stable multiloops through the elimination of dangling bonds due to enhanced carbon mobility at higher temperatures. Multiloops are typically built by 2 to 6 adjacent graphitic layers. Typically, single-loop structures are formed between 900 and 1200°C, while 1500°C is considered as the threshold for the formation of multilayer loops.<sup>128</sup> The radius of curvature of the outer layer is similar to the average radius of double-walled nanotubes.<sup>131</sup>

### 4.3.3 PROPERTIES AND APPLICATIONS

#### 4.3.3.1 Electronic Band Structure

Electronic properties of cylindrical single- and multiwall carbon nanotubes have been widely studied both theoretically and experimentally over the past 15 years, and findings have been summarized in several books about carbon nanotubes,<sup>71,132</sup> as well as in Chapter 2 of this book.

Electronic structure of polygonal single-wall carbon nanotubes has been investigated theoretically within tight-binding and *ab initio* frameworks,<sup>133,134</sup> and it has been found that polygonization changes the electronic band structure qualitatively and quantitatively. An example of a zigzag nanotube is given. Considered is the (10, 0) tube with: a circular (a) and pentagonal (b) cross section (Figure 4.21). The (10, 0) carbon nanotube with a circular cross section is a semiconductor, with a band gap of 0.82 eV. In calculating the band structure of a polygonal tube, it is reasonable to assume that the zones of strong curvatures near the edges of the polygonal tube will introduce a  $\sigma^*-\pi^*$  hybridization of carbon bonds. This local variation of bonding with strong  $sp^3$  character in the folds creates a sort of defect line in the  $sp^2$  carbon network.<sup>135</sup> In addition to the effect of bond hybridization, polygonization of the cross section lowers the symmetry from a ten- to a fivefold axis.

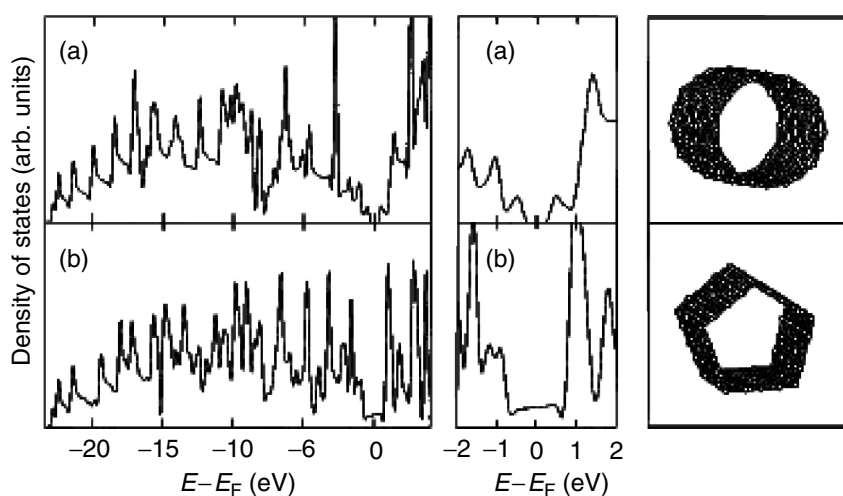


**FIGURE 4.21** Tight-binding densities of states (states/eV/cell) for the (10, 0) cylindrical (a), and the (10, 0)<sup>5</sup> pentagonal (b) cross-section nanotubes. The Fermi level is positioned at zero energy. Both nanotubes are also represented in inset on the right of their respective DOS.<sup>134</sup>

Furthermore, out-of-plane bending of the hexagonal carbon rings along the polygonal edges brings new pairs of atoms closer than the second-neighbor distance in graphite. All this leads to the modification of the electronic band structure, and as a consequence, the semiconducting band gap of the (10, 0) polygonal tube is almost completely closed (Figure 4.21b). The *ab initio* calculations<sup>134</sup> confirm these tight-binding results and predict a gap of 0.08 eV for the pentagonal cross section. Electronic behavior of metallic armchair nanotubes is not so strongly altered with polygonization because the  $\sigma^*-\pi^*$  hybridization is not possible in the case of armchair configurations.

Theoretical studies also suggest that the perturbation of electronic properties of carbon nanotubes will be different for various degrees of polygonization (i.e., various numbers of facets).<sup>134</sup> An example is given for a (12, 0) nanotube. Zigzag (12, 0) nanotube of circular cross section is metallic. When different polygonal cross sections (triangle, square, and hexagon) are considered, the results indicate that all kinds of electronic properties arise (Figure 4.22). The first two cases are metallic, while the third is a 0.5 eV band gap semiconductor. It is important to remember here that these calculations are given for a carbon nanotube comprised of a single shell.

### 4.3.3.2 Raman Spectra

Vibrational properties of GPCs have been studied by means of Raman spectroscopy,<sup>42,102,115</sup> and it has been confirmed that they are highly graphitized structures with the distinct disorder-induced (D) band and the strong graphitic (G) band of about the same full-width at half-maximum (FWHM = 14  $\text{cm}^{-1}$ ) as in crystals of natural graphite.<sup>136</sup> The selective micro-Raman spectra from the crystal's side face and tip are shown in Figure 4.23. Spectra from the crystal faces correspond to perfect graphite with a narrow G band at 1580  $\text{cm}^{-1}$ . In addition to 1580  $\text{cm}^{-1}$  peak, the spectra from the tips feature a weak D band at 1352  $\text{cm}^{-1}$ , and an unusually strong 2-D (2706  $\text{cm}^{-1}$ ) overtone that exceeds the intensity of the G band. A similar effect was observed on graphite scrolls (Figure 4.15). Raman spectra of GPCs contain two additional bands in the second-order frequency range at ca. 1895 and 2045  $\text{cm}^{-1}$  (Figure 4.23). A number of weak low-frequency bands including a doublet at 184/192  $\text{cm}^{-1}$  have been observed in some samples.<sup>42</sup> These low-frequency bands, typical for single-wall nanotubes,<sup>137</sup> may come from the innermost carbon nanotube shells protruding

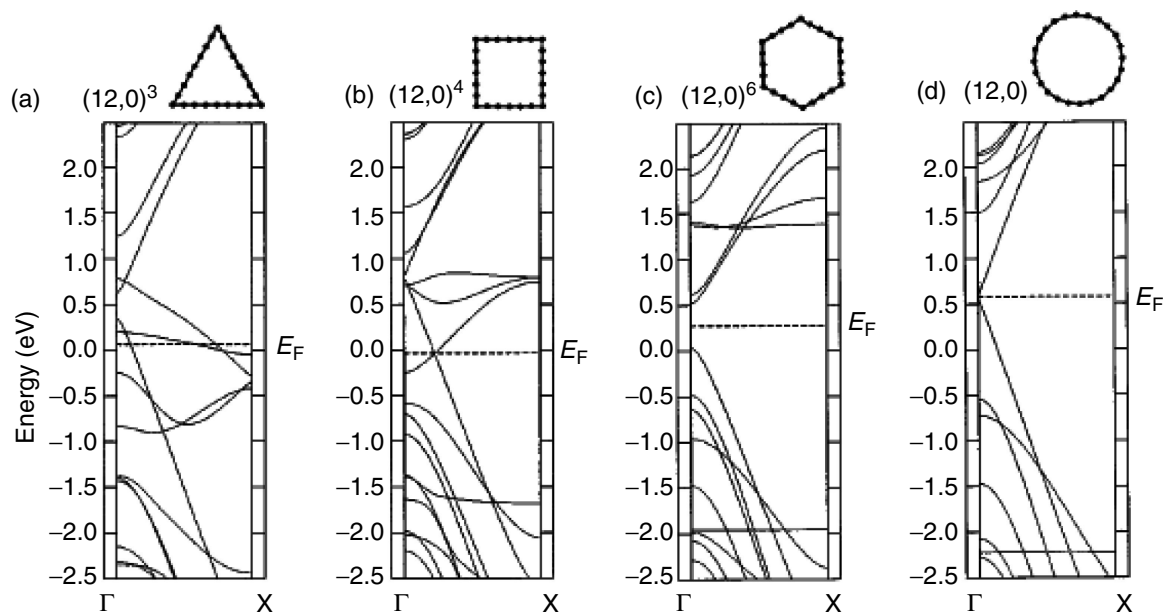


**FIGURE 4.22** Tight-binding band structures of the metallic (12, 0) nanotube, illustrating the effect of the degree of polygonization of the cross section on electronic behavior. Given here are examples of (a) the triangle (12, 0)<sup>3</sup>, (b) square (12, 0)<sup>4</sup>, and (c) hexagonal (12, 0)<sup>6</sup> geometries that are compared to the pure cylinder case tube (d).<sup>134</sup>



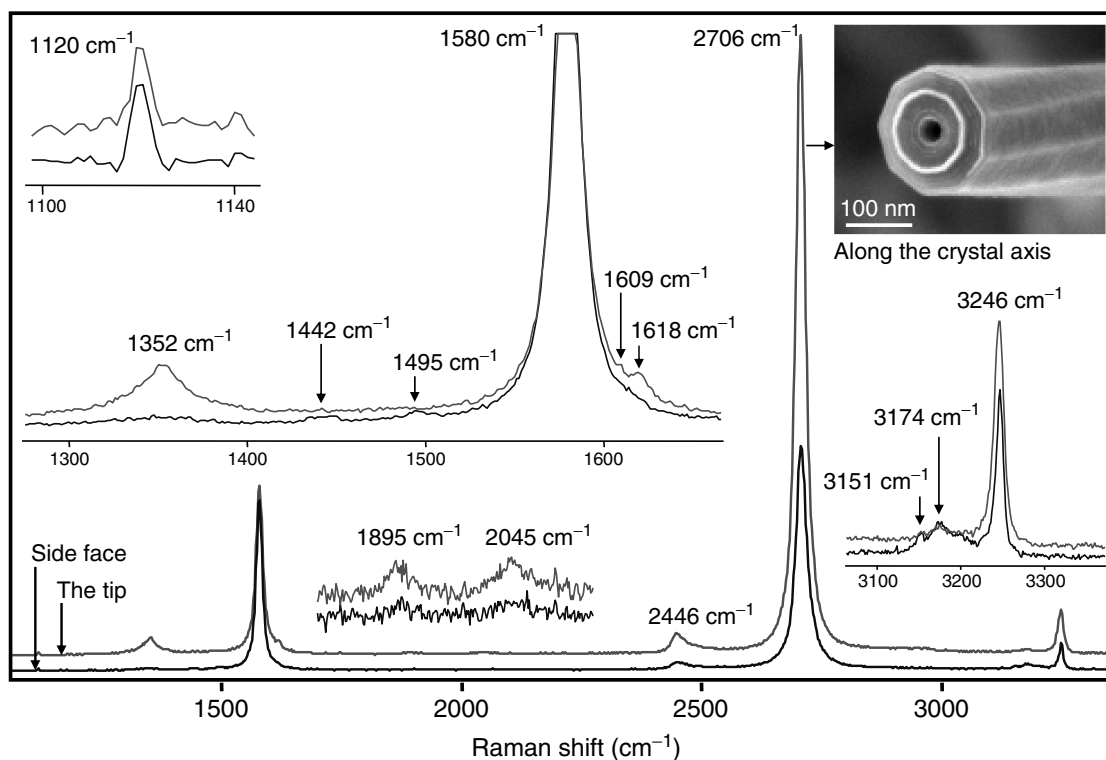


**FIGURE 4.23** Fundamental modes, combination modes, and overtones in Raman spectra taken from the side face and the tip of an individual graphite polyhedral crystal (514.5 nm excitation). Inset: an SEM micrograph of a different crystal having structure similar to the one used to record Raman spectra.<sup>102</sup>

sometimes from the GPCs (see Figure 4.17b). Low-intensity bands are also present in the range 1440 to 1500  $\text{cm}^{-1}$  (Figure 4.24), the origin of which has not been unambiguously determined yet.

#### 4.3.3.3 Chemical, Thermal, and Mechanical Stability

Functionalization and chemical activity of carbon nanotubes is the subject of intensive study, and many breakthroughs have been made in this field over the past 5 years. Side walls of single-wall carbon nanotubes have been successfully functionalized with fluorine,<sup>138</sup> carboxylic acid groups,<sup>139</sup> isocyanate groups,<sup>140</sup> dichlorocarbene,<sup>141</sup> poly-methyl methacrylate,<sup>142</sup> and polystyrene.<sup>143</sup> Various functional groups have been attached to tube edge sites. This has made it possible to utilize carbon nanotubes and other tubular carbon materials in the fabrication of sorbents,<sup>144</sup> catalyst supports,<sup>145,146</sup> gas storage materials,<sup>147</sup> and polymer matrix composites.<sup>148,149</sup> The effect of polygonization on chemical behavior of carbon nanotubes has not been thoroughly investigated yet; however it is expected that polygonal tubes have chemical properties similar to those of circular multiwall carbon nanotubes and graphite, and that they may be more reactive (less stable) along the polygonal edges than in the extended near-planar regions.<sup>120</sup> Another interesting property of GPCs is polygonized hemitoroidal edge plane terminations.<sup>150</sup> Transformation of active sites into loops promotes the GPC into a more stable (or chemically inert) structure. Moreover, due to their specific spatial conformation, they allow for easier intercalation with foreign atoms such as lithium and others.<sup>127,151</sup>

Several methods have been utilized to probe the chemical activity of polygonal tubes. In one of them, GPCs were intercalated with 50:50  $\text{H}_2\text{SO}_4/\text{HNO}_3$  for 1 h, washed in deionized water, dried for 24 h, and then exfoliated by rapid heating at about 980°C for about 15 sec or until maximum volume expansion is reached. GPCs survived very severe intercalation and exfoliation conditions, most of them retaining their original shape of faceted axial whiskers, although damage in the form of cracks along the axis and striations on the hemitoroidal surfaces was observed on most of the

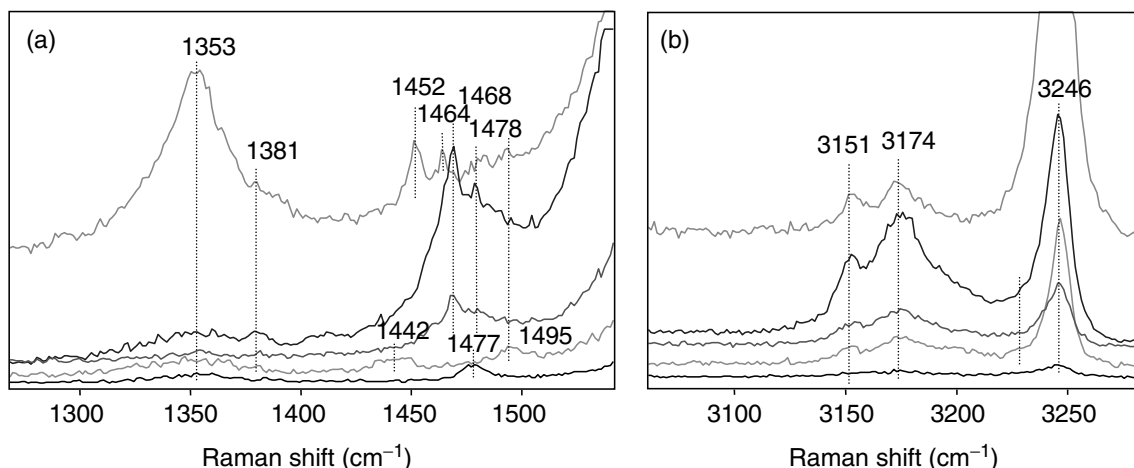


**FIGURE 4.24** Raman spectra of graphite polyhedral crystals showing additional weak bands in the range: (a) 1400 to 1500  $\text{cm}^{-1}$  and (b) 3100 to 3200  $\text{cm}^{-1}$  (for 514.5 nm excitation).<sup>102</sup>

crystals. Corrosion studies of graphitic polyhedral crystals showed that exposure of GPCs to overheated steam at normal pressure for 1 h will cause their complete oxidation at temperatures between 600 and 700°C. Similarly, 700°C was determined as an onset temperature for oxidation in air. However, they were more stable than disordered glassy carbon in supercritical water.<sup>42</sup>

Polygonization of the cross section of a tube is not expected to significantly affect its tensile strength, nor should it drastically affect the bending modulus of the tube. However, for a helical polygonal multiwall nanotube, the pull-out strength is expected to be higher than in the case of its cylindrical counterpart, because of the more favorable stress distribution upon loading.

#### 4.4 CONCLUSIONS

Extended growth of nanotubes or fullerene cones leads to formation of a myriad of nano- and microstructures, which are larger relatives of carbon nanotubes. Graphite cones and whiskers have much in common with carbon nanotubes and nanofibers. They inherit the conical structure of scrolled tubes (also known as “herring-bone” structure in carbon nanotubes). Seamless graphite nano- and microcones can have five different apex angles with “magic” numbers of 19.2, 38.9, 60.0, 83.6, and 112.9°, which correspond to 60, 120, 180, 240, and 300° disclinations in graphite. Scrolled conical structures may have virtually any apex angle, and very small (2 to 3°) angles have been observed. A few other specific values also occur more frequently as they are energetically preferred because they allow the registry between graphene sheets in the cone.

Polygonization of nanotubes accompanied by growth in the radial direction leads to the formation of GPCs. They have nanotube cores and graphite crystal faces. Unusual symmetries have been observed in GPCs. Most of them are built of co-axial graphite shells.

Cones and large nanotubes have been produced synthetically in the laboratory, and several methods for their synthesis are known. GPCs have only been discovered in synthetic carbon materials and can be grown by CVD or hydrothermally. However, since many natural graphites have been formed from hydrothermal deposits in nature, it would not be surprising to learn that GPCs exist in nature as well. Large carbon nanotubes have already been observed in natural deposits along with carbon cones.

Cones, whiskers, and GPC can bridge the nano- and microworlds and may have numerous applications, where sizes between nanotubes and carbon fibers are required. They may also have interesting electronic and mechanical properties determined by their geometry. However, while their structure has been well understood, very little is known about their properties. Properties need to be studied before their wide-scale applications can be explored.

## ACKNOWLEDGMENT

This work was supported by the US Department of Energy grant DE-FJ02-01ER45932.

## REFERENCES

1. B. T. Kelly, *Physics of Graphite*, Applied Science Publishers, London, 1981.
2. S. Iijima, *Nature*, 354, 56, 1991.
3. T. Tsuzuku, *Proceedings of the 3rd Conference on Carbon*, Pergamon Press, University of Buffalo, New York, 1957, p. 433.
4. T. Tsuzuku, *J. Phys. Soc. Jpn.*, 12, 778, 1957.
5. S. Amelinckx, W. Luyten, T. Krekels, et al., *J. Cryst. Growth*, 121, 543, 1992.
6. M. Ge and K. Sattler, *Chem. Phys. Lett.*, 220, 192, 1994.
7. K. Sattler, *Carbon*, 33, 915, 1995.
8. A. Krishnan, E. Dujardin, M. M. J. Treacy, et al., *Nature*, 388, 451, 1997.
9. H. W. Kroto, J.R. Heath, S.C.O'Brien, et al., *Nature*, 318, 162, 1985.
10. S. Iijima, *MRS Bull.*, 19, 43, 1994.
11. R. Bacon, *J. Appl. Phys.*, 31, 283, 1960.
12. D. W. McKee, *Annu. Rev. Mater. Sci.*, 03, 195, 1973.
13. P. M. Ajayan, J. M. Nugent, R. W. Siegel, et al., *Nature*, 404, 243, 2000.
14. M. Hillert and N. Lange, *Z. Kristallogr. Kristallgeometrie Kristallphys. Kristallchem.*, 111, 24, 1958.
15. S. D. Robertson, *Carbon*, 8, 365, 1970.
16. P. L. J. Walker, J. F. Rakaszawski, and G. R. Imperial, *J. Phys. Chem.* 63, 133, 1959.
17. M. L. Lieberman, C. R. Hills, and C. J. Miglionico, *Carbon*, 9, 633, 1971.
18. P. A. Tesner, E. Y. Robinovich, I. S. Rafalkes, et al., *Carbon*, 8, 435, 1970.
19. W. R. Davis, R. J. Slawson, and G. R. Rigby, *Trans. Br. Ceram. Soc.*, 56, 67, 1957.
20. A. Fonseca, K. Hernadi, P. Piedigrosso, et al., *Appl. Phys. A: Mater. Sci. Process.*, 67, 11, 1998.
21. H. B. Haanstra, W. F. Knippenberg, and G. Verspui, *J. Cryst. Growth*, 16, 71, 1972.
22. J. H. Knox, B. Kaur, and G. R. Millward, *J. Chromatogr.*, 352, 3, 1986.
23. J. Dong, W. Shen, B. Zhang, et al., *Carbon*, 39, 2325, 2001.
24. J. Dong, W. Shen, F. Kang, et al., *J. Cryst. Growth*, 245, 77, 2002.
25. P. T. B. Shaffer, *Plenum Press Handbooks of High-Temperature Materials No. 1 Materials Index*, Plenum Press, New York, 1964.
26. J. Gillot, W. Bollman, and B. Lux, *Carbon*, 6, 381, 1968.
27. D. D. Double and A. Hellawell, *Acta Metall.*, 22, 481, 1974.
28. S. Iijima, T. Ichihashi, and Y. Ando, *Nature*, 356, 776, 1992.
29. P. M. Ajayan, T. Ichihashi, and S. Iijima, *Chem. Phys. Lett.*, 202, 384, 1993.
30. P. M. Ajayan and S. Iijima, *Nature*, 358, 23, 1992.
31. T. W. Ebbesen, *Annu. Rev. Mater. Sci.*, 24, 235, 1994.
32. T. W. Ebbesen and T. Takada, *Carbon*, 33, 973, 1995.
33. A. L. Mackay and H. Terrones, *Nature*, 352, 762, 1991.
34. H. Terrones and A. L. Mackay, *Carbon*, 30, 1251, 1992.
35. B. I. Dunlap, *Phys. Rev. B.*, 46, 1933, 1992.
36. W. Luyten, T. Krekels, S. Amelinckx, et al., *Ultramicroscopy*, 49, 123, 1993.
37. S. Amelinckx, A. Lucas, and P. Lambin, *Rep. Prog. Phys.*, 62, 1471, 1999.
38. H. P. Boehm, *Carbon*, 35, 581, 1997.
39. G. R. Millward and D. A. Jefferson, in *Chemistry and Physics of Carbon*, Vol. 14, P. L. J. Walker and P. A. Thrower, Eds., Dekker, New York, 1978, p. 1.
40. S. Dimovski, J. Libera, and Y. Gogotsi, *Mat. Res. Soc. Symp. Proc.*, 706, Z6.27.1, 2002.
41. Y. Gogotsi, S. Dimovski, and J. A. Libera, *Carbon*, 40, 2263, 2002.
42. Y. Gogotsi, J. A. Libera, N. Kalashinkov, et al., *Science*, 290, 2000.
43. N. Muradov and A. Schwitler, *Nano Lett.*, 2, 673, 2002.
44. J. Liu, W. Lin, X. Chen, et al., *Carbon*, 42, 669, 2004.
45. S. F. Braga, V. R. Coluci, S. B. Legoas, et al., *Nano Lett.*, 4, 881, 2004.
46. L. M. Viculis, J. J. Mack, and R. B. Kaner, *Science*, 299, 1361, 2003.

47. N. M. Rodriguez, A. Chambers, and R. T. K. Baker, *Langmuir*, 11, 3862, 1995.
48. V. I. Merkulov, A. V. Melechko, M. A. Guillorn, et al., *Chem. Phys. Lett.*, 350, 381, 2001.
49. V. I. Merkulov, M. A. Guillorn, D. H. Lowndes, et al., *Appl. Phys. Lett.*, 79, 1178, 2001.
50. H. Terrones, T. Hayashi, M. Muños-Navia, et al., *Chem. Phys. Lett.*, 343, 241, 2001.
51. M. Endo, Y. A. Kim, T. Hayashi, et al., *Appl. Phys. Lett.*, 80, 1267, 2002.
52. G. Y. Zhang, X. Jiang, and E. G. Wang, *Science*, 300, 472, 2003.
53. Y. Hayashi, T. Tokunaga, T. Soga, et al., *Appl. Phys. Lett.*, 84, 2886, 2004.
54. R. C. Mani, X. Li, M. K. Sunkara, et al., *Nano Lett.*, 3, 671, 2003.
55. P. Liu, Y. W. Zhang, and C. Lu, *Appl. Phys. Lett.*, 85, 1778, 2004.
56. Z. F. Ren, Z. P. Huang, D. Z. Wang, et al., *Appl. Phys. Lett.*, 75, 1086, 1999.
57. Q. Yang, C. Xiao, W. Chen, et al., *Diamond Relat. Mater.*, 13, 433, 2004.
58. H. Lim, H. Jung, and S.-K. Joo, *Microelectron. Eng.*, 69, 81, 2003.
59. Y. K. Yap, J. Menda, L. K. Vanga, et al., *Mat. Res. Soc. Symp. Proc.*, 821, P3.7.1, 2004.
60. A. R. Patel and S. V. Deshpande, *Carbon*, 8, 242, 1970.
61. J. A. Jaszczak, G. W. Robinson, S. Dimovski, et al., *Carbon*, 41, 2085, 2003.
62. S. Dimovski, J. A. Jaszczak, G. W. Robinson, et al. Extended Abstracts of Carbon 2004, Biennial Conference on Carbon, American Carbon Society, RI, 2004.
63. J. A. Jaszczak, in *Mesomolecules: From Molecules to Materials*, G. D. Mendenhall, A. Greenberg, and J. F. Liebman, Eds., Chapman & Hall, New York, 1995, p. 161.
64. V. N. Kvasnitsa and V. G. Yatsenko, *Mineralogicheskii Zh.*, 13, 95, 1991.
65. V. G. Kvasnitsa, V. N. Yatsenko, and V. M. Zagnitko, *Mineralogicheskii Zh.*, 20, 34, 1998.
66. C. Lemanski, *Picking Table*, 32, 1, 1991.
67. B. A. Van der Pluijm and K. A. Carlson, *Geology*, 17, 161, 1989.
68. Carlson, B. A. Van der Pluijm, and S. Hanmer, *Geol. Soc. Am. Bull.*, 102, 174, 1990.
69. J. A. Jaszczak and G. W. Robinson, *Rocks Miner.*, 75, 172, 2000.
70. S. N. Britvin, G. U. Ivanyuk, and V. N. Yakovenchuk, *World of Stones*, 5/6, 26, 1995.
71. P. J. F. Harris, *Carbon Nanotubes and Related Structures*, Cambridge University Press, Cambridge, 1999.
72. E. A. Lord and C. B. Wilson, *The Mathematical Description of Shape and Form*, Halsted Press, New York, 1984.
73. S. Ihara, S. Itoh, K. Akagi, et al., *Phys. Rev. B*, 54, 14713, 1996.
74. M. Endo, K. Takeuchi, K. Kobori, et al., *Carbon*, 33, 873, 1995.
75. J. R. Dias, *Carbon*, 22, 107, 1984.
76. A. T. Balaban, D. J. Klein, and X. Liu, *Carbon*, 32, 357, 1994.
77. D. J. Klein, *Phys. Chem. Chem. Phys.*, 4, 2099, 2002.
78. D. J. Klein, *Intl. J. Quantum Chem.*, 95, 600, 2003.
79. K. Kobayashi, *Phys. Rev. B*, 61, 8496, 2000.
80. Mizes and J. S. Foster, *Science*, 244, 559, 1989.
81. R. Tamura, K. Akagi, M. Tsukada, et al., *Phys. Rev. B*, 56, 1404, 1997.
82. R. Tamura and M. Tsukada, *Phys. Rev. B*, 52, 6015, 1995.
83. R. Tamura and M. Tsukada, *Phys. Rev. B*, 49, 7697, 1994.
84. D. L. Carroll, P. Redlich, P. M. Ajayan, et al., *Phys. Rev. Lett.*, 78, 2811, 1997.
85. B. I. Dunlap, *Phys. Rev. B*, 49, 5643, 1994.
86. J. W. Mintmire, B. I. Dunlap, and C. T. White, *Phys. Rev. Lett.*, 68, 631, 1992.
87. R. Saito, M. Fujita, G. Dresselhaus, et al., *Phys. Rev. B*, 46, 1804, 1992.
88. J.-C. Charlier and J.-P. Issi, *Appl. Phys. A: Mater. Sci. Process*, 67, 79, 1998.
89. J. W. G. Wilder, L. C. Venema, A. G. Rinzler, et al., *Nature*, 391, 1998.
90. J. C. Charlier, T. W. Ebbesen, and P. Lambin, *Phys. Rev. B*, 53, 11108, 1996.
91. S. Berber, Y.-K. Kwon, and D. Tománek, *Phys. Rev. B*, 62, 2291, 2000.
92. R. Vidano and D. B. Fischbach, *J. Am. Cer. Soc.*, 61, 13, 1978.
93. P. Lespade, R. Al-Jishi, and M. S. Dresselhaus, *Carbon*, 20, 427, 1982.
94. G. Katagiri, H. Ishida, and A. Ishitani, *Carbon*, 26, 565, 1988.
95. Y. Kawashima and G. Katagiri, *Phys. Rev. B*, 52, 10053, 1995.
96. G. G. Samsonidze, R. Saito, A. Jorio, et al., *Phys. Rev. Lett.*, 90, 027403, 2003.
97. F. Tuinstra and J. L. Koenig, *J. Chem. Phys.*, 53, 1126, 1970.
98. R. J. Nemanich and S. A. Solin, *Phys. Rev. B*, 20, 392, 1979.
99. P. H. Tan, Y. M. Deng, and Q. Zhao, *Phys. Rev. B*, 58, 5435, 1998.

100. P. H. Tan, C. Y. Hu, J. Dong, et al., *Phys. Rev. B*, 6421, 214301, 2001.
101. J. Dong, W. C. Shen, and B. Tatarchuk, *Appl. Phys. Lett.*, 80, 3733, 2002.
102. P. H. Tan, S. Dimovski, and Y. Gogotsi, *Phil. Trans. Royal Soc. Lond. A*, 362, 2289, 2004.
103. Thomsen, C. and Reich, S. *Phys. Rev. Lett.*, 85, 5214, 2000.
104. M. Q. Liu and J. M. Cowley, *Mater. Sci. Eng. A*, 185, 131, 1994.
105. M. Liu and J. M. Cowley, *Ultramicroscopy*, 53, 333, 1994.
106. S. Amelinckx, D. Bernaerts, X. B. Zhang, et al., *Science*, 267, 1334, 1995.
107. N. G. Chopra, L. X. Benedict, V. H. Crespi, et al., *Nature*, 377, 135, 1995.
108. M. Liu and J. M. Cowley, *Carbon*, 32, 393, 1994.
109. J. S. Speck, M. Endo, and M. S. Dresselhaus, *J. Cryst. Growth*, 94, 834, 1989.
110. X. F. Zhang, X. B. Zhang, G. Van Tendeloo, et al., *J. Cryst. Growth*, 130, 368, 1993.
111. W. Kratschmer, L. D. Lamb, K. Fostiropoulos, et al., *Nature*, 347, 354, 1990.
112. C.-H. Kiang, M. Endo, P. M. Ajayan, et al., *Phys. Rev. Lett.*, 81, 1869, 1998.
113. Y. Saito, T. Yoshikawa, S. Bandow, et al., *Phys. Rev. B*, 48, 1907, 1993.
114. M. Bretz, B. G. Demczyk, and L. Zhang, *J. Cryst. Growth*, 141, 304, 1994.
115. H. Okuno, A. Palnichenko, J.-F. Despres, et al., *Carbon*, 43, 692, 2005.
116. J. M. Calderon-Moreno and M. Yoshimura, *Mater. Trans.*, 42, 1681, 2001.
117. J. M. Calderon Moreno and M. Yoshimura, *J. Am. Chem. Soc.*, 123, 741, 2001.
118. S. Iijima, *J. Cryst. Growth*, 50, 675, 1980.
119. D. Ugarte, *Nature*, 359, 707, 1992.
120. Y. Maniwa, R. Fujiwara, H. Kira, et al., *Phys. Rev. B*, 64, 073105, 2001.
121. L. A. Bursill, P. Ju-Lin, and F. Xu-Dong, *Philos. Mag. A (Phys. Condens. Matter, Defects Mech. Prop.)*, 71, 1161, 1995.
122. S. Q. Feng, D. P. Yu, G. Hub, et al., *J. Phys. Chem. Solids*, 58, 1887, 1997.
123. G. Hu, X. F. Zhang, D. P. Yu, et al., *Solid State Commun.*, 98, 547, 1996.
124. J.-B. Park, Y.-S. Cho, S.-Y. Hong, et al., *Thin Solid Films*, 415, 78, 2002.
125. S. V. Rotkin and Y. Gogotsi, *Mater. Res. Innovations*, 5, 191, 2002.
126. A. Sarkar, H. W. Kroto, and M. Endo, *Carbon*, 33, 51, 1995.
127. K. Moriguchi, Y. Itoh, S. Munetoh, et al., *Phys. B: Condens. Matter*, 323, 127, 2002.
128. M. Endo, B. J. Lee, Y. A. Kim, et al., *New J. Phys.*, 5, 121.1, 2003.
129. H. Murayama and T. Maeda, *Nature*, 345, 791, 1990.
130. M. Endo, Y. A. Kim, T. Hayashi, et al., *Carbon*, 41, 1941, 2003.
131. Z. Zhou, L. Ci, X. Chen, et al., *Carbon*, 41, 337, 2003.
132. M. S. Dresselhaus, G. Dresselhaus, and P. C. Eklund, *Science of Fullerenes and Carbon Nanotubes*, Academic Press, New York, 1996.
133. P. Lambin, A. A. Lucas, and J.-C. Charlier, *J. Phys. Chem. Solids*, 58, 1833, 1997.
134. J.-C. Charlier, P. Lambin, and T. W. Ebbesen, *Phys. Rev. B*, 54, R8377, 1996.
135. H. Hiura, T. W. Ebbesen, J. Fujita, et al., *Nature*, 367, 148, 1994.
136. K. Ray and R. L. McCreery, *Analyt. Chem.*, 69, 4680, 1997.
137. A. M. Rao, E. Richter, S. Bandow, et al., *Science*, 275, 187, 1997.
138. E. T. Mickelson, I. W. Chiang, J. L. Zimmerman, et al., *J. Phys. Chem. B*, 103, 4318, 1999.
139. J. Chen, M. A. Hamon, H. Hu, et al., *Science*, 282, 95, 1998.
140. C. Zhao, L. Ji, H. Liu, et al., *J. Solid State Chem.*, 177, 4394, 2004.
141. H. Hu, B. Zhao, M. A. Hamon, et al., *J. Am. Chem. Soc.*, 125, 14893, 2003.
142. H. Kong, C. Gao, and D. Yan, *J. Am. Chem. Soc.*, 126, 412, 2004.
143. G. Viswanathan, N. Chakrapani, H. Yang, et al., *J. Am. Chem. Soc.*, 125, 9258, 2003.
144. Y. Xu, J. W. Zondlo, H. O. Finklea, et al., *Fuel Process Technol.*, 68, 189, 2000.
145. J. Ma, C. Park, N. M. Rodriguez, et al., *J. Phys. Chem B*, 105, 11994, 2001.
146. M. Endo, Y. A. Kim, M. Ezaka, et al., *Nano Lett.*, 3, 723, 2003.
147. A. Chambers, C. Park, R. T. K. Baker, et al., *J. Phys. Chem. B*, 102, 4253, 1998.
148. R. Andrews and M. C. Weisenberger, *Curr. Opinion Solid State Mater. Sci.*, 8, 31, 2004.
149. V. Datsyuk, C. Guerret-Piecourt, S. Dagreou, et al., *Carbon*, 43, 873, 2005.
150. J. Han, *Chem. Phys. Lett.*, 282, 187, 1998.
151. K. Moriguchi, S. Munetoh, M. Abe, et al., *J. Appl. Phys.*, 88, 6369, 2000.

---

# 5 Nanocrystalline Diamond

*Olga Shenderova and Gary McGuire*

International Technology Center, Research Triangle Park,  
North Carolina

## CONTENTS

5.1	Introduction .....	175
5.2	Stability of Nanodiamond .....	176
5.3	Types of Nanodiamond and Methods of Their Synthesis .....	180
5.3.1	Zero-Dimensional Nanodiamond Structures .....	181
5.3.2	One-Dimensional Nanodiamond Structures .....	186
5.3.3	Two-Dimensional Nanodiamond Structures .....	189
5.3.4	Three-Dimensional Nanodiamond Structures .....	189
5.4	Ultrananocrystalline Diamond Particulate Produced by Explosive Detonation .....	191
5.4.1	Synthesis and Properties .....	191
5.4.2	Applications of Ultrananocrystalline Diamond Particulate .....	197
5.5	Ultrananocrystalline Diamond Films Produced by Chemical Vapor Deposition .....	199
5.6	Carbide-Derived Diamond-Structured Carbon .....	200
5.7	Medical and Biological Applications of Nanodiamond .....	201
5.8	Conclusion .....	204
	References .....	205

## 5.1 INTRODUCTION

The term “nanodiamond” is broadly used for a variety of diamond-based materials at the nanoscale (lengths in the scale of ~1 to 100 nm), including pure-phase diamond films, diamond particles, and their structural assemblies, such as loosely bound particle agglomerates or particles incorporated into other material matrices. The recently fabricated one-dimensional (1-D) diamond nanorods (DNR) and 2-D diamond nanoplates complete the set of possible dimensionalities of these structures. There is a special class of nanodiamond material called “ultrananocrystalline” diamonds (UNCD), the basic diamond constituents whose length is of the order of a few nanometers. They are called “ultra-nanocrystalline,” to distinguish them from other diamond-based nanostructures with characteristic sizes above ~10 nm. Among UNCD materials, the most promising for nanotechnological applications in the immediate future are *UNCD particles* produced by detonation of carbon explosive materials (characteristic size of primary particles ~5 nm) developed in the former USSR in the 1960s, and pure-phase *UNCD films* produced by chemical vapor deposition (CVD) (characteristic size of grains 2 to 5 nm) recently developed in the Argon National Laboratory [1]. UNCD particles and films possess unique properties, and have different niche applications. These two technologically important materials have been the focus of several recent reviews [1–4], monographs [5–7], as well as recent nanodiamond conferences [8–10], and will be major topics of this chapter.

Methods for synthesizing diamond powder in the form of single particles with micro- and nanometer sizes were developed in the beginning of the 1960s by DuPont de Nemours (USA) and the product has been commercially available since the 1970s (Mypolex™). DuPont produced polycrystalline diamond particles up to 50 μm in size, using shock wave compression of carbon materials (graphite, carbon black) mixed with catalyst. The size of the primary grains in the polycrystalline particles is about 20 nm. Recently, the Mypolex polycrystalline diamond business has been acquired from DuPont by Microdiamant AG, Switzerland, a company specializing in the micron and submicron diamond market. The finest diamond fraction, produced by milling followed by grading, encompasses the range of 0 to 50 nm with an average particle size of about 25 nm. In addition to Mypolex polycrystalline diamond, Microdiamant AG also provides the finest fractions of particles of size down to 0 to 50 nm processed from high-pressure high-temperature (HPHT) synthetic diamond (both mono- and polycrystalline) as well as from natural diamond powders. The commercialization of this nanodiamond material has matured and it has been in use for high-precision polishing applications for a long time. An approach for producing UNCD powder with a characteristic size of primary particles of ~5 nm is the conversion of carbon-containing explosive compounds into diamond during firing of explosives in hermetic tanks. Details on the fascinating history of the discovery of the UNCD particulate can be found in [3,5,11]. This method was initiated in Russia in the early 1960s, soon after DuPont's work on shock wave synthesis. A large-scale production foundry, "ALTAI," was founded in Russia in 1983 to commercialize the process of detonation diamond production in bulk quantities (of the order of tons of the product per year) [5]. According to a USSR government report (1989) on UNCD particulate production, the plan was to increase UNCD production by up to 250 million carats per year [5]. Presently, however, the production of detonation diamond by ALTAI is limited. Currently, there are several commercial centers in Russia, Ukraine, Byelorussia, Germany, Japan, and China, producing UNCD particulates by explosives detonation. Although discovered several decades ago, UNCD particles have become an object of keen interest outside of Russia only within the last few years [8,10] as the field of nanotechnology has developed.

While developed relatively recently [1] as compared to UNCD particles, UNCD films are close to successful commercialization. Their ultrananocrystallinity is the result of a new growth and nucleation mechanism, which uses argon-rich plasmas instead of the hydrogen-rich plasmas normally used to deposit microcrystalline diamond films. Ultrananocrystalline diamond films are superior in many ways to traditional microcrystalline diamond films: they are smooth, dense, pinhole-free, phase-pure, and can be deposited conformally on a wide variety of materials and high-aspect-ratio structures [1].

Diamonds with characteristic sizes encompassing several nanometers have also been synthesized by other methods, particularly by chlorination of carbides [12], ion irradiation of graphite [13], electron irradiation of carbon onions [14], and in the vapor phase in a substrate-free, low-pressure, microwave-plasma CVD reactor [15]. Astronomical observations suggest that as much as 10 to 20% of the interstellar carbon is in the form of nanodiamonds [16]. The questions of when and how a nanodiamond originates in the Cosmos remain open.

This chapter is organized as follows: After a short section on the carbon phase diagram at the nanoscale and theoretical predictions of nanodiamond stability, nanodiamond structures of different dimensionalities synthesized to date will be summarized. Next, the synthesis, properties, and applications of UNCD particles of detonation origin, which have been on the market in FSU countries for decades, UNCD films that possess very unique properties, and carbide-derived UNCD films that are distinct by the simplicity of their production, will be discussed in more detail. These UNCD materials are synthesized by completely different techniques and have rather different properties, providing each of them specific application niches.

## 5.2 STABILITY OF NANODIAMOND

It is well known that the most stable carbon phase on the macroscale is graphite and that diamond is metastable. The energy difference between the two phases is only 0.02 eV/atom. However, because

of the high activation barrier for a phase transition ( $\sim 0.4$  eV/atom), very high temperatures and pressures and the use of a catalyst are required to realize the phase transformation. At the nanoscale, however, the carbon phase diagram has to be re-considered by introducing in addition to pressure and temperature a third parameter — cluster size [17,18]. In the expressions for the Gibbs free energy per atom of a cluster of  $n$  atoms in a given phase, the surface energy contribution has to be added to the bulk free energy. Estimates of the displacement of phase equilibrium lines for small carbon particles containing several hundred to several tens of thousands of atoms have been made recently [17,18] (Figure 5.1a). The authors report better agreement with calculations for experimental shock

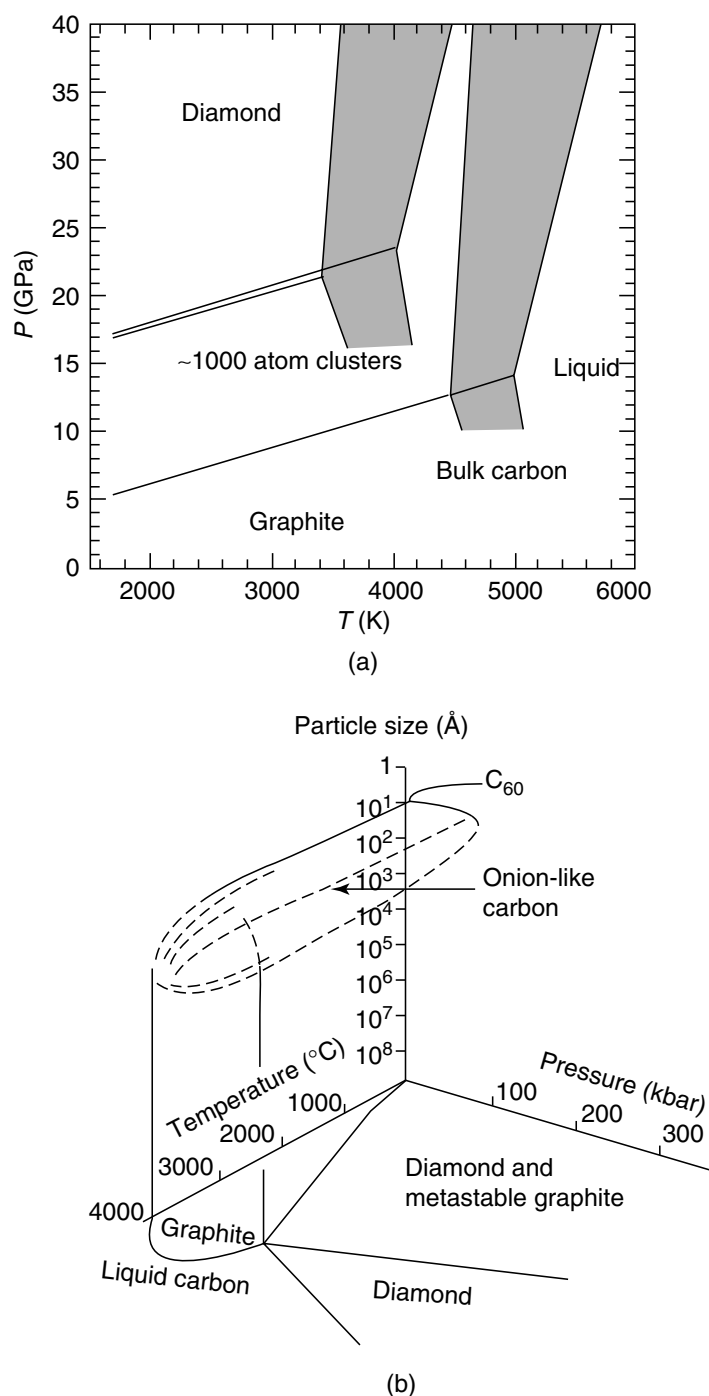


**FIGURE 5.1** Approximate phase diagram for 1000 atom carbon cluster. Shaded region corresponds to estimated uncertainties in location of equilibrium lines derived from available experimental data. Schematic three-dimensional phase diagram including fullerenes. (a: From Viecelli, J.A. and Ree, F.H., *J. Appl. Phys.*, 88, 683–690, 2000; b: from Kuznetsov, V.L. et al., *Mater. Res. Soc. Proc.*, 359, Pittsburgh, PA, 1995, 105. With permission.)



pressure–volume and temperature data using “nanocarbon phase diagram” than for those obtained with a bulk carbon equation of state. The results also suggest that carbon particles of the order of  $10^3$  to  $10^4$  atoms can exist in the liquid state at lower temperatures than bulk carbon. As a further extension of the carbon phase diagram, according to the fact that at sizes below 1.8 nm other carbon forms such as fullerenes and onions are abundant, it has been suggested to assign the corresponding region of the state diagram to fullerenes and onions [19], as shown schematically in Figure 5.1b.

However, analysis of the optimized geometries of the bare nanodiamond surfaces showed that the stability of nanocarbon species is quite complicated. Recent *ab initio* simulations demonstrate that within the size range of 1 [20–22] to 3 nm for spherical clusters [23]), the crystal morphology plays a very important role in cluster stability. While surfaces of cubic crystals exhibit structures similar to bulk diamonds, surfaces of octahedral, cuboctahedral, and spherical clusters show a transition from  $sp^3$  to  $sp^2$  bonding. The preferential exfoliation of the (1 1 1) surfaces begins for clusters in the subnanometer size range and promotes cluster transition to endo-fullerene for small clusters (~tens of atoms) and onion-like shells with diamond cores (buckydiamond) for larger clusters [20] (Figure 5.2b and Figure 5.3a). Recently, Barnard and colleagues included fullerenes, onions, and buckydiamonds in the “traditional” analysis of the relative stability of diamond and graphite at the nanoscale, and defined size regions of the stability of these structures [24]. According to the results in [24], as the system size for all-carbon structures is increased, the most stable carbon form at the nanoscale changes from fullerene — to onions — to buckydiamond — to nanodiamond — to graphite. The crossover from fullerenes to closed nanotubes has also been analyzed recently [25]. Regarding small carbon clusters, three regions of stability can be outlined [26]: below 20 atoms, the most stable geometries are one-dimensional ring clusters; between 20 and 28 atoms, clusters with quite different types of geometry have similar energetics; for larger clusters, fullerenes should be more stable. The hierarchy of the stabilities of carbon forms at the nanoscale is summarized in Figure 5.4. In general, for all-carbon nanostructures, it has been demonstrated by the highest level of sophisticated computational approaches that nanodiamonds are more stable thermodynamically than graphite when the particle size is less than 5 to 10 nm in contrast to the macroscale where diamond is metastable. At the same time, computational methods indicate that nanodiamond stability is restricted by the smallest sizes of ~1.9 nm, below which fullerene-related structures are more stable.

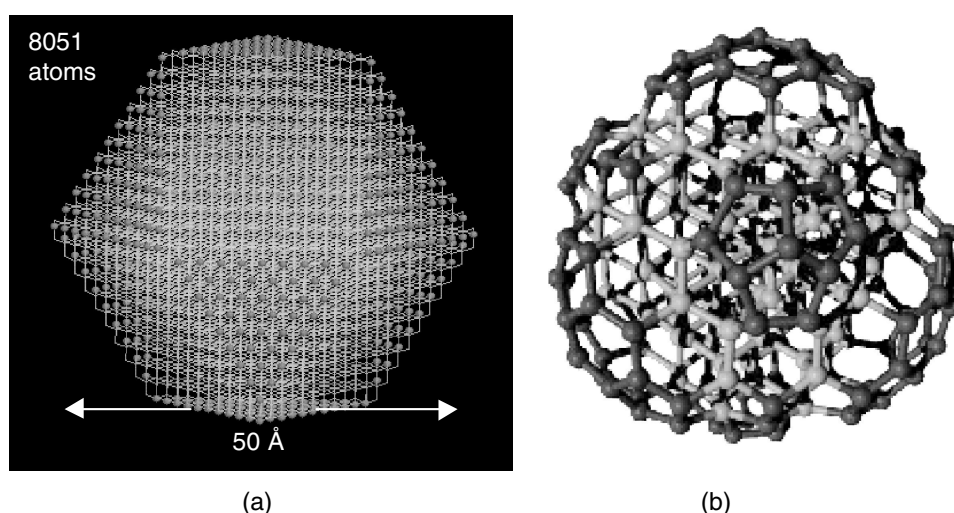


**FIGURE 5.2** Structural models of nanodiamond clusters. Polyhedral (a) (cuboctahedron) shape with all four-coordinated carbon atoms can be preserved if cluster surface is terminated by hydrogen. Three- and two-coordinated atoms on the surface of the cuboctahedral cluster are orange and white colored, respectively. (b) Bare surface of nonhydrogenated diamond clusters experience surface reconstruction, resulting in a cluster with a diamond core and a fullerene-like shell. Red colored atoms are  $sp^2$  carbon atoms. (b: Courtesy of Guilia Galli, Lawrence Livermore National Laboratory.)

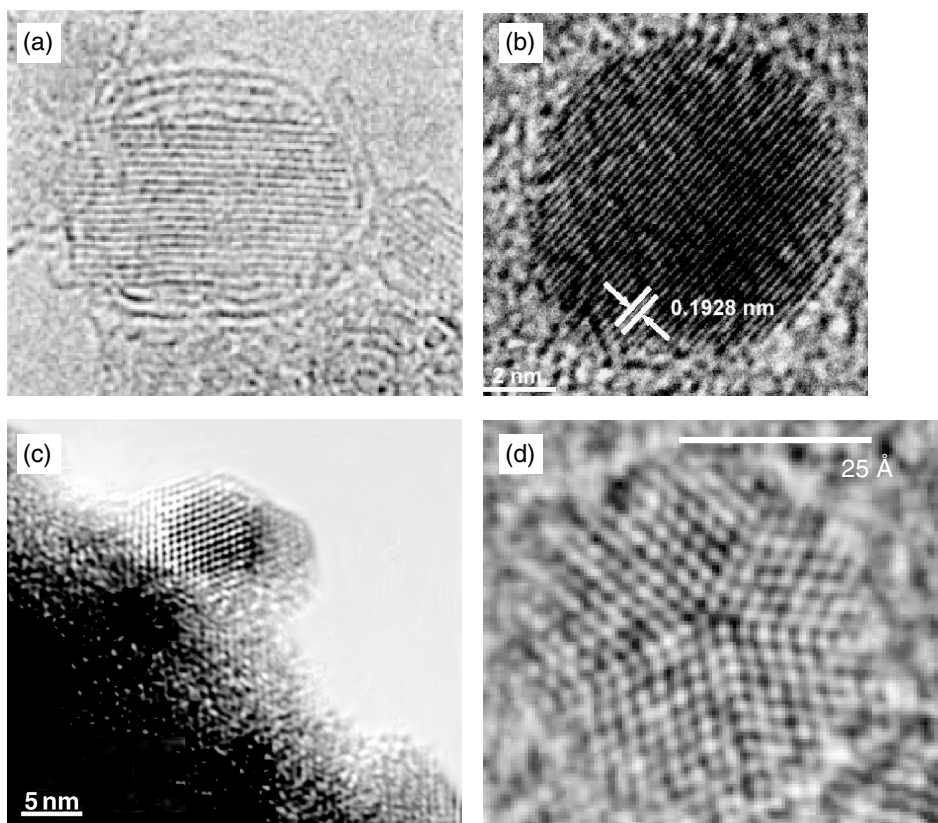


**FIGURE 5.3** HRTEM images of a bucky-diamond formed from a UNCD particle of detonation origin (a), spherical diamond in a carbide matrix synthesized by carbide chlorination process (b), polyhedral particle of detonation UNCD (c), and multiple twin particles of a presolar diamond (d). (Courtesy of T.L. Daulton, Naval Research Laboratory.) (a: From Kuznetsov, V.L. et al., *J. Appl. Phys.*, 86, 863, 1999; b: from Welz, S. et al., *J. Appl. Phys.*, 93, 4207, 2003; c: from Tyler, T. et al., *Appl. Phys. Lett.*, 82, 2904, 2003. With permission.)

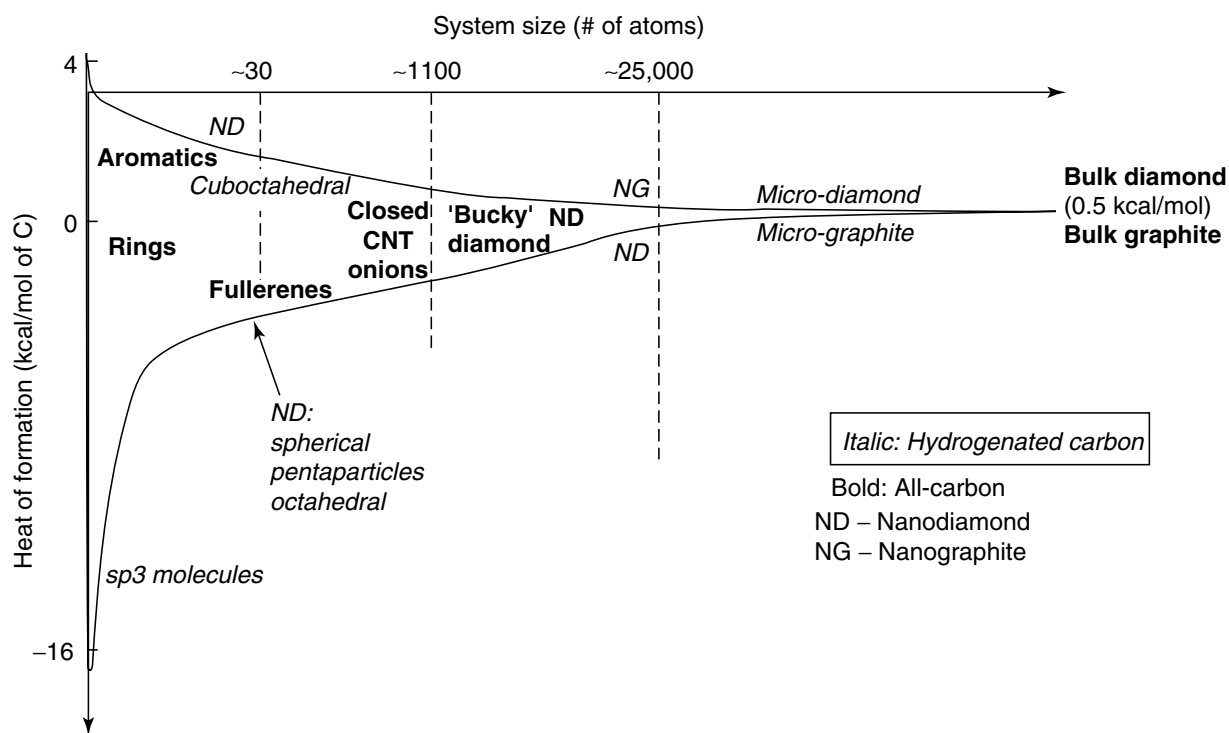


**FIGURE 5.4** Schematic representation of the most stable carbon phase (all-carbon and hydrogenated species) depending on the size of the carbon structure.

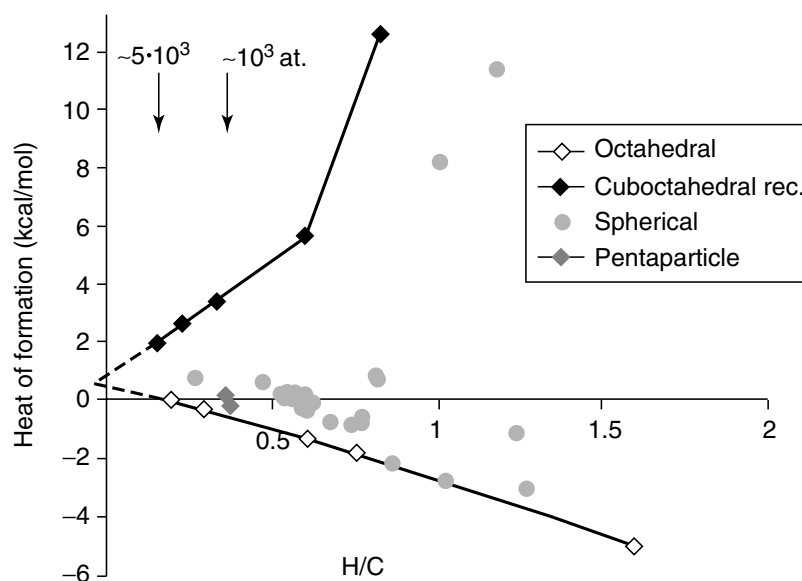


**FIGURE 5.5** Heats of formation for hydrogenated octahedra, (0 0 1)  $2 \times 1$  reconstructed cuboctahedra, spherical clusters, and two clusters with pentagonal shape.

The relative stability of different nanodiamond morphologies changes if one considers saturation of the dangling bonds on a particle surface by specific functional groups on an isolated particle surface, or on the interface between a UNCD particle and the surrounding matrix if a particle is incorporated into a matrix (as, for example, UNCD grains in CVD films, nanodiamond in agglomerates, etc.). Until recently, most of the experimental work dealing with nanodiamonds produced by means of detonation described the shape of clusters as being spherical. Figure 5.3b illustrates the perfect spherical shape of nanodiamond particles; in this case, a particle surrounded by carbide material during synthesis by a carbide chlorination process. However, high-resolution transmission electron microscopy (HRTEM) images of a single nanodiamond cluster on the surface of a Mo tip clearly indicate the presence of facets on the particle surface, with the cluster resembling a polyhedral shape (Figure 5.3c) [29]. In order to address the most stable shapes of the hydrogenated nanodiamond particles, heats of formation have been calculated for several nanodiamond series for particles relaxed with bond order potential [30]. Results of calculations for cuboctahedral, octahedral, spherical particles, and pentaparticles are illustrated in Figure 5.5. All of the series are bounded by curves corresponding to hydrogenated octahedra and (0 0 1)  $2 \times 1$  reconstructed cuboctahedra. Extrapolated curves intersect the ordinate axis at a point corresponding to the heat of formation of bulk diamond ( $\sim 0.5$  kcal/mol). It can be concluded that the most stable morphologies for hydrogenated nanodiamond are octahedra, pentaparticles, and groups of spherical particles. Obviously, there are many more series of different nanodiamond morphologies that can be constructed, which, however, will probably be bound by the octahedral (0 0 1)  $2 \times 1$  reconstructed cuboctahedra curves. In combination with the above analysis on all-carbon clusters, the hierarchy of the stabilities of H-containing carbon forms at the nanoscale is summarized in Figure 5.4. The region of the relative stability of different forms of hydrogenated carbon is highlighted in order to emphasize the plurality of possible morphologies for nanodiamond particles that comprise this region as demonstrated above. To make the overall scheme more quantitative, all related simulations need to be done using the same computational approach (of *ab initio*) level.

### 5.3 TYPES OF NANODIAMOND AND METHODS OF THEIR SYNTHESIS

There are numerous reports on experimental observations of nanosized diamond, summarized in [3]. Reported methods of nanodiamond synthesis are very diverse, involving methods such as a

gas-phase nucleation at ambient pressure [15], chlorination of carbide material at moderate temperatures [12], HPHT graphite/nanocarbon transformation within a shock wave [31,32], and carbon condensation during explosive detonation [2].

The information on types of nanodiamonds is arranged below according to the dimensionality of the diamond constituents. We discuss systems of increasing complexity, beginning with the zero-dimensional structures in the form of isolated particles, going on to particles embedded within a matrix of another material, followed by recently synthesized exotic forms of 1-D and 2-D nanodiamond structures. Finally, three-dimensional assemblies of diamond nanocrystals grown as thin films or compacted from UNCD powder to preformed bulk shapes are reviewed.

### 5.3.1 ZERO-DIMENSIONAL NANODIAMOND STRUCTURES

We discuss below methods of synthesis of nanodiamond particles according to the characteristic sizes of the primary particles. We start with a discussion of nanocrystalline particles, followed by a discussion of UNCD, and then diamond molecules. Information on the characteristic sizes of commercially available isolated diamond particles is summarized in [Figure 5.6](#).

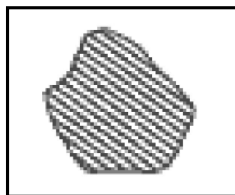
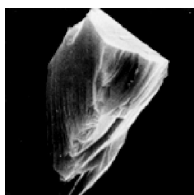
Isolated nanodiamond particles with sizes of several tens of nanometers may be monocrystalline or polycrystalline ([Figure 5.6](#)). These are obtained by processing micron-sized diamond particles, which are, in turn, a by-product of natural diamond or HPHT diamond synthesis. Synthetic diamond with sizes below 50  $\mu\text{m}$  represent the raw material for making micron and submicron diamond sizes. The processing of micron-sized diamond particles to smaller fractions includes the processes of milling, purification, and grading of the powder. Monocrystalline nanodiamond particles have rather sharp edges ([Figure 5.6](#)).

Polycrystalline nanodiamond powder ([Figure 5.6](#)) can be processed from micron-sized polycrystalline diamond particles obtained by shock synthesis [32] ([Figure 5.6](#)). Under suitable conditions, explosively produced shock waves can create high-pressure ( $\sim 140$  GPa) high-temperature conditions in confined volumes for a sufficient duration to achieve partial conversion of graphite into nanometer-sized diamond grains ( $\sim 20$  nm), which compact into micron-sized, polycrystalline particles ([Figure 5.6](#)). In order to avoid transformation of the diamond back to graphite, copper is mixed with graphite used in shock wave synthesis. This enables faster heat dissipation at the high temperatures that are reached during the explosion [5]. Polycrystalline diamond particles of micron size are more friable than monocrystalline diamond microparticles (natural or produced by HPHT), and are widely used in fine polishing applications. It is important to note that agglomerate-free suspensions of nanocrystalline diamond particles (for both mono- and polycrystalline forms) in water and oil have been developed [33]. Some recent studies have reported that low dynamic pressures up to 15 GPa are sufficient to produce diamond from ordered pyrolytic graphite (with voids between particles), using planar shock waves parallel to the basal plane of the graphite [34]. Diamond particles consisting of crystallites with grain sizes of several tens of nanometers have been observed by high-resolution electron microscopy (HREM) in postshock samples. There are several modifications of the shock wave process for diamond synthesis. Particularly, graphite (or other carbonaceous materials such as carbon black, and coal, etc.) can be loaded into explosives [35] vs. loading in a fixture, external to the explosives.

Primary particles of UNCD with characteristic sizes of about 5 nm ([Figure 5.3](#) and [Figure 5.6](#)) are obtained by the detonation of solid explosives in an inert atmosphere. This class of nanodiamond material is technologically important since detonation UNCD can be produced in bulk quantities. The product obtained in detonation synthesis, called detonation soot, contains the diamond phase, which is separated from soot by chemical treatment. More details on synthesis of UNCD particles will be provided in [Section 5.4.1](#). While it is possible to isolate the smallest UNCD particles,  $\sim 2$  to 5 nm in size ([Figure 5.3](#) and [Figure 5.6](#)), under laboratory conditions, in general, agglomeration of the particles remains one of the most serious problems in “true” nanotechnological applications. At the same time there are several very recent reports that suspensions of

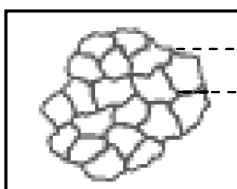
### Nanocrystalline diamond particulate

Range of smallest fraction sizes: 0–50 nm; average size: ~25 nm  
other fractions: 0–100 nm (average size 50 nm) and up



#### Monocrystalline:

Natural  
Synthetic HPHT



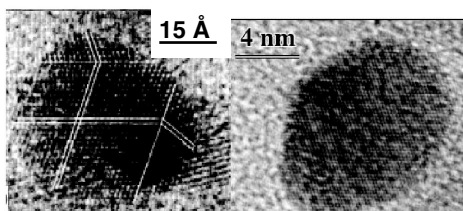
20 nm

#### Polycrystalline:

Shock wave compression of graphite (DuPont process)  
Grain size ~20 nm

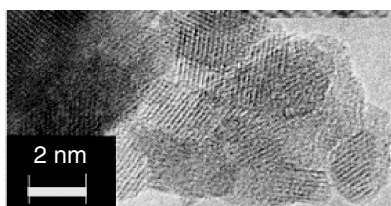
### Ultrananocrystalline diamond particulate

Range of primary particle sizes: 0–10 nm; average size: ~4–5 nm



#### Substantially monocrystalline (often with multiple twins)

Detonation synthesis  
Vapor grown  
Chlorination of carbide  
Ion irradiation of graphite  
Other methods



#### Tend to form agglomerates

Smallest sizes of agglomerates in stable suspensions obtained by practical ways are ~30–40 nm.

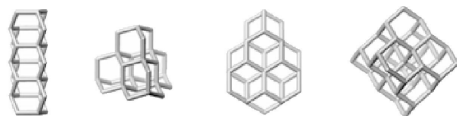


#### Polycrystalline detonation diamond

Sintering of detonation UNCD particles by detonation. Fractions: tens/hundreds of microns.

### Highest diamondoids

Hydrogenated molecules with sizes 1–2 nm



Isolated from petroleum

**FIGURE 5.6** Summary of nanodiamond particle sizes and structures. (Pictures of nanocrystalline diamond are courtesy of Microdiamant AG, Switzerland. Pictures of UNCD single particles are courtesy of T.L. Daulton, Naval Research Laboratory. Picture of polycrystalline detonation diamond is courtesy of Alit, Kiev. Examples of higher diamondoids from petroleum, 1 to 2 nm hydrogen-terminated diamond molecules (left to right): rod-shaped [1 2 1 2] pentamantane  $C_{26}H_{32}$ , pyramid-shaped [1 (2, 3) 4] pentamantane  $C_{26}H_{32}$ , irregular disc-shaped [1 2 1 3 2 1] heptamantane  $C_{30}H_{34}$ , octahedral [1 2 3 1 2 4 1 (2) 3] decamantane  $C_{35}H_{36}$ . (Graphics courtesy of Chevron Texaco Molecular Diamond Technologies, Richmond, CA.)

detonation UNCD particles of sizes ranging from ten to several tens of nanometers have been developed [10]. Another interesting particulate material obtained from UNCD of detonation origin is micron-sized polycrystalline particles. This is obtained by detonation sintering using the initial UNCD powder (Figure 5.6) [7]. Owing to its more rounded form than Myporex and monocrystalline diamond particles, this new type of diamond particulate is expected to have different niche applications [7].

Recently, a whole family of hydrogen-terminated diamond species, ~1 to ~2 nm size, has been discovered, literally filling the gap between adamantane molecules that are the smallest crystals of H-terminated cubic diamond containing only ten carbon atoms, and the wide plethora of UNCD particles with sizes more than 2 nm described above. These so-called higher diamondoids (number of crystal diamond cages more than 3) extracted from petroleum, are diamond molecules that are nanometer-sized rods, helices, discs, pyramids, etc. [36,37] (Figure 5.6). Their highly rigid, well-defined, and readily derivatizable structures make them valuable molecular building blocks for nanotechnology. Certain higher diamondoids can now be produced in gram quantities and are available through Molecular Diamond Technologies, Inc., Richmond, CA. The exact mechanisms of the formation of these higher diamondoids in petroleum is still a mystery [37]. So far it has not been possible to synthesize higher diamondoids. Higher diamondoid molecules crystallize into a variety of crystal systems [36]. For example, depending on the isomer type, crystals of pentamantane can be orthorhombic, triclinic, or monoclinic. Rod-shaped [1 2 1 2] pentamantane molecules form orthorhombic crystals (Figure 5.7), in which they are aligned parallel to their long axis, perpendicular to their diamond (1 1 0) lattice faces [37].

In the above section different classes of commercially available nanodiamond particles were discussed. In the following section we will provide a brief overview of nanodiamond particles synthesized at the laboratory scale. In order to systemize the currently known methods of nanodiamond synthesis, a tentative scheme is suggested in Figure 5.8.

While a particular class of commercial nanodiamonds is obtained as a by-product of HPHT synthesis, there are laboratory studies of HPHT conversion of exotic carbon forms to nanodiamond. The HPHT process requires approximately 6 GPa pressure and 1500°C to convert graphite powder into diamond in the presence of a catalyst. Synthesis of diamonds starting from exotic precursor materials such as fullerenes [38] as well as carbon nanotubes [39] takes place at much

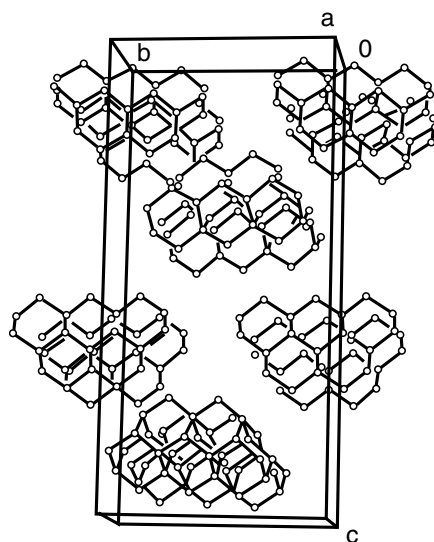


**FIGURE 5.7** Higher diamondoids are diamond molecules that can be isolated in high purity and crystallized. Illustrated is the unit cell of [1 2 1 2] pentamantane determined by x-ray crystallography on a single orthorhombic crystal (space group  $P2_12_12_1$ ). (Graphics courtesy of Chevron Texaco Molecular Diamond Technologies, Richmond, CA.)

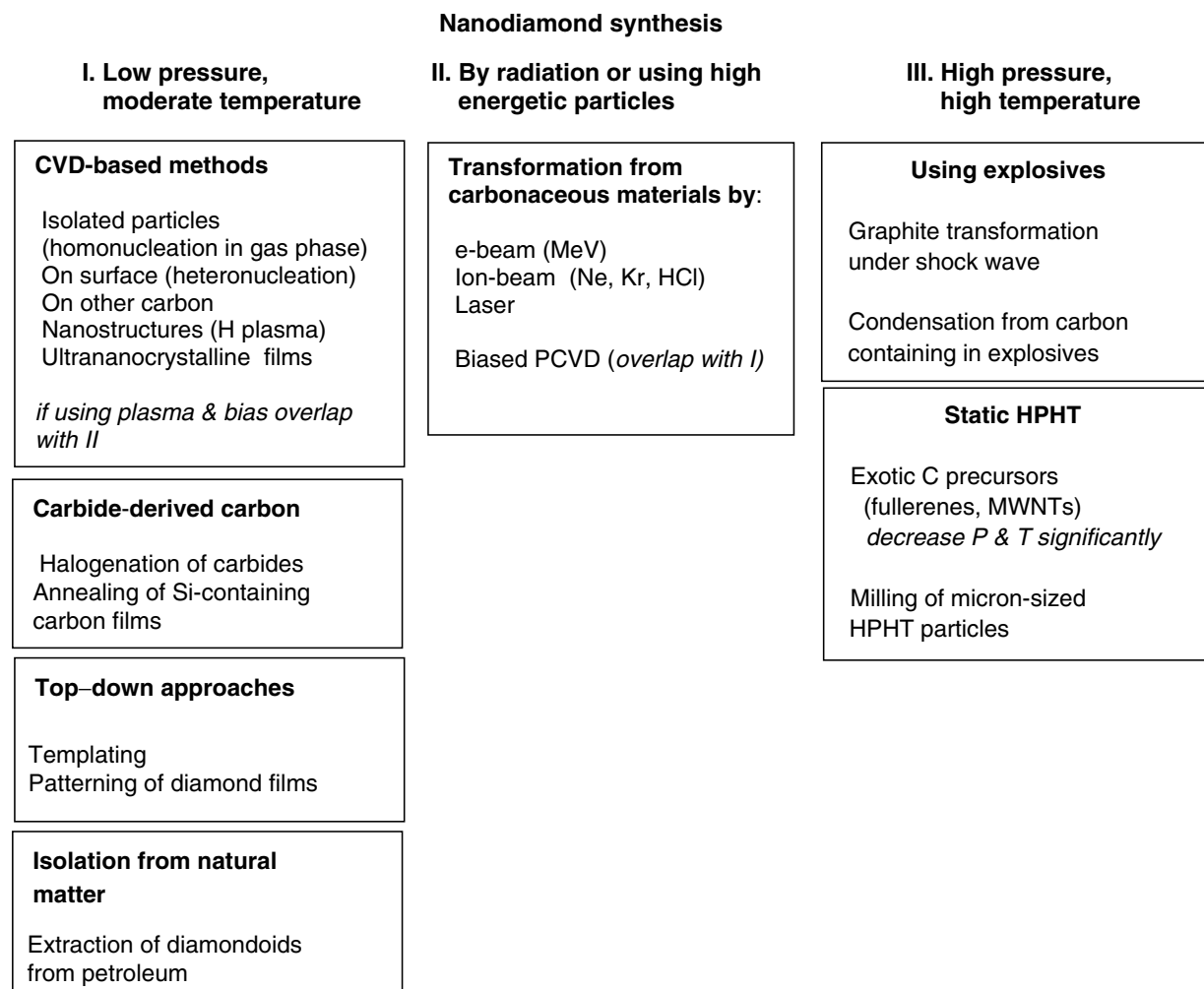


**FIGURE 5.8** Tentative scheme summarizing methods of synthesis of diamond nanostructures.

lower temperatures and externally applied pressures as compared to graphite. For example, the transformation of buckyballs to diamond at high static pressure can be performed at room temperature and does not require a catalyst [38]. Another group of authors reported conversion of fullerenes into diamond under “moderate” conditions of 5.0 to 5.5 GPa and 1400°C [40]. Carbon nanotubes have been converted to diamond at 4.5 GPa and 1300°C using NiMnCo catalyst [39]. On the basis of HRTEM observations, the authors suggest that under HPHT conditions the tubular structures collapse and broken graphitic shells curl up and close into spheroidal networks to eliminate the dangling bonds at the edges. The high curvature of the nested graphitic shells formed, and cross-links between the layers in the onion-like structures that are formed, lead to an increased fraction of  $sp^3$  bonds, which facilitates the formation of diamond.

We discuss below methods of nanodiamond synthesis based upon the CVD technique as well as methods using radiation and high energetic particles. Frenklach and coworkers [42] studied nucleation and growth of nanodiamond powder directly from the vapor phase in a substrate-free, low-pressure, microwave-plasma CVD reactor. The particles were collected downstream of the reaction zone on a filter within the tubular flow reactor, and subjected to wet oxidation to remove nondiamond carbon. Homogeneous diamond nucleation took place when dichloromethane–oxygen and trichloroethylene–oxygen mixture were used as source material. The particles formed had crystalline shapes with an average particle size around 50 nm. A mixture of diamond polytypes was observed in the powder.

Frenklach et al. [15] also studied the effects of heteroatom addition on the nucleation of solid carbon in a low-pressure plasma reactor. The addition of diborane ( $B_2H_6$ ) resulted in substantial production of diamond particles, 5 to 450 nm in diameter, under the same conditions that show no diamond formation without the presence of diborane. The yield of oxidation-resistant powder produced in boron-containing mixtures was observed to be as high as 1.3 mg/h. It was found that nanodiamonds in the CVD residue have an abundance of linear twins and star-twin microstructures consistent with radial (isotropic) gas-phase growth conditions. Studies of diamond nucleation directly from an activated gas phase have important implications in revealing mechanisms of interstellar dust formation.

Another example of homogeneous diamond nucleation in the gas phase is laser-induced decomposition of  $C_2H_4$  at low pressures and temperatures [43], which results in diamond powder formation with grain diameters of 6 nm to 18  $\mu m$ . According to Buerki and Leutwyler [43], high-purity, homogeneously nucleated diamond nanoparticles had spherical and faceted morphology.

Another group of methods of nanodiamond formation include direct transformation of carbon solids to nanodiamond. Recent experiments have shown that heavy ion or electron irradiation induces nucleation of diamond crystallites inside concentric nested carbon fullerenes [14,44]. High-energy electron irradiation (1.2 MeV,  $>10^{24}$  e/cm<sup>2</sup>;  $\sim 100$  dPa) was successfully used to convert the cores of concentric-shell graphitic onions into nanometer-size diamonds at irradiation temperatures above 900 K [14]. These experiments were performed *in situ* in an electron microscope, which allowed continuous observation of the formation process. A strong compression in the interior of the onion was inferred by the reduction observed in the spacing between adjacent concentric shells during irradiation. Ion beam irradiation of carbon solids also resulted in the formation of nanodiamond [44]. Irradiation with  $Ne^+$  (3 MeV,  $4 \times 10^{19}$  cm<sup>-2</sup>;  $\sim 600$  dPa) at temperatures between 700 and 1100°C converted graphitic carbon soot into nanometer-size diamonds [44]. Again the diamonds were found to nucleate in the cores of graphitic onions that developed under irradiation. The increased diamond yield through this process as compared to e-beam irradiation is explained by the higher displacement cross section, the higher energy transfer, and the higher total beam current on the specimen. Other carbon materials can also be transformed to nanodiamond by using laser pulses, MeV electron, or ion beams. Nanodiamond particles have been synthesized from fine particles of carbon black exposed to intense laser irradiation [45]. Similarly, the transformation from carbon nanotubes to carbon onions and then to nanodiamond as a result of laser irradiation has been reported in [46]. Nanodiamond nucleation inside graphite occurs under ion irradiation at ambient temperature, when implanted with  $Kr^+$  ions (350 MeV,  $6 \times 10^{12}$  cm<sup>-2</sup>) [13]. The residue of the ion-irradiated graphite was found to contain nanodiamonds with an average diameter of 7.5 nm. Another example of nanodiamond formation includes irradiation of highly oriented pyrolytic graphite surfaces using a highly charged ion (HCl) [47]. In [41], multiwalled carbon nanotubes (MWCNT) were heated in a diamond anvil cell by a laser, above 17 GPa and 2500 K. The recovered product comprised of nanosized octahedral crystals (diamond) of less than 50 nm. The tubular structure completely changed to granular, and grain sizes corresponded to the diameter of nanotubes. The grain size of the diamond suggests that the transformation took place by direct conversion of nanotubes. This might provide a means to control diamond size by the choice of the multiwall (carbon) nanotubes (MWNT) size.

In contrast to the above works, transformation of spherical carbon onions to diamond by low-temperature heat treatment at 500°C in air without electron and ion irradiation has also been reported [48]. High-resolution transmission electron microscopy images showed that diamond particles, several tens of nanometers in diameter, co-exist with carbon onions after the heat treatment in air. From detailed HRTEM and electron energy-loss spectroscopy studies, the authors [48] suggest that  $sp^3$  sites in the onions and the presence of oxygen during the heat treatment play important roles in transformation in the absence of irradiation.

Structural phase transformation from MWCNT to nanocrystalline diamond has been recently achieved by posttreatment of 20 to 40-nm-diameter MWCNT samples in hydrogen plasma. Nanocrystalline diamond particles with diameters ranging from 5 to 30 nm were embedded in an



amorphous matrix (Figure 5.9a). It was proposed that the diamond formation and growth mechanism were a consequence of the formation of  $sp^3$ -bonded amorphous carbon clusters. As discussed by Sun et al. [49], hydrogen chemisorption on the curved graphite network and energy deposition on carbon nanotubes by continuous impingement of activated molecular or atomic hydrogen are responsible for the formation of an amorphous carbon matrix. Similar to the role of hydrogen in conventional CVD diamond growth, hydrogen plasma etching prevents graphite formation in the thermally activated processes.

Nanodiamond nucleation in amorphous carbon films also takes place via the bias-enhanced CVD method, in which the substrate is negatively biased and exposed to CVD plasma. Diamond nuclei of 5 to 10 nm in diameter have been recently observed in amorphous carbon films grown using bias-enhanced CVD [50]. The authors suggested a general model for diamond nucleation by energetic species (for example, using bias-enhanced CVD or with direct ion beam bombardment). This process involves spontaneous bulk nucleation of a diamond embryo cluster in a dense, amorphous carbon hydrogenated matrix; stabilization of the cluster by favorable boundary conditions of nucleation sites and hydrogen termination; and ion bombardment-induced growth through a preferential displacement mechanism. Formation of a dense amorphous hydrogenated carbon phase occurs via a subimplantation process, wherein energetic carbon, hydrocarbon, and hydrogen species bombard the surface and get incorporated into subsurface layers.

Finally, a new class of nanostructured carbon has been recently synthesized, in which nanodiamond particles form hybrid structures with singlewall (carbon) nanotubes (SWNTs) [51]. The deposition experiments have been carried out in a hot-filament CVD reactor equipped with an apparatus to allow the introduction of powder. The reactants were carbon powder (40 nm in diameter) and atomic H. The Si substrate was coated by submicron catalytic Fe particles that promoted initial growth of SWNTs. In the first stage of the growth sequence, aligned bundles of SWNT up to 15  $\mu\text{m}$  long were formed, followed by synthesis at the outer parts of the SWNTs, of well-shaped diamond crystallites with diameters in the 20 to 100 nm range (Figure 5.9b). Terranova et al. [51] attribute the nanodiamond nucleation and growth to the presence of an unusually high concentration of atomic H.

### 5.3.2 ONE-DIMENSIONAL NANODIAMOND STRUCTURES

First, aligned diamond whiskers were formed by a “top-down” approach by air plasma etching of polycrystalline diamond films, particularly of as-grown diamond films and films with molybdenum

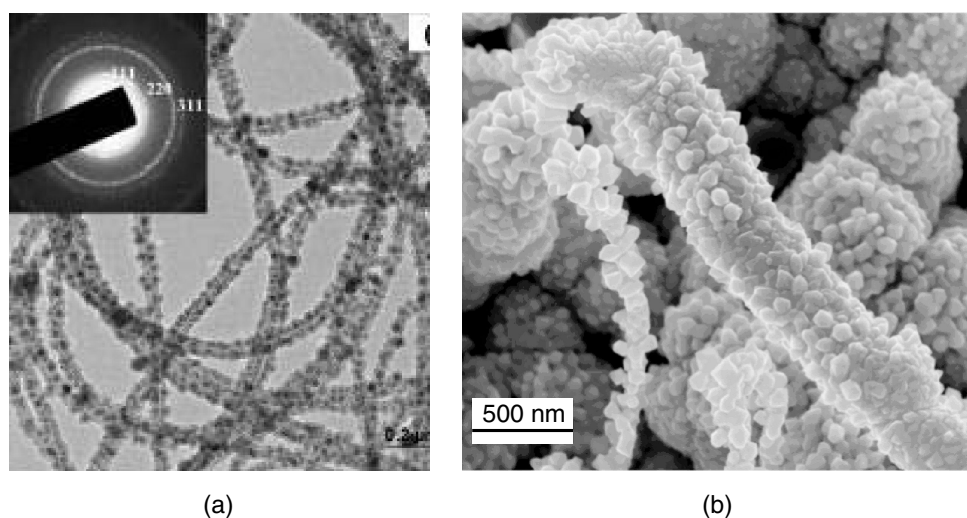


**FIGURE 5.9** (a) TEM image shows diamond crystallites embedded in amorphous carbon clusters and partial reservation of CNT hollow structure after hydrogen plasma-treated MWCNTs. (b) Nanodiamond-carbon nanotube composites grown by CVD method. (a: From Sun, L.T. et al., *Appl. Phys. Lett.*, 84, 2901, 2004; b: from Terranova, M.L. et al., *Chem. Mater.*, 17, 3214, 2005. With permission.)

deposited as an etch-resistant mask [52] (Figure 5.10). In the case of the as-grown diamond films, nanowhiskers were found to form preferentially at the grain boundaries of diamond crystals. On dry etching of diamond films with preformed Mo deposits, well-aligned whiskers of 60 nm diameter were formed uniformly over the entire film surface with a density of  $50 \mu\text{m}^{-2}$ .

Micron-diameter filaments formed by colloidal assemblies of UNCD particles have been observed in [53]. After extracting and drying, the filaments were similar to glass fibers, but no measurements of mechanical properties have been performed. Koscheev et al. [53] also succeeded in the synthesis of submicron-diameter filaments consisting of UNCD particles, obtained by laser ablation of pressed nanodiamond pellets. In contrast to dense filaments in colloids, every laser-ablated fiber is a network of nanoparticle chains (Figure 5.11). Studies of the elemental composition as well as the infrared (IR) and Raman spectra of filaments confirmed that they consist of the original nanoparticles, which still retained diamond structure. After extraction from the vacuum chamber, the whole assembly behaved like an aerogel. In both examples of UNCD-based filaments, the filament networks are rather tangled.

Polycrystalline diamond nanocylinders have been grown on anodic aluminum oxide templates using microwave plasma-assisted CVD and 50 nm nanodiamond particles as seeds [54]. Ordered 300 nm diamond nanocylinder arrays with cylinder lengths of about 5  $\mu\text{m}$  are illustrated in Figure 5.12.

Most recently, monocrystalline diamond nanorods have been fabricated by Ando et al. [55] using reactive ion etching. The HPHT synthetic single-crystal diamond substrates with (1 0 0) and (1 1 0)-oriented surfaces were etched with oxide impurities acting as micro-masks; another mask set consisted of arrays of Al dots. Fabricated arrays of DNR were 50 to 200 nm in diameter and several microns in height (Figure 5.13).

Theoretical aspects of thermodynamic stability of DNR and preferable morphologies have been investigated by Barnard [56] and are summarized in a recent review. By first principle modeling of

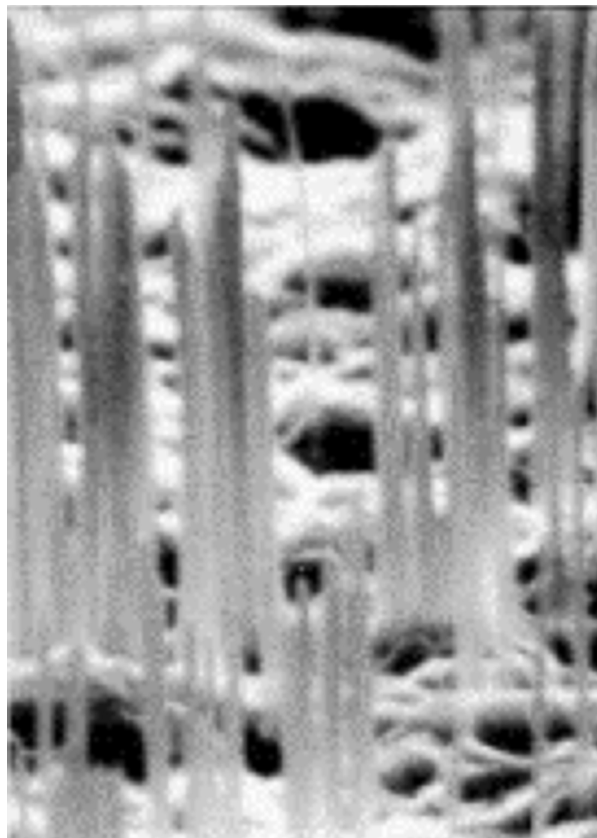


**FIGURE 5.10** Magnified SEM micrograph of diamond nanowhiskers 60 nm in diameter ( $2.5 \mu\text{m}$  across the picture). (From Baik, E.S., *Thin Solid Films*, 377, 295, 2000. With permission.)

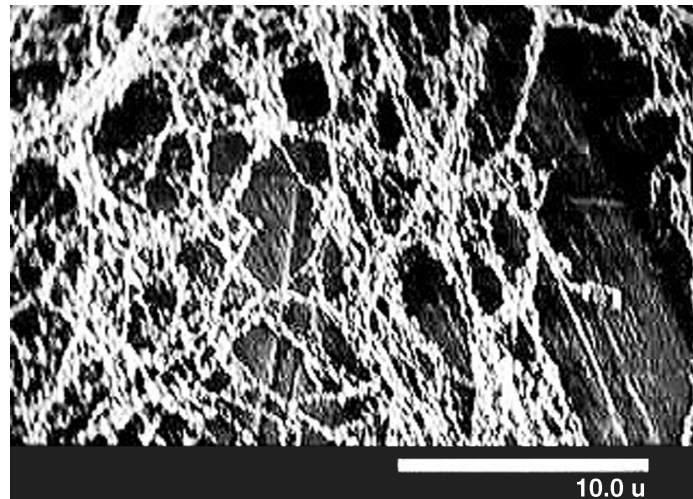


**FIGURE 5.11** Diamond filaments obtained by laser ablation of pressed UNCD particle pellets. (Image courtesy of A. Koscheev.)

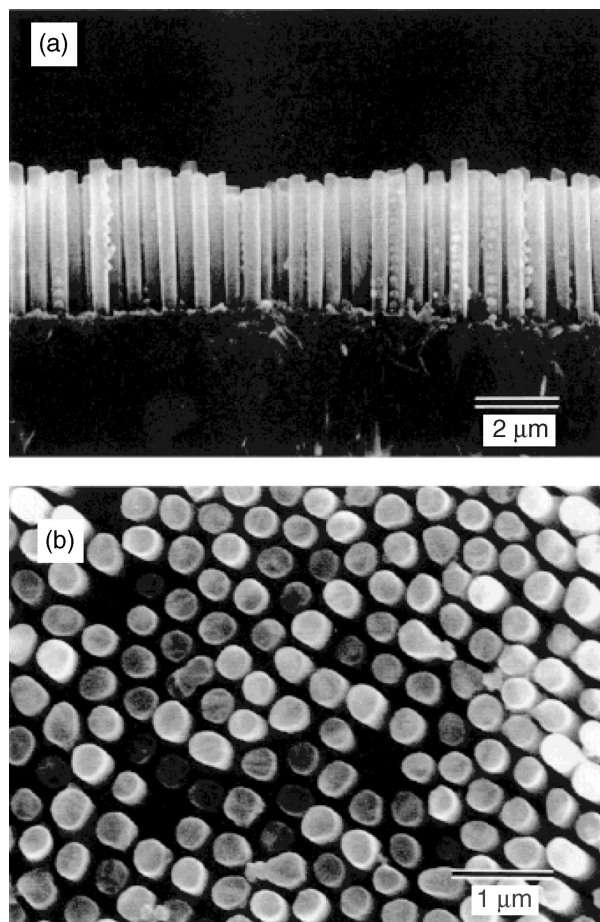


**FIGURE 5.12** SEM micrographs of nanodiamond cylindrical structure. (a) Cross-sectional view of the diamond cylinder membrane after dissolving the alumina template. (b) Top view of the cylinder membrane. (From Masuda, H. et al., *Adv. Mater.*, 13, 247, 2001. With permission.)

different DNR morphologies, the role of surface hydrogenation was emphasized for reliably obtaining DNR with structural properties analogous to bulk diamond. It was also theoretically predicted that the band gaps of DNR with diameters less than  $\sim 1.8$  nm are significantly smaller than bulk diamond [57]. According to [57], DNR may be semimetallic or semiconducting depending on the

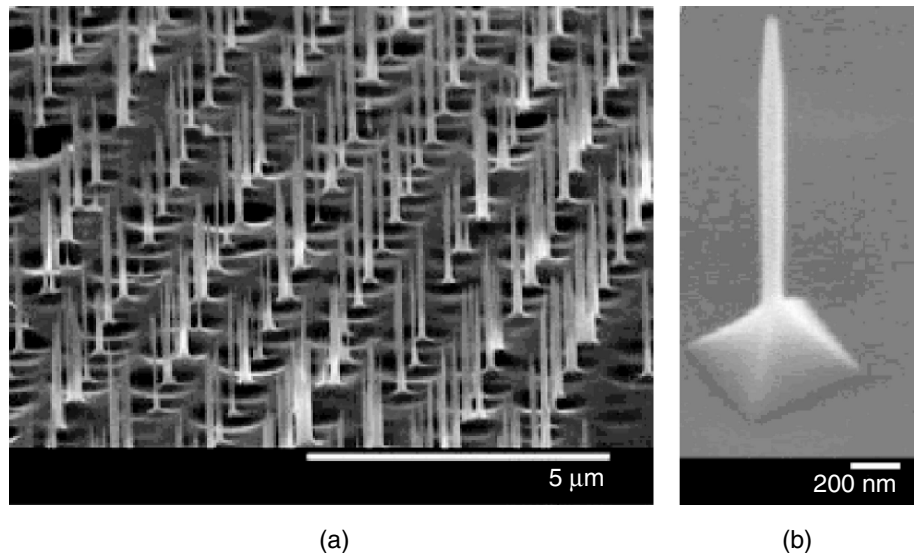


**FIGURE 5.13** SEM micrographs of (a) array of diamond rods fabricated by reactive ion etching and (b) single nanorod. (From Ando, Y. et al., *Diam. Rel. Mater.*, 13, 633, 2004. With permission.)

nanowire diameter, surface morphology, and degree of surface hydrogenation. Another theoretical prediction based on literature *ab initio* data [58] suggests that DNR would have a brittle fracture force and stiffness that exceeds that of carbon nanotubes for radii greater than  $\sim 1$  to 3 nm, depending on the orientation of DNR. In general, it becomes evident that DNR represent an important and viable target structure for synthesis.

### 5.3.3 TWO-DIMENSIONAL NANODIAMOND STRUCTURES

Single-crystalline diamond nanoplatelets have recently been grown on polycrystalline diamond substrates [59] coated with a 100-nm-thick film of nickel before deposition. Deposition was carried out at a temperature above  $1000^{\circ}\text{C}$  in a microwave plasma CVD reactor using a 3%  $\text{CH}_4/\text{H}_2$  gas mixture. Scanning electron microscope and transmission electron microscope (TEM) micrographs revealed that these nanoplatelets had regular shapes of triangles and parallelograms with well-faceted surfaces, their thickness ranging from 30 to 70 nm, and length from several hundred nanometers to a few micrometers (Figure 5.14). The edges of the platelets are along  $\langle 110 \rangle$  directions, with top and bottom surfaces parallel to  $\{111\}$  planes. The platelet morphology suggests that they are formed by lateral growth, although the influence of Ni on the formation of diamond nanoplatelets is unknown [59]. This result, in combination with the results on growth of DNR discussed above, proves that the synthesis of single-crystalline nanodiamond of desired dimensionality has become a reality.

### 5.3.4 THREE-DIMENSIONAL NANODIAMOND STRUCTURES

Three types of three-dimensional UNCD structures that are currently being commercialized are UNCD films, carbide-derived diamond-structured carbon, and bulk sintered UNCD particles of detonation origin. The synthesis and applications of the former two materials will be discussed in more detail in Sections 5.5 and 5.6, respectively.

UNCD films with 2 to 5 nm grains have been synthesized in Argon National Laboratory by Gruen and colleagues [1,60,61], using a new plasma deposition process which utilizes a high content of noble gas. Ultrananocrystalline diamond films are superior in many ways to traditional microcrystalline diamond films: they are smooth, dense, pinhole-free, and phase-pure, and can be conformally coated on a wide variety of materials and high-aspect-ratio structures.

Recently, a method for the synthesis of diamond-structured carbon has been developed by Gogotsi et al. [12]. The method is based on extracting silicon from silicon carbide or metal carbide

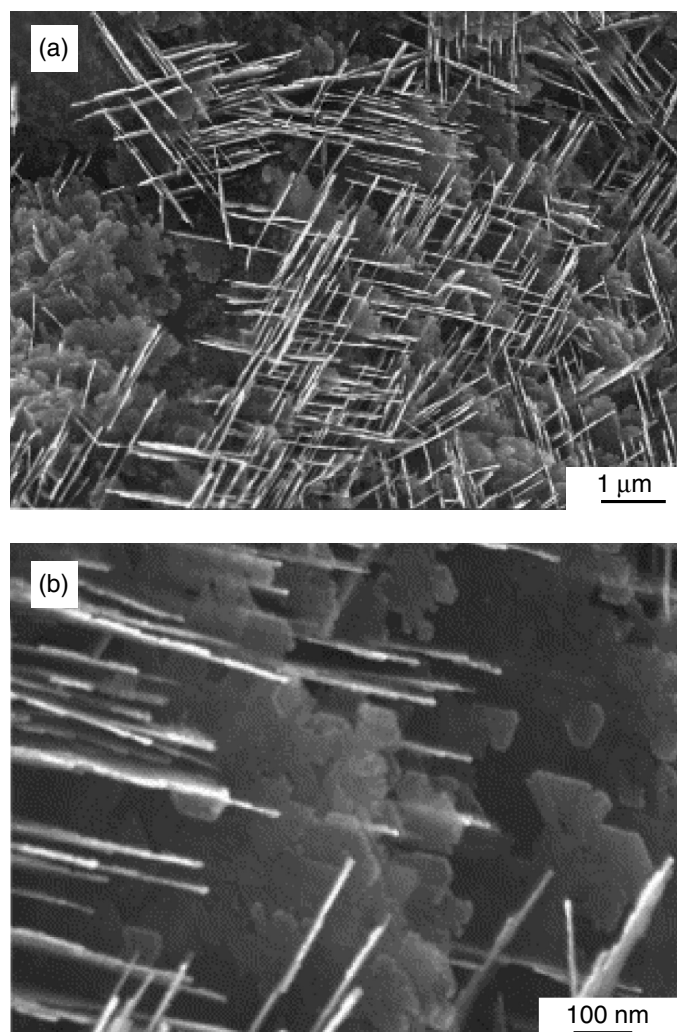


**FIGURE 5.14** SEM micrographs of diamond nanoplatelets with different magnifications. (b) demonstrates that the thickness of platelets is approximately 30 nm. (From Chen, H. and Chang, L., *Diam. Rel. Mat.*, 13, 545, 2004. With permission.)

in chlorine-containing gases at ambient pressure and temperatures not exceeding 1000°C. Nanocrystalline diamonds with an average crystallite size of 5 nm are formed after extraction of silicon or metal from the carbide. Figure 5.3b demonstrates a diamond particle with an average size of 5 nm, embedded in an amorphous matrix formed during chlorination of TiC [28]; the absolutely round particle shape is worth noting. An amorphous carbon/nanodiamond structure has been recently produced in a similar way by annealing Si-containing carbon films [62]. Carbon and silicon were simultaneously evaporated on amorphous carbon substrates at room temperature in a vacuum of  $10^{-4}$  Pa. Nanodiamond grains of 1.2 nm size were detected in the as-deposited Si-containing carbon film. Then the as-deposited films were heated at 400 to 800°C in a vacuum. At this stage, diamond grains of 5 to 30 nm size were grown depending on the annealing temperature. The growth of diamond and  $\beta$ -SiC were controllable by adjusting the heating temperature and the proportion of Si. The role of Si as a catalyst in this process was revealed; when Ge was substituted for Si, nanodiamond formation was not observed.

Another interesting bulk form of nanodiamond particles is the so-called nanodiamond composite [63], which consists of UNCD particles connected by a pyrocarbon matrix. The UNCD powder is placed in a container of a predetermined shape, and bonded together by pyrocarbon formed by means of methane decomposition through the entire volume of the diamond powder [63]. This material is characterized by a high porosity (50 to 70%) and demonstrates a relatively high Young's

modulus of 30 GPa. The reported pore size is not greater than 20 to 30 nm, with an average radius of 4.5 nm. Owing to the high density of nanopores, the material possesses a high sorption activity, particularly for large biomolecules (e.g., trypsin) [63]. The production of the material has been realized at Skeleton Technologies, Inc., Baar, Switzerland.

In summary, a rich plethora of new methods of nanodiamond synthesis have appeared within the last few years.

## 5.4 ULTRANANOCRYSTALLINE DIAMOND PARTICULATE PRODUCED BY EXPLOSIVE DETONATION

### 5.4.1 SYNTHESIS AND PROPERTIES

In the method of using energy from an explosion for diamond production, diamond clusters are formed from carbon atoms contained within explosive molecules themselves, so only the explosive material is used as a precursor material. A wide variety of explosive materials can be used. A typical explosive is a mixture of TNT (2-methyl-1,3,5-trinitrobenzene) and hexogen (in the proportion 60:40) composed of C, N, O, and H with a negative oxygen balance (i.e., with the oxygen content lower than the stoichiometric value), so that “excess” carbon is present in the system. A negative oxygen balance in the system is an important condition for UNCD formation. The explosion takes place in a nonoxidizing medium (Figure 5.15) of either gas ( $N_2$ ,  $CO_2$ , Ar, or other medium that can be under pressure) or water (ice), called “dry” or “wet” synthesis respectively. The medium acts as a coolant. In order to prevent the UNCD formed in the detonation wave from transforming into graphite at the high temperature generated by the detonation, the cooling rate of the reaction products should be no less than 3000 K/min [5]. The initial shock from a detonator compresses the high-explosive material, heating it and causing chemical decomposition, thereby releasing enormous amounts of energy in a fraction of a microsecond (Figure 5.15). As the detonation wave propagates through the material it generates high temperatures (3000 to 4000 K) and high pressures (20 to 30 GPa) which correspond to the region of thermodynamic stability for diamond (Figure 5.16). During detonation, the free carbon coagulates into small clusters, which grow larger by diffusion [17,18]. The product of detonation synthesis, called

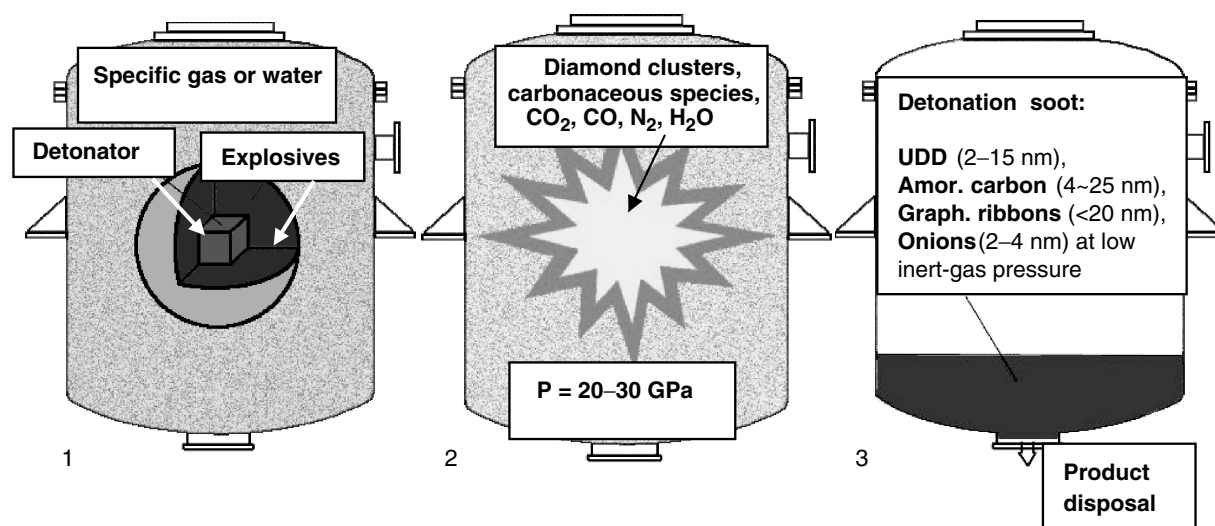


**FIGURE 5.15** Schematic illustration of steps of controlled detonation synthesis of nanodiamond from carbon-containing explosives (1). During explosion, (2) the highly dispersed carbon medium condenses from free explosive carbon in a fraction of a microsecond. After disposal, the product has to undergo several stages of purification. Big industrial detonation reactors are able to deliver tons of detonation diamond per month. (Pictures are based on pictures of the detonation process. Courtesy of PlasmaChem GmbH, Mainz, Germany.)

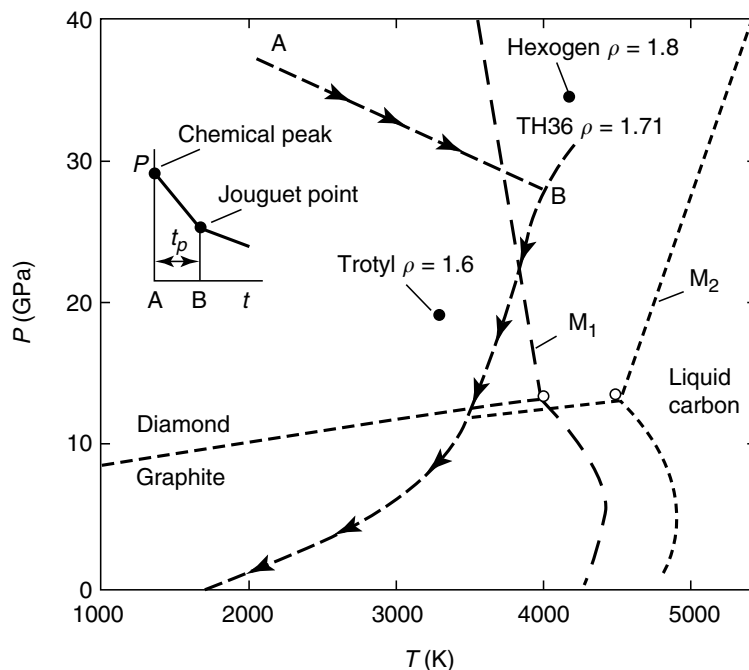


**FIGURE 5.16** Phase diagram of carbon and explosives detonation process path. The inset illustrates the pressure profile in a detonation wave: A corresponds to the shock compression of the explosives (chemical peak), AB corresponds to decomposition of explosive molecules and condensation of free carbon to UNCD at pressures higher than 20 GPa; B represents termination of decomposition (the Jouguet point), and  $t_p$  the duration of decomposition. In the diagram,  $M_1$  and  $M_2$  are possible melting lines of carbon according to Danilenko [11], and  $\rho$  is density (in  $\text{g/cm}^3$ ). (From Danilenko, V.V., *Phys. Solid State*, 46, 595, 2004. With permission.)

detonation soot or diamond blend, contains 40 to 80 wt% of the diamond phase depending on the detonation conditions. The carbon yield is 4 to 10% of the explosive weight.

In general, there are two major technical requirements for UNCD synthesis using explosives: the composition of the explosives must provide the thermodynamic conditions for diamond formation, and the composition of gas atmosphere must provide the necessary quenching rate (by appropriate thermal capacity) to prevent diamond oxidation. The diamond yield depends to a large extent on the explosive mixture [17]. The shape of the explosive also influences the yield: the ideal shape is spherical but, for convenience, a cylindrical one is regularly used [5]. The relationship between the mass of the explosives and the mass of the surrounding media also influences the yield (for example, 5 kg of explosive requires a detonation chamber of  $\sim 11 \text{ m}^3$  with gas media at ambient pressure to provide the necessary quenching rate) [5].

In addition to UNCD, the diamond blend contains graphite-like structures (35 to 45 wt%), and incombustible impurities (metals and their oxides — 1 to 5 wt%) [2]. Using x-ray diffraction and small-angle x-ray scattering, it was shown that an UNCD cluster in detonation soot has a complex structure consisting of a diamond core of about 4.3 nm in size and a shell made up of  $\text{sp}^2$ -coordinated carbon atoms [64].

UNCD purification is performed by mechanical and chemical methods. After mechanical removal of process admixtures, the diamond-carbon powder is subjected, for example, to thermal oxidation with nitric acid under pressure to separate the diamond phase [2]. In this method, metals are dissolved and nondiamond carbon is oxidized simultaneously. The diamond needs to be flushed with water after separation from the acidic media. After purification typically, powders of UNCD can be considered as a composite consisting of different forms of carbon (80 to 89%), nitrogen (2 to 3%), hydrogen (0.5 to 1.5%), oxygen (up to 10%) and an incombustible residue (0.5 to 8%) [2]. The carbon phase consists of a mix of diamond (90 to 99%) and nondiamond carbon (1 to 10%). In general, methods of UNCD purification as well as UNCD purity vary from vendor to vendor.

The impurity content of nanodiamonds produced by detonation synthesis is higher when compared with other artificial diamonds (for instance, HPHT diamonds contain no less than 96% carbon). Commercial products of purification have the following grades: a water suspension of diamond and powder obtained from suspensions by drying and grinding of UNCD. To remove non-carbon impurities, the chemically purified product is subjected in some cases to additional purification using ion-exchange and membrane technologies.

In general, UNCD production consists of detonation synthesis, chemical purification and acid washing of UNCD, product conditioning, and modification of the diamond.

The properties of UNCD particles are mainly defined by their nanometer-scale sizes (4 to 6 nm in diameter), which are in the transitional size range between macromolecules and crystalline solids. Half of all atoms in such particles are on the surface, and therefore are unavoidably bound to adsorbed atoms, molecules, and functional groups. These adsorbed atoms, which may exceed the number of atoms in the diamond particle, can strongly affect the physical and chemical properties of the particles. Different functional groups, which in principle can be attached to the diamond surface or have been detected on UNCD particles, surfaces are schematically illustrated in Figure 5.17. To minimize surface energy, the primary UNCD particles with diameters of ~4 nm form larger clusters, 20 to 30 nm in size that, in their turn, form larger weakly bound aggregates (of an order of magnitude of hundreds of nanometers).

Reviews [2–4] summarize a wide variety of experimental data on UNCD powder characterization including x-ray, electronic, electron paramagnetic resonance (EPR), nuclear magnetic resonance (NMR), IR, Raman, Auger, photoluminescent spectra, results of HRTEM as well as results of other measurements. Table 5.1 shows selected properties of UNCD particulates. Note that these are collective properties of UNCD powders. Below in this section, we provide results related to the fundamental studies of electrical and electronic properties of UNCD particulates. Properties of detonation nanodiamonds related to practical aspects (e.g., purity of UNCD produced by different vendors, dispersivity, stability in suspensions, maximum concentration in stable suspensions, and controlled surface functionalization) can be found in [2,6,10,65].

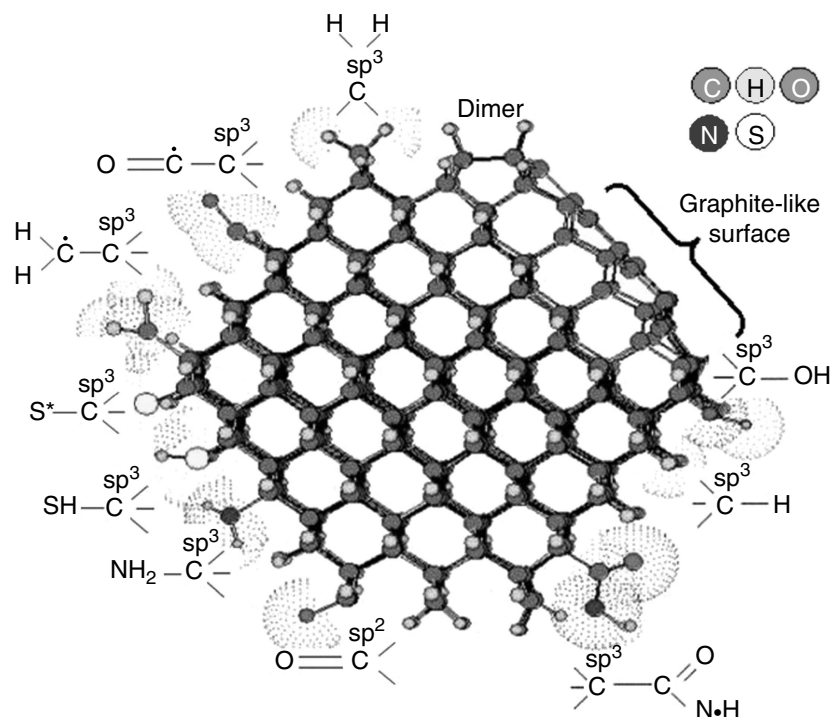


**FIGURE 5.17** Schematic illustration of different functional groups on surface of UNCD particle detected after different purification/surface modification treatments. One of the facets corresponds to a buckydiamond structure. (Courtesy of O. Shenderova, I.V. Shugalei, and Y.V. Dolmatov.)



**TABLE 5.1**  
**Selected Properties of Ultradispersed Diamond Based on Refs. [2,10,63]**

Structure	Cubic ( $a = 0.3573 \pm 0.0005$ nm)
Density	3.30 g/cm <sup>3</sup>
Crystal lattice parameter	0.3562 $\pm$ 0.0004 nm
Size of crystallites	2–10 nm
Average monocrystal size	4.3 nm
Size of smallest aggregates	20–50 nm
Specific surface area	300–400 m <sup>2</sup> /g
Pore volume in powder	0.3–1 sm <sup>3</sup> /g
Density of dislocations	$1.8 \times 10^{17}$
Composition (at%)	C (90–100); O, N, H (0–10)
Incombustible impurities (wt%)	0.2–1.4 (Fe, Cr, Si, Al, Na, Cu, Ca, Mg, Mn, Ti)
Raman frequencies	1321–1322 cm <sup>-1</sup>
Initial air oxidation temperature (depends on purity)	430°C
Initial vacuum graphitization temperature	1100–1200°C
Resistivity	$7.7 \times 10^9$ $\Omega$ m
Electrophoretic surface charge	–78.44 mV
Refractive index	~2.55 (at $\lambda = 580$ nm)

The surface and electronic properties of nanometer-sized diamond particles have been studied by x-ray photoelectron spectroscopy (XPS) and UV photoelectron spectroscopy (UPS) [66]. In these experiments, nanodiamonds (NdO from Table 5.2) were deposited on Si(100) substrates by electrophoresis. According to XPS analysis, the UNCD powder did not contain any detectable impurities except nitrogen. The N content was estimated to be 1 to 2 at%. The as-deposited UNCD powder films showed a strong oxygen peak. After treatment in a hydrogen microwave plasma and transfer in air to the XPS system, the nanodiamond films were found to be almost free from oxygen contamination. HeI ( $h\nu = 21.2$  eV) and HeII ( $h\nu = 40.8$  eV) UPS measurements have been performed on as-deposited and hydrogen plasma-treated nanodiamond films. The emission width of the as-deposited sample was 15.0 eV with a low-energy cutoff at 3.1 eV, which results in a positive value of electron affinity of +0.7 eV, assuming the band gap is  $E_g = 5.5$  eV. After H<sub>2</sub> plasma treatment, the samples showed an emission width of 15.9 eV with a very sharp, low-energy cutoff at 2.1 eV, indicating a negative electron affinity of –0.2 eV.

Some measurements of collective electrical characteristics of powders and suspensions are given in Table 5.1. Gordeev et al. [67] reported a resistivity for bulk nanodiamond composites obtained by pressing UNCD powders. The room-temperature resistivity of such UNCD composites was  $1.2 \times 10^9$  W m, consistent with the resistivity reported by Dolmatov [2] (Table 5.1).

Belobrov et al. [68] reported results of studies on UNCD powders of different surface modifications by electron paramagnetic resonance and NMR [68]. They found that the nanodiamond EPR signal is independent of the chemical modification of the nanodiamond surface. The  $g$ -factor for UNCD was found to be 2.0027(5) [68]. Hence they concluded that the paramagnetic properties of nanodiamonds are determined only by the sp<sup>3</sup> core of the diamond particle. Analyzing <sup>13</sup>C-NMR spectrum for nanodiamonds, the authors [68] concluded that the resonance line is asymmetric and well decomposed into two Gaussian components. The authors interpreted the narrow line with  $\delta = 35.1$  ppm as relating to diamond carbon, and the wide line with  $\delta = 34.2$  ppm as being caused by distortion of the tetrahedral coordination. The authors [68] concluded that only 30% of bonds in nanodiamonds are nondistorted sp<sup>3</sup> bonds; 70% of carbon bonds are distorted and these distorted bonds also have sp<sup>3</sup> hybridization. For comparison, natural jewel-quality diamonds have a characteristic chemical shift  $\delta = 50$  ppm.

**TABLE 5.2**  
**Properties of Three Types of Detonation Nanodiamond Particles Produced at Russian Federal Research Center, All-Union Research Institute of Technical Physics, Snezhinsk, Russia, and Field Electron Emission Parameters of Corresponding Nanodiamond Coatings**

Nanodiamond Type	Nd	NdP1	NdO
Description	Standard (chromic acid purification)	Nd with additional acid and high-temperature treatment; “bottom” fraction	NdP1 with additional ozone treatment
Impurities	O, N, H ~8–10%	O, N, H ~2–4%	N, O ~6%
pH of 10% water suspension	5.6–6.2	3.5–4.5	1.6–2.0
<i>Field electron emission parameters</i>			
Change in field emission threshold, compared to bare Si field emitter (%)	–15	–25	–15
Change in normalized integral transconductance compared to bare Si field emitter (%)	–37	–30	+33

Zhirnov et al. [69,70] characterized UNCD particles using field electron emission measurements by depositing small amounts (0.2  $\mu\text{m}$  in thickness) of UNCD on metal or silicon tips by electrophoresis. In these experiments, the field emission characteristics of tips with UNCD coatings were compared with characteristics of bare tips. The emission experiments showed that the emission characteristics differ significantly for different UNCD coating conditions. The different UNCD coating conditions were obtained from one original UNCD powder (marked as Nd in Table 5.2) using different physical and chemical treatments. The modifications differed in concentration of impurities, pH of water suspension, and density as shown in Table 5.2. Table 5.2 also contains a summary of emission characteristics for different UNCD coatings. It can be seen from Table 5.2 that all three types of nanodiamond coatings showed improvement in field emission threshold. Additional hydrogen plasma treatment was used to modify the surface properties of emitters with NdO and NdP1. Figures 5.18a and b show emission characteristics before and after the plasma treatment. As can be seen, the effect of hydrogen plasma treatment is very different for the two types of nanodiamond particles. The in-depth discussion of the possible influence of different surface groups on field emission properties of nanodiamond particles is given in [71]. In general, it is concluded that nanodiamonds purified by ozone treatment followed by hydrogen plasma modification are most promising for field emission applications.

The smallest amount of diamond matter, which can be prepared and studied in isolation, are primary particles of UNCD. Recently Tyler et al. [29] reported a new technique for isolating individual nanodiamond particles by depositing them on sharp (radius of 10 to 50 nm) metal tips by pulsed electrophoresis of alcohol suspensions of UNCD. Apparently, a very high electric field near the sharp tip breaks the agglomerates, and thus it is possible to manipulate individual nanodiamond particles. The typical size of diamond nanoparticles as measured in TEM was about 3 nm (Figure 5.3c). It should be noted that in all cases, only particles with faceted shape were observed.

Results of field emission characterization of UNCD reveal a considerable difference in emission behavior of single isolated diamond nanoparticles and multiparticle nanodiamond thin films [29]. A substantial increase (~30%) in threshold voltage was observed for a tip capped with a single isolated diamond nanoparticle, in comparison with the bare Mo tip (Figure 5.18c). The  $I$ - $V$  curves also exhibited non-Fowler–Nordheim behavior. However, after the additional deposition of nanodiamond and the formation of a thicker nanodiamond film (~20 nm), a drastic decrease in

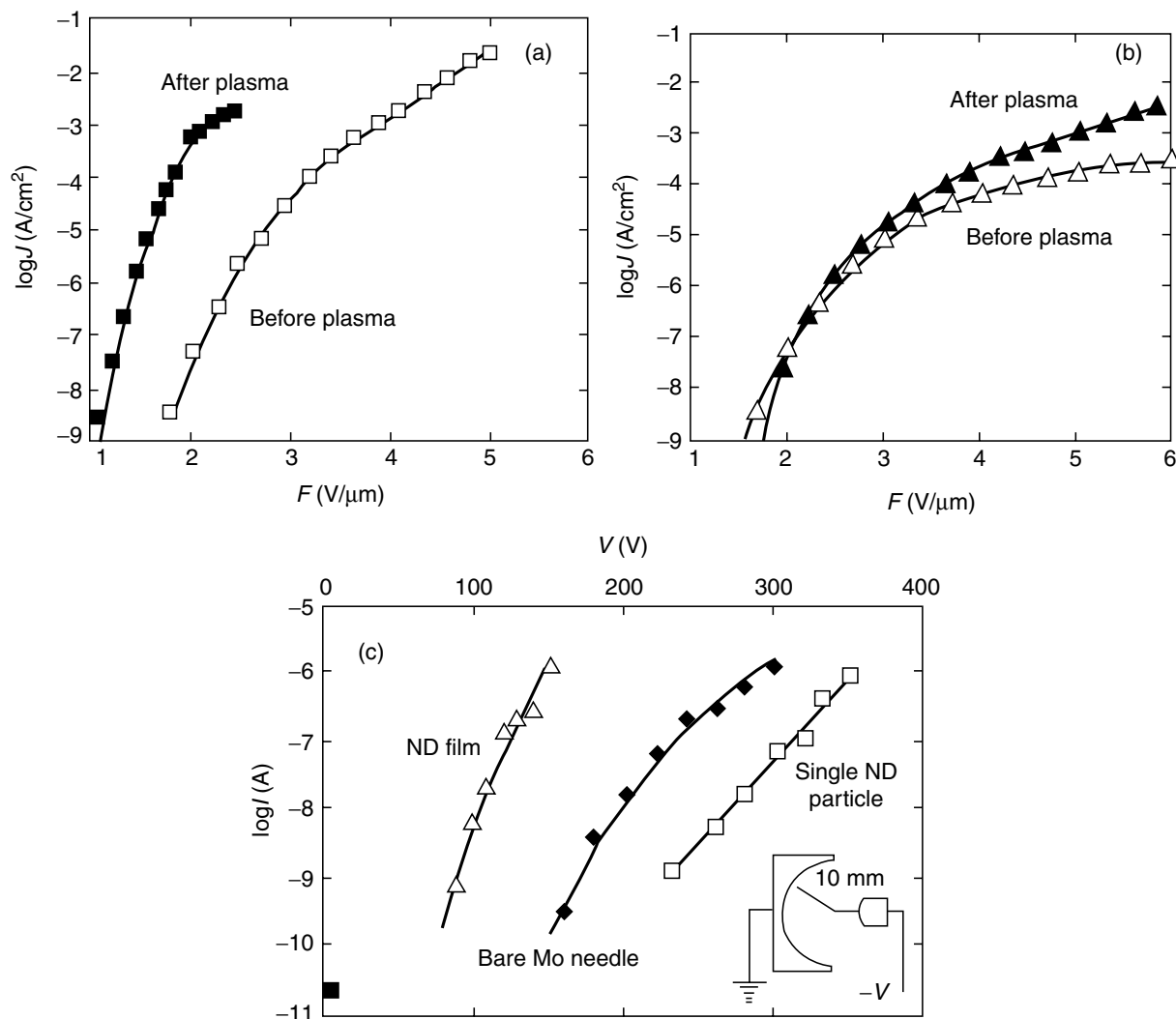


**FIGURE 5.18** Field emission characteristics of detonation nanodiamond: hydrogen plasma effect on coatings of NdO (a) and NdP1 (b); for an isolated nanodiamond particle and a nanodiamond film, compared to a bare tip (c). Inset in (c): schematic of experimental set-up. (From Zhirnov V.V. et al., *Phys. Solid State*, 46, 641, 2004. With permission.)

threshold voltage (~48%) and an increase in transconductance (~115%) were observed – characteristics typical of nanodiamond coated tips. The emission suppression in a structure with a single UNCD particle can be explained on the basis of triple junction effect [72], due to the local suppression of electric field at the metal–dielectric–vacuum boundary. Obviously, there are no triple junction interfaces in coatings containing more than one monolayer of particles.

Very interesting transformations between carbon forms at the nanoscale were discovered in the mid-1990s. Upon annealing at temperatures between 1300 and 1800 K, nanodiamond particles transform to carbon onions with a transformation temperature that depends upon the particle size [73]. X-ray diffraction data show graphitic phase formation at  $T > 1200$  K [74]. The diamond–graphite phase transition temperature observed in UNCD ( $T_{pt} > 1200$  K) is considerably lower than the phase transition temperature of bulk single-crystal diamonds ( $T_{pt} > 1900$  K).

In summary, detonation nanodiamond particles have been investigated in great detail after their invention 40 years ago. In most cases, it was collective properties of UNCD powders that have been investigated; only very recently have nanodiamond particles been isolated and their structural, compositional, and electronic properties begun to be studied. Among the current active areas of research, the most important one from the practical point of view is developing an understanding of the relationships

between the surface chemistry of the particles, and conditions needed to maintain stable colloidal suspensions of nanodiamonds of ultrahigh dispersivity (particle sizes of 5 to 30 nm).

#### 5.4.2 APPLICATIONS OF ULTRANANOCRYSTALLINE DIAMOND PARTICULATE

Applications of UNCD particles of detonation origin can be categorized as *traditional* — those on which work has been going on for the last couple of decades; and *novel* — those on which work has started only recently owing to advances in nanotechnology throughout the world. Within the novel applications, *biological* applications should be considered separately due to their high specificity. Biological applications of detonation UNCD will be discussed in Section 5.7. Technological applications of UNCD particles have been summarized in [2–7,65]; review [4] particularly provides an extensive discussion of biological applications of UNCD particulates. The bibliographic index [9] contains references on categorized nanodiamond applications.

Traditional UNCD particulate applications include metal–diamond galvanic coatings, polishing pastes and suspensions, polymer composites, lubricating oils, greases, and lubricant coolants.

Electrochemical deposition of UNCD together with metals, using standard galvanic equipment, has been demonstrated to be useful in a variety of applications for coatings of components of transportation units, tools for electronics, electrical engineering, medicine, watches, and the jewelry industry [2,6]. The advantages of adding UNCD to galvanic coatings include increase in wear resistance (2 to 13 times depending on metal); microhardness (may be up to 2 times depending on the metal); an increase in corrosion resistance (2 to 6 times depending on the metal); decrease in porosity (pores can be completely eliminated depending on the metal); significant decrease of friction coefficient; considerable improvement of adhesion and cohesion; and high throwing power of the electrolyte. According to [2,6], the service life of products is increased 2 to 10 times, even when coating thicknesses are decreased by a factor of 2 to 3. The strengthening effect is observed in coatings of many metals, including silver, gold, and platinum, which are employed in electronic applications. Particularly, UNCD is most widely used in strengthening chromium coatings deposited using an electrolytic process. In this process, UNCD-containing additives are added to the chrome-plating electrolyte without any modification of the standard production line. Such coatings increase the operating life of molds, high-precision bearing surfaces and other similar components by a few times [6]. The UNCD content in a metal coating averages 0.3 to 0.5 wt%. The amount of UNCD consumed for a metal layer of 1 mm thickness is 0.2 g (1 carat)/m<sup>2</sup>.

UNCD particles are being used for finishing precision polished materials for electronics, radio engineering, optics, medical, and jewelry industries [2]. The compositions with UNCD allow one to obtain a surface of complex geometrical form, with a relief height roughness of 2 to 8 nm. Recently, 4 Å roughness has been achieved for polished Al<sub>2</sub>O<sub>3</sub>, and SiC surfaces using UNCD suspensions (according to the Alit, Inc., Kiev, Ukraine). UNCD is employed in polishing compositions used for the final treatment of silicon wafers in the microelectronics industry. UNCD has also been used in the electronics industry as a component of heat-removal pastes, and compounds for chip packaging, replacing the highly toxic beryllium oxide that has been traditionally used. The amount of UNCD consumed for this application is 1 to 10 g/m<sup>2</sup>.

The addition of UNCD to polymers provides an increase in their mechanical strength, wear-resistance, and heat-aging resistance [2,6]. According to [2], highly effective coatings based on the incorporation of UNCD into fluoroelastomers and polysiloxanes have been developed; the elastic strength of rubbers based on polyisoprene, butadiene–styrene, butadiene–nitrile, and natural rubbers has been considerably improved. For example, for fluoroelastomers filled with UNCD particles, the tensile modulus at 100% elongation and the conditional rupture strength increased more than tenfold (from 8.5 to 92 MPa and from 15.7 to 173 MPa, respectively). In this case, the elongation increased by a factor of 1.6 (from 280 to 480%). An increase in cross-linking is one of the mechanisms to which the influence of UNCD particles on the strength properties of polymer composites has been attributed [2]. According to [2], addition of UNCD into rubbers decreases attrition wear

by an average of 3 to 5 times, increases rupture strength by 30%, and breaking temperature by 15%. Epoxy adhesives, which incorporate UNCD, have high adhesion and cohesion properties. The specific consumption of UNCD or diamond blend (mix containing UNCD and significant percent of other carbon-based products of detonation explosion) is 1 to 5 kg/1000 kg of rubber (polymer) and 1 to 5 kg/1000 m<sup>2</sup> of polymer coating or film.

The addition of UNCD and diamond blend to oils allows one to obtain sedimentation-stable and environmentally safe systems with particle sizes of less than 0.5 μm [2]. According to [2], the use of nanodiamonds in oils increases the service life of motors and transmissions, reduces friction torque by 20 to 40%, and decreases wear of rubbed surfaces by 30 to 40%. Recently, UNCD particulates have been examined for thermal conductivity enhancement of dielectric oils [75]. It was demonstrated that dispersion of nanodiamonds (1 wt%) in oil (XO-class) can increase the overall thermal conductivity of cooling oils; those, e.g., for use in power transformers by over 25% [75]. The specific consumption of UNCD or diamond blend in oils is 0.01 to 0.2 kg/1000 kg of oil [2].

Novel UNCD niche applications developed recently [10,65] include UNCD for systems of magnetic recording, as adsorbents of a new type, as components in the production of diamond ceramics and molds made of diamond-containing materials, as coatings in field emission devices, in heterogeneous and electrochemical catalysis, and in proton-conducting nanocomposite membranes in fuel cells applications. UNCDs have also been employed for seeding substrates used in the CVD growth of diamond films. Dry UNCD is known to absorb and retain water in amounts that are four times the weight of the UNCD. This allows its use as an inert solid water absorber in materials like magnetic carriers, whose quality is determined by the residual water content.

In systems of magnetic recording, UNCD is used as an antifriction additive and as a physical modifier for ferro-lacquer coating of magnetic tapes and disks, and also as an additive to solutions for electrochemical deposition of composite magneto-recording tapes to improve the properties of magnetic recording devices [76]. The addition of UNCD decreases ferro-magnetic grain size, thus allowing an increase in recording density while reducing abrasive wear and friction coefficient.

Carbon-containing adsorbents are widely used in various industries such as medicine and pharmacology. The most abundant of them are activated coals and graphitized thermal carbon black. Synthetic diamonds, particularly submicron diamond composites as well as sintered UNCDs, represent a new class of carbon-containing adsorbents [77], characterized by chemical inertness and high strength. Another beneficial effect is the possibility of using the adsorbent repeatedly, by modifying and recovering the diamond surface.

A very interesting application of nanodiamonds for advanced information processing is the generation of light sources that are able to emit individual photons on demand. While nanodiamond particles of nondetonation origin have been reported by Beveratos et al. [78,79], nothing prevents the use of nanodiamond of different origins in this application. Beveratos et al. investigated the quantum properties of the light emitted by diamond nanocrystals containing a single nitrogen-vacancy color center [78]. The typical size of diamond particles used in these experiments was 40 nm. According to the authors, there are several very important optical properties of diamond nanocrystals, which contribute to their usefulness as individual photon light sources. First, the sub-wavelength size of these nanocrystals renders refraction irrelevant. A nanocrystal can be regarded as a point light source. Second, the very small volume of diamond excited by the pump light yields very small background light. This is very important for single-photon sources. By exciting nanodiamond crystals using a YAG laser ( $\lambda = 532$  nm), the authors were able to observe fluorescence with almost background-free photon antibunching from single nitrogen-vacancy centers in diamond nanocrystals at room temperature. The excited state lifetime in the bulk is  $t_b = 11.6$  ns. The measured lifetime in the nanocrystals was 25 ns. The authors argue that this lifetime modification is a quantum electrodynamic effect. In a later paper by Beveratos et al. [78], a full implementation of a quantum cryptography protocol using a stream of single photon pulses generated by a stable and efficient source operating at room temperature has been reported. The quantum bit error rate was less than 4.6% and the secure bit rate was 7700 bits/sec. The overall performances of the system

were reported to be at a stage where single photons have a measurable advantage over an equivalent system based on attenuated light pulses.

In summary, there is striking evidence that niche applications for nanodiamonds, particularly nanodiamonds of detonation origin which are a commercial product, are expanding significantly. A big advantage of nanodiamonds of detonation origin is their affordability due to low cost, and the well-developed infrastructure for the scale-up production.

## 5.5 ULTRANANOCRYSTALLINE DIAMOND FILMS PRODUCED BY CHEMICAL VAPOR DEPOSITION

Ultrananocrystalline diamond films with 2 to 5 nm grains (both H-containing and H-free) have been recently synthesized in the Argonne National Laboratory, Illinois, USA, by Gruen and colleagues [1,60,69,79], using a microwave plasma-assisted chemical vapor deposition process. The UNCD thin films were synthesized using argon-rich plasmas instead of the hydrogen-rich plasmas normally used to deposit microcrystalline diamond. By adjusting the noble gas:hydrogen ratio in the gas mixture, a continuous transition from micro- to nanocrystallinity was achieved. The controlled, continuous transition from the micro- to nanoscale is a unique feature of the method [1].

The use of small amounts of carbon-containing source gases ( $C_{60}$ ,  $CH_4$ ,  $C_2H_2$ ) along with argon leads to the formation of  $C_2$ -dimers, which is the growth species for all UNCD thin films. The nanocrystallinity is the result of a new growth and nucleation mechanism, which involves the insertion of  $C_2$  into the  $\pi$  bonds of the nonhydrogenated reconstructed (1 0 0) surface of diamond. Then, unattached carbon atoms react with other  $C_2$  molecules from the gas phase to nucleate new diamond crystallites [1,80]. This results in an extremely high, heterogeneous nucleation rate ( $10^{10} \text{ cm}^{-2}\text{sec}^{-1}$ , which is  $10^6$  times higher than from conventional  $CH_4/H_2$  plasmas). The UNCD grown from  $C_2$  precursors consists of ultrasmall (2 to 5 nm) grains and atomically sharp grain boundaries. Up to 10% of the total carbon in the nanocrystalline films is located within the 2 to 4 atom-wide grain boundaries. Because the grain boundary carbon is  $\pi$  bonded, the mechanical, electrical, and optical properties of nanocrystalline diamond particles are profoundly altered. More subtle control of the properties of UNCD films can be accomplished via the addition of supplementary gases to the plasma ( $N_2$ ,  $H_2$ ,  $B_2H_6$ ,  $PH_3$ ) and changes in the growth conditions (biasing, power). For instance, the addition of hydrogen leads to highly insulating films with large columnar grains. Adding nitrogen leads to the formation of CN in addition to  $C_2$  in the plasma. The presence of CN results in decreased renucleation rates during growth, which leads to larger grains and grain boundary widths.

Ultrananocrystalline diamond films are superior in many ways to traditional microcrystalline diamond films: they are smooth, dense, pinhole free, and phase-pure, and can be conformally coated on a wide variety of materials and high-aspect-ratio structures [1]. The set of unique properties include mechanical (high hardness  $\sim 100$  GPa, and Young's modulus  $\sim 960$  GPa), tribological (extremely low friction  $\sim 0.01$ ), transport (tunable electrical conductivity, high thermal conductivity), electrochemical (wide working potential window), and electron emission (low, stable threshold voltage).

In studies of UNCD-coated flat substrates and microtip arrays for cold cathodes applications [1,81], consistently low threshold fields (1 to 2 V/ $\mu\text{m}$ ) and current densities of  $4 \times 10^{-4} \text{ A/cm}^2$  at 4 V/mm have been achieved using thin films of UNCD grown from  $C_{60} - 80\% \text{ Ar} - 20\% \text{ H}_2$  microwave plasmas [1].

Ultrananocrystalline diamond is slightly p-type as it grows [82]. As nitrogen is added, this material becomes n-type, with a very shallow activation energy. The origin of this conductivity is related to disorders and  $\pi$  bonding at the grain boundaries, which introduce states within the gap and band tails, resulting in high carrier concentrations and low mobilities. Ultrananocrystalline diamond particles have been grown with the incorporation of nitrogen up to  $8 \times 10^{20} \text{ atoms/cm}^3$  by the addition of nitrogen to plasmas during the CVD growth of diamond films [81]. This is the highest carrier concentration seen for any n-type diamond material to date, resulting in several orders of magnitude

increase in UNCD conductivity. This has promising applications in heterojunction electronic devices. The maximum conductivity measured was  $400 \Omega^{-1}\text{cm}^{-1}$  for 20%  $\text{N}_2$  in the gas phase [82]. Recently, high-temperature operation of a heterostructure diode utilizing n-type UNCD as an electrode has been demonstrated [82].

UNCD electrodes exhibit a wide working potential window, a low background current, and a high degree of electrochemical activity for redox systems. These results, in combination with the biocompatibility properties of UNCD, could lead to the application of UNCD electrodes for nerve stimulation [1].

UNCDs have been considered for a variety of applications including micro-electro-mechanical systems (MEMS) and moving mechanical assembly (MMA) devices, surface acoustic wave devices, biosensors and electrochemical sensors, coatings for field emission arrays, photonic and radio frequency (RF) switching, and neural prostheses. Particularly, in the future, MEMS applications that involve significant rolling or sliding contact (MEMS MMAs) will require the use of new materials with significantly improved mechanical and tribological properties, and the ability to perform in harsh environments. Since the feature resolution in polycrystalline MEMS is limited by grain size, the use of MEMS made by conventional CVD diamond methods is limited. In addition, the conventional CVD diamond films have large grain size ( $\sim 1 \mu\text{m}$ ), high internal stress, poor inter-granular adhesion, and rough surfaces (rms  $\sim 1 \mu\text{m}$ ). Diamond-like coatings, generally grown by physical vapor deposition, cannot cover high-aspect-ratio features conformally for applications such as MEMS, and require high-temperature postdeposition processing to relieve stress, which compromises their mechanical properties. UNCD coatings possess morphological and mechanical properties that are ideally suited for MEMS applications in general, and MMA use in particular [1,82]. The roughness of the film is about 20 to 40 nm and the friction coefficient can be as low as 0.01. The surfaces are very smooth (rms  $\sim 30$  to 40 nm) and the hardness is as high as  $\sim 100$  GPa. As compared to Si-based MEMS, the brittle fracture strength is 23 times that of Si, and the projected wear life of MEMS MMAs from diamond is 10,000 times greater than that of Si MMAs. The group from the Argonne National Laboratory have demonstrated three dimensional MEMS structures fabricated from UNCD material, including cantilevers and multilevel devices, acting as precursors to microbearings and gears.

Although discovered very recently, UNCD films have found a surprisingly wide range of niche applications. In many cases, prototype devices have been demonstrated.

## 5.6 CARBIDE-DERIVED DIAMOND-STRUCTURED CARBON

Recently, a completely different method, distinct by its simplicity, from what has been discussed in the previous two sections, has been developed for the synthesis of diamond-structured carbon in bulk quantities [12,28]. The method developed by Gogotsi et al is based on extracting silicon from silicon carbide or metal carbide, using chlorine-containing gases at ambient pressure and temperatures not exceeding  $1000^\circ\text{C}$ . Nanocrystalline diamond particles with an average crystallite size of 5 nm are formed, as is illustrated in [Figure 5.3b](#) for a diamond nanocrystal embedded in amorphous carbon in carbide-derived carbon produced by chlorination of TiC [28].

Following continued heat treatment at low hydrogen content, a typical film microstructure obtained by chlorination of SiC consists of a nanocrystalline diamond layer several microns thick near the SiC-carbon interface, followed by a region of diamond nanocrystals surrounded by carbon onions and disordered carbon. The third, closest to the surface layer, consists of carbon onions, as well as curved graphite sheets, some planar graphite, and porous and disordered amorphous carbon [12]. Initially, for stable conversion of silicon carbide into the diamond phase, the presence of hydrogen in the gas mixture was considered essential to saturate dangling bonds on the surface of the diamond particles [12]. Nanocrystalline diamond films grown up to  $50 \mu\text{m}$  thick at high hydrogen content has been demonstrated [84]. However, later, large nanocrystalline diamond areas were found in some regions of SiC samples treated in pure chlorine with no hydrogen [28]. The fact that hydrogen is not essential for the growth of diamonds using the carbide chlorination process outside

its range of thermodynamic stability is consistent with the conditions necessary for diamond synthesis from fullerene [1] or during codeposition of carbon and Si [62].

The specific feature of diamond-structured carbon is multiple diamond structures including cubic, hexagonal (lonsdalite) structures, as well as a variety of other diamond polytypes [12,28]. It is also possible to vary the pore size from angstroms to a few nanometers, depending on the carbide precursor type leading to the growth of nanoporous carbon or nanoporous diamond [12,83].

In principle, chlorination of carbides for the production of carbon-based materials and particularly, nanoporous carbon, is a relatively mature technology that has been commercialized (see, for example, <http://www.skeleton-technologies.com>). However, the synthesis of nanocrystalline diamonds by this technique [12] is a recent achievement. Coatings of diamond-structured carbon produced by this route show hardness values in excess of 50 GPa and Young's moduli up to 800 GPa.

Carbide-derived carbon and diamond coatings show excellent tribological behavior in both room air and dry nitrogen, and are at the stage of commercialization for tribological applications, particularly as nanodiamond coatings for SiC dynamic seals for water pumps [84]. The coatings are self-lubricating with remarkably low friction coefficients which can be tailored by altering the reaction parameters, and show no measurable wear. Favorable tribological properties of carbide-derived nanodiamond make it a potential candidate for applications in the manufacture of different types of prosthesis [84].

Conformal coatings produced by selective etching can be useful in MEMS applications where very thin and uniform coatings are required. In addition, permeability of films produced by chlorination of SiC and an extremely narrow pore size distribution in carbide-derived carbon provide effective molecular sieves, high-surface area electrodes and other applications, where vapor-deposited diamond films cannot be applied. The large-scale, solid-state synthesis of technical diamonds at ambient pressure and moderate temperatures with no plasma activation can provide diamond materials at low cost for a variety of high-volume applications such as brake pads, where diamond could not be used previously because of its cost.

## 5.7 MEDICAL AND BIOLOGICAL APPLICATIONS OF NANODIAMOND

All major forms of carbon at the nanoscale (fullerenes, nanotubes, and nanodiamond — both particulate and films) appear to be valuable resources for biomedical applications [85]. In the mid-1990s it was demonstrated that fullerene compounds have biological activity, and their potential as therapeutic products for the treatment of several diseases has been reported. As a result, a private biopharmaceutical company, C Sixty Inc., Houston, TX, was created, with a primary focus on the discovery and the development of a new class of therapeutics based on the fullerene molecule. At 7.2 Å in diameter, C<sub>60</sub> is similar in size to steroid hormones or peptide  $\alpha$ -helices, and thus fullerene compounds are ideal molecules to serve as ligands for enzymes and receptors [86]. In the last few years, a number of useful fullerene-based applications have been reported, including therapeutics such as antiviral agents and anticancer drugs, as biosensors for diagnostic applications [87,88], as a protective agent against iron-induced oxidative stress [89], and as an *in vitro* antibacterial agent [90]. Fullerenes have also been demonstrated to be useful in DNA-templated assemblies of inorganic–organic building blocks [91].

The exploration of buckytubes in biomedical applications is also underway. Multiwall carbon nanotubes have been used for the immobilization of proteins, enzymes, and oligonucleotides [92–94]. Significant progress has been made in the last few years in the effort to overcome some of the fundamental and technical barriers toward bioapplications, especially with regard to issues concerning the aqueous solubility, and biocompatibility of carbon nanotubes, modifications of carbon nanotubes with various biological and bioactive species, and on the design and fabrication of prototype biosensors. A comprehensive review of the advances in this fast-moving research field has recently been published by Lin et al. [95].

CVD diamond films (both conventional and UNCD) have been suggested as an ideal platform for future biochips and biosensors because of their superior mechanical, thermal, and chemical



properties as compared to glass, silicon, and gold surfaces [96]. Outstanding biocompatibility of diamond films and micron-sized particles with living cells has been demonstrated, and related research is summarized in [85]. The immobilization of biomolecules on diamond for the fabrication of integrated biochips and sensors requires surface activation processing such as sequential plasma treatment, amination, and carboxylation steps [98,99] in order to form covalent linkages to amino- or phosphate-modified DNA. The electrochemical deposition of polyaniline (PANI)/polyimide (PAA) conducting polymer layer on boron-doped diamond film has also been reported [97]. The PANI/PAA thin film provides freely accessible carboxylic groups that have high chemical specificity in the covalent immobilization of oligonucleotides. Recently, Yang et al. [96] used photochemical methods to create a homogeneous layer of amine groups on nanocrystalline and UNCD films, which served as binding sites for DNA attachment. By comparing DNA-modified ultra- and nanocrystalline diamond films with other commonly used surfaces for biological modification, such as gold, silicon, glass and glassy carbon, Yang et al. [96] concluded that diamond is unique in many ways: its ability to achieve very high stability while gold–thiol bonds, for example, are very susceptible to oxidation, leading to solubilization of the attached layers; chemically modified surfaces involving Si–O linkages degrade under basic conditions; both crystalline silicon and SiO<sub>2</sub> surfaces are susceptible to amine-induced degradation because oxidation of silicon is catalyzed by amines. It was also emphasized [97] that nanodiamond surfaces possess superior sensitivity while also being compatible with microelectronics processing technologies.

Nanocrystalline diamond coatings on suitable substrates are promising materials for medical implants, cardiovascular surgery, and for coating of certain components of artificial heart valves, due to their extremely high chemical inertness, smoothness of the surface, and good adhesion of the coatings to the substrate [100]. Nanocrystalline diamond coating (reported grain size ~10 nm) deposited by radio-frequency plasma chemical vapor deposition (RF-PCVD) of methane with nitrogen on millimeter-sized steel implants demonstrated excellent biocompatibility and biostability in situations where the implant had been inserted to tissue and bones for up to 52 weeks [100].

The first biomedical applications of UNCD particulate was reported by Kossovsky et al. [101], where nanodiamond was used for immobilization of antigens. Nanodiamond was chosen because of requirements of high surface area, high surface energy, and nontoxicity, as compared, for example, with toxic tin oxide particles. General Electric, Inc. (GE) powder of blocky 5 to 10 nm particles was treated with cellobiose (4 to 6 nm layer) following adsorption of antigen mussel adhesive protein (MAP) by dialysis. The resulting colloidal system of nanodiamond/cellobiose/MAP aggregates of 300 nm in size was used as antigen delivery vehicles for prolonged production of antibody.

An extensive set of experiments on biological activity of UNCD particles and their potential applications has been carried out by Puzyr et al. [102–107]. Reference [102] demonstrates the possibility of preparation of materials composed of particles with significantly different chemical structure and physical properties, using protein molecules as a cross-linking agent. Particularly promising for design of new composites biomaterials is the nanodiamond–protein–Al<sub>2</sub>O<sub>3</sub> complex, where UNCD particles and  $\delta$ -Al<sub>2</sub>O<sub>3</sub> were used as building blocks and protein as cross-linking agents. In the first stage, a recombinant apoobelin (a light-emitting protein) was adsorbed on nanodiamond particles, and in the second stage, the nanodiamond–protein complex was adsorbed onto the  $\delta$ -Al<sub>2</sub>O<sub>3</sub> particles. As an extension of that work, obelin–nanodiamond particle complexes were immobilized on a plane aluminum oxide structure [103], which allowed them to devise a bioluminescent test system to record calcium ions, as an alternative to the well-known methods of calcium measurement performed within the volume of the reaction mixture. Importantly, biological activity of apoobelin in the composites was retained even for a dry plate, so that the analyzed solution can be placed on a dry plate. It is claimed that the designed plane luminescent sensors (biochips) are capable of operating under “extraordinary” conditions [103]. For example, prolonged space missions are known to promote decalcination of human bone tissue. The express method of analysis that does not require any solution other than the one under analysis eliminates the problem of working with a variety of liquids under microgravity, and makes it much easier to obtain information on

the dynamics of calcium ions in physiological liquids (saliva, urine, blood, or tears). Recently, a luminescent biochip prototype for use in bioluminescent analysis has been designed, whose main element consists of detonation UNCD particles functionalized with light-emitting proteins such as bacterial luciferase and obelin [107]. It was demonstrated that, in these structures, the enzyme retains the catalytic activity.

Detonation nanodiamond has also been used for the separation and purification of recombinant apoobelin and recombinant luciferase from bacterial cells of *Escherichia coli* [105] in bulk. It has been demonstrated that the application of nanodiamonds simplifies the procedures for purifying the proteins, decreases the time of their separation to 30 to 40 min (as compared to conventional methods which take several days), eliminates the necessity of using special chromatographic equipment, and makes it possible to prepare high-purity apoobelin and luciferase materials with protein yields of 35 to 45% and 45 to 60%, respectively. As possible mechanisms of interaction of proteins with particle surfaces formation of S–S bridges, coordination bonds, or multiple points interaction of a protein molecule with different functional groups on a particle surface was considered [105].

Puzyr et al. [104] performed a study of the effects of UNCDs on human white and red blood cells *in vitro*. Experiments were carried out using seven different samples of detonation UNCD purified from by-products of explosion-induced synthesis by different methods and obtained from different vendors. Two parameters were used to understand the effects of nanodiamond particles on white blood cells: (1) the kinetics of generation of active oxygen species (AOS) and (2) the cell viability. The kinetics of AOS generation was measured using the chemiluminescence luminol reaction (CLR), and cell viability was tested by staining with a trypan blue solution. It was observed that the detonation UNCD had a damaging effect on both white cells and erythrocytes [104]. The results of the study suggest that nanodiamond particles in whole blood interact with white blood cells and activate AOS generation in these cells. On the other hand, there was almost no correlation between the physicochemical characteristics of the nanodiamond samples used in the study and their effects on the whole blood CLR kinetics. It was concluded [104] that the active functional groups that are exposed on the surface of nanoparticles, rather than their diamond core, are the decisive factor of the UNCD-induced effect on cells. On the other hand, experiments performed by a group from Poland [108] demonstrated that detonation UNCD increases blood cells' survivability in systems with high concentration of free radicals as compared to nanodiamond particles synthesized by other means. Definitely, this important area requires more work to be done to reveal the mechanisms of interaction of UNCD with blood cells as well as other types of cells. Figure 5.19 is a TEM micrograph of an ultrathin section of a mammalian cell, demonstrating results of incubation of modified UNCD with a cell. White arrows highlight places where presumably UNCD particles penetrated the cell membrane. This is an important fact demonstrating that, in principle, UNCD particles (at least modified UNCD [106]) can serve as delivery vehicles for different substances into cells. Also, UNCD particulates have been specifically modified with the ultimate goal of adapting them to biological investigations [106]. Powders of modified nanodiamonds are characterized by a high colloidal stability of the particles, virtually independent of particle concentration. They form stable hydrosols on simple addition of water, and do not need ultrasonic dispersion. After repeated removal of the dispersive medium and subsequent addition of water to the dry, modified nanodiamond powder, again a stable hydrosol can be obtained. The use of highly stable colloidal solutions of modified UNCD in biological investigations (buffer solutions, culture media, physiological liquids), and for achieving a uniform distribution of nanoparticles in an agar gel, has been demonstrated. It was also reported [106] that organosols with modified UNCD possess high colloidal stability over a wide range of temperatures, namely, from the boiling point to the freezing point of the dispersive medium. After freezing and melting, the organosol retains the colloidal stability.

Another group active in the development of biological and medical applications of UNCDs is the team led by Dolmatov [2]. In preliminary experiments on animals with Erlich carcinoma, and several clinical tests on terminally ill cancer patients, the research team [109] found that treatment with aqueous suspensions of nanodiamonds resulted in improvement of the overall condition of the

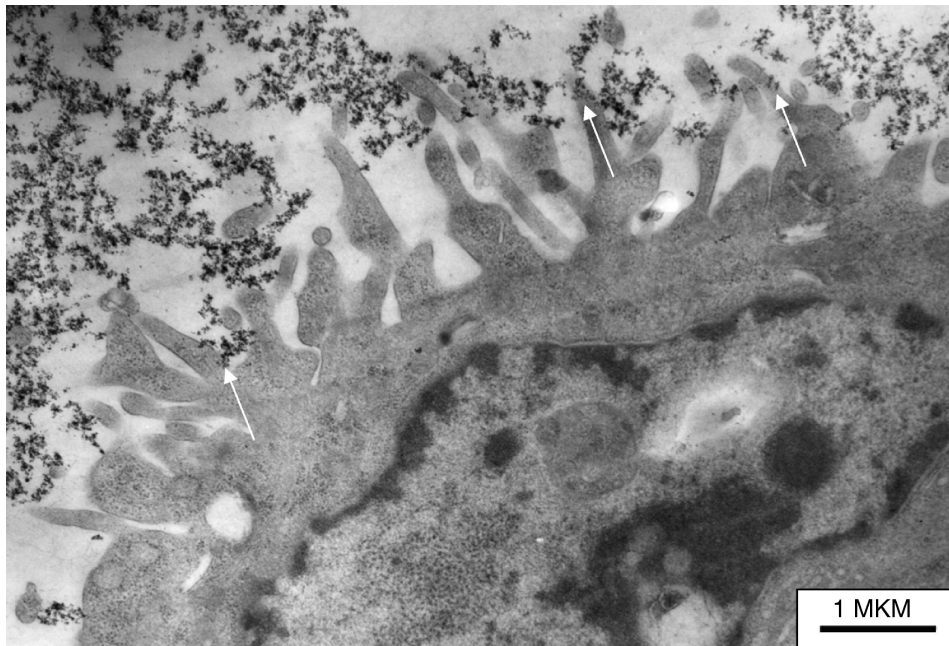


**FIGURE 5.19** TEM micrograph of an ultrathin section of a mammalian cell, demonstrating results of incubation of modified UNCD with a cell. (Courtesy of A.P. Puzyr, O.A. Mogilnaya, and V.S. Bondar.)

patients, normalization of gastrointestinal function, decrease in the intoxication and, in some cases, reduction of the tumor size [2,109]. However, no detailed mechanism-of-action studies have been conducted so far. According to Dolmatov et al. [2,109], UNCD can be considered as a potential medical agent (not just drug-delivery agent) in oncology, gastroenterology, and vascular disease, and an efficient remedy for the after-effects of burns, in skin diseases, and intoxication. The characteristics of UNCDs which make them suitable for medical applications are the anomalously high adsorption capacity, high specific surface areas, abundance of free electrons on the surface (a multiple radical donor), nanoscale size, significant amount of oxygen-containing functional groups on the surface, chemically inert cores, and hydrophobicity of the surface [2]. According to Dolmatov [2], owing to their high adsorption capacities, UNCDs exhibit extremely high absorbing/bonding activities with respect to pathogenic viruses, microbes, and bacteria. The absorbing/bonding may be selective to particular drugs that can enhance the drugs' activity. According to [2,109], UNCDs exhibit no carcinogenic or mutagenic properties and are not toxic.

While the preliminary results, particularly in oncology, are encouraging [109], a very limited amount of research has been conducted so far on the pharmacological effects of UNCD, and extensive fundamental studies will be required before a clear understanding of the benefits can be developed.

## 5.8 CONCLUSION

Nanodiamond particles have very diverse structures at the nanoscale, ranging from individual clusters to high-purity films, can be produced by very diverse techniques such as the detonation explosives method, low-pressure CVD, and the chlorination of carbides. Different types of nanodiamond are at varying stages of commercialization. Production of nanodiamond particulates for polishing applications, obtained by fractioning and grinding of micron-sized monocrystalline and polycrystalline particles, is a very mature technology. The purity of nanodiamond for polishing applications is not as critical as it is for other applications, so the specifications for nanodiamond quality in this application are more relaxed. The recently developed process of depositing UNCD films with very unique properties is at the very early stage of commercialization. The process of producing UNCD films by the carbide-derivation process is distinct due to its simplicity and is being rapidly implemented in some market niches because of the existing infrastructure for producing carbide films.

It is interesting that before nanotechnology became widely popular, there was a long history of application of detonation UCND in traditional areas such as in polymer composites and polishing compounds, as additions to lubricants, and in solutions for galvanic coatings, in the countries of the former Soviet Union.

UNCDs can be easily produced in tons quantities; however, it is very hard to produce UNCD completely free of contamination due to the incombustible impurities (metals, nonmetals, and their oxides), which are located in inter-particle areas within agglomerates of UNCD particles. High purity of UNCD is not required, however, for the traditional applications mentioned above. Depending on the application, technologies developed earlier for UNCD purification, surface modification as well as generation of aggregate-free UNCD suspensions, are now being scaled up for industrial use. Application-specific modification of UNCDs is underway. It should be emphasized that developing an understanding of the relationship between the complex structure of the surface of UNCDs and their physical properties is an area of very active research. Especially important, although very challenging, is developing an understanding of the properties of individual nanodiamond particles. Regarding novel applications of UNCD, we have pointed out that biomedical applications is an area of research that is just beginning to emerge.

In conclusion, nanocrystalline diamond with a wide diversity of forms is a rapidly developing area from both the point of view of fundamental research as well as the current perspective of application in many areas of nanotechnology.

## REFERENCES

1. Gruen, D.M., Nanocrystalline diamond films, *Annu. Rev. Mater. Sci.*, 29, 211, 1999.
2. Dolmatov, V.Y., Detonation synthesis ultradispersed diamonds: properties and applications, *Russian Chem. Rev.*, 70, 607, 2001.
3. Shenderova, O.A., Zhirnov, V.V., and Brenner, D.W., Carbon nanostructures, *Crit. Rev. Solid State Mater. Sci.*, 27, 227, 2002.
4. Belobrov, P.I., Nature of nanodiamond state and new applications of diamond nanotechnology, Proceedings of the IX International Conference on "High-tech for Russian Industry," Moscow, Russia, 11–13 September, 2003, 1: 235–269 (in Russian).
5. Vereschagin, A.L., *Detonation Nanodiamonds*, Altai State Technical University, Barnaul, Russian Federation, 2001 (in Russian).
6. Dolmatov, V.Y., *Ultradisperse Diamonds of Detonation Synthesis: Production, Properties and Applications*, St. Petersburg, State Polytechnical University, 2003.
7. Danilenko, V.V., *Synthesis and Sintering of Diamond by Detonation*, Energoatomizdat, 2003 (in Russian).
8. Benedek, G., Milani, P., and Ralchenko, V.G., Eds., *Nanostructured Carbon for Advanced Applications*, NATO Science Series, Vol. 24, Kluwer Academic, Dordrecht, 2001.
9. Vul, A., Dolmatov, V., and Shenderova, O., *Detonation Nanodiamonds and Related Materials*, Bibliography Index, First Issue, "FIZINTEL," St. Petersburg, Russia, 2003.
10. Gruen, D., Vul, A., and Shenderova, O., Eds., *Ultrananocrystalline Diamond: Synthesis, Properties and Applications*, NATO Science Series, Springer, 2005.
11. Danilenko, V.V., On the history of the discovery of nanodiamond synthesis, *Phys. Solid State*, 46, 595, 2004.
12. Gogotsi, Y., Welz, S., Ersoy, D.A., and McNallan, M.J., Conversion of silicon carbide to crystalline diamond-structured carbon at ambient pressure. *Nature*, 411, 283, 2001.
13. Daulton, T.L., Kirk, M.A., Lewis, R.S., and Rehn, L.E., Production of nanodiamonds by high-energy ion irradiation of graphite at room temperature, *Nucl. Instrum. Methods B*, 175, 12, 2001.
14. Banhart, F. and Ajayan, P.M., Carbon onion as nanoscopic pressure cell for diamond formation, *Nature*, 382, 433, 1996.
15. Frenklach, M., Howard, W., Huang, D., Yuan, J., Spear K.E., and Koba, R., Induced nucleation of diamond powder. *Appl. Phys. Lett.*, 59, 546, 1991.
16. Tielens A., Seab, C., Hollenbach, D.J., and Mckee, C.F., Shock processing of interstellar dust — diamonds in the sky, *Astrophys. J.*, 319, L109, 1987.

17. Vicelli, J.A. and Ree, F.H., Carbon particle phase transformation kinetics in detonation waves, *J. Appl. Phys.*, 88, 683–690, 2000.
18. Vicelli, J.A., Bastea, S., Glosli, J.N., and Ree, F.H., Phase transformations of nanometer size carbon particles in shocked hydrocarbons and explosives, *J. Chem. Phys.*, 115, 2730, 2001.
19. Kuznetsov, V.L., Chuvilin, A.L., Butenko, Yu.V., and Usoltseva, A., Carbon phase diagram at the nanoscale, in *Science and Technology of Fullerene Materials*, Bernier, P., Ebbesen, T.W., Bethune, D.S., Metzger, R.M., Chiang, L.Y., and Mintmire, J.W., Eds., *Mater. Res. Soc. Proc.*, vol. 359, Pittsburgh, PA, p. 105, 1995.
20. Barnard, A.S., Russo, S.P., and Snook, I.K., Structural relaxation and relative stability of nanodiamond morphologies, *Diam. Rel. Mater.*, 12, 1867, 2003.
21. Barnard, A.S., Russo, S.P., and Snook, I.K., Size dependent phase stability of carbon nanoparticles: nanodiamond versus fullerenes, *J. Chem. Phys.*, 118, 5094, 2003.
22. Barnard, A.S., Russo, S.P., and Snook, I.K., Ab initio modelling of the stability of nanocrystalline diamond morphologies, *Phil. Mag. Lett.*, 83, 39, 2003.
23. Raty, J.Y., Galli, G., Bostedt, C., van Buuren, T.W., and Terminello, L.J., Quantum confinement and fullerene-like surface reconstructions in nanodiamonds, *Phys. Rev. Lett.*, 90, 037401, 2003.
24. Barnard, A., Russo, S., and Snook, I.K., Coexistence of bucky diamond with nanodiamond and fullerene carbon phases, *Phys. Rev. B*, 68, 073406, 2003.
25. Park, N., Lee, K., Han, S.W., Yu, J.J., and Ihm, J., Energetics of large carbon clusters: crossover from fullerenes to nanotubes, *Phys. Rev. B*, 65, 121405, 2002.
26. Tomanek, D. and Schluter, M.A., Growth regimes of carbon clusters, *Phys. Rev. Lett.*, 67, 2331–2335, 1991.
27. Kuznetsov, V.L., Zilberberg, I.L., Butenko, Y.V., Chuvilin, A.L., and Segall, B., Theoretical study of the formation of closed curved graphite-like structures during annealing of diamond surface, *J. Appl. Phys.*, 86, 863, 1999.
28. Welz, S., Gogotsi, Y., and McNallan, M.J., Nucleation, growth, and graphitization of diamond nanocrystals during chlorination of carbides, *J. Appl. Phys.*, 93, 4207, 2003.
29. Tyler, T., Zhirnov, V., Kvit, A., Kang, D., and Hren, J., Electron emission from diamond nanoparticles on metal tips, *Appl. Phys. Lett.*, 82, 2904, 2003.
30. Brenner, D.W., Shenderova, O.A., Harrison, J.A., and Sinnott, S., Second generation reactive empirical bond order (REBO) potential energy expression for hydrocarbons, *J. Phys.: Condens. Matter*, 14, 783, 2002.
31. Zhu, Y.Q., Sekine, T., Kobayashi, T., Takazawa, E., Terrones, M., and Terrones, H., Collapsing carbon nanotubes and diamond formation under shock waves, *Chem. Phys. Lett.*, 287, 689, 1998.
32. DeCarli, P. and Jamieson, J., Formation of diamond by explosive shock, *Science*, 133, 1821, 1961.
33. Website of Microdiamant, AG Lengwil, Switzerland, [www.microdiamant.com](http://www.microdiamant.com).
34. Yamada, K. and Tanabe, Y., Shock-induced phase transition of oriented pyrolytic graphite to diamond at pressures up to 15 GPa, *Carbon*, 40, 261–269, 2002.
35. Adadurov, G.A., Bavina, T.V., Breusov, O.N., Drobyshev, V.N., Messinev, M.J., Rogacheva, A.I., Ananiin, A.V., Apollonov, V.N., Dremmin, A.N., Doronin, V.N., Dubovitsky, F.I., Zemlyakova, L.G., Pershin, S.V., and Tatsy, V.F., Method of producing diamond and/or diamond-like modifications of boron nitride, U.S. Patent 4,483,836, 1984.
36. Dahl, J.E., Liu, S.G., and Carlson, R.M.K., Isolation and structure of higher diamondoids, nanometer-sized diamond molecules, *Science*, 299, 96, 2003.
37. Carlson, R.M.K., Dahl, J.E.P., and Liu, S.G., in *Diamond Molecules Found in Petroleum*, in *Ultrananocrystalline Diamond: Synthesis, Properties and Applications*, Gruen, D., Vul, A., and Shenderova, O., Eds., NATO Science Series, Springer, 2005, p. 63.
38. Núñez-Regueiro, M., Monceau, P., and Hodeau, J.-L., Crushing C60 to diamond at room temperature, *Nature*, 355, 237–239, 1992.
39. Cao, L.M., Gao, C.X., Sun, H.P., Zou, G.T., Zhang, Z., Zhang, X.Y., He, M., Zhang, M., Li, Y.C., Zhang, J., Dai, D.Y., Sun, L.L., and Wang, W.K., Synthesis of diamond from carbon nanotubes under high pressure and high temperature, *Carbon*, 39, 311, 2001.
40. Ma, Y.Z., Zou, G.T., Yang, H.B., and Meng, J.F. Conversion of fullerenes to diamond under high pressure and high temperature, *Appl. Phys. Lett.*, 65, 822, 1994.
41. Yusa, H., Nanocrystalline diamond directly transformed from carbon nanotubes under high pressure, *Diam. Relat. Mater.*, 11, 87, 2002.

42. Frenklach, M., Kematick, R., Huang, D., Howard, W., Spear, K.E., Phelps, A.W., and Koba, R., Homogeneous nucleation of diamond powder in the gas phase, *J. Appl. Phys.*, 66, 395–399, 1989.
43. Buerki, P.R. and Leutwyler, S., Homogeneous nucleation of diamond powder by CO<sub>2</sub> laser-driven reactions, *J. Appl. Phys.*, 69, 3739, 1991.
44. Wesolowski, P., Lyutovich, Y., Banhart, F., Carstanjen, H.D., and Kronmuller, H., Formation of diamond in carbon onions under MeV ion irradiation, *Appl. Phys. Lett.*, 71, 1948, 1997.
45. Fedoseev, D.V., Bukhovets, V.L., Varshavskaya, I.G., Lavrentev, A.V., and Derjaguin, B.V., Transition of graphite into diamond in a solid state under the atmospheric pressure, *Carbon*, 21, 237, 1983.
46. Wei, B., Zhang, J., Liang, J., and Wu, D., The mechanism of phase transformation from carbon nanotube to diamond, *Carbon*, 36, 997, 1998.
47. Meguro, T., Hida, A., Suzuki, M., Koguchi, Y., Takai, H., Yamamoto, Y., Maeda, K., and Aoyagi, Y., Creation of nanodiamonds by single impacts of highly charged ions upon graphite, *Appl. Phys. Lett.* 79, 3866, 2001.
48. Tomita, S., Fujii, M., Hayashi, S., and Yamamoto, K., Transformation of carbon onions to diamond by low-temperature heat treatment in air, *Diam. Rel. Mater.*, 9, 856, 2000.
49. Sun, L.T., Gong, J.L., Zhu, Z.Y., Zhu, D.Z., He, S.X., Wang, Z.X., Chen, Y., and Hu, G., Nanocrystalline diamond from carbon nanotubes, *Appl. Phys. Lett.*, 84, 2901, 2004.
50. Lifshitz, Y., Kohler, T., Frauenheim, T., Guzman, I., Hoffman, A., Zhang, R.Q., Zhou, X.T., and Lee, S.T., The mechanism of diamond nucleation from energetic species, *Science*, 297, 1531, 2002.
51. Terranova, M.L., Orlanducci, S., Fiori, A., Tamburri, E., Sessa, V., Rossi, M., and Barnard, A.S., Controlled evolution of carbon nanotubes coated by nanodiamond: the realization of a new class of hybrid nanomaterials, *Chem. Mater.*, 17, 3214, 2005.
52. Baik, E.S., Fabrication of diamond nanowhiskers, *Thin Solid Films*, 377, 295, 2000.
53. *Ximia i zizn (Chemistry and Life)*, 1, 14–16, 1999 (in Russian; about work of Koscheev, A.)
54. Masuda, H., Yanagishita, T., Yasui, K., Nishio, K., Yagi, I., Rao, T.N., and Fujishima, A., Synthesis of well aligned diamond nanocylinders, *Adv. Mater.*, 13, 247, 2001.
55. Ando, Y., Nishibayashi, Y., and Sawabe, A., Nano-rods of single crystalline diamond, *Diam. Rel. Mater.*, 13, 633, 2004.
56. Barnard, A.S., Structural properties of diamond nanowires: theoretical predictions and experimental progress, *Rev. Adv. Mater. Sci.*, 6, 94, 2004.
57. Barnard, A., From nanodiamond to nanowires, in *Ultrananocrystalline Diamond: Synthesis, Properties and Applications*, Gruen, D., Vul, A., and Shenderova, O., Eds., NATO Science Series, Springer, 2005, p. 25.
58. Shenderova, O., Brenner, D., and Ruoff, R.S., Would diamond nanorods be stronger than fullerene nanotubes? *Nano Lett.*, 3, 805, 2003.
59. Chen, H. and Chang, L., Characterization of diamond nanoplatelets, *Diam. Rel. Mater.*, 13, 545, 2004.
60. Gruen, D.M., Liu, S.Z., Krauss, A.R., and Pan, X.Z., Buckyball microwave plasmas: fragmentation and diamond-film growth, *J. Appl. Phys.*, 75, 1758, 1994; *Appl. Phys. Lett.*, 64, 1502, 1994.
61. Gruen, D.M., 356350 Ultracrystalline diamond in the laboratory and the cosmos, *MRS Bull.*, 26, 771–776, 2001.
62. Kimura, Y. and Kaito, C., Production of nanodiamond from carbon film containing silicon, *J. Cryst. Growth*, 255, 282, 2003.
63. Gordeev, S.K., in *Nanostructured Carbon for Advanced Applications*, Benedek, G., Milani, P., and Ralchenko, V.G., Eds., NATO Science Series, Vol. 24, Kluwer Academic, Dordrecht, 2001, pp. 71–88.
64. Aleksenskii, A.E., Baidakova, M.V., Vul', A.Y., and Siklitskii, V.I., The structure of diamond nanoclusters, *Phys. Solid State*, 41, 668–671, 1999.
65. *Proceedings of the 1st International Symposium, Detonation Nanodiamond: Synthesis, Properties, and Applications*, St Petersburg, 7–9 July, 2003, *Phys. Solid State*, 46, 2004.
66. Maillard-Schaller, E., Kuettel, O.M., Diederich, L., and Zhirnov, V., Surface properties of nanodiamond films deposited by electrophoresis on Si(100), *Diam. Rel. Mater.*, 8, 805, 1999.
67. Gordeev, S.K., Belobrov, P.I., Kiselev, N.I., Petrakovskaya, E.A., and Ekstrom, T.C., Novel solid nano diamond/pyrocarbon semiconductor materials, *Mater. Res. Soc. Symp. Proc.*, 63, F14.16.1, 2001.
68. Belobrov, P.I., Gordeev, S.K., Petrakovskaya, E.A., and Falaleev, O.V., Paramagnetic properties of nanodiamond, *Doklady Phys.*, 46, 459, 2001.

69. Zhirnov, V.V., Kuttel, O.M., Groning, O., Alimova, A.N., Detkov, P.Y., Belobrov, P.I., Maillard-Schaller, E., and Schlapbach, L., Characterization of field emission cathodes with different forms of diamond coatings, *J. Vac. Sci. Technol.*, 17, 666, 1999.
70. Alimova, A.N., Chubun, N.N., Belobrov, P.I., Detkov, P.Y., and Zhirnov, V.V., Electrophoresis of nanodiamond powder for cold cathode fabrication, *J. Vac. Sci. Technol. B*, 17, 715, 1999.
71. Zhirnov, V.V., Shenderova, O.A., Jaeger, D.L., and Brenner, D., Electron emission properties of detonation nanodiamonds, *Phys. Solid State*, 46, 641, 2004.
72. Jaeger, D.L., Tyler, T., Kvit, A.K., Zhirnov, V.V., and Hren, J.J., Electrostatic factors affecting emission from discrete isolated diamond nanodots, *Proceedings of Cold Cathodes II*, Electrochemical Society, Philadelphia, PA, 2002, p. 291.
73. Kuznetsov, V.L., Chuvilin, A.L., Butenko, Yu.V., Malkov, I.Yu., and Titov, V.M., Onion-like carbon from ultra-disperse diamond, *Chem. Phys. Lett.*, 222, 343, 1994.
74. Aleksenskii, A.E., Baidakova, M.V., Vul, A.Y., Davydov, V.Y., and Pevtsova, Y.A., Diamond-graphite phase transition in ultradisperse-diamond clusters, *Phys. Solid State*, 39, 1007, 1997.
75. Davidson, W.P. and Kang, J.L., *Applying CVD Diamond and Particulate Nanodiamond*, in *Ultrananocrystalline Diamond: Synthesis, Properties and Applications*, Gruen, D., Vul, A., and Shenderova, O., NATO Science Series, Springer, 2005, p. 357.
76. Timoshkov, Y.V., Danilyuk, A.L., Molchan, I.S., *Galvanotekhnika and Obrabotka Poverkhnosti*, 7, 20–26, 1999 (in Russian).
77. Bogatyreva, G.P., Marinich, M.A., and Gvyazdovskaya, V.L., Diamond — an adsorbent of a new type *Dia. Rel. Mater.*, 9, 2002–2005, 2000.
78. Beveratos, A., Brouri, R., Gacoin, T., Poizat, J.P., and Grangier, P., Nonclassical radiation from diamond nanocrystals, *Phys. Rev. A*, 64, 1802, 2001.
79. Curtiss, L.A., Zapol, P., Sternberg, M., and Gruen, D., *Quantum Chemical Studies of Growth Mechanisms of Ultrananocrystalline Diamond*, in *Ultrananocrystalline Diamond: Synthesis, Properties and Applications*, Gruen, D., Vul, A., and Shenderova, O., Eds., NATO Science Series, Springer, 2005, p. 39.
80. Corrigan, T.D., Gruen, D.M., Krauss, A.R., Zapol, P., and Chang, R.P.H., The effect of nitrogen addition to Ar/CH<sub>4</sub> plasmas on the growth, morphology and field emission of ultrananocrystalline diamond, *Diam. Rel. Mater.*, 11, 43–48, 2002.
81. Williams, O., Zimmermann, T., Kubovic, M., and Gruen, D., *Electronic Properties and Applications of Ultrananocrystalline Diamond*, in *Ultrananocrystalline Diamond: Synthesis, properties and Applications*, Gruen, D., Vul, A., and Shenderova, O., Eds., NATO Science Series, Springer, 2005, p. 373.
82. Krauss, A.R., Auciello, O., Gruen, D.M., Jayatissa, A., Sumant, A., Tucek, J., Mancini, D.C., Moldovan, N., Erdemir, A., Ersoy, D., Gardos, M.N., Busmann, H.G., Meyer, E.M., and Ding, M.Q., Ultrananocrystalline diamond thin films for MEMS and moving mechanical assembly devices, *Diam. Rel. Mater.*, 10, 1952–1961, 2001.
83. Gordeev, S.K., in *Nanostructured Carbon for Advanced Applications*, Benedek, G., Milani, P., and Ralchenko, V.G., Eds., NATO Science Series, Vol. 24, Kluwer Academic, Dordrecht, 2001, pp. 71–88.
84. Gogotsi, Yu., personal communication, 2003.
85. Frietas, R.A., *Nanomedicine*, Volume 1: *Basic Capabilities*, Landes Bioscience, 1999; *Nanomedicine*, Volume IIA: *Biocompatibility*, Landes Bioscience, 2003.
86. Wilson, S.R., Biological aspects of fullerenes, in *Fullerenes: Chemistry, Physics, and Technology*, Kadish, K.M., and Ruoff, R.S., Eds., Wiley, New York, 2000.
87. Nanotechnology in Biology: The Good of Small Things, *The Economist*, December 22, 2001.
88. <http://www.csixty.com>
89. Lin, A.M.Y., Chyi, B.Y., Wang, S.D., Yu, H.H., Kanakamma, P.P., Luh, T.Y., Chou, C.K., and Ho, L.T., Carboxyfullerene prevents iron-induced oxidative stress in rat brain, *J. Neurochem.*, 72, 1634–1640, 1999.
90. DaRos, T., Prato, M., Novello, F., Maggini, M., and Banfi, E., Easy access to water-soluble fullerene derivatives via 1,3-dipolar cycloadditions of azomethine ylides to C<sub>60</sub>, *J. Org. Chem.*, 61, 9070, 1996.
91. Niemeyer, C.M., Nanoparticles, proteins, and nucleic acids: biotechnology meets materials science, *Angew. Chem. Int. Ed.*, 40, 4128–4158, 2001.

92. Tsang, S.C., Davis, J.J., Chen, Y.K., Green, M.L.H., Hill, H.A.O., Hambley, T.W., and Sadler, P.J., Immobilization of small proteins in carbon nanotubes — high-resolution transmission electron-microscopy study and catalytic activity, *J. Chem. Soc. Chem. Commun.*, 12, 1803–1805, 1995.
93. Tsang, S.C., Guo, Z.J., Chen, Y.K., Green, M.M.H., Hill, H.A.O., Hambley, T.W., and Sadler, P.J., Immobilization of platinated and iodinated oligonucleotides on carbon nanotubes, *Angew. Chem. Int. Ed.*, 36, 2198–2200, 1997.
94. Davis, J.J., Green, M.L., Hill, H.A., Leung, Y.C., Sadler, P.J., Sloan, J., Xavier, A.V., and Tsang, S.C., The immobilization of proteins in carbon nanotubes, *Inorg. Chim. Acta*, 272, 261–266, 1998.
95. Lin, Y., Taylor, S., Li, H.P., Fernando, K.A.S., Qu, L.W., Wang, W., Gu, L.R., Zhou, B., and Sun, Y.P., Advances toward bioapplications of carbon nanotubes, *J. Mater. Chem.*, 14, 527, 2004.
96. Yang, W.S., Auciello, O., Butler, J.E., Cai, W., Carlisle, J.A., Gerbi, J., Gruen, D.M., Knickerbocker, T., Lasseter, T.L., Russell, J.N., Smith, L.M., and Hamers, R.J., DNA-modified nanocrystalline diamond thin-films as stable, biologically active substrates, *Nat. Mater.*, 1, 253, 2002.
97. Gu, H., Su, X., and Loh, K.P., Conductive polymer-modified boron-doped diamond for DNA hybridization analysis, *Chem. Phys. Lett.*, 388, 483, 2004.
98. Takahashi, K., Tanga, M., Takai, O., and Okamura, H., DNA preservation using diamond chips *Diam. Rel. Mater.*, 12, 572, 2003.
99. Ushizawa, K., Sato, Y., Mitsumori, T., Machinami, T., Ueda, T., and Ando, T., Covalent immobilization of DNA on diamond and its verification by diffuse reflectance infrared spectroscopy, *Chem. Phys. Lett.*, 351, 105, 2002.
100. Mitura, S., Mitura, A., Niedzielski, P., and Couvrat, P., Nanocrystalline diamond coatings, *Chaos Solitons Fractals*, 10, 2165, 1999.
101. Kossovsky, N., Gelman, A., Hnatyszyn, H.J., Rajguru, S., Garrell, R.L., Torbati, S., Freitas, S.S.F., and Chow, G.M., Surface modified diamond nanoparticles as antigen delivery vehicles, *Bioconjugate Chem.*, 6, 507, 1995.
102. Puzyr, A.P., Bondar, V.S., Belobrov, P.I., and Bukaemskii, A.A., Preparation of nanodiamond-protein- $\delta$ -aluminum oxide complex, *Dokl. Acad. Sci. USSR*, 373, 408, 2000.
103. Purtov, K.V., Bondar', V.S., and Puzyr', A.P., Supramolecular structure of nanodiamond particles and obelin built up on a two-dimensional plate, *Dokl. Akad. Nauk.*, 380, 339, 2001.
104. Puzyr, A.P., Neshumayev, D.A., Tarskikh, S.V., Makarskaya, G.V., Dolmatov, V.Y., and Bondar, V.S., Damaging effect of detonation diamonds on human white and red blood cells in vitro, *Dokl. Biochem. Biophys.*, 385, 201, 2002.
105. Bondar', V.S., Pozdnyakova, I.O., and Puzyr', A.P., Applications of nanodiamonds for separation and purification of proteins *Phys. Solid State*, 46, 758–760, 2004.
106. Bondar', V.S. and Puzyr', A.P., Nanodiamonds for biological investigations *Phys. Solid State*, 46, 716–719, 2004.
107. Puzyr', A.P., Pozdnyakova, I.O., and Bondar', V.S., Design of a luminescent biochip with nanodiamonds and bacterial luciferase, *Phys. Solid State*, 46, 761–763, 2004.
108. Bakowicz, K. and Mitura, S., Influence of bioactive diamond powder particles on human red blood cells in conditions of oxidative free radical damage. Abstract for IVC-16/ICSS-12/NANO-8/AIV-17, June 28–July 2, Venice, Italy, 2004.
109. Dolmatov, V.Yu. and Kostrova, L.N., Detonation-synthesized nanodiamonds and the possibility to develop a new generation of medicines, *J. Superhard Mater.*, 3, 79, 2000.



---

# 6 Carbide-Derived Carbon

*Gleb Yushin, Alexi Nikitin, and Yury Gogotsi*  
Department of Materials Science and Engineering,  
Drexel University, Philadelphia, Pennsylvania

## CONTENTS

Abstract .....	212
6.1 Introduction .....	212
6.2 Selective Etching of Carbides by Halogens .....	213
6.2.1 Chlorination of Carbides for Production of Chlorides .....	213
6.2.2 Thermodynamic Simulations .....	214
6.2.3 Historic Overview of Carbide-Derived Carbon Studies .....	215
6.2.4 Kinetics of Halogenation of Carbides .....	217
6.2.5 Conservation of Shape .....	218
6.2.6 Nanoporous Structure and Adsorption Properties .....	218
6.2.6.1 Pore Formation .....	218
6.2.6.2 Effect of the Chlorination Temperature .....	220
6.2.6.3 Effect of the Carbide Structure .....	224
6.2.6.4 Effect of Catalysts on the Surface Area and Microstructure of CDC .....	226
6.2.6.5 Effect of a Halogen .....	226
6.2.6.6 Effect of the Initial Carbide Porosity .....	227
6.2.6.7 CDC Composites .....	227
6.2.7 Analysis of CDC Structure .....	228
6.2.7.1 Graphitization and Detection of Nanocrystals .....	228
6.2.7.2 Carbon Nanostructures .....	230
6.3 Selective Etching of Carbides by Melts and Supercritical Water .....	232
6.3.1 Reaction of Calcium Carbide with Inorganic Salts .....	232
6.3.2 Hydrothermal Leaching of Carbides .....	233
6.3.2.1 Thermodynamic Analysis .....	233
6.3.2.2 Experimental Results .....	234
6.4 Thermal Decomposition of Carbides .....	235
6.4.1 Carbon Structure and Conservation of Shape .....	235
6.4.2 Synthesis of Carbon Nanotubes and Carbon Onions .....	237
6.5 Applications .....	241
6.5.1 Supercapacitors .....	241
6.5.2 Hydrogen Storage .....	242
6.5.3 Methane Storage .....	243
6.5.4 Lithium-Ion Batteries .....	243
6.5.5 Pt Catalyst on CDC Support .....	244
6.5.6 Tribological Coatings .....	244

8.6 Conclusions .....	245
Acknowledgments .....	245
References .....	245

## ABSTRACT

This chapter gives a comprehensive overview of various nanostructured carbon materials produced from carbides by selective etching in halogens, molten salts, and supercritical water, as well as by vacuum decomposition. Both experimental results and thermodynamic modeling of carbon formation are provided. Amorphous and nanocrystalline graphitic carbon, nanotubes, fullerene-like structures, carbon onions, nanocrystalline diamond, and ordered graphite can be produced by selective etching or decomposition of metal carbides. The discussed method of carbon synthesis offers unique control over carbon microstructure and porosity at the nanoscale, thus allowing optimization of material properties for improved performance in advanced applications. These applications include hydrogen and methane storage media, electrodes in electrochemical energy-storage systems, tribological coatings, sorbents, and catalyst supports, among others.

## 6.1 INTRODUCTION

Carbon is a very special element. It plays a dominant role in the chemistry of all living organisms and is considered to be the only truly biocompatible material in all its forms. Carbon is the backbone of all organic substances and a whole class of materials — polymers — is based on carbon compounds. Being the sixth most common element in the universe, it is present in most of the things that surround us. In addition, carbon is the only element that has a major monthly scientific journal named after it — *Carbon*, published by Elsevier Science. This journal publishes papers dealing with carbon materials only: mainly amorphous carbons, graphite, diamond, fullerene-like structures, and nanotubes, which have numerous practical applications. Moreover, some of the carbon allotropes, diamond and fullerene, have journals dedicated to them as well (*Diamond and Related Materials*, *Fullerene Science and Technology*, and others).

There has been a new wave of interest in carbon materials caused by the recent “nano-” revolution, which has affected all science and engineering fields. Many nanotechnology papers are devoted to carbon-based nanostructures. Not only nanotubes and fullerenes but also nanodiamond, nanographite, carbon onions, and nanoporous carbons are steadily attracting increasing attention [1–7]. Biocompatibility of carbons may provide them a unique place in medical applications of nanotechnology [3,8–11].

The range of mechanical, optical, and electrical properties that carbon materials can provide is amazing. For example, diamond is one of the hardest materials known (microhardness of >100 GPa) and is used to make cutting tools and abrasives, while graphite is one of the softest materials (microhardness is about 1 GPa) and is used as a solid lubricant. While diamond is an optically transparent material, being a wide-band-gap semiconductor, graphite is not transparent, being a good electric conductor. The recently discovered carbon nanotubes (CNTs) are considered to be the strongest fibers known. Depending on their crystallographic structure, CNTs may have the conductivity of copper (metallic single-wall nanotubes) or silicon (semiconducting single-wall nanotubes). In addition to the known carbon allotropes, amorphous or disordered carbons form a whole new class of materials for which all properties, such as electrical conductivity, hardness, wear resistance, gas permeability, optical transparency, and many others can be finely tuned by controlling the  $sp^2/sp^3$  carbon ratio, porosity/density, size, and ordering of nanocrystals, and inclusions of various allotropic forms of carbon and other elements.

There are many ways to produce carbon materials. Very high temperatures are typically required for the synthesis of ordered graphite because of a very low mobility of carbon atoms in its

covalently bonded layers. Diamond is produced either at high pressures or by using plasma and other high-energy activation techniques. Many carbon nanostructures such as fullerenes, carbon onions, and nanotubes can be produced by vaporization of graphite (e.g., by electric current, laser heating, explosion, plasma, etc.) in the presence of an inert quenching gas. Chemical vapor deposition (CVD) is currently a common method for the synthesis of thin and thick films of disordered graphitic carbon, diamond, and nanotubes. Many porous and disordered carbons, including carbon fibers and activated carbons, are made by thermal decomposition of organic compounds.

The age of nanotechnology requires new methods that enable engineers to control the growth of carbon materials at the atomic level, and provide a better control over the structure of carbon materials as well as capability to produce selectively novel carbon structures such as nanotubes, onions, nanocrystalline diamond, or nanoporous carbon with a narrow pore-size distribution for gas storage, batteries, supercapacitors, and other applications.

Selective etching of carbides is considered to be a promising technique for the synthesis of various carbon structures [12]. Carbon produced by extraction of metals from metal carbides (MeCs) is called carbide-derived carbon (CDC). Leaching in supercritical water, high-temperature treatment in halogens, vacuum decomposition, and other methods can be used to remove metals from carbides, producing carbon coatings or bulk and powdered carbon. The linear reaction kinetics, which were demonstrated for chlorination of both bulk-sintered polycrystalline SiC [13] and single-crystalline SiC nanowhiskers [14], allow transformation to any depth, until the complete particle or component is converted into carbon. Carbide-derived carbon demonstrates a variety of carbon phases depending on experimental conditions. Amorphous and nanocrystalline graphitic carbon [15], nanotubes [16], fullerene-like structures [17], carbon onions [17,18], nanocrystalline diamond [19,20], and ordered graphite [21] have been reported. Thus, this method allows the synthesis of almost all carbon allotropes. Since the metal carbide lattice is used as a template and metal is extracted layer-by-layer, atomic-level control can be achieved in the synthesis process and the structure of the carbon can be templated by the carbide structure, with an opportunity for further structure modification by controlling the temperature, composition of the environment, and other process variables. An important advantage of the CDC process over the CVD or the PVD process for coating synthesis is that the transformation is conformal and does not lead to a change in the carbide sample size and shape. This may be of particular importance in nanotechnology when nanometer-range accuracy must be achieved.

Significant progress in CDC synthesis has been achieved over the past decade and a review of the synthesis has been published [22]. However, during the last few years, a significantly better understanding of the mechanisms involved in CDC formation has been achieved and better control over CDC properties has been developed. This chapter presents an up-to-date summary of the work done in this exciting area, which shows various approaches to CDC synthesis (leaching by supercritical water, halogens, salts, and decomposition in vacuum), analyzes similarities and differences between different techniques, and describes the variety of structures produced, their applications as well as the potential of the method for producing new carbon structures with required properties.

## 6.2 SELECTIVE ETCHING OF CARBIDES BY HALOGENS

### 6.2.1 CHLORINATION OF CARBIDES FOR PRODUCTION OF CHLORIDES

A manufacturing process based on the reaction of silicon carbide with chlorine gas was reported in 1918 for the first time [23]. Hutchins patented a method for the production of silicon tetrachloride using the reaction



The reaction was conducted by passing dry chlorine over silicon carbide heated to a temperature of 1000°C or above. The main product of the reaction, silicon tetrachloride vapor, passed through the

outlet pipe into a condenser. Residual carbon was disposed of. A development of this method was patented in 1956 [24]. In order to remove carbon without cooling off the reactor, air was periodically blown through it to burn the carbon waste. This method was widely used until the 1960s, when the availability of large quantities of inexpensive Si manufactured for the semiconductor industry led to the replacement of SiC with Si in SiCl<sub>4</sub> production.

Treatment of other MeCs in chlorine gas has been used to produce corresponding chlorides. Therefore, kinetics of chlorination of titanium and niobium carbides [25] and zirconium carbide [26] were studied. The reactions



(where  $x = 4$  when Me = Ti, Zr; and  $x = 5$  when Me = Nb) were conducted in a quartz-tube flow reactor in the temperature range 600 to 800°C in the case of TiC and NbC, and 450 to 950°C in the case of ZrC. Samples were produced by hot-pressing the carbide powders. The rates of the reactions were controlled by measuring the weight loss and the amount of chlorides. Carbon that formed on the surface of the samples in the course of the reaction was considered to be porous graphite or carbonaceous “cinder.” This layer did not affect the reaction rate at 400°C but at higher temperatures the diffusion resistance was considerable. In the case of niobium carbide, the chlorination rate at 600°C was higher than at 800°C. This phenomenon was attributed to the increased adhesion of the carbon layer to the carbide surface, but our recent work shows that it should primarily be attributed to changes in the CDC structure. For some carbides, the mechanism of the interaction with chlorine and the composition of reaction products may change with temperature. Therefore, it is important to consider the thermodynamics of the reactions of carbides with halogens.

## 6.2.2 THERMODYNAMIC SIMULATIONS

Thermodynamic simulations can be utilized to estimate the effect of various process parameters on CDC formation and help in choosing the optimum synthesis conditions [27]. Such simulations were performed on a number of carbides [28–32]. The Gibbs free energy minimization program (such as FactSage or ChemSage from GTT Technologies, Germany) was employed to estimate the equilibrium amounts of reaction species as a function of the chlorination temperature for different amounts of chlorine. The calculations were always done for a closed system with a constant total pressure of 1 atm. The gas phase was considered to be a mixture of ideal gases, and the solid phase was treated as a mechanical mixture of compounds with unit activities. It was found that carbon formation is possible by the halogenation of SiC, TiC, ZrC, V<sub>2</sub>C, NbC, Nb<sub>2</sub>C, TaC, Ta<sub>2</sub>C, Cr<sub>3</sub>C<sub>2</sub>, Mo<sub>2</sub>C, MoC, W<sub>2</sub>C, WC, BaC<sub>2</sub>, CaC<sub>2</sub>, SrC<sub>2</sub>, Al<sub>4</sub>C<sub>3</sub>, B<sub>4</sub>C, Fe<sub>3</sub>C, Ti<sub>3</sub>SiC<sub>2</sub>, and Ti<sub>2</sub>AlC. We will use the designation “MeC CDC” for carbon produced from a metal carbide (MeC) by selective removal of the metal.

Figure 6.1 shows an example of the thermodynamic calculations discussed with regard to the formation of carbon from ZrC for different amounts of initial Cl<sub>2</sub> content. Low content of Cl<sub>2</sub> in the reaction mixture limits the CDC conversion efficiency and the reaction products contain a considerable amount of untransformed carbide (Figure 6.1a). Adding more Cl<sub>2</sub> into the system results in the complete conversion of ZrC into ZrCl<sub>4</sub>, CCl<sub>4</sub>, and C. Different temperature ranges can be distinguished. In the low-temperature range (range I), no CDC synthesis is thermodynamically possible under equilibrium conditions due to the preferential formation of CCl<sub>4</sub> over solid C. The medium-temperature range (range II) corresponds to the formation of both CDC and CCl<sub>4</sub>. As can be seen from Figure 6.1, increasing the temperature leads to a higher CDC yield. In the high-temperature region (range III), no loss of carbon as CCl<sub>4</sub> is observed. Each range depends on the amount of Cl<sub>2</sub> used in the calculation. Range II, for example, changed from ~50–700°C to ~350–800°C and to ~450–870°C when the amount of Cl<sub>2</sub> changed from 3 to 5 and to 10 mol, respectively, while the amount of ZrC was kept constant (1 mol). The thermodynamic simulations suggest an optimum Cl<sub>2</sub>/ZrC ratio, where maximum carbon yield is achieved over a large temperature range. Adding too much or too little Cl<sub>2</sub> will affect the temperature range yielding maximum

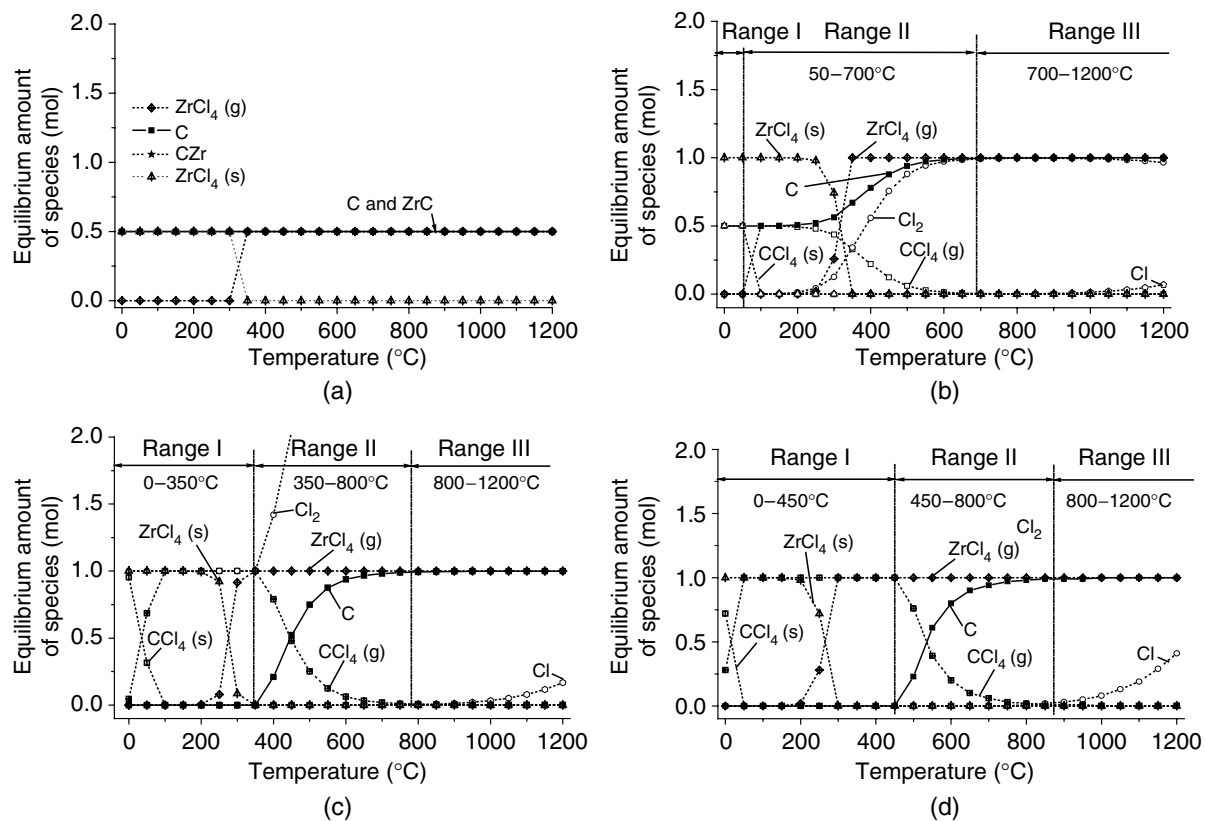


**FIGURE 6.1** Example of thermodynamic analysis for zirconium carbide chlorination: equilibrium amount of species vs. chlorination temperature for 1 mol (a), 3 mol (b), 5 mol (c), and 10 mol (d) of Cl<sub>2</sub> (From Dash, R.K. et al., Synthesis, structure and porosity analysis of microporous and mesoporous carbon derived from zirconium carbide, *Microporous and Mesoporous Mater.*, **86**, 50–57, 2005. Generally, three temperature ranges can be distinguished: range-I with no CDC formation predicted due to high stability of CCl<sub>4</sub> at low temperatures, range-II corresponding to the increase of CDC amount with temperature, and range-III is where CDC efficiently forms due to the higher stabilities of gaseous ZrCl<sub>4</sub> and solid C compared to CCl<sub>4</sub>. Each range clearly depends on the amount of Cl<sub>2</sub> in the system. Formation of solid ZrCl<sub>4</sub> is expected at temperatures below 300°C. Incomplete reaction takes place in case of insufficient Cl<sub>2</sub> amount.

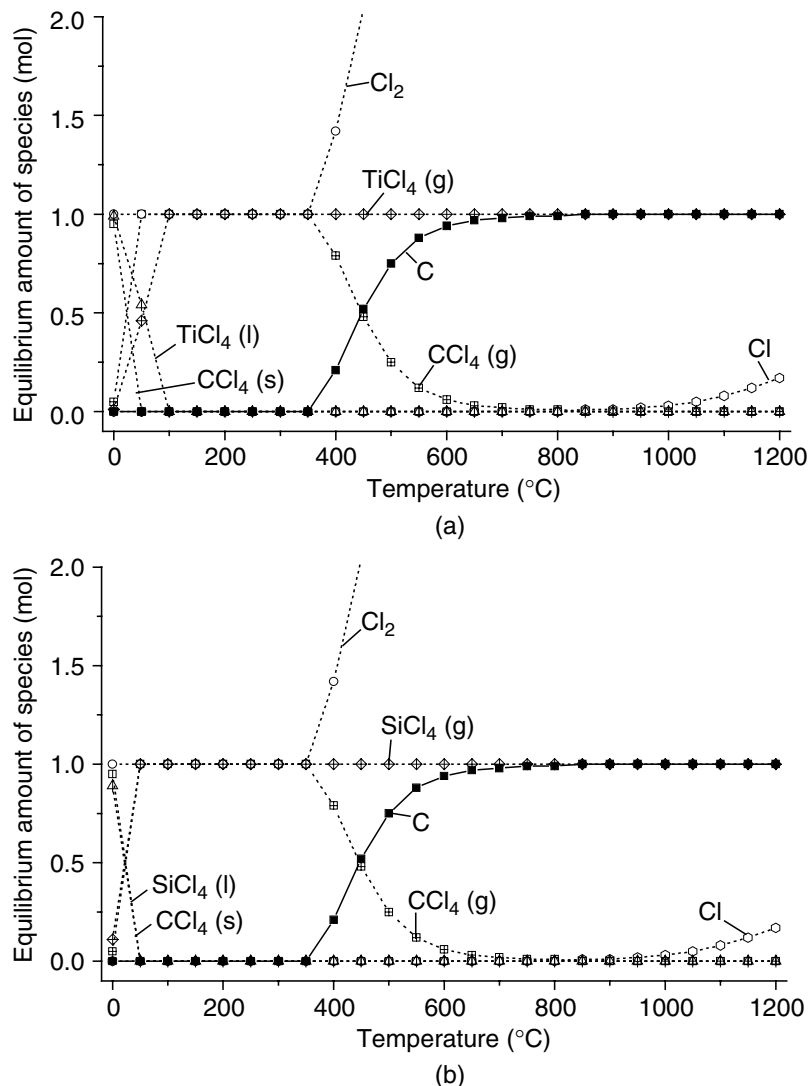
carbon. Undesirable formation of solid zirconium chloride is expected at temperatures below 300 to 350°C, depending on the initial Cl<sub>2</sub> amount.

Figure 6.2 shows equilibrium compositions for TiC/Cl<sub>2</sub> and SiC/Cl<sub>2</sub> systems (1:5 molar ratio) at ambient pressure. In both cases, no formation of solid chlorides is predicted and CDC forms in high yield at above 600°C. We have also conducted thermodynamic simulations for interactions of a variety of carbides with other halogens such as F and I and halogen-containing gases such as HCl and HF (data not shown), and confirmed the possibility of CDC formation in nonchlorine environments.

The thermodynamic calculations provide information about a closed system in equilibrium. The experimental set-up used for CDC synthesis is in most cases an open system, where gaseous reaction products are continuously removed with a gas flow, and the actual product composition may be determined by the kinetics of the process. However, the results obtained provide general guidelines for the experimental design. They show that selective removal of metals is possible by using small amounts of Cl<sub>2</sub>, as well as suggesting that a moderate amount of Cl<sub>2</sub> is the key to efficient CDC synthesis. Excess Cl<sub>2</sub> can be used at high temperatures, when CCl<sub>4</sub> is unstable to accelerate the process.

### 6.2.3 HISTORIC OVERVIEW OF CARBIDE-DERIVED CARBON STUDIES

Carbide-derived carbon did not attract major attention from researchers until 1959, when Mohun [15] introduced “a fourth class of amorphous carbons” along with the three known ones (hard carbons,



**FIGURE 6.2** Examples of thermodynamic analysis for chlorination of TiC (a) and SiC (b) in 5 mol of  $\text{Cl}_2$ , demonstrating efficient formation of CDC at above  $600^\circ\text{C}$ .

soft carbons, and carbon black). The term “mineral carbons” was proposed for carbons formed by the chlorination of inorganic carbides to distinguish them from carbons of organic origin. Unlike organic carbon, which also includes substantial quantities of hydrogen and other elements, CDC was claimed to be real elemental amorphous carbon. Chlorination of silicon, aluminum, boron, titanium, zirconium carbides, and zirconium carbonitride was carried out in the temperature range from  $150$  for  $\text{ZrC} \cdot \text{ZrN}$  to  $1650^\circ\text{C}$  for SiC in chlorine flow. Reactor tubes were made of quartz or mullite and were provided with an external electric heater. Owing to the strong exothermic effect of the reaction and the substantial size of the samples (20 to 250 g), temperature of the sample was rather difficult to control. After the chlorination process was completed, carbon samples were cooled in an atmosphere of chlorine or dry nitrogen and treated to remove the residual chlorine.

Mohun extended his study and eventually patented the new materials and the processes of their production [33,34]. Figure 6.3 shows some sorption properties of SiC CDC reported in these patents as a function of chlorination temperature and the cooling environment. Vapor adsorption capacity of the CDC generally peaked at some intermediate chlorinated temperatures and decreased when the processing temperature increased to  $1650^\circ\text{C}$ , possibly due to the graphitization of the CDC and the corresponding decrease of the specific surface area (SSA, surface area of material per unit weight) as we know from our experiments. Vapor adsorption also noticeably increased when samples were

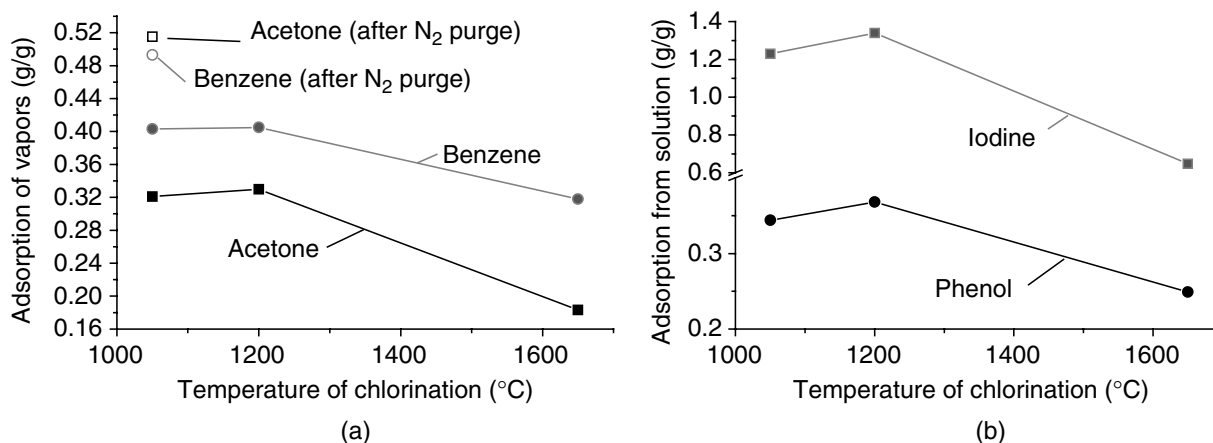


**FIGURE 6.3** Adsorption capacity of SiC CDC cooled in Cl<sub>2</sub> as a function of chlorination temperature: vapor adsorption (a) and adsorption from solution (b). A maximum adsorption at intermediate temperature was observed. Dechlorination of SiC CDC prepared at 1050°C by purging N<sub>2</sub> through it resulted in a noticeable increase of the vapor adsorption capacity.

cooled in N<sub>2</sub> rather than in Cl<sub>2</sub>, demonstrating the importance of the dechlorination procedure. The patents also give a detailed description of all the methods employed for the dechlorination of the CDC samples. The techniques described include heating in static air, heating in gas stream (air, nitrogen, water vapor, and carbon dioxide), vacuum dechlorination, and wet dechlorination with the use of various washing solutions. Chlorine content in the samples was controlled by weight loss during dechlorination, and measuring the pH of the aqueous suspension. It was found that the flow of nitrogen or other gases over the sample heated at 150°C at atmospheric pressure provided rapid and complete dechlorination. Of considerable importance are the chlorides, which remain trapped in the carbon when reaction is complete. It was shown that they are readily removed by any cyclic fluctuation in temperature or pressure carried out at the same time as dechlorination. Another interesting property of CDCs discovered in the studies was the absence of measurable paramagnetic electron spin absorption. This distinguishes CDCs from organic chars in which free radicals are trapped during carbonization of organic matter.

The chlorination set-up used in most of the CDC experiments is a common set-up for treatment of the solid samples in the gas flow at elevated temperatures. Figure 6.4 shows a version of the experimental apparatus.

#### 6.2.4 KINETICS OF HALOGENATION OF CARBIDES

The kinetics of CDC formation has been studied for various carbides. In 1960, Kirillova et al. [25] investigated the chlorination of bulk TiC and NbC and observed a linear increase in the CDC layer thickness with time, suggesting that the transformation rate is not controlled by the diffusion of gases. The chlorination rates were determined, and activation energies of CDC synthesis in the 400 to 800°C range were found to be 50 and 38 kJ/mol for TiC CDC and NbC CDC, respectively. The chlorination kinetics of a lower zirconium carbide was discussed in the Ph.D. dissertation of Vasilenko [35] in 1956. Experiments were carried out in the 400 to 800°C range on bulk and powder samples. It was shown that CDC synthesis follows linear reaction kinetics and that the chlorination temperature has only a small influence on the CDC synthesis rate.

In 1964, Kuriakose and Murgrave published the results of their studies on the fluorination of bulk ZrC and HfC in the 300 to 900°C range [36,37]. They determined the activation energies of the fluorination to be 92 kJ/mol and observed a constant fluorination rate with time. In 1966 Orekhov et al. [26] performed in-depth studies of chlorination kinetics of bulk ZrC in the 450 to 950°C range. The activation energy of the chlorination was found to increase from ~67 to

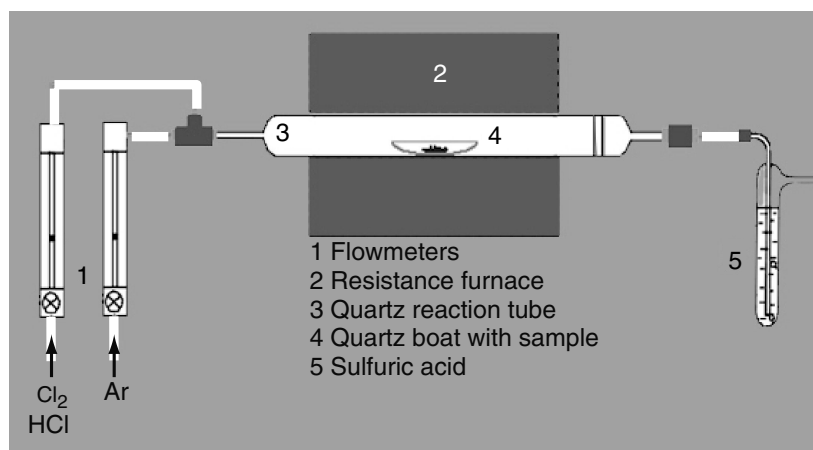


**FIGURE 6.4** Typical experimental set-ups used for the chlorination of carbides.

~121 kJ/mol with an increase in the chlorination temperature. Chlorination rates were determined for various temperatures and Cl<sub>2</sub> gas velocities. The increase of CDC thickness was linear with time for relatively thin coatings (<500 μm). However, for thicker CDC layers, the diffusion became the limiting factor of the transformation rate, resulting in a parabolic dependence of the CDC thickness over time. More recent studies of the halogenation of various carbides (see, [38]) generally confirmed the linear transformation kinetics of bulk polycrystalline carbides to CDC, which allows easy and precise control over the coating thickness, desirable for most of the applications. Recent transmission electron microscopy (TEM) studies on the chlorination of SiC nanowhiskers [14] revealed linear kinetics for CDC transformation of single-crystalline carbides starting from the initial stage, when a nanometer-thick coating is formed.

### 6.2.5 CONSERVATION OF SHAPE

As mentioned in the introduction, halogenation of carbides results in a conformal transformation. Conservation of shape during the CDC synthesis had been observed in macro and microscopic objects [38,39] for a long time. However, most studies were conducted on powders, fibers, and bulk samples, and until very recently [14], it was not known how precisely the carbon formed could follow the original shape of the carbide crystal. In addition, it was not known if the stresses existing at the interface between CDC and the substrate might destroy nanoscale objects having a high aspect ratio (e.g., components of SiC-based microelectromechanical systems [MEMS], during the transformation). Our recent TEM studies [14] provided direct nanoscale observations of all stages of the CDC transformation (Figure 6.5). They revealed that no matter what the final structure of the transformed carbon or what metal extraction method was employed, a complex shape of a carbide nano-object could be preserved.

### 6.2.6 NANOPOROUS STRUCTURE AND ADSORPTION PROPERTIES

#### 6.2.6.1 Pore Formation

Selective removal of metals from MeCs generally results in the formation of porous carbon with a density lower than that of graphite. The size of pores in the CDC is influenced by the distribution of carbon atoms in the initial carbide, the CDC's atomic structure, the amounts of chlorides and chlorine trapped in the CDC, the size of the chloride molecule, the presence of catalytic particles, and the effect of optional post-treatments, such as activation, or mild oxidation.

Porous structure and molecular sieve properties of CDC were first investigated by Boehm and Warnecke [40] in 1975. Carbon samples were prepared by treating tantalum and silicon carbides in



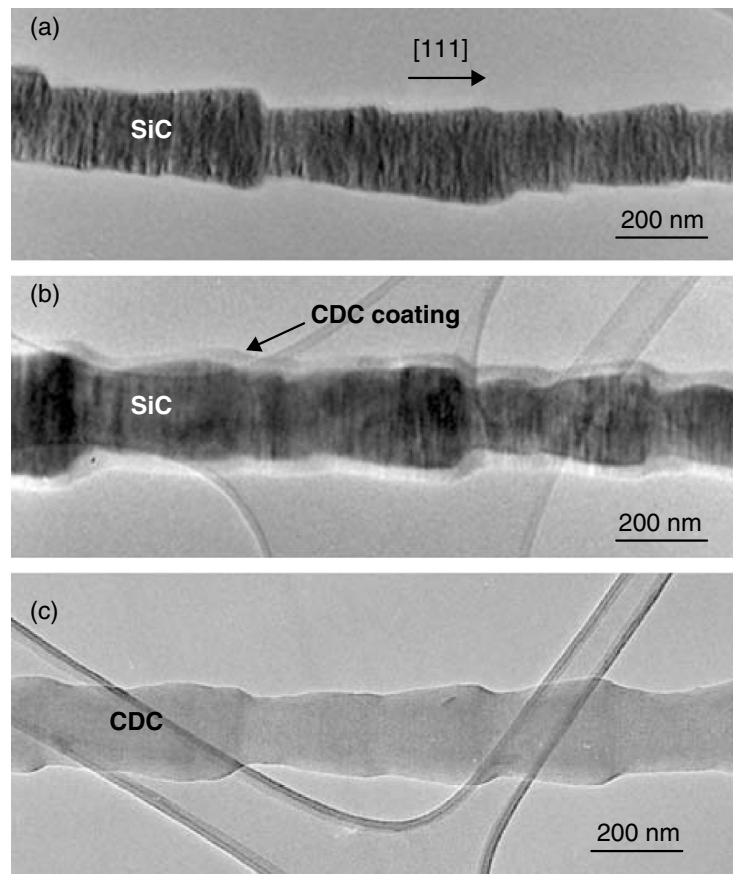


**FIGURE 6.5** Transmission electron microscopy micrographs of SiC whiskers at different stages of the transformation to carbon: (a) initial: as-received SiC whisker, (b) intermediate: carbon coating on a SiC whisker, and (c) final: completely transformed to amorphous carbon. (From Cambaz, Z.G. et al., Conservation of shape during formation of carbide-derived carbon on silicon carbide nano-whiskers, *J. Am. Ceram. Soc.*, 2005, in press.) The whiskers were treated in  $\text{Cl}_2$  at 700°C (b) and 1200°C (c).

chlorine flow at 500 and 900°C, respectively. The completeness of the reaction was confirmed by the disappearance of the x-ray diffraction (XRD) peaks of the original carbides. The CDC samples produced from TaC were additionally heat-treated at various temperatures. Sorption isotherms (the quantity of the gas adsorbed onto or desorbed from the solid adsorbent surface at a constant temperature in the range of equilibrium vapor pressures) of CDCs were measured for  $\text{N}_2$  at  $-196^\circ\text{C}$ , for  $\text{CO}_2$  at  $0^\circ\text{C}$ , and for a variety of organic adsorptives at  $25^\circ\text{C}$ . All isotherms were of Type I in the Brunauer classification, which indicated the nanoporous structure of the CDC samples. There was a peak in  $\text{N}_2$  uptake for CDC from TaC after heat treatment at  $1450^\circ\text{C}$ . The low sorption capacity of the CDC prepared at  $500^\circ\text{C}$  was explained by the presence of tantalum pentachloride, which blocked a considerable part of the pore volume. However, our experience shows that a very small pore size can also limit the applicability of sorption techniques for the analysis of CDC produced from transition MeCs at  $\sim 500^\circ\text{C}$ . The maximum pore volume accessible to  $\text{N}_2$  in CDC after heat treatment at  $1450^\circ\text{C}$  was  $0.644 \text{ cm}^3/\text{g}$ , which is in excellent agreement with the theoretically calculated pore volume value of  $0.645 \text{ cm}^3/\text{g}$ . Evaluation of the  $\text{CO}_2$  isotherms of the CDCs heat-treated in the range 500 to  $1100^\circ\text{C}$  gave a maximum pore volume of  $0.273 \text{ cm}^3/\text{g}$ , indicating that not all the pores were accessible to larger  $\text{CO}_2$  molecules. Adsorption of organic vapors (benzene, tetrachloromethane, toluene, and  $\alpha$ -pinene) demonstrated strong molecular sieve effects for CDC from TaC heat-treated above  $1500^\circ\text{C}$ . CDC from SiC post-treated in hydrogen at  $800^\circ\text{C}$  was proven to be suitable for gas chromatography. It was possible to separate low-molecular weight gases with its use. For example,  $\text{O}_2$ ,  $\text{N}_2$ ,  $\text{CO}$ , and  $\text{CO}_2$  could be separated with a 1 m column at  $30^\circ\text{C}$  and  $\text{CH}_4$ ,  $\text{C}_2\text{H}_2$ ,  $\text{C}_2\text{H}_4$ , and  $\text{C}_2\text{H}_6$  at  $100^\circ\text{C}$ .

The porous structure and adsorption properties of CDC from silicon carbide and carbides of transition metals of IV to VI groups were studied by Fedorov et al. [41–44] in the early 1980s. Three forms of SiC (green and black  $\alpha$ -SiC and  $\beta$ -SiC, temperature is not indicated) [41]; TiC in the temperature range 500 to 1100°C [42]; ZrC, HfC, VC, NbC, WC, Cr<sub>3</sub>C<sub>2</sub>, Mo<sub>2</sub>C, B<sub>4</sub>C, and UC at 700°C [43] were treated in chlorine gas flow in the quartz-tube reactor. Vapors of bromine and iodine, besides chlorine gas, were used for etching zirconium carbide [44]. Completeness of the reaction was controlled by the weight loss during the process and by the carbide contents in the sample. The porous structure of the CDCs obtained was studied by a combination of pycnometric, mercury-porosimetric, and sorption methods. Theoretical values of the apparent density  $\delta$  were calculated assuming that no shrinkage of the samples occurred during the chlorination process (confirmed by electron microscopy), using the following formula:

$$\delta = dA \quad (6.3)$$

where  $d$  is carbide density and  $A$  is the mass fraction of carbon in the carbide. Theoretical total pore volume  $V_{\Sigma}$  was calculated on the basis of pycnometric density of carbon ( $d_c = 2.00 \text{ g/cm}^3$ ) by the formula

$$V_{\Sigma} = \frac{1}{\delta} - \frac{1}{d_c} \quad (6.4)$$

It was found that the theoretical  $\delta$  and  $V_{\Sigma}$  values are generally in satisfactory agreement with experimental data taking into account the porosity of the initial carbide granules.

According to the IUPAC definition, porosity in solids is classified by pore size [45]:

1. pores with widths exceeding about 50 nm are called *macropores*;
2. pores of widths between 2 and 50 nm are called *mesopores*;
3. pores with widths not exceeding about 2 nm are called *micropores*.

As currently accepted, we use the term *nanopores* for the pores of  $\leq 2$  nm, which reflects their actual size more appropriately.

Sorption analysis was carried out with the use of benzene vapor as an adsorptive agent. Isotherms were generally of Type I in the Brunauer classification that characterizes these carbons as nanoporous adsorbents. The sole exception was Mo<sub>2</sub>C CDC, which developed mesopore volume. This was explained by the larger distances between the carbon atoms in Mo<sub>2</sub>C compared to the other transition MeCs, and the correspondingly smaller density of Mo<sub>2</sub>C CDC. Our experience shows that the pore-size distribution may also be affected by many other parameters, including the CDC microstructure, which, in turn, depends on the carbide and the temperature of its chlorination. The isotherms were evaluated using Dubinin's theory of volume filling of nanopores [46,47]. The characteristic energy of adsorption, which is the principal parameter of nanoporous structure of CDCs, was at the level of the values for the best activated carbons.

A mechanism of nanopore formation in carbon materials produced by the interaction of carbides with chlorine was proposed in [48]. In essence, this theory is as follows: a series of nonlinear chemical reactions proceed in the course of a chemical interaction between chlorine and carbide. If the external parameters, the component fluxes, and the diffusion rates satisfy certain relations, the self-organization process can occur. This process results in the creation of a periodic nanoporous structure in the carbon material formed. A mathematical model was proposed, the main characteristics of the process were calculated, and the restrictions on the parameters at which the formation of the porous structure becomes possible were found.

### 6.2.6.2 Effect of the Chlorination Temperature

Temperature dependence of the pore-size distribution, BET specific surface area ( $S_{\text{BET}}$ ) [216], and microstructure of Ti<sub>3</sub>SiC<sub>2</sub>, Ti<sub>2</sub>AlC, B<sub>4</sub>C, ZrC, and SiC CDCs were studied in the range of 200 to 1200°C

[30,31,49–52]. Samples were prepared in a horizontal tube furnace (Figure 6.4). After chlorination, the samples were purged with Ar for ~15 min at the chlorination temperature and then cooled down in an Ar atmosphere. A combination of TEM, Raman spectroscopy, and XRD was employed for the analysis of carbon microstructure. Pore structure was studied using Ar or CH<sub>3</sub>Cl sorption, or small-angle x-ray scattering (SAXS). It was discovered that chlorination temperature might control the pore structure and the pore size with sub-angstrom accuracy. Figure 6.6 shows the differential pore-size distributions for Ti<sub>3</sub>SiC<sub>2</sub> CDC and the dependence of the pore size on the processing temperature. Low-temperature chlorination resulted in very uniform pores [49]. Pore-size distribution for these CDCs was narrower than that of single-walled carbon nanotubes (SWCNT) and activated carbons, and comparable to that of zeolites. Increasing CDC synthesis temperature generally leads to pore enlargement and eventually (above 1100°C in case of Ti<sub>3</sub>SiC<sub>2</sub> CDC) to a broader distribution of pore sizes. Similar dependences were demonstrated for CDCs produced from other carbides. Figure 6.7 and Figure 6.8 show the differential pore-size distribution of Ti<sub>2</sub>AlC CDC and ZrC CDC in the temperature range 400 to 1200°C.

The observed changes in the pore structure are inherently connected to the changes in the microstructure of the CDCs. Uniform, relatively small pores formed during chlorination at lower temperatures were found to be associated with the amorphous structure of the CDCs, while less uniform and generally larger pores formed at higher synthesis temperatures were linked to graphitic ribbon network structure (see Figure 6.7 and Figure 6.8).

$S_{\text{BET}}$  as a function of synthesis temperature of the as-prepared CDCs generally follows a “bell-shape” curve (Figure 6.9). Samples prepared at low temperature are of amorphous structure, have pores filled with considerable amounts of trapped chlorine and chlorides, and thus show a small effective  $S_{\text{BET}}$ . It is also possible that some of the pores are too small to be fully accessible to N<sub>2</sub> or Ar molecules used for  $S_{\text{BET}}$  measurement. As CDC processing temperature increases, the size of pores in the CDC increases as well. This allows chloride molecules to be removed from the pores more efficiently, and the effective  $S_{\text{BET}}$  to be increased. In addition, high processing temperatures increase the diffusion rates of gases (chlorides, chlorine, Ar, etc.) into and out of pores, thus contributing to the CDC cleaning efficiency and the corresponding increase in an accessible CDC surface area. However, above a certain temperature, multiwalled graphitic structures start forming in

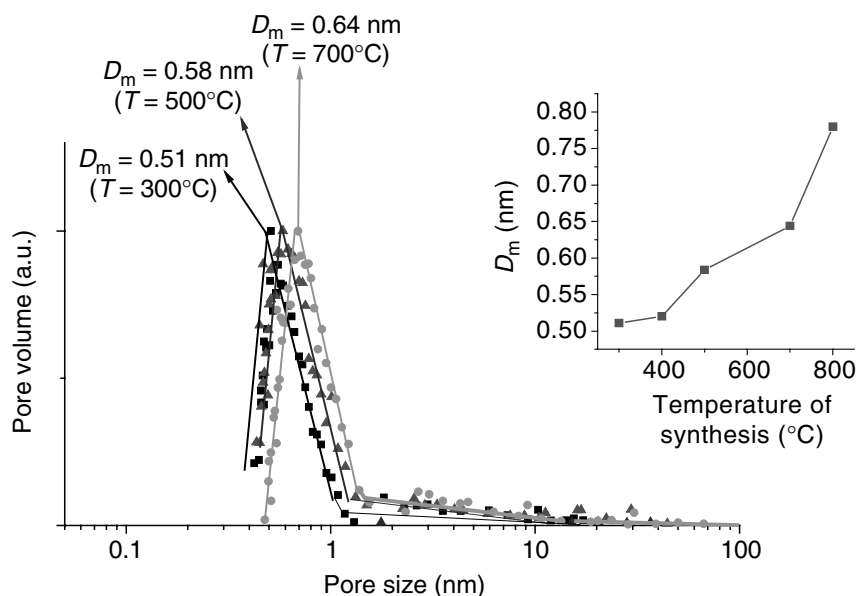


**FIGURE 6.6** Pore-size distributions of Ti<sub>3</sub>SiC<sub>2</sub> CDC showing uniform pore size when produced at low temperatures (From Gogotsi, Y. et al., Nanoporous carbide-derived carbon with tunable pore size, *Nature Mater.*, **2**, 591–594, 2003.). The calculations were performed using the Horvath–Kawazoe method and assuming a slit pore model. Inset (top right): demonstrates fine tunability of the pores by varying the synthesis temperature.  $D_m$  represents the maximum pore-size distribution.

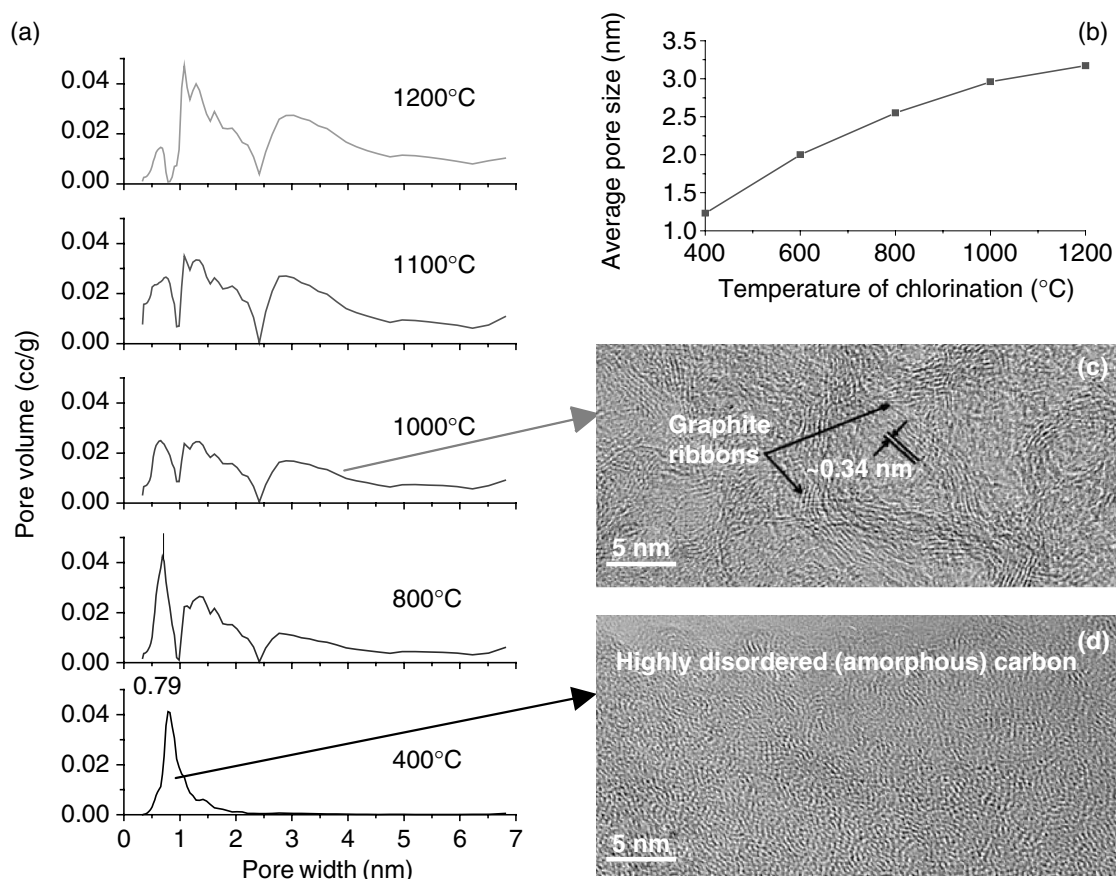


**FIGURE 6.7** Pore-size distribution (a) and the weighted average pore size (b) of  $\text{Ti}_2\text{AlC}$  CDC as a function of chlorination temperature, showing drastic changes in the pore structure (From Hoffman, E.N. et al., Synthesis of carbide-derived carbon by chlorination of  $\text{Ti}_2\text{AlC}$ , *Chem. Mater.*, **17**, 2317–2322, 2005.). The distributions were calculated using DFT, assuming slit pores. The pore volume was used as a weighting factor for the calculation of the average pore size in the 1–7 nm range. The TEM micrographs show the structure of the  $\text{Ti}_2\text{AlC}$  CDC produced at 1000°C (c) and 400°C (d), revealing the correlation between the microstructure and the porosity.

CDC. The area between the walls in such structures is generally not accessible to  $\text{N}_2$  and Ar, as the interwall spacing is generally close to interplanar spacing in graphite (0.335 nm), which is too small for  $\text{N}_2$  or Ar to fit in between. As such, formation of a substantial amount of well-organized multiwalled graphite ribbons in CDC may lower its  $S_{\text{BET}}$  value. The optimum synthesis temperature for large  $S_{\text{BET}}$  CDC would correspond to the conditions when all of the pores formed in the CDC are open; large enough to be accessible to inert gases and free from contaminants, while the amount of multiwalled graphite ribbons in the CDC is limited.

The temperature of graphite formation in CDC seems to depend strongly on the initial carbide, its purity, presence of catalyst particles, and halogen chosen. SiC CDC, for example, shows very limited formation of graphite ribbons even at 1200°C synthesis temperature and its  $S_{\text{BET}}$  does not decrease substantially at temperatures below 1200°C (Figure 6.9). In contrast, Dimovski et al. [21] observed the formation of planar microcrystalline graphite during the CDC synthesis from  $\text{Fe}_3\text{C}$  at 1200°C. It was suggested that above the eutectic temperature in the Fe– $\text{Fe}_3\text{C}$  system (1130°C) a liquid phase formed, which was further supersaturated with carbon due to the removal of Fe upon interaction with  $\text{Cl}_2$ , and that graphite crystals nucleated and grew from this melt. It should also be mentioned that significant graphitization was observed even at lower temperatures (above 600°C). The catalytic effect of iron played a significant role in the phenomena observed.

Temperature dependence of  $\text{Al}_4\text{C}_3$  CDC structure was reported in [53,54]. The nitrogen sorption isotherm of a low-temperature  $\text{Al}_4\text{C}_3$  CDC (300°C) was of a type I in the Brunauer classification,

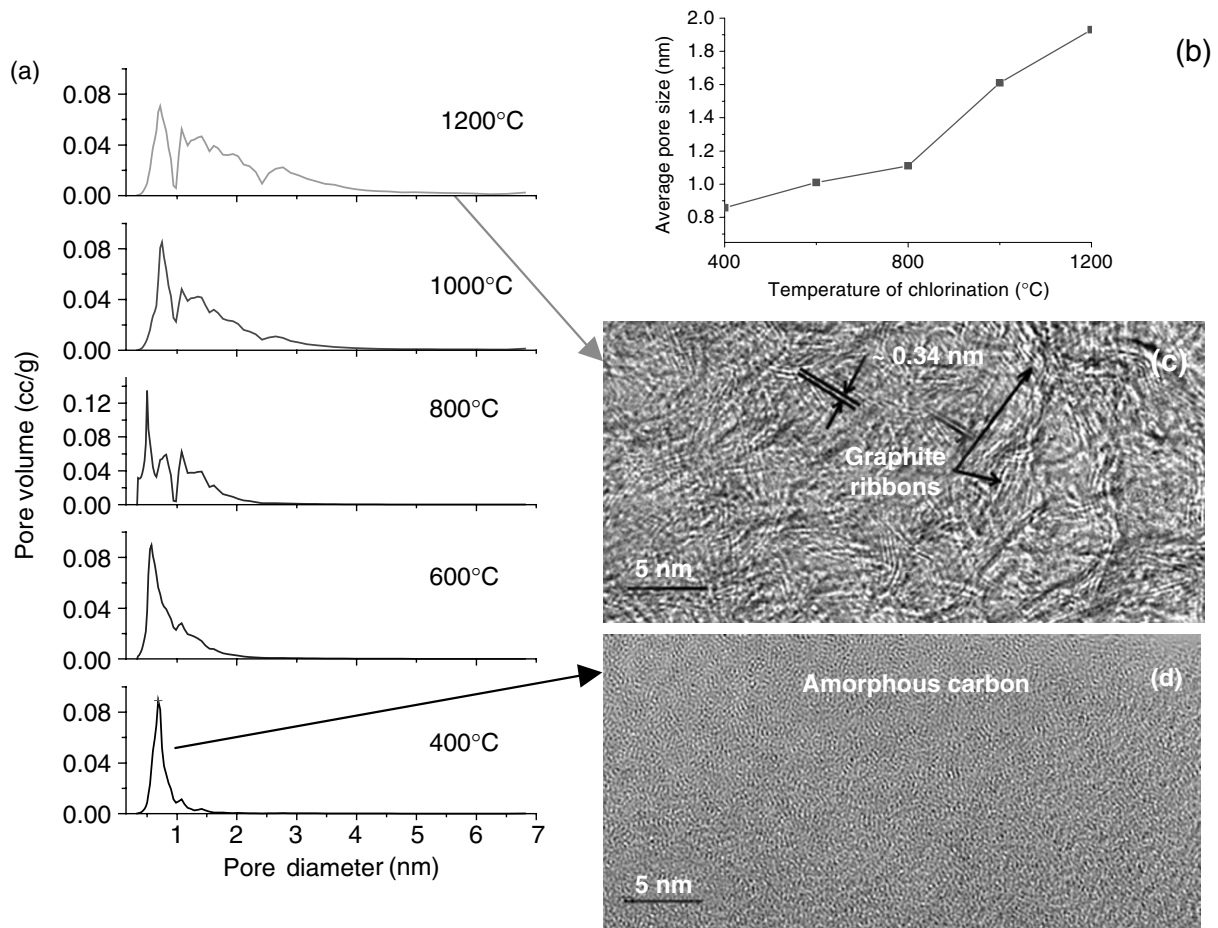


**FIGURE 6.8** The DFT pore-size distribution (a) and the weighted average pore size (b) of the ZrC CDC as a function of chlorination temperature. (From Dash, R.K. et al., Synthesis, structure and porosity analysis of microporous and mesoporous carbon derived from zirconium carbide, *Microporous and Mesoporous Mater.*, **86**, 50–57, 2005.), showing similar dependence to that observed for  $\text{Ti}_2\text{AlC}$  CDC. Slit pores were assumed for DFT calculations and the pore volume was used as a weighting factor for the calculation of the average pore size. The TEM micrographs show the structure of the ZrC CDC produced at 1000°C (c) and 300°C (d).

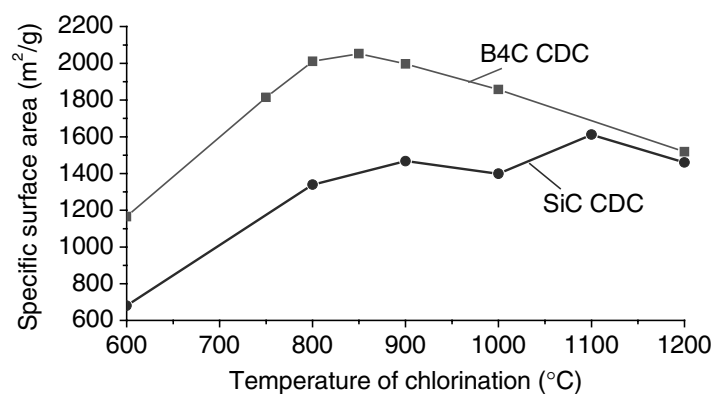


**FIGURE 6.9** The BET specific surface area of the B<sub>4</sub>C CDC and SiC CDC as a function of chlorination temperature, showing the maximum value at intermediate temperatures (From Dash, R.K. et al., *Microporous carbon derived from boron carbide*, *Microporous Mesoporous Mater.*, **72**, 203–208, 2004; Gogotsi, Y. et al., Effect of synthesis temperature on structure and properties of nanoporous carbon derived from silicon carbide, *Carbon*, 2005, in press.). Clogging of the CDC pores when synthesis is performed at low temperature and graphitization observed at higher temperatures limit the surface area achieved. The decrease in the surface area in SiC CDC is not pronounced even at 1200°C as in this material noticeable graphitization starts at higher temperatures.

indicating that this sample had a nanoporous structure. High-resolution transmission electron microscopy (HRTEM) revealed the amorphous structure of the material. However, CDCs produced at 500 to 900°C demonstrated considerable graphitization, as confirmed by both HRTEM and XRD, and their sorption isotherms were of a type IV, which indicates the presence of mesopores [45]. The average pore size was calculated according to the Barrett Joyner Halenda (BJH) theory [55] and the  $S_{\text{BET}}$  values of  $\text{Al}_4\text{C}_3$  CDC were plotted as a function of chlorination temperature in Figure 6.10. The large  $S_{\text{BET}}$  of  $\text{Al}_4\text{C}_3$  CDC synthesized at 300°C is probably related to the efficient removal of the chlorides and the relatively large pores fully accessible to  $\text{N}_2$ . Upon increasing the processing temperature,  $S_{\text{BET}}$  steadily decreased as a result of CDC graphitization. It is necessary to note that the presence of condensed  $\text{AlCl}_3$ , which has a melting point of 192°C, can affect the pore structure of this CDC.

Temperature dependence of the pore structure of TiC CDC was investigated in [56]. As in some of the previous studies, TiC CDC sample chlorinated at a lower temperature demonstrated an apparent density higher than the theoretical value. The presence of  $\text{TiCl}_4$  in a significant part of the pore volume provided a possible explanation. Samples produced in the 700 to 1100°C range showed virtually equal values of total pore volume, while their pore-size distributions were different. Volume occupied by mesopores increased with increasing chlorination temperature as a result of the ordering of turbostratic carbon structures. Figure 6.11 shows the mesopore volume measured by means of benzene adsorption and mercury porosimetry as a function of the synthesis temperature. The differences in the mesopore volume obtained by these two techniques are explained by the failure of mercury porosimetry to detect pores of equivalent radius below 3 nm. CDC produced at 1100°C evidently had some mesopores of less than 3 nm in equivalent size.

### 8.2.6.3 Effect of the Carbide Structure

The distribution of carbon atoms within carbides may differ substantially even when densities of the corresponding CDCs are similar. The carbide microstructure discussed may have a strong influence on the microstructure of the CDC produced and thus on its pore shape and pore size. Figure 6.12 shows a layered C structure in a hexagonal  $\text{Ti}_3\text{SiC}_2$  and a uniform distribution of C in a cubic SiC (3C polytype), while Figure 6.13 compares the microstructure of the CDCs obtained at 1200°C. It is clearly seen that under the same processing conditions, CDC obtained from  $\text{Ti}_3\text{SiC}_2$  consists of a disordered network of graphite ribbons (Figure 6.13a), whereas CDC from SiC shows an amorphous structure (Figure 6.13b).

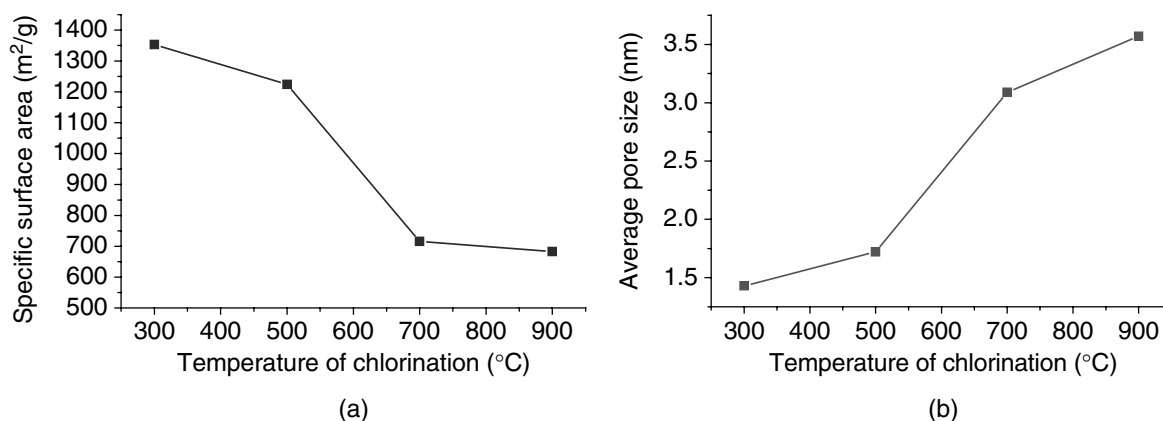


**FIGURE 6.10** The BET-specific surface area (a) and the calculated average pore size using the BJH theory (b) of  $\text{Al}_4\text{C}_3$  CDC as a function of chlorination temperature. (From Leis, J. et al., Carbon nanostructures produced by chlorinating aluminium carbide, *Carbon*, **39**, 2043–2048, 2001.) A sharp decrease in the surface area and increase of the pore size value occur at 500°C as a result of low-temperature formation of graphitic structures in such material. It is believed that formation of these structures was facilitated by the presence of transition metal impurities in the  $\text{Al}_4\text{C}_3$ .

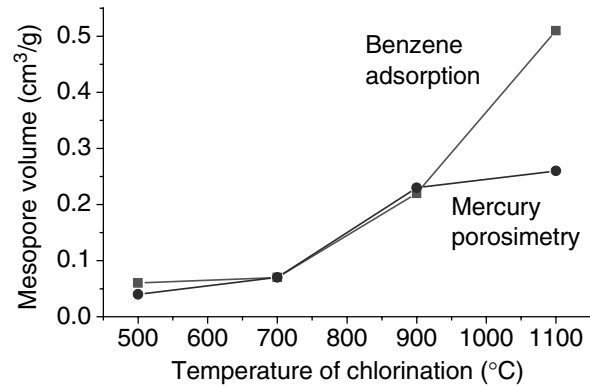


**FIGURE 6.11** The mesopore volume of TiC CDC measured using benzene adsorption and mercury porosimetry as a function of chlorination temperature (From Fedorov, N.F. et al., Porous structure of carbon adsorbents from titanium carbide, *Z. Prikladnoi Khimii*, **55**, 46–50, 1982 [in Russian]). Inability of mercury porosimetry to detect pores smaller than 3 nm resulted in considerable difference in the mesopore volume measured in the material processed at 1100°C.

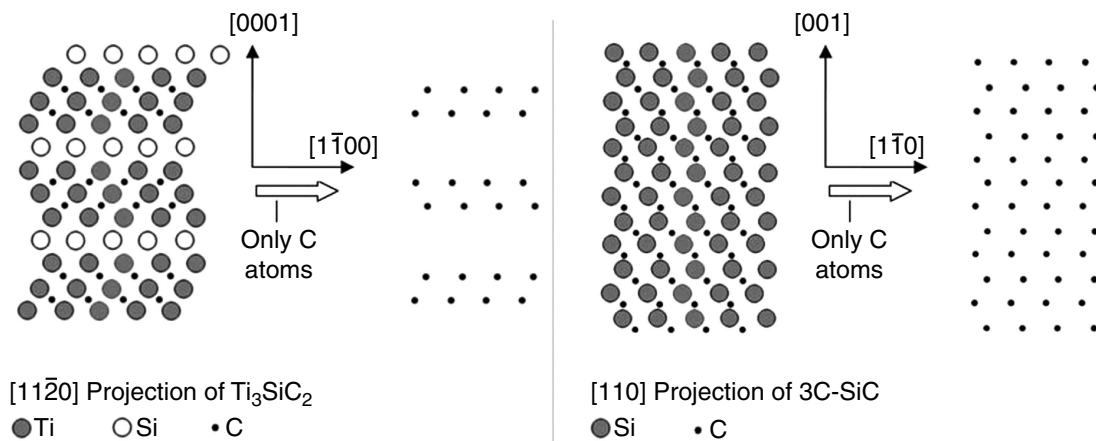


**FIGURE 6.12** Schematic of the lattice structure of  $Ti_3SiC_2$  with and without Ti and Si atoms shown (a), and schematic of the lattice structure of SiC with and without Si atoms shown (b).

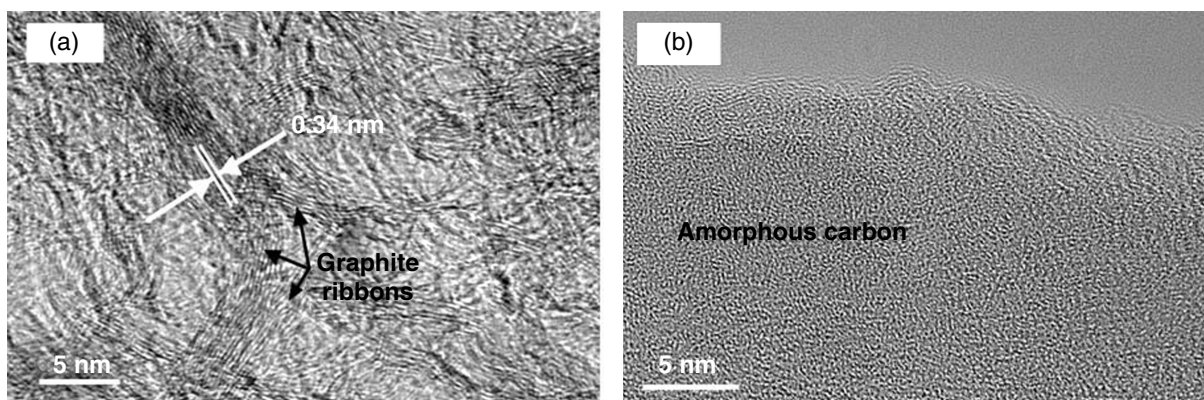


**FIGURE 6.13** High-resolution TEM of CDC produced at 1200°C from  $Ti_3SiC_2$  (a) and SiC (b) at 1200°C. (From Yushin, G. et al., Synthesis of nanoporous carbide-derived carbon by chlorination of titanium silicon carbide, *Carbon*, **43**, 2075–2082, 2005; Gogotsi, Y. et al., Effect of synthesis temperature on structure and properties of nanoporous carbon derived from silicon carbide, *Carbon*, 2006, in press.)

#### 6.2.6.4 Effect of Catalysts on the Surface Area and Microstructure of CDC

The influence of 3d-transition metal catalysts on the temperature dependence of the microstructure and  $S_{\text{BET}}$  of TiC CDC was studied in [57]. Titanium carbide powder samples were chlorinated for 1 h in the temperature range 400 to 1200°C. Pure TiC samples as well as TiC with an added mixture of Co, Ni, and Fe chlorides (~73 mg of each chloride per gram of TiC) were converted into CDC.  $S_{\text{BET}}$  was calculated from the data of  $\text{N}_2$  sorption at  $-196^\circ\text{C}$  (Figure 6.14a); micropore volume was determined by measuring dynamic benzene adsorption at room temperature (Figure 6.14b). The  $S_{\text{BET}}$  temperature dependence followed the expected bell-like curve, where the trapped chlorides lowered the accessible surface area in samples processed at low temperatures, and graphitization of carbon with the formation of multiwalled graphite structures limited the surface area of the material formed at higher temperatures. The slow increase in the micropore volume with an increase in chlorination temperature could be explained by mild oxidation or structural change during the CDC synthesis. The effect of metal catalysts was not significant at temperatures below 700°C. But at higher temperatures, the catalysts strongly increased the graphitization degree and correspondingly lowered the  $S_{\text{BET}}$  value. Judging from the  $S_{\text{BET}}$  values and XRD spectra, TiC sample chlorinated at 900°C in the presence of catalysts showed a higher degree of graphitization (thickness of graphitic structures in the 0 0 2 direction) than the pure TiC sample chlorinated at 1200°C.

#### 6.2.6.5 Effect of a Halogen

The influence of the nature of reacting halogens on the porous structure of CDC was demonstrated in [44]. In that study, ZrC CDC was synthesized by treatment in chlorine, bromine, and iodine at 800°C. Equal values of the total pore volume were found by measuring benzene adsorption in all the samples. At the same time, their sorption capacities for halogens differed significantly. The highest capacities for bromine vapor and iodine adsorption were observed in the case of the CDC sample prepared by bromination and iodination, respectively. This was considered evidence that the porous structure of CDC was affected by the size of the halogen and evolving zirconium tetrahalogenide molecules as well as by surface termination of CDC produced using different halogens.

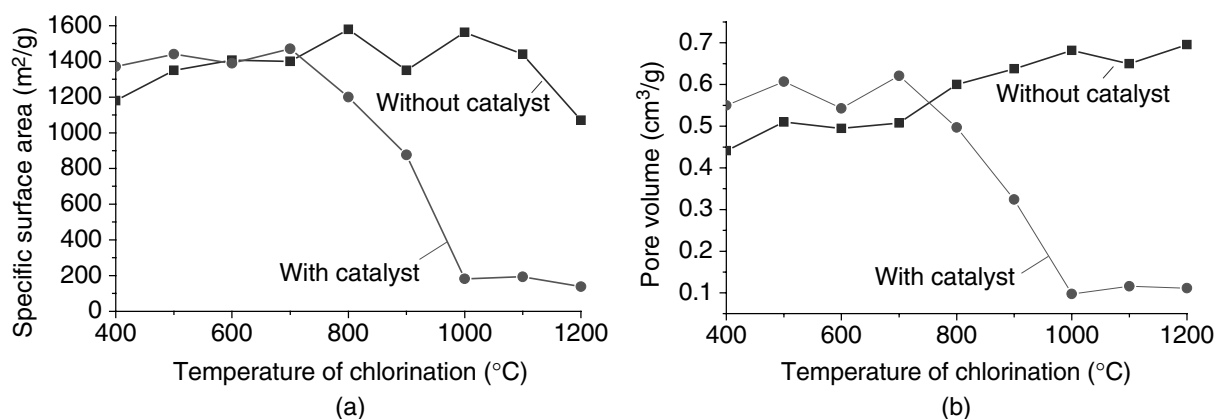


**FIGURE 6.14** The BET-specific surface area (a) and the pore volume (b) of TiC CDC as a function of processing temperature, showing the effect of the metal chloride catalysts present in TiC before the synthesis (From Leis, J. et al., Catalytic effect of metals of the iron subgroup on the chlorination of titanium carbide to form nanostructural carbon, *Carbon*, **40**, 1559–1564, 2002.). Graphitization at lower temperature caused by the catalysts resulted in the decrease of the surface area and pore volume at temperatures above 700°C. The catalyst mixture consisted of  $\text{CoCl}_2$ ,  $\text{NiCl}_2$ , and  $\text{FeCl}_3$  solutions in ethanol with a final content of 73 mg of each chloride per gram of carbide.



### 6.2.6.6 Effect of the Initial Carbide Porosity

Carbide-derived carbons from carbide single crystals do not possess macroporosity, unlike carbons produced from porous sintered samples of carbides having initial porosity of 6 to 16% (by vol.). This means that the original macropore volume of sintered carbides does not change during the chlorination process and can be controlled by controlling the porosity of carbides. Kukushkina et al. [58,59] studied the influence of the initial porosity in polycrystalline carbides on the porosity of the corresponding CDC. The chlorine treatment of the dense polycrystalline carbides (SiC, TiC, HfC, and ZrC) at 600 to 1100°C resulted in completely nanoporous CDCs, similar to the CDCs produced from single crystals, with the experimental values of apparent density and total pore volume in good agreement with the theoretically expected ones. The chlorination of polycrystalline SiC with various initial porosities revealed a linear relationship between the total pore volume of the synthesized CDC and the initial pore volume.

Total volume and characteristic dimensions of meso- and nanopores can be predicted and achieved by the selection of proper binary or ternary carbides or carbide mixtures, and variation of the chlorination process parameters. This statement is illustrated with an example of the CDC produced from TiC and HfC solid solutions of variable composition. Linear dependence of the total pore volume measured by benzene adsorption on the composition is shown in Figure 6.15.

The above considerations allow simple calculations to be used for the evaluation of the total pore volume in CDC [60]:

$$V_V = d(1 - \varepsilon_0) \left( \frac{1}{d} \frac{\varepsilon_0}{1 - \varepsilon_0} + \frac{\alpha}{d} - \frac{\alpha}{d_c} \frac{M_C}{M} \right) \quad (6.5)$$

where  $V_V$  is the total volume of pores per total material volume ( $\text{cm}^3/\text{cm}^3$ ),  $\varepsilon_0$  is the relative pore volume of the initial carbide,  $\alpha$  is the fractional conversion of the chlorination reaction,  $M_C$  and  $M$  are the molecular masses of carbon and the carbide, respectively, and  $d$  and  $d_c$  are the densities of carbon and the carbide, respectively.

### 6.2.6.7 CDC Composites

Fedorov et al. [61] and later Gordeev et al. [62–64] offered a method for production of nanoporous carbon bodies of any shape having sufficient mechanical strength and open pores. The method consists of forming an intermediate blank of MeC having porosity in the range of 30 to 50% (by vol.) in the desired shape (e.g., by sintering). The blank is then impregnated with carbon as a binder by exposure to a gaseous hydrocarbon mixture at a temperature exceeding the decomposition temperature of hydrocarbons (700 to 1000°C) until the mass of the blank increases by 10 to 25% due to formation of pyrocarbon. The blank is then treated in chlorine at 900 to 1100°C. A nanoporous

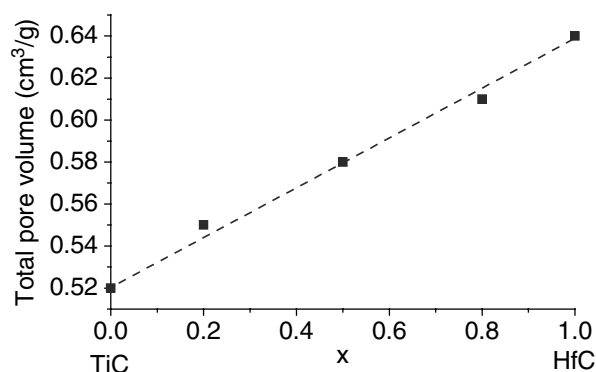


**FIGURE 6.15** Pore volume of CDC produced from solid solution of  $\text{Ti}_{1-x}\text{Hf}_x\text{C}$  as a function of composition showing a linear dependence (From Kukushkina, et al., Parameters of the porous structure of carbon produced by thermochemical treatment of nanoporous carbides, *Russ. J. Appl. Chem.*, **69**, 620–622, 1996).

structure is formed after the removal of volatile chlorides of carbide-forming elements according to Equation (6.2). As a version of the method, the blank made of silicon carbide may be impregnated with liquid silicon. Then the hydrocarbon mixture interacts with the liquid silicon to form a secondary silicon carbide. It was shown that macroporosity that developed in the course of formation of the carbide–pyrocarbon composite remained unchanged after thermochemical treatment in chlorine [61]. The influence of pyrocarbon content on the porous structure and physical properties, including resistivity, heat conductivity, and compression strength, were systematically studied for the SiC CDC–pyrocarbon composites [65].

## 6.2.7 ANALYSIS OF CDC STRUCTURE

As discussed to some extent in the previous subsections, CDCs of different hybridization, microstructure, density, and porosity can be produced by chlorination. Since the structure of CDC has a strong effect on its mechanical, electrical, and sorption properties, it is important to review the studies on the structure of CDCs obtained from various carbides under various experimental conditions.

### 6.2.7.1 Graphitization and Detection of Nanocrystals

By using the Scherrer equation and the FWHM of the carbon peaks, the average thickness of the graphite crystals in  $[0\ 0\ 2]$  ( $L_c$ ) and  $[1\ 0\ 0]$  ( $L_a$ ) directions could be estimated. Although the use of the Scherrer equation for the estimation of the crystallite size in carbons with a low degree of ordering has been demonstrated to provide adequate results [66], one should realize that the values obtained might be affected by the short-range order in the amorphous material, as well as by the irregularity and distortion of the crystalline structure. Nevertheless, qualitatively, XRD is clearly capable of providing valuable information on the CDC structure even when the CDC is produced at low temperatures and is disordered.

Mohun [15,33,34] used XRD to determine the degree of graphitization and the average size of graphite crystallites in CDC produced from a variety of carbides. As in most other studies, significant graphitization was observed only in samples obtained at higher temperatures. Unfortunately, he did not publish systematic results on the changes of XRD patterns of CDC produced from different carbides as a function of the chlorination temperature. However, he reported the general dependencies and some random data for CDC. For instance, he determined the thickness of graphite crystallites ( $L_c$ ) in SiC CDC at the highest investigated temperature of 1650°C (2.5 h) to be ~4 nm. Mohun was the first to point out that graphitization degree also depends on the duration of the chlorination process: CDC samples produced at 1050°C (24 h) and 825°C (630 h) demonstrated the same graphitization degree. As such, graphitization was clearly determined to be a kinetically controlled process. CDC samples produced at low temperatures were completely amorphous and showed absolutely no diffraction pattern when chlorinated for 24 h.

The structure of SiC CDC was investigated by XRD in another early work [67]. CDC for that study was produced in the course of neutron activation analysis of silicon carbide [68].  $\beta$ -SiC was treated in the chlorine gas flow in the quartz tube reactor at 1200 to 1250°C. Some samples were slowly cooled after the chlorination and stored for several months prior to the XRD measurement. Debye–Scherrer films of these samples showed only the diffuse rings typical for amorphous substances. Another sample of CDC, which was subjected to XRD was fresh (2 days old) and had been rapidly cooled after chlorination in a stream of cold nitrogen. In this case, Debye–Scherrer films showed in addition to the diffuse rings, a number of spotty lines, most of which were identified as  $\beta$ -SiC. In the first case, the samples were easy to break with the touch of fingertips, while the quenched samples were hard and brittle. It was noted that the size and shape of the bodies did not change during the reaction.

$L_a$  and  $L_c$  values for the heat-treated TaC CDC and SiC CDC were calculated from the corresponding XRD patterns in [40]. The  $L_a$  values were larger than for conventional activated carbons treated to the same temperatures. In contrast, the  $L_c$  dimensions were very low as presented in

Figure 6.16, indicating the formation of thin and wide graphitic structure. In the case of TaC CDC, distinct graphite reflexes became apparent after heat treatment at 1700°C (see Figure 6.16), while temperatures above 2000°C were needed for pronounced graphite peaks to appear in diffraction patterns of SiC CDC samples. The authors suggested that as-prepared CDC from SiC and TaC consisted of disordered bent graphene layers with very little parallel stacking. We performed the analysis of similar samples by TEM in our laboratory and confirmed a low degree of ordering in as-prepared SiC CDC. After heat treatment, the diameter of the coherently scattering segments of the layers clearly increased and, in consequence, the mesopore volume increased as well. The open structure began to collapse at 1500°C for TaC CDC; the stacks of carbon layers grew in height and the distance between these stacks decreased to that of the ordered graphite. In the case of TaC CDC, the pore volume decreased to nearly zero at 1900°C, and the layers aligned to the perfect graphite structure at 2800°C.

Formation of carbon films and carbon-rich surface layers was repeatedly observed in the course of investigating high-temperature corrosion of SiC-based ceramics in mixed oxygen–chlorine environments [69–75] and during etching of SiC surfaces with chlorine and fluorine-containing gases for electronic device fabrication [76–79]. Study of the properties and the structure of carbon was not the object of the cited studies; moreover its formation was frequently considered to be undesirable.

Further investigations of CDC structure were reported in a number of papers by Gordeev et al. [48,80–84]. X-ray scattering studies of the structure of CDC prepared at 700 to 1000°C from 6H-SiC single crystals, polycrystalline  $\alpha$ -SiC and polycrystalline SiC, TiC, and Mo<sub>2</sub>C were conducted. The angular dependences of the scattering intensity obtained were treated as a result of scattering from nanoparticles of different size. By unfolding the experimental curves into components corresponding to particles with different gyration radii  $R_g$ , scattering distribution functions with respect to gyration radius were calculated. Samples prepared from different carbides differed in the degree of nanoparticle uniformity. The most uniform in size were the nanoparticles in the samples prepared from SiC. The size of the particles was found to depend on the carbide source (and possibly purity) as well as on its crystallinity. In CDC produced from polycrystalline SiC, the average  $R_g$  was <0.6 nm, while in CDC from  $\alpha$ -SiC and 6H-SiC single crystals, most of the particles had  $R_g \approx 1.0$  to 1.2 nm [80]. A possible cause of the larger particle formation in the case of single crystals is their lower chlorination rate and consequently longer time of treatment. In the report [81], irrespective of the type of the starting carbide, particles with  $R_g \approx 0.5$  nm made up the largest fraction in porous carbon. In other studies [82], nanoparticles in CDC produced from different carbides varied in size. A study of the temperature dependences of the electrical resistivity, Hall coefficient, and thermoelectromotive force in the temperature range 1.5 to 300 K for the materials characterized by SAXS in [82] showed that the structural units responsible for the character of charge transport in

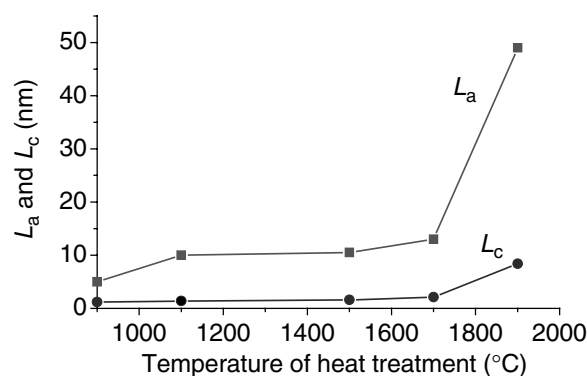


**FIGURE 6.16** Dimensions of graphite crystallites in heat-treated TaC-CDC produced at 500°C as a function of the annealing temperature, showing pronounced graphitization at temperatures above 1700°C (From Boehm, H.P. et al., Structural parameters and molecular sieve properties of carbons prepared from metal carbides, *Proceedings of the 12th Biennial Conference on Carbon*, Pergamon, Oxford, 1975, pp. 149–150).

these materials were carbon nanoclusters of 1 to 3 nm in size [84]. SiC CDC produced from powders with various particle sizes (8 to 10, 180 to 200, and 800 to 1000  $\mu\text{m}$ ) was analyzed by XRD and SAXS [83], and it was shown that the mean size and number of nanoparticles (presumably graphite nanostructures) increases with increasing particle size. Possibly longer times required for carbonization of coarser grains were responsible for the higher graphitization degree observed. The XRD and SAXS data on the CDC structure from [80–82] were revised and later summarized with confirmation from the HRTEM images in [85]. It is noticeable that besides amorphous and partially graphitized carbon, some diamond nanocrystallites were detected in the CDC from SiC [85].

Carbon coatings on silicon carbide powders and monolithic specimens produced by treatment in diluted chlorine and chlorine–hydrogen mixtures were examined by Gogotsi and McNallan in a series of works [12,13,19,28,86–89]. The  $\beta$ -SiC powder was treated in the  $\text{Cl}_2$  (2 to 3.5%)– $\text{H}_2$  (0 to 2%)–balance Ar gas mixtures in the temperature range 500 to 1000°C at ambient pressure [28,86,87]. Experiments were continued for 5 to 72 h depending on the material. The progress of the reactions conducted at 800°C was monitored by thermogravimetric analysis. The mass decreases approximately linearly with time, approaching a minimum value, which is dependent on the ratio of chlorine to hydrogen. Gas mixtures that were low in hydrogen produced the highest reaction rates. Uniform amorphous carbon or nanocrystalline graphite films were produced by treatment in  $\text{Cl}_2$ –Ar media as shown by XRD, Raman spectroscopy, and TEM. In the Raman spectra, D and G bands of disordered graphite were observed. From the relative intensities of these bands, the size ( $L_a$ ) of the graphite crystallites was evaluated to be 2 to 4 nm. As the temperature of the treatment increases, the size of these crystallites and the thickness of the film formed after a fixed period of exposure increase. BET SSAs of carbon layers were calculated using the results of  $\text{N}_2$  or Ar sorption measurements and taking into account the presence of unreacted silicon carbide. High values of surface area (Figure 6.9) provide the evidence that nanoporous CDC was produced.

Raman spectra of CDC prepared from polycrystalline  $\alpha$ -SiC and TiC [90] support a cluster structure of nanoporous carbon and size quantization of the electronic and vibrational spectra in carbon nanoclusters. The presence of fragments of strained cubic or hexagonal diamond was observed in a number of cases.

Chlorination of SiC fibers was also studied [91,92]. Fibers from polymer precursors are nanoscale mixtures of SiC, carbon, and  $\text{SiC}_x\text{O}_y$ . Their chlorination can be conducted at 400°C and above, thus well below the temperatures necessary to produce CDC on SiC crystals or micropowders.

### 6.2.7.2 Carbon Nanostructures

It has been previously discussed that the major part of the CDC structure generally consists either of amorphous (highly disordered) nanoporous carbon or a porous network of graphite ribbons. However, recent TEM studies revealed the formation of various carbon nanostructures, including nanodiamond, carbon onions, nanotubes, barrel-like particles, and fullerene-like structures during the chlorination of carbides (Figure 6.17).

Studies performed by Gogotsi et al. [12,13,19,88] revealed that addition of hydrogen into the reaction mixture of  $\text{Cl}_2$ –Ar used for chlorination of carbides not only reduced the reaction rate but also influenced the composition and properties of the products. The sharp diamond band at  $\sim 1330\text{ cm}^{-1}$  was observed in the Raman spectra of the powder treated in 2.6%  $\text{Cl}_2$ –1.3%  $\text{H}_2$ –Ar at 950°C, and diamond regions were clearly visible under an optical microscope. Other bands, which may correspond to crystallized and amorphous diamond, were present in the Raman spectra as well. Thus, hydrogen plays a significant role in the formation of diamond by stabilizing dangling bonds of cubic diamond formed from  $\beta$ -SiC upon extraction of silicon. Chlorination of monolithic sintered and CVD samples of  $\alpha$ - and  $\beta$ -SiC under the conditions described above [28] resulted in the formation of gray and translucent areas in thin section films in cases of low  $\text{Cl}_2/\text{H}_2$  ratios in the reaction mixture [12,13,19,88]. These films probably acted as a diffusion barrier and prevented further

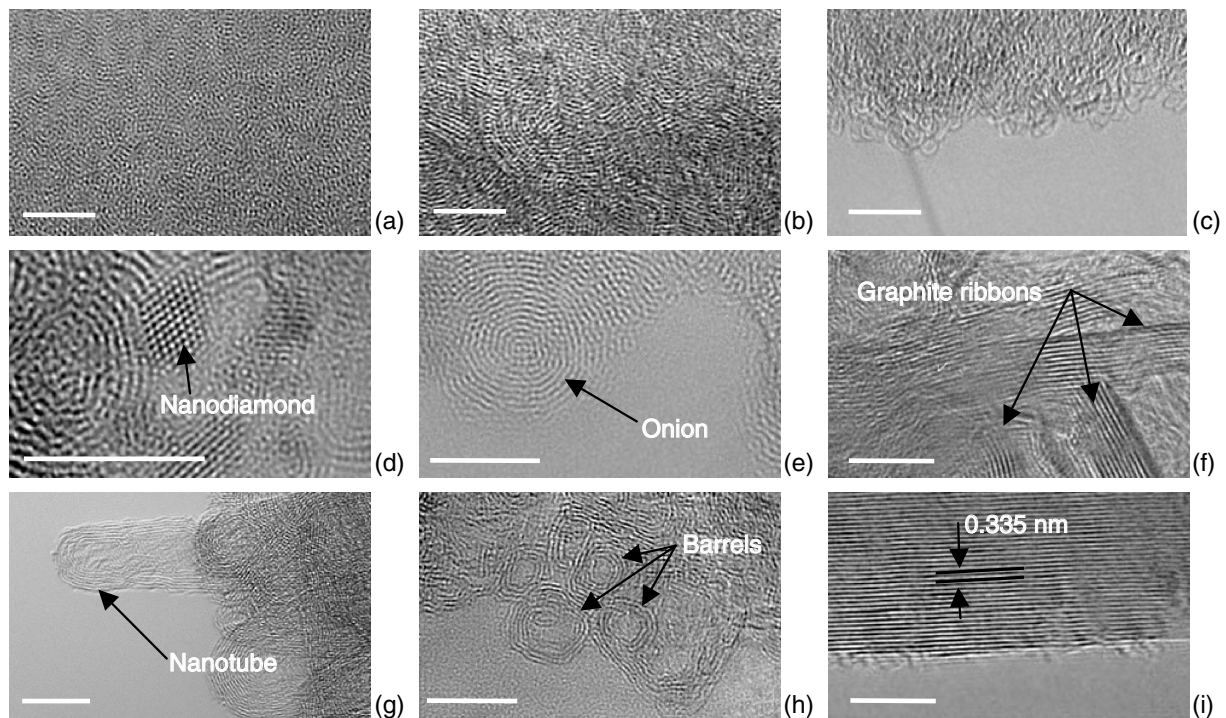


**FIGURE 6.17** High-resolution TEM images of various carbon structures produced by chlorination of carbides: amorphous carbon (a), turbostratic graphite (b), fullerene-like carbon (c), nanodiamond (d), carbon onion (e), graphite ribbons (f), CNTs (g), barrel-like particles (h), and ordered graphite. Scale bar, 5 nm.

reaction. Lattice fringing (Figure 6.17d), electron diffraction patterns, and electron energy-loss spectroscopy (EELS) confirmed the formation of nanocrystalline diamond-structured carbon. The analysis of Raman spectra supported the presence of  $sp^3$  bonding, which is also confirmed by a very high hardness (up to 50 GPa) and Young's modulus (up to 600 GPa) of these coatings. CDC coatings produced by treatment in chlorine or chlorine–hydrogen mixtures at  $Cl_2/H_2 \geq 2:1$  consisted of a loosely attached, powdery top carbon layer with a dense, highly disordered, adherent amorphous or nanocrystalline layer below it. The adherent layers were shown to be composed of a mixture of graphitic and diamond-structured carbon [19] or highly disordered  $sp^2$  carbon [13]. The thickness of the carbon layer increased linearly during the process. Because the kinetics is linear, the controlling factor of the reaction is not the diffusion of reactant species through the growing carbon layer.

Detailed HRTEM study of diamond crystals, produced by treatment of SiC in the gas mixtures of 1 to 3.5%  $Cl_2$  and 0 to 2%  $H_2$ –Ar at 1000°C, showed local epitaxial growth of diamond on the SiC surface [93]. It has been shown that the presence of hydrogen in the environment is not required for diamond synthesis. However, hydrogen can stabilize the nanocrystals and lead to an increased diamond content in CDC. If no hydrogen is added, diamond nanocrystals transform to graphitic carbon, forming carbon onions and other curved graphitic structures. Diamond formation is also favored by low temperature of synthesis providing moderate carbon mobility. This result is in accordance with the x-ray photoelectron spectra of CDC from SiC, TiC, and ZrC produced at various temperatures [94]. It was shown that the degree of  $sp^3$  hybridization increases as the temperature of the process is reduced from 1100 to 350°C.

When Danishevskii et al. [95] studied the effects of preparation conditions on nanodiamond formation during chlorination of SiC they observed that smaller SiC grains generally lead to smaller sized diamond. When SiC precursor contained pyrocarbon, the formation of diamond was hindered. The researchers suggested that the fast propagation velocity of the reaction front and the correspondingly strong nonequilibrium conditions favor diamond nucleation.

Theoretical studies of graphite and diamond growth on the (1 0 0 0) Si-surface of 6H-SiC were carried out using molecular dynamics simulation [12,96]. It was shown that very high lattice strains do not allow continuous growth of diamond on SiC, and fragmentation occurs leading to nanocrystalline material. Small diamond clusters on SiC are predicted to have a good adhesion to the substrate and maintain  $sp^3$  coordination of carbon atoms in the cluster. Transmission electron microscopy studies [19] proved that SiC was converted to  $sp^3$  carbon, and formation of crystalline diamond-structured carbon occurred from disordered Si-depleted SiC within nanometers of the SiC/C interface. Growth of larger crystals of diamond-structured carbon was probably the result of coalescence of continuous nanocrystalline regions. The presence of hydrogen helps to maintain  $sp^3$  hybridization of carbon, stabilizing the dangling bonds.

Carbon onions in CDC were first observed during the chlorination of titanium carbide [97] near particle edges. These structures with concentric spherical graphitic shells were observed to have outer diameters in the range 15 to 35 nm. The distance between graphitic planes in the shells was 0.34 nm, slightly larger than the interplanar distance in graphite. As a comparison, HRTEM images of CDC from SiC produced at 1000°C did not indicate onion-like shells. However, our work showed the formation of carbon onions in CDC produced from SiC [19]. The mechanism of their formation via diamond nanoparticles is described in [98]. High-resolution TEM images of carbon onions and other carbon shells found in CDC are presented in Figures 6.17d, e, and h.

It is interesting to note that according to Boehm [99], CNTs were first observed in 1972, during the TEM analysis of SiC CDC. Boehm observed multiwall CNTs and carbon onions only occasionally in CDCs, and concluded that these structures were present in SiC before the chlorination. However, we believe that nanotube synthesis may have occurred during the CDC production (Figure 6.17g). Gogotsi et al. [19,100] reported the formation of carbon onions and CNT in SiC CDC formed at 1000–1200°C. Wertz [98] observed CNT and carbon onions in CDC produced from SiC and TiC at similar temperatures. Hoffman et al. [50] observed the formation of short CNT on the surface of  $Ti_2AlC$  CDC particles formed at ~800°C. Higher temperatures resulted in the formation of graphite ribbon networks and amorphous carbon. No tubular graphitic structures were found in these samples. The CDC produced at 600°C consisted only of porous amorphous carbon. Similar curved graphitic structures with characteristics similar to short CNT or elongated carbon onions were observed in the CDC produced from  $Ti_3SiC_2$  at 800°C [31]. A considerable amount of amorphous and turbostratic carbon was also present in this sample.

Similar multiwall nanostructures, called “nano-barrels” were also observed in CDCs produced from  $Al_4C_3$  [101–103]. The CDC from  $Al_4C_3$  produced at 700°C consisted, to a large part (~80%), of barrel-like multiwall nanoparticles and nanotubes. The sample chlorinated at 900°C was primarily turbostratic carbon forming randomly oriented band-like graphitic lamellae and large sheets. The observed nanobarrels were considered to be intermediates between empty onion-like particles and multiwall nanotubes and patented as a “nanotubular carbon material” [101]. We observed nano-barrels in CDC produced from other carbides, including TiC and SiC (Figure 6.17h), however, the yield was noticeably smaller than that observed in  $Al_4C_3$  CDC.

The mechanisms governing the growth of various nanostructures during chlorination of carbides are not yet clear. A catalytic effect of impurities present in carbides [102], metals, or metal chlorides might play a significant role in nanostructure formation. Carbide structure and optimum temperature regime also seem to be important parameters for the selective synthesis of various nanostructures. Further investigation is needed to clarify the phenomena observed.

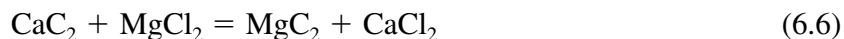
## 6.3 SELECTIVE ETCHING OF CARBIDES BY MELTS AND SUPERCRITICAL WATER

### 6.3.1 REACTION OF CALCIUM CARBIDE WITH INORGANIC SALTS

Salt-like carbides react at elevated temperatures with a number of reagents, resulting in the formation of carbon formation along with other reaction products [104]. The few reports there are on this

carbide-thermal process and the resulting carbon material have all been devoted to calcium carbide reactions with metal salts [105–111]. Generally, the process can be considered as the high-temperature exchange reaction of calcium carbide and metal salt producing a calcium salt and a new unstable salt-like carbide, decomposing to give free metal and carbon [110].

This method was first applied for the production of macrocrystalline graphite with the use of magnesium chloride [105]. The process included the following exchange and decomposition reactions:



The reaction mixture was heated to 600 to 1275°C for 1 to 5 h. The best yield and quality of graphite were achieved in the range 950 to 1200°C. After removal of the unreacted carbides and salts and amorphous carbon the yield was up to 85%. X-ray diffraction showed that both graphitic and turbostratic carbon were present in the product. It is important to note that since  $\text{CaCl}_2$  has a high melting point of 772°C and low vapor pressure, pure CDC cannot be produced by chlorination of  $\text{CaC}_2$ .

The porous structure and adsorption properties of the CDC material prepared by the carbide-thermal process were first studied by Fedorov et al. [106]. Reaction of calcium carbide with sodium chloride according to the overall equation



was conducted in the temperature range 400 to 900°C and resulted in a sorption-active carbon material. Parameters of the porous structure were determined by measuring benzene sorption isotherms. Carbonaceous materials from  $\text{CaC}_2$  had an extensive and variable mesopore volume of up to 0.63 cm<sup>3</sup>/g, but a relatively low specific surface area (below 330 m<sup>2</sup>/g) compared to the CDC produced by chlorination of carbides.

Measurements of the yield of free carbon for various  $\text{CaC}_2/\text{NaCl}$  ratios in the initial mixture showed that two routes of reaction are possible at 900°C [109]. Decomposition of  $\text{CaC}_2$  catalyzed by chloride takes place at low  $\text{CaC}_2/\text{NaCl}$  ratios (1:0.03–1.2 eq.). Reaction (6.9) proceeds at higher  $\text{CaC}_2/\text{NaCl}$  ratios.

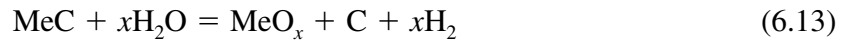
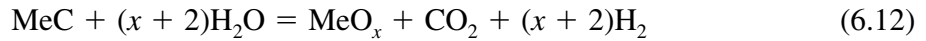
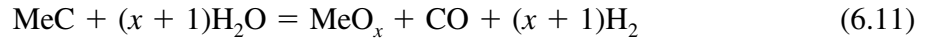
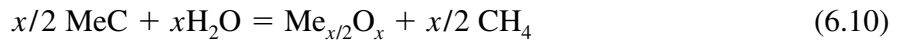
The technique of producing CDC adsorbents from  $\text{CaC}_2$  includes the following steps: mixing of the initial components with the particle size of 100 to 300 μm in the ratio 1:(1–3); compaction at 5 to 40 MPa; and thermal treatment at 600 to 1000°C in the inert gas medium, followed by cleansing in water or acid, drying, and crushing. These sorbents can be used as soil detoxicants, gas drying agents, chemical adsorbents, and catalysts [111].

### 6.3.2 HYDROTHERMAL LEACHING OF CARBIDES

#### 6.3.2.1 Thermodynamic Analysis

Thermodynamic stability of a number of MeCs under hydrothermal conditions has been analyzed [27]. The possible reaction routes and products were predicted using Gibbs energy minimization. Thermodynamic calculations were conducted in the temperature range from 300 to 1000°C and pressures in the range between 2 and 200 MPa for the  $\text{M}_x\text{C}-n\text{H}_2\text{O}(\text{g})$  system, where  $n = 2$  and 10, and  $x = \text{Si}, \text{Ti}, \text{Ta}, \text{Nb}, \text{W},$  and  $\text{B}$ . The following idealization was used to carry out these calculations: hydrothermal fluid is treated as steam, solid phase is a mechanical mixture of compounds with unit activities, and gas phase is a mixture of ideal gases. Also kinetic factors and effects such as pH were not taken into consideration.

The analysis indicated that carbon,  $\text{MeO}_x$ ,  $\text{CH}_4$ ,  $\text{CO}_2$ ,  $\text{CO}$ , and  $\text{H}_2$  are the main products of hydrothermal reactions in the temperature range of the study and principal reactions in the  $\text{M}_x\text{C}-n\text{H}_2\text{O}(\text{g})$  system can be written as follows:



Thermodynamic calculations show that the formation of carbon on the surface of SiC depends crucially on the  $\text{H}_2\text{O}/\text{SiC}$  ratio and three regimes can be identified. At low  $\text{H}_2\text{O}/\text{SiC}$  ratios (regime 1), both carbon and silica are deposited on the surface. At intermediate  $\text{H}_2\text{O}/\text{SiC}$  ratios (regime 2), carbon and silica are formed. Silica is dissolved in water according to Equation (6.14). Thus, reaction (6.13) tends to move further to the right. At higher  $\text{H}_2\text{O}/\text{SiC}$  ratios (regime 3), since they dissolve in the excess water, neither carbon nor silica precipitates.

It was shown that the yield of methane, which is unstable at high temperatures, decreases with temperature and thus the yield of elemental carbon, which is produced due to instability of  $\text{CH}_4$  increases. Higher pressures led to a slight increase in stability of methane and, accordingly, to a lower yield of carbon.

The behavior of TaC, TiC, and NbC is very similar to that of SiC. Tantalum carbide seems to be more stable at low water contents. Carbon formation was calculated for TaC at temperatures  $>700^\circ\text{C}$  and only at relatively low pressures. However, it is important to remember that most metal oxides, unlike silica, cannot be easily dissolved in supercritical water. Thus, a mixture of carbon and metal oxide (or hydroxide) is produced. The behavior calculated for WC is somewhat different as compared with previously discussed carbides. A lower carbide  $\text{W}_2\text{C}$  and a number of stable oxides exist. Free carbon is predicted to form only at the lower temperatures. Boron carbide is the only carbide from the group studied that is not predicted to convert to free carbon under hydrothermal conditions. The present calculations provide some general guidelines and, as will be shown, are generally in good agreement with experimental results.

The formation of carbon-rich layers on the surface of carbides was repeatedly detected in the course of investigations on controlled oxidation of HfC [112–117], ZrC [116–121], and TiC [115,117] at low pressures of oxygen (0.02 to 16 kPa). These layers contained up to 25 at% of carbon in addition to metal oxides and oxycarbides. As characterized by Raman spectroscopy, this carbon was mainly amorphous. In some cases, formation of carbon in the form of hexagonal diamonds was reported [118].

### 6.3.2.2 Experimental Results

Formation of carbon from carbides after hydrothermal treatment was first reported by Gogotsi and Yoshimura in 1994 [87,122–125]. This phenomenon was observed in the course of corrosion studies of amorphous SiC (Tyranno) fibers at 300 to  $800^\circ\text{C}$  and about 100 MPa. Tyranno is a type of silicon carbide fiber containing titanium and oxygen, made by pyrolysis of an organometallic polymer precursor. It consists of SiC nanocrystals, which are connected by Si–O–C and Ti–O (Ti–C–O) interlayers and can be considered as an amorphous  $\text{SiO}_x\text{C}_y$  matrix with nanometer-size  $\beta$ -SiC inclusions. The outer surface of the fibers treated at temperatures up to  $450^\circ\text{C}$  remained smooth and almost featureless. Auger electron spectroscopy depth analysis of the surface layer showed that a



carbon layer containing traces of silicon was formed [123]. The thickness of this layer varied from 10 to 20 nm to 1 to 2  $\mu\text{m}$ . Raman spectra of the fibers showed a band of graphite (G) and a disorder-induced band (D), thus confirming the formation of amorphous or nanocrystalline carbon [122]. The crystallites were of very small grain size and  $\text{sp}^2$  C–C bonds dominated.

Formation of amorphous carbon has been reported on the surface of Tyranno fibers after hydrothermal treatment at 300 to 400°C and 100 MPa [87,91,126,127]; CVD-SiC fibers after treatment at 400 to 700°C and 200 MPa [128];  $\alpha$ - and  $\beta$ -SiC platelets, whiskers, and powders at 600 to 800°C [27,87,126,127,129]. Some amounts of disordered diamond as well as graphite and amorphous carbon were found on the surface of  $\alpha$ - and  $\beta$ -SiC powder and single crystals after treatment at 300 to 800°C and 100 to 500 MPa [130–134]. The hydrothermal method was also found to be suitable for preparation of CDC from other carbides including WC, TaC, NbC, and TiC at 500 to 750°C and 100 to 170 MPa [27].

## 6.4 THERMAL DECOMPOSITION OF CARBIDES

It is known that silicon carbide and many other carbides decompose at high temperatures [104]. This thermal decomposition in vacuum or inert environment is accompanied by the formation of carbon and preferential evaporation of the carbide-forming element due to the low vapor pressure of graphite at elevated temperatures compared to that of most metals.

A consideration of transport processes leading to the formation of carbon during the thermal decomposition of SiC was attempted by Motzfeldt and Steinmo [135]. Vapor pressure over the SiC(s)–C(s) was studied by means of Knudsen effusion method for three different orifice sizes. It was found that surface diffusion is of great importance in the process. The overall process was visualized in the following way: The outermost layer of the SiC crystal loses silicon by evaporation from the surface, and a layer of microporous carbon is left. A gradient in silicon is established through this layer and silicon from the interior moves through it by surface diffusion and then evaporates from the surface. One can find indirect evidence of silicon surface migration during the silicon carbide decomposition in the report [136] published in 1970.

### 6.4.1 CARBON STRUCTURE AND CONSERVATION OF SHAPE

The first documented observation of carbon formation after heat treatment of SiC in vacuum at temperatures up to 2000°C was published in 1960 [67]. As in the case of CDC prepared by chlorination of silicon carbide, the size and shape of the large particles did not change noticeably after the treatment. The same phenomenon was observed in 1963 in the course of the study of SiC dissociation [137].

Several attempts to investigate the structure of carbon obtained by decomposition of silicon carbide have been reported. An X-ray diffraction study was conducted by Badami [138,139]. Single crystals of  $\alpha$ -SiC (6H) were heated in a vacuum ( $10^{-5}$  Torr) at 2050–2280°C for 1 h. The sample produced by heating to 2050°C had undergone only partial decomposition as demonstrated by its diffraction pattern. On the basis of an examination of various parts of the samples produced at 2050°C, the author concluded that the carbon produced consisted of a matrix of turbostratic carbon with strong preferred orientation of the carbon layers parallel and perpendicular to the layers of silicon carbide and graphite nanocrystals having a common  $c$  axis and axial symmetry about it. Samples produced at 2280°C exhibited a gradually changing structure. The outer layers of carbon consisted mainly of crystalline graphite with small amounts of turbostratic graphite. Deeper inside the sample, there was turbostratic graphite and, finally, completely disordered carbon. Higher levels of graphite ordering at the particle surface could be explained by surface diffusion and effectively longer time of carbon annealing. Silicon atoms migrating from inside the particles to the surface may also provide an additional transport mechanism for the reorganization of carbon atoms.

Selected area electron diffraction was used to investigate the decomposition of single-crystal  $\beta$ -SiC whiskers [140]. Whiskers, averaging about 300 nm in diameter, were heated to about 2400°C at  $10^{-6}$  Torr for 2 to 3 min. In spite of such a high temperature, whiskers were found at various stages of decomposition. Graphite crystallites about 10 nm or less in diameter were observed at the outer surface of the partially decomposed whiskers. It was concluded on the basis of selected area diffraction patterns that the crystallites were grown with their basal planes tangential to the whisker surface.

It should be mentioned that, in our experience, the level of decomposition depends not only on temperature but also on the position of a microcrystal (SiC particle or whisker) in a sample holder. Particles from the outer layer transform at a higher rate, possibly due to the gradient in pressure and composition of the residual gas across the sample holder inside the vacuum chamber. As a result, a thicker layer of particles may lead to the retarded decomposition.

In recent electron microscopy studies of  $\beta$ -SiC whiskers annealed in vacuum ( $10^{-5}$  Torr) at 1700–2000°C, conservation of shape during carbide decomposition has been shown [14]. We observed that at lower temperatures the shape of the whiskers does not change considerably. However, we found some distortion of the sharp features at the surface of nanoobjects at higher temperatures. Figure 6.18 shows graphitic CDC structures obtained by annealing of SiC whiskers in vacuum. Similar to the CDC processes described previously, the whiskers annealed at 1700°C retained their original shape as shown in both SEM (Figure 6.18a) and TEM (Figure 6.18c) micrographs. When we increased the vacuum treatment temperature to 2000°C, all SiC transformed to well-ordered graphitic carbon. The same cross-sectional shape was found by TEM studies (Figure 6.18d). SEM investigations (Figure 6.18b) revealed that the general hexagonal cross-section was preserved; however, the edges of the hexagonal platelets were not straight any more, and a wrinkled graphitic structure was formed.

Later research on SiC surfaces at elevated temperatures was triggered by the demand of the electronics industry for the development of good metal-semiconductor contacts and thus the need to perfect a procedure for producing atomically clean SiC crystal surface [141]. These studies were mainly conducted on (0 0 0 1) (Si) and (0 0 0  $\bar{1}$ ) (C) faces of 6H and (1 1 1) (Si-) and (1 1 1) (C-) faces of 3C SiC.

Bommen et al. [142] studied thermal decomposition of Si and C faces of 6H SiC crystals in vacuum ( $10^{-10}$  Torr) by low-energy electron diffraction (LEED) and Auger electron spectroscopy (AES). They observed the formation of a graphite monolayer at temperatures as low as 800°C. On

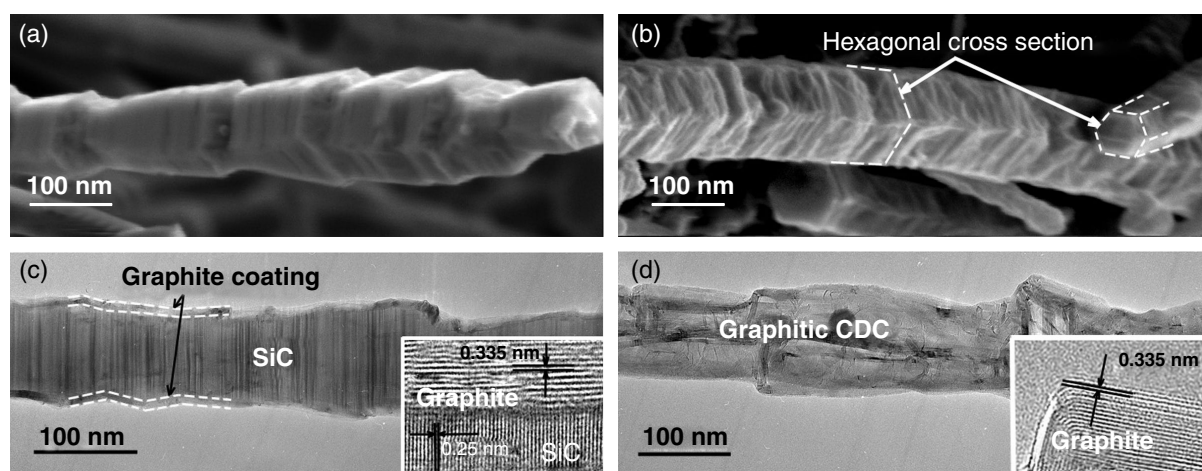


**FIGURE 6.18** Scanning electron microscopy (a, b) and TEM (c, d) images of the whiskers obtained by annealing of SiC whiskers in vacuum at 1700°C (a, c) and 2000°C (b, d) for 30 min. (From Cambaz, Z.G. et al., Conservation of shape during formation of carbide-derived carbon on silicon carbide nano-whiskers, *J. Am. Ceram. Soc.*, 2005, in press.) The insets in (c) and (d) show HRTEM of the surface of the whiskers annealed at 1700°C and 2000°C, respectively, revealing highly ordered graphite structures.

the Si face, this monolayer is monocrystalline with the unit cell rotated  $30^\circ$  with respect to the SiC unit cell. On the C face, this layer was polycrystalline with no preferred orientation. These results agree well with the ellipsometry [143], scanning probe microscopy (SPM) [144–146], angle-resolved inverse photoemission spectroscopy (KRIPS) [147], and EELS [148,149] studies as well as with further LEED [144,147,150–155] investigations performed by other research groups, who studied surface reconstruction on the (0 0 0 1) and (0 0 0  $\bar{1}$ ) surfaces of SiC crystals at high temperatures. It was also shown that the rate of carbon layer growth on the carbon face is higher than that on the Si face. Bonzo et al. [156] and Muehlhoff et al. [148] performed a detailed study of the surface graphitization of SiC in vacuum ( $10^{-9}$  Torr) as a function of temperature by using X-ray photoelectron spectroscopy (XPS) and AES techniques. A short annealing time of 5 min at 300 to 1400 K was chosen for their studies. Four temperature ranges were distinguished. At temperatures below 900 K (range I), no evidence for carbon segregation was found on either SiC face. At temperatures between 900 and 1100 K (range II), carbon segregation occurred on the C face of SiC and the amount of carbon formed in the surface layer increased slightly with temperature from 1 to 1.3 C/Si ratio. At temperatures between 1100 and 1300 K (range III), carbon also formed only on the C face of SiC but the C/Si ratio did not vary with temperature. Above 1300 K (range IV), strong graphitization took place on both SiC faces with the C face showing a higher rate of carbon growth. However, due to a short annealing time and moderate experimental temperatures ( $<1400$  K), the thickness of the graphite layer was limited to below 1 nm.

Iijima [157] studied the decomposition of silicon carbide under electron beam irradiation in 1982. Small flakes of 6H SiC were irradiated with the electron beam at a pressure of  $10^{-6}$  Torr. The decomposition was controlled to some extent by halting the irradiation after a short exposure to the beam. Electron diffraction patterns showed a gradual disappearance of the SiC reflections and graphitization of the sample at the same time. The preferred orientation of graphite was similar to the data of the XRD by Badami [138]. However, the decomposition did not completely preserve the particle shape, as shown by electron micrographs. Many ordered graphite bands and no regions of amorphous or turbostratic carbon were recognized in these micrographs. Images of the interface between SiC and graphite clearly showed the topotaxial mechanism of the reaction.

The only published source on the thermal decomposition of carbides other than SiC is the report by Foster et al. [158]. Decomposition of aluminum carbide at  $2400^\circ\text{C}$  and atmospheric pressure for 2 h in argon resulted in the formation of graphite crystals with a low  $c$ -spacing (0.33545 nm), chemical purity, large size, and the general absence of cleavage and twinning.

#### 6.4.2 SYNTHESIS OF CARBON NANOTUBES AND CARBON ONIONS

A new interest in the thermal decomposition of SiC arose in 1997 when Kusunoki et al. [16,159–164] discovered growth of self-organized carbon nanotube (CNT) films during the decomposition of SiC. In contrast to the more conventional CVD growth technique, this technique allows the formation of highly aligned nanotubes and no catalyst is required for the CNT development. Moreover, selective preparation of CNTs of the zigzag type is possible [163]. To the best of our knowledge, this is currently the only method that permits preparation of CNTs of the same chirality. Other methods, such as arc-discharge, laser evaporation, and CVD, usually result in zigzag, armchair, and chiral tubes coexisting in the products.

Initial studies were conducted on  $\beta$ -SiC particles heated to  $1700^\circ\text{C}$  at  $10^{-9}$  Torr for a few minutes in a TEM equipped with a YAG laser-heating holder [16]. Overlapped CNT with caps of 2 to 5 nm oriented along the [1 1 1] direction on [1 1 1] surface plane of  $\beta$ -SiC single crystal were observed on the heated samples. Further research of this group was focused on the production of large-area continuous films or membranes of aligned and interconnected CNT [159,162,165] (Figure 6.19) and on understanding the mechanisms governing the CNT growth [160,161,164].

It was found that resistive heating of SiC in vacuum also results in CNT formation and thus laser heating is not essential for successful growth. More important conditions for the growth seem to be

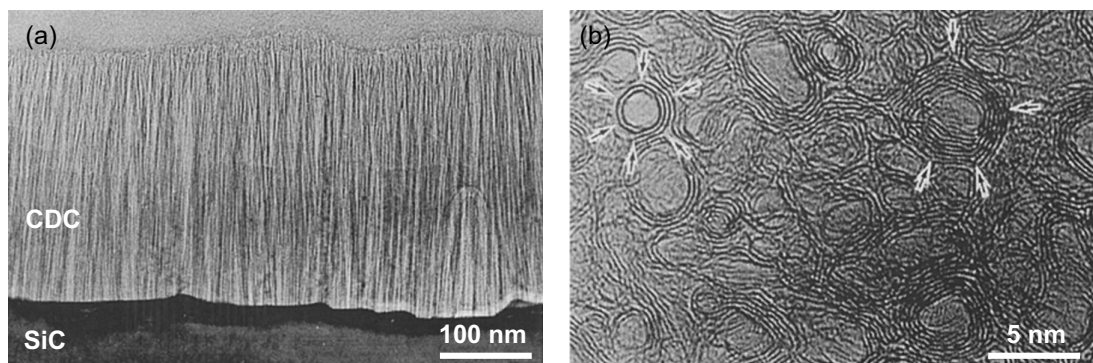


**FIGURE 6.19** Transmission electron microscopy images of a CNT film grown by thermal decomposition of the C-face of 6H-SiC. Cross-sectional TEM micrograph (a) and plain-view HRTEM image (b). (From Kusunoki, M. et al., Formation of self-aligned carbon nanotube films by surface decomposition of silicon carbide, *Phil. Mag. Lett.*, **79**, 153–161, 1999. Courtesy of Dr. M. Kusunoki of Japan Fine Ceramic Center.)

the orientation and face of SiC crystals, level of vacuum, crystal morphology, and heating rate. A remarkable difference between the carbon structures formed on (0 0 0 1) (Si) and (0 0 0 1) (C) faces of a 6H-SiC single crystal was found [161,162]. While CNT growth was observed under various experimental conditions on the C-face, only flat graphite sheets parallel to the surface were found on the Si-face. Similar face dependence was observed in  $\beta$ -SiC (1 1 1) films [165]. When the structure of the uppermost layers of SiC was changed by using laser irradiation, the structure of the carbon formed changed dramatically [164]. Porous amorphous carbon layer formed on both the C- and Si-faces during the vacuum annealing of the irradiated areas of the sample, while CNT and thin ordered graphite formed on the nonmodified areas of the C- and Si-terminated faces, respectively. Clearly, atomic structure of the very top SiC surface is a key factor that governs the structure of the CDC formed. The observed segregation of oxygen at the interface between the CNT film and SiC plane led Kusunoki [160] to suggest that residual oxygen in the vacuum chamber may play an important role in the formation of CNTs. Lower CNT growth rate in higher vacuum [160] supported this hypothesis. Further HRTEM analyses of various stages of CNT formation allowed the authors to propose a model, which consisted of three stages. At temperatures above 1000°C (stage I), several graphite sheets are formed parallel to the (0 0 0 1)<sub>SiC</sub> plane. At a temperature of ~1300°C (stage II), carbon nanocaps are formed by generation of bubbles of SiO gas. At stage III, the graphite sheets stand up and CNTs grow toward the interior of the SiC crystal. Possibly, stronger bonding of graphite layer to the Si-face of SiC prohibits formation of nanocaps, and thus further CNT growth.

Interestingly, in a later study by Derycke et al. [166] using scanning tunneling microscopy (STM) and atomic force microscopy (AFM), CNTs were found on an Si face of partially decomposed 6H SiC wafers. Samples were rapidly heated in ultra-high vacuum ( $<10^{-9}$  Torr) to 1650°C by passing a DC current through them, and maintained at this temperature for 15 min. Scanning tunneling microscopy and AFM images clearly showed highly ordered SWNT networks on and below the surface with their axes parallel to it. The nanotubes had a very narrow size distribution in the 1.2–1.6 nm range.

The initial growth process of CNT from SiC was also investigated *in situ* by time-resolved HRTEM [167]. The sample of 3C SiC single crystal was slowly heated to 1360°C at  $\sim 10^{-9}$  Torr. Dynamic observation was conducted at a time resolution of 1/60 sec. Two types of CNTs were observed with diameters 0.8 and 1.5 nm. It was shown that first amorphous carbon was formed and then it crystallized to graphene sheets parallel to the (1 1 1) plane. Carbon nanotubes were formed by the lift of a part of the graphene sheet along the [1 1 1] direction.

The influence of SiC morphology on the CDC structure is worth a separate discussion. Kusunoki et al. [160] investigated the interface between the CNT film and C-face SiC (Figure 6.20). As previously discussed, all graphite (0 0 0 2) planes are perpendicular to the (0 0 0 1) plane of SiC (CNTs grow perpendicular to the basal planes of SiC). However, on a step of SiC, graphite sheets

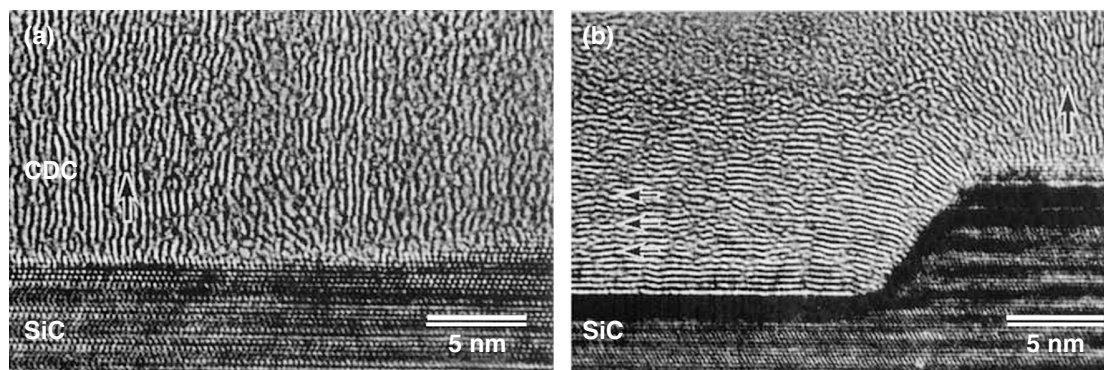


**FIGURE 6.20** Cross-sectional HRTEM images of the interface between CDC film and C-face SiC annealed for 30 min at 1700–2000°C in vacuum, showing the effect of morphology on the orientation of graphite (0 0 2) planes relative to the (0 0 1) planes of SiC (From Kusunoki, M. et al., Formation of self-aligned carbon nanotube films by surface decomposition of silicon carbide, *Phil. Mag. Lett.*, **79**, 153–161, 1999.). In case of a flat SiC surface, all graphite (0 0 2) planes grow perpendicular to the SiC basal plane (a) while at an SiC step, graphite sheets lie down gradually, and on a large area, graphite sheets are oriented parallel to the SiC basal plane (b). (Courtesy of Dr. M. Kusunoki of Japan Fine Ceramic Center.)

lie down and become oriented parallel to the SiC basal planes, which suppresses CNT formation. During our investigation of  $\beta$ -SiC whiskers grown along the [1 1 1] direction and annealed in a vacuum using a resistive heater, we generally did not observe CNT formation on the tip of the whiskers as we initially expected. Only occasionally when the tip of the whisker was broken and a sufficiently large flat area of the C-face SiC basal plane was exposed to the vacuum during the annealing, some large multiwall CNT-like structures were produced (Figure 6.21). As one may notice, due to the irregular shape of the whisker, its relatively small diameter and thus strong effect of the edges, the shape of the nanotubes is highly distorted and the average wall thickness of the formed structures noticeably exceeds that of CNTs obtained by Kusunoki et al. (Figure 6.19). Possibly, CNT formation from the irregularly shaped SiC particles reported earlier [16] could be explained by the rapid heating of the particles by laser as compared to regular heating at a rate of 1–15°C/min by using a graphite-resistive heater. Since planar graphite structures are more thermodynamically stable than CNTs, nonequilibrium processes may favor CNT growth. The relatively large size of the SiC particles as compared to the whiskers may also play a role in CNT formation.

The possibility of the transformation of SiC to nanotubes on larger SiC particles by means of rapid heating of the particles in a vacuum resistance furnace was also investigated [168]. Silicon carbide powder was heated to 1600 to 1700°C within 5 min, kept for another 10 to 15 min at high temperatures and then cooled to room temperature. Dense layers of elongated carbon structures (possibly MWCNTs), typically 20 to 50 nm in diameter and up to 1  $\mu$ m in length, were observed on the surface of 40% of the SiC powder. Unfortunately, no TEM analysis was performed on the CDC produced to reveal its microstructure.

Botti et al. [169] reported catalyst-free formation of SWCNT by rapid laser annealing of cold-pressed pellets of silicon carbide nanoparticles. The size of the nanoparticles varied from 30 to 70 nm, while the pellets were 13 mm in diameter and 3 mm in thickness. A defocused (10 mm) beam of the CO<sub>2</sub> laser with a power of 80 W irradiated SiC samples for 5 min in low vacuum (10<sup>-3</sup> Torr), was used, achieving temperatures of 1050°C. CDC was produced in the form of CNT bundles 60 to 80 nm in diameter. Raman spectroscopy suggested the presence of SWCNT in the bundles. However, it is important to note that double- or triple-walled CNT, similar to the ones reported by Kusunoki, can also produce radial breathing modes (RBM) in Raman spectra.

The same research group reported the formation of CNT by laser heating of amorphous SiC film in vacuum (10<sup>-4</sup> Torr) [170]. The 300-nm-thin SiC films were grown on HF-etched Si wafer

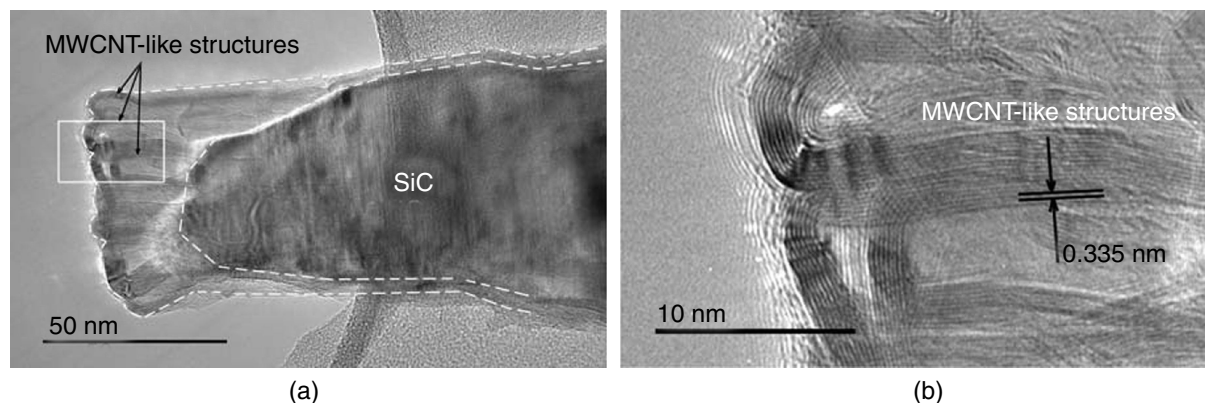


**FIGURE 6.21** Tip of a broken SiC whisker annealed in vacuum at 1700°C for 30 min: TEM (a) and HRTEM of the framed section of the whisker (b), demonstrating growing MWCNT-like structures.

by CVD from disilane and acetylene. By using a CO<sub>2</sub> laser, the amorphous films were heated to 950 or 1050°C and maintained at these temperatures for 90 and 30 min, respectively. The resultant CDC in the form of nanofilaments consisted of SWCNT and MWCNT. The diameter of the nanotube bundles increased from 14 to 20 to 30 to 50 nm when the synthesis temperature increased from 950 to 1050°C. Samples processed at higher temperature were more ordered, but distribution of tube diameters was similar at both temperatures, as observed by Raman spectroscopy.

Gorelik et al. [171] produced carbon onions from amorphous silicon carbide using a single shot of a KrF laser (pulse duration 25 ns, energy density 800 mJ/cm<sup>2</sup>, wavelength 248 nm). The temperature of the surface layer during the laser shot was estimated from numerical calculations to reach ~4000 K. Amorphous SiC films were produced either by laser ablation from a sintered SiC target or by ion implantation (Ge ions) into 6H-SiC. No difference of the CDC/SiC structure formed after laser irradiation of either type of substrate was detected. In each case, the irradiation resulted in the material crystallizing into the nanocrystalline cubic ( $\beta$ ) structure of SiC in the near-surface region down to 50 to 100 nm and formation of ~10 nm carbonaceous (CDC) layer at the very surface due to the preferential evaporation of Si from the surface. The size of SiC crystals ranged from 5 to 50 nm with larger crystals situated at the surface and smaller crystals at the interface between the crystallized and unaffected material. Carbon onions were observed both inside the polycrystalline SiC region and inside the carbonaceous surface layer. However, onions formed inside the SiC region were larger and less defective, suggesting different formation mechanisms.

Lower temperatures of crystalline silicon carbide decomposition may be required to form CNTs in the presence of metal catalysts [172]. The metal-coated substrates of polycrystalline SiC were heated to 1000 to 1200°C at 10<sup>-2</sup> Torr in a vacuum electric furnace. As a result, in the case of Pt, Ni, Co, Rh, and PtPd, carbon tubular nanostructures (tubes and fibers) grew at 1200°C. The SEM observation revealed that the synthesized structures range from 100 nm to 10  $\mu$ m in length. According to TEM images, the synthesized CNTs are multiwalled, ranging from 2 to 10 nm in diameter. Most of the tubular structures included a metal particle at the tip. The growth mechanism is thought to be similar to a CVD process.

We have shown previously that SiC whiskers generally decompose during high-temperature vacuum annealing into irregular porous graphitic structures (Figure 6.18). However, when SiC whiskers were synthesized using a Fe(CO)<sub>5</sub> catalyst with a considerable amount of Fe left in the whisker tip, we observed transformation of an SiC whisker into a single multiwalled carbon nanotube (MWCNT) (Figure 6.22). At the tip of the CNT, one may see a hollow onion-like structure, where a catalyst particle was presumably located prior to evaporation. The presence of metal has been reported to enhance SiC graphitization [173]. We assume that decomposition of the whisker started from the tip and continued along the whisker growth axis, leading to the CNT formation.

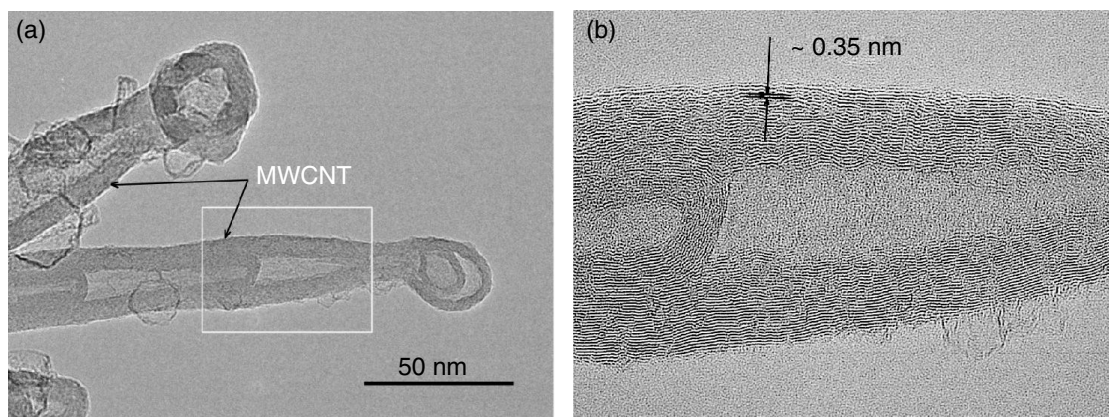


**FIGURE 6.22** Two SiC whiskers transformed into two MWCNTs during 1700°C annealing for 30 min in vacuum: TEM (a) and HRTEM of the framed section of the CNT (b). SiC whiskers were synthesized using  $\text{Fe}(\text{CO})_5$  catalyst and had a considerable amount of Fe impurities left in the tips.

## 6.5 APPLICATIONS

It has already been mentioned that CDC has a variety of applications including molecular sieves, sorbents for gas chromatography, soil detoxification, dehumidification, and catalysis. This section describes other potential applications of CDC in more detail.

### 6.5.1 SUPERCAPACITORS

Supercapacitors, which are also called ultracapacitors or electrical double-layer capacitors, are rechargeable devices for electrical energy storage. They are poised to begin displacing batteries in applications where high power and low weight are essential. As batteries rely on slow rate-determining chemical reactions, they lack the ability to supply quick power bursts. In addition, chemical reactions in batteries contribute to 20 to 25% of the charging energy being lost. Most high-power batteries offer limited lifetime, require narrow temperature window for efficient operation, and are not environmentally friendly. Supercapacitors offering long-cycle life (>100,000 cycles), high efficiency (>90%), and fast charging/discharging are competitive alternatives to batteries for such applications as personal electronic devices, mobile telecommunications, back-up power storage, and peak power sources for hybrid electric, electric, and traditional vehicles, among others [174–178].

A supercapacitor consists of two porous electrodes with high surface area separated by an ion-conducting membrane. Energy is stored as a charge separation in a thin double layer at the interface between the electrode and the electrolyte. To increase energy storage, the electrodes in a supercapacitor should have as high a surface area accessible to the electrolyte as possible. To date, various carbon materials have been used as electrodes in double-layer capacitors, including activated carbons, carbon fiber composites, and CNT. The main disadvantage of high surface area activated carbons used in supercapacitors is their wide pore-size distribution. A large fraction of the pores is too small to permit the electrolyte ions to freely diffuse in and out of pores, so that only a fraction of the total surface area is utilized to form a double layer (Figure 6.23). The presence of very small pores also increases the electrode resistance. Very large pores that are present in activated carbons are not so efficient for energy storage. Electrodes made from carbon fibers and CNT also suffer from a wide pore-size distribution. In the ideal case, the electrode material should have a narrow pore-size distribution with an average pore size tailored to suit the electrolyte used.

CDC produced by halogenation of carbides is an attractive material for supercapacitor electrodes. Among the advantages of CDC, high specific surface area and controlled pore size distribution (Figure 6.7 and Figure 6.8) are the most important. By choosing an appropriate precursor and synthesis conditions, and by using various post-treatments (e.g., activation), one can design CDCs

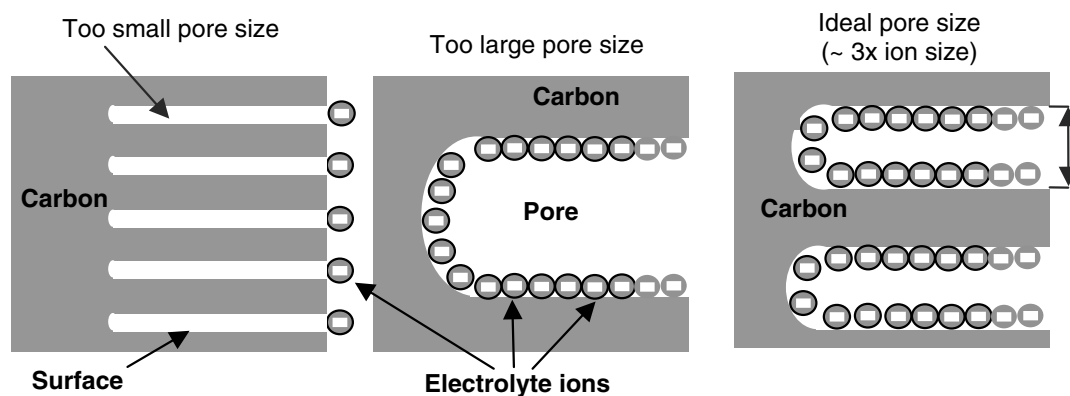


**FIGURE 6.23** Schematic explanation of the optimum pore size for the highest surface area accessible by the electrolyte ions.

with pore size tuned for the most efficient electrode performance. Two approaches to the design of CDC electrode bodies have been proposed. The first one suggests production of CDC–pyrocarbon composites that offer an increased mechanical strength [63,64,179]. This method was employed for preparation of supercapacitor electrodes with specific capacitance of up to  $39 \text{ F/cm}^3$  in aqueous electrolyte [180–182]. The second approach is conventional: CDC powder is mixed with an appropriate binder and then formed into a 100 to 400- $\mu\text{m}$ -thick film [183–190]. Specific capacitance values above 140 F/g (in case of organic electrolyte) and above 250 F/g (in the case of aqueous electrolyte) have been demonstrated. These values are considerably higher than those achieved with most activated carbons and CNT-based electrodes (20–100 F/g) [191]. Additional optimization of the CDC structure should further improve its electrochemical performance.

### 6.5.2 HYDROGEN STORAGE

The success of any future hydrogen economy depends, in large part, on our ability to develop inexpensive high-tech materials with sufficiently high hydrogen-storage capacity. Many types of materials have been tried or suggested for use as hydrogen-storage media. These include nano-materials, high-surface-area materials, synthetic metals, and chemical and metal hydrides. There are presently three generic routes known for the storage of hydrogen in materials; namely (1) *physisorption* as in the case of many porous carbon and zeolite materials, (2) *chemisorption* as in hydrogen storage in metal hydrides, and finally (3) *chemical reaction* such as complex metal hydrides and chemical hydrides. The sorption process typically requires highly porous materials to maximize the surface area available for hydrogen sorption to occur and to allow for easy uptake and release of hydrogen from the material. Among different types of hydrogen-storage materials discussed above, the carbon-based materials have received considerable attention. This is mainly due to carbon's light weight and low cost, its large abundance in nature, its nontoxic behavior (compared to metal hydrides), and high  $S_{\text{BET}}$  [192]. It is intuitive to suggest that hydrogen adsorption on porous carbon materials with similar structure should depend linearly on its specific surface area. This concept has been further generalized to include even dissimilar carbons [193]. However, in our experience, other parameters of nanoporous carbons, including their pore size, surface chemistry, and structure, may play a vital role in improved hydrogen (or any other gas) adsorption. We observed that CDC with  $S_{\text{BET}}$  under 1400  $\text{m}^2/\text{g}$  adsorbed twice as much hydrogen as other porous carbons with  $S_{\text{BET}}$  of over 2000  $\text{m}^2/\text{g}$ .

Compared to other carbons, CDCs offer independent control over pore shape, pore size, surface area, surface termination, and microstructure of carbon. As such, CDCs can be tuned for maximum sorption of a given gas (e.g., hydrogen).

Gordeev et al. [194,195] evaluated hydrogen sorption by some CDC at high temperatures of 300 to 700°C and both high (above 90 atm) and low (below 0.1 atm) pressures using the method of thermodesorption spectrometry. Hydrogenation at elevated temperatures leads to chemisorption of



hydrogen. Thermodesorption spectra registered in the temperature range up to 1500°C consisted of several phases. The desorption peaks observed at 500 to 550°C and 800 to 850°C were attributed to the hydrogen adsorbed on dangling carbon bonds and graphite-like carbon surfaces, respectively. The apparent activation energy and heat of sorption were estimated. It was also shown that doping the CDC samples with 0.5 wt% of palladium increased hydrogen uptake about 2.5 times.

Johansson et al. [196] were the first to study the low-temperature hydrogen uptake by CDC. Nanoporous CDC was prepared from  $Al_4C_3$  and SiC by chlorination and hydrogen sorption was measured at  $-196$ ,  $-78$ , and  $27^\circ C$ . At liquid nitrogen temperatures and pressure of  $\sim 100$  atm, the CDC demonstrated hydrogen uptake of up to 4.1 wt%.

Our preliminary testing has shown that at  $-196^\circ C$  and 1 atm, CDC samples exhibit  $H_2$  storage capacity up to 3 wt%, which is one of the highest reported for carbon materials. Interestingly, the SSA of these samples was only 1400  $m^2/g$ . Further optimization of CDC structure and an increase in the SSA to 3000  $m^2/g$  may allow the  $H_2$  uptake of above 6 wt%.

### 6.5.3 METHANE STORAGE

The use of natural gas (methane) as an automotive fuel offers considerable advantages, including reduced emission, lower maintenance, and, most importantly, lower fuel cost relative to gasoline. Moreover, the worldwide reserves of natural gas considerably exceed the oil reserves and thus natural gas may offer a solution when oil wells run dry. However, in order to compete with gasoline now (and offer comparable driving distance for vehicles before refueling), advanced methane storage units with large volumetric and gravimetric methane storage capacity need to be developed. Storing natural gas in a compressed form has the disadvantage of high cost of high-pressure cylinders needed to provide adequate methane storage capacity in a reasonably small volume. The use of inexpensive carbon adsorbent materials may allow the storage of considerable amounts of natural gas at relatively low pressure ( $<40$  bar), making it more attractive for practical use.

Similar to hydrogen-storage applications, CDC can be optimized to adsorb a large quantity of methane. We performed preliminary experiments on a selected CDC prepared from SiC and having SSA of 1200  $m^2/g$  and pore size of 0.82 nm [52], which is close to the theoretically calculated ideal pore size of 0.74 nm for high methane uptake [197]. This CDC outperforms commercially available activated carbons, offering 2.8 wt% methane storage at room temperature and atmospheric ( $\approx 1$  bar) pressure. Pressurizing methane to 40 atm generally increases the porous carbon sorption capacity 10 to 20 times [198–200].

### 6.5.4 LITHIUM-ION BATTERIES

The lithium battery industry is rapidly expanding. Presently, it represents the largest segment of the portable battery business, dominating the cell phone, camera, and laptop and notebook computer power source market sections. The first lithium batteries had metallic lithium as negative electrodes (anode, the source of lithium). However, it was found to produce dendrites, growing during the battery operation and inducing short circuits. Thus, metallic lithium anodes are not used any longer. Graphite is considered a good material for anodes in lithium-ion batteries as it may intercalate a considerable amount of lithium at low potential. One Li ion per six C atoms ( $LiC_6$ ) can be reached, which corresponds to a theoretical reversible specific capacity of 372 Ah/kg. Higher capacity values have been obtained for less ordered carbons [201–203], where two types of Li ions contribute to the charge transfer: intercalated Li and quasimetallic Li. Quasimetallic Li, occupying the nanopores, is responsible for very good reversible capacity at very low voltages [202]. Disorganized carbons may offer a longer life cycle and faster charging/discharging rates as compared to graphite, where Li ions have to diffuse a long distance between the closed-spaced graphene layers, leading to fast material degradation. It should be noted, however, that some issues, including relatively large irreversible capacity, still need to be resolved. Additionally, further increase in the reversible Li insertion amount by electrochemistry is highly desirable.

CDC can be prepared at a controlled level of ordering and porosity and thus may be an ideal material for systematic studies of the influence of these parameters on reversible Li insertion degree, ionic conductivity, lifetime, etc. These studies should allow fabrication of advanced Li-ion batteries with high specific power and energy density, longer lifetime, and higher efficiency.

A preliminary study has been performed on CDCs prepared from SiC, TiC, and Mo<sub>2</sub>C [204, 205]. Bulk CDC samples were lithiated over the temperature range 30–200°C. Concentration profiles of Li in CDCs were measured using the nuclear reaction <sup>7</sup>Li(p,a)<sup>4</sup>He. Diffusion coefficients obtained were in the range 10<sup>-9</sup>–10<sup>-7</sup> cm<sup>2</sup>/sec and dependent on the pore size and the diffusion process duration. A mechanism for the process proposed on this basis is mainly Li diffusion along pore walls and Li accumulation in pores followed by the formation of metal clusters [204].

### 6.5.5 Pt CATALYST ON CDC SUPPORT

Platinum supported on carbon (Pt/C) is widely used as a catalyst for hydrogenation and oxidation reactions. The porous structure of the carbon support is of primary importance in the catalyst performance. CDC provides an advantage of a narrow pore-size distribution and variable pore diameters. Pt/C catalysts are usually prepared by adsorption of platinum-containing species from the solution on the selected carbon material followed by the reduction of the platinum compound to metal state (see, e.g., [206]). This method is applicable to CDC. A novel one-stage method for preparation of Pt/C catalysts from SiC was proposed by McNallan and Gogotsi [207,208]. Silicon carbide ceramics were treated in Cl<sub>2</sub>–H<sub>2</sub>–Ar gas mixtures according to the technique described in the reports [28,86,87]. Additionally, metallic platinum was present in the reaction zone in the form of foil or wire. In this case, Pt particles were dispersed in the produced material forming interlayers in the carbon layer. The proposed mechanism of the process begins with platinum transport to the SiC/C interface via the gas phase in the form of triplatinum trichloride. Then Pt<sub>3</sub>Cl<sub>3</sub> reacts with Si from the SiC resulting in Pt and SiCl<sub>4</sub>.

### 6.5.6 TRIBOLOGICAL COATINGS

Metal carbides are widely used in a variety of machining and sliding contact applications. Despite their high corrosion and wear resistance, these materials are not lubricious. A novel process for the formation of a low-friction carbon layer on the SiC surface was recently introduced [13,88]. Tribological characterization of the CDC-coated silicon carbide ceramics was carried out in [209]. Sintered  $\alpha$ -SiC and CVD  $\beta$ -SiC specimens were treated in Cl<sub>2</sub>–H<sub>2</sub>–Ar mixtures of various compositions at temperatures from 700 to 1000°C and ambient pressure. Tribological tests consisting of measuring the friction coefficients and wear rates by means of standard ball-on-disk method were performed. It was observed that the produced articles had friction coefficients seven times lower than the untreated SiC. The friction coefficients of ~0.1 were almost independent of the type of initial material and parameters of the ball-on-disk test including contact load and sliding speed. As evidenced by the wear track features, the primary deformation process appears to be plastic flow of the carbon layer, resulting in smooth surface as the wear process progresses.

Further work [210–212] confirmed good tribological properties of CDC coatings in humid environments (air or water) but it also revealed that CDC shows a remarkably low friction coefficient (<0.03) with minimal wear in dry (nitrogen or vacuum) ambient. This behavior is unlike that of graphite and other sp<sup>2</sup> modifications of carbon, where the presence of water vapors is required for lubricity and long-time stability of the coatings. The presence of carbon onions and termination of dangling carbon bonds with hydrogen can explain the excellent performance of CDC in dry atmospheres. Potential applications of CDC coatings (with or without lubricants) include bearings, SiC-based MEMS, and dynamic seals of water pumps, to name a few.

CDC coatings on SiC fibers could be used to improve pull-out behavior and damage tolerance in composite materials [92,213]. Moreover, CDC can be used as a sacrificial layer for the formation of BN and Al–O–N coatings, which offer better oxidation resistance than carbon [214,215]. These

novel methods of coating synthesis by carbothermal nitridation consist of several steps. First CDC layer is produced on SiC fibers, then CDC is infiltrated with either boric acid (for BN formation) or aluminum chloride solution (for Al–O–N formation), and finally samples are treated in ammonia at atmospheric pressure and elevated temperatures to produce BN (or Al–O–N) coatings. The intermediate CDC layer helps to build a strong bonding between the fiber and coating. Formation of BN coatings did not result in any degradation in tensile strength of the SiC fibers. Synthesis of Al–O–N coatings led to more than 65% improvement in the tensile strength and a threefold increase in the Weibull modulus for the fiber with 200 nm coating compared to those for the as-received fibers. The coated fiber exceeds the strength of all other small-diameter SiC fibers reported in literature.

## 6.6 CONCLUSIONS

The synthesis of almost all known carbon structures, including amorphous and nanocrystalline graphitic carbon, graphite ribbons, CNTs, carbon onions, nanodiamond, and ordered graphite, is possible by the extraction of metals from carbides. In addition, CDC synthesis allows formation of highly porous carbon materials with good mechanical properties. Microstructure, pore size, pore shape, and surface termination of nanoporous CDC can be precisely controlled by the process parameters and the composition and structure of the initial carbide precursor. As such, the process allows optimization of nanoporous CDC for various applications.

Thermodynamic analysis shows the possibility of carbon synthesis from almost any carbide under appropriate process conditions (temperature, pressure, and etchant). While more experimental data have been obtained on SiC, about 20 other carbides have been successfully used to produce CDC.

Along with conventional applications for porous carbon as sorbents, new applications are enabled by tailorable structure and porosity of CDC. Tests performed to investigate the hydrogen and methane storage capabilities of CDC revealed that CDC could outperform the entire spectrum of commercial porous carbons and most of the other novel carbon materials. As such, CDC is a very promising material for numerous energy-related applications. CDC as a storage medium of active chlorine may be used for various sanitization purposes. Tribological testing of CDC coatings in humid and dry (nitrogen or vacuum) ambient showed the low friction coefficient and high mechanical stability of this material. Carbothermal nitridation of CDC coatings allows formation of well-adhered oxidation-resistant nitride coatings on SiC. Preliminary results on the performance of CDC as electrodes in supercapacitors or Li-ion batteries are also very promising. However, for most of the applications discussed, more research needs to be done in order to understand the mechanisms behind the interaction of CDC with gases, liquids, and organic molecules and to improve further the performance of CDC.

## ACKNOWLEDGMENTS

This work was supported by DARPA via ONR contract. Y. Gogotsi acknowledges the productive collaboration with Professor M.J. McNallan (UIC) and help from his students and postdoctoral associates H. Ye, B. Carroll, L. Chen, R. Dash, J. Chmiola, E. Hoffman, and Z.G. Cambaz at Drexel University, and S. Welz at University of Illinois at Chicago, who worked with him on the development of new CDC materials.

## REFERENCES

1. O.A. Shenderova, V.V. Zhirnov, and D.W. Brenner, Carbon nanostructures, *Critical Rev. Solid State Mat. Sci.*, **27**, 227–356, 2004.
2. A.L. Vereshchagin, *Detonation Nanodiamonds*, Altai State Technical University, Barnaul, Russia, 2001.
3. V.Y. Dolmatov, Detonation synthesis of ultradispersed diamonds: properties and applications, *Russ. Chem. Rev.*, **70**, 607–626, 2001.

4. M. Inagaki, *New Carbons*. Elsevier, Amsterdam, 2000.
5. S. Subramoney, Novel nanocarbons — structure, properties, and potential applications. *Adv. Mater.*, **10**, 1157, 1998.
6. R.W. Baker, Future directions of membrane gas separation technology. *Ind. Eng. Chem. Res.*, **41**, 1393–1411, 2002.
7. T. Duren, L. Sarkisov, O.M. Yaghi, and R.Q. Snurr, Design of new materials for methane storage, *Langmuir*, **20**, 2683–2689, 2004.
8. V.Y. Dolmatov and L.N. Kostrova, Detonation synthesis of nanodiamonds and the feasibility of developing a new generation of drugs, *J. Superhard Mater.*, **3**, 79–82, 2000.
9. G.P. Bogatyreva and M.A. Marinich, *NATO Advanced Research Workshop on Nanostructured Materials and Coatings for Biomedical and Sensor Applications*, Y. Gogotsi and I. Uvarova, Eds., Kiev, Ukraine, 2002.
10. S.V. Mikhalovsky, Emerging technologies in extracorporeal treatment: focus on adsorption, *Perfusion-UK*, **18**, 47–54, 2003.
11. R.A. Freitas, *Nanomedicine*, Landes Bioscience, TX, USA, 2003.
12. Y. Gogotsi, V. Kamyshenko, V. Shevchenko, S. Welz, D.A. Ersoy, and M.J. McNallan, Nanostructured carbon coatings on silicon carbide: experimental and theoretical study, in *NATO ASI on Functional Gradient Materials and Surface Layers Prepared by Fine Particles Technology*, M.-I. Baraton and I. Uvarova, Eds., Kluwer Academic, Dordrecht, 2001, pp. 239–255.
13. D.A. Ersoy, M.J. McNallan, and Y. Gogotsi, Carbon coatings produced by high temperature chlorination of silicon carbide ceramics, *Mat. Res. Innovat.*, **5**, 55–62, 2001.
14. Z.G. Cambaz, G.N. Yushin, K.L. Vyshnyakova, L.N. Pereseltseva, and Y.G. Gogotsi, Conservation of shape during formation of carbide-derived carbon on silicon carbide nano-whiskers, *J. Am. Ceram. Soc.*, 2005, in press.
15. W.A. Mohun, A novel amorphous carbon, *Proceedings of the 4th Biennial Conference on Carbon*, Pergamon, Oxford, 1959, pp. 443–453.
16. M. Kusunoki, M. Rokkaku, and T. Suzuki, Epitaxial carbon nanotube film self-organized by decomposition of silicon carbide, *Appl. Phys. Lett.*, **71**, 2620–2622, 1997.
17. S. Welz, Identification of carbon structures synthesized by chlorination of SiC and TiC. Ph.D. dissertation, University of Illinois at Chicago, Chicago, 2003.
18. J. Zhang, T.C. Ekstrom, S.K. Gordeev, and M. Jacob, Carbon with an onion-like structure obtained by chlorinating titanium carbide, *J. Mater. Chem.*, **10**, 1039–1041, 2000.
19. Y. Gogotsi, S. Weltz, D.A. Ersoy, and M.J. McNallan, Conversion of silicon carbide to crystalline diamond-structured carbon at ambient pressure, *Nature*, **411**, 283–287, 2001.
20. A.M. Danishevski, G.N. Mosina, E.A. Smorgonskaya, S.K. Gordeev, A.V. Grechinskaya, C. Jardin, R. Meaudre, and O. Marty, Effect of preparation conditions on diamond cluster formation in bulk nanoporous carbon, *Diam. Relat. Mater.*, **12**, 378–382, 2003.
21. S. Dimovski, A. Nikitin, H. Ye, and Y. Gogotsi, Synthesis of graphite by chlorination of iron carbide at moderate temperatures, *J. Mater. Chem.*, **14**, 238–243, 2004.
22. A. Nikitin and Y. Gogotsi, Nanostructured carbide-derived carbon, in *Encyclopedia of Nanoscience and Nanotechnology*, Vol. 7, H.S. Nalwa, Ed., American Scientific Publishers, Stevenson Ranch, CA, USA, 2003, pp. 553–574.
23. O. Hutchins, Method for the Production of Silicon Tetrachloride, US Patent 1271713, 1918.
24. J.N. Andersen, Silicon Tetrachloride Manufacture, US Patent 2739041, 1956.
25. G.F. Kirillova, G.A. Meerson, and A.N. Zelikman, Kinetics of chlorination of titanium and niobium carbides, *Izvestiya vuzov, Tsvetnaya. Metallurgiya.*, **3**, 90–96, 1960.
26. V.P. Orekhov, G.V. Seryakov, A.N. Zelikman, T.M. Starobina, T.I. Kahzanova, K.V. Petrova, and P.M. Sverchkov, Kinetics of chlorination of zirconium carbide briquets. *J. Appl. Chem. USSR*, **42**, 230–237, 1969.
27. N.S. Jacobson, Y.G. Gogotsi, and M. Yoshimura, Thermodynamic and Experimental Study of Carbon Formation on Carbides under Hydrothermal Conditions. *J. Mater. Chem.*, **5**, 595–601, 1995.
28. Y.G. Gogotsi, I.-D. Jeon, and M.J. McNallan, Carbon coatings on silicon carbide by reaction with chlorine-containing gases, *J. Mater. Chem.*, **7**, 1841–1848, 1997.
29. M.J. McNallan, Y.G. Gogotsi, and I. Jeon, Preparation of carbon films by high temperature chlorination of metal carbides, *Proceedings of the 9th International Conference on High Temperature Materials Chemistry*, Vol. 97–39, K.E. Spear, Ed., The Electrochemical Society, Inc., Pennington, NJ, 1997.

30. R.K. Dash, G. Yushin, and Y. Gogotsi, Synthesis, structure and porosity analysis of microporous and mesoporous carbon derived from zirconium carbide, *Microporous and Mesoporous Mater.*, **86**, 50–57, 2005.
31. G. Yushin, E. Hoffman, A. Nikitin, H. Ye, M.W. Barsoum, and Y. Gogotsi, Synthesis of nanoporous carbide-derived carbon by chlorination of titanium silicon carbide. *Carbon*, **43**, 2075–2082, 2005.
32. R.K. Dash, A. Nikitin, and Y. Gogotsi, Nanoporous carbon derived from boron carbide. *Microporous Mesoporous Mater.*, **72**, 203–208, 2004.
33. Nillok Chemicals, Improvements in and Relating to Mineral Active Carbons and to a Process for Their Preparation. Great Britain Patent 971943, 1964.
34. W.A. Mohun, Mineral Active Carbon and Process for Producing Same, US Patent 3066099, 1962.
35. B.D. Vasilenko, Ph.D. Dissertation, Studies of carbide chlorination, Mintsvetmetzoloto, Moscow, USSR, 1956.
36. A.K. Kuriakose and J.L. Murgrave, Kinetics of reactions of elemental fluorine — 1, *J. Phys. Chem.*, **68**, 290–295, 1964.
37. A.K. Kuriakose and J.L. Murgrave, Kinetics of reactions of elemental fluorine — 2, *J. Phys. Chem.*, **68**, 2343–2345, 1964.
38. D. Ersoy, M.J. McNallan, and Y.G. Gogotsi, Carbon coatings produced by high temperature chlorination of silicon carbide ceramics, *Mater. Res. Innov.*, **5**, 55–62, 2001.
39. L. Chen, H. Ye, Y. Gogotsi, and M. McNallan, Carbothermal synthesis of boron nitride coatings on silicon carbide. *J. Am. Ceram. Soc.*, **86**, 1830–1837, 2003.
40. H.P. Boehm and H.H. Warnecke, Structural parameters and molecular sieve properties of carbons prepared from metal carbides, *Proceedings of the 12th Biennial Conference on Carbon*, Pergamon, Oxford, 1975, pp. 149–150.
41. N.F. Fedorov, G.K. Ivakhnyuk, V.V. Tetenov, and G.V. Matyukhin, Carbon adsorbents based on silicon carbide, *J. Appl. Chem. USSR*, **54**, 1239–1242, 1981.
42. N.F. Fedorov, G.K. Ivakhnyuk, and D.N. Gavrilov, Porous structure of carbon adsorbents from titanium carbide, *Z. Prikladnoi Khimii*, **55**, 46–50, 1982.
43. N.F. Fedorov, G.K. Ivakhnyuk, and D.N. Gavrilov, Carbon adsorbents from carbides of the IV–VI groups transition metals, *Z. Prikladnoi Khimii*, **55**, 272–275, 1982.
44. O.E. Babkin, G.K. Ivakhnyuk, and N.F. Fedorov, Porous structure of carbon adsorbents from zirconium carbide, *Z. Prikladnoi Khimii*, **57**, 504–508, 1984.
45. K.S.W. Sing, D.H. Everett, R.A.V. Haul, L. Moscou, R.A. Pierotti, J. Rouquerol, and T. Siemieniewska, Reporting physisorption data for gas/solid systems, *Pure Appl. Chem.*, **57**, 603–619, 1985.
46. M.M. Dubinin, Microporous structures and absorption properties of carbonaceous adsorbents, *Carbon*, **21**, 359–366, 1983.
47. M.M. Dubinin, Generalization of the theory of volume filling of micropores to nonhomogeneous microporous structures, *Carbon*, **23**, 373–380, 1985.
48. S.K. Gordeev, S.A. Kukushkin, A.V. Osipov, and Y.V. Pavlov, Self-organization in the formation of a nanoporous carbon material, *Phys. Solid State*, **42**, 2314–2317, 2000.
49. Y. Gogotsi, A. Nikitin, H. Ye, W. Zhou, J.E. Fischer, B. Yi, H.C. Foley, and M.W. Barsoum, Nanoporous carbide-derived carbon with tunable pore size, *Nature Mater.*, **2**, 591–594, 2003.
50. E.N. Hoffman, G. Yushin, M.W. Barsoum, and Y. Gogotsi, Synthesis of carbide-derived carbon by chlorination of  $Ti_2AlC$ , *Chem. Mater.*, **17**, 2317–2322, 2005.
51. R.K. Dash, A. Nikitin, and Y. Gogotsi, Microporous carbon derived from boron carbide. *Microporous Mesoporous Mater.*, **72**, 203–208, 2004.
52. Y. Gogotsi, V.L. Kuznetsov, G.N. Yushin, A. Nikitin, A.V. Okotrub, A.I. Romanenko, A.I. Boronin, and E. Pozhetnov, Effect of synthesis temperature on structure and properties of nanoporous carbon derived from silicon carbide, *Carbon*, 2006, in press.
53. J. Leis, A. Perkson, M. Arulepp, M. Kaarik, and G. Svensson, Carbon nanostructures produced by chlorinating aluminium carbide, *Carbon*, **39**, 2043–2048, 2001.
54. M. Jacob, U. Palmqvist, P. Alberius-Henning, and T. Ekstrom, Bulk synthesis of nanotube-like carbon material. *Mat. Res. Soc. Symp. Proc.*, **593**, 87–92, 2000.
55. E.P. Barrett, L.G. Joyner, and P.P. Halenda, The determination of the pore volume and area distributions in porous substances: computations from nitrogen isotherms, *J. Am. Ceram. Soc.*, **73**, 373–380, 1951.
56. N.F. Fedorov, G.K. Ivakhnyuk, and D.N. Gavrilov, Porous structure of carbon adsorbents from titanium carbide, *Z. Prikladnoi Khimii*, **55**, 46–50, 1982 [in Russian].

57. J. Leis, A. Perkson, M. Arulepp, P. Nigu, and G. Svensson, Catalytic effect of metals of the iron subgroup on the chlorination of titanium carbide to form nanostructural carbon, *Carbon*, **40**, 1559–1564, 2002.
58. Y.A. Kukushkina, R.G. Avarbe, and V.V. Sokolov, Parameters of the porous structure of carbon produced by thermochemical treatment of nonporous carbides, *Russ. J. Appl. Chem.*, **69**, 620–622, 1996.
59. Y.A. Kukushkina, R.G. Avarbe, V.V. Sokolov, and T.V. Mazaeva, Properties of tubular carbon articles prepared by chlorination of silicon carbide with various initial porosities, *Russ. J. Appl. Chem.*, **69**, 623–625, 1996.
60. S.K. Gordeev and A.V. Vartanova, Porosity of materials produced by chlorination of covalent and metal-like carbides, *Z. Prikladnoi Khimii*, **64**, 1178–1182, 1991 [in Russian].
61. G.K. Ivakhnyuk, O.E. Babkin, and N.F. Fedorov, Technological principles of the synthesis of model adsorbent for chromatography, *Russ. J. Phys. Chem.*, **67**, 1849–1852, 1993.
62. S.K. Gordeev and A.V. Vartanova, Porosity variation in the process of forming of carbide materials and making compact carbon adsorbents on their basis, *Z. Prikladnoi Khimii*, **67**, 1080–1084, 1994 [in Russian].
63. S.K. Gordeev, R.G. Avarbz, A.E. Kravtjik, J.A. Kukuşjkina, V.V. Sokolov, T.V. Mazaeva, and A. Grechinskaya, A method for Producing a Porous Article and an Article Produced Thereby, PCT Patent WO 98/54111, 1998.
64. S.K. Gordeev and A.V. Vartanova, Novel approach for obtaining of bulk microporous materials, *Z. Prikladnoi Khimii*, **67**, 1375–1377, 1994 [in Russian].
65. Y.A. Kukushkina, R.G. Avarbe, V.V. Sokolov, and A.E. Kravchik, Influence of pyrocarbon content on properties of carbon–carbon sorption-active composites, *Russ. J. Appl. Chem.*, **72**, 2144–2145, 1999.
66. A. Manivannan, M. Chirila, N.C. Giles, and M.S. Seehra, Microstructure, dangling bonds and impurities in activated carbons, *Carbon*, **37**, 1741–1747, 1999.
67. F. Euler and E.R. Czerlinsky, X-ray studies of amorphous carbon from silicon carbide, *Proceedings of the Conference on Silicon Carbide. A High Temperature Semiconductor*, J. Smiltens, Ed., Pergamon Press, Oxford, 1960, pp. 155–161.
68. L.F. Lowe, H.D. Thompson, and J.P. Cali, Neutron activation analysis of silicon carbide, *Proceedings of the Conference on Silicon Carbide. A High Temperature Semiconductor*, J. Smiltens, Ed., Pergamon Press, Oxford, 1960, pp. 221–226.
69. M.J. McNallan, S.Y. Ip, S. Saam, and W.W. Liang, High Temperature corrosion of SiC based ceramics in chlorine containing environments, in *High Temperature Materials Chemistry — III*, D. Cubicciotti, Ed., The Electrochemical Society, Pennington, NJ, 1986, pp. 328–338.
70. S.Y. Ip, M.J. McNallan, and M.E. Schreiner, Oxidation of SiC ceramic heat exchanger materials in the presence of chlorine at 1300°C, in *Silicon Carbide '87 Ceramic Transactions*, Vol. 2, C.E. Semler, Ed., The American Ceramic Society: Columbus, OH, 1989, pp. 289–299.
71. M.J. McNallan, S.Y. Ip, S.Y. Lee, and C. Park, Corrosion of silicon-based ceramics in mixed oxygen–chlorine environments, in *Corrosion and Corrosive Degradation of Ceramics, Ceramic Transactions*, Vol. 10, M.J. McNallan, Ed., The American Ceramic Society: Columbus, OH, 1990, pp. 309–332.
72. D.S. Park, M.J. McNallan, C. Park, and W.W. Liang, Active corrosion of alpha-silicon carbide in oxygen–chlorine gases at elevated temperatures, *J. Am. Ceram. Soc.*, **73**, 1323–1329, 1990.
73. J.E. Marra, E.R. Kreidler, N.S. Jacobson, and D.S. Fox, Reactions of silicon-based ceramics in mixed oxidation chlorination environments, *J. Am. Ceram. Soc.*, **71**, 1067–1073, 1988.
74. J.E. Marra, E.R. Kreidler, N.S. Jacobson, and D.S. Fox, The behavior of SiC and Si<sub>3</sub>N<sub>4</sub> ceramics in mixed oxidation/chlorination environments, in *Silicon Carbide '87. Ceramic Transactions*, Vol. 2, C.E. Semler, Ed., The American Ceramic Society, Columbus, OH, 1989, pp. 275–286.
75. J.E. Marra, E.R. Kreidler, N.S. Jacobson, and D.S. Fox, Direct mass spectromic identification of silicon oxychloride compounds, *J. Electrochem. Soc.*, **135**, 1571–1574, 1988.
76. M. Balooch and D.R. Olander, Etching of silicon carbide by chlorine, *Surf. Sci.*, **261**, 321–324, 1992.
77. W.-S. Pan and A.J. Steckl, Reactive ion etching of SiC thin films by mixtures of fluorinated gases and oxygen, *J. Electrochem. Soc.*, **137**, 212–220, 1990.
78. P.H. Yih and A.J. Steckl, Effects of hydrogen additive on obtaining residue-free reactive ion etching beta-SiC in fluorinated plasmas, *J. Electrochem. Soc.*, **140**, 1813–1824, 1993.
79. P.H. Yih and A.J. Steckl, Residue-free reactive ion etching of 3C-SiC and 6H-SiC in fluorinated mixture plasmas, *J. Electrochem. Soc.*, **142**, 2853–2860, 1995.

80. R.N. Kyutt, É.A. Smorgonskaya, A.M. Danishevskii, S.K. Gordeev, and A.V. Grechinskaya, Structural studies of nanoporous carbon produced from silicon carbide, *Phys. Solid State*, **41**, 808–810, 1999.
81. R.N. Kyutt, É.A. Smorgonskaya, A.M. Danishevskii, S.K. Gordeev, and A.V. Grechinskaya, Structural study of nanoporous carbon produced from polycrystalline carbide materials: small-angle x-ray scattering, *Phys. Solid State*, **41**, 1359–1363, 1999.
82. É.A. Smorgonskaya, R.N. Kyutt, S.K. Gordeev, A.V. Grechinskaya, Y.A. Kukushkina, and A.M. Danishevskii, On fractal nature of the structure of nanoporous carbon obtained from carbides, *Phys. Solid State*, **42**, 1176–1181, 2000.
83. É.A. Smorgonskaya, R.N. Kyutt, A.V. Shchukarev, S.K. Gordeev, and A.V. Grechinskaya, X-ray studies of nanoporous carbon powders produced from silicon carbide, *Semiconductors*, **35**, 661–665, 2001.
84. V.V. Popov, S.K. Gordeev, A.V. Grechinskaya, and A.M. Danishevskii, Electrical and thermoelectric properties of nanoporous carbon, *Phys. Solid State*, **44**, 789–792, 2002.
85. E. Smorgonskaya, R. Kyutt, A. Danishevskii, C. Jardin, R. Meaudre, O. Marty, S. Gordeev, and A. Grechinskaya, X-ray and HRTEM structural studies of bulk nanoporous carbon materials produced from carbides, *J. Non-Crystalline Solids*, **299–302**, 810–814, 2002.
86. I.D. Jeon, M.J. McNallan, and Y.G. Gogotsi, Formation of carbon coatings on silicon carbide by reactions in halogen containing media, in *Proceedings of the Symposium on Fundamental Aspects of High Temperature Corrosion*, Vol. 96–26, P.Y. Hou, Ed., The Electrochemical Society: Pennington, NJ, 1996, pp. 256–268.
87. Y.G. Gogotsi, Formation of carbon coatings on carbide fibers and particles by disproportionation reactions, in *Advanced Multilayered and Fibre-Reinforced Composites*, Y.M. Haddad, Ed., Kluwer Academic Publishers: Dordrecht, 1998, pp. 217–230.
88. D.A. Ersoy, M.J. McNallan, and Y. Gogotsi, High temperature chlorination of SiC for preparation of tribological carbon films, *Proceedings of the Symposium on High Temperature Corrosion and Materials Chemistry*, Vol. 98–99, P.Y. Hou, M.J. McNallan, R. Oltra, E.J. Opila, and D.A. Shores, Eds., The Electrochemical Society, Inc.: Pennington, NJ, 1998, pp. 324–333.
89. Y. Gogotsi, V.L. Kuznetsov, G.N. Yushin, A. Nikitin, A.V. Okotrub, A.I. Romanenko, A.I. Boronin, and E. Pozhetnov, Effect of synthesis temperature on structure and properties of nanoporous carbon derived from silicon carbide, *Carbon*, 2006, in press.
90. A.M. Danishevskii, É.A. Smorgonskaya, S.K. Gordeev, and A.V. Grechinskaya, Raman light scattering in nanoporous carbon obtained from silicon and titanium carbides, *Phys. Solid State*, **43**, 137–144, 2001.
91. Y.G. Gogotsi, S. Welz, J. Daghfal, M.J. McNallan, I.-D. Jeon, K.G. Nickel, and T. Kraft, Formation of carbon coatings on SiC fibers by selective etching in halogens and supercritical water, *The 22th Annual Conference on Composites, Advanced Ceramics, Materials and Structures: A*, D. Bray, Ed., Am. Ceram. Soc., Westerville, OH, 1998, pp. 87–94.
92. M.J. McNallan, Y. Gogotsi, and D.A. Ersoy, Reaction formed coatings for SiC fibers in ceramic matrix composites, in *Elevated Temperature Coatings: Science and Technology III*, J.M. Hampikian and N.B. Dahotre, Eds., The Minerals, Metals & Materials Society, Warrendale, PA, USA, 1999, pp. 351–359.
93. S. Welz, Y. Gogotsi, and M. McNallan, Nucleation, growth, and graphitization of diamond nanocrystals during chlorination of carbides, *J. Appl. Phys.*, **93**, 4207–4214, 2003.
94. O.E. Babkin, G.K. Ivakhnyuk, Y.N. Lukin, and N.F. Fedorov, Study of structure of carbide derived carbon by XPS, *Z. Prikladnoi Khimii*, **57**, 1719–1721, 1984.
95. A.M. Danishevskii, G.N. Mosina, E.A. Smorgonskaya, S.K. Gordeev, A.V. Grechinskaya, C. Jardin, R. Meaudre, and O. Marty, Effect of preparation conditions on diamond cluster formation in bulk nanoporous carbon, *Diam. Relat. Mater.*, **12**, 378–382, 2003.
96. V.V. Kamysenko, V.I. Shevchenko, Y.G. Gogotsi, and V.V. Kartuzov, Theoretical studies of diamond film growth on (1 1 1) SiC surface, in *Mathematical Models and Computing Experiment in Materials Science*, Vol. 5, B.A. Galanov, Ed., Frantsevich Institute for Problems of Materials Science, Kiev, 2001, pp. 65–71.
97. J. Zheng, T.C. Eckström, S.K. Gordeev, and M. Jacob, Carbon with an onion-like structure obtained by chlorinating titanium carbide, *J. Mater. Chem.*, **10**, 1039–1041, 2000.
98. S. Weltz, Identification of Carbon Structures Synthesized by Chlorination of SiC and TiC, Ph.D. dissertation, University of Illinois at Chicago, Chicago, 2003.
99. H.P. Boehm, The first observation of carbon nanotubes, *Carbon*, **35**, 581–584, 1997.

100. Y. Gogotsi, A. Nikitin, H. Ye, W. Zhou, J.E. Fischer, B. Yi, H.C. Foley, and M.W. Barsoum, Nanoporous carbide-derived carbon with tunable pore size, *Nature Mater.*, **2**, 591–594, 2003.
101. T. Ekstrom, M. Jacob, J. Zheng, P. Berius-Henning, U. Palmqvist, J. Leis, and A. Perkson, Method for Producing a Nanotubular Carbon Material and the Material Produced Thereby, PCT Patent WO 01/16023, 2001.
102. A. Perkson, J. Leis, M. Arulepp, M. Kaarik, S. Urbonaite, and G. Svensson, Barrel-like carbon nanoparticles from carbide by catalyst assisted chlorination, *Carbon*, **41**, 1729–1735, 2003.
103. J. Leis, A. Perkson, M. Arulepp, M. Kaarik, and G. Svensson, Carbon nanostructures produced by chlorinating aluminium carbide, *Carbon*, **39**, 2043–2048, 2001.
104. T.Y. Kosolapova, *Carbides. Properties, Production, and Applications*, Plenum Press, New York, 1971.
105. D. Osetzky, Macrocrystalline graphite from magnesium carbide, *Carbon*, **12**, 517–523, 1974.
106. N.F. Fedorov, G.K. Ivakhnyuk, and V.V. Samonin, Mesoporous carbon adsorbents from calcium carbide, *J. Appl. Chem. USSR*, **54**, 2253–2255, 1981.
107. G.K. Ivakhnyuk, V.V. Samonin, N.F. Fedorov, V.A. Vladimirov, L.V. Stepanova, and O.M. Kas'yanova, Carbon enriched calcium carbide and possibility of its application, *Z. Prikladnoi Khimii*, **60**, 852–856, 1987.
108. G.K. Ivakhnyuk, V.V. Samonin, and N.F. Fedorov, Study of properties of carbon derived from calcium carbide in the presence of nitrogen, *Z. Prikladnoi Khimii*, **60**, 1413–1415, 1987.
109. V.V. Samonin, G.K. Ivakhnyuk, and N.F. Fedorov, On mechanism of interaction between calcium carbide and metal chlorides, *Z. Prikladnoi Khimii*, **60**, 2357–2358, 1987.
110. N.F. Fedorov and V.V. Samonin, Theoretical foundations of carbide-thermal technology for production of activated carbon and sorption-active materials, *Russ. J. Appl. Chem.*, **71**, 584–588, 1998.
111. N.F. Fedorov and V.V. Samonin, Production, pore structure, adsorption properties, and fields of application of composite sorbents from calcium carbide, *Russ. J. Appl. Chem.*, **71**, 795–798, 1998.
112. S. Shimada, M. Inagaki, and K. Matsui, Oxidation kinetics of hafnium carbide in the temperature range of 480–600°C, *J. Am. Ceram. Soc.*, **75**, 2671–2678, 1992.
113. C.B. Bargerion and R.C. Benson, Oxidation of hafnium carbide in the temperature range 1400–2060°C, *J. Am. Ceram. Soc.*, **76**, 1040–1046, 1993.
114. S. Shimada, K. Nakajima, and M. Inagaki, Oxidation of single crystals of hafnium carbide in a temperature range of 600–900°C, *J. Am. Ceram. Soc.*, **80**, 1749–1756, 1997.
115. S. Shimada, F. Yunazar, and S. Otani, Oxidation of hafnium carbide and titanium carbide single crystals with the formation of carbon at high temperatures and low oxygen pressures, *J. Am. Ceram. Soc.*, **83**, 721–728, 2000.
116. S. Shimada, Formation and mechanism of carbon-containing oxide scales by oxidation of carbides (ZrC, HfC, TiC), *Mater. Sci. Forum*, **369–372**, 377–384, 2001.
117. S. Shimada, A thermoanalytical study on the oxidation of ZrC and HfC powders with formation of carbon, *Solid State Ionics*, **149**, 319–326, 2002.
118. S. Shimada and T. Ishii, Oxidation kinetics of zirconium carbide at relatively low temperatures, *J. Am. Ceram. Soc.*, **73**, 2804–2808, 1990.
119. S. Shimada, M. Nishisako, M. Inagaki, and K. Yamamoto, Formation and microstructure of carbon-containing oxide scales by oxidation of single crystals of zirconium carbide, *J. Am. Ceram. Soc.*, **78**, 41–48, 1995.
120. S. Shimada, Microstructural observations of ZrO<sub>2</sub> scales formed by oxidation of ZrC single crystals with formation of carbon, *Solid State Ionics*, **101–103**, 749–753, 1997.
121. S. Shimada, M. Yoshimatsu, M. Inagaki, and S. Otani, Formation and characterization of carbon at the ZrC/ZrO<sub>2</sub> interface by oxidation of ZrC single crystals, *Carbon*, **36**, 1125–1131, 1998.
122. Y.G. Gogotsi and M. Yoshimura, Formation of carbon films on carbides under hydrothermal conditions, *Nature*, **367**, 628–630, 1994.
123. Y.G. Gogotsi and M. Yoshimura, Low-temperature oxidation, hydrothermal corrosion, and their effects on properties of SiC (Tyranno) fibers, *J. Am. Ceram. Soc.*, **78**, 1439–1450, 1995.
124. Y. Gogotsi and M. Yoshimura, Degradation of SiC (Tyranno) fibers in high-temperature, high-pressure water, *J. Mater. Sci. Lett.*, **14**, 755–759, 1995.
125. Y.G. Gogotsi, Y. Tanabe, E. Yasuda, and M. Yoshimura, Effect of oxidation and hydrothermal corrosion on strength of SiC fibres, in *Advanced Materials '93, I/A: Ceramics, Powders, Corrosion and Advanced Processing*, N. Mizutani, Ed., Elsevier, Amsterdam, Netherlands, 1994.



126. Y. Gogotsi, *Hydrothermale Korrosion von SiC — Betrachtung der schädlichen und nützlichen Aspekte*, in *Korrosion und Verschleiß von keramischen Werkstoffen*, R. Telle and P. Quirnbach, Eds., Deutsche Keramische Gesellschaft, Aachen, 1994, pp. 114–122.
127. Y.G. Gogotsi, M. Yoshimura, M. Kakihana, Y. Kanno, and M. Shibuya, Hydrothermal synthesis of carbon films on SiC fibers and particles, in *Ceramic Processing Science and Technology*, H. Hausner, G.L. Messing, and S.-I. Hirano, Eds., American Ceramic Society, Westerville, OH, 1995, pp. 243–247.
128. T. Kraft, K.G. Nickel, and Y.G. Gogotsi, Hydrothermal degradation of chemical vapour deposited SiC fibres, *J. Mater. Sci.*, **33**, 4357–4364, 1998.
129. T. Kraft and K.G. Nickel, Carbon formed by hydrothermal treatment of alpha-SiC crystals, *J. Mater. Chem.*, **10**, 671–680, 2000.
130. Y.G. Gogotsi, K.G. Nickel, and P. Kofstad, Hydrothermal synthesis of diamond from diamond-seeded  $\beta$ -SiC powder, *J. Mater. Chem.*, **5**, 2313–2314, 1995.
131. Y.G. Gogotsi, P. Kofstad, M. Yoshimura, and K.G. Nickel, Formation of  $sp^3$ -bonded carbon upon hydrothermal treatment of SiC, *Diamond Relat. Mater.*, **5**, 151–162, 1996.
132. Y.G. Gogotsi and K.G. Nickel, Hydrothermal synthesis of diamond: challenges and opportunities, *The 21st Annual Conference on Composites, Advanced Ceramics, Materials and Structures — B*, American Ceramic Society, Westerville, OH, 1997, pp. 747–754.
133. R. Roy, D. Ravichandran, A. Badzian, and E. Breval, Attempted hydrothermal synthesis of diamond by hydrolysis of  $\beta$ -SiC powder, *Diamond Relat. Mater.*, **5**, 973–976, 1996.
134. K.G. Nickel, T. Kraft, and Y.G. Gogotsi, Hydrothermal synthesis of diamond, in *Handbook of Ceramic Hard Materials*, R. Riedel, Ed., Wiley-VCH, Weinheim, 2000, pp. 374–389.
135. K. Motzfeldt and M. Steinmo, Transport processes in the thermal decomposition of silicon carbide, *Proceedings of the Ninth International Conference on High Temperature Materials Chemistry*, Vol. 97–39, K.E. Spear, Ed., The Electrochemical Society, Inc., Pennington, NJ, 1997, pp. 523–528.
136. N.I. Voronin, V.L. Kuznetsova, and R.I. Bresker, Durability of silicon carbide heaters in various gaseous media, in *Silicon Carbide*, I.N. Frantsevich, Ed., Consultants Bureau, New York, 1970, pp. 81–87.
137. W.F. Knippenberg, Growth phenomena in silicon carbide, *Philips Res. Reports*, **18**, 161–274, 1963.
138. D.V. Badami, Graphitisation of alpha-silicon carbide, *Nature (London)*, **193**, 569–570, 1962.
139. D.V. Badami, X-ray studies of graphite formed by decomposing silicon carbide carbon, *Carbon*, **3**, 53–57, 1965.
140. J.J. Comer, Electron microscopy and diffraction data of thermally decomposed  $\beta$ -silicon carbide whiskers, *J. Appl. Cryst.*, **4**, 12–15, 1971.
141. M.J. Bozack, Surface studies on SiC as related to contacts, *Phys. Stat. Sol. (b)*, **202**, 549–580, 1997.
142. A.J. van Bommel, J.E. Crombeen, and A. van Tooren, LEED and Auger electron observations of the SiC(0 0 0 1) surface, *Surf. Sci.*, **48**, 463–472, 1975.
143. F. Meyer and G.J. Loyen, Ellipsometry applied to surface problems, *Acta Electron.*, **18**, 33–38, 1975.
144. C.S. Chang, I.S.T. Tsong, Y.C. Wang, and R.F. Davis, Scanning tunneling microscopy and spectroscopy of cubic -SiC(1 1 1) surfaces, *Surf. Sci.*, **256**, 354–360, 1991.
145. M.A. Kulakov, P. Heuell, V.F. Tsvetkov, and B. Bullemer, Scanning tunnelling microscopy on the 6H SiC(0 0 0 1) surface, *Surf. Sci.*, **315**, 248–254, 1994.
146. F. Owman and P. Martensson, Scanning tunneling microscopy study of SiC(0 0 0 1) surface reconstructions, *J. Vac. Sci. Technol. B*, **14**, 933–937, 1996.
147. I. Forbeaux, J.-M. Themlin, and J.-M. Debever, High-temperature graphitization of the 6H-SiC (0 0 0–1) face, **442**, 1999.
148. L. Muehlhoff, W.J. Choyke, M.J. Bozack, and J.T. Yates, Comparative electron spectroscopic studies of surface segregation on SiC(0 0 0 1) and SiC(0 0 0–1), *J. Appl. Phys.*, **60**, 2842–2853, 1986.
149. T. Angot, M. Portail, I. Forbeaux, and J.M. Layet, Graphitization of the 6H-SiC(0 0 0 1) surface studied by HREELS, *Surf. Sci.*, **502–503**, 81–85, 2002.
150. S. Nakanishi, H. Tokutaka, K. Nishimori, S. Kishida, and N. Ishihara, The difference between 6H-SiC (0 0 0 1) and (0 0 0) faces observed by AES, LEED and ESCA, *Appl. Surf. Sci.*, **41/42**, 44, 1989.
151. R. Kaplan, Surface structure and composition of 6H-SiC, *Surf. Sci.*, **215**, 111–134, 1989.
152. U. Starke, C. Bram, P.-R. Steiner, W. Hartner, L. Hammer, K. Heinz, and K. Müller, The (0 0 0 1) — surface of 6H-SiC: morphology, composition and structure, *Appl. Surf. Sci.*, **89**, 175–185, 1995.
153. J. Schardt, C. Bram, S. Müller, U. Starke, K. Heinz, and K. Müller, LEED structure determination of hexagonal SiC surfaces, *Surf. Sci.*, **337**, 232–242, 1995.

154. K. Heinz, U. Starke, J. Bernhardt, and J. Schardt, Surface structure of hexagonal SiC surfaces: key to crystal growth and interface formation? *Appl. Surf. Sci.*, **162–163**, 9–18, 2000.
155. I. Forbeaux, J.M. Themlin, A. Charrier, F. Thibaudau, and J.M. Debever, Solid-state graphitization mechanisms of silicon carbide 6H-SiC polar faces, *Appl. Surf. Sci.*, **162**, 406–412, 2000.
156. F. Bonzo, L. Muehlhoff, M. Trenary, W.J. Choyke, and J.T. Yates, Electron spectroscopy study of SiC, *J. Vac. Sci. Technol. A*, **2**, 1271–1274, 1984.
157. S. Iijima, Graphitization of silicon carbide due to electron beam irradiation, *J. Solid State Chem.*, **42**, 101–105, 1982.
158. L.M. Foster, G. Long, and H.C. Stumpf, Production of graphite single crystals by the thermal decomposition of aluminum carbide, *Am. Mineral.*, **43**, 285–296, 1958.
159. M. Kusunoki, J. Shibata, M. Rokkaku, and T. Hirayama, Aligned carbon nanotube film self-organized on a SiC wafer, *Jpn. J. Appl. Phys.*, **37(5B)**, L605–L606, 1998.
160. M. Kusunoki, T. Suzuki, K. Kaneko, and M. Ito, Formation of self-aligned carbon nanotube films by surface decomposition of silicon carbide, *Phil. Mag. Lett.*, **79**, 153–161, 1999.
161. M. Kusunoki, T. Suzuki, T. Hirayama, J. Shibata, and K. Kaneko, A formation mechanism of carbon nanotube films on SiC(0 0 0 1), *Appl. Phys. Lett.*, **77**, 531–533, 2000.
162. M. Kusunoki, T. Suzuki, T. Hirayama, and N. Shibata, Aligned carbon nanotube films on SiC(0 0 0 1) wafers, *Physica B*, **323**, 296–298, 2002.
163. M. Kusunoki, T. Suzuki, C. Honjo, T. Hirayama, and N. Shibata, Selective synthesis of zigzag-type aligned carbon nanotubes on SiC (0 0 0 1) wafers, *Chem. Phys. Lett.*, **366**, 458–462, 2002.
164. H. Konishi, H. Matsuoka, N. Toyama, M. Naitoh, S. Nishigaki, and M. Kusunoki, Growth control of carbon nanotubes on silicon carbide surfaces using the laser irradiation effect, *Thin Solid Films*, **464–465**, 295–298, 2004.
165. T. Shimizu, Y. Ishikawa, M. Kusunoki, T. Nagano, and N. Shibata, Creation of highly oriented free-standing carbon nanotube film by sublimating decomposition of silicon carbide film, *Jpn. J. Appl. Phys.*, **39**, L1057–L1059, 2000.
166. V. Derycke, R. Martel, M. Radosavljevic, F.M. Ross, and P. Avouris, Catalyst-free growth of ordered single-walled carbon nanotube networks, *Nano Lett.*, **2**, 1043–1046, 2002.
167. H. Watanabe, Y. Hisada, S. Mukainakano, and N. Tanaka, *In situ* observation of the initial growth process of carbon nanotubes by time resolved high-resolution transmission electron microscopy. *J. Microscop.*, **203**, 40–46, 2001.
168. H. Takikawa, R. Miyano, M. Yatsuki, and T. Sakakibara, Carbon nanotubes on SiC powder surface grown by a vacuum heating process, *Jpn. J. Appl. Phys.*, **37**, L187–L189, 1998.
169. S. Botti, R. Ciardi, L. Asilyan, L. De Dominicis, F. Fabbri, S. Orlanducci, and A. Fiori, Carbon nanotubes grown by laser-annealing of SiC nanoparticles, *Chem. Phys. Lett.*, **400**, 264–267, 2004.
170. S. Botti, L.S. Asilyan, R. Ciardi, F. Fabbri, S. Lorety, A. Santoni, and S. Orlanducci, Catalyst-free growth of carbon nanotubes by laser annealing of amorphous SiC films, *Chem. Phys. Lett.*, **396**, 1–5, 2004.
171. T. Gorelik, S. Urban, F. Falk, U. Kaiser, and U. Glatzel, Carbon onions produced by laser irradiation of amorphous silicon carbide, *Chem. Phys. Lett.*, **373**, 642–645, 2003.
172. K. Tsugawa, A. Goto, and Y. Koga, Carbon nanotubes and carbon nanofibers synthesized by sublimating decomposition of silicon carbide with catalysts, *Proceedings of the 6th ADC/FCT Conference*, 2001, pp. 800–804.
173. A. Hahnel and J. Woltersdorf, Platinum-enhanced graphitization in sandwich structures of silicon carbide and borosilicate glass, *Mat. Chem. Phys.*, **83**, 380–388, 2004.
174. A. Burke, Ultracapacitors: why, how, and where is the technology? *J. Power Sources*, **91**, 37–50, 2000.
175. B.E. Conway, W.G. Pell, Double-layer and pseudocapacitance types of electrochemical capacitors and their applications to the development of hybrid devices, *J. Solid State Electrochem.*, **7**, 637–644, 2003.
176. Q. Jiang, M.Z. Qu, B.L. Zhang, Z.L. Yu, Progress of research on electrode materials for electrochemical supercapacitors, *J. Inorganic Mater.*, **17**, 649–656, 2002.
177. R.A. Huggins, Supercapacitors and electrochemical pulse sources, *Solid State Ionics*, **134**, 179–195, 2000.
178. B.E. Conway, *Electrochemical Supercapacitors*, Vol. 1, Kluwer Academic/Plenum Publishers, New York, 1999, p. 698.
179. S.K. Gordeev and A.V. Vartanova, Porosity variation in the process of forming of carbide materials and making compact carbon adsorbents on their basis, *Z. Prikladnoi Khimii*, **67**, 1080–1084, 1994.

180. R.G. Avarbz, A.V. Vartanova, S.K. Gordeev, S.G. Zjukov, B.A. Zelenov, A.E. Kravtjik, V.P. Kuznetsov, J.A. Kukusjkina, T.V. Mazaeva, O.S. Pankina, and V.V. Sokolov, Double Layer Capacitor with Porous Carbon Electrodes and Method for Manufacturing These Electrodes, PCT Patent WO 97/20333, 1997.
181. R.G. Avarbz, A.V. Vartanova, S.K. Gordeev, S.G. Zjukov, B.A. Zelenov, A.E. Kravtjik, V.P. Kuznetsov, J.A. Kukusjkina, T.V. Mazaeva, O.S. Pankina, and V.V. Sokolov, Process of Manufacturing a Porous Carbon Material and a Capacitor Having the Same, US Patent 5876787, 1999.
182. R.G. Avarbz, A.V. Vartanova, S.K. Gordeev, S.G. Zjukov, B.A. Zelenov, A.E. Kravtjik, V.P. Kuznetsov, J.A. Kukusjkina, T.V. Mazaeva, O.S. Pankina, and V.V. Sokolov, Electrode Having a Carbon Material with a Carbon Skeleton Network and a Capacitor Having the Same, US Patent 6110335, 2000.
183. Y.A. Maletin, N.G. Strizhakova, V.G. Izotov, A.A. Mironova, S.G. Kozachkov, V.G. Danilin, S.N. Podmogilny, M. Arulepp, J.A. Kukusjkina, A.E. Kravtjik, V.V. Sokolov, A. Perkson, J. Leis, J. Zheng, S.K. Gordeev, J.Y. Kolotilova, J. Cederstrom, and C.L. Wallace, A Supercapacitor and a Method of Manufacturing Such a Supercapacitor, PCT Patent WO 02/39468, 2002.
184. J. Chmiola, G. Yushin, R.K. Dash, and Y. Gogotsi, Effect of pore size and surface area of carbide derived carbons on specific capacitance, *J. Power Sources*, 2005, accepted.
185. A. Arulepp, L. Permann, J. Leis, A. Perkson, K. Rumma, A. Janes, and E. Lust, Influence of the solvent properties on the characteristics of a double layer capacitor, *J. Power Sources*, **133**, 320–328, 2004.
186. E. Lust, A. Janes, and M. Arulepp, Influence of electrolyte characteristics on the electrochemical parameters of electrical double layer capacitors, *J. Solid State Chem.*, **8**, 488–496, 2004.
187. E. Lust, G. Nurk, A. Janes, M. Arulepp, P. Nigu, P. Moller, S. Kallip, and V. Sammelselg, Electrochemical properties of nanoporous carbon electrodes in various nonaqueous electrolytes, *J. Solid State Electrochem.*, **7**, 91–105, 2003.
188. A. Janes, L. Permann, M. Arulepp, and E. Lust, Electrochemical characteristics of nanoporous carbide-derived carbon materials in non-aqueous electrolyte solutions, *Electrochem. Commun.*, **6**, 313–318, 2004.
189. E. Lust, A. Janes, T. Parn, and P. Nigu, Influence of nanoporous carbon electrode thickness on the electrochemical characteristics of a nanoporous carbon/tetraethylammonium tetrafluoroborate in acetonitrile solution interface, *J. Solid State Electrochem.*, **8**, 224–237, 2004.
190. A. Janes, L. Permann, M. Arulepp, and E. Lust, Voltammetric and electrochemical impedance spectroscopy studies of the nanoporous carbon vertical bar 1 M (C<sub>2</sub>H<sub>5</sub>)<sub>3</sub>CH<sub>3</sub>NBF<sub>4</sub> electrolyte solution interface, *J. Electroanalyt. Chem.*, **569**, 257–269, 2004.
191. J. Chmiola, G. Yushin, R.K. Dash, E.N. Hoffman, J.E. Fischer, M.W. Barsoum, and Y. Gogotsi, Double-layer capacitance of selected carbide-derived carbons in sulfuric acid, *Electrochem. Solid State Commun.*, **8**, A357–A360, 2005.
192. L. Schlapbach and A. Zuttel, Hydrogen-storage materials for mobile applications, *Nature*, **414**, 353–358, 2001.
193. M.G. Nijkamp, J.E.M.J. Raaymakers, A.J. van Dillen, and K.P. de Jong, Hydrogen storage using physisorption — materials demands, *Appl. Phys. A*, **72**, 619–623, 2001.
194. E.A. Evard, A.P. Voit, S.K. Gordeev, and I.E. Gabis, Kinetics of sorption and release of hydrogen by nanoporous carbon, *Mater. Sci.*, **36**, 499–505, 2000.
195. I.E. Gabis, E.A. Evard, S.K. Gordeev, and T. Ekstrom, Carbon nanomaterial for hydrogen uptake and storage, in *Hydrogen Materials Science and Chemistry of Metal Hydrides*, M.D. Hampton, Ed., Kluwer Academic, Dordrecht, 2002, pp. 383–390.
196. E. Johansson, B. Hjorvarsson, T. Ekström, and M. Jacob, Hydrogen in carbon nanostructures, *J. Alloys Compounds*, **330–332**, 670–675, 2002.
197. X.S. Chena, B. Mceaneya, T.J. Maysa, J. Alcaniz-Mongeb, D. Cazorla-Amorosb, and A. Linares-Solanob, Theoretical and experimental studies of methane adsorption on microporous carbons, *Carbon*, **35**, 1251–1258, 1997.
198. K.R. Matranga, A.L. Myers, and E.D. Glandt, Storage of natural gas by adsorption on activated carbon, *Chem. Eng. Sci.*, **47**, 1569–1579, 1992.
199. D. Lozano-Castello, D. Cazorla-Amoros, A. Linares-Solano, and D.F. Quinn, Influence of pore-size distribution on methane storage at relatively low pressure preparation of activated carbon with optimum pore size, *Carbon*, **40**, 989–1002, 2002.
200. D. Lozano-Castello, D. Cazorla-Amoros, and A. Linares-Solano, Powered activated carbons and activated carbon fibers for methane storage: a comparative study, *Energy Fuels*, **16**, 1321–1328, 2002.

201. S. Gautier, F. Leroux, E. Frackowiak, A.M. Faugere, J.-N. Rouzaud, and F. Beguin, Influence of the pyrolysis conditions on the nature of lithium inserted in hard carbons, *J. Phys. Chem. A*, **105**, 5794–5800, 2001.
202. M. Letellier, F. Chevallier, F. Beguin, E. Frackowiak, and J.-N. Rouzaud, The first *in situ* Li NMR study of reversible lithium insertion mechanism in disordered carbons, *J. Phys. Chem. Solids*, **65**, 245–251, 2004.
203. S. Flandrois and B. Simon, Carbon materials for lithium-ion rechargeable batteries, *Carbon*, **37**, 165–180, 1999.
204. I.M. Kotina, V.M. Lebedev, A.G. Ilves, G.V. Patsekina, L.M. Tuhkonen, S.K. Gordeev, M.A. Yagovkina, and T. Ekström, Study of the lithium diffusion in nanoporous carbon materials produced from carbides, *J. Non-Cryst. Solids*, **299–302**, 815–819, 2002.
205. I.M. Kotina, V.M. Lebedev, A.G. Ilves, G.V. Patsekina, L.M. Tuhkonen, S.K. Gordeev, M.A. Yagovkina, and T. Ekström, The Phase Composition of the Lithiated Samples of Nanoporous Carbon Materials Produced from Carbides, *J. Non-Cryst. Solids*, **299–302**, 820–823, 2002.
206. E. Antolini, F. Gardellini, E. Giacometti, and G. Squadrito, Study of the formation of Pt/C catalysts by non-oxidized active carbon support and a sulfur-based reducing agent, *J. Mater. Sci.*, **37**, 133–139, 2002.
207. D.A. Ersoy, M.J. McNallan, and Y. Gogotsi, *Platinum Reactions with Carbon Coatings Produced by High-Temperature Chlorination of Silicon Carbide*, Vol. 99–38, The Electrochemical Society, Inc., Pennington, NJ, 1999, pp. 456–467.
208. D.A. Ersoy, M.J. McNallan, and Y. Gogotsi, Platinum reactions with carbon coatings produced by high-temperature chlorination of silicon carbide, *J. Electrochem. Soc.*, **148**, C774–C779, 2001.
209. D.A. Ersoy, M.J. McNallan, Y. Gogotsi, and A. Erdemir, Tribological properties of carbon coatings produced by high-temperature chlorination of silicon carbide STLE, *Tribol. Trans.*, **43**, 809–815, 2000.
210. B. Carroll, Y. Gogotsi, A.M. Koval'chenko, A. Erdemir, and M. McNallan, in *NATO Advanced Research Workshop on Nanostructured Materials and Coatings for Biomedical and Sensor Applications*, Y. Gogotsi, Ed., Kluwer Academic Publishers, Dordrecht, 2002.
211. B. Carroll, Y. Gogotsi, A. Kovalchenko, A. Erdemir, and M.J. McNallan, Effect of humidity on the tribological properties of carbide-derived carbon (CDC) films on silicon carbide, *Tribology Lett.*, **15**, 51–55, 2003.
212. B. Carroll, Y. Gogotsi, A. Kovalchenko, A. Erdemir, and M. McNallan, Tribological characterization of carbide-derived carbon layers on silicon carbide for dry friction applications. Euro Ceramics VIII, PTS 1-3 *Key Eng.*, **264–268**, 465–468, 2004.
213. L. Chen, G. Behlau, Y. Gogotsi, and M.J. McNallan, Carbide-derived carbon (CDC) coatings for Tyranno ZMI SiC fibers, *Ceram. Eng. Sci. Proc.*, **24**, 57–62, 2003.
214. L. Chen, H. Ye, Y. Gogotsi, and M.J. McNallan, Carbothermal synthesis of boron nitride coatings on silicon carbide, *J. Am. Ceram. Soc.*, **86**, 1830–1837, 2003.
215. L. Chen, H. Ye, and Y. Gogotsi, Carbothermal synthesis of Al–O–N coatings increasing strength of SiC fibers, *Int. J. Appl. Ceramic Technol.*, **1**, 68–75, 2004.
216. S. Brunauer, P. Emmett, and E. Teller, Adsorption of gases in multimolecular layers, *J. Am. Chem. Soc.*, **60**, 309–319, 1938.

---

# 7 Nanotubes in Multifunctional Polymer Nanocomposites

*Fangming Du*

Department of Chemical and Biomolecular Engineering,  
University of Pennsylvania, Philadelphia, Pennsylvania

*Karen I. Winey*

Department of Materials Science and Engineering,  
University of Pennsylvania, Philadelphia, Pennsylvania

## CONTENTS

7.1	Introduction .....	255
7.2	Nanocomposite Fabrication and Nanotube Alignment .....	257
7.3	Mechanical Properties .....	261
7.4	Thermal and Rheological Properties .....	263
7.5	Electrical Conductivity .....	266
7.6	Thermal Conductivity and Flammability .....	268
7.7	Conclusions .....	269
	Acknowledgments .....	271
	References .....	271

## 7.1 INTRODUCTION

Polymer nanocomposites have attracted great attention due to the unique properties introduced by nanofillers, which typically refer to carbon blacks, silicas, clays, or carbon nanotubes (CNT). The polymer matrix acts as a supporting medium and the improvement in the properties of the nanocomposites generally originates from the nature of these nanofillers. Compared to other nanofillers, the unique structures of CNT potentially provide superior mechanical, electrical, and thermal properties. There are two types of CNT with high structural perfection, single-walled nanotubes (SWNT) and multi-walled nanotubes (MWNT) (Figure 7.1). SWNT can be considered as a single graphite sheet seamlessly wrapped into a cylindrical tube. MWNT comprise an array of such nanotubes that are concentrically nested. Theoretical and experimental results<sup>1</sup> on individual CNT have shown extremely high elastic modulus, greater than 1TPa, and their reported strength is many times higher than the strongest steel at a fraction of the weight. The fiber-like structure of CNT with low density makes them particularly attractive for reinforcement of composite materials. The nearly one dimensional (1D) electronic structure of CNT allows electrons to be transported along the nanotubes without scattering, enabling them to carry high current with essentially no heating. Phonons also propagate easily along the nanotubes, such that the measured room temperature thermal conductivity for an individual MWNT<sup>2</sup> (>3000 W/m K) is greater than that of natural diamond (~2000 W/m K). The thermal

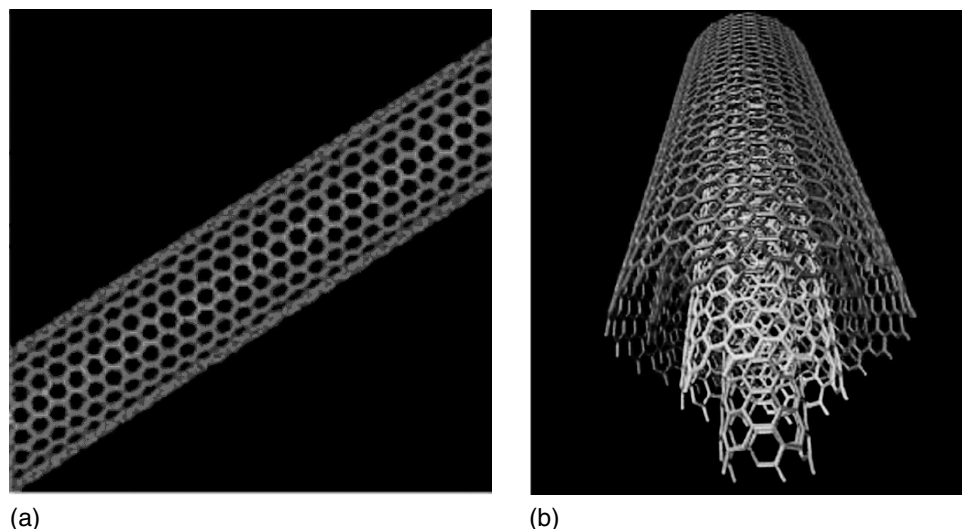


**FIGURE 7.1** (a) Image of SWNT. (Copyright, Dr. Smalley Group, Rice University, 2004; (b) Image of MWNT. (Copyright, Rochefort, Nano-CERCA, University of Montreal, Canada, 2004.)

conductivity of an individual SWNT is expected to be even higher.<sup>3</sup> The high aspect ratio (length/diameter) of CNT suggests lower percolation thresholds for both electrical and thermal conductivity in their nanocomposites. Therefore, CNT have considerable potential in multifunctional polymer nanocomposites for structural, electrical, and thermal applications.

To date this potential has not yet been fully realized, although many researchers are devoting much attention to developing CNT/polymer nanocomposites. One significant challenge is to obtain uniform nanotube dispersion within the polymer matrix. CNT have diameters on the nanoscale and substantial van der Waals attractions between them, so CNT tend to agglomerate. As shown in [Figure 7.2](#), these SWNT (synthesized by a high-pressure carbon monoxide method at Rice University)<sup>4</sup> are highly entangled and the diameter of the nanotube bundles is tens of nanometers, indicating hundreds of individual nanotubes in one bundle. Unfortunately, the nanotube bundles have significantly lower aspect ratios and inferior mechanical (due to slipping of nanotubes inside the bundles)<sup>5</sup> and electrical properties. Lower aspect ratios are likely to lead to higher percolation thresholds for both electrical and thermal conductivity in these nanocomposites. Therefore, uniformly dispersed nanotubes within the polymer matrix is critical for improved properties at the minimal CNT content. Various nanotube processing procedures and nanocomposite fabrication methods have been used toward this goal.<sup>6–8</sup> The second challenge is to understand the effect of nanotube alignment on nanocomposite properties because the nanotubes have asymmetric structures and properties. For example, nanotube alignment increases the elastic modulus<sup>6</sup> and increases the electrical conductivity<sup>9</sup> of the nanocomposites along the nanotube alignment direction. The third challenge is to create strong physical or chemical bonds between the nanotubes and the polymer matrix. These bonds can efficiently transfer load from the polymer matrix to the nanotubes, which is important for mechanical reinforcement. Covalent bonds can also benefit phonon transferring between the nanotubes and the polymer matrix, which is a key factor for improving thermal conductivity of the nanocomposites. Therefore, various surfactants and chemical functionalization procedures have been adopted to modify the surface of nanotubes, so as to enable more adhesion to the polymer matrix.

It is to be noted that nanotubes are synthesized by a variety of methods that give rise to different mean lengths, mean diameters, distributions in lengths and diameters, relative amounts of conductive nanotubes, and concentrations and types of impurities.<sup>10</sup> Furthermore, we have found important differences between different batches of nanotubes produced by seemingly equivalent synthetic processes. Added to this complexity are the observations that nanotube distribution and alignment significantly influence properties and it is expected that the physical properties of

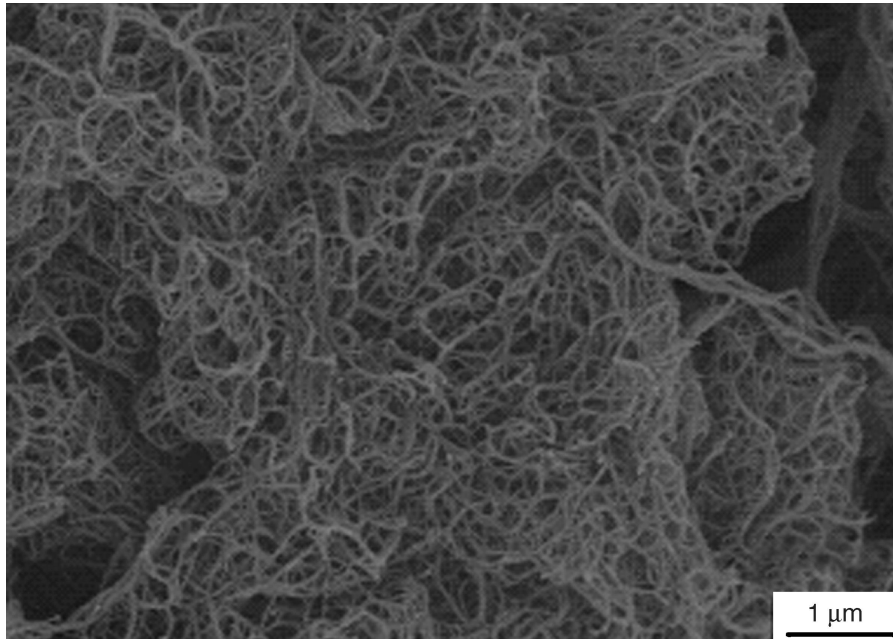


**FIGURE 7.2** SEM image of as-produced SWNT, showing that nanotube bundles are highly entangled. (Copyright, Winey group.)

nanotube/polymer composites will vary dramatically in the published literature. Thus, this chapter focuses on trends rather than absolute values for elastic modulus, electrical percolation, and so forth, because the nanotubes and composite processing methods employed by different researchers are substantially different. After reviewing various methods for producing nanotube/polymer nanocomposites, the mechanical, rheological, electrical, and thermal conductivities will be discussed separately.

## 7.2 NANOCOMPOSITE FABRICATION AND NANOTUBE ALIGNMENT

Solvent casting and melt mixing are two common fabrication methods for the nanotube-based nanocomposites. Solvent casting involves preparing a suspension of nanotubes in a polymer solution and then allowing the solvent to evaporate to produce a nanotube/polymer nanocomposite. Qian et al.<sup>11</sup> cast a MWNT/polystyrene (PS)/toluene suspension after sonication into a dish to produce the nanocomposites with enhanced elastic modulus and break stress. Benoit et al.<sup>7</sup> obtained electrically conductive nanocomposites by dispersing SWNT and poly(methyl methacrylate) (PMMA) in toluene, followed by drop casting the mixture on substrates. Nanocomposites with other thermoplastic matrices with enhanced properties have also been fabricated by solvent casting,<sup>12</sup> but nanotubes tend to agglomerate during solvent evaporation, which leads to inhomogeneous nanotube distribution in the polymer matrix. Unlike solvent casting methods, in which nanotubes are typically dispersed by sonication, melt mixing uses elevated temperatures and high shear forces to disrupt the nanotube bundles. Bhattacharyya et al.<sup>13</sup> made a 1 wt% SWNT/polypropylene (PP) nanocomposite by melt mixing, but found that melt mixing alone did not provide uniform nanotube dispersion. A subsequent processing step, namely passing the 1 wt% nanocomposite through a stainless-steel filter at 240°C, removed the larger SWNT agglomerates and reduced the nanotube loading to 0.8 wt%.

Some researchers use combined methods, such as solvent casting in conjunction with sonication, followed by melt mixing. For example, Haggenueller et al.<sup>6</sup> first demonstrated the combination of solvent casting and melt mixing for SWNT/PMMA composites with considerable improvement in nanotube dispersion. They dissolved PMMA in dimethylformamide that was also used to disperse SWNT by sonication and the resulting suspension was then cast into a dish.

After drying, the nanocomposite film exhibited heterogeneous nanotube dispersion when subjected to optical microscopy. These SWNT/PMMA films prepared by solvent casting alone contained micron-scale nanotube agglomerates due to reaggregation during solvent evaporation. Thus, the nanocomposite films were broken into pieces, stacked together, and then hot pressed. This hot pressing procedure was repeated for up to 20 times and the state of dispersion steadily improved with each additional melt mixing cycle. This combination of solvent casting and melt processing produced superior SWNT dispersion.

As seen above, solvent casting can allow CNT to agglomerate during solvent evaporation. There have been some attempts to reduce the solvent evaporation time by spin casting or drop casting.<sup>7,14,15</sup> Spin casting, also called spin coating, involves putting a nanotube/polymer suspension on a rotating substrate, so that the solvent evaporates within seconds. Drop casting involves dropping a nanotube/polymer suspension on a hot substrate, so that the solvent can evaporate very quickly. To better eliminate nanotube reagglomeration, Du et al.<sup>8</sup> developed a coagulation method to produce nanotube-based nanocomposites with uniform dispersion. Optical microscopy (Figure 7.3a) shows that there are no obvious agglomerations of the nanotubes in a 1 wt% SWNT/PMMA nanocomposite fabricated by the coagulation method, indicating that the nanotubes are uniformly distributed within the polymer matrix. Scanning electron microscopy (SEM) of a 7 wt% nanocomposite (Figure 7.3b) shows that the nanotubes are also uniformly distributed on a sub-micrometer scale. This coagulation method begins with a nanotube/polymer suspension in which the nanotubes have been well dispersed by sonication, and then poured into an excess of a nonsolvent, causing the polymer to precipitate and entrap the nanotube bundles. This precipitation process is rapid, so the nanotubes apparently do not aggregate or flocculate during the coagulation process.<sup>16</sup> Therefore, the coagulation method provides better nanotube dispersion.

In addition to the solvent casting, melt mixing, and coagulation methods, which combine nanotubes with high molecular weight polymers, *in situ* polymerization methods have also been used to make nanotube-based nanocomposites starting with nanotubes and monomers. The most common *in situ* polymerization methods involve epoxy in which the resins (monomers) and hardeners are combined with SWNT or MWNT prior to curing (polymerizing).<sup>17,18</sup> Epoxy is the most commonly used thermoset polymer. Its resin can be crosslinked after mixing with a hardener of an appropriate ratio (resin/hardener) based on the number of functional groups on them. In addition to thermoset matrixes, a few examples of thermoplastic nanocomposites have been prepared by *in situ* polymerization. Park et al.<sup>19</sup> performed *in situ* polymerization of polyimide while sonicating to keep the nanotubes dispersed in the reaction medium. The role of sonication during polymerization is to disperse the SWNT in the low-viscosity monomer solution. As polymerization progresses, the

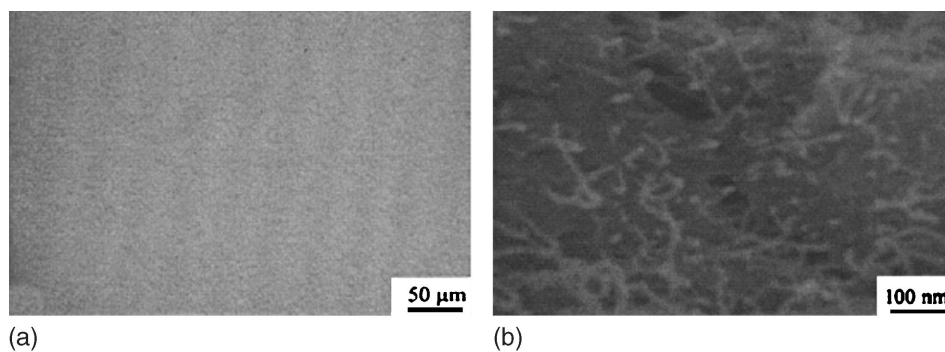


**FIGURE 7.3** (a) Optical micrograph of a 1wt% SWNT/PMMA nanocomposite thin film illustrating the absence of nanotube agglomerates; (b) SEM image of a 7wt% SWNT/PMMA nanocomposite. These nanocomposites were fabricated by the coagulation method and show uniform nanotube distribution. (Adapted from Du, F. et al.<sup>8</sup> *J. Poly. Sci.: Part B: Poly. Phys.* 41, 3333–3338, 2003.)



high-molecular-weight polymer increases the solution viscosity, restricts Brownian motion and sedimentation of the nanotubes, and stabilizes the nanotube dispersion against agglomeration.

Many of the fabrication methods described above require nanotubes to be well dispersed in solvents. The nanotube dispersion in the polymer matrix largely depends on the state of nanotube dispersion in a solvent, assuming that the following processing procedures effectively avoid nanotube flocculation. However, the chemical structure of CNT makes dissolving long CNT in common solvents to form true solutions virtually impossible. Most nanotube/solvent systems are suspensions of nanotube bundles where the size and concentration of the bundles dictate how long the suspensions persist before flocculation. To date, large fractions of individual nanotubes have only been achieved either by functionalizing the nanotubes or by surrounding the nanotubes with dispersing agents, such as surfactants and polymers. The improved nanotube suspensions resulting from functionalization or dispersing agents can be employed in many of the methods described above to make nanotube nanocomposites with improved nanotube dispersion. Furthermore, functionalized CNT might also allow covalent bonds between the nanotubes and the polymer matrix.

Nanotube functionalization typically begins with oxidative conditions, such as refluxing in nitric acid, to attach carboxylic acid moieties to the defect sites on the nanotube's surface.<sup>20,21</sup> These acid moieties can be further transformed to more reactive groups, like  $-\text{COCl}$ , or  $-\text{CONH}_2$ . These reactive groups allow CNT to chemically bond with the polymer chains through certain chemical reactions. Hill et al.<sup>22</sup> showed that SWNT and MWNT could be chemically bonded to a PS copolymer based on esterification. Lin et al.<sup>23</sup> also reported that the carboxylic acid on the surface of MWNT could attach aminopolymers via the formation of amide linkages. As functionalization chemistries advance, those interested in nanocomposites will continue to adapt these methods for the preparation of nanotube/polymer nanocomposites. One caveat in this regard is the degradation of properties, particularly aspect ratio and electrical conductivity, as the bonding of the CNT is disrupted by attaching functional groups to the nanotubes. There is likely to be an optimal level and type of nanotube functionalization that captures the advantages of better nanotube dispersion while minimizing the disadvantages of reduced nanotube performance.

The addition of dispersing agents, particularly surfactants, to nanotube/solvent systems has also shown improved dispersion.<sup>24</sup> Islam et al.<sup>24</sup> reported that sodium dodecylbenzene sulfonate was an effective surfactant to solubilize high-molecular-weight SWNT fractions in water by sonication. Their atomic force microscopy (AFM) showed that  $\sim 63 \pm 5\%$  of SWNT bundles exfoliated into single tubes even at 20 mg(SWNT)/ml( $\text{H}_2\text{O}$ ). Barrau et al.<sup>25</sup> used palmitic acid as a surfactant to disperse SWNT into the epoxy resin, followed by a curing procedure in the presence of the hardener. In comparison with nanocomposites not using palmitic acid, the use of palmitic acid lowers the threshold of the electrical conductivity percolation, indicating better SWNT dispersion in the epoxy. Polymers can also solubilize nanotubes in water by a noncovalent association. O'Connell et al.<sup>26</sup> first reported improved nanotube dispersion in water associated with modest concentration of polyvinyl pyrrolidone and also found that the nanotubes can be disassociated by changing the solvent system. Star et al.<sup>27</sup> discovered that starch improves the dispersion of SWNT in water and Barisci et al.<sup>28</sup> found that DNA could disperse SWNT well in water. Many groups investigating the interactions between nanotubes and polymers describe the mechanism by which nanotubes show improved dispersion as "polymer wrapping."<sup>26,27</sup> While there might be a few examples in which a polymer chain finds it energetically favorable to assume a periodic helical conformation about an isolated nanotube, it is far more likely that the improved nanotube solubility is accomplished with a more random association between the polymers and nanotubes. Regardless of the polymer conformations and mechanisms, improved nanotube solubility with the addition of surfactants and polymers provides a means to improve the nanotube dispersion in nanocomposites by improving the initial state of dispersion and by hindering the reaggregation during solvent casting and other fabrication methods.

Nanotubes can be aligned by magnetic force<sup>29–31</sup> (Figure 7.4a) and by polymer flow introduced by mechanical stretching,<sup>32</sup> spin casting,<sup>33</sup> or melt fiber spinning,<sup>6,8</sup> (Figure 7.4b). Magnetic fields have been used to align nanotubes in low-viscosity suspensions based on the anisotropic magnetic susceptibility of nanotubes. While magnetic alignment has shown some promise in the preparation of nanotube samples or buckypapers, this method is less appealing in nanotube/polymer composites due to the higher viscosities of the nanotube/polymer suspensions. Alternatively, polymer flow elongates and orients polymer molecules along the flow direction and the frictional forces of this process align nanotubes within the polymer matrix. Of the mechanical methods used to align nanotubes in a polymer matrix, melt fiber spinning methods exhibit the greatest degree of alignment.

The characterization of dispersion and alignment requires special attention in nanotube/polymer nanocomposites, because the physical properties are quite sensitive to these morphological attributes. Transmission electron microscopy (TEM) is a direct method to characterize MWNT/polymer composites, although there has been little success with SWNT/polymer composites due to the small size of the filler. Figure 7.5 is an aligned 5 wt% MWNT/PS nanocomposite film made by melt mixing and the MWNT were further aligned by drawing the nanocomposite in the molten state.<sup>34</sup> It shows that the nanocomposite has quite good dispersion and the nanotubes are well aligned along the polymer flow direction. In contrast to the qualitative measurements by TEM, polarized Raman spectroscopy and x-ray scattering provide quantitative descriptions of the degree of nanotube alignment in the nanocomposites. Besides detecting nanotube alignment, Raman spectroscopy can also be used to measure quantitatively nanotube dispersion in the polymer matrix.<sup>16</sup>

Nanotubes show a resonance-enhanced Raman scattering effect when a visible or near-infrared laser is used as the excitation source, while most polymers do not. By taking advantage of this scattering effect, polarized Raman spectra are recorded for the nanocomposites with the nanotube alignment direction at some angles with respect to the incident polarization axis. In the recorded spectra, the intensity of the unique nanotube scattering mode as a function of angle can be fitted by a Lorentzian or a Gaussian

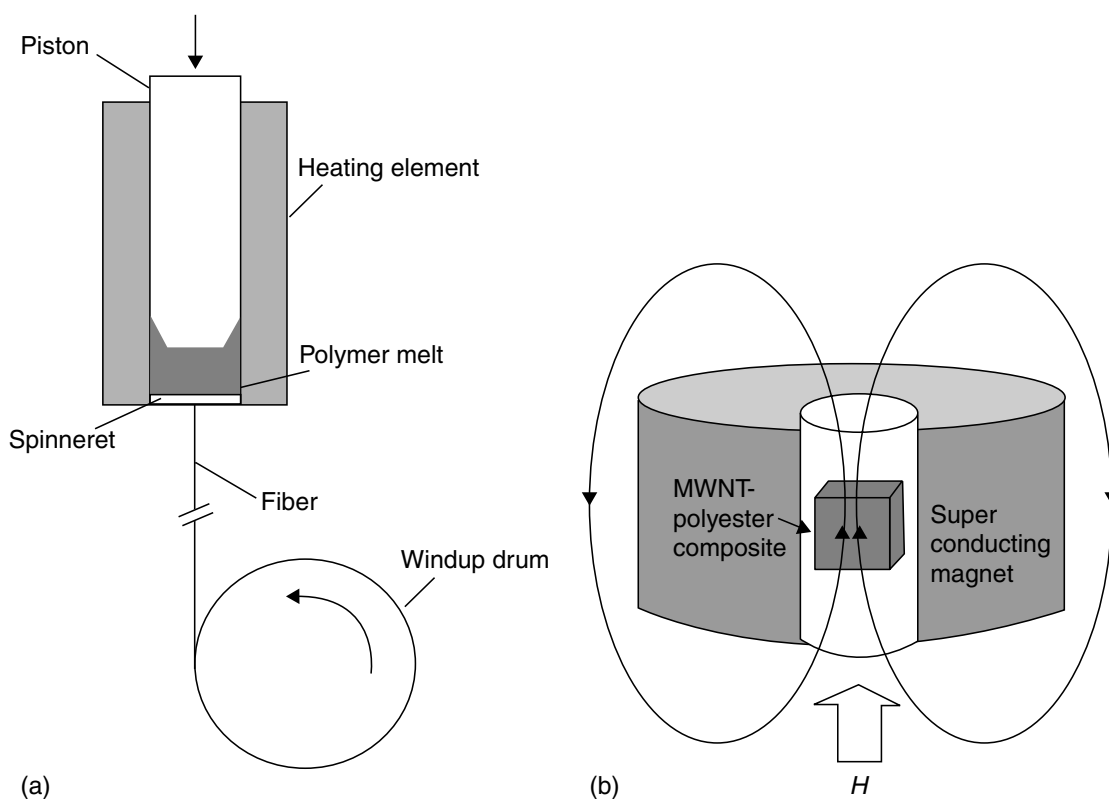


**FIGURE 7.4** Schematics for aligning nanotubes in nanocomposites (a) by melt fiber spinning using extensional polymer flow and (b) by a magnetic field. (Adapted from Kimura, T. et al., *Adv. Mater.*, 14, 1380–1383, 2002.)

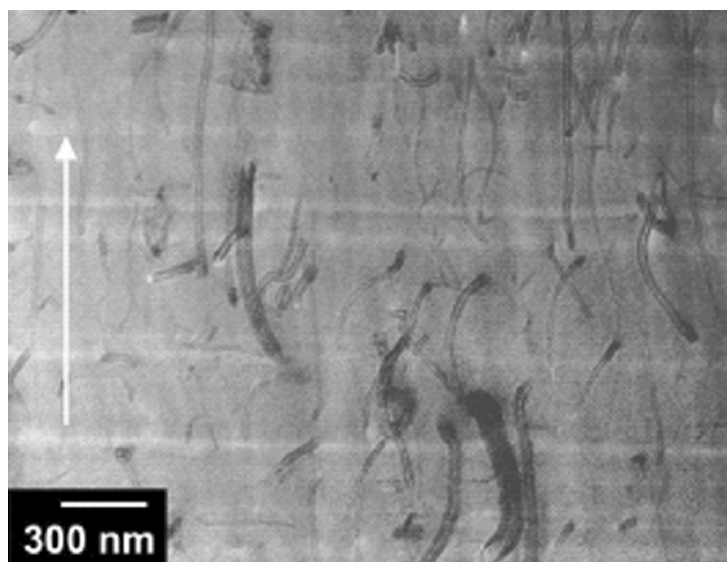


**FIGURE 7.5** TEM image of a 5wt% MWNT/PS nanocomposite film showing strong nanotube alignment after mechanical stretching. The arrow indicates the stretch direction. (Adapted from Thostenson, E.T. et al., *Compos. Sci. Technol.*, 61, 1899–1912, 2001.)

function whose full-width at half-maximum (FWHM) can quantitatively determine the extent of nanotube alignment. For example, Haggenueller et al.<sup>35</sup> obtained the degree of nanotube alignment for their SWNT/polyethylene (PE) fibers aligned by melt spinning with polarized Raman spectroscopy.

However, Raman spectroscopy is surface sensitive because the penetration depth of the incident beam is generally no more than several micrometers, depending on the nanotube loading. This problem can be solved by x-ray scattering, which is a bulk measurement for the nanocomposite in transmission and can describe the degree of nanotube alignment. Jin et al.<sup>32</sup> aligned nanotubes in a 50% MWNT/polyhydroxyaminoether nanocomposite film by mechanical stretching. Wide-angle x-ray scattering patterns that were dominated by a strong Bragg peak resulting from the intershell of MWNT ((002) peak) were collected from both unstretched and stretched samples. The 2D scattering intensity,  $I$ , was then integrated along the  $2\theta$  axis and plotted as  $I$  vs. azimuth,  $f$ , after subtracting the background intensity, as shown in Figure 7.6 for the unstretched and stretched samples, respectively. The scattering intensity from the unstretched sample is essentially a constant over the whole  $f$  range, as shown in Figure 7.6a, indicating random nanotube orientation. The spectrum in Figure 7.6b was fitted by 2D Lorentzian function with a FWHM of  $46.4^\circ$ , corresponding to a mosaic angle of  $\pm 23.2^\circ$  around the stretching direction. Du et al.<sup>8</sup> used small-angle x-ray scattering to characterize the degree of nanotube alignment in the SWNT/PMMA nanocomposites, in which SWNT were aligned by melt spinning. X-ray intensity from SWNT nanocomposites in the small-angle range ( $0.01 \text{ \AA} < q < 0.1 \text{ \AA}$ ) was mainly from the form factor scattering of SWNT and SWNT bundles. They observed that the aligned 1 wt% SWNT/PMMA had a FWHM of  $16^\circ$ , indicating that SWNT were highly aligned.

### 7.3 MECHANICAL PROPERTIES

Nanotubes were first considered as reinforcing fillers in polymer matrices due to their fiber-like structure and their exceptionally high axial strengths and axial Young's moduli. To date, the mechanical properties of various polymer matrices have shown only moderate improvements with the addition of either SWNT or MWNT.

Qian et al.<sup>11</sup> measured mechanical properties of MWNT/PS nanocomposites. With the addition of only 1 wt% MWNT the nanocomposite exhibited a 36–42% increase in the elastic stiffness and a 25% increase in the tensile strength. Haggenueller et al.<sup>6</sup> investigated the effect of both nanotube

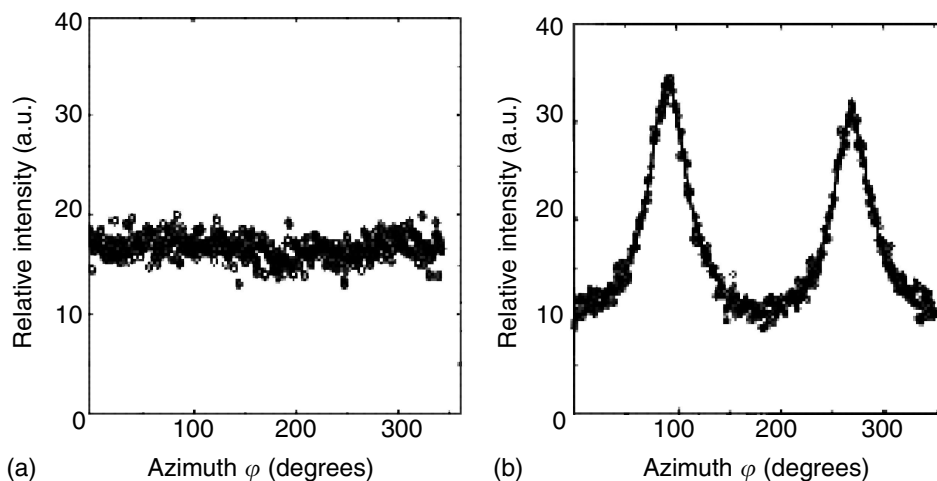


**FIGURE 7.6** Integrated x-ray intensity (along the  $2\theta$  axis) vs. the azimuth for (a) an as-cast 50% MWNT/polyhydroxyaminoether nanocomposite film, and (b) the nanocomposite after being mechanically stretched. The solid line is a fit to the data by two Lorentzian functions and a constant background. (Adapted from Jin, L. et al., *Appl. Phys. Lett.*, 84, 2660–2669, 2002.)

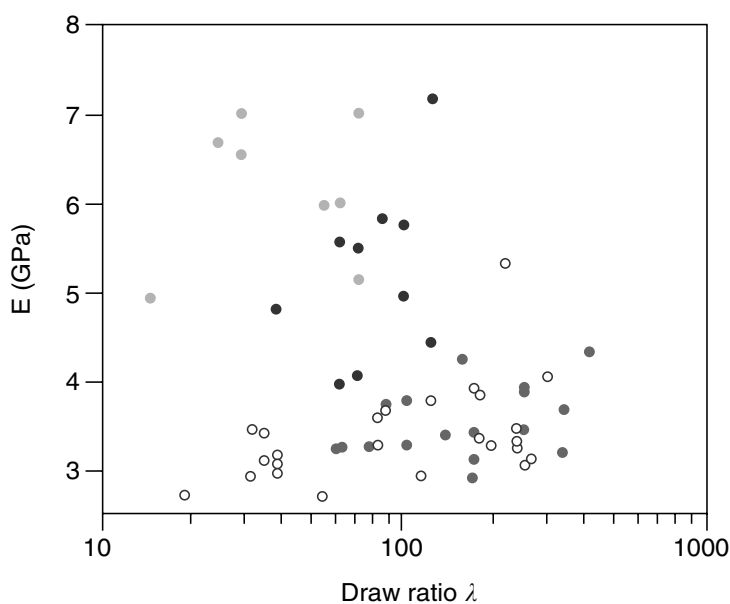


**FIGURE 7.7** Elastic modulus as a function of draw ratio  $\lambda$  for the SWNT/PMMA nanocomposites melt spun fibers containing 0wt% (white), 1wt% (blue), 5wt% (red), or 8wt% (green) of SWNT. (Adapted from Haggenueller, R. et al., *Chem. Phys. Lett.*, 330, 219–225, 2000.)

loading and nanotube alignment on the elastic modulus of SWNT/PMMA nanocomposite fibers. Nanotube alignment was achieved by melt fiber spinning and characterized by polarized resonant Raman spectroscopy. The elastic modulus of the nanocomposite fibers increased with nanotube loading and nanotube alignment, as shown in Figure 7.7. Note that the x-axis in Figure 7.7 is the draw ratio, where higher draw ratios correspond to better nanotube alignment. Andrews et al.<sup>36</sup> also reported that the tensile strength and modulus of a 5 wt% SWNT/pitch nanocomposite fiber were enhanced by  $\sim 90$  and  $\sim 150\%$ , respectively, as compared to pure pitch fiber.

To enhance mechanical properties, mechanical load has to be efficiently transferred from the polymer matrix to the nanotubes. Lordi and Yao<sup>37</sup> suggest that the strength of the interface might result from molecular-level entanglement of pristine nanotubes and polymer chains. Thus, many

researchers have investigated the interactions and load transfer between nanotubes and polymer matrices in nanocomposites. Lourie et al.<sup>38</sup> collected TEM images showing good epoxy-nanotube wetting and significant nanotube-epoxy interfacial adhesion, and concluded SWNT-epoxy interfacial affinity. This group also performed *in situ* deformation studies within the TEM and followed the rupture of SWNT, another indication of strong nanotube/epoxy interfaces. Wagner and co-workers<sup>39</sup> performed reproducible nano-pullout experiments using AFM to measure the force required to separate a CNT from poly(ethylene-co-butene) and found a separation stress of 47 MPa. In comparison, composite materials containing fiber reinforcements with weak fiber/polymer interactions typically have separation stresses of <10 MPa.<sup>39</sup> Simulating nanotube pullout in a CNT/PS nanocomposite, Liao and Li<sup>40</sup> obtained an interfacial shear stress of ~160 MPa, corresponding to a strong interface. These results from TEM, AFM, and simulation indicate that CNT can form strong interfaces with various polymer matrices.

Stress transfer can be most directly investigated by Raman spectroscopy, because the second-order (disorder-induced) Raman peak for nanotubes shifts with applied strain. If nanotubes within a nanocomposite carry part of the mechanical strain, then the Raman peak shifts with increasing applied strain. Cooper et al.<sup>41</sup> observed that when their SWNT/epoxy nanocomposite was mechanically strained the  $G'$  Raman band ( $2610\text{ cm}^{-1}$ ) shifted to a lower wave number. This shift in the  $G'$  Raman band corresponds to strain in the nanotube graphite structure, indicating stress transfer between the epoxy matrix and nanotubes, and hence reinforcement by the nanotubes.

In addition to the publications showing improvements in mechanical properties along with good interfacial adhesion and load transfer, other reports have been less promising and highlight the sensitivity of nanotube/polymer composites to all aspects of materials and fabrication. Fisher et al.<sup>42</sup> used a combined finite element and micromechanical approach and found that the nanotube waviness significantly reduced the effective reinforcement when compared to straight nanotubes. Cooper et al.<sup>43</sup> investigated the detachment of MWNT from an epoxy matrix using a pullout test for individual MWNT. Observed values for the interfacial shear strength ranged from 35 to 376 MPa, and the authors attribute this variability to differences in structure, morphology, or surface properties of the nanotubes. This structural variety in nanotubes occurs during their synthesis, but can also be introduced during purification and other processing procedures.<sup>10</sup> Defects to the nanotube structure are expected to reduce significantly the mechanical properties of nanotubes.<sup>44</sup> Some methods of handling nanotubes, including acid treatments and high- as well as low-power sonication for extended periods of time, are known to shorten nanotubes.<sup>10</sup> Shorter nanotubes and thereby reduced aspect ratios are detrimental to mechanical properties. In contrast, some purification and processing steps might also introduce functional groups, such as carboxylic acid to the nanotube surface that subsequently form secondary bonds, such as hydrogen bonds, between the nanotubes and polymer matrices. Such functional groups might improve interfacial strength and promote nanotube compatibility and composite properties. Given the complexity of the starting materials (raw nanotubes), the range of chemical and physical processing methods and the breadth of polymer matrices being explored, variability in the mechanical properties in nanotube/polymer composites will persist.

Although improvements in mechanical properties have been reported for various nanotube/polymer nanocomposites, the gains are modest and fall far below simple estimates. Haggenueller et al.<sup>35</sup> applied the Halpin-Tsai composite theory to their SWNT nanocomposites and found their experimental elastic modulus more than an order of magnitude smaller than predicted. They attribute this large difference mainly to the lack of perfect load transfer from the nanotube to the matrix, but other sources of uncertainty in the model include the aspect ratio and modulus of the nanotubes.

## 7.4 THERMAL AND RHEOLOGICAL PROPERTIES

The glass transition temperature ( $T_g$ ) is a measure of the thermal energy required to allow polymer motion involving 10 to 15 monomeric units and corresponds to the softening of a polymer. Park et al.<sup>19</sup> reported that  $T_g$  did not change for their *in situ* polymerized SWNT/polyimide nanocomposites.

The SWNT/PMMA nanocomposites produced by the coagulation method have the same  $T_g$  over a wide range of nanotube loadings.<sup>16</sup> The addition of nanotubes does not change the glass transition temperature in nanotube/polymer nanocomposites, because in the absence of strong interfacial bonds and at low nanotube loadings, the majority of polymers are locally constrained only by other polymers.

In contrast, at larger length scales, nanotubes do impede the motion of polymer molecules as measured by rheology. Rheological (or dynamic mechanical) measurements at low frequencies probe the longest relaxation times of polymers that correspond to time required for an entire polymer molecule to change conformation. Du et al.<sup>16</sup> found that although it has little effect on polymer motion at the length scales comparable to or less than an entanglement length, the presence of nanotubes has a substantial influence at large length scales corresponding to an entire polymer chain. The storage modulus,  $G'$ , at low frequencies becomes almost independent of the frequency as nanotube loading increases (Figure 7.8a). These data show a transition from liquid-like behavior (short relaxation times) to solid-like behavior (infinite relaxation times) with increasing nanotube loading. By plotting  $G'$

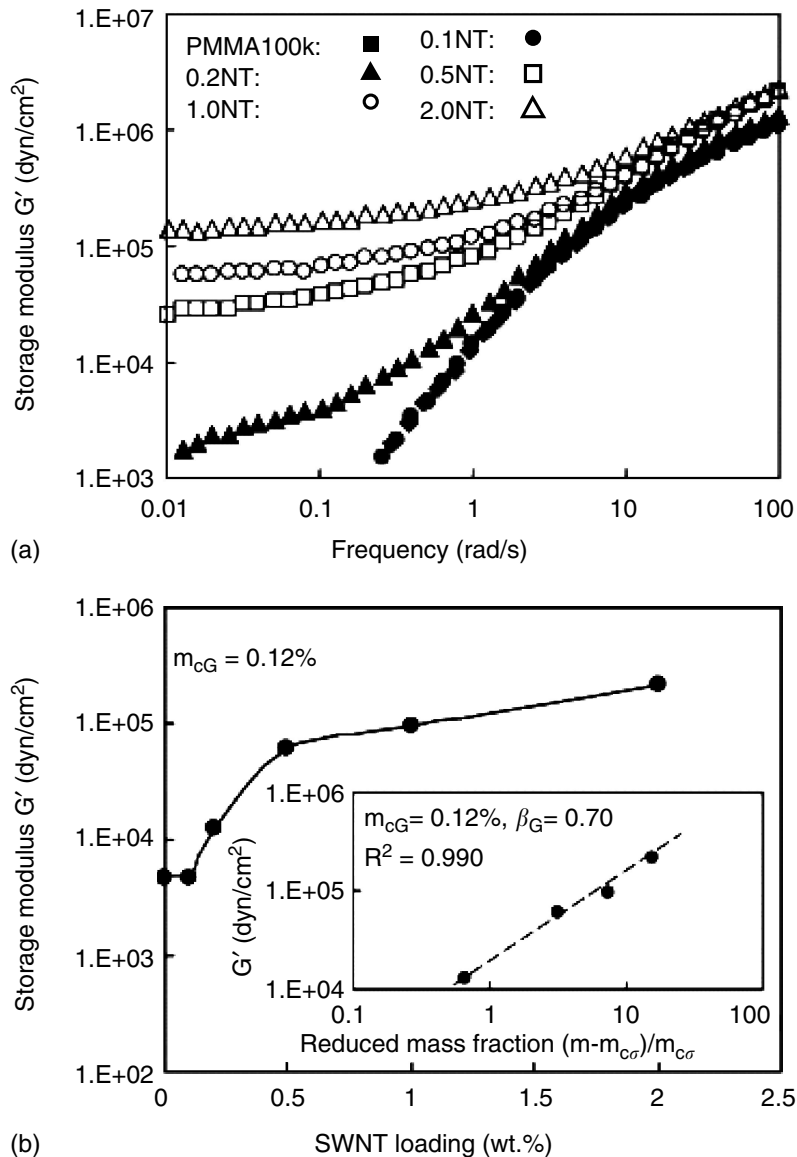


**FIGURE 7.8** (a) Storage modulus ( $G'$ ) vs. shear frequency for SWNT/PMMA nanocomposites with various nanotube loadings; (b)  $G'$  as a function of the nanotube loading for SWNT/PMMA nanocomposites at a fixed frequency, 0.5rad/sec. The inset is a power law plot of  $G'$  of the nanocomposites vs. reduced mass fraction on a logarithmic scale. (Adapted from Du, F. et al., *Macromolecules*, 37, 9048–9055, 2004.)

versus nanotube loading and fitting with a power law function, the rheological threshold of these nanocomposites is  $\sim 0.12$  wt% (Figure 7.8b). This rheological threshold can be attributed to a hydrodynamic nanotube network that impedes the large-scale motion of polymer molecules. This phenomenon has previously been reported in polymer nanocomposites filled with nanoclays by Krishnamoorti et al.<sup>45</sup> A network of nanoscale fillers restrains polymer relaxations, leading to solid-like or nonterminal rheological behavior. Therefore, any factor that changes the morphology of the nanotube network will influence the low-frequency rheological properties of the nanocomposites.

Du et al.<sup>16</sup> found that better nanotube dispersion, less nanotube alignment, and longer polymer chains result in more restraint on the mobility of the polymer chains; i.e., the onset of solid-like behavior occurs at low nanotube concentrations. In addition to the loading, dispersion, and alignment of the nanotubes, the size, aspect ratio, and interfacial properties of the nanotubes are expected to influence the rheological response in nanocomposites. For example, at a fixed loading, nanotubes with smaller nanotube diameters and larger aspect ratios will produce a network with smaller mesh size and larger surface area/volume, which might restrain polymer motion to a greater extent. Experimental results support this hypothesis. Lozano et al.<sup>46</sup> observed a rheological threshold of 10–20 wt% in carbon nanofiber/PP nanocomposites in which the diameter of the carbon nanofiber is  $\sim 150$  nm. The rheological threshold is  $\sim 1.5$  wt% in MWNT/polycarbonate nanocomposites,<sup>47</sup> and only 0.12 wt% for the SWNT/PMMA system.<sup>16</sup> Although these three systems have different polymer matrices and their states of dispersion are unclear, the diameters of carbon nanofibers, MWNT, and SWNT differ by orders of magnitude. As the filler size decreases, the filler loading required for solid-like behavior increases substantially.

The constraints imposed by nanotubes on polymers in nanocomposites are also evident in the polymer crystallization behavior. Bhattacharyya et al.<sup>13</sup> studied crystallization in 0.8 wt% SWNT/PP nanocomposites using optical microscopy (with cross-polarizers) and differential scanning calorimetry (DSC) (Figure 7.9). The spherulite size in PP is much larger than in SWNT/PP nanocomposites. DSC results show that upon cooling, the SWNT/PP nanocomposites begin crystallizing at  $\sim 11^\circ\text{C}$  higher than PP, suggesting that nanotubes act as nucleating sites for PP crystallization. They also observed that both melting and crystallization peaks in the nanocomposite are narrower than in pure PP. The authors proposed that higher thermal conductivity of the CNT as compared to that of the polymer, at least in part may be responsible for the sharper but narrower crystallization and melting peaks, as heat will be more evenly distributed in the samples containing the nanotubes.

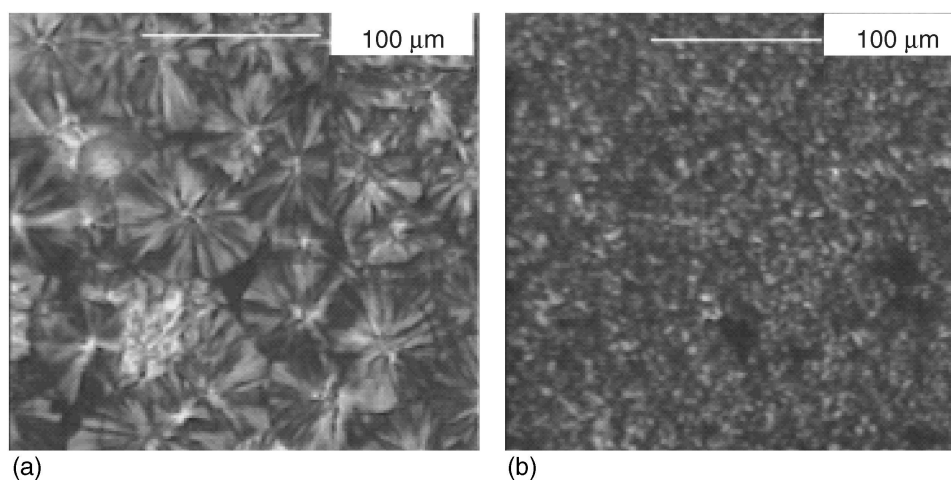


**FIGURE 7.9** Optical micrographs using cross-polarizers of (a) pure PP and (b) a 0.8wt% SWNT/PP nanocomposite, showing that the nanocomposite has much smaller spherulite size compared to pure PP. (Adapted from Bhattacharyya, A.R. et al., *Polymer*, 44, 2373–2377, 2003.)

## 7.5 ELECTRICAL CONDUCTIVITY

A variety of applications are being pursued using electrically conductive nanotube/polymer nanocomposites, including electrostatic dissipation, electromagnetic interference shielding, printable circuit wiring, and transparent conductive coatings. For example, charge buildup can lead to explosions in automotive gas lines and filters, and carbon black is typically added to plastics to dissipate the charge. Nanotube/polymer composites also dissipate charge and have the added advantage that the barrier properties against fuel diffusion are superior to composites made with carbon black.<sup>48</sup> Compared to carbon black's globular shape and micron-scale size, nanotubes are cylindrical in shape and with diameter in nanometer-scale. The larger aspect ratios and smaller diameters of nanotubes led to improved electrical conductivity in polymers at lower filler concentrations as compared to carbon black, so that a polymer's other desired performance aspects, such as mechanical and permeability properties, can be preserved.

Figure 7.10a shows the conductivity of SWNT/PS nanocomposites as a function of nanotube loading measured by Ramasubramaniam et al.<sup>49</sup> The conductivity of the nanocomposite increases sharply between 0.02 and 0.05 wt% SWNT loading, indicating the formation of a conductive nanotube network; this behavior is typical of percolation. According to percolation theory, the conductance should follow the following power law close to the threshold concentration:  $\sigma \sim (v-v_c)^\beta$ , where  $v$  is the volume fraction of the conductive component and  $\beta$  is the critical exponent for the conductivity. Most

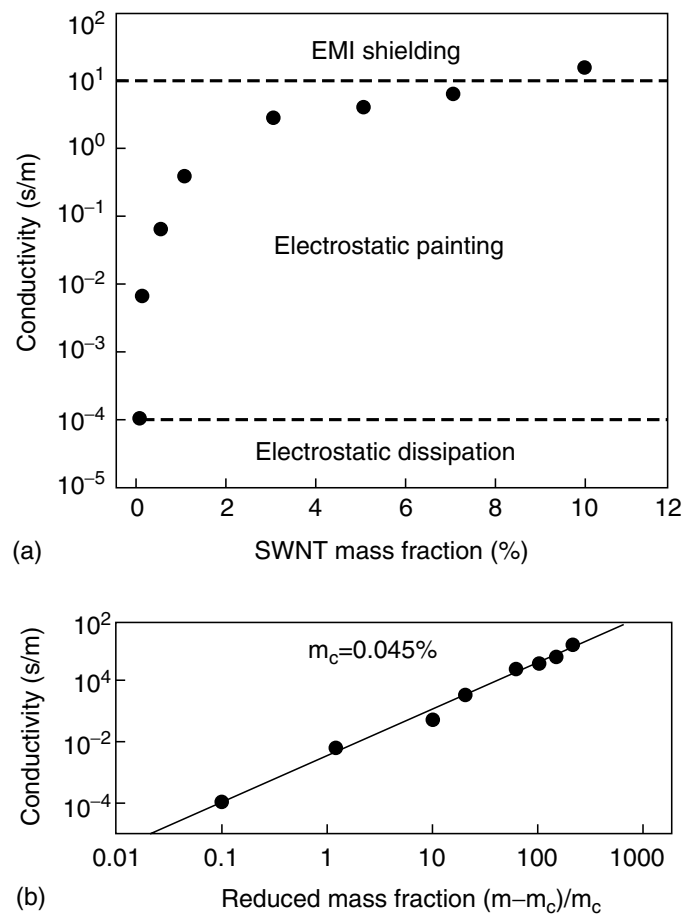


**FIGURE 7.10** (a) Electrical conductivity of SWNT/PS nanocomposites as a function of nanotube loading, showing a typical percolation behavior. Dashed lines represent the lower limits of electrical conductivity required for the specified applications, (b) Electrical conductivity as a function of reduced mass fraction of nanotubes, showing a threshold of 0.045wt%. (Adapted from Ramasubramaniam, R. et al., *Appl. Phys. Lett.*, 83, 2928–2930, 2003.)



researchers assume that the nanotube volume fraction is comparable to the nanotube mass fraction, because the densities of nanotubes and polymers are similar. The power law expression for percolation fits the conductivity data for SWNT/PS nanocomposites giving a low percolation threshold, 0.045 wt%. Ounaies et al.<sup>50</sup> also observed percolation behavior for electrical conductivity in SWNT/polyimide nanocomposites with a percolation threshold of 0.1 vol%. Their current–voltage measurements exhibited nonohmic behavior, which is most likely due to a tunneling conduction mechanism. Conduction probably occurs by electron hopping between adjacent nanotubes when their separation distance is small. At concentrations greater than the percolation threshold, conductive paths are formed through the whole nanocomposite, because the distance between the conductive filler (nanotubes or nanotube bundles) is small enough to allow efficient electron hopping. Ounaies et al.<sup>50</sup> developed an analytical model and numerical simulation using high aspect ratio and rigid spherocylinders in a unit cube to mimic SWNT/polymer nanocomposites to aid in understanding these results. The predictions from both the analytical model and the numerical simulation were in good agreement with the experimental results.

As presented earlier, a hydrodynamic nanotube network forms upon increasing nanotube loading and leads to the nonterminal rheological behavior. Similarly, a conductive nanotube network turns polymers from insulating to conducting. Du et al.<sup>16</sup> have compared the hydrodynamic and the conductive nanotube networks. In their SWNT/PMMA nanocomposites, the rheological percolation threshold, 0.12 wt%, is significantly smaller than the percolation threshold for electrical conductivity, 0.39 wt%. They understand this difference in the percolation threshold in terms of the smaller nanotube–nanotube distance required for electrical conductivity as compared to that required to impede polymer mobility. Specifically, the proposed electron hopping mechanism requires tube–tube distance of less than ~5 nm, while for rheological percolation the important length scale is comparable to the size of the polymer chain, which is ~18 nm for PMMA ( $M = 100$  kDa). Thus, they conclude that a less dense nanotube network can restrict polymer motion than can conduct electricity.

Three main factors that influence the percolation threshold for the electrical conductivity are nanotube dispersion, aspect ratio, and alignment. Barrau et al.<sup>25</sup> used palmitic acid as a surfactant to improve the nanotube dispersion in SWNT/epoxy nanocomposites and reduced the threshold concentration for electrical conductivity from ~0.18 to ~0.08 wt%. Bai and Allaoui<sup>51</sup> pretreated MWNT to alter their aspect ratios before preparing MWNT/epoxy nanocomposites and found that the threshold concentration for electrical conductivity varied from 0.5 to >4 wt% with decreasing aspect ratio. This observation is consistent with the predictions from Balberg's model.<sup>52</sup> As the quality of nanotube dispersion improves and the aspect ratios of nanotubes increase, lower nanotube loadings are required to increase the electrical conductivities and these loadings are smaller than the loading required, obtaining comparable conductivities by adding other conductive fillers, like carbon black and graphite.<sup>53</sup>

Owing to their highly anisotropic shape the alignment of nanotubes must be considered when studying the properties, including electrical conductivity of nanotube/polymer nanocomposites. Du et al.<sup>8</sup> found that the electrical conductivity of a 2 wt% SWNT/PMMA nanocomposite decreased significantly (from  $\sim 10^{-4}$  to  $\sim 10^{-10}$  S/cm) when the SWNT were highly aligned (FWHM =  $20^\circ$  as measured by x-ray scattering as described above). This decrease in electrical conductivity is the result of fewer contacts between nanotubes when they are highly aligned as compared to having an isotropic orientation. In contrast, Choi et al.<sup>9</sup> observed that nanotube alignment increased the conductivity of a 3 wt% SWNT/epoxy nanocomposite from  $\sim 10^{-7}$  to  $\sim 10^{-6}$  S/cm. Note that nanotubes in the SWNT/PMMA systems<sup>8</sup> were aligned by melt spinning, while they were aligned in the SWNT/epoxy<sup>9</sup> by magnetic force during fabrication. Although Choi et al. did not quantify the degree of alignment, it is reasonable to assume that SWNT are better aligned by the extensional flow of melt fiber spinning. More recently, we found an optimal degree of nanotube alignment that yields a maximum electrical conductivity.<sup>63</sup> The degree of nanotube alignment was varied by controlling the melt fiber spinning conditions and was characterized by x-ray scattering. In all cases, the SWNT/PMMA nanocomposites with isotropic nanotube orientation have greater electrical conductivity than the nanocomposites with highly aligned nanotubes. Furthermore, at low nanotube

concentrations, there are intermediate levels of nanotube alignment with higher electrical conductivities than the isotropic condition. We attribute the maximum electrical conductivity at an intermediate nanotube alignment observed in the competition between the number of tube–tube contacts and the distance between these contacts.

The electrical properties of nanocomposites made from electrically conductive conjugated polymers have also been studied.<sup>14,54</sup> Tchmutin et al.<sup>55</sup> compared the electrical conductivity behavior of SWNT/polyaniline (PA) and SWNT/PP nanocomposites produced by the same method. The nanocomposites prepared with PA have a lower threshold for electrical conductivity than SWNT/PP nanocomposites, specifically ~2 vol% compared to ~4 vol%. They attribute this lower threshold to a “double percolation,” involving both the nanotubes and the conjugated polymer matrix, where the PA becomes conductive when injected with charge carriers from the nanotubes. In SWNT/PA composites, the nanotubes are surrounded by PA domains of higher conductivity that increase the effective volume of conductive nanotubes and thereby reduce the concentrations required for percolation in these nanocomposites.

## 7.6 THERMAL CONDUCTIVITY AND FLAMMABILITY

Nanotube/polymer nanocomposites are expected to have superior thermal conductivity due to the exceptionally high thermal conductivities reported for nanotubes. Biercuk et al.<sup>56</sup> first reported the improvement in thermal conductivity for SWNT/polymer nanocomposites; their 1 wt% SWNT/epoxy nanocomposite showed a 70% increase in thermal conductivity at 40 K, increasing to 125% at room temperature. Choi et al.<sup>9</sup> reported a 300% increase in thermal conductivity at room temperature with 3 wt% SWNT in epoxy. The thermal conductivity of individual nanotube is approximately four orders of magnitude higher than that of typical polymers (~0.2 W/m K), so these reported enhancements are smaller than expected if one assumes perfect phonon transfer between nanotubes in the composite. A more appropriate benchmark for thermal conductivities in nanotube/polymer composites is the thermal conductivity of nanotube buckypaper (a low-density felt or mat of nanotubes typically made via filtration of nanotube suspensions) so as to account for the thermal resistance between nanotubes. Hone et al.<sup>17</sup> used a comparative method to measure the thermal conductivity of an unaligned SWNT buckypaper at room temperature and found it to be ~30 W/m K. In the absence of thermal resistance between nanotubes, this value would be expected to be less of the order of  $10^3$  W/m K. Researchers are currently exploring the extent to which substantial interfacial thermal resistance is intrinsic to nanotubes.

A comparison of the electrical and thermal conductivity behaviors in nanotube-based nanocomposites provides some insight to heat transport. A 2 wt% SWNT/PMMA nanocomposite is well above the threshold concentration for electrical conductivity (~0.4 wt%),<sup>16</sup> but has the thermal conductivity of pure PMMA.<sup>64</sup> In other words, the electrically conductive nanotube network in the 2 wt% SWNT/PMMA is not thermally conductive. This can be explained by the different transport mechanisms for electrons and phonons. As we discussed above, an electron hopping mechanism has been applied to nanotube-based nanocomposites, which requires close proximity (but not direct contact) of the nanotubes or nanotube bundles in the composites. However, heat transport inside nanotube-based nanocomposites proceeds by phonon transfer. The nanotubes and polymer matrix are coupled only by a small number of low-frequency vibrational modes in the absence of covalent bonds at the interface. Thus, thermal energy contained in high-frequency phonon modes within the CNT must first be transferred to low frequencies through phonon–phonon couplings before being exchanged with the surrounding medium.<sup>57</sup> This is the origin of the high interfacial thermal resistance in nanotube/polymer composites. Huxtable et al.<sup>57</sup> used picosecond transient absorption to measure the interface thermal conductance of CNT suspended in surfactant micelles in water, a system comparable to polymer-based composites. They estimated that the thermal resistance posed by the nanotube–polymer interface was equivalent to the resistance of a 20-nm-thick layer of polymer. This finding indicates that heat transport in a

nanotube-based nanocomposite material will be limited by the exceptionally small interface thermal conductance and is in marked contrast to the findings regarding electrical conduction in these composites. Thus, the thermal conductivity of nanotube/polymer nanocomposite will be much lower than the value estimated from the intrinsic thermal conductivity of nanotubes. Improvements in thermal conductivity will require strategies for overcoming the interfacial thermal resistance, perhaps by interfacial covalent bonding.

In addition to interfacial bonding, nanotube dispersion, alignment, and aspect ratio are expected to influence the thermal conductivity of the nanocomposites. There are a limited number of reports on thermal conductivity of nanotube-based nanocomposites, due at least in part to the difficulty of the experiments. Thus, only an incomplete view of how these parameters influence thermal conductivity is available. Choi et al.<sup>9</sup> showed that the thermal conductivity of the magnetically aligned 3 wt% SWNT/epoxy was 10% higher than that of the unaligned nanocomposite with the same loading.

Like silica<sup>58</sup> and clay,<sup>59,60</sup> nanotubes also improve the thermal stability of polymer matrices in nanocomposites. In these nanocomposites, the filler particles absorb a disproportionate amount of thermal energy, thereby retarding the thermal degradation of the polymer. Du et al.<sup>8</sup> showed that the temperature of the maximum weight loss peak shifts from 300°C for pure PMMA to 370°C for the 0.5 wt% SWNT/PMMA nanocomposite, as determined by thermal gravimetric analysis. Similar results were also found using MWNT in various polymer matrices.<sup>12,61</sup>

Nanotubes have also proven to be effective flame-retardant additives. Kashiwagi et al.<sup>12,31</sup> reported that small amounts of MWNT greatly improve the flammability of PP, as measured both by cone calorimetry and radiant gasification in nitrogen. Mass loss rates decrease with increasing MWNT concentration (Figure 7.11a) indicating that the addition of MWNT effectively prolongs the burning of PP. The sample residue collected after nitrogen gasification (Figure 7.11b) is nearly the same shape as the original sample and is a low-density, self-supporting structure of nanotubes, a nanotube network. Kashiwagi et al.<sup>62</sup> attribute the improvement in flammability to nanotube networks spanning the nanocomposite that dissipate heat and thereby reduce the external radiant heat transmitted to the PP in the sample. A recent study<sup>62</sup> of SWNT/PMMA nanocomposites also shows similar flame retardancy effectiveness with lower concentrations of SWNT.

Kashiwagi et al.<sup>31</sup> compared MWNT/PP and carbon black/PP nanocomposites. With the same carbon loading, 1 wt%, carbon black is much less flame retardant than MWNT. The residue of the 1 wt% carbon black/PP nanocomposite after nitrogen gasification contains discrete aggregates and granular particles in contrast to the residue from the MWNT/PP composites having a MWNT network. The presence of the nanotube network is critical to improving the flame retardancy, because this morphology provides efficient heat dissipation. A similar network was observed in clay/PP nanocomposites with 5 wt% filler,<sup>59</sup> but the residue was brittle. At only 0.5 wt% loading, intact nanotube networks form in both SWNT and MWNT nanocomposites, indicating that nanotubes are more potent flame-retardant additives than nanosilicates. As with other properties of nanotube/polymer composites, the flame-retardant performance will depend on nanotube dispersion,<sup>62</sup> aspect ratio, and alignment.

## 7.7 CONCLUSIONS

Polymers are frequently modified to improve their physical properties for specific applications. Among the additives now available are CNT that provide unique opportunities to improve mechanical, electrical, and thermal properties of a variety of polymer matrices. We have summarized the current state of this field, though each month brings new publications that expand the understanding of nanotube/polymer nanocomposites. The published literature, as presented above, is only a fraction of the current activity as companies pursue research and development on nanotube/polymer materials. Upon review of the available literature the following generalizations are evident:

1. In addition to nanotube concentration, the properties of nanotube/polymer composites strongly depend on the nanotube dispersion within the matrix, the aspect ratio of the

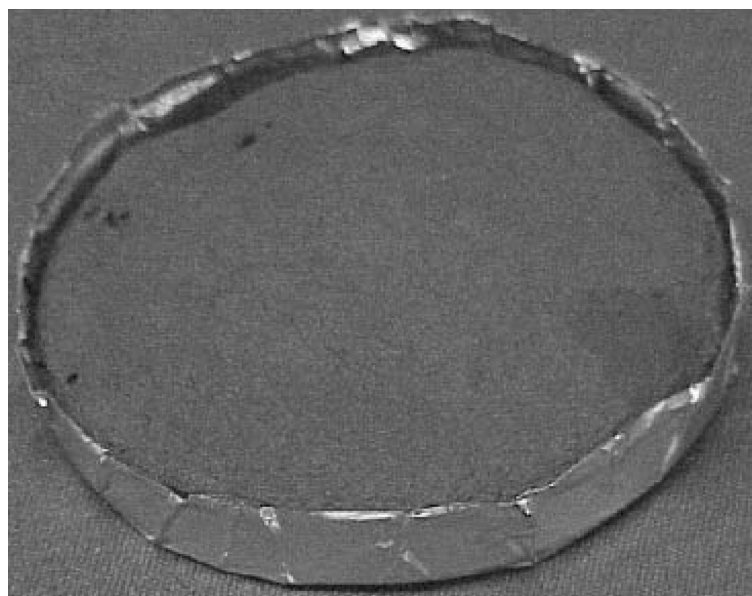
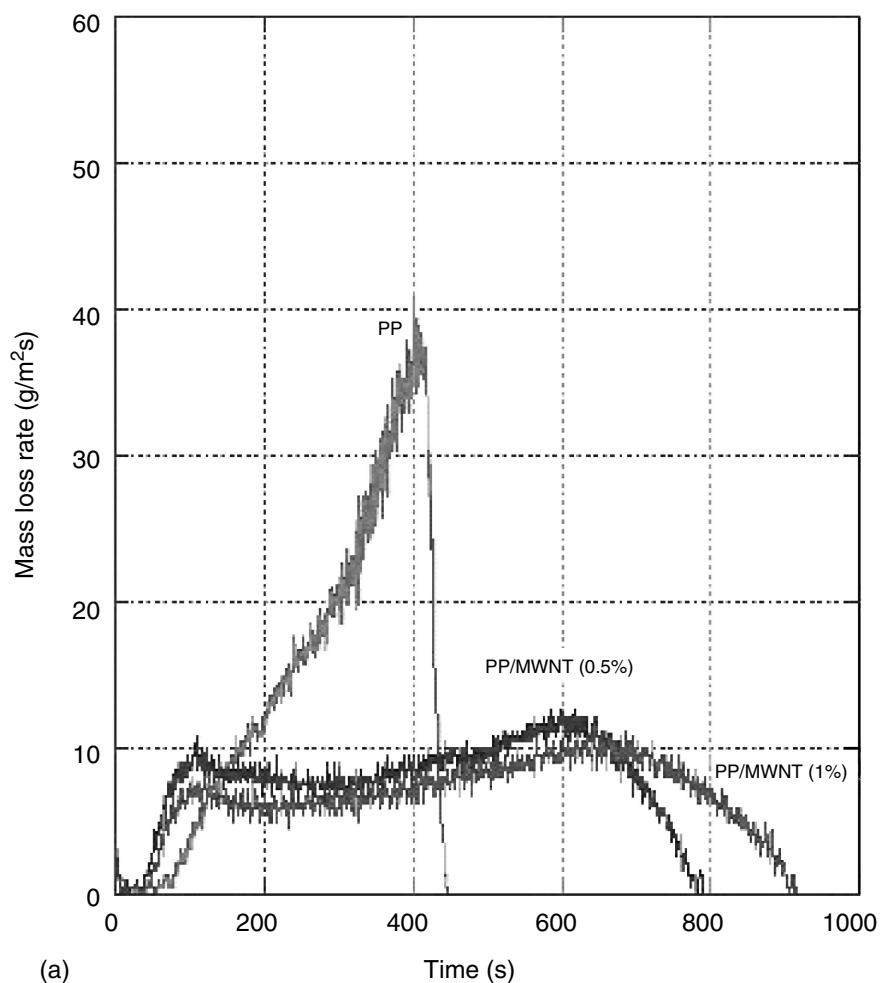


**FIGURE 7.11** (a) Mass loss rate for PP and MWNT/PP nanocomposites in nitrogen gasification, showing that the addition of MWNT slows the thermal degradation of the polymer matrix; (b) highly porous residue of the 1wt% MWNT/PP nanocomposite after nitrogen gasification suggesting the presence of a nanotube network in the nanocomposite. (Adapted from Kashiwagi et al.<sup>31</sup>)

nanotubes and the alignment of the nanotubes within the polymer matrix. These traits, dispersion, aspect ratio, and alignment, are difficult and tedious to determine, and many publications fail even to attempt a qualitative description of these characteristics of their composites. As these traits are not independent (e.g., shorter nanotubes are easier to disperse) control experiments are challenging. Nanotube dispersion in a nanocomposite must be explored over a range of length scales from nm to mm. The aspect ratios of nanotubes depend on the synthetic route of the nanotubes with batch-to-batch variations that are considerable. In addition, postsynthesis processing to increase purity and improve dispersion can alter the distribution of aspect ratios. The high aspect ratios of nanotubes make them prone to alignment by even modest applied forces (e.g., during solvent casting gravity is sufficient to bias the spatial distribution of nanotubes to be preferentially horizontal). These nuances are important to nanotube/polymer composites and their properties and serve to caution researchers in the field.

2. The concept of networks of nanotubes provides strong correlations between nanocomposite morphology and properties. Nanotube networks are structures in which interconnected nanotubes form an open and irregular framework of nanotubes that span across the nanocomposites. Such nanotube networks are readily detected by dynamic mechanical (rheological) or electrical conductivity measurements. In fact, the detection of a nanotube network provides a reliable, though indirect and qualitative, measure of the relative nanotube dispersion and aspect ratio. For example, the presence of solid-like behavior indicates better dispersion than a comparable nanocomposite with the same nanotube loading and aspect ratio having liquid-like behavior. The presence of nanotube networks in nanocomposites provides a framework for discussing rheological, electrical, and flame-retardant properties. This framework is inappropriate for properties such as mechanical and thermal properties in which the interfacial properties of the nanotube/polymer nanocomposite are dominant.
3. Nanotubes are certainly capable of improving the physical properties of polymers. As with any filler, there will be a balance of advantages and disadvantages. The higher electrical conductivity available at low nanotube loadings will be balanced with the onset of solid-like behavior that will make the nanocomposite more difficult to process. The current cost of nanotubes is such that loadings as small as 1 wt% could be prohibitive over the next few years, except in highly selective markets. Because the cost of nanotubes will continue to drop, research with available nanotube materials should continue in earnest. At the moment, improvements in the electrical and thermal properties are perhaps the most promising, although mechanical properties of nanotube/polymer composites will benefit substantially from the emerging availability of all nanotube fibers.

In conclusion, nanotube/polymer nanocomposites have demonstrated their promise as multifunctional materials. Attention to the challenges detailed above will maximize their potential as a new class of nanocomposites for a variety of applications in the coming decades.

## ACKNOWLEDGMENTS

The authors thank the Office of Naval Research (N00014-3-1-0890) for funding and Dr. Fischer, Dr. Kashiwagi, Dr. Lukes, R. Haggenueller, and C. Guthy for helpful discussions.

## REFERENCES

1. Thostenson, E.T., Ren, Z., and Chou, T.W., *Comp. Sci. Technol.*, 61, 1899–1912, 2001.
2. Kim, P., Shi, L., Majumdar, A., and McEuen, P.L., *Phys. Rev. Lett.*, 87, 21550201–21550204, 2001.
3. Maruyama, S., *Physica B*, 323, 193–195, 2002.
4. Bronilowski, M.J., Willis, P.A., Colbert, D.T., Smith, K.A., and Smalley, R. E., *J. Vac. Sci. Technol. A*, 19, 1800–1805, 2001.

5. Salvetat, J.P., Andrew, G., Briggs, D., Bonard, J.M., Bacsa, R.R., Kulik, A.J., Stockli, T., Burnham, N.A., and Forro, L., *Phys. Rev. Lett.*, 82, 944–947, 1999.
6. Haggemueller, R., Commans, H.H., Rinzler, A.G., Fischer, J.E., and Winey, K.I., *Chem. Phys. Lett.*, 330, 219–225, 2000.
7. Benoit, J.M., Corraze, B., Lefrant, S., Blau, W., Bernier, P., and Chauvet, O., *Synth. Met.*, 121, 1215–1216, 2001.
8. Du, F., Fischer, J.E., and Winey, K.I., *J. Polym. Sci.: Part B: Polym. Phys.* 41, 3333–3338, 2003.
9. Choi, E.S., Brooks, J.S., Eaton, D.L., Al-Haik, M.S., Hussaini, M.Y., Garmestani, H., Li, D., and Dahmen, K., *J. Appl. Phys.*, 94, 6034–6039, 2003.
10. Furtado, C.A., Kin, U.J., Gutierrez, H.R., Pan, L., Dickey, E.C., and Eklund, P.C., *J. Am. Chem. Soc.*, 126, 6095–6105, 2004.
11. Qian, D., Dickey, E.C., Andrews, R., and Rantell, T., *Appl. Phys. Lett.*, 76, 2868–2870, 2000.
12. Kashiwagi, T., Grulke, E., Hilding, J., Harris, R., Awad, W., and Douglas, J., *Macromol. Rapid Commun.*, 23, 761–765, 2002.
13. Bhattacharyya, A.R., Sreekumar, T.V., Liu, T., Kumar, S., Ericson, L.M., Hauge, R.H., and Smalley, R.E., *Polymer*, 44, 2373–2377, 2003.
14. Coleman, J.N., Curran, S., Dalton, A.B., Davey, A.P., McCarthy, B., Blau, W., and Barklie, R.C., *Phys. Rev. B*, 58, 57–60, 1998.
15. Benoit, J.M., Corraze, B., and Chauvet, O., *Phys. Rev. B*, 65, 24140501–24140504, 2002.
16. Du, F., Scogna, R.C., Zhou, W., Brand, S., Fischer, J.E., and Winey, K.I., *Macromolecules*, 37, 9048–9055, 2004.
17. Hone, J., Batlogg, B., Benes, Z., Llaguno, M.C., Nemes, N.M., Johnson, A.T., and Fischer, J.E., *Mater. Res. Soc. Symp. Proc.*, 633, A17.11.11–A17.11.12, 2001.
18. Ajayan, P.M., Schadler, L.S., Giannaris, C., and Rubio, A., *Adv. Mater.*, 12, 750–753, 2000.
19. Park, C., Ounaies, Z., Watson, K.A., Crooks, R.E., Smith, J., Jr., Lowther, S.E., Connell, J.W., Siochi, E.J., Harrison, J.S., and Clair, T.L.S., *Chem. Phys. Lett.*, 364, 303–308, 2002.
20. Sun, Y., Fu, K., Lin, Y., and Huang, W., *Acc. Chem. Res.*, 35, 1096–1104, 2002.
21. Chen, J., Hamon, M.A., Hu, H., Chen, Y., Rao, A.M., Eklund, P.C., and Haddon, R.C., *Science*, 282, 95–98, 1998.
22. Hill, D.E., Lin, Y., Rao, A.M., Allard, L.F., and Sun, Y., *Macromolecules*, 35, 9466–9471, 2002.
23. Lin, Y., Rao, A.M., Sadanadan, B., Kenik, E.A., and Sun, Y., *J. Phys. Chem. B*, 106, 1294–1298, 2001.
24. Islam, M.F., Rojas, E., Bergey, D.M., Johnson, A.T., and Yodh, A.G., *Nano Lett.*, 3, 269–273, 2003.
25. Barrau, S., Demont, P., and Perez, E., *Macromolecules*, 36, 9678–9680, 2003.
26. O’Connell, M.J., Boul, P., Ericson, L.M., Huffman, C., Wang, Y., Haroz, E., Kuper, C., Tour, J., Ausman, K.D., and Smalley, R.E., *Chem. Phys. Lett.*, 342, 265–271, 2001.
27. Star, A., Steuerman, D.W., Heath, J.R., and Stoddart, J.F., *Angew. Chem. Int. Ed.*, 41, 2508–2512, 2002.
28. Barisci, J.N., Tahhan, M., Wallace, G.G., Badaire, S., Vaugien, T., Maugey, M., and Poulin, P., *Adv. Funct. Mater.*, 14, 133–138, 2004.
29. Kimura, T., Ago, H., Tobita, M., Ohshima, S., Kyotani, M., and Yumura, M., *Adv. Mater.*, 14, 1380–1383, 2002.
30. Walters, D.A., Casavant, M.J., Qin, X.C., Huffman, C.B., Boul, P.J., Ericson, L.M., Haroz, E.H., O’Connell, M.J., Smith, K., Colbert, D.T., and Smalley, R.E., *Chem. Phys. Lett.*, 338, 14–20, 2001.
31. Kashiwagi, T., Grulke, E., Hilding, J., Groth, K., Harris, R., Shields, J., Kathryn, B., Kharchenko, S., and Douglas, J., *Polymer*, 45, 4227–4239, 2004.
32. Jin, L., Bower, C., and Zhou, O., *Appl. Phys. Lett.*, 73, 1197–1199, 1998.
33. Safadi, B., Andrews, R., and Grulke, E.A., *J. Appl. Poly. Sci.*, 84, 2660–2669, 2002.
34. Thostenson, E.T., and Chou, T.-W., *J. Phy. D: Appl. Phy.*, 35, 77–80, 2002.
35. Haggemueller, R., Zhou, W., Fischer, J.E., and Winey, K.I., *J. Nanosci. Nanotechnol.*, 3, 104–108, 2003.
36. Andrews, R., Jacques, D., Rao, A.M., Rantell, T., Derbyshire, F., Chen, Y., Chen, J., and Haddon, R.C., *Appl. Phys. Lett.*, 75, 1329–1331, 1999.
37. Lordi, N., and Yao, V., *J. Mater. Res.*, 15, 2770–2779, 2000.
38. Lourie, O., and Wagner, H.D., *Appl. Phys. Lett.*, 73, 3527–3529, 1998.
39. Barber, A.H., Cohen, S.R., and Wagner, H.D., *Appl. Phys. Lett.*, 82, 4140–4142, 2003.
40. Liao, K., and Li, S., *Appl. Phys. Lett.*, 79, 4225–4227, 2001.
41. Cooper, C.A., Young, R.J., and Halsall, M., *Comp. Part A: Appl. Sci. Manuf.*, 32, 401–411, 2001.

42. Fisher, F.T., Bradshaw, R.D., and Brinson, L.C., *Appl. Phys. Lett.*, 80, 4647–4649, 2002.
43. Cooper, C.A., Cohen, S.R., Barber, A.H., and Wagner, H.D., *Appl. Phys. Lett.*, 81, 3873–3875, 2002.
44. Wagner, H.D., *Chem. Phys. Lett.*, 361, 57–61, 2002.
45. Krishnamoorti, R., and Giannelis, E.P., *Macromolecules*, 30, 4097–4102, 1997.
46. Lozano, K., Bonilla-Rios, J., and Barrera, E.V., *J. Appl. Poly. Sci.*, 80, 1162–1172, 2000.
47. Cumings, J., and Zettl, A., *Science*, 602, 289–291, 2000.
48. Baughman, R.H., Zakhidov, A.A., and deHeer, W.A., *Science*, 297, 787–792, 2002.
49. Ramasubramaniam, R., Chen, J., and Liu, H., *Appl. Phys. Lett.*, 83, 2928–2930, 2003.
50. Ounaies, Z., Park, C., Wise, K.E., Siochi, E.J., and Harrison, J.S., *Comp. Sci. Technol*, 63, 1637–1646, 2003.
51. Bai, J.B., and Allaoui, A., *Comp. Part A: Appl. Sci. Manuf.*, 34, 689–694, 2003.
52. Balberg, I., and Binenbaum, N., *Phys. Rev. B*, 28, 3799–3812, 1983.
53. Lau, K., Shi, S., and Cheng, H., *Comp. Sci. Technol.*, 63, 1161–1164, 2003.
54. Kymakis, E., Alexandou, I., and Amaratunga, G.A.J., *Synthetic Metals*, 127, 59–62, 2002.
55. Tchmutin, I.A., Ponomarenko, A.T., Krinichnaya, E.P., Kozub, G.I., and Efimov, O.N., *Carbon*, 41, 1391–1395, 2003.
56. Biercuk, M.J., Llaguno, M.C., Radosavljevic, M., Hyun, J.K., Johnson, A.T., and Fischer, J.E., *Appl. Phys. Lett.*, 80, 2767–2739, 2002.
57. Huxtable, S.T., Cahill, D.G., Shenogin, S., Xue, L., Ozisik, R., Barone, P., Usrey, M., Strano, M.S., Siddons, G., Shim, M., and Koblinski, P., *Nat. Mater.*, 2, 731–734, 2003.
58. Morgan, A.B., Antonucci, J.M., VanLandingham, M.R., Harris, R.H., and Kashiwagi, T., *Polym. Mater. Sci. Eng.*, 83, 57–58, 2000.
59. Marosi, G., Marton, A., Szep, A., Csontos, I., Keszei, S., Zimonyi, E., Toth, A., Almeras, X., and Le Bras, M., *Polym. Degrad. Stabil.*, 82, 379–385, 2003.
60. Qin, H., Su, Q., Zhang, S., Zhao, B., and Yang, M., *Polymer*, 44, 7533–7538, 2003.
61. Pötschke, P., Fornes, T.D., and Paul, D.R., *Polymer*, 43, 3247–3255, 2002.
62. Kashiwagi, T., Du, F., Winey, K.I., Groth, K.M., Shields, J.R., Bellayer, S.P., Kim, H., and Douglas, J.F., *Polymer*, 46, 471–481, 2005.
63. Du, F., Fischer, J.E., and Winey, K.I., *Phys. Rev. B*, 72, 12140401–12140404, 2005.
64. Du, F., Guthy, C., Kashiwagi, T., Fischer, J.E., and Winey, K.I., in preparation.

---

# 8 Nanostructured Materials for Field Emission Devices

*J.D. Carey and S.R.P. Silva*  
Advanced Technology Institute, University of Surrey,  
Guildford, United Kingdom

## CONTENTS

Abstract .....	275
8.1 Introduction to Field Emission and Criteria for Practical Electron Sources .....	275
8.2 Carbon Nanomaterial Based Cold Cathodes .....	278
8.3 Field Emission from Different Types of Amorphous Carbon .....	281
8.3.1 Polymer-Like Amorphous Carbon Films .....	281
8.3.2 Diamond-Like Amorphous Carbon Films .....	282
8.3.3 Tetrahedral Amorphous Carbon Films .....	285
8.3.4 Graphite-Like Amorphous Carbon Films .....	286
8.3.5 Nanocomposite Amorphous Carbon Films .....	286
8.3.6 Ultrananocrystalline Diamond Thin Films .....	286
8.4 Field Emission and Dielectric Inhomogeneity .....	287
8.5 Field Emission as a Function of Conditioning .....	288
8.6 Surface Modifications .....	290
8.7 Summary and Outlook for the Future .....	292
References .....	292

## ABSTRACT

In this review, the state of the art in the use of thin film nanomaterials for use as electron sources is described. We first begin with a discussion of the phenomena of electron field emission and a discussion of the minimum specifications required for practical device fabrication. The bulk of the review concentrates on what is known about thin film emitters, based on amorphous carbon. The concept and importance of dielectric inhomogeneity is discussed. Extensions to other nanomaterial systems are also presented and examples of the use of amorphous silicon and excimer laser-processed amorphous silicon for the fabrication of thin film cold cathodes will also be introduced. Finally, we describe how external treatments can be used to improve the field emission characteristics.

## 8.1 INTRODUCTION TO FIELD EMISSION AND CRITERIA FOR PRACTICAL ELECTRON SOURCES

The ability to extract electrons from a material has a ready number of applications ranging from field emission based displays (FEDs) to electron sources for microwave applications. Such



applications are generally considered as being within the realm of vacuum micro- and nanoelectronics. (For a comprehensive review of the physics and applications of amorphous carbon-thin films, see [1].) Field-induced electron emission from a surface is primarily determined by the strength of the *local* electric field and the potential barrier to emission. In a metal, the barrier would correspond to the work function of the material. The other key aspect in the discussion of FE is the concept of the local field, which differs from the applied macroscopic field. In the usual two-terminal experimental set-up, described in Figure 8.1, an anode at a potential  $V$  is separated by a distance  $D$  from a grounded cathode. The applied field is then  $V/D$ . The local field is enhanced relative to the applied field and this increase is characterized by the field enhancement factor or field magnification factor  $\beta$ . For tip-based emitters such as Spindt tips or carbon nanotubes, the enhancement factor usually depends on the geometric properties of the emitter tip, such as height and radius. For example, the field-enhancement factor for a single-grounded hemisphere is calculated to be 3. The enhancement factor may also depend on the location of the anode plane if the anode–cathode separation becomes comparable with the anode–tip separation. In the case of semiconductors, field penetration becomes an important consideration when compared with metallic emitters, where no penetration into the cathode is present.

The application of an electric field to the surface of an emitter can have several effects and they are summarized in Figure 8.2. As the electric field is increased, thermionic emission over the top of the surface barrier occurs. This is followed by emission over the field-reduced barrier (Schottky emission). Emission will then occur partly over and partly through the barrier if the temperature is high enough. As the temperature is lowered, emission will result from electrons tunneling through the barrier from electron states at the Fermi level. This is known as Fowler–Nordheim (FN) tunneling. Finally, at very high fields, emission occurs from electron states below the Fermi level (ballistic electron emission). In Figure 8.2, the simple triangular potential can be taken to be of the form

$$V(z) = h - eEz \quad (8.1)$$

where  $h$  is the surface barrier height (eV), often regarded as the work function ( $\Phi$ ) of the material.

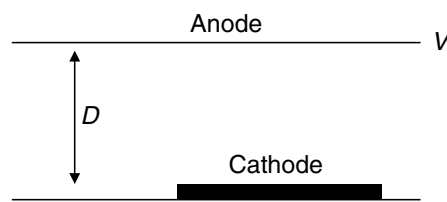


**FIGURE 8.1** Two terminal field emission arrangement in which the anode, at potential  $V$ , is separated from a grounded cathode by a distance  $D$ . The macroscopic electric field is  $V/D$ .

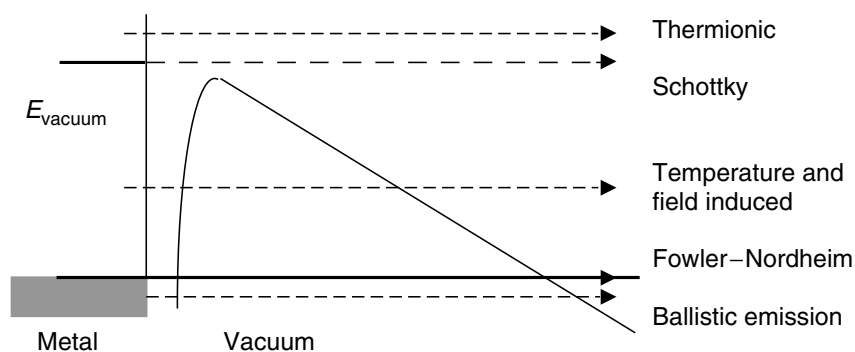


**FIGURE 8.2** Electron emission processes that can occur in the presence of an electric field.

The second rounded potential in Figure 8.2 incorporates the image charge effects and adds an additional term to Equation (8.1) to give

$$V(z) = h - eEz - \frac{e^2}{16\pi\epsilon\epsilon_0 z} \quad (8.2)$$

The effect of this additional term is to round off the overall potential barrier and lower the overall barrier height by an amount

$$\Delta h = 3.975 \times 10^{-5} E^{1/2}, \quad (8.3)$$

where the field  $E$  is measured in V/m. For a field of 20 V/ $\mu\text{m}$  the barrier lowering due to image charge effects is approximately 0.17 eV. It is evident from Figure 8.2 that the emission of electrons is a quantum mechanical tunneling process and various forms of the FN theory and equation have been employed. Indeed, the FN theory has been applied to explain the emission from gated emitter arrays, chemical vapor deposition (CVD) grown diamond films incorporating grain boundaries, atomically smooth amorphous carbon thin films and carbon nanotubes, both single and multiwall, and as such its application to these structures is somewhat remarkable when considering the assumptions on which the theory is based. The standard FN theory makes the following assumptions [2]:

1. The emitter is an atomically smooth and clean metal surface.
2. The metal has a free electron band structure and the electrons in the metal obey Fermi–Dirac statistics.
3. Emission occurs at 0 K and the barrier to emission (work function) is uniform and independent of applied electric field.
4. Electron tunneling can be described in terms of the Wentzel–Kramers–Brillouin approximation.
5. The barrier to emission can be represented by a triangular potential onto which a classical image potential is superimposed.

It is useful to examine the final form(s) of the FN equation and discuss its application to FE data. Representing the applied electric field by  $E$  and the barrier height by  $\Phi$ , the emission current  $I$  can be expressed as

$$I = \frac{aA(\beta E)^2}{\Phi} \exp \left[ \frac{-b\Phi^{3/2}}{\beta E} \right] \quad (8.4)$$

where  $a$  and  $b$  are constants with values of  $1.54 \times 10^{-6}$  A eV/V<sup>2</sup> and  $6.8 \times 10^9$  eV<sup>-3/2</sup> V/m, respectively, and  $A$  is the emission area. Here,  $\beta E$  represents the local electric field and in this context  $\beta$  represents the enhancement of the applied electric field. FE measurements are usually performed in either a diode arrangement in which an anode, either a parallel plate or spherical ball electrode, is located above a grounded cathode or in a triode arrangement in which a gated electrode is located nearby. Analysis of FE  $I$ – $V$  characteristics using the FN equation can be performed by plotting  $\log(I/E^2)$  against  $1/E$ , the slope being  $-b\Phi^{3/2}/\beta$ . It is not possible from an FE measurement to determine both  $\beta$  and  $\Phi$  independently, although the latter can be determined via other methods. Armed with a knowledge of the work function, considerable attention has been paid to the significance of the value and origin of the enhancement factor. However, some care must be exercised in the interpretation of enhancement factors since complications arise in comparing theory with experiment. The levels of sophistication that have been developed in understanding the application of an electric field to a clean metal surface (or other material) are often masked by experimental factors such as the presence of

absorbates on the cathode surface. For example, different atoms can induce dipoles on the surface, which can change the work function of a metal, or the work function itself may possess a dependence on the electric field and nano-protrusions on the surface may act to increase the local electric field.

Finally, it is worth noting that FE from semiconductors is complicated by the possibility of emission from either the conduction or valence bands, from the Fermi level or from surface states. In addition, the effects of band bending, field penetration, and internal FE, particularly in wide-gap semiconductors, as well as the possibility of negative electron affinity, need to be taken into account. There is also the issue of “conditioning” of the cathode, in which the onset of stable and reproducible emission is sometimes only observed after several cycles of the voltage, a process that will be discussed later. Despite these potential complications in understanding the mechanism of emission, because of their inherently simpler fabrication process and ability to scale up production, semiconductor thin film emitters have a number of advantages over tip-based arrays. First, electron emission from a thin film comes from a much larger area than from a tip array. This results in a low current density at emission points for a given emission current. Second, the absence of highly focused electric fields reduces the ion bombardment and sputter erosion of the thin film. With these advantages in mind, we now discuss some common nano-material cold cathodes based on amorphous carbon.

For a practical flat panel display, it is necessary to have typically 100 Cd/m<sup>2</sup> brightness but with FE most devices will exceed 300 Cd/m<sup>2</sup>. In general, emission current densities of 10 mA/cm<sup>2</sup> will be sufficient to give suitable output from conventional phosphor cathodes with ideally emission sites in excess of 10<sup>6</sup> cm<sup>-2</sup> in order to obtain uniform emission from a high-density display without correction optics.

## 8.2 CARBON NANOMATERIAL BASED COLD CATHODES

Nanomaterials based on amorphous carbon have attracted particular attention since it is possible to deposit thin films over large areas and at low temperatures [1]. The latter point is of notable importance since it is possible to deposit films onto organic or plastic substrates. In addition, the softening temperature of most common display glass is around 400°C and as a result deposition processes which significantly exceed this temperature are not compatible with current technology. Fortunately, the low-temperature deposition of amorphous carbon makes it an ideal candidate as a potential cathode material. Early interest in carbon films as cold cathodes was driven by the hope that these films possessed negative electron affinity (NEA) [3] in the same way that certain H-terminated diamond films can possess an NEA surface. As a result, once electrons were injected into the conduction band of the film, there would be a steady supply of electrons which could emerge at the film/vacuum interface. However, it is important to realize at this stage that there are many different types of amorphous carbon films that are possible, based upon different configurations of bonding hybridizations that are available to carbon. These include tetrahedral sp<sup>3</sup> bonds, trigonal sp<sup>2</sup> bonds, and linear sp<sup>1</sup> bonds as shown in Figure 8.3. As in the crystalline case, each of these bond variations is available to its amorphous counterpart, and this enables the unique and large variation in the physical and material properties to be extended to amorphous carbon (a-C) thin films. The sp<sup>3</sup> phase in low density a-C films tends to be found in aliphatic chains, whereas the sp<sup>2</sup> phase tends to cluster into olefinic chains or aromatic rings. Amorphous carbon is the generic term used here to describe most disordered carbon films. Although there is no long-range order present, both short- and medium-range order is preserved, which gives rise to physical properties that can mimic those found in the crystalline material. In these materials, by examining the nearest neighbor distance and the next-nearest-neighbor distance, it is clear that the short-/medium-range order is very close to its crystalline counterpart. It is generally the bond angle, not bond length, that is different from that of the crystalline case which gives a-C no long-range order. Such bond angle disorder can also give rise to the narrowing of the band gap by virtue of it creating highly localized states within the band gap [4].

The description of a-C films can be broken down into two distinct categories; hydrogenated and non-hydrogenated films. Whenever a hydrocarbon source gas or plasma system is used to deposit

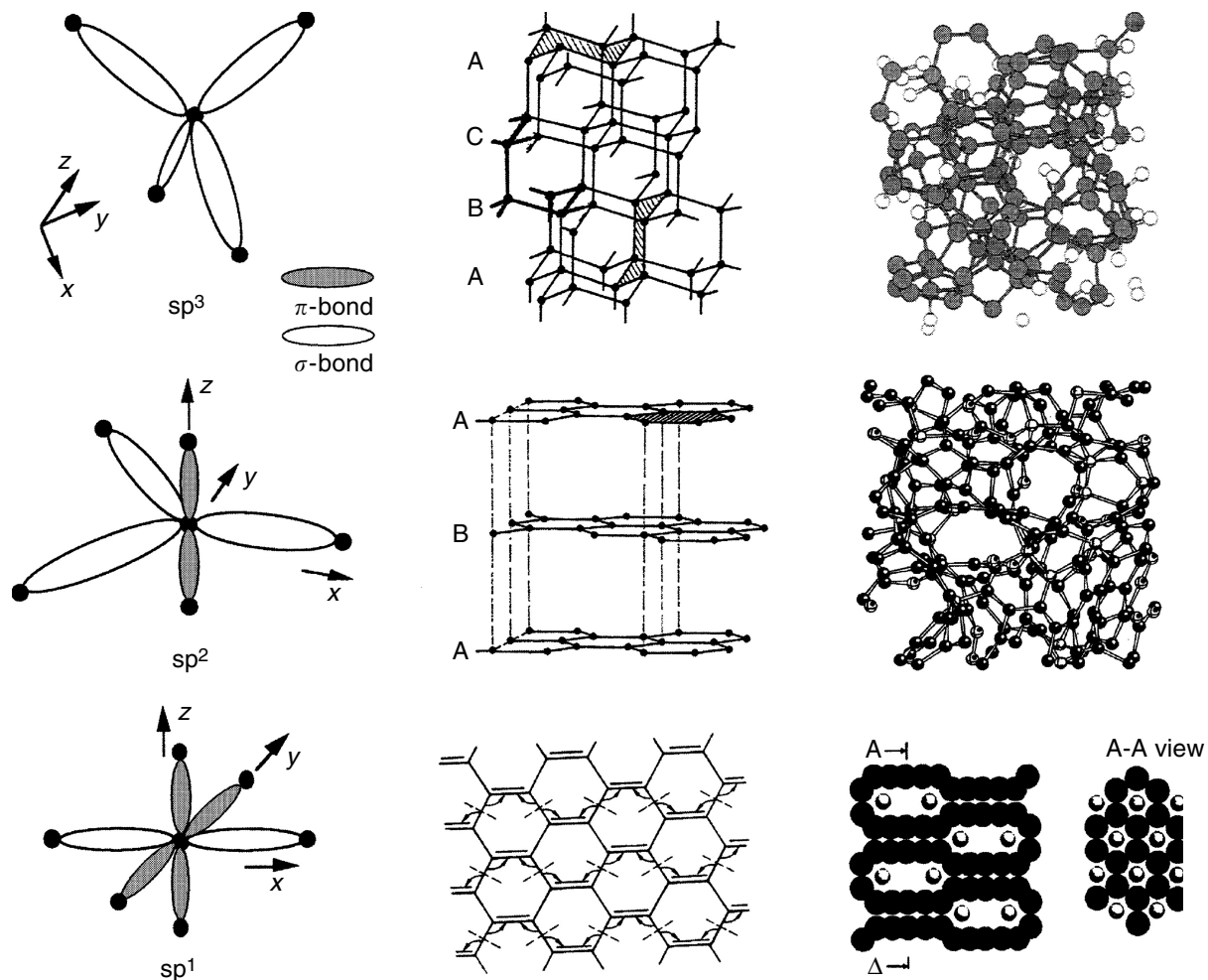


**FIGURE 8.3** A schematic representation of  $sp^1$ -,  $sp^2$ -, and  $sp^3$ -hybridized bonds and the resultant crystalline and model amorphous structures.

films, some quantity of hydrogen gets incorporated within its microstructure [1]. Since hydrogen prefers to bond in an  $sp^3$  hybridized manner by terminating single bonds, they tend to enhance the  $sp^3$  or tetrahedral nature within the films. Using techniques such as the plasma beam source, an  $sp^3$  content as high as 80% has been recorded in the presence of 30% hydrogen within these highly tetrahedral hydrogenated a-C (ta-C:H) films [5]. This is in contrast to the more usual 40–60%  $sp^3$  bonding found in the diamond-like carbon (DLC) films deposited using radio frequency plasma-enhanced chemical vapor deposition (r.f. PECVD) with ion bombardment (and H contents of ~30–40 at.%). When no ion bombardment is used, as in the case of film growth on the earthed electrode of a r.f. PECVD systems, highly polymer-like a-C:H (PAC) films are deposited [6]. These films have an  $sp^3$  content between 60 and 80% (but mostly in the form of C–H bonds with little  $sp^3$  C–C bonds) and high hydrogen contents (H content up to 55 at.%). At the high end of the hydrogen content, thin films deposited are more similar to hydrocarbon polymers such as polythene which possesses 66 at.% H. Tetrahedral amorphous carbon (ta-C) can also be produced, which tends to have a high  $sp^3$  content and is grown by arc or laser ablation methods. The different types of films are summarized in the ternary phase diagram presented in Figure 8.4. We will use this classification to describe the a-C films below.

Polymer-like films tend to be grown under low-energy conditions, such as those found with low negative self-bias in r.f. PECVD, whereas DLC films tend to be grown under higher deposition self-bias (energy) conditions. Examples of DLC films are those deposited on the driven electrode of an r.f. PECVD system, where during the growth process there is also ion beam “subplantation” of growth species involved. In other deposition systems such as sputtering, a similar result could be

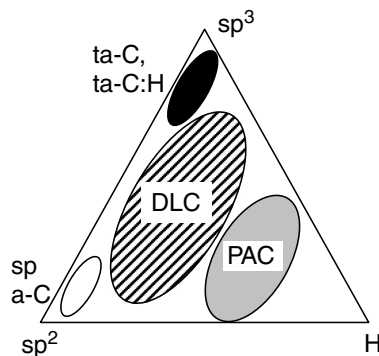


**FIGURE 8.4** Ternary phase diagram for amorphous carbon system. Not shown is  $sp^1$  bonding which is considered not to be present in sufficient quantities.

achieved by either having a second ion source that is used purely to ion-bombard the growth surface or by the application of a negative self-bias to the growth substrate. Graphite-like a-C (GAC) are also possible with very high-energy C ion sources. It is worth highlighting that it is imperative that to understand the FE characteristics of these nanomaterials, detailed knowledge of the film's electronic properties is required. For example, the films deposited by Gröning et al. [7] have been compared by a number of authors to films deposited by Amaratunga and Silva [8] using rf PECVD. A closer examination of the material properties shows that Gröning's films are graphite-like GAC films with no optical band gap while the DLC films by Amaratunga and Silva have an optical band gap close to 2 eV. Therefore, few parallels can be made in terms of FE models and transfer of experimental results for films that have material properties that are dissimilar.

It is worth categorizing several types of a-C films for the analysis of their electron field emission process. Progressing with ascending energies required for the growth of the films, we will consider emission from PAC, DLC, ta-C, GAC, as well as nanocomposite amorphous carbon (NAC) films. It is also worth discussing that in the case of a-C films that do not possess large numbers of defect states within the films or graphitic or conducting regions in their microstructure, a conditioning process is often required before the emission of electrons takes place. Subsequent to the initiation voltage required in the conditioning, emission takes place at successively lower threshold fields which reaches a minimum value after about four cycles. The hysteresis observed in this process of conditioning is shown clearly in Figure 8.5, and is non-reversible, i.e., once a cathode has been conditioned, it will remain conditioned despite being exposed to atmospheric condition for several days. This points to the fact that surface termination or the front surface dipole effects may play less of a role than originally thought for these types of film. Other types of both carbon- and noncarbon-based nanomaterials will also be considered.

Since there are different types of a-C and a-C:H film possible with very different properties, it is not surprising that there is more than one possible emission mechanism. One immediate feature for the need of different models concerns the application of an electric field to the surface of a semiconductor. It is well known that the degree of field penetration into a semiconductor film depends on the conductivity of the sample. The higher the conductivity, the smaller the extent that the externally applied field will penetrate into the film. In the ultimate limit of a metallic conductor, there will be no penetration of the field into the film. As the  $sp^2$  phase is associated with the more conductive clusters within the film, the field lines from the anode will terminate on these clusters. As a result there is an immediate link between the emission mechanism and the extent of field penetration. In some cases, field penetration will extend to the film/substrate interface, where the emission mechanism will be referred to as a "back contact" controlled emission. Such an emission mechanism differs in films for which there is little field penetration and where the emission is controlled by the properties at or near to the front of the film/vacuum interface, referred to as the "front surface" controlled mechanism. The origin of these two different types of mechanism will be explored in detail below.

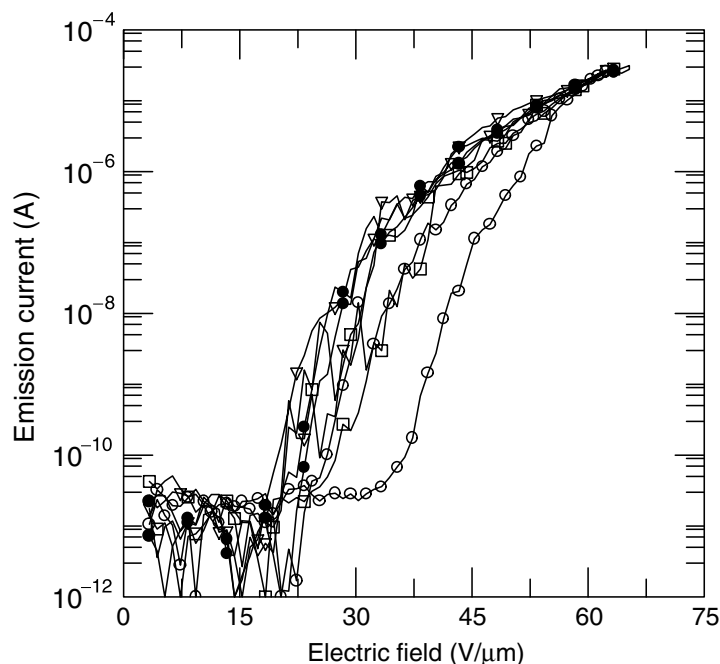


**FIGURE 8.5** Emission current vs. macroscopic electric field for a 67-nm-thick polymer-like a-C:H film. The applied field is cycled up and down four times: (○) run 1; (□) run 2; (●) run 3; (▽) run 4.

Finally, to produce a satisfactory model for electron emission, three fundamental questions are worth addressing before continuing the discussion of the mechanisms that are responsible for emission from these materials. First, what is the source of the electrons? Second, how are the electrons transported through the film? Finally, how are the electrons emitted into vacuum?

## 8.3 FIELD EMISSION FROM DIFFERENT TYPES OF AMORPHOUS CARBON

### 8.3.1 POLYMER-LIKE AMORPHOUS CARBON FILMS

There are a number of reports of electron field emission properties of these types of films [9,10]. These films have low defect densities and often require a high initiation electric field for emission to take place. Significant hysteresis is often observed in the first cycle after initiation (as shown in Figure 8.5). Subsequent to the initiation process, the threshold field for electron emission has been shown to vary between 10 and 70 V/μm by changing the thickness of the undoped films by Forrest et al. [9] (Figure 8.6). Despite some of these films being subject to very high electric fields of the order of 70 V/μm, no surface morphological change was observed with a scanning electron microscope after emission. The data show a very strong dependence of the conditioned threshold field on film thickness, with the required field showing a minimum turning point at a film thickness close to 60 nm. The threshold field needed for emission increases on either side of this optimum thickness, with the surface of the films not exhibiting any morphological changes when examined by an atomic force microscope (AFM), as a function of film thickness.

As will be described later, the degree of sp<sup>2</sup> clustering is shown to be a major factor in the control of FE from a-C films. However, the growth conditions in the study of Forrest et al. have been kept constant throughout the deposition process and so no changes in the microstructure of the film is expected. The observed variations with film thickness in these films were explained using the inter-layer model based on space-charge-induced band bending. In this model, the a-C films act as an interlayer with the true cathode being the underlying Si or metal substrate, with the crucial factor being the heterojunction (or in other materials if formed, the Schottky barrier) that is formed at the back contact. This model, proposed by Amaratunga and Silva [8], is based on

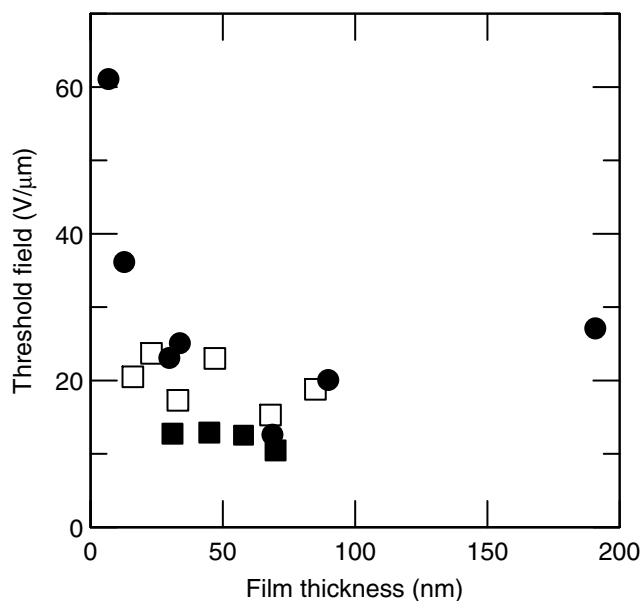


**FIGURE 8.6** Variation of threshold field as a function of thickness for a polymer-like film (●) and for DLC films deposited at  $-90$  V (□) and  $-265$  V (■) self-bias.

assuming that the a-C thin film is n-doped and has an electron affinity close to 2.5 eV, a Fermi level of 0.5 eV as shown in Figure 8.7a.

When a bias is applied to the heterojunction and the anode becomes positive, and the applied field is large enough to fully deplete the carbon thin film, it was shown [8,9] that the field experienced by the electrons that tunnel through the heterojunction barrier into the conduction band is larger than the applied electric field, due to space charge considerations. This field decreases parabolically within the film, as it traverses toward the surface of the semiconductor (Figure 8.7b). According to the band diagram, the pool of electrons gathered at the n-Si/a-C interface has a built-in barrier that prevents the tunneling/thermal excitation of electrons into the conduction band of the a-C layer before the inter-layer band bending is large enough for the electrons to overcome the energy barrier for emission into the vacuum. The electrons can now lose up to 3 eV in phonon scattering and still retain sufficient kinetic energy to enter the vacuum level in the a-C thin films and thus emit into the vacuum. In the case of electrons that do not have enough energy to reach the vacuum, they will collect at the front surface of the a-C thin film and decrease the band bending in the space charge layer as shown in Figure 8.7c. Until the total band bending is lost, there will be some electrons emitted from the a-C thin films. This is an example of a back contact controlled mechanism. Similar arguments may be applied to any material which allows field penetration and this includes wide-gap semiconductor materials.

### 8.3.2 DIAMOND-LIKE AMORPHOUS CARBON FILMS

The higher energy deposition found in DLC films produces more defect states near the Fermi level. In the a-C system, the defect states are those associated with the conductive  $sp^2$  clusters, which themselves may be distorted or undistorted. The location of the  $sp^2$  clusters in the energy gap depends on two factors: whether they consist of even or odd numbers of carbon atoms and whether they are distorted. Undistorted even-numbered clusters will give rise to states near the Fermi level ( $E_F$ ) only if they are sufficiently large. This differs from the case of odd-numbered clusters, which can give rise to gap states even if composed of a small number of atoms. In general, distorted clusters give rise to a state that is closer to  $E_F$  than undistorted clusters. In this way, electron spin resonance (ESR) can give a measure of the density of  $sp^2$  states at the Fermi level, provided that a majority of these states have a net unpaired electron spin present. Note that measurements of ESR spin densities do not themselves measure the  $sp^2$  content [11].

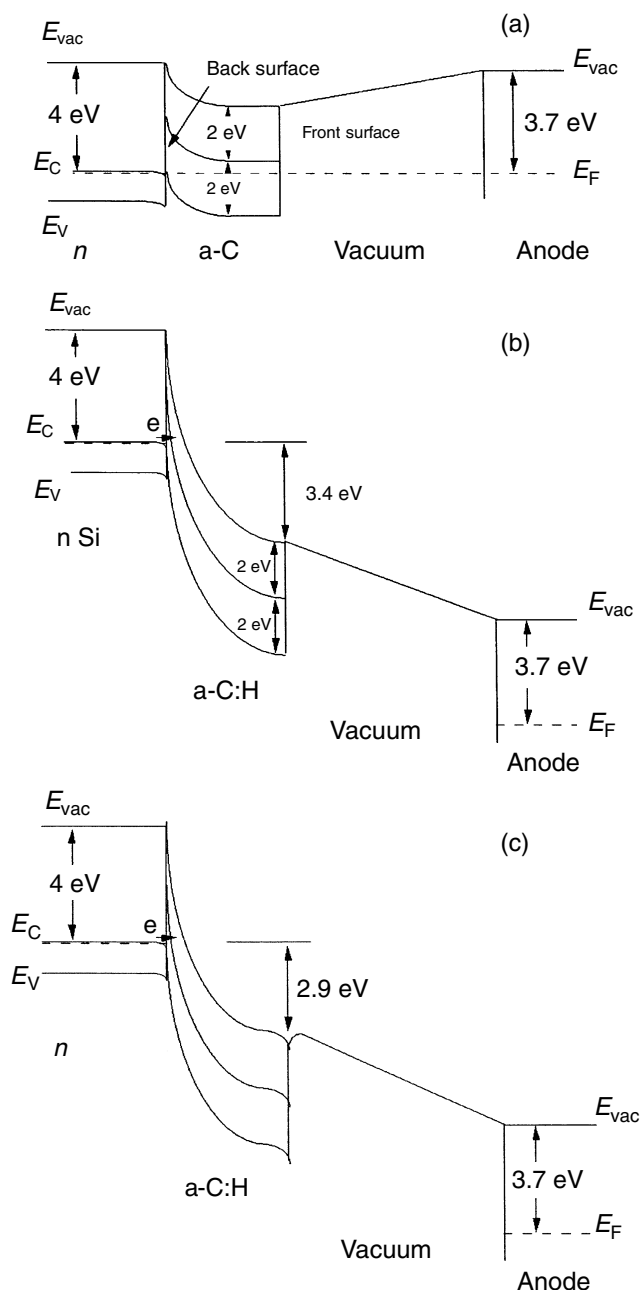


**FIGURE 8.7** Space-charge-induced band bending for field emission in low defect density materials for zero bias (a) and two different levels of bias (b, c).

Films were deposited using a standard capacitively coupled rf PECVD system with feed gases of  $\text{CH}_4$  and He. The negative DC self-bias developed across the plasma sheath was varied in the range  $-50$  to  $-265$  V at a fixed pressure of 200 mT. The films were deposited on  $n^{++}$ -Si substrates, which were degreased and then Ar (He) plasma-cleaned prior to deposition. The variation of (a) threshold field and (b) spin density with negative self-bias is shown in Figure 8.8. As the self-bias is increased from  $-50$  to  $-90$  V, the threshold field increases from a value of  $18$  V/ $\mu\text{m}$  to a value close to  $26$  V/ $\mu\text{m}$ . For bias values above  $-90$  V, the threshold field decreases to around  $12$  V/ $\mu\text{m}$ , where it remains approximately constant in this bias regime. The measured spin density,  $N_s$ , of these films rises rapidly from  $3 \times 10^{17}$  to  $1.1 \times 10^{20}$   $\text{cm}^{-3}$  at  $-125$  V. At higher biases,  $N_s$  increases only very gradually, finally reaching  $1.6 \times 10^{20}$   $\text{cm}^{-3}$ . The Tauc gap, which is a measure of the  $\pi$ - $\pi^*$  separation, falls rapidly from  $2.6$  ( $-50$  V bias) to  $1.3$  eV ( $-125$  V), and then falls gradually to about  $1.1$  eV at the highest bias voltages, as shown in Figure 8.9. In the case of the peak-to-peak ESR linewidth,



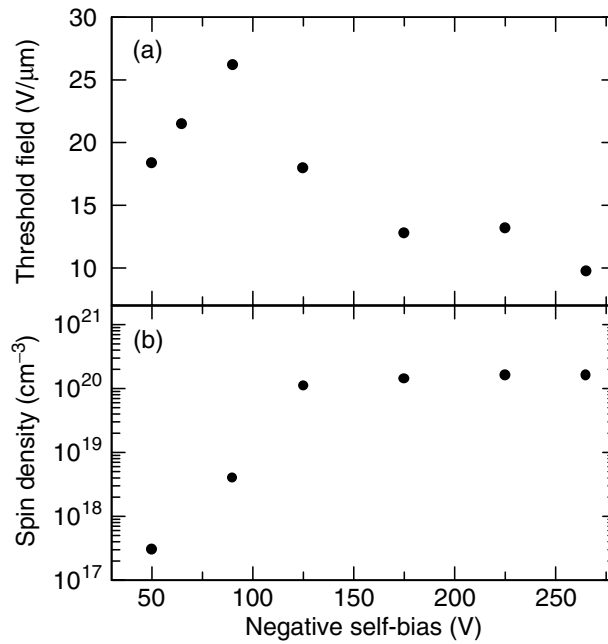


**FIGURE 8.8** Variation of (a) threshold field and (b) spin density for a-C:H films as a function of negative self-bias. Increasing the bias results in a change from polymer-like films to DLC films.

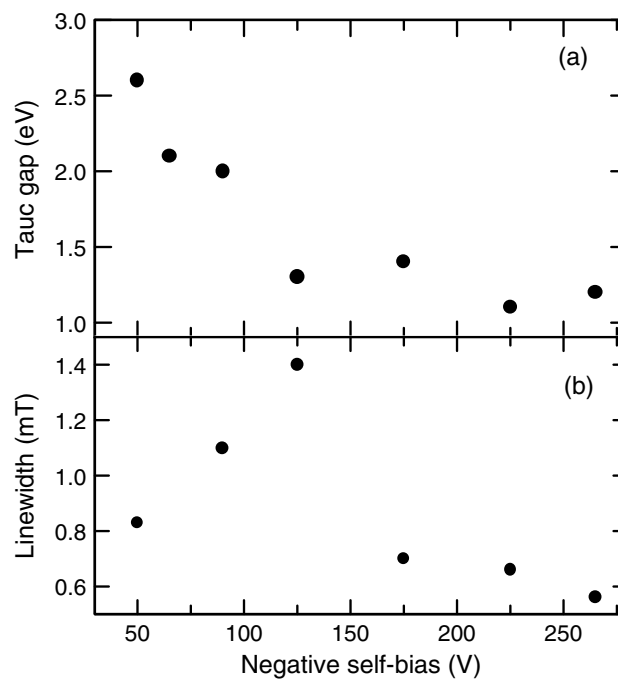


**FIGURE 8.9** Variation of (a) Tauc gap and (b) ESR linewidth for a-C:H films as a function of negative self-bias. Increasing the bias results in a change from polymer-like films to DLC films.

$\Delta B_{pp}$ , there is an initial increase in the linewidth, reaching a maximum of 1.4 mT at  $-125$  V bias followed by a rapid decrease to 0.7 mT, which continues to decrease to 0.56 mT at  $-265$  V bias. These results suggest the existence of two regimes, above and below  $-125$  V bias, and it is therefore convenient to discuss the results from the two regimes separately.

For the sample deposited at  $-125$  V bias, the measured spin density is  $1.1 \times 10^{20} \text{ cm}^{-3}$  and the observed linewidth is 1.4 mT. The Lorentzian line shape can be explained using dipolar broadening. Above  $-125$  V, it is thought that the narrowing of the linewidth is due to rapid exchange of spins as the  $sp^2$  clusters increase in size [12]. This is consistent with the narrowing of the band gap,

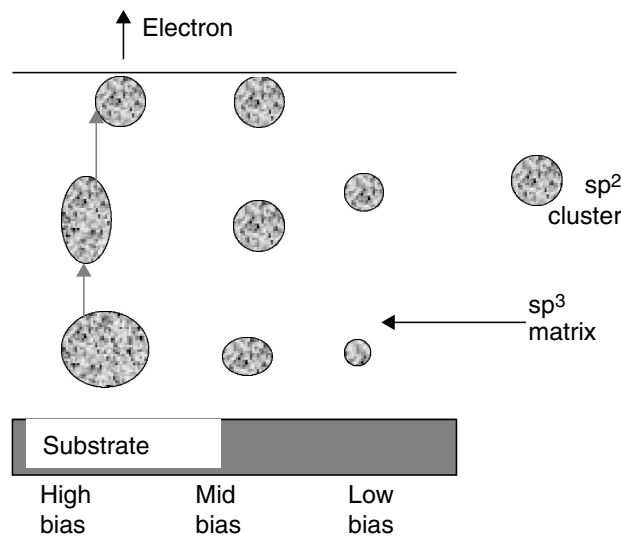


**FIGURE 8.10** Cluster arrangements in low-, mid-, and high-bias samples showing the variation of density and size of the clusters present. As the cluster size gets larger, hopping between clusters becomes easier, which contributes to the conduction in the material. The higher the cluster density, the lower the extent of field penetration.

and the reason for the convergence of the threshold field to a limiting value close to  $12 \text{ V}/\mu\text{m}$  for these films. These films have a high  $\text{sp}^2$  content ( $>65\%$ ) as well as a high band gap ( $>2 \text{ eV}$ ) and as a consequence the wave function overlap of the clusters will result in electron delocalization or enhanced hopping between the clusters that will enhance the connectivity, as shown in Figure 8.10. Application of an external electric field results in extraction of electrons from the film surface. Replenishment of the emitted electrons to the surface layer is accomplished due to the good connectivity between the clusters. Emission from these high  $\text{sp}^2$ -rich films would be characterized as a “front surface”-type emission. The high conductivity of these samples means the films would not be able to sustain any form of space charge. As the films have a high concentration of defect states ( $10^{20} \text{ cm}^{-3}$ ), it would not be possible to form a “leak-free” barrier (Schottky or heterojunction) at the back contact to the film. As a result the emission process will not be controlled by the back contact as described earlier for PAC films.

Reducing the self-bias to  $-90 \text{ V}$  decreases the spin density by about two orders of magnitude and gives rise to an increase in the Tauc gap. The rise in the Tauc gap shows that major structural changes in the film are occurring at low bias voltages with the films likely to have a lower  $\text{sp}^2$  content due to C–H bonding. At low self-biases, a low concentration of small isolated  $\text{sp}^2$  clusters forms. Initially, the number of C atoms in each cluster is small (as inferred from the large Tauc gap), but the greater energy available at higher biases allows the formation of a greater number of larger, but still isolated, clusters. This results in a reduction in the Tauc gap and an increase in the spin density, although the electron delocalization in the cluster or hopping between clusters is kept to a minimum. This leads to poor connectivity and explains why the threshold field is higher at the lower bias voltages when compared with the films deposited at higher biases. The subsequent drop in threshold field for the film at the lowest bias voltages indicates that another emission mechanism is also present in these low defect, polymer-like, wide energy gap films. The low concentration of  $\text{sp}^2$  clusters is unable to screen the field at the front surface. In this way, emission from these low bias deposited films would be more correctly described as being determined by the “back contact” model discussed earlier rather than being a “front surface”-dominated process. This view is further supported by the lack of a significant variation in the threshold field as a function of film thickness for two series of films grown under higher bias (see Figure 8.6).

### 8.3.3 TETRAHEDRAL AMORPHOUS CARBON FILMS

Tetrahedral amorphous carbon films can be produced using a filtered cathodic arc system. The films produced are highly tetrahedral in nature ( $>80\% \text{ sp}^3$ ) and extremely hard (with hardnesses

approaching 60% of that of diamond and a Young's modulus close to 500 GPa). Their properties, such as  $sp^2$  content, can be controlled by the ion energy of the carbon arc used for deposition and any negative bias applied to the substrate. It is well established that the  $sp^2$  content in ta-C films is primarily controlled by the deposition ion energy [13], which also controls many of the microstructural [14] and electronic [15] properties. It should be noted at the outset that the ta-C films discussed here have a large defect concentration comparable to that found in DLC films. On the basis of the analysis by Ilie et al. [16], it was suggested that the clustering of  $sp^2$  states plays an important role. As a result, emission from this type of nanomaterial will be front surface-dominated. Indeed, this was demonstrated by Hart et al. [17] for ~25 nm thick films deposited onto substrates of different metals (varying work functions). It was stated that several of these substrates (Ti, Mo, Si, and Cr) can form interfacial carbides, which could lower the barrier at the back contact and possibly lead to the formation of an Ohmic contact. However, the authors noted that since there was a significant spread in the measured values of threshold field between the carbide and noncarbide forming substrates, the back contact does not play a significant role in determining the emission characteristics of ta-C films, as would be predicted from a front surface-controlled electron emission process. A forming process or initiation field is sometimes needed before stable emission could be observed from some of the films [18]. Once more no surface damage was observed after forming. Field emission studies on ta-C films have also been performed by Cheah et al. [19], with low threshold fields reported.

#### 8.3.4 GRAPHITE-LIKE AMORPHOUS CARBON FILMS

Cluster beam growth of macro-aggregates having 500–2000 atoms loosely bound together are formed by an adiabatic expansion of evaporated material through a nozzle into a high-vacuum chamber. The advantages associated with the technique are due to the fact that any charge placed upon the cluster is equally distributed across each of the constituent atoms and thereby its use for ultra-shallow implants cannot be overemphasized. Each of the atoms imparts precisely the total ion energy given to the cluster divided by the size of the cluster upon impact with a surface. So the growth process possesses very low charge to mass ratios for the ionized cluster which prevents the buildup of surface space charge. Electron emission has also been reported from polycrystalline graphite films produced by supersonic cluster beam assembly techniques [20,21]. Owing to the high  $sp^2$  content the FN theory was applied since emission was assumed to originate for the Fermi level. Assuming a work function of 5 eV, a field-enhancement factor of 350 was obtained.

#### 8.3.5 NANOCOMPOSITE AMORPHOUS CARBON FILMS

Nanocomposite films consist of crystalline nanoparticles, in the form of multiwall carbon nanotubes, intentionally embedded into an amorphous carbon matrix [22]. The nanoparticles were formed by having a cathode striker in a high pressure of He or N<sub>2</sub>. Low thresholds for emission of 4.5 V/ $\mu\text{m}$  were obtained, which could be reduced by etching of the front surface. The emission mechanism was explained in terms of FN tunneling and hot electron emission in which the matrix acts as an interlayer that moderates the emission. Amaratunga et al. [22] also used the interlayer model described earlier to explain successfully the variations of their films. In this case, the internal junctions of the particles and the a-C matrix allow for heating of electrons within the thin film, with the emission process at the outer end of the particle being purely due to FN tunneling.

#### 8.3.6 ULTRANANOCRYSTALLINE DIAMOND THIN FILMS

It is interesting to compare the results obtained from the FE and scanning tunneling microscope (STM) studies from amorphous DLC film with those from ultrananocrystalline (UNCD) films carried out by Krauss et al. [23] Despite the difference in the long- and medium-range order, the bonding in the two materials can be described as mixed  $sp^2$  and  $sp^3$  phases. In the study by Krauss et al., it was shown that UNCD films have grain sizes between 2 and 5 nm in size and grain boundaries

<0.4 nm in thickness. It was observed that when UNCD films were deposited on Si micro tips there was little variation in the threshold field with either the film thickness or the Si tip radius. Furthermore, STM results showed that the emission sites from the UNCD films could not be related to any surface asperities. Both electrical and theoretical calculations show that the grain boundaries are the most probable path for conduction from the substrate. It is also worth noting that the tight binding calculations for UNCD showed the presence of a continuum density of states throughout the bulk diamond gap. Since the  $sp^2$  grain boundary is less than 0.4 nm in thickness and surrounds a 2 to 5 nm size diamond  $sp^3$  grain, this is similar to the situation encountered above in amorphous DLC type films. The study by Krauss et al. shows the importance of nanoscale inhomogeneities to the FE process. These studies also show the importance of understanding the nature of the cathode material at a nanometer level.

## 8.4 FIELD EMISSION AND DIELECTRIC INHOMOGENEITY

From the discussion in Section 8.3, it is apparent that the role of  $sp^2$  clusters embedded in an  $sp^3$  matrix plays an important role for a-C and a-C:H films. For films with a high  $sp^2$  content and good inter-cluster interactions, FE is determined by the properties of the film near to the front surface. It is known from AFM images of DLC films that they are atomically flat with a typical RMS roughness of less than 1 nm. If an FN emission process is present then it is necessary to explain the large enhancement factors, typically several hundreds, required to lower a barrier by 4 eV. Since there are no surface features to aid the geometric enhancement of the electric field, we have examined the possibility of a non-geometric internal enhancement mechanism. The results of a high-resolution STM study of the DLC film deposited at  $-265$  V are presented in Figure 8.11. It is apparent that the conductivity of the film is not uniform, with a number of localized high conductivity regions of a few nm in size surrounded by a more insulating matrix. The STM results can be interpreted as resulting from a series of closely spaced localized conductive  $sp^2$  regions which, under the action of the applied field, allows electrons to hop from one spatially localized cluster to another, as in Figure 8.10. In the continuous limit, this would produce a conducting channel or filament that can extend through the bulk of the film. High-resolution electron microscopy studies of a-C films have never revealed such a feature, leading us to conclude that an alternative enhancement mechanism is present.

We propose that the enhancement is due to the different intrinsic dielectric and conductive properties of nanometer-sized  $sp^2$  clusters embedded in the surrounding  $sp^3$  insulating matrix. It is well

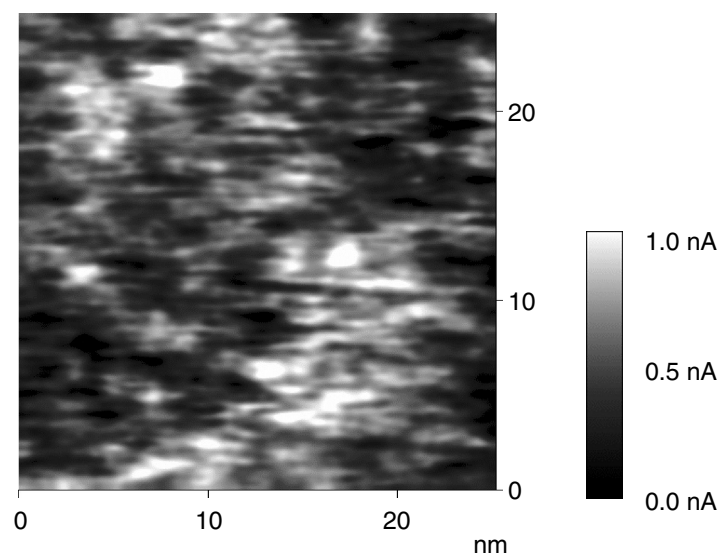


**FIGURE 8.11** High resolution scanning tunneling microscopy measurement made on a DLC film showing regions of electrical nonuniformity.

known that the electric field near a single conductive dielectric sphere in an insulating matrix is increased by a factor of up to 2 due to the dielectric mismatch between the sphere and the matrix. It has been calculated that in the presence of two closely spaced spheres with the conductivity of gold, an enhancement of the electric field by a factor of 56 is possible if the spheres have a separation of 5 nm [24]. This enhancement increases as the separation between the spheres is reduced, reaching a factor of 400 for a sphere–sphere separation of 1 nm. Although the conductivity of the  $sp^2$  clusters will not be as high as Au, these calculations demonstrate that high enhancement factors can be obtained by considering the effects of just two conductive spheres near the surface.

In this manner, the emission process for DLC films can be explained as follows: the high density of defects will act to localize and attract the field lines from the anode to a thin region near the surface of the film. High-field enhancement factors are present if two (or more)  $sp^2$  conductive clusters are nearby. Once the electrons are emitted from the clusters near the surface of the film, they can be replaced by electrons from clusters deeper within the film. Such a description aids us in explaining the spotty nonuniform (on the nano- to microscale) nature of the emission across the surface of the film in which the *local* arrangement of the clusters below the surface is important.

Other nanomaterials for which dielectric inhomogeneity have been suggested to play a role include B-doped Si nanoparticles. A turn on field of 6 V/ $\mu\text{m}$  was reported for B-doped Si nanoparticles which is lower than that reported for undoped particles (9 V/ $\mu\text{m}$ ) [25]. Tsang et al. [26] studied electron field emission from ion beam synthesized SiC layers. They reported that in as-implanted film the field enhancement was attributed to dielectric inhomogeneity; however, after annealing the surface morphology changed and nanoprotusions aid in the observation of emission at low fields. The presence of a large amount of N aids in the clustering of the  $sp^2$  phase, which was reported as being important for a- $\text{CN}_x$  film grown by excimer laser ablation [27]. Liao [28] reported that the inhomogeneous nature of  $\text{HfN}_x\text{O}_y$  films comprising nanoscale conductive hafnium nitride grains embedded in a matrix of dielectric oxide or oxynitride played an important role in the FE from these materials. Finally, another study has examined the electron field emission of radio frequency magnetron-sputtered  $\text{CN}_x$  films annealed at different temperatures and also concluded that the film's nanostructure is important [29].

In the case of excimer laser crystallized amorphous silicon a low turn on a field of 10 V/ $\mu\text{m}$  without any hysteresis were reported [30]. Techniques for producing a self aligned and gated FE device using a single mask process have also been shown to be possible [31]. Taking into account that in the case of active matrix liquid crystal displays, polysilicon driver circuitry can be produced on glass flat panel on the scale of 1  $\text{m}^2$ , having fully integrating large areas, single mask technology comparable with current flat panel display (FPD) production lines makes this material system very valuable and technologically important. In the case of excimer laser produced materials, the aspect ratio for the enhancement factors cannot account for the observation of FE at low applied fields. The apparent discrepancy was reconciled with an FN type emission if nanoscale inhomogeneity also plays an important role.

## 8.5 FIELD EMISSION AS A FUNCTION OF CONDITIONING

We have previously discussed conditioning, i.e. the need to apply several voltage cycles before the onset of stable emission (cf. Figure 8.5) [32,33]. Similar conditioning treatments have also been reported necessary in ta-C [16,34] and in diamond films grown by chemical vapor deposition [35]. The exact nature of this conditioning step and the role of any damage-induced surface micro-protrusions is not fully understood, although conditioning may involve an increase in the concentration of threefold coordinated carbon atoms at the expense of fourfold coordinated atoms [36]. For practical a-C:H-based display applications, the values of the threshold field must be as reproducible as possible. Furthermore, to limit the spread in the drive voltages, the hysteresis in the current–voltage ( $I$ – $V$ ) characteristics should be kept to a minimum. Current stressing has been shown to overcome the need for a voltage-controlled conditioning cycle [37]. It should be noted that in improperly

conditioned films there may be significant differences in values of  $E_{th}$  depending on whether the current is recorded on the upward voltage cycle or on the downward cycle. As a measure of this “hysteresis effect,” the difference in the applied fields between the upward and downward voltage cycles at a current of 1 nA is used. Current stressing of the films was performed by contacting the anode to the film and passing a current through the film up to a predetermined level [37]. Each film was tested before stressing by applying a field of up to 100 V/ $\mu\text{m}$  and only those samples which *did not* emit after this preliminary test were subject to current stressing. For the current stressing measurements, several identical films from the same deposition run were examined. For reference, the typical value of  $E_{th}$  for films which did emit after conventional conditioning is about 30 V/ $\mu\text{m}$ .

The three current stress levels chosen were  $\times 10^{-8}$ ,  $5.2 \times 10^{-8}$ , and  $2 \times 10^{-7}$  A. The FE characteristics of the film stressed to  $\times 10^{-8}$  A (not shown) exhibited emission but with an  $E_{th}$  of over 85 V/ $\mu\text{m}$  and a full width (at half maximum) of the first cycle hysteresis loop of over 20 V/ $\mu\text{m}$ . Subsequent voltage cycles resulted in a reduction of  $E_{th}$ , although the average threshold field obtained from the latter three cycles was  $66 \pm 4$  V/ $\mu\text{m}$ . Stressing to a higher current of  $5.2 \times 10^{-8}$  A results in an initial emission at a field of 48 V/ $\mu\text{m}$  through a hysteresis width of 20 V/ $\mu\text{m}$ , as shown in Figure 8.12. The  $I$ - $V$  characteristics of the film before stressing is also presented and shows that no emission had occurred from this film even up to fields of 90 V/ $\mu\text{m}$ . The threshold field continued to decrease after subsequent voltage cycles and finally reached 40 V/ $\mu\text{m}$  after the 4th cycle. The average value of  $E_{th}$  obtained from this film is  $38 \pm 10$  V/ $\mu\text{m}$ , higher than that obtained from a film that underwent the conventional conditioning treatment. Since the width of the first cycle is 20 V/ $\mu\text{m}$ , the film is not fully conditioned.

The  $I$ - $V$  characteristic of the film stressed to  $2 \times 10^{-7}$  A is shown in Figure 8.13, where the value of  $E_{th}$  for the 1st cycle was only 34 V/ $\mu\text{m}$ , which subsequently decreased to 30, 26, and 27 V/ $\mu\text{m}$  in the remaining three cycles. The average  $E_{th}$  of  $28 \pm 2$  V/ $\mu\text{m}$  is comparable to the values of  $E_{th}$  for films that have undergone a conventional conditioning treatment. The width of the  $I$ - $V$  hysteresis loop is about 2 V/ $\mu\text{m}$  in each run and no evidence of a conditioning cycle after current stressing is observed. Since the FE characteristics are different and are observed to improve with higher stress currents, the mechanical effects of contacting between the anode and film as the primary reason for the improvements were eliminated.

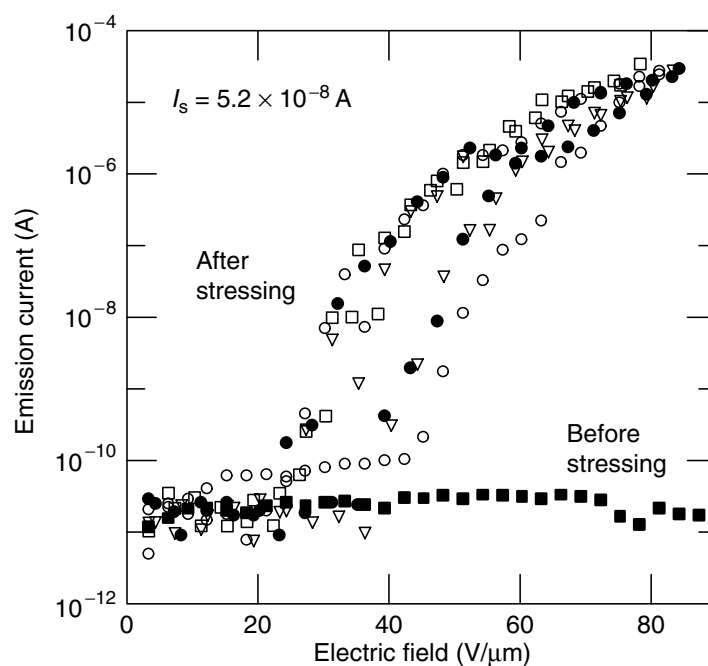


**FIGURE 8.12** Emission current vs. electric field for films stressed to  $5 \times 10^{-8}$  A. The applied field is cycled up and down four times: (○) run 1; (□) run 2; (●) run 3; (▽) run 4. The emission current for the film before stressing is indicated by (■).

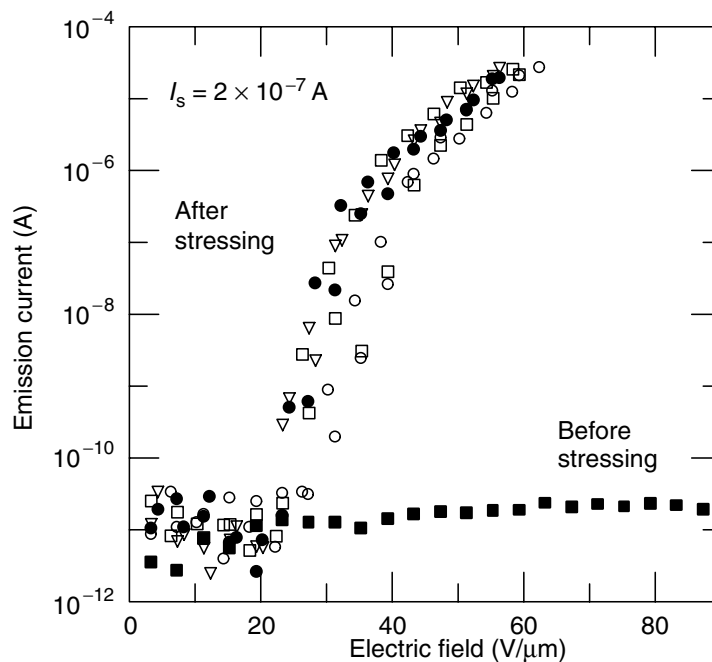


**FIGURE 8.13** Emission current vs. electric field for films stressed to  $2 \times 10^{-7}$  A. The applied field is cycled up and down four times: (○) run 1; (□) run 2; (●) run 3; (▽) run 4. The emission current for the film before stressing is indicated by (■).

In order to examine whether the current-induced conditioning was permanent, the films were retested some hours after the initial stressing had been performed. In order to prevent any possible atmospheric contamination, the samples were kept held under vacuum during this period. Figure 8.14a shows that even after just 15 h in the sample that was stressed to  $5.2 \times 10^{-8}$  A,  $E_{th}$  had increased to about 50 V/μm, similar to the value obtained in the first cycle after this sample had just been stressed, indicating that some form of “healing” process had occurred. By contrast, Figure 8.14b shows that in the film stressed to  $2 \times 10^{-7}$  A, no evidence of a conditioning cycle is required 23 h after the original current stressing had occurred. Only the first two  $I$ - $V$  characteristics are presented in Figure 8.14b and values of  $E_{th}$  obtained after 23 h are 30 and 32 V/μm with a hysteresis width of 2 to 3 V/μm. Testing after 87 h revealed similar results to those obtained after testing after 23 h, with the values of  $E_{th}$  for the first two cycles being 31 and 32 V/μm, again showing that the film remains conditioned.

In a study by Mercer et al. [36] an STM tip was used to effectively current stress ta-C films by generating a highly spatially localized electric field. They observed that after ramping the tip-sample bias and current, nanostructures of about 100 nm in the extent form are produced. By using high-resolution spatially resolved electron energy loss spectroscopy, they showed that the predominant bonding configuration changes from predominately four-fold coordinated C to three-fold coordinated. The net effect of the conditioning or the current stressing treatment may well be to generate conductive  $sp^2$ -rich areas either in the form of filaments or clusters through localized Joule heating. Missert et al. [38] proposed that the presence of conductive filaments is related to the deposition conditions under which the film was grown. Since the deposition conditions for the films in this study were kept the same, the current stressing may well increase the number of such filaments/clusters extending through the film.

## 8.6 SURFACE MODIFICATIONS

Shi et al. [39] and Hart et al. [17] have studied the effects of post-deposition surface treatments using ion beam bombardment and ion plasmas, respectively. In the study performed by Shi et al., undoped and  $n^+$  doped ta-C deposited at 100 eV using the filtered cathodic vacuum arc (FCVA) method were subjected to H, O and Ar ion bombardment. Growth at 100 eV in undoped ta-C

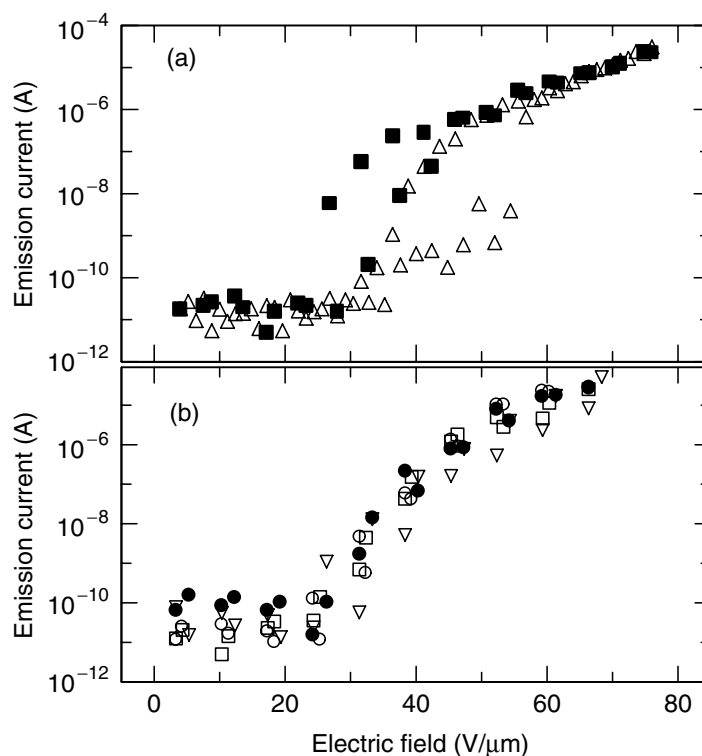


**FIGURE 8.14** Emission current vs. electric field for films (a) stressed to  $5 \times 10^{-8}$  A and retested after 15 h ( $\Delta$ ,  $\blacksquare$ ) and (b) stressed to  $2 \times 10^{-7}$  A and retested after 23 ( $\circ$ ,  $\square$ ) and 87 h ( $\bullet$ ,  $\nabla$ ). Only the first two cycles of each retest are shown for clarity.

resulted in the maximum  $sp^2$  content and n-type doping was achieved by the addition of N. They noted that the threshold field in the undoped films decreased from 18 to 14  $V/\mu m$  after treatment with each of the ions and  $n^+$ -ta-C ion beam treatment resulted in a decrease from 12 to 8  $V/\mu m$ . The saturated emission current density of the post-treated films was noted to improve by about an order of magnitude and appeared to be independent of the ion used. Shi et al. also measured the effects on the threshold field of undoped ta-C by varying the H ion energy from 50 to 800 eV. In this ion energy range, the threshold field increased from 14 to 22  $V/\mu m$ . Hart et al. studied the effects of reactive ion etching using  $H_2$ ,  $O_2$  and Ar gases. By varying the etching time, it is possible to remove different thicknesses from the surface layer. Such a consideration is important since ta-C has a  $sp^2$ -rich surface layer extending about 1 nm from the surface. As-deposited films had a threshold field of 8  $V/\mu m$ . Removal of 0.5 nm resulted in the threshold field reducing to 3.0  $V/\mu m$  and removal of 2 nm resulted in the threshold field reducing to 3.9  $V/\mu m$ . The former treatment corresponds to incomplete  $sp^2$  surface layer removal whereas the latter corresponds to complete removal. For  $O_2$  etching, the threshold field decreased to 5  $V/\mu m$  for both 0.5 and 2 nm etch. Ar-plasma etching reduced the threshold field to 6  $V/\mu m$ . Finally, emission maps using an ITO anode as a phosphor showed that the emission site density measured at 20  $V/\mu m$  increased from about 50 to 100  $cm^{-2}$  in as-deposited films to 1000  $cm^{-2}$  for  $O_2$ -etched films, 2000  $cm^{-2}$  for Ar-etched films, and 4000  $cm^{-2}$  for  $H_2$ -etched films. Treatment with  $H_2$  plasmas is predicted to increase the probability of C-H surface termination and, therefore, within the confines of the negative electron affinity model, would be expected to reduce the emission barrier at the front ta-C/vacuum interface. However, a reduction in the threshold field was also observed for  $O_2$  plasma treatment, which should raise the front surface barrier since the surface would be terminated with C-O bonds. Since Hart et al. used a parallel plate geometry to measure FE characteristics, the lowering of the threshold field is due to a higher emission site density and thus a greater distribution of sites with lower threshold fields. Atomic force microscopy showed that the RMS roughness of films did not change after plasma treatment and therefore surface features do not play a significant role.



## 8.7 SUMMARY AND OUTLOOK FOR THE FUTURE

In summary, there are a plethora of different carbon films from which electron emission has been obtained at relatively low threshold fields. Threshold fields below  $30 \text{ V}/\mu\text{m}$  can be integrated into gated structures using commercial CMOS technology, provided that any hysteresis is kept to a minimum. Amorphous carbon films appear to be unique in that most forms of carbon films give FE at low fields. Each of these films has a unique structure with some common features with the categorized a-C films discussed in this review. It is important that researchers first understand the basic microstructure of their a-C films before venturing into postulating a possible electron field emission mechanism in their films. There are a few more established emission models that can explain the electron emission from a number of these films as well as the variations with the physical properties. Extensions to noncarbon-based nanomaterials have also been presented.

In terms of future prospects, the scene is currently set with researchers having an excellent working knowledge of the emission characteristics of planar amorphous carbon cathodes. When this is coupled with high brightness that can be obtained from FED devices and the lifetime studies of FED prototype structures, it is only a matter of time before these properties will be exploited in FE-type display applications.

## REFERENCES

1. Silva, S.R.P., Carey, J.D., Khan, R.U.A., Gerstner, E.G., and Anguita, J.V., Amorphous carbon thin films, in *Handbook of Thin Film Materials*, Vol. 4, Nalwa, H.S., Ed., Academic Press, Orlando FL, 2002, Chap. 9, pp. 403–506.
2. Ed. by The Proceedings of the International Vacuum Microelectronics Conference; *J. Vac. Sci. Technol.*
3. Robertson, J., *Diamond Relat. Mater.*, 5, 797, 1996.
4. Fanchini, G. and Taliaferro, A., *Appl. Phys. Lett.*, 85, 730, 2004.
5. Weiler, M., Sattel, S., Jung, K., Erhardt, H., Veerasamy, V.S., and Robertson, J., *Appl. Phys. Lett.*, 64, 2798, 1994.
6. Silva, S.R.P., Ed., *Properties of Amorphous Carbon*, EMIS Datareviews series no. 29, IEE, London, 2002.
7. Gröning, O., Küttel, O.M., Gröning, P., and Schlapbach, L., *Appl. Phys. Lett.*, 71, 2253, 1997.
8. Amaratunga, G.A.J. and Silva, S.R.P., *Appl. Phys. Lett.*, 68, 2529, 1996.
9. Forrest, R.D., Burden, A.P., Silva, S.R.P., Cheah, L.K., and Shi, X., *Appl. Phys. Lett.*, 73, 3784, 1998.
10. Burden, A.P., Forrest, R.D., and Silva, S.R.P., *Thin Solid Films*, 337, 257, 1999.
11. Carey, J.D., Forrest, R.D., Khan, R.U.A., and Silva, S.R.P., *Appl. Phys. Lett.*, 77, 2006, 2000.
12. Carey, J.D., Forrest, R.D., and Silva, S.R.P., *Appl. Phys. Lett.*, 78, 2339, 2001.
13. Silva, S.R.P., Xu, S., Tay, B.K., Tan, H.S., and Milne, W.I., *Appl. Phys. Lett.*, 69, 491, 1996.
14. Fallon, P.J., Veerasamy, V.S., Davis, C.A., Robertson, J., Amaratunga, G.A.J., Milne, W.I., and Koskinen, J., *Phys. Rev. B*, 48, 4777, 1993.
15. Veerasamy, V.S., Yuan, J., Amaratunga, G.A.J., Milne, W.I., Gilkes, K.W.R., Weiler, M., and Brown, L.M., *Phys. Rev. B*, 48, 17954, 1993.
16. Ilie, A., Ferrari, A.C., Yagi, T., and Robertson, J., *Appl. Phys. Lett.*, 76, 2627, 2000.
17. Hart, A., Satyanarayana, B.S., Robertson, J., and Milne, W.I., *Appl. Phys. Lett.*, 74, 1594, 1999.
18. Satyanarayana, B.S., Hart, A., Milne, W.I., and Robertson, J., *Diam. Relat. Mater.*, 7, 656, 1998.
19. Cheah, L.K., Shi, X., Tay, B.K., Silva, S.R.P., and Sun, Z., *Diam. Relat. Mater.*, 7, 640, 1998.
20. Milani, P., Ferretti, M., Piseri, M., Bottani, C.E., Ferrari, A., Bassi, A.L., Guizzetti, G., and Patrini, M., *J. Appl. Phys.*, 82, 5793, 1997.
21. Ferrari, A.C., Satyanarayana, B.S., Robertson, J., Milne, W.I., Barborini, E., Piseri, P., and Milani, P., *Europhys. Lett.*, 46, 245, 1999.
22. Amaratunga, G.A.J., et al., *New Diam. Front. C. Technol.*, 9, 31, 1999.
23. Krauss, A.R., Auciello, O., Ding, M.Q., Gruen, D.M., Huang, Y., Zhirnov, V.V., Givargizov, E.I., Breskin, A., Chechen, R., Shefer, E., Konov, V., Pimenov, S., Karabutov, A., Rakhimov, A., and Suetin, N., *J. Appl. Phys.*, 89, 2958, 2001.

24. Chaumet, P.C. and Dufour, J.P., *J. Electrostat.*, 43, 145, 1998.
25. Tang, Y.H., Sun, X.H., Au, F.C.K., Liao, L.S., Peng, H.Y., Lee, C.S., Lee, S.T., and Sham, T.K., *Appl. Phys. Lett.*, 79, 1673, 2001.
26. Tsang, W.M., Wong, S.P., and Lindner, J.K.N., *Appl. Phys. Lett.*, 81, 3942, 2002.
27. Fogarassy, E., Szorenyi, T., Antoni, F., Pirio, G., Olivier, J., Legagneux, P., and Boher, P., *Appl. Phys. A*, 76, 15, 2003.
28. Liao, M.Y., Gotoh, Y., Tsuji, H., and Ishikawa, J., *Appl. Phys. Lett.*, 83, 1626, 2003.
29. Li, J.J., Zheng, W.T., Jin, Z.S., Wang, X., Bian, H.J., Gu, G.R., Zhao, Y.N., Meng, S.H., He, X.D., and Han, J.C., *J. Vac. Sci. Technol. B*, 21, 2382, 2003.
30. Tang, Y.F., Silva, S.R.P., and Rose, M.J., *Appl. Phys. Lett.*, 78, 186, 2001.
31. Forrest, R.D., Cox, D.C., Tang, Y.F., Shannon, J.M., and Silva, S.R.P., *J. Vac. Sci. Technol. B*, 21, 1560, 2003.
32. May, P.W., Hohn, S., Wang, W.N., and Fox, N.A., *Appl. Phys. Lett.*, 72, 2182, 1998.
33. Carey, J.D., Poa, C.H., Forrest, R.D., Burden, A.P., and Silva, S.R.P., *J. Vac. Sci. Technol. B*, 18, 1051, 2000.
34. Talin, A.A., Felter, T.E., Friedmann, T.A., Sullivan, J.P., and Siegal, M.P., *J. Vac. Sci. Technol. A*, 14, 1719, 1996.
35. Sowers, A.T., Ward, B.L., English, S.L., and Nemanich, R.J., *J. Appl. Phys.*, 86, 3973, 1999.
36. Mercer, T.W., DiNardo, N.J., Rothman, J.B., Siegal, M.P., Friedmann, T.A., Martinez Miranda, L.J., *Appl. Phys. Lett.*, 72, 2244, 1998.
37. Carey, J.D. and Silva, S.R.P., *Appl. Phys. Lett.*, 78, 347, 2001.
38. Missert, N., Friedmann, T.A., Sullivan, J.P., Copeland, R.G., *Appl. Phys. Lett.* 70, 1995, 1997.
39. Shi, X., Cheah, L.K., Tay, B.K., and Silva, S.R.P., *Appl. Phys. Lett.*, 74, 833, 1999.

---

# 9 Nanotextured Carbons for Electrochemical Energy Storage

*François Béguin*

Centre de Recherche sur la Matière Divisée, CNRS-Université,  
Orléans, France

*Elzbieta Frackowiak*

Institute of Chemistry and Technical Electrochemistry,  
Poznań University of Technology, Poznań, Poland

## CONTENTS

9.1	General Properties of Carbons for Energy Storage .....	295
9.2	Supercapacitors .....	296
9.2.1	Performance of Supercapacitors .....	296
9.2.2	Carbons for Pure Electrochemical Double-Layer Capacitors .....	300
9.2.2.1	Activated Carbons .....	300
9.2.2.2	Porous Carbons Prepared by the Template Technique .....	301
9.2.3	Electrochemical Capacitors from Carbons with Pseudocapacitance Properties .....	302
9.2.4	Carbon Nanotubes as a Composite Component .....	305
9.3	Electrochemical Hydrogen Storage .....	308
9.3.1	Introduction .....	308
9.3.2	Mechanism of Reversible Hydrogen Insertion .....	309
9.3.2.1	Mechanism in Aqueous KOH Medium .....	310
9.3.2.2	Mechanism in Aqueous H <sub>2</sub> SO <sub>4</sub> Medium .....	312
9.3.2.3	Comparison of Galvanostatic Charge/Discharge in Acidic and Basic Media .....	312
9.3.2.4	Relation between the Reversible Hydrogen Storage Capacity and the Nanotextural Characteristics of Porous Carbons .....	313
9.4	Conclusions and Perspectives .....	315
	References .....	316

## 9.1 GENERAL PROPERTIES OF CARBONS FOR ENERGY STORAGE

The exponential growth of the portable electronic devices' market together with the development of electric vehicles has created a continuously increasing demand for lightweight and compact electric power sources of high energy and power density. Among the many topics under investigation in industry and academic laboratories, the development of new materials is one of the most important.

For many years, nanotextured carbons have been shown as a basic material for the realization of high-performance power sources, e.g., supercapacitors, lithium-ion accumulators, or fuel cells.

The key factors that dictate the selection of carbon for this target are its accessibility, low cost, easy processability, as well as the different forms attainable (powder, fibers, foams, fabrics, composites) [1], adaptable porosity [2,3], and surface functionality [4,5]. Carbon electrodes are well polarizable, chemically stable in different solutions (acidic, basic, aprotic) and in a wide range of temperatures. The amphoteric character of carbons, both electron donor/acceptor, and the simultaneous presence of acidic/basic surface groups allows the electrochemical properties of materials based on this element to be extensively varied. A wide variety of carbon materials, e.g., graphites, cokes, mesocarbon microbeads, activated carbons, aerogels, xerogels, carbon blacks, carbon nanotubes, carbons from templates, etc. have been extensively considered as electrode materials for energy storage.

The nanotextural and chemical properties of carbons determine their efficiency for electrochemical application as electrodes. A strict control of the carbonization process (time, temperature, gas flow), the kind of natural or synthetic precursor, and/or chemical vapor deposition conditions allow carbons with almost defined nanotexture and surface functionality to be prepared. The modification of carbon by an activation process gives a further possibility of modifying the properties, especially by highly developing the specific surface area [2]. Oxygenated surface groups can be created by treatment with liquid oxidants (e.g., aqueous solutions of  $\text{HNO}_3$ ,  $\text{H}_2\text{O}_2$ ,  $\text{NaOCl}$ ). Alternatively, heat treatment of carbons under neutral atmosphere up to 700 to 800°C strongly diminishes the concentration of surface groups. Various advanced forms of carbon can be designed and prepared by a careful selection of templates with different dimensionalities, in such a way that one-, two-, or three-dimensional carbons can be obtained easily [6]. Taking into account the versatility for preparing various forms, there is a great interest in designing carbons for different energy storage devices.

The main preferred characteristics of carbon for all electrochemical applications are a good conductivity and wettability. Wettability is generally improved by the presence of a rich surface functionality, whereas electrical conductivity depends mainly on the thermal treatment conditions, nanotexture, hybridization of carbon, and content of heteroatoms. However, the electrolyte may be also decomposed by reaction with the surface groups of carbon that causes performance fading during cycling of the energy-storage systems. Therefore, the type of surface functionality must be perfectly adapted to the kind of device developed. Moreover, each electrochemical application involves completely different nanotextural properties of carbon characterized by its specific surface area, the presence of micro- and mesopores, their ratio, pore shapes, and so on. It is well known, for example, that carbon materials used as catalyst support in fuel cells should have a moderate surface area. By contrast, a highly developed surface area is required for good performance of supercapacitors; also, pore size must be adapted to ion size in order to ensure quick charge propagation.

Finally, besides its role of catalyst support or active electrode material, carbon can also be used in power sources as a conductivity additive. The most widely applied percolators are carbon blacks because of their availability and low cost. Recently, carbon nanotubes have been shown to be more efficient than carbon black [7], allowing new kinds of composite electrodes to be developed.

The use of carbons for anodes of lithium-ion batteries is extensively discussed in the literature [8–10]. Therefore, in this chapter, we prefer to describe only the new trends related to the use of carbons for energy storage and, consequently, to focus mainly on the application of carbons in supercapacitors and for electrochemical hydrogen storage. An additional reason for this choice is related to very close electrochemical concepts for both applications where highly porous carbon materials are generally required.

## 9.2 SUPERCAPACITORS

### 9.2.1 PERFORMANCE OF SUPERCAPACITORS

Electrochemical capacitors (often called supercapacitors or ultracapacitors) [11–13] are very attractive power sources for portable systems and automotive applications due to their high specific

power and very long durability. In most cases, being often associated to a battery, they are used to deliver a high power during a short time, which in turn provides a high specific energy. Some applications of supercapacitors are hybrid power sources for electrical vehicles, computers, UPS, pulse laser technique, starters for engines, etc.

In a true electrochemical capacitor the charges are accumulated in the electrical double layer at the electrode/electrolyte interface. In contrast with typical accumulators, this process occurs without any charge transfer (faradaic) reaction. As shown in the schematic representation of Figure 9.1, an electrochemical capacitor is constituted of two electrodes on which the ions are fixed, the positive one with electron deficiency and the second one with electron excess (negative). The capacitance  $C_n$  of one electrode is given by

$$C_n = \frac{\epsilon S}{d} \quad (9.1)$$

where  $\epsilon$  is the permittivity or dielectric constant of the solution,  $S$  the surface area of the electrode/electrolyte interface, i.e., the electrode surface, and  $d$  the thickness of the electrical double layer. Taking into account that  $d$  is generally less than 1 nm, Equation (9.1) shows immediately the technological advantage of supercapacitors over conventional capacitors, giving rise to specific capacitances of approximately 0.1 F/m<sup>2</sup>. Moreover, if high-specific surface area activated carbons are used as substrate for ion adsorption, high values of capacitance may be reached. For example, assuming a specific capacitance of 0.1 F/m<sup>2</sup> and a specific surface area of 1000 m<sup>2</sup>/g, it gives a capacitance value of 100 F/g of carbon.

From Figure 9.1, it is noteworthy that the overall capacitance  $C$  of the device results from the series connection of two capacitors  $C_1$  and  $C_2$ , according to

$$\frac{1}{C} = \frac{1}{C_1} + \frac{1}{C_2} \quad (9.2)$$

where  $C_1$  and  $C_2$  represent the capacitance of each electrode. Hence, in the case of a capacitor built from electrodes of different surfaces, or more generally of different capacitances, the component with the smallest capacitance contributes more to the total value  $C$  due to the inverse dependence in formula (9.2).

The capacitance is expressed in F, which is the charge (in C) accumulated in a defined voltage range (1 F = 1 C/1 V). Depending on the applied objective, the specific capacitance can be related to the electrode mass (F/g), to its volume (F/cm<sup>3</sup>), or to its surface area (F/cm<sup>2</sup>).

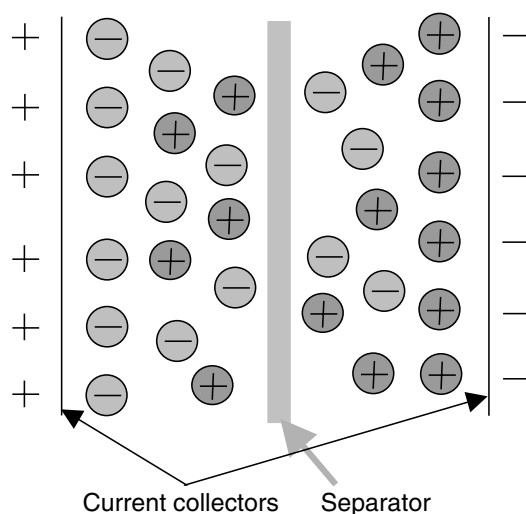


**FIGURE 9.1** Schematic representation of an electrochemical capacitor:  $\oplus$  cations of the electrolyte;  $\ominus$  anions of the electrolyte.

The amount of electrical energy  $W$  accumulated in an electrochemical capacitor is proportional to capacitance  $C$  and square of voltage  $U$

$$W = \frac{1}{2}CU^2 \quad (9.3)$$

The capacitance  $C$  depends essentially on the electrode material used, whereas the operating voltage is determined by the stability window of the electrolyte. Capacitors in an organic electrolyte can easily operate in the range 2 to 2.5 V, and using ionic liquids it is even possible to extend this range to 3.5–4 V [14], whereas in aqueous solution it is generally below 1 V. Hence, at least for symmetric systems, about one order of magnitude higher capacitance can be expected with organic electrolytes or ionic liquids compared to water medium.

Since the electrodes do not undergo any phase transformation as in accumulators, the main advantage of an electrochemical double-layer capacitor (EDLC) lies in its ability of high dynamic charge propagation that allows a rapid withdrawing of energy, i.e., a high power. The power  $P$  of a supercapacitor is given by

$$P = \frac{U^2}{4R_s} \quad (9.4)$$

where  $R_s$  is the internal resistance, i.e., commonly the equivalent series resistance (ESR). The ESR of the entire device is the sum of the resistances of all the materials between the external contacts, i.e., substrate, carbon, binder, separator, and electrolyte. Since the main function of supercapacitors is their use in high-power applications, it is essential to lower the series resistance  $R_s$  by using high-conductivity additives.

The electrochemical capacitors where carbon is an electrode component are of two types, depending on the charge-storage mechanism. In the EDLCs, a pure electrostatic attraction occurs between the ions and the charged surface of the electrode that is generally from activated carbon. The electrons involved in double-layer charging are the de-localized conduction-band electrons of the carbon electrode. The capacitance of activated carbons is limited both by their specific surface capacitance, close to  $10 \mu\text{F}/\text{cm}^2$  [11–13], and their specific surface area, which cannot be higher than 2500 to 3000  $\text{m}^2/\text{g}$ . In the second type of capacitors, called pseudocapacitors, electrons are additionally involved in quick faradaic reactions and are transferred to or from the valence states of the redox cathode or anode reagent, although they may arrive in or depart from the conduction band of carbon [11,13]. In this case, contrary to a battery redox process, the charge transferred is proportional to voltage, as in a real capacitor, therefore it is called pseudocapacitance. Electrode materials with pseudocapacitance properties are generally metal oxides ( $\text{RuO}_2$ ,  $\text{MnO}_2$ , etc.) [7,15–17] or conducting polymers [18–21]. Examples of pseudofaradaic reactions are illustrated by Equations (9.5) and (9.6) for polypyrrole (PPy) and ruthenium oxide, respectively,



Pseudocapacitance may also be realized through special doping of carbons via the presence of heteroatoms, e.g., oxygen or nitrogen [22,23]. The values of capacitance are strictly connected to the nature and surface of the electrode/electrolyte interface [24,25] as well as to the amount of pseudocapacitive additive.

The most useful techniques for investigating the performance of supercapacitors are galvanostatic charge/discharge and cyclic voltammetry. In the first case, a constant current — generally in the range of 1 mA/g of carbon to 1 A/g — is passed through the device, and the voltage is measured as a function of time. In the case of an ideal capacitor — where  $Q = C \times V$  — the curve  $V = f(t)$

should be perfectly triangular, as shown in Figure 9.2 for a carbon obtained by KOH activation of pitch mesophase [26]. In the case of the voltammetry technique, a linear variation of voltage is imposed in the limits of the electrolyte stability window — generally at scan rates between 1 to 100 mV/sec — and the charging current is measured. In the case of an EDLC with a low value of ESR, the curve  $I = f(V)$  has a rectangular box-like shape, as shown in Figure 9.3 for activated carbon from pitch mesophase [26]. The value of capacitance  $C$  is easily evaluated either from the slope of the galvanostatic characteristics or from the current  $I$  measured on the voltammetry curve using

$$C = \frac{I}{v} \quad (9.7)$$

where  $v$  represents the voltage scan rate. In general, the most reliable values are obtained from galvanostatic discharge measurements.

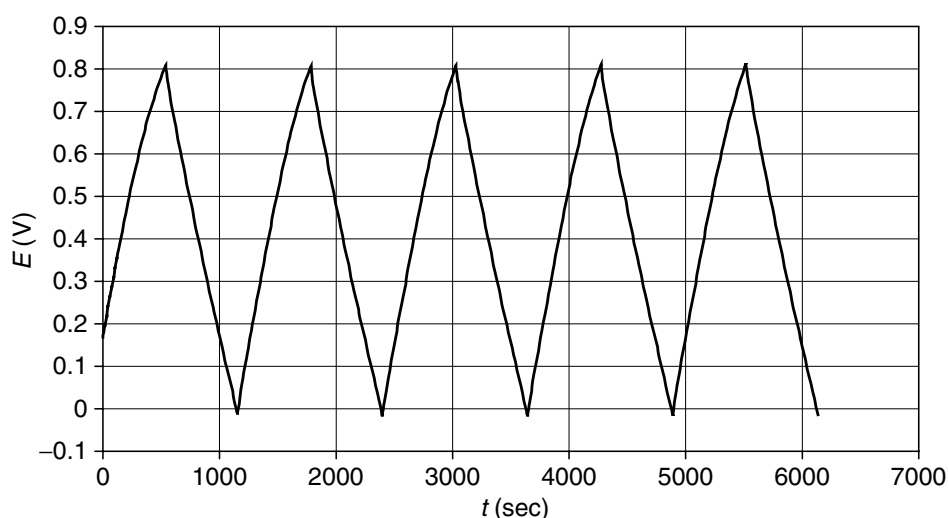


**FIGURE 9.2** Galvanostatic ( $I = 2$  mA) charge/discharge characteristics of a capacitor built with AC electrodes obtained by KOH activation of pitch mesophase. Electrolytic solution 1 mol/L  $\text{H}_2\text{SO}_4$ . (From Kierzek, K. et al., *Electrochim. Acta*, 49, 515, 2004.)

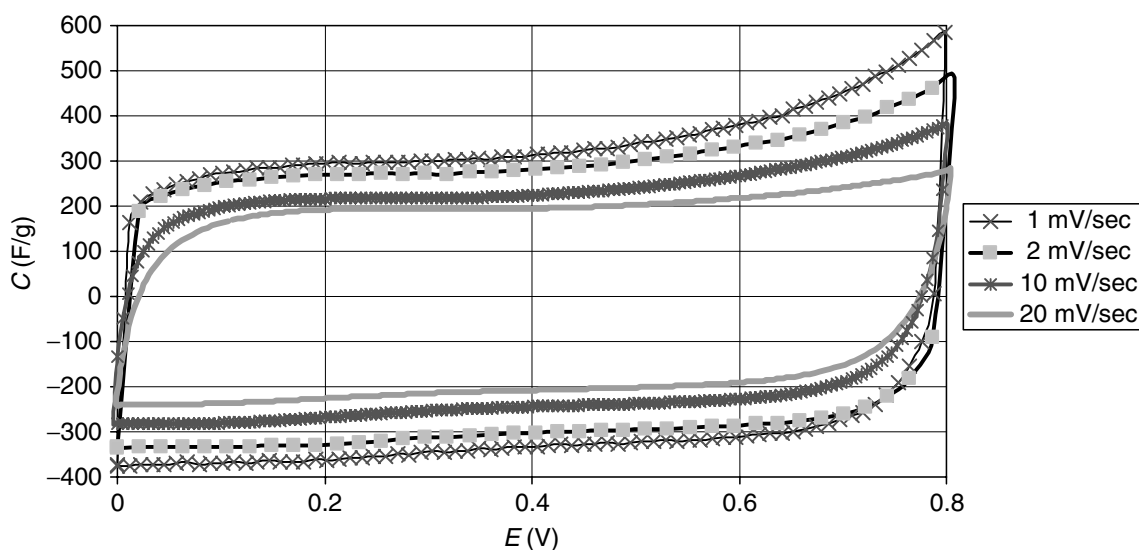


**FIGURE 9.3** Cyclic voltammograms of a capacitor built with activated carbon electrodes obtained by KOH activation of pitch mesophase at different scan rates. Electrolytic solution 1 mol/L  $\text{H}_2\text{SO}_4$ . (From Kierzek, K. et al., *Electrochim. Acta*, 49, 515, 2004.)

## 9.2.2 CARBONS FOR PURE ELECTROCHEMICAL DOUBLE-LAYER CAPACITORS

### 9.2.2.1 Activated Carbons

A highly developed surface area of carbon is a crucial factor for trapping a high amount of ions in the electrode/electrolyte interface [12,13]. Generally, the more developed the specific surface area of carbon, the higher the ability for charge accumulation. However, this surface must be electrochemically accessible to ions. Therefore, apart from the high values of specific surface area determined by micropores (with a diameter less than 2 nm), where the ions are adsorbed forming the electrical double layer, the presence of mesopores (diameter from 2 to 50 nm) is essential for a quick transportation of ions in the bulk of the electrode material. The availability and wettability of pores, with dimensions adapted to the size of solvated anions and cations, which have to be transported from the electrolytic solution, is crucial for the high performance of the capacitor. Besides the maximum value of capacitance that can be realized with a given activated carbon/electrolyte interface, a quick charge transportation can fulfill the so-called frequency response, i.e., the ability for energy extraction at higher frequencies (e.g., 1 Hz).

Activated carbons prepared from different precursors and by different activation processes have been widely used in supercapacitors [24–26]. Natural precursors such as coal- and pitch-derived carbonaceous materials are of high interest due to their low cost and availability [26]. Among many physical (e.g., water, carbon dioxide) and chemical activation procedures, KOH activation seems to be the most adapted one for obtaining carbons with extensively developed porosity, where micropores efficiently contribute to the value of capacitance [26–29]. However, taking into account the low values of specific surface capacitance, which are generally reported in the literature ( $10 \mu\text{F}/\text{cm}^2$  when only charging of the double-layer is involved), one can assume that not all micropores are effective in charge accumulation. For this reason, it is easy to understand why capacitance is generally not proportional to the specific surface area [30,31]. Taking into account that most activated carbons are characterized by a relatively wide pore-size distribution, it is clear that the micropores not adapted to the size of the solvated ions do not take part in the double-layer charging [32]. Moreover, even if the pore size is high enough, the micropores may be filled at different rates, which will affect considerably the frequency dependence and power. Highly micro-porous carbons always pose some diffusion limitation. This effect can be observed at quick scan rates during voltammetry or impedance spectroscopy experiments. For example, for an activated carbon with a BET specific surface area of  $2130 \text{m}^2/\text{g}$ , it has been shown by impedance spectroscopy in KOH medium that pores with a size larger than 1.1 nm can be reached by electrolyte ions within less than 0.1 sec, while 5 sec are necessary to access pores of size 0.6 nm [24]. An optimized material for EDLCs should be highly micro-porous to ensure a high capacity and should contain a high enough proportion of mesopores for quick dynamics of charge propagation reflected by a small time constant (RC). The clue for fulfilling both conditions is to design carbon materials with interconnected micropores and mesopores in well-balanced proportion as, for example the micro/meso-porous carbons prepared by the template techniques [33]. Nevertheless, even if such conditions are realized, due to the different size of solvated cations and anions, it is obvious that the efficiency of such optimized materials may be different for both electrodes. Therefore, asymmetric capacitors with electrodes of activated carbons with different distributions of pore diameters adapted to the size of both kinds of ions have been proposed to circumvent the size differences between cations and anions [34].

Although it is well demonstrated that nanotexture plays a key role in the determination of EDLCs' properties, the charging of the double layer remains a very complex process which, besides accessibility of micropores, depends also on a number of other parameters such as the affinity of the electrolyte ions for the electrode material, the hydrophobic–hydrophilic character, the particles' conductivity and their size. Among all, surface functionality is certainly an important parameter that should be taken into account for explaining the difficulties in establishing a direct relationship between the capacitance and the nanotextural parameters of the carbon material [29,31].



Though most of the fundamental work on carbon-based EDLCs focuses on obtaining high values of capacitance, the practical application of these devices is essentially determined by other important parameters. Generally, carbon materials are investigated with three-electrode cells, while using a limited potential range. When the same materials are applied in the real two-electrode cells, the results may be completely different. First, depending on the sizes of both cations and anions, the efficiency of porosity may be different at each electrode. Second, contrary to a three-electrode cell, the potential at which each electrode operates cannot be controlled, which imposes a limit of maximum cell voltage to 0.6 to 0.7 V in aqueous medium for avoiding electrolyte decomposition. Third, in an organic medium some different redox decomposition processes may occur at each electrode, depending on its polarity. Therefore, even if the preliminary investigation of activated carbons shows high capacitance values, other parameters must be investigated to demonstrate the applicability of a given system. To be applicable, a two-electrode supercapacitor must demonstrate a low-performance fading during cycling, a quick charge propagation at different loads, and a low self-discharge. The micropores are not easily wetted by the electrolyte and the exposed surface in micropores may not be utilized for charge storage. Moreover, even in the situation wherein the micropores are wetted by the electrolyte, ionic motion in such small pores may be so slow that the high rate capability, which is one of the advantages of EDLCs, may not be realized.

### 9.2.2.2 Porous Carbons Prepared by the Template Technique

As stated above, both charge storage and rate capability are further limited if the pores are randomly connected. Therefore, high-surface area carbon materials containing regularly interconnected micro- and mesopores are highly desirable for EDLC electrodes. Recently, many groups have synthesized ordered meso-porous silica, which could be used later as a template for the preparation of carbons with well-sized pores [35–38], meeting the above-mentioned capacitor requirements. The templates are mesostructured silicas such as MCM48, MCM41, SBA15, whereas the carbon source is a liquid or gas phase, e.g., sucrose solution, polyfurfuryl alcohol, propylene, or pitch [33,39–41]. The steps of the preparation process are schematized in Figure 9.4. After its deposition inside the pores of the template, the carbon precursor is carbonized at temperatures close to 800°C. The last step is the removal of the silica template by dissolution in hydrofluoric acid.

In an attempt to correlate the electrochemical performance of template carbons with their nanotextural parameters, a perfect linear relationship has been found between the capacitance values in aqueous or organic medium and the micro-pore volume determined by CO<sub>2</sub> adsorption at 273 K (Figure 9.5) [33]. It clearly proves that, with this kind of porous carbon, the ions are essentially trapped in ultramicropores, i.e., pores with size <0.7 nm. Comparison of the measured value of capacitance in aqueous solution with the available volume of ultramicropores shows that most of them take part in trapping nonsolvated ions in the electrical double layer. In these template carbons, micro- and mesopores are perfectly interconnected, mesopores being the former walls of the silica matrix, whereas the carbonaceous walls are microporous. Under the application of an electrical polarization, the solvated ions easily diffuse in the mesopores (playing the role of corridors) for being finally trapped as nonsolvated in ultramicropores. In a typical microporous activated carbon, the situation is completely different. The pathway for solvated ions to reach the active surface is very tortuous and long, with several bottlenecks (gates). Therefore, the limiting pore size in this case is probably higher than the size of the

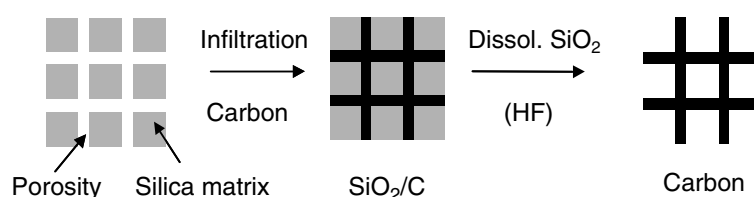


**FIGURE 9.4** Schematic representation of the elaboration of porous carbon by the template technique.

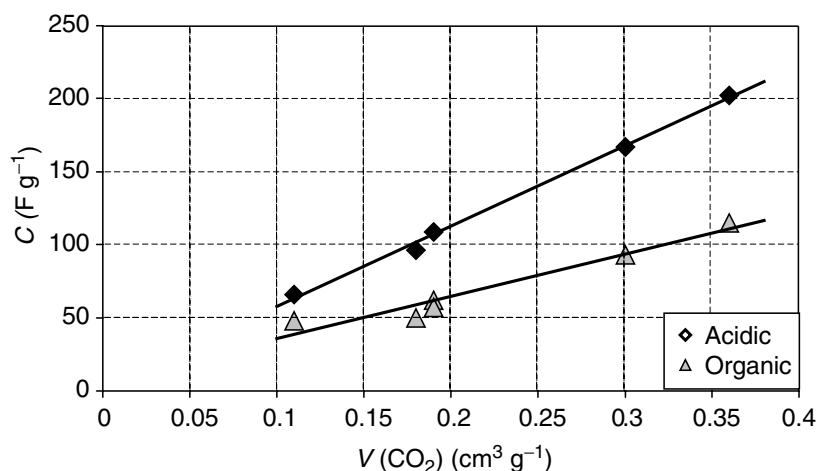


**FIGURE 9.5** Capacitance values in aqueous and organic media of the nanotextured carbons synthesized with different carbon precursors and templates vs. their micro-pore volume determined by  $\text{CO}_2$  adsorption. (From Vix-Guterl, C. et al., *Carbon*, 43, 1293, 2005.)

pores where the ions are finally accumulated. Templated carbons, in spite of the difficulty in their preparation and relatively high cost, are certainly a good means for supplying important information about pore-size effects on electrical double-layer charging.

### 9.2.3 ELECTROCHEMICAL CAPACITORS FROM CARBONS WITH PSEUDOCAPACITANCE PROPERTIES

Many commercially available activated carbons already reach the theoretical value of specific surface area for a single graphene layer, i.e.,  $2600 \text{ m}^2/\text{g}$ . Hence, according to formula (9.1), the only possibility of enhancing capacitance with this kind of material is by improving the access to micropores. However, high BET surface-area-activated carbons possess a high number of active sites or surface groups, which considerably reduce the life cycle of supercapacitors due to side reactions [42]. Therefore, instead of developing the specific surface area largely, an alternative is to introduce pseudofaradaic properties by doping of carbon through foreign elements. The presence of different heteroatoms (oxygen, nitrogen) substituted for carbon in the graphene layers or occurring as functional groups has been considered for modifying the electronic properties that can further influence the electrochemical performance [43,44]. The foreign atoms modify the electron donor/acceptor properties of the graphene layers, and are consequently expected to affect the charging of the electrical double layer and to give pseudocapacitance faradaic reactions. The main dopant studied in literature is nitrogen [45–48]. A part of the nitrogen can be substituted to carbon (“lattice nitrogen”), and the other can be chemically bound to the edge carbon atoms (“chemical nitrogen”).

The effect of substitutional nitrogen in the graphitic network on the pseudocapacitance properties has been studied recently. A series of nitrogen-enriched carbons has been prepared by carbonization of polyacrylonitrile (PAN) or oxidized poly (4-vinylpyridine) cross-linked with 25 wt% of divinylbenzene (PVPox) and of their blends with pitch (P). Then, they have been activated by steam to give activated carbons that were tested in two electrode capacitors [23,49]. The detailed nanotextural characteristics together with elemental composition expressed by N/C, O/C, and N/O atomic ratios and the potential of zero charge are presented in Table 9.1. The BET-specific surface area of the activated carbons ranges from  $800$  to  $1400 \text{ m}^2/\text{g}$ , and their nitrogen content from 1.9 to 7.2 wt%. It is also noteworthy that the higher the amount of nitrogen, the higher the basicity of carbon. The voltammetry characteristics for activated carbon from PAN (Figure 9.6) show a perfect rectangular shape at  $2 \text{ mV}/\text{sec}$  and a slight aggravation from  $10$  to  $20 \text{ mV}/\text{s}$ , supporting the hypothesis that faradaic reactions in the presence of nitrogen proceed with limitations at higher load. The galvanostatic charge/discharge curves for the

**TABLE 9.1**  
**Characteristics of the Activated Carbons from N-polymers and Their Blends with Pitch P**

Sample	Porosity			Elemental Composition			pH <sub>PZC</sub>
	S <sub>BET</sub> (m <sup>2</sup> /g)	V <sub>μ</sub> /V <sub>T</sub>	N (wt%)	(N/C) <sub>at</sub>	(O/C) <sub>at</sub>	(N/O) <sub>at</sub>	
PAN	807	0.93	7.2	0.071	0.050	1.42	9.3
P/PAN 1:1	832	0.89	4.2	0.041	0.042	0.98	8.5
P/PAN 3:1	747	0.84	3.1	0.029	0.037	0.78	7.7
PVPox	1420	0.92	2.6	0.025	0.043	0.58	7.6
P/PVPox 1:1	889	0.87	1.9	0.018	0.033	0.55	7.4

Source: From Lota, G. et al., *Chem. Phys. Lett.*, 404, 53, 2005.

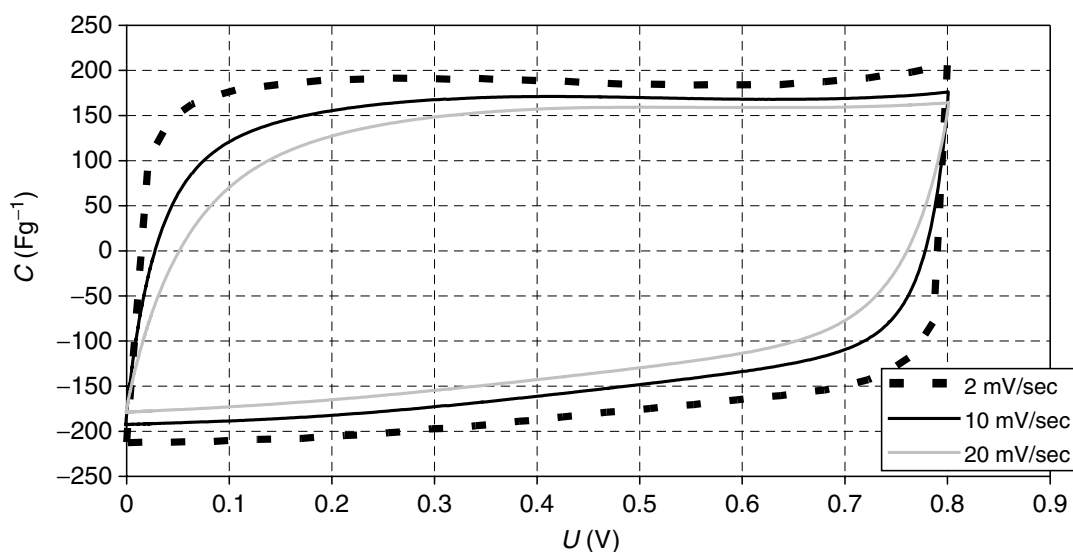
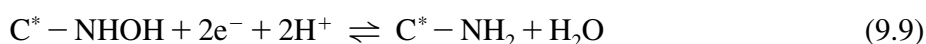


**FIGURE 9.6** Voltammetry characteristics of a two-electrode capacitor built with the AC from PAN (electrolytic medium: 1 mol/L H<sub>2</sub>SO<sub>4</sub>) at three different scan rates. (From Frackowiak, E. et al., *Electrochim. Acta*, in press, 2005.)

nitrogenated material from PVPox, which contains roughly three times less nitrogen than that from PAN, are of the triangular shape typical of a good capacitor even at a high load of 1000 mA/g (Figure 9.7), demonstrating that upon reducing the amount of substitutional nitrogen, the faradaic perturbations are less visible. The capacitance values of nitrogenated carbons are strongly affected by the nature of the electrolyte and the electronic structure induced by nitrogen. A careful analysis of the results obtained for samples with comparable nanotextural properties, i.e., S<sub>BET</sub> ≈ 800 m<sup>2</sup>/g, shows no remarkable differences in organic medium, whereas capacitance is proportional to the N content and pH<sub>PZC</sub> in acidic medium (Figure 9.8) [49]. The extrapolation to a nitrogen content of 0 wt% gives a capacitance of 85 F/g, which is the order generally found for activated carbons with a specific surface area of 800 m<sup>2</sup>/g. The enhancement of the capacitance values in H<sub>2</sub>SO<sub>4</sub> medium was interpreted by pseudofaradaic reactions due to the nitrogen functionality, as illustrated by the following equations [49,50]:



where C\* stands for the carbon network. Figure 9.9 shows the capacitance vs. frequency dependence for capacitors built in 1 mol/L H<sub>2</sub>SO<sub>4</sub> from the two activated carbons from PVPox and P/PAN

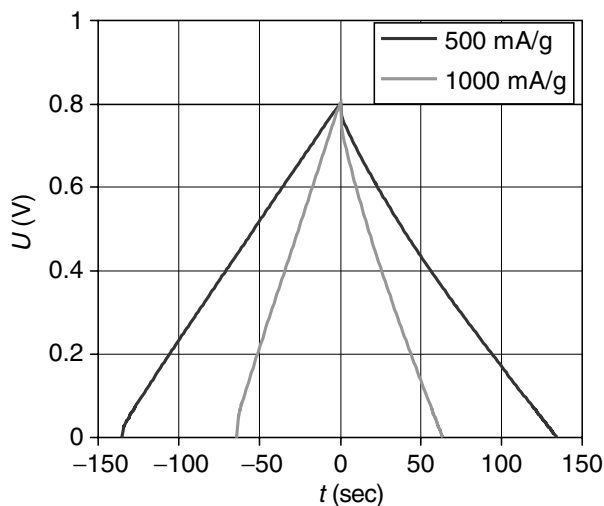


**FIGURE 9.7** Galvanostatic charge/discharge of a two-electrode capacitor built with the AC from PVPox (electrolytic medium: 1 mol/L  $H_2SO_4$ ) at two different current loads. (From Lota, G. et al., *Chem. Phys. Lett.*, 404, 53, 2005.)

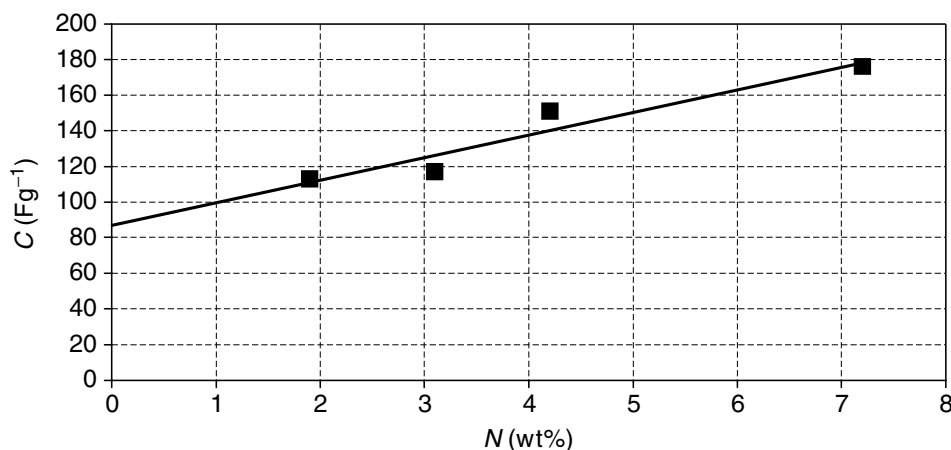


**FIGURE 9.8** Capacitance values (F/g) in acidic medium vs. nitrogen content (wt%) for the ACs from PAN-A, P/PAN 1:1, P/PAN 3:1, P/PVPox 1:1. (From Frackowiak, E. et al., *Electrochim. Acta*, in press, 2005.)

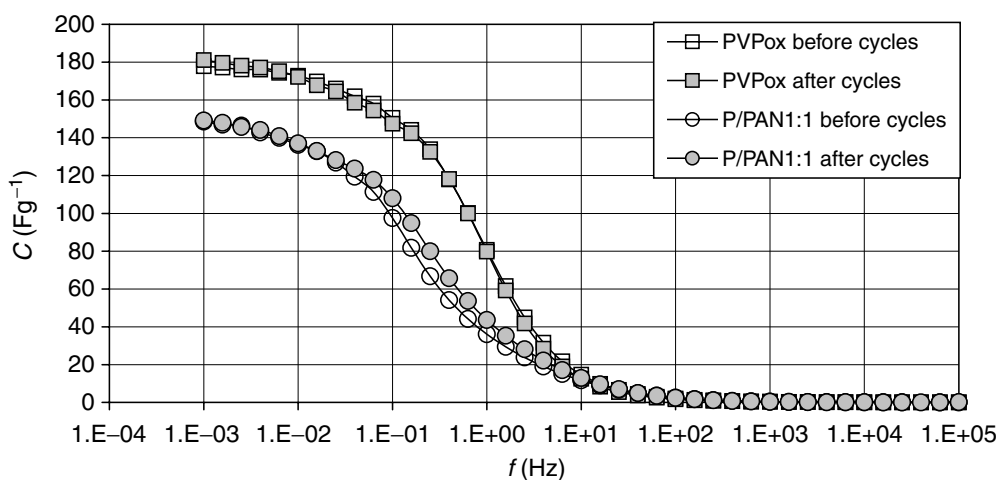


**FIGURE 9.9** Capacitance values vs. frequency for two activated carbons from PVPox and P/PAN 1:1 before and after 3000 cycles at 500 mA/g current load. Electrolytic solution: 1 mol/L  $H_2SO_4$ . (From Frackowiak, E. et al., *Electrochim. Acta*, in press, 2005.)

as 1:1, before and after 3000 cycles at 500 mA/g current load. The fact that the before and after cycling curves are almost superimposed proves that the pseudocapacitance effect introduced by nitrogen is stable with cycling. Moreover, capacitance only slightly decreases at low frequency, as would be the case for an electrochemical double-layer capacitor.

Hence, it is clear that noticeable capacitance values can be obtained when heteroatoms are incorporated into the network of activated carbons, even if their specific surface area is quite moderate. These kinds of materials open new insights for the development of high-performance supercapacitors. It also confirms that the pseudofaradaic effects due to heteroatoms are an additional factor that apart from nanotextural parameters may contribute to the determination of capacitance [31].

#### 9.2.4 CARBON NANOTUBES AS A COMPOSITE COMPONENT

As already explained in Section 9.2.1, materials with pseudocapacitance properties, such as oxides [16,17] or electronically conducting polymers (ECPs) [19,21] may be a promising alternative for the development of high-performance supercapacitors. However, in most reports, a very thin layer of the active material coats a metallic current collector — very often platinum — that is far from the requirements for an industrial application. Moreover, swelling and shrinkage may occur during doping/de-doping of the active film, which leads to mechanical degradation of the electrode and fading of the electrochemical performance during cycling. Such problems have been partly overcome in the case of ECPs by adding an insulating polymer with good mechanical properties such as poly-*N*-vinylalcohol [51], but as a result the electrical conductivity of the composite material is lower than in the pristine ECP. Adding carbon [52], and especially carbon nanotubes, is the most interesting solution that has been proposed to improve the mechanical and electrochemical properties of the electrodes [7,18]. Carbon nanotubes (CNTs), due to their unique morphology and extended graphitic layers, are characterized by exceptional conducting and mechanical properties that allow them to be used directly as three-dimensional support for active materials. With nanotubes, the percolation of the active particles is more efficient than with traditional carbon blacks, which are generally used for the manufacture of electrodes [7]. On the other hand, the open mesoporous network formed by the entanglement of nanotubes, allows the ions to diffuse easily to the active surface of the composite components. The two latter properties are essential to lower the ESR and consequently increase the power of the device. Finally, since nanotubular materials are characterized by a high resiliency, the composite electrodes can easily adapt to the volumetric changes during charge and discharge, which drastically improves the cycling performance. For all these reasons, composites incorporating a nanotubular backbone coated by an active phase with pseudocapacitive properties represent an interesting breakthrough for developing a new generation of supercapacitors.

Chemical and electrochemical polymerization of the monomer have been considered in order to get an ECP layer — the most investigated being polypyrrole (PPy) — on nanotubular materials. The TEM micrograph presented in Figure 9.10 for a material prepared by PPy electrochemical deposition shows a very uniform polymer coating [53]. Coating by a thin layer of polypyrrole has been realized on multiwalled nanotubes (MWNTs) [18,54,55], well-aligned MWNTs [56], and single-wall nanotubes (SWNTs) [57]. When MWNTs are oxidized, their surface is covered with oxygen-containing groups, which can be used as anionic dopant of a PPy film electrodeposited on the MWNTs [58]. These films are notably less brittle and more adhesive to the electrode than those formed using an aqueous electrolyte as a source of counterion. The electrochemical behavior of ECP/CNT composites has been studied either in two- or three-electrode cells. Comparison of the redox performance of PPy films on aligned MWNTs and on flat Ti and Pt surfaces shows a noticeable improvement in the case of the composites with MWNTs due to the high-accessible surface area of CNTs in the aligned arrays [56]. By contrast, the results found with SWNT/PPy nanocomposites [57] are probably of limited application because (1) the nickel foam used as a current collector supplies an additional capacity in the alkaline solution used for the study; and (2) PPy degrades quickly in alkaline solution. With the electrochemically obtained MWNTs/PPy

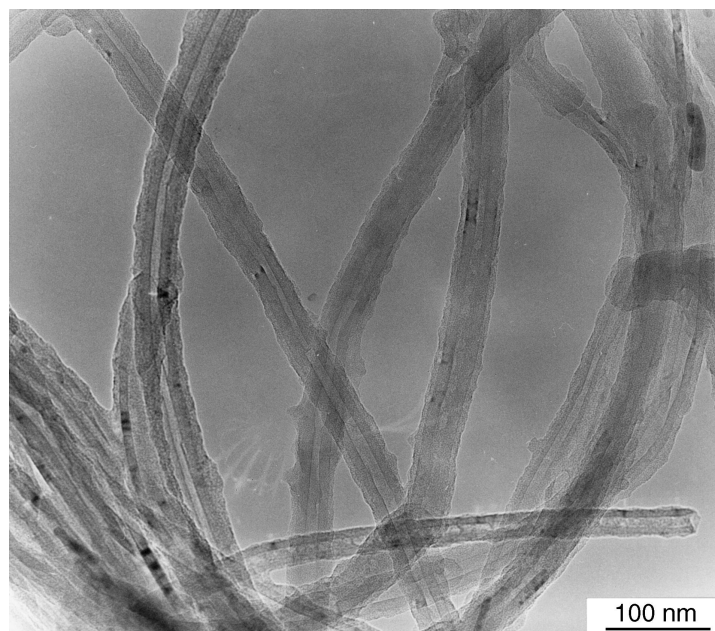


**FIGURE 9.10** Multiwalled carbon nanotubes electrochemically coated by a thin layer of polypyrrole. The coating thickness is estimated to be 5 nm. (From Frackowiak, E. et al., *Polish J. Chem.*, 78, 1345, 2004.)

composite, the capacitance values reach ca. 170 F/g with a good cyclic performance over 2000 cycles [18]. In fact, it has been shown that the capacitance values for composites with polyaniline (PANI) and PPy strongly depend on the cell construction [59]. With chemically deposited ECPs, extremely high values of specific capacitance can be found — from 250 to 1100 F/g — using a three-electrode cell, whereas smaller values of 190 F/g for MWNTs/PPy and 360 F/g for MWNTs/PANI have been measured in a two-electrode cell. It highlights the fact that only two-electrode cells allow the material's performance to be estimated well in electrochemical capacitors. The applied voltage was found to be the key factor influencing the specific capacitance of ECP-based nanocomposites. Generally, it cannot exceed 0.6 to 0.8 V due to oxygen evolution in the positive range of potentials and switching to an insulating state in the negative values [59]. The high values of capacitance found with MWNT/ECP composites is due to the unique property of the entangled nanotubes that supply a perfect three-dimensional volumetric charge distribution and a well-accessible electrode/electrolyte interface. Comparing the results of the two coating techniques, the non-homogeneous PPy layer deposited chemically is more porous and less compact than the electrochemically deposited one. Consequently, the diffusion of ions proceeds more easily, giving a better efficiency for charge storage [59]. [Figure 9.11](#) illustrates the electrochemical performance obtained in a two-electrode capacitor with the chemically deposited PPy. The square shape of the voltammogram and linear galvanostatic charge/discharge demonstrate perfect capacitance behavior, even if pure PPy itself gives more irregular characteristics [59].

Carbon nanotubes can also be a perfect support for cheap transition metal oxides of poor electrical conductivity, such as amorphous manganese oxide ( $\alpha\text{-MnO}_2 \cdot n\text{H}_2\text{O}$ ) [7]. The  $\alpha\text{-MnO}_2$ /MWNTs composite can be prepared by precipitation of  $\alpha\text{-MnO}_2$  from a  $\text{KMnO}_4 + \text{Mn}(\text{OAc})_2 \cdot 4\text{H}_2\text{O}$  mixture that contains a predetermined amount of CNTs. The scanning electron microscopy (SEM) image presented in [Figure 9.12](#) for an  $\alpha\text{-MnO}_2$ /MWNT composite containing 15 wt% of nanotubes shows a remarkable template effect of the entangled nanotubes framework. Consequently, the composite electrodes have a good resiliency, and their porosity is high enough to favor the access of ions to the bulk of the active material. The other interesting property of this composite is an extremely good adhesion of the coating layer on the CNTs that is reflected by low values of electrical resistance. In order to demonstrate the advantage of this material, two-electrode capacitors were built in aqueous medium with two kinds of  $\alpha\text{-MnO}_2$ -based composite

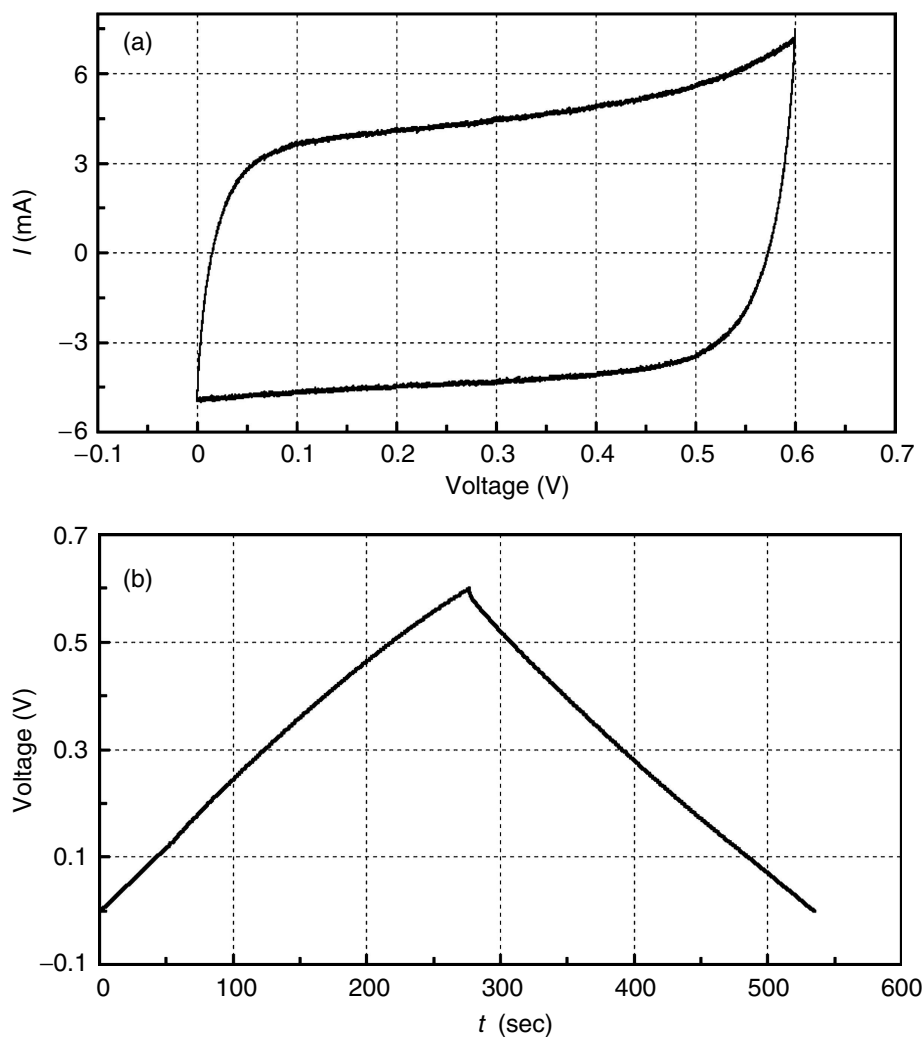


**FIGURE 9.11** Electrochemical characteristics of a symmetric capacitor based on PPy/MWNTs composite electrodes (mass of each electrode = 8.6 mg). (a) cyclic voltammogram (5 mV/s); (b) galvanostatic charge/discharge at 2 mA. (From Khomenko, V. et al., *Electrochim. Acta*, 50, 2499, 2005.)

containing either 15 wt% of carbon black or 15 wt% of MWNTs. The shape of the characteristics in the presence of carbon black demonstrates a resistive behavior of the electrodes, whereas a perfectly rectangular voltammogram was observed with the a-MnO<sub>2</sub>/MWNTs composite [7]; the corresponding values of ESR were 50 and 2 Ωcm<sup>2</sup>, respectively. The a-MnO<sub>2</sub>/MWNTs composite supplies a capacitance of 140 F/g with good cyclability and high dynamic of charge propagation. However, the voltage window of MnO<sub>2</sub>-based capacitors is limited to 0.6 V, due to the irreversible reactions Mn(IV) to Mn(II) at the negative electrode and Mn(IV) to Mn(VII) at the positive. In order to circumvent this drawback, an asymmetric configuration has been proposed, where the positive electrode consists of a-MnO<sub>2</sub> and the negative is built from activated carbon [61–63]. When the a-MnO<sub>2</sub>/MWNTs composite is used as the positive electrode, the supercapacitor demonstrates perfectly rectangular voltammograms (Figure 9.13) and it can be operated up to 2 V in aqueous medium with an extremely good cyclability [63]. High energy and power density can be reached in aqueous electrolyte, 10.5 Wh/kg and 123 kW/kg, respectively, due both to the large voltage window and to the presence of MWNTs [63]. While being environment-friendly, this system offers electrochemical characteristics comparable with EDLCs in organic electrolytes. Hence, it demonstrates perfectly that combining materials with pseudocapacitance properties in an asymmetric construction is a very promising direction for developing a new generation of high-performance supercapacitors.

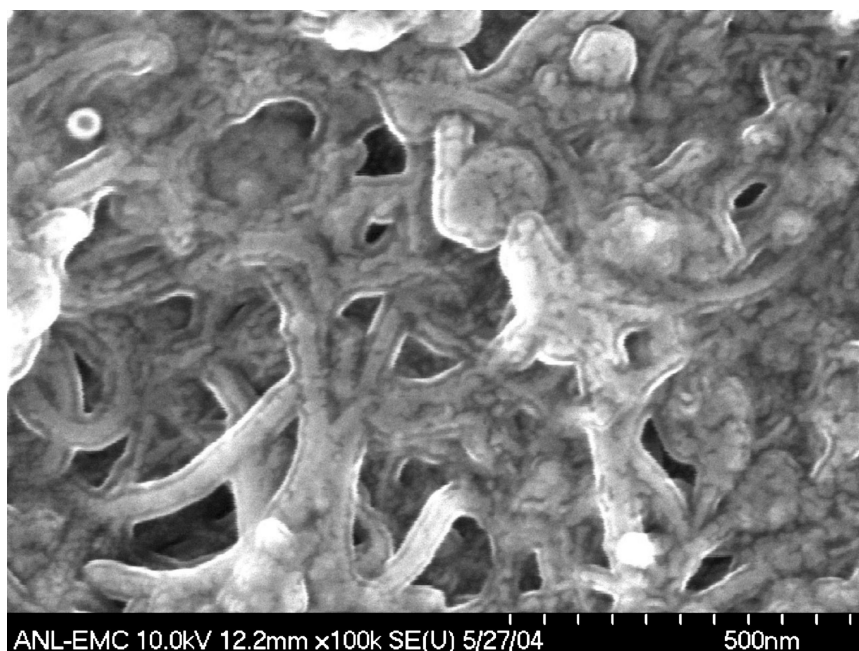


**FIGURE 9.12** Scanning electron microscopy image of an a-MnO<sub>2</sub>/MWNTs composite containing 15 wt% of nanotubes. (Courtesy of M. Thackeray, Argonne National Laboratory, USA.)

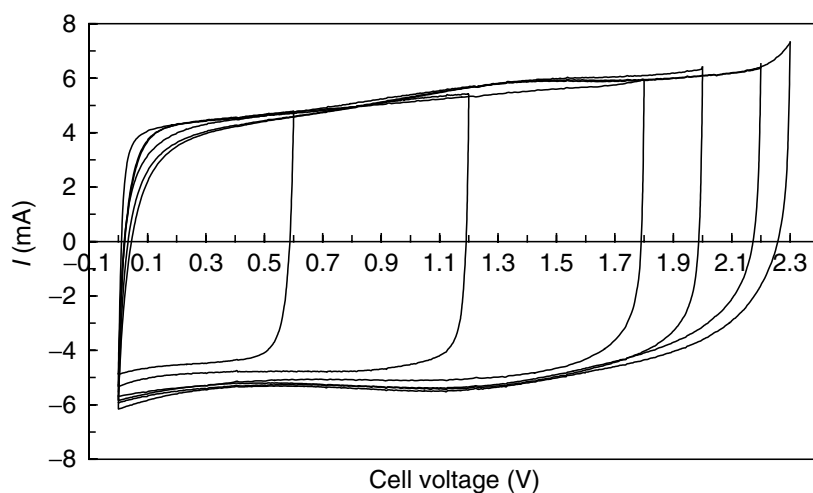


**FIGURE 9.13** Voltammograms of an asymmetric capacitor in 2 mol/L KNO<sub>3</sub> where the positive electrode is from the a-MnO<sub>2</sub>/MWNTs composite and the negative electrode is from AC. Scan rate 10 mV/sec. (From Khomenko, V. et al., *J. Power Sourc.*, in press, 2005.)

## 9.3 ELECTROCHEMICAL HYDROGEN STORAGE

### 9.3.1 INTRODUCTION

In the last few decades, hydrogen has been recognized as an ideal fuel for many energy converters because of its high efficiency and nonpolluting nature. However, the major drawback for practical usage of hydrogen is the difficulty to store it safely and economically. Storage neither as compressed gas nor as a cryogenic liquid appears to be suitable for wide application. Hydrogen storage in metal alloys by absorption or electrodecomposition of a water solution [64] is an interesting alternative, but these materials are not cheap and their reversible capacity, ca. 1.5 wt%, is still far from the US Department of Energy benchmark (5 wt%), as far as powering of vehicles with a hydrogen



fuel-based system is considered. Therefore, the realization of economical and efficient hydrogen-storage techniques is a critical requirement for hydrogen-fueled transportation that stimulates ongoing search for new possibilities.

Although many papers have claimed that nanostructured carbons and nanotubes are able to store large amounts of hydrogen, there is a high discrepancy among all the values published [9,65–78]. Moreover, the factors that allow storage to be optimized are not clearly elucidated. As far as di-hydrogen adsorption is considered, it seems that high pressure (at least 10 MPa) or low temperature (77 K) are necessary for getting noticeable values. Especially in the case of SWNTs and MWNTs, the values of hydrogen capacity are very scarce and doubtful, ranging from 0.2 to 3.7 wt% [67–71]. The possible reasons for the fluctuations in the results may not only be due to experimental errors, but also a large amount of impurities in the samples (e.g., metallic particles and microporous carbon), and the use of additives for conductivity enhancement of the electrodes when an electrochemical technique is used. Investigating high-purity SWNTs and MWNTs, the storage capacity by electrodecomposition of water does not exceed 0.2–0.4 wt% [72]. This fits well also with the di-hydrogen adsorption studies in the gas phase on a number of carbon materials, which confirms the poor efficiency of CNTs for this process [73,74]. By contrast, using activated carbons, the values of reversible hydrogen sorption reach ca. 2 wt% by cathodic electrodecomposition of water at room temperature [72,75–77], and by adsorption of the gas, they range from 1 to 5 wt% depending on whether high pressure (up to 70 MPa) and low temperature (77 K) are applied together or not [65,66,79,80].

The accuracy of the techniques used for measuring the di-hydrogen uptake — volumetric and gravimetric methods, thermo-programmed desorption coupled to mass spectrometry — is quite doubtful. On the contrary, hydrogen storage by galvanostatic electrochemical decomposition of an aqueous basic medium, where the measured variable is the discharging time, is a very accurate method [67,75–77]. Moreover, this reversible process is attractive from the point of view of energy efficiency since it associates in a unique step the hydrogen production by water electrolysis and its simultaneous storage in the carbon substrate. The *in situ* produced hydrogen easily penetrates into the nanopores of carbon, where it is adsorbed due to the driving force of the negative polarization. By this process, higher pressures (approximately calculated from the Nernst law) than in the gas phase can be reached [77]. The overall charge/discharge phenomenon can be represented as



where  $\langle CH_x \rangle$  stands for hydrogen inserted into the nanotextured carbon during charging and oxidized during discharging.

### 9.3.2 MECHANISM OF REVERSIBLE HYDROGEN INSERTION

The mechanism of electrochemical hydrogen storage in nanoporous activated carbon should be taken into account in order to detect the possible optimizations of this process. The electrochemical hydrogen capacities of carbons depend on various parameters such as their physicochemical properties, the nature of the electrolytic medium, and its concentration, the potential cutoff. The carbon sample should contain a noticeable amount of ultramicropores (<0.7 nm) [81], which are generally supposed to be highly efficient for hydrogen sorption [80,82].

Potentiodynamic cycling is a well-adapted electrochemical technique to obtain information on the mechanism and kinetics of reversible hydrogen storage. Examples of voltammetry experiments using an activated carbon (AC) cloth in 3 mol/L KOH and H<sub>2</sub>SO<sub>4</sub>, are shown in Figure 9.14 and Figure 9.15, respectively. The various curves have been recorded with a stepwise (100 mV) shift of potential cutoff to more negative values, it means towards hydrogen evolution. In both electrolytic media, it is obvious that the two phenomena of charging the electrical double layer and hydrogen adsorption during electrochemical decomposition of water are very much linked. When

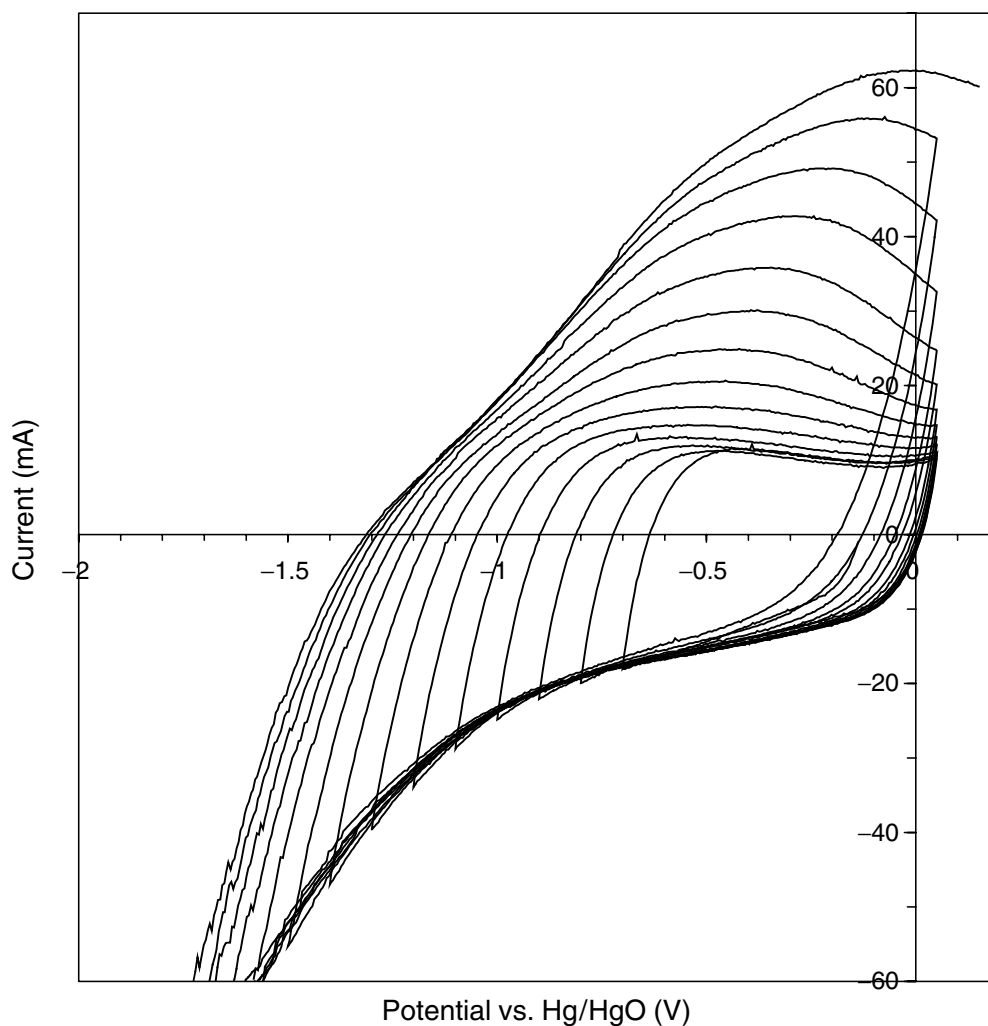


**FIGURE 9.14** Dependence of the voltammetry characteristics of an activated cloth AC (15.2 mg) with the value of negative potential cutoff. Electrolyte: 3 mol/L KOH. Scan rate of potential: 5 mV/sec. The various loops are obtained by stepwise (100 mV) shifting of the potential cutoff to more negative values. (From Jurewicz, K. et al., *Appl. Phys. A*, 78, 981, 2004.)

the electrode potential is higher than the thermodynamic value that corresponds to water decomposition, only the electrical double layer is charged, whereas when it becomes lower than this value, not only the double layer is charged, but hydrogen is also adsorbed in the pores of carbon. In the latter case, the two processes contribute to the amount of electrical energy, which is reversibly stored [77].

### 9.3.2.1 Mechanism in Aqueous KOH Medium

In the case of the voltammetry experiment in aqueous KOH (Figure 9.14), the almost rectangular shape of the curves down to a potential cutoff of  $-0.8\text{ V}$  vs. Hg/HgO proves entirely the pure capacitive and reversible behavior of AC. The negative current reflects the number of hydrated potassium ions,  $\text{K}_{\text{aq}}^+$ , which are accumulated in the carbon/electrolyte interface during the negative polarization of AC, whereas the positive current corresponds to the desorption of  $\text{K}_{\text{aq}}^+$ . The faradaic water decomposition starts gradually to take place from the third loop when the potential cutoff is lower than the equilibrium potential (the theoretical value of the equilibrium potential in 3 mol/L KOH is  $-0.856\text{ V}$  vs. NHE, i.e.,  $-0.908\text{ V}$  vs. Hg/HgO). The increase in positive current during the anodic scan is the proof that the hydrogen that was adsorbed in the pores as  $\text{H}_{\text{ad}}$  during water reduction is now electrooxidized when the potential is higher than the equilibrium value.

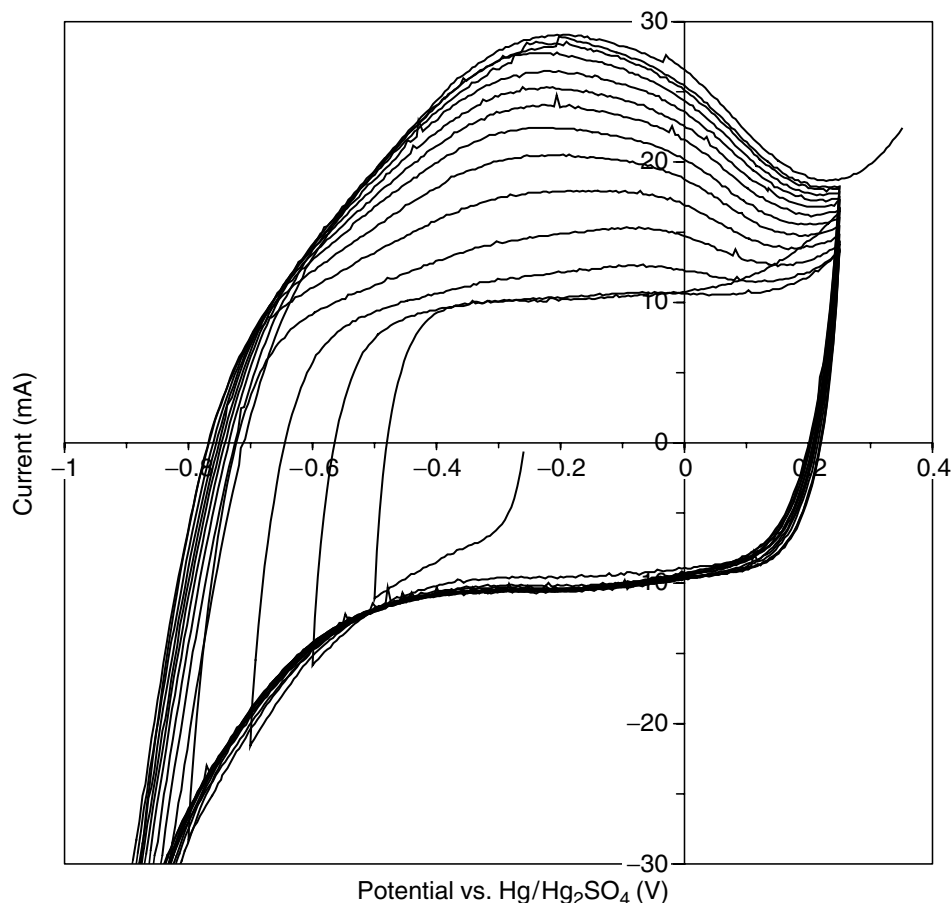


**FIGURE 9.15** Dependence of the voltammetry characteristics of an activated cloth AC (14.1 mg) with the value of negative potential cutoff. Electrolyte: 3 mol/L H<sub>2</sub>SO<sub>4</sub>. Scan rate of potential: 5 mV/s. The various loops are obtained by stepwise (100 mV) shifting of the potential cutoff to more negative values. (From Jurewicz, K., et al., *Appl. Phys. A*, 78, 981, 2004.)

In alkaline solution, water is reduced according to



The nascent hydrogen formed in the reaction (9.11) is adsorbed on the pores surface (reaction [9.12]):



and/or it recombines to form H<sub>2</sub> molecules through one of the processes described in the following:



These steps are often distinguished as Volmer (9.11), Heyrovsky (9.13) and Tafel (9.14) reactions. If the hydrogen adsorption energy is smaller than the energy released in the Tafel or Heyrovsky reactions, and if the activation barrier for one of these processes is low enough, then the recombination

of  $H_{ad}$  takes place and molecular hydrogen evolves by chemical or electrochemical processes, respectively. If not, the adsorbed hydrogen can further diffuse in the bulk of the carbon host occupying sites with higher adsorption energy; this process is strongly dependent on the sizes and shapes of the pores.

During the oxidation step, the above reactions run in opposite directions. When during charging the value of the cutoff potential is below  $-0.8$  V vs. Hg/HgO, the hydrogen oxidation is well observed on the anodic part of the voltammetry characteristics. The positive current due to hydrogen oxidation increases with the decrease of potential cutoff and a more and more pronounced hump shifts towards more positive values of potential. When the negative potential cutoff reaches  $-2$  V vs. Hg/HgO, the hump is located close to  $0$  V vs. Hg/HgO, i.e.,  $+0.052$  V vs. NHE. The latter value is very high compared with the equilibrium potential for reaction (9.11) in  $3$  mol/L KOH, i.e.,  $-0.856$  V vs. NHE. This high over-voltage required for hydrogen oxidation is a clear proof that hydrogen stored at very negative values of potential is strongly trapped in the porous carbon bulk. The high difference of positive and negative currents measured at  $0$  V vs. Hg/HgO indicates that a part of hydrogen remains irreversibly trapped in the carbon material. The dangling bonds present at the edge of the graphene layers may be responsible for trapping hydrogen more energetically than it can be the case for classical physisorption [83].

### 9.3.2.2 Mechanism in Aqueous $H_2SO_4$ Medium

In sulfuric acid,  $H_3O^+$  is the available proton source for the initial charge transfer step according to



The theoretical value of the equilibrium potential for reaction (9.16) in  $3$  mol/L  $H_2SO_4$  is  $0.046$  V vs. NHE, i.e.,  $-0.566$  V vs. Hg/Hg<sub>2</sub>SO<sub>4</sub>. Figure 9.15 presents the voltammetry characteristics of AC in  $H_2SO_4$  with a stepwise shift ( $100$  mV) of negative potential cutoff from  $-0.5$  to  $-1.8$  V vs. Hg/Hg<sub>2</sub>SO<sub>4</sub>. During the first cycle, the solvated  $H_3O^+$  ions are accumulated in the electrical double layer during the cathodic sweep, and the anodic one corresponds to their repulsion. In Figure 9.15, one can see that the faradaic reaction according to (9.16) proceeds at more negative values than  $-0.6$  V vs. Hg/Hg<sub>2</sub>SO<sub>4</sub>. It is noteworthy that the voltammetry response differs significantly from the alkali medium. The intermediate region where hydrogen adsorption takes place during the cathodic polarization is almost absent, and di-hydrogen evolution starts almost immediately after the region of pure capacitance behavior. It is clear that the Tafel recombination (Equation [9.14]) determines the process, i.e., is quicker than hydrogen diffusion and incorporation into the bulk of AC. Owing to this phenomenon, the oxidation current is lower in  $3$  mol/L  $H_2SO_4$  (Figure 9.15) than in  $3$  mol/L KOH (Figure 9.14), which means  $30$  mA against  $60$  mA for equivalent masses of AC. Moreover, in contrast to the KOH medium, the oxidation hump locates at a constant position, ca.  $-0.2$  V vs. Hg/Hg<sub>2</sub>SO<sub>4</sub>, i.e.,  $+0.4$  V vs. NHE. The latter value is only slightly higher than the equilibrium potential in  $3$  mol/L  $H_2SO_4$  medium. In acidic medium, the hydrogen evolution as well as its oxidation proceed more easily, i.e., with a smaller polarization than in the KOH medium, because the protons are directly available in the electrode/electrolyte interface for the redox process. In conclusion, hydrogen is mainly trapped in a state close to physisorption when electrodecomposition is performed in aqueous  $H_2SO_4$  medium.

### 9.3.2.3 Comparison of Galvanostatic Charge/Discharge in Acidic and Basic Media

The amount of hydrogen stored reversibly in both alkaline and acidic electrolytes is estimated quantitatively by galvanostatic charge/discharge (Figure 9.16). The hydrogen insertion into AC proceeds spontaneously during the decomposition of the electrolytic solution using a current load of  $-500$  mA/g. After saturation of the samples using a charge excess, the system is allowed to relax for  $1/2$  to  $1$  h, and the amount of hydrogen reversibly stored in the AC is determined by measuring the time of galvanostatic discharge at a current load of  $25$  mA/g. Taking into account the Faraday law,  $1$  wt% of hydrogen corresponds to a charge of  $270$  mAh/g.

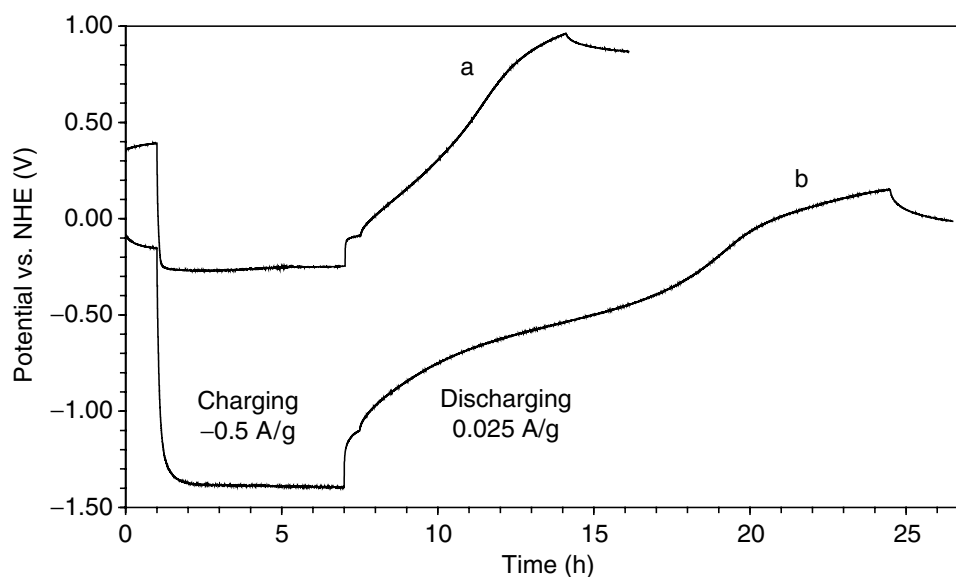


**FIGURE 9.16** Galvanostatic charge/discharge of hydrogen in AC: (a) in 3 mol/L  $\text{H}_2\text{SO}_4$  (mass of AC = 19.4 mg); (b) in 3 mol/L KOH (mass of AC = 20.0 mg). The system is first allowed to equilibrate for 1 h; then a negative current of  $-0.5 \text{ A/g}$  is applied for 6 h. After a relaxation period of 30 min, a positive current of  $0.025 \text{ A/g}$  is applied in order to oxidize the inserted hydrogen. (From Jurewicz, K. et al., *Appl. Phys. A*, 78, 981, 2004.)

Considering the values of equilibrium potentials, a significant over-voltage  $\eta$  for di-hydrogen evolution is observed in basic and in acidic medium, i.e., 0.55 and 0.32 V, respectively. It confirms the previous observations from potentiodynamic investigations that hydrogen adsorption is favored in alkaline medium. The well-defined potential plateau at  $-0.55 \text{ V}$  vs. NHE on the discharge curve in 3 mol/L KOH is a typical proof of hydrogen electro-desorption from the material. By contrast, in 3 mol/L  $\text{H}_2\text{SO}_4$  there is almost a monotonic increase in potential with time, which demonstrates a lack of distinct energy sites in this medium (Figure 9.16). Hence, both potentiodynamic and galvanostatic experiments confirm that the storage conditions are better in KOH than in  $\text{H}_2\text{SO}_4$ , and that charging of the electrical double layer is the main contribution to charge storage in acidic medium.

Under appropriate conditions, the reversible capacity of AC in 6 mol/L KOH can reach 480 mAh/g [77], i.e., 1.8 wt%, which is quite interesting for battery application by comparison with metallic hydrides [64]. Moreover, this value is much better than that found when di-hydrogen is adsorbed in the same material under a pressure of 70 bar at 273 K, e.g., 0.4 wt% [75]. Such a difference between the two techniques is easily explained by an estimation of the local pressure during a galvanostatic charge. Activated carbon is first submitted to a prolonged galvanostatic charge in 6 mol/L KOH, and then the system is allowed to relax for 1 h before measuring the open circuit voltage (OCV). From the value of OCV, a local hydrogen pressure of  $1.3 \times 10^2 \text{ MPa}$  is estimated by the application of the Nernst equation to reaction (9.11) [77]. This high value of pressure, which cannot be easily reached with conventional systems in the gas phase, justifies the better efficiency of the electrochemical process for hydrogen storage [75].

#### 9.3.2.4 Relation between the Reversible Hydrogen Storage Capacity and the Nanotextural Characteristics of Porous Carbons

Taking into account that the part of hydrogen that can be reversibly recovered is in a state close to physisorption, the adsorption capacity should be influenced by the porous nanotexture of the carbon material. Therefore, in order to find the possible directions of optimization, some correlations were tentatively established with the nanotextural parameters of carbons.

The electrochemical storage capacity of various nanostructured carbons, including high-surface area graphites, ACs, SWNTs, and MWNTs, seems to slightly correlate with the BET specific surface area [72,84]. From the slope of the capacity vs. surface area plot (Figure 9.17), an uptake of

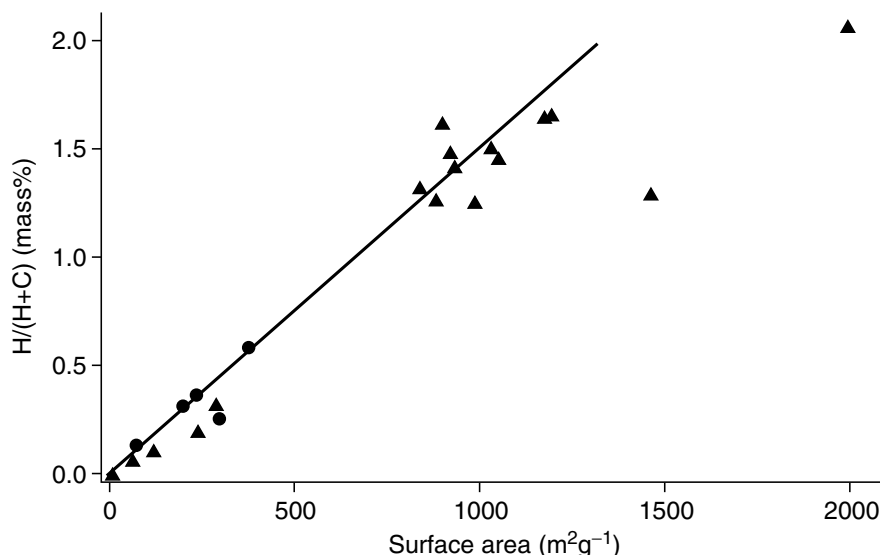


**FIGURE 9.17** Desorbed amount of hydrogen vs. the BET specific surface area for carbon nanotubes and high surface area graphite samples. (From Züttel, A. et al., *Int. J. Hydrogen Energy*, 27, 203, 2002.)

1.5 wt% for 1000 m<sup>2</sup>/g is estimated. However, Figure 9.17 shows clearly that it is only a trend, several points being quite out of linearity. A similar tendency vs.  $S_{\text{BET}}$  has been found under di-hydrogen pressures up to 12.5 MPa at room temperature, but most of the experimental points are quite scarce and the linear relationship is not so obvious [78]. The hydrogen adsorption under higher pressures of 10 and 70 MPa at room temperature was also tentatively correlated with the micro-pore volume measured by nitrogen adsorption at 77 K, showing a trend to proportionality, but for some carbons the values are quite out of the proposed correlation [79].

Although authors often propose a correlation of the electrochemical properties of nanoporous carbons with their BET area, this parameter does not take into account that in most cases only micropores with an appropriate size are efficient. Moreover, the total capacity, which is measured by galvanostatic cycling, includes also the capacity due to the charging of the double layer, which should be subtracted to get values typical of hydrogen uptake. The surface functionality may play an additional role in shifting the electrochemical behavior from a tight correlation with any nanotextural parameter. Recently, a significant effort has been undertaken to depict ideal nanotextured carbons for hydrogen storage. Experimental or theoretical studies have shown that the presence of ultramicropores, i.e., smaller than 0.7 nm [81], determines the hydrogen adsorption capacity. However, some discrepancy exists between the theoretical results regarding the optimal pore size for hydrogen adsorption. From Reference [82], the optimum pore size is close to 0.35 nm, which corresponds to a monolayer of adsorbed hydrogen; whereas Reference [85] indicates a size of 0.56 nm that is compatible with two layers of adsorbed hydrogen. The theoretical information obtained in Reference [85] seems to agree with the experimental results obtained either by nitrogen [79] or by CO<sub>2</sub> adsorption [80] on activated carbons.

Hence, a strict control of the pore size is strongly required if one wants to optimize the electrochemical hydrogen storage process. Additionally, as already explained above in the case of supercapacitors, besides the micropores, the presence of mesopores may be very useful to facilitate the diffusion of ions to the pores where they will be adsorbed and subsequently reduced. Unfortunately, most of the commercially available carbon adsorbents display a wide pore-size distribution and their adjustment to required values is not easy. Therefore, the reversible hydrogen capacity has been determined for a series of template carbons and correlated with the volume of ultramicropores measured by CO<sub>2</sub> adsorption at 273 K [33]. The tendency for the amount of hydrogen stored to increase with the total surface area is confirmed, but without any proportionality, in agreement with previous works carried out on CNTs or high surface area graphites [78]. By contrast, if the amount of hydrogen reversibly stored is plotted vs.  $V(\text{CO}_2)$ , a perfect linear relationship is observed (Figure 9.18),

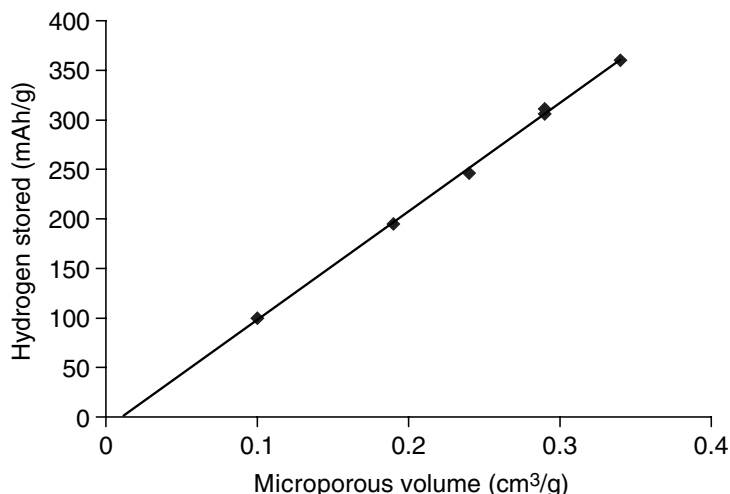


**FIGURE 9.18** Hydrogen storage capacity of various nanotextured carbons prepared by a template technique vs. their ultramicropore volume determined by CO<sub>2</sub> adsorption. (From Vix-Guterl, C. et al., *Carbon*, 43, 1293, 2005.)

confirming the theoretical predictions that hydrogen adsorption is strongly related to the presence of ultramicropores [33]. Taking into account that such a perfect correlation with the ultramicropore volume is not so well observed for all kinds of porous carbons [86], it is obvious once more that the electrochemical performance for hydrogen storage is strongly controlled by the presence of mesopores connected to the micropores. The mesopores are essential to “feed” the micropores with ions or water molecules, which will be further reduced giving hydrogen the ability to be fixed in the ultramicropores.

## 9.4 CONCLUSIONS AND PERSPECTIVES

This chapter shows that all the electrochemical parameters related with capacitance properties and hydrogen storage are strongly correlated with nanotexture and surface functionality of carbons. In most of the literature reports, the effect of surface functionality is neglected, considering rather nanotextured carbons as hosts with inert pores, whose properties would only be dependent on pore volume development. The surface groups not only affect the wettability of porous carbons and their redox properties, but also the cycling performance. Therefore, for future developments, they should be taken more into account and strategies should be developed to efficiently control their nature and amount. Electrochemical grafting of carbon surfaces with well-defined functions would certainly be an adapted technique to reach such objectives.

The most used materials for electrochemical double-layer capacitors are ACs, because they are commercially available and cheap, and they can be produced with large specific surface area. However, many pores are not useful because they cannot be reached by ions. Therefore, the objective is not to develop high surface area carbons, but porous carbons with micropores of small size, which are perfectly connected to a framework of mesopores. A fundamental study establishing the respective sizes of pores and ions to reach optimal capacitance performance would be very useful. Also, it should not be neglected that an asymmetric construction where the pores of the positive and negative electrodes are adapted to the size of the ions to be trapped is preferable to a symmetric cell. Finally, as far as the energy density is concerned, the voltage window must be extended as much as possible. Substitutional heteroatoms in the carbon network might be profitable in shifting the operating potential range of each electrode, leading to a possible voltage increase without electrolyte decomposition.

One of the drawbacks of porous carbons is the poor volumetric capacity that can be reached with these materials. Carbons obtained by one-step pyrolysis of organic precursors are very interesting,

because they present a higher density than the ACs. In this case, the lack of porosity available for charging the electrical double layer must be compensated by pseudofaradaic properties. For this objective, the pyrolysis of nitrogen carriers seems to be very promising.

Another important use of carbon materials for supercapacitors, and more generally for energy storage systems, is their presence as electrode components for improving both the electrical conductivity and mechanical properties. In this sense, CNTs are more efficient than carbon black, because they form a three-dimensional and interconnected framework on which the active material can be deposited. In this chapter, extremely interesting properties of composites incorporating nanotubes and an active material, such as electrically conducting polymers or  $\alpha\text{-MnO}_2$ , have been shown. Taking into account that noticeable improvements cannot be expected with ACs, the nanotube-based composites probably represent an important breakthrough. It will be nevertheless necessary to have the ability to ensure their homogeneous dispersion in the composite materials in order to enhance their efficiency.

In the case of electrochemical hydrogen storage, knowledge is still in the state of seeking. During the last few years, the scientific aspect has been poorly considered, with many authors wishing to demonstrate the exceptional properties of CNTs, without any fundamental background that could justify the choice of this material. All the serious studies published in the last 3 to 4 years agree that the hydrogen uptake with nanotubes is less than 0.5 wt%, irrespective of the experimental conditions. Activated carbons, as cheap and versatile materials, offer definitely better performance and promises. Independent studies, in gas phase or by water decomposition, demonstrate that ultramicropores ( $<0.7\text{ nm}$ ) are essential in this process. Further work should focus on designing carbon materials with a highly developed porosity in this range of size. Other probe molecules, such as  $\text{CF}_4$ ,  $\text{SF}_6$ , should also be used to analyze more correctly the pore sizes. Finally, an important aspect would be to determine to which extent the pore shape affects the hydrogen adsorption properties. Presently, this is probably the most difficult task, because of the lack of an available technique for this kind of analysis. Nevertheless, without any optimization, carbon materials already demonstrate better gravimetric capacity than metallic alloys during the electrodecomposition of alkaline solutions; therefore they should be more extensively investigated as electrode materials for hydrogen storage.

## REFERENCES

1. Inagaki, M., *New Carbons: Control of Structure and Functions*, Elsevier, Amsterdam, 2000.
2. Bansal, R.C., Donnet, J., and Stoeckli, F., *Active Carbon*, Marcel Dekker, New York, 1988.
3. Py, X., Guillot, A., and Cagnon, B., Activated carbon porosity tailoring by cyclic sorption/decomposition of molecular oxygen, *Carbon*, 41, 1533, 2003.
4. Boehm, H.P., Some aspects of the surface chemistry of carbon blacks and other carbons, *Carbon*, 32, 759, 1994.
5. Montes-Moran, M.A., Suárez, D., Menéndez, J.A., Fuente, E., Radovic, L.R., Cannon, F.S., and Strelko, V., On the nature of basic sites on carbon surfaces: an overview, *Carbon*, 42, 1219, 2004.
6. Huczko, A., Template-based synthesis of nanomaterials, *Appl. Phys. A*, 70, 365, 2000.
7. Raymundo-Piñero, E., Khomeiko, V., Frackowiak, E., and Béguin, F., Performance of manganese oxide/CNTs composites as electrode materials for electrochemical capacitors, *J. Electrochem. Soc.*, 152, A229, 2005.
8. Zheng, T. and Dahn, J.R., Applications of carbon in lithium-ion batteries, in *Carbon Materials for Advanced Technologies*, Burchell, T.D., Ed., Elsevier, Oxford, 1999, p. 341.
9. Frackowiak, E. and Béguin, F., Electrochemical storage of energy in carbon nanotubes and nanostructured carbons, *Carbon*, 40, 1775, 2002.
10. Flandrois, S. and Simon, B., Carbon materials for lithium-ion rechargeable batteries, *Carbon*, 37, 165, 1999.
11. Conway, B.E., *Electrochemical supercapacitors — scientific fundamentals and technological applications*, Kluwer Academic/Plenum, New York, 1999.



12. Kötz, R. and Carlen, M., Principles and applications of electrochemical capacitors, *Electrochim. Acta*, 45, 2483, 2000.
13. Frackowiak, E. and Béguin, F., Carbon materials for the electrochemical storage of energy in capacitors, *Carbon*, 39, 937, 2001.
14. Balducci, A., Bardi, U., Caporali, S., Mastragostino, M., and Soavi, F., Ionic liquids for hybrid supercapacitors, *Electrochem. Commun.* 6, 566, 2004.
15. Toupin, M., Brousse, T., and Bélanger, D., Influence of microtexture on the charge storage properties of chemically synthesized manganese dioxide, *Chem. Mater.*, 14, 3946, 2002.
16. Wu, N.L., Nanocrystalline oxide supercapacitors, *Mater. Chem. Phys.*, 75, 6, 2002.
17. Miller, J.M., Dunn, B., Tran, T.D., and Pekala, R.W., Morphology and electrochemistry of ruthenium/carbon/aerogel nanostructures, *Langmuir*, 15, 799, 1999.
18. Jurewicz, K., Delpoux, S., Bertagna, V., Béguin, F., and Frackowiak, E., Supercapacitors from nanotubes/polypyrrole composites, *Chem. Phys. Lett.*, 347, 36, 2001.
19. Laforgue, A., Simon, P., Sarrazin, Ch., and Fauvarque, J.-F., Polythiophene-based supercapacitors, *J. Power Sourc.* 80, 142, 1999.
20. Arbizzani, C., Mastragostino, M., and Soavi, F., New trends in electrochemical supercapacitors, *J. Power Sourc.*, 100, 164, 2001.
21. Mastragostino, M., Arbizzani, C., and Soavi, F., Conducting polymers as electrode materials in supercapacitors, *Solid State Ionics*, 148, 493, 2002.
22. Jurewicz, K., Babel, K., Ziolkowski, A., and Wachowska, H., Ammoxidation of active carbons for improvement of supercapacitor characteristics, *Electrochim. Acta*, 48, 1491, 2003.
23. Lota, G., Grzyb, B., Machnikowska, H., Machnikowski, J., and Frackowiak, E., Effect of nitrogen in carbon electrode on the supercapacitor performance, *Chem. Phys. Lett.*, 404, 53, 2005.
24. Qu, D. and Shi, H., Studies of activated carbons used in double-layer capacitors, *J. Power Sourc.*, 74, 99, 1998.
25. Gambly, J., Taberna, P.L., Simon, P., Fauvarque, J.F., and Chesneau, M., Studies and characterization of various activated carbons used for carbon/carbon supercapacitors, *J. Power Sourc.*, 101, 109, 2001.
26. Kierzek, K., Frackowiak, E., Lota, G., Gryglewicz, G., and Machnikowski, J., Electrochemical capacitors based on highly porous carbons prepared by KOH activation, *Electrochim. Acta*, 49, 515, 2004.
27. Raymundo-Pinero, E., Cazorla-Amoros, D., Linares-Solano, A., Delpoux, S., Frackowiak, E., Szostak, K., and Béguin, F., High surface area carbon nanotubes prepared by chemical activation, *Carbon*, 40, 1614, 2002.
28. Frackowiak, E., Delpoux, S., Jurewicz, K., Szostak, K., Cazorla-Amoros, D., and Béguin, F., Enhanced capacitance of carbon nanotubes through chemical activation, *Chem. Phys. Lett.* 361, 35, 2002.
29. Lozano-Castelló, D., Cazorla-Amorós, D., Linares-Solano, A., Shiraiishi, S., Kurihara H., and Oya, A., Influence of pore structure and surface chemistry on electric double layer capacitance in non-aqueous electrolyte, *Carbon*, 41, 1765, 2003.
30. Shi, H., Activated carbons and double layer capacitance, *Electrochim. Acta*, 41, 1633, 1996.
31. Guo, Y., Qi, J., Jiang, Y., Yang, S., Wang, Z., and Xu, H., Performance of electrical double-layer capacitors with porous carbons derived from rice husk, *Mat. Chem. Phys.*, 80, 704, 2003.
32. Salitra, G., Soffer, A., Eliad, L., Cohen, Y., and Aurbach, D., Carbon electrodes for double-layer capacitors. I. Relations between ion and pore dimensions, *J. Electrochem. Soc.*, 147, 2486, 2000.
33. Vix-Guterl, C., Frackowiak, E., Jurewicz, K., Friebe, M., Parmentier, J., and Béguin, F., Electrochemical energy storage in ordered porous carbon materials, *Carbon*, 43, 1293, 2005.
34. Okamura, M., Electric Double Layer Capacitor, U.S. Patent 6,064,562 and JP11067608, JEOL Ltd., 2000.
35. Kyotani, T., Control of pore structure in carbon, *Carbon*, 38, 269, 2000.
36. Ryoo, R., Joo, S.H., Kruk, M., and Jaroniec, M., Ordered mesoporous carbons, *Adv. Mater.*, 13, 677, 2001.
37. Han, S., Lee, K.T., Oh, S.M., and Hyeon, T., The effect of silica template structure on the pore structure of mesoporous carbons, *Carbon*, 41, 1049, 2003.
38. Fuertes, A.B., Template synthesis of mesoporous carbons with a controlled particle size, *J. Mater. Chem.*, 13, 3085, 2003.
39. Lee, J., Yoon, S., Hyeon, T., Oh, S.M., and Kim, K.B., Synthesis of a new mesoporous carbon and its application to electrochemical double-layer capacitors, *Chem. Comm.*, 2177, 1999.

40. Jurewicz, K., Vix, C., Frackowiak, E., Saadallah, S., Reda, M., Parmentier, J., Patarin, J., and Béguin, F., Capacitance properties of ordered porous carbon materials prepared by a templating procedure, *J. Phys. Chem. Solids*, 65, 287, 2004.
41. Yoon, S., Lee, J., Hyeon, T., and Oh, S.M., Electric double-layer capacitor performance of a new mesoporous carbon, *J. Electrochem. Soc.*, 147, 2507, 2000.
42. Pillay, B. and Newman, J., The influence of side reactions on the performance of electrochemical double-layer capacitors, *J. Electrochem. Soc.*, 143, 1806, 1996.
43. Biniak, S., Świątkowski, A., and Pakuła, M., in *Chemistry and Physics of Carbon*, Vol. 27, Radovic, L.R., Ed., Marcel Dekker, New York, 2001, p. 125.
44. Laszlo, K., Tombacz, E., and Josepovits, K., Effect of activation on the surface chemistry of carbons from polymer precursors, *Carbon*, 39, 1217, 2001.
45. Pels, J.R., Kaptein, F., Moulijn, J.A., Zhu, Q., and Thomas, K.M., Evolution of nitrogen functionalities in carbonaceous materials during pyrolysis, *Carbon*, 33, 1641, 1995.
46. Kaptein, F., Moulijn, J.A., Matzner, S., and Boehm, H.P., The development of nitrogen functionality in model chars during gasification in CO<sub>2</sub> and O<sub>2</sub>, *Carbon*, 37, 1143, 1999.
47. Grzyb, B., Machnikowski, J., Weber, J.V., Koch, A., and Heintz, O., Mechanism of co-pyrolysis of coal-tar pitch with polyacrylonitrile, *J. Anal. Appl. Pyrolysis*, 67, 77, 2003.
48. Grzyb, B., Machnikowski, J., and Weber, J.V., Mechanism of co-pyrolysis of coal-tar pitch with polyvinylpyridine, *J. Anal. Appl. Pyrolysis*, 72, 121, 2004.
49. Frackowiak, E., Lota, G., Machnikowski, J., Vix-Guterl, C., and Béguin, F., Optimisation of supercapacitors using carbons with controlled nanotexture and nitrogen content, *Electrochim. Acta*, on line, 2005.
50. Grimshaw, J., *Electrochemical Reactions and Mechanisms in Organic Chemistry*, Elsevier, Amsterdam, 2000, chapters 10 and 11.
51. Campomanes, R.S., Bittencourt, E., and Campos, J.S.C., Study of conductivity of polypyrrole-poly(vinyl alcohol) composites obtained photochemically, *Synth. Met.*, 102, 1230, 1999.
52. Wampler, W.A., Wei, C., and Rajeshwar, K., Electrocomposites of polypyrrole and carbon black, *J. Electrochem. Soc.*, 141, L13, 1994.
53. Frackowiak, E., Jurewicz, K., and Béguin, F., Development of new supercapacitor electrodes based on carbon nanotubes, *Polish J. Chem.*, 78, 1345, 2004.
54. Frackowiak, E., Jurewicz, K., Delpeux, S., and Béguin, F., Nanotubular materials for supercapacitors, *J. Power Sourc.*, 97–98, 822, 2001.
55. Xiao, Q. and Zhou, X., The study of multiwalled carbon nanotube deposited with conducting polymer for supercapacitor, *Electrochim. Acta*, 48, 575, 2003.
56. Chen, J.H., Huang, Z.P., Wang, D.Z., Yang, S.X., Li, W.Z., Wen, J.G., and Ren, Z.F., Electrochemical synthesis of polypyrrole films over each of well-aligned carbon nanotubes, *Synth. Met.*, 125, 289, 2002.
57. An, K.H., Jeon, K.K., Heo, J.K., Lim, S.C., Bae, D.J., and Lee, Y.H., High-capacitance supercapacitor using a nanocomposite electrode of single-walled carbon nanotube and polypyrrole, *J. Electrochem. Soc.*, 149, A1058, 2002.
58. Chen, G.Z., Shaffer, M.S.P., Coleby, D., Dixon, G., Zhou, W., Fray, D.J., and Windle, A.H., Carbon nanotube and polypyrrole composites: coating and doping, *Adv. Mater.*, 12, 522, 2000.
59. Khomenko, V., Frackowiak, E., and Béguin, F., Determination of specific capacitance of conducting polymers/nanotubes composite electrodes using different cell configurations, *Electrochim. Acta*, 50, 2499, 2005.
60. Lee, H.Y. and Goodenough, J.B., Supercapacitor behavior with KCl electrolyte, *J. Solid State Chem.*, 144, 220, 1999.
61. Hong, M.S., Lee, S.H., and Kim, S.W., Use of KCl aqueous electrolyte for 2V manganese oxide/activated carbon hybrid capacitor, *Electrochem. Solid State Lett.*, 5, A227, 2002.
62. Brousse, T., Toupin, M., and Bélanger, D., A hybrid activated carbon–manganese dioxide capacitor using mild aqueous electrolyte, *J. Electrochem. Soc.*, 151, A614, 2004.
63. Khomenko, V., Raymundo-Piñero, E., and Béguin F., Optimisation of an asymmetric manganese oxide/activated carbon capacitor working at 2V in aqueous medium, *J. Power Sourc.*, in press, 2005.
64. Cuevas, F., Joubert, J.-M., Latroche, M., and Percheron-Guégan, A., Intermetallic compounds as negative electrodes of Ni/MH batteries, *Appl. Phys. A*, 72, 225, 2001.

65. Carpetis, C. and Peschka, W., A study on hydrogen storage by use of cryoadsorbents, *Int. J. Hyd. Energy*, 5, 539, 1980.
66. Agarwal, R.K., Noh, J.S., Schwarz, J.A., and Davini, P., Effect of surface acidity of activated carbon on hydrogen storage, *Carbon*, 25, 219, 1987.
67. Nützenadel, C., Züttel, A., Chartouni, D., and Schlapbach, L., Electrochemical storage of hydrogen in nanotube materials, *Electrochem. Solid State Lett.*, 2, 30, 1999.
68. Qin, X., Gao, X.P., Liu, H., Yuan, H.T., Yan, D.Y., Gong, W.L., and Song, D.Y., Electrochemical hydrogen storage of multiwalled carbon nanotubes, *Electrochem. Solid State Lett.*, 3, 532, 2000.
69. Rajalakshmi, N., Dhathathreyan, K.S., Govindaraj, A., and Satishkumar, B.C., Electrochemical investigation of single-walled carbon nanotubes for hydrogen storage, *Electrochim. Acta*, 45, 4511, 2000.
70. Kibria, A.K.M., Mo, Y.H., Park, K.S., Nahm, K.S., and Yun, M.Y., Electrochemical hydrogen storage behaviours of CVD, AD, and LA grown carbon nanotubes in KOH medium, *Int. J. Hydrogen Energy*, 26, 823, 2001.
71. Gundiah, G., Govindaraj, A., Rajalakshmi, N., Dhathathreyan, K.S., and Rao, C.N.R., Hydrogen storage in carbon nanotubes and related materials, *J. Mat. Chem.*, 13, 209, 2003.
72. Züttel, A., Sudan, P., Mauron, P., Kioyobayashi, T., Emmenegger, C., and Schlapbach, L., Hydrogen storage in carbon nanostructures, *Int. J. Hydrogen Energy*, 27, 203, 2002.
73. Tibbetts, G.G., Meisner, G.P., and Olk, C. H., Hydrogen storage capacity of carbon nanotubes, filaments, and vapor-grown fibres, *Carbon*, 39, 2291, 2001.
74. Hirscher, M., and Becher, M., Hydrogen storage in carbon nanotubes, *J. Nanosci. Nanotech.*, 3, 3, 2003.
75. Jurewicz, K., Frackowiak, E., and Béguin, F., Enhancement of reversible hydrogen capacity into activated carbon through water electrolysis, *Electrochem. Solid State Lett.*, 4, A27, 2001.
76. Jurewicz, K., Frackowiak, E., and Béguin, F., Electrochemical storage of hydrogen in activated carbons, *Fuel Process. Tech.*, 77–78, 415, 2002.
77. Jurewicz, K., Frackowiak, E., and Béguin, F., Towards the mechanism of electrochemical hydrogen storage in nanostructured carbon materials, *Appl. Phys. A*, 78, 981, 2004.
78. Ströbel, R., Jörissen, L., Schliermann, T., Trapp, V., Schütz, W., Bohmhammel, K., Wolf, G., and Garche, J., Hydrogen adsorption on carbon materials, *J. Power Sourc.*, 84, 221, 1999.
79. De la Casa-Lillo, M.A., Lamari-Darkrim, F., Cazorla-Amoros, D., and Linares-Solano, A., Hydrogen storage in activated carbons and activated carbon fibers, *J. Phys. Chem. B*, 106, 10930, 2002.
80. Texier-Mandoki, N., Dentzer, J., Piquero, T., Saadallah, S., David, P., and Vix-Guterl, C., Hydrogen storage in activated carbon materials: role of the nanoporous texture, *Carbon*, 42, 2744, 2004.
81. Cazorla Amorós, D., Alcañiz Monge, J., De la Casa Lillo, M.A., and Linares-Solano, A., CO<sub>2</sub> as an adsorptive to characterize carbon molecular sieves and activated carbons, *Langmuir*, 14, 4589, 1998.
82. Rzepka, M., Lamp, P., and De la Casa-Lillo, M.A., Physisorption of hydrogen on microporous carbons and carbon nanotubes, *J. Phys. Chem. B*, 102, 10894, 1998.
83. Béguin, F., Vix-Guterl, C., Dentzer, J., Friebe, M., Jurewicz, K., and Frackowiak, E., Mechanism of electrochemical hydrogen storage in nanotextured carbons, *Carbon*, submitted.
84. Nijkamp, M.G., Raaymakers, J.E.M.G., van Dillen, A.J., de Jong, K.P., Hydrogen storage using physisorption: materials demands, *Appl. Phys. A*, 72, 619, 2001.
85. Wang, Q. and Johnson, J.K., Molecular simulation of hydrogen adsorption in single-walled carbon nanotubes and idealized carbon slit pores, *J. Chem. Phys.*, 110, 577, 1999.
86. Béguin, F., Kierzek, K., Friebe, M., Jankowska, A., Machnikowski, J., Jurewicz, K., and Frackowiak, E., Effect of various porous nanotextures on the reversible electrochemical sorption of hydrogen in activated carbons, *Electrochim. Acta*, in press, 2005.

# Other Related Titles of Interest by Taylor & Francis

Adsorption and Transport at the Nanoscale

Nick Quirke

ISBN: 0415327016

Carbon Nanotubes: Science and Applications

M. Meyyappan

ISBN: 0849321115

Handbook of Nanoscience, Engineering, and Technology

William A. Goddard III, Donald W. Brenner, Sergey Edward Lyshevski, and Gerald J. Iafrate

ISBN: 0849312000

Nanoengineering of Structural, Functional and Smart Materials

Mark J. Schulz, Ajit D. Kelkar, and Mannur J. Sundaresan

ISBN: 0849316537

Nanoparticle Assemblies and Superstructures

Nicholas Kotov

ISBN: 0824725247

New Materials, Processes, and Methods Technology

Mel Schwartz

ISBN: 0849320534